

# MAGNETOM Flash

The Magazine of MRI

Issue Number 2/2013

ISMRM Edition

Not for distribution in the USA

SIEMENS

## Clinical

Advanced Techniques  
in MR Neuroimaging  
Page 6

Neuroimaging of Stroke  
Page 36

Improved EPI DWI of  
the Head and Neck  
using *syngo* ZOOMit  
Page 68

Combining Throughput  
and Highest Quality  
MRI in an Optimized  
Clinical Workflow  
Page 82

Indications for 24 Hours /  
7 Days Emergency MRI  
Page 128

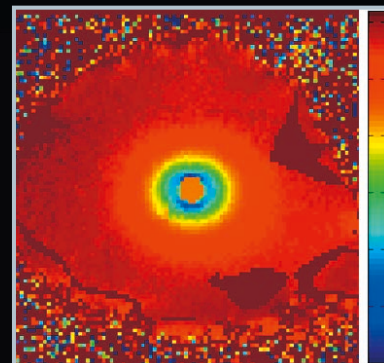
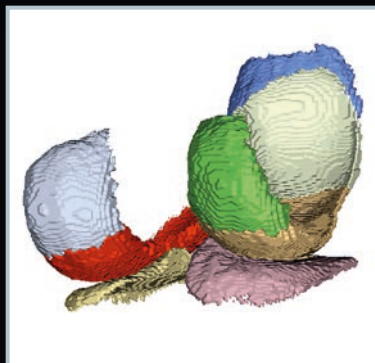
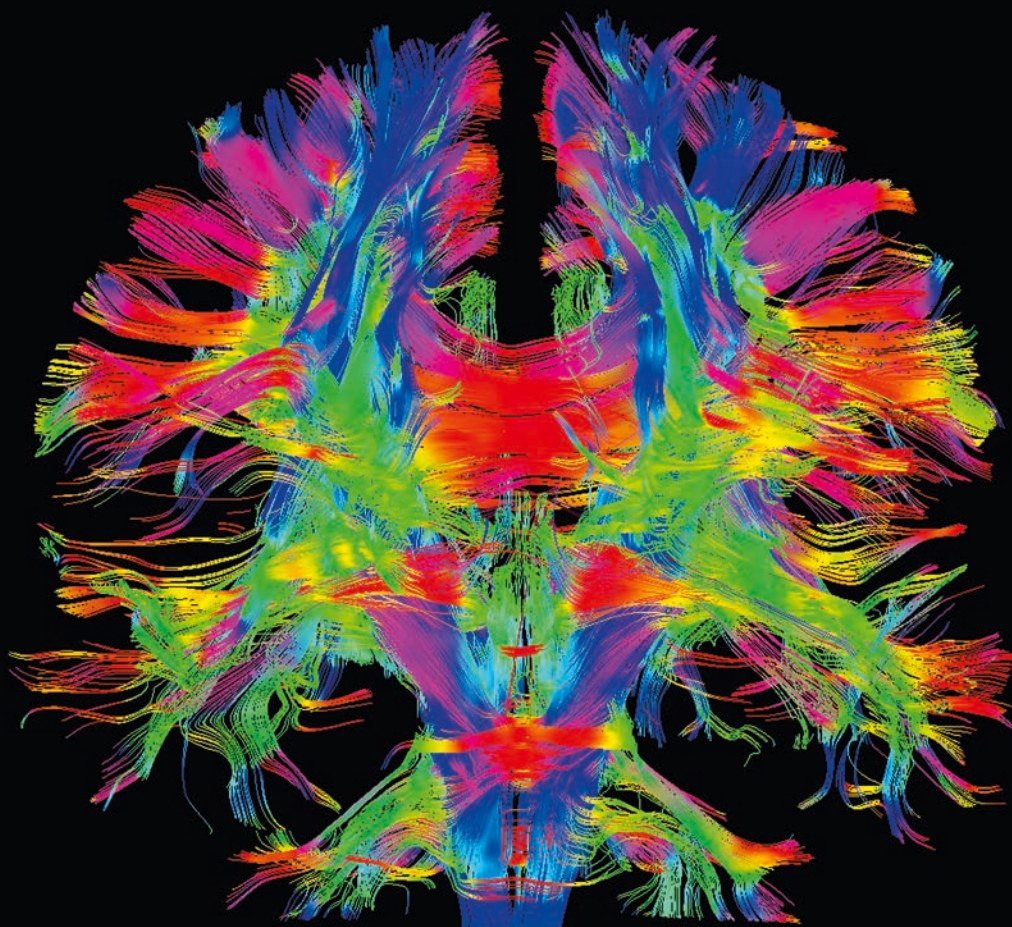
Automated Morphological  
Knee Cartilage Analysis  
of 3D MRI at 3T  
Page 146

## Product News

The New MR Gradient  
System XR 80/200  
Page 160

## Technology

PRFS Thermometry  
Proximal to  
Cryoablation Ice-ball  
Page 164





Milind Dhamankar, M.D.  
Editor-in-Chief

## Dear MAGNETOM users,

I am excited to be taking on this new role as Editor-in-Chief of MAGNETOM Flash. I would best describe myself as a student and a teacher. What inspires me is the desire to learn new things and apply that learning to my work. I will continue the tradition of focusing on making a difference to our readers, by providing **information, education and context**.

With changing healthcare economics, attention to patient outcomes and efficiency is critical. MAGNETOM Flash helps to inform on innovations, products and new applications – for example, Daniel Fischer's XR 80/200 gradient\* article provides insight in hardware changes. Marc-André Weber and Jürgen Biederer have contributed an article on Indications for Emergency MRI. Why do we provide this information? Because we all must grow in our understanding of the clinical applications. It is important to define the right 'context' when applying technology in clinical practice. That will help align patient needs. The patient is the focus and accurate results will help speed up treatment decisions and will help reduce uncertainty and anxiety in patients. This is where I think MAGNETOM Flash plays an important role by informing, educating and providing the context to you, our readers.

While change is permanent, consistency and continuity are critical. In that regard, my predecessor Matthias Lichy and I would like to thank Associate Editor Antje Hellwich for her help over the last years without which our Flash magazine would not have achieved the caliber and reputation that it enjoys today.



सप्रेम नमस्कार

Sincerely,

*Milind*

We value your feedback. Please take a moment to complete a brief reader survey at  
[www.siemens.com/flash-survey](http://www.siemens.com/flash-survey)

\*The product is still under development and not commercially available yet. Its future availability cannot be ensured.

## Editorial Board

We appreciate your comments.

Please contact us at [magnetomworld.med@siemens.com](mailto:magnetomworld.med@siemens.com)



**Antje Hellwich**  
*Associate Editor*



**Wellesley Were**  
*MR Business Development  
Manager Australia and New  
Zealand*



**Ralph Strecker**  
*MR Collaborations Manager,  
Sao Paulo, Brazil*



**Sven Zühlsdorff, Ph.D.**  
*Clinical Collaboration Manager,  
Chicago, IL, USA*



**Gary R. McNeal, MS (BME)**  
*Advanced Application Specialist,  
Cardiovascular MR Imaging  
Hoffman Estates, IL, USA*



**Peter Kreisler, Ph.D.**  
*Collaborations & Applications,  
Erlangen, Germany*

## Review Board

Lisa **Chua**, Ph.D., Global Marketing Manager Neurology

Wilhelm **Horger**, Application Development Oncology

Michelle **Kessler**, US Installed Base Manager

Berthold **Kiefer**, Ph.D., Oncological and Interventional Applications

Sunil **Kumar S.L.**, Ph.D., Senior Manager Applications

Reto **Merges**, Head of Outbound Marketing MR Applications

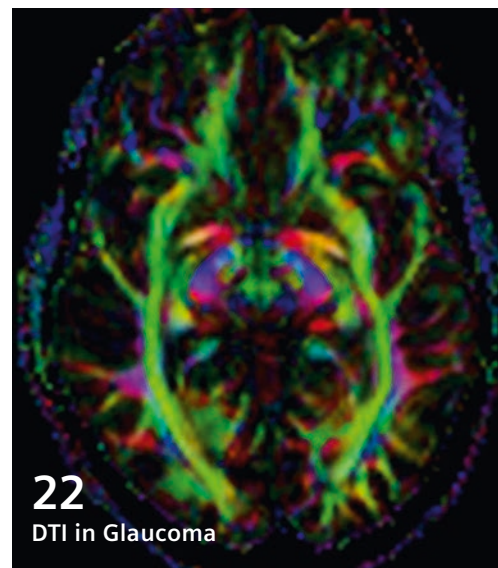
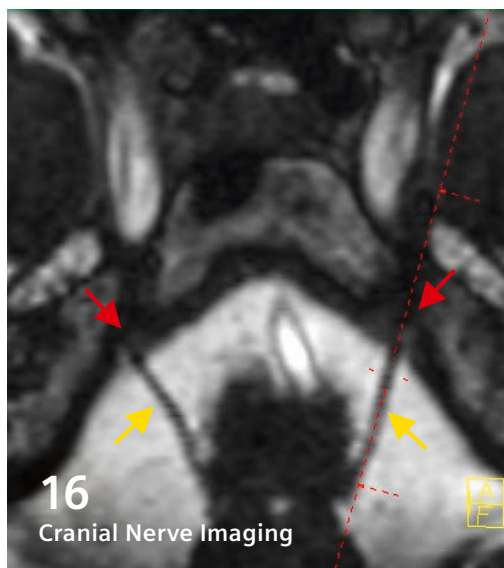
Heiko **Meyer**, Ph.D., Neuro and Orthopedic Applications

Nashiely Sofia **Pineda Alonso**, Ph.D., Global Marketing Manager Men's and Women's Health

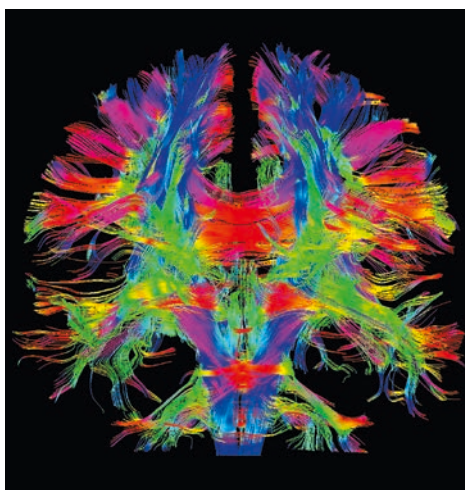
Silke **Quick**, Global Marketing Manager Body Imaging

Heike **Weh**, Clinical Data Manager

# Content



## Cover

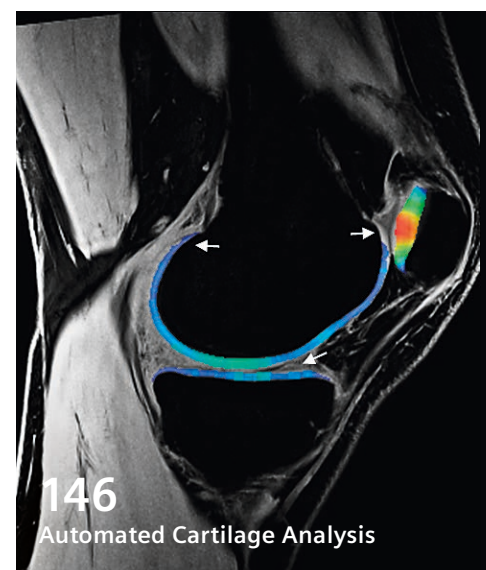
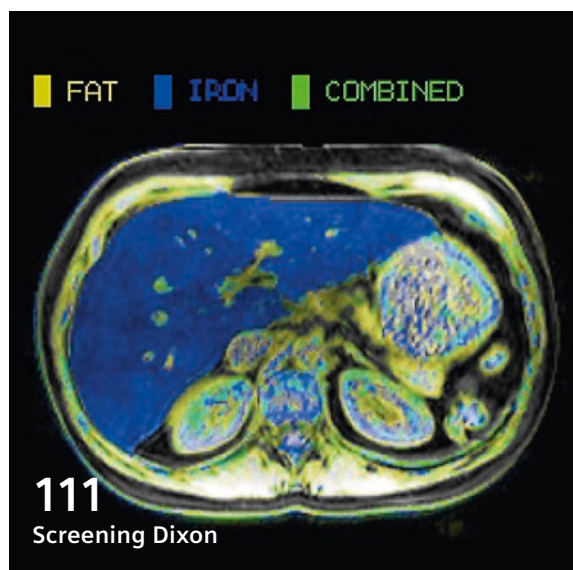
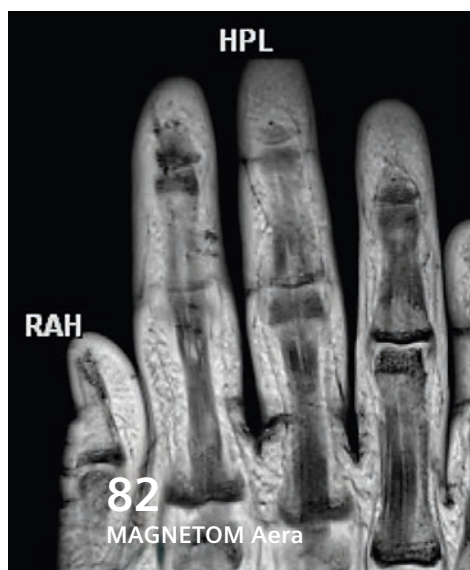


3T MAGNETOM Prisma  
Diffusion Tensor Imaging,  
64 directions,  
syngo DTI with high  
resolution.

The information presented in MAGNETOM Flash is for illustration only and is not intended to be relied upon by the reader for instruction as to the practice of medicine. Any health care practitioner reading this information is reminded that they must use their own learning, training and expertise in dealing with their individual patients. This material does not substitute for that duty and is not intended by Siemens Medical Solutions to be used for any purpose in that regard. The treating physician bears the sole responsibility for the diagnosis and treatment of patients, including drugs and doses prescribed in connection with such use. The Operating Instructions must always be strictly followed when operating the MR System. The source for the technical data is the corresponding data sheets.

## Clinical Neurology

- 6** Introduction to Advanced Techniques in MR Neuroimaging  
*Bernhard Schuknecht, Krisztina Baràth*
- 16** **How-I-do-it:** Imaging of Diseases of the Cranial Nerves: Tips and Tricks  
*Bernd F. Tomandl, et al.*
- 22** 3T DTI in Patients with Glaucoma. New Approaches for Data Analysis & Clinical Implications  
*Tobias Engelhorn, et al.*
- 32** Case Study: Murray Valley Encephalitis (MVE)  
*Jan Neal*
- 36** Neuroimaging of Stroke. The Complementary Roles of CT and MRI  
*Karl-Olof Löfvblad, Vitor Mendes Pereira*
- 44** Implication of Brain Susceptibility-Weighted Imaging  
*Fong Y Tsai, et al.*
- 53** Pseudoprogression and Pseudo-response: Imaging Challenges in the Assessment of Post Treatment Glioma  
*L. Celso Hygino Cruz Jr., Nina Ventura*



## Technology

- 58** Imaging and Spectroscopy at 9.4 Tesla: First Results on Patients and Volunteers  
*Klaus Scheffler, et al.*

## Clinical Oncology

- 68** Improved Echo Planar Diffusion-Weighted imaging of the Head and Neck using syngo ZOOMit  
*Philipp Riffel, Henrik J. Michaely*
- 72** Sodium ( $^{23}\text{Na}$ )-Imaging as Therapy Monitoring in Oncology – Future Prospects  
*Stefan Haneder, et al.*

## Clinical Pediatric Imaging

- 78** A novel 2D Pulsed Arterial Spin Labeling Protocol for Pediatric Cases with Brain Tumor  
*Yang Wang, et al.*

## Clinical Head-to-Toe Imaging

- 82** MAGNETOM Aera – Combining Throughput and Highest Quality MRI in an Optimized Clinical Workflow  
*Johan Dehem*

- 94** Initial Experience with Whole-Body Diffusion-Weighted Imaging in Oncological and Non-Oncological Patients  
*Marcos Vieira Godinho, et al.*

- 104** Parallel Transmission and its Clinical Implementation: Enabling new Clinical Imaging Paradigms  
*Fernando Boada, et al.*

## Clinical Abdominal Imaging

- 111** Liver Imaging Today  
*Tobias Heye, Mustafa R. Bashir*
- 118** **How-I-do-it:** Faster Abdominal MRI Examinations by Limiting Table Movement  
*Mustafa Rifaat Bashir, et al.*

## How-I-do-it

- 121** Bandwidth in MRI?  
*Joachim Graessner*
- 128** Indications for 24 Hours / 7 Days Emergency MRI  
*Marc-André Weber, Jürgen Biederer*

## Clinical Orthopedic Imaging

- 132** **How-I-do-it:** Musculoskeletal Imaging at 3T with Simultaneous Use of Multipurpose Loop Coils  
*Elena Ferrer, Rafael Coronado Santos*
- 146** Automated Morphological Knee Cartilage Analysis of 3D MRI at 3T  
*Jurgen Fripp, et al.*

## Product News

- 157** Image Gallery  
MAGNETOM Prisma
- 160** The New, High-Performance MR Gradient System XR 80/200.  
*Daniel Fischer; Eva Eberlein*

## Technology

- 164** PRFS Thermometry Proximal to Cryoablation Ice-ball  
*Antje Kickhefel, et al.*

# Introduction to Advanced Techniques in MR Neuroimaging

Bernhard Schuknecht, M.D.; Krisztina Baràth, M.D.

*Diagnostic, Vascular and Interventional Neuroradiology, Medizinisch Radiologisches Institut MRI Zürich, Bethanien Hospital, Zürich, Switzerland*

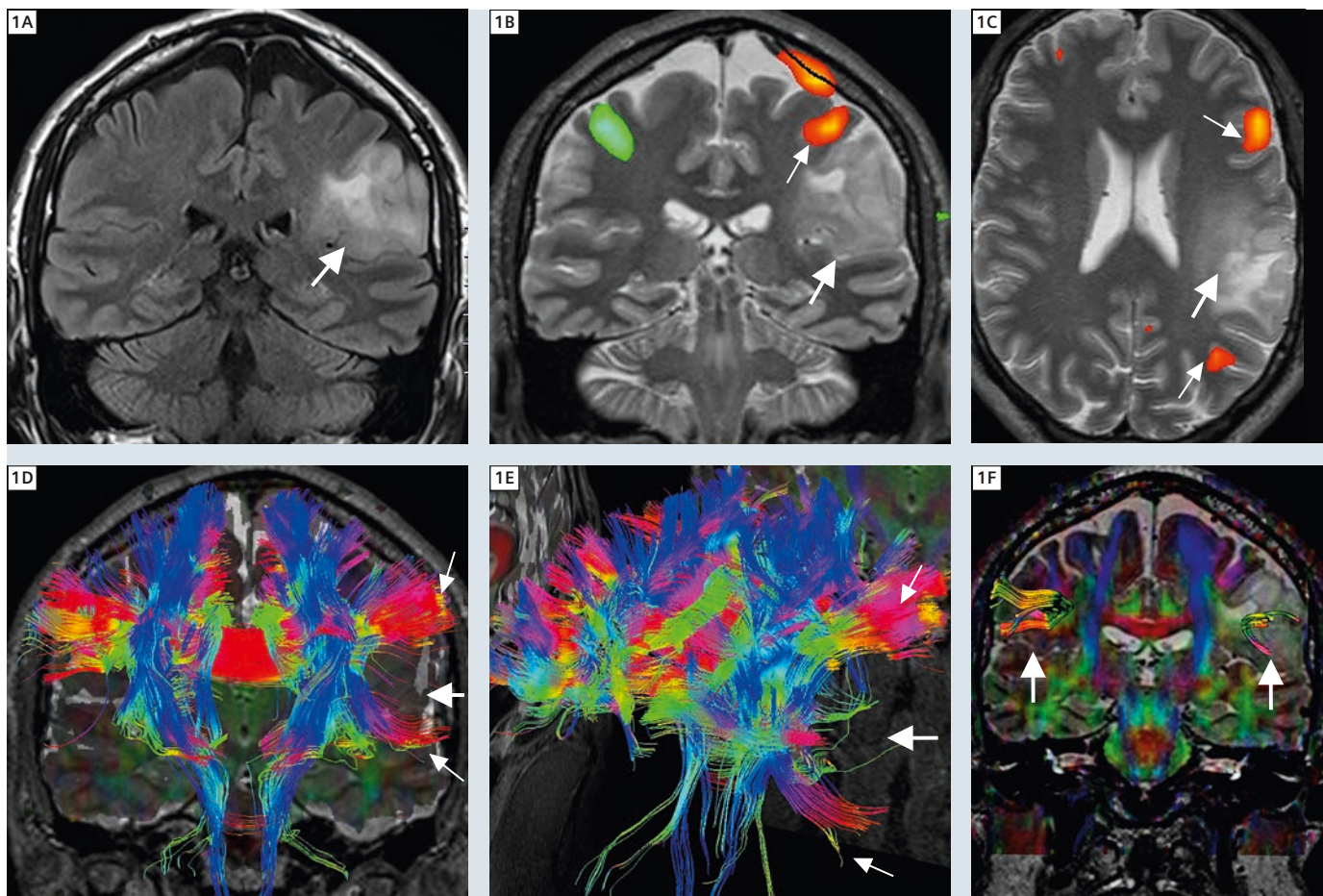
## Functional MRI (fMRI )

Functional magnetic resonance imaging (fMRI) is based on the blood oxygenation level dependent (BOLD) effect. BOLD contrast rises with neural activation and

depends on the variables blood flow and oxygenation. Augmentation of regional cerebral blood flow (CBF) is accompanied by a local increase in oxygen extraction

due to a rise in the cerebral metabolic rate of oxygen consumption. The ferrous iron in deoxyhemoglobin adopts paramagnetic properties contrary to the

## fMRI and DTI of a brain tumor: function and structure



**1** (1A) Brain tumor (oligodendroglioma) (arrow) in the subcentral gyrus/inferior parietal lobule on the left shown on a FLAIR sequence. (1B) Activation of the primary motor cortex (thin arrow) close to the tumor (arrow) during finger tapping. Red = movement on the right, Green = movement on the left. (1C) Activation of the motor speech area and the sensory speech area (thin arrows) far away from the tumor (arrow). The DTI sequence (1D–E) shows the deviated U-fibers (thin arrow) due to the tumor (arrow). The Broca- and Wernicke areas are connected through the arcuate fibers, which makes a combination of fMRI and DTI for the preoperative planning necessary. (1F) The thinning of the left arcuate fibers indicates an infiltration of the speech-network.

diamagnetic effect in oxyhemoglobin. This results in a susceptibility induced field shift and leads to an increase in  $T2^*$  value and a signal increase in  $T2^*$  gradient echo or echo planar imaging (EPI) studies. The high sensitivity of EPI sequences enables real time visualization of activation of different parts of the brain in comparison to a resting state. In a functional MR paradigm the patient is asked to alternatively perform tasks or is stimulated to trigger several processes or emotions. Threshold functional MRI activation maps are spatially addressed (Fig. 1A) and therefore typically overlaid in colour on a high resolution anatomical T1 MPRAGE or SPACE FLAIR MR image (Figs. 1B, C).

fMRI was first employed for mapping of neuronal activation during visual perception tasks and motor activation in the early nineties. Since then fMRI has evolved into an invaluable research tool, e.g. in cognitive neuroscience or neuropharmacology as well as a routinely applied clinical MR technique.

Clinical applications comprise mainly neurosurgical planning in order to determine resection margins in relation to functional 'eloquent' areas. With fMRI brain functional plasticity may also be visualized in recovery after stroke or surgery. Furthermore fMRI can be used to evaluate specific brain functions in a range of neuro-degenerative diseases. Despite existing limitations of fMRI, a significant increase in spatial and temporal resolution has been achieved in order to improve localization of specific brain function and individualize treatment.

### Diffusion Tensor Tractography (Diffusion Tensor Imaging, DTI)

DTI is a non-invasive MR technique to study brain tissue composition and architecture *in vivo*. DTI is based on the concept that water diffusion is anisotropic in organized tissues. Cerebral white matter is composed of axons, myelin sheaths and neuroglia which are aligned to form fiber tracts. DTI provides information on water diffusion properties regarding the extent of diffusion anisotropy and its orientation. A pair of magnetic dephas-

ing and rephasing field gradients is successively applied in distinct directions in 3D space. The resulting images exhibit signal attenuation in the direction of the applied gradient which is proportional to water diffusivity. The largest principal axis of the diffusion tensor aligns with the predominant fiber orientation in an MRI voxel. A diffusion tensor or the mean diffusivity may be estimated from as few as 6 diffusion-weighted images acquired along non-collinear directions and 1 minimally =  $T2$ -weighted ( $b_0$ ) image. From the diffusion tensor, the DTI indices derived include the mean diffusion coefficient (ADC), calculated eigenvalues and eigenvectors and an index of diffusion anisotropy, e.g. fractional anisotropy (FA). To achieve a high signal-to-noise ratio DTI employs more than the minimum of 6 diffusion-weighting angulations and/or acquires repeated measurements of diffusion directions. Despite substantial improvement in technique, spatial resolution of DTI in the order of 1–4 mm per dimension, reflects limitations imposed by using a macroscopic technique to visualize microscopic restrictions. DTI is performed in combination with fMRI for preoperative localization of fiber tracts in proximity to a lesion (Figs. 1D–F), and for preoperative differentiation of white matter tract infiltration from displacement in patients with low grade glioma in particular.

Following hemorrhagic or ischemic stroke and trauma DTI has become an important tool to assess white matter tract involvement beyond findings by morphologic imaging. This holds also true for white matter alterations in patients suffering from neurodegenerative and movement disorders, and to visualize secondary neurodegeneration in inflammatory conditions such as multiple sclerosis.

### Diffusion-Weighted Imaging (DWI)

Diffusion-weighted MR imaging renders microscopic molecular motion of water visible within tissues. The anisotropic nature of diffusion in the brain can be visualized by comparing images obtained

with DWI gradients applied in three orthogonal directions. DWI consists of an echo planar spin-echo T2w pulse sequence. Alternative DWI sequences are based on a single-shot gradient or single-shot fast spin-echo technique, 'line-scan' and spiral DWI technique. The signal intensity obtained by DWI corresponds to the signal on T2w images decreased by a signal amount that is related to the rate of diffusion in the direction of the applied gradients. Pathology therefore is reflected by high signal on diffusion-weighted images and by decreased signal on apparent diffusion coefficient (ADC) maps. While DWI is highly sensitive in reflecting the physical properties of diffusion, the observation of restricted water diffusion is relatively non-specific for pathology. Restricted diffusion is the earliest detectable MR sign of ischemia. However diffusion changes are also seen with infection, inflammation and neoplasms. In an abscess restricted diffusion and low ADC values are attributed to increased fluid viscosity and higher cellularity present in pus. Metastases and tumors may have a similar appearance to an abscess on morphologic images but present with normal diffusion and high ADC values in areas of necrosis.

DWI is gaining increasing importance in oncology both for the initial diagnosis and as a sensitive tool to assess tumor response to treatment. Low ADC values in a lesion are an indicator for a malignant compression fracture in the spine as well as for malignant lymphadenopathy in the neck. In cerebral gliomas ADC values inversely correlate with the grading of gliomas, and low values indicate the higher grade component in a 'mixed' glioma. Lower ADC values in the edema of gliomas compared to metastases are an early sign of brain infiltration beyond macroscopic visible margins. Restricted diffusion in the early postoperative phase is more likely to correspond to ischemia and reparative changes, while after 6–8 weeks may indicate true progression or pseudoprogression. Increasing ADC values in a solid lesion like a glioma, lymphoma or metastasis are a more sensitive

parameter to chemo-radiotherapy treatment response than the contrast enhanced T1 images.

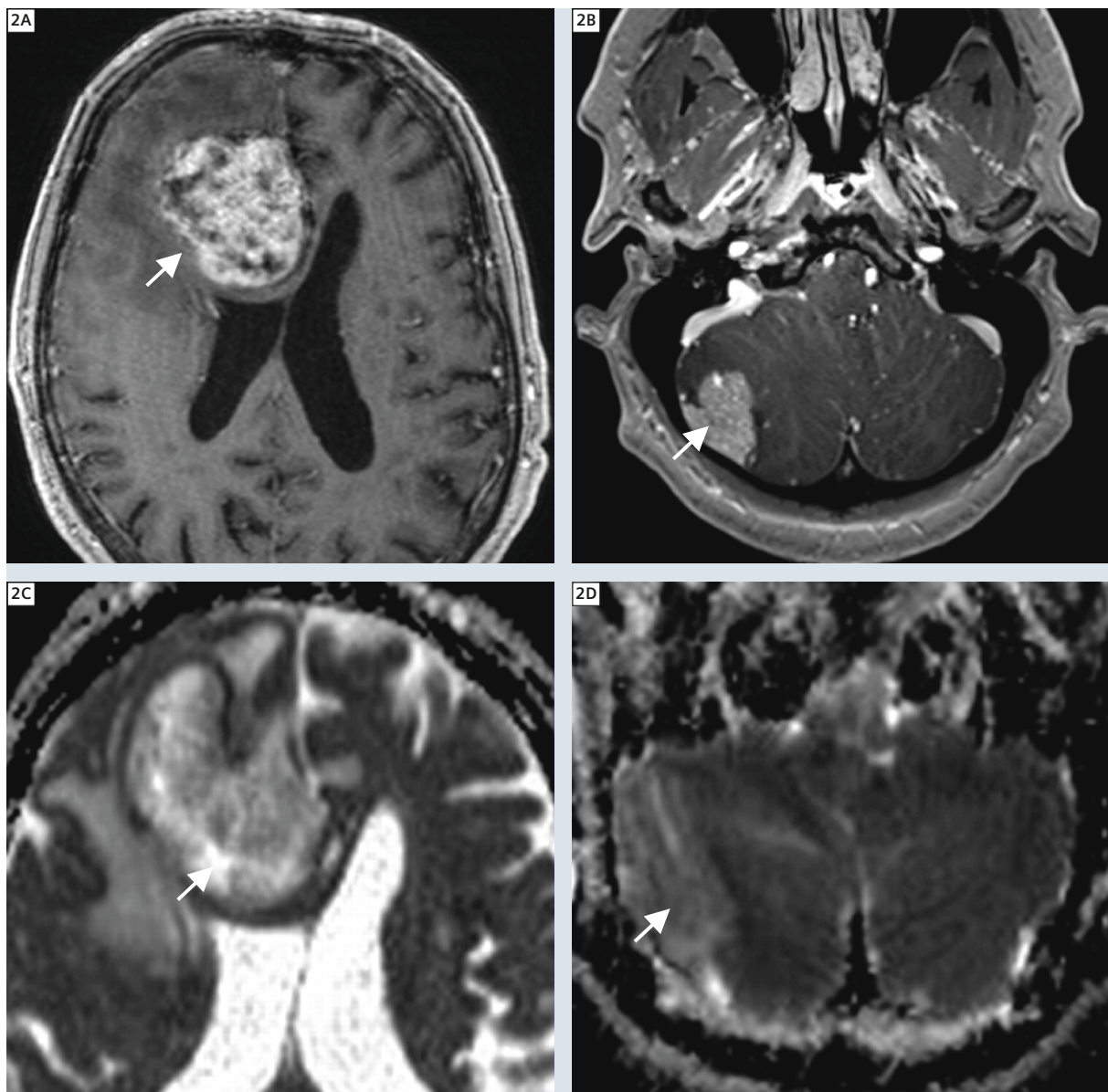
Metastases and glial tumors can be differentiated by low ADC due to their high grade cellularity (metastases) and by areas of high ADC due to necrosis (glial tumors) (Figs. 2A–D).

### Perfusion-MRI (PWI = Perfusion-weighted imaging)

Perfusion MRI relies on two different techniques: dynamic contrast enhanced (DCE) perfusion MRI consists of a T1w 3D FLASH sequence which is used to depict cerebral microcirculation and is a direct measure of vascular permeability. On the other hand dynamic susceptibility

contrast (DSC) MR perfusion is based on a gradient-echo echo planar sequence. DSC provides a measure of vascularity, microvascular density or relative cerebral blood volume (rCBV) and therefore is complementary to DCE perfusion. Both sequences require a bolus of contrast media injected into a peripheral vein.

### Diffusion in glioma and metastasis: cellularity and tissue ultrastructure



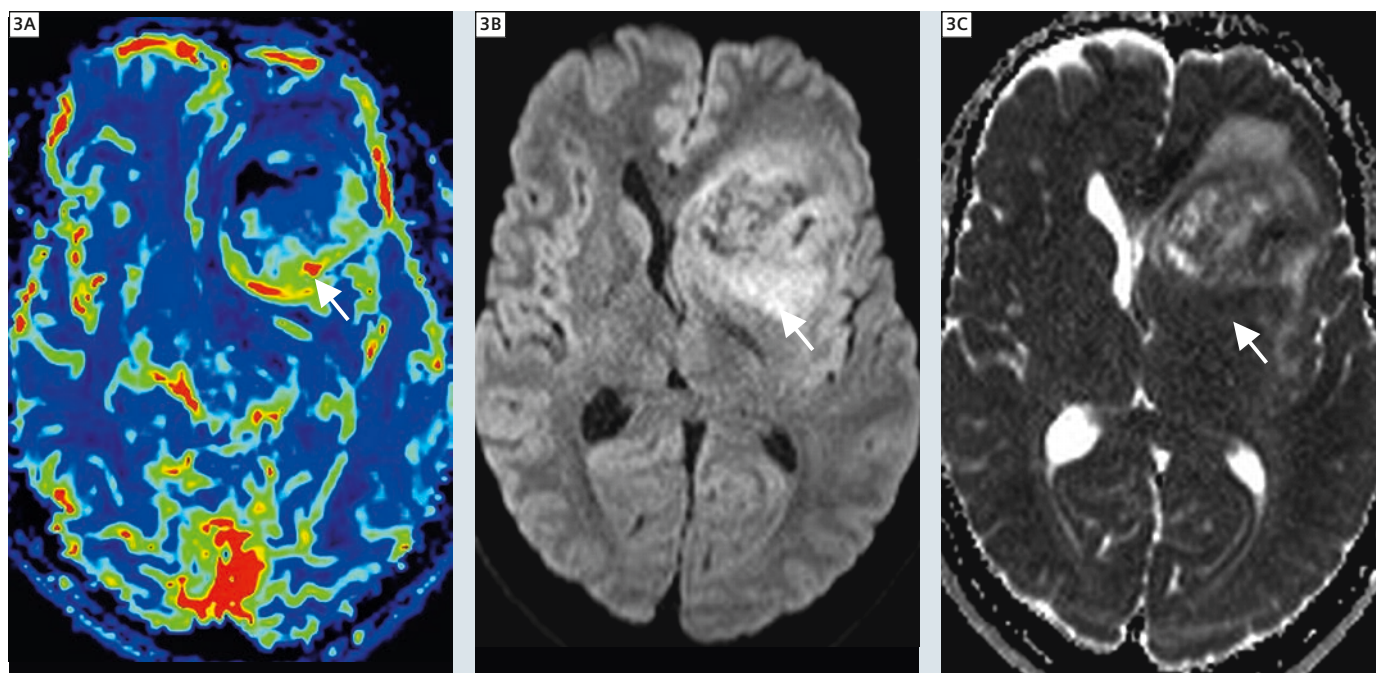
**2** Contrast enhanced MRI does not reliably distinguish a glioblastoma multiforme (**2A**) from a metastasis (**2B**). Focal high ADC values (bright) indicate necrotic components in a glioma (arrow **2C**). Low ADC values represent a solid metastasis (**2B**) as in this case or a lymphoma with dense cellularity (**2D**). ADC values are lower within the edema of a glioma due to microscopic infiltration which is usually not present within the edema of a metastasis.

Perfusion MR in combination with diffusion-weighted imaging has been routinely applied in the setting of acute stroke. The initial perfusion – diffusion mismatch correlates with the ischemic penumbra, the tissue at risk and the extent of the definite infarct size. In brain neoplasms vascular proliferation and neoangiogenesis are hallmarks of dif-

ferentiation to higher grades of malignancy. rCBV values as obtained by DSC show a significant correlation with tumor grade (Figs. 3 A–C), microvascular density and in case of increase predict malignant transformation. Frequently, changes of these parameters during cytostatic, anti-angiogenic and radiation therapy (Figs. 4A–C) precede tumor volume reduction. DCE is

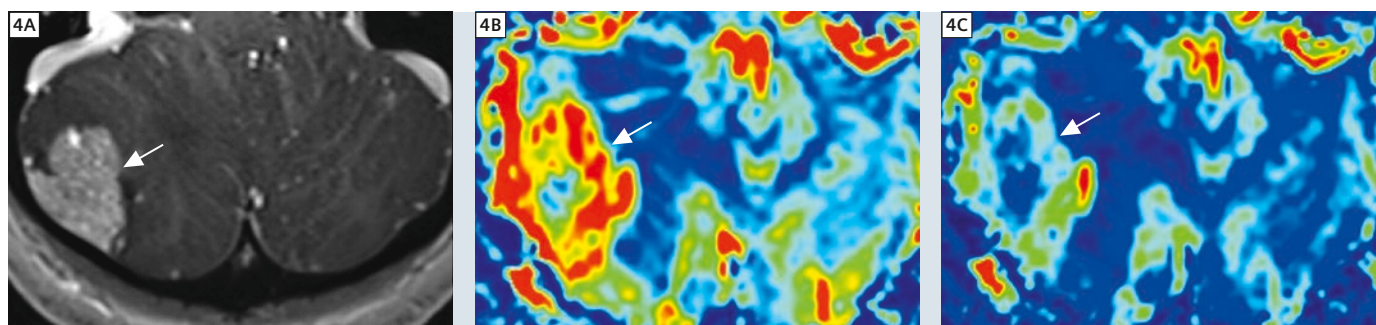
applied to assess the degree of tumor angiogenesis and vessel permeability. Dynamic contrast enhanced perfusion (DCE) in combination with dynamic susceptibility contrast (DSC) perfusion (Fig. 5B) and MR spectroscopy (Fig. 6C) is applied to distinguish treatment related effects (pseudoprogression or pseudoresponse) from true progression and true response respectively.

### Perfusion and diffusion in brain tumor imaging: vascularisation, neo-angiogenesis, capillary permeability – cellularity vs. extracellular space



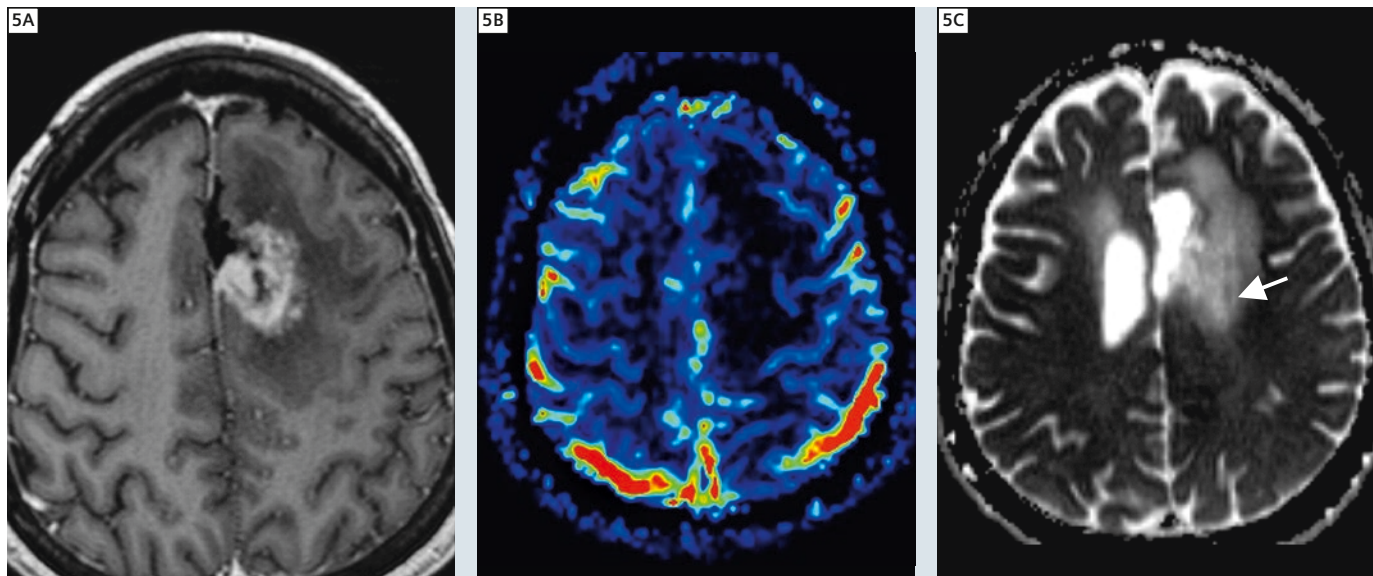
**3** Perfusion MRI of an anaplastic glioma with high rCBV within the component of higher malignancy in the posterior part (arrow 3A) with restricted diffusion (3B) and low ADC values (3C) as additional signs of a highly cellular anaplastic component.

### Treatment monitoring: decreased vascularity



**4** (4A) Cerebellar metastasis of renal cell carcinoma with subtle peripheral vessels indicated on the contrast enhanced T1w image. DSC perfusion MRI depicts markedly increased vascularity within the entire metastasis with high rCBV values before (4B) and with decreased rCBV values under radiotherapy (4C).

## Treatment related effects: low perfusion – low cellularity



**5** T1w contrast enhanced image one year following resection and chemo-radiotherapy of a glioblastoma. Recurrence and treatment related necrosis cannot be reliably differentiated based on morphology (**5A**). Perfusion MRI depicts low rCBV values (**5B**) contrary to high rCBV values indicating recurrence in a high grade glioma (compare to Fig. 3A). High ADC values (**5C**) denote low cellularity indicative of a necrosis confirmed by subsequent histology.

### ASL Arterial Spin labelling

MR imaging with ASL is an alternative method to measure perfusion. Contrary to dynamic contrast enhanced (DCE) and dynamic susceptibility contrast (DSC) perfusion MRI, ASL uses electromagnetically labelled arterial blood water as a freely diffusible intrinsic tracer. In clinical applications, the ASL technique proved reproducible and reliable to assess cerebral blood flow (CBF) despite a relatively low signal intensity-to-noise ratio. ASL has been evaluated in various pathological states including cerebrovascular and neurodegenerative disease and for the assessment of glioma grading and tumor angiogenesis. Quantitative assessment of blood flow in gliomas by ASL yielded results and reproducibility comparable to DSC perfusion MR imaging.

### MR Spectroscopy (MRS)

MR spectroscopy provides a measure of brain metabolic composition or chemistry. Each metabolite appears at a specific ppm (Fig. 6 A–C), and each one reflects specific cellular and biochemical processes. N-Acetyl-Aspartat (NAA) is

a neuronal marker and decreases with any disease that adversely affects neuronal integrity. Creatine provides a measure of energy stores. Choline is a measure of increased cellular turnover and is elevated in tumors and inflammatory processes. Lactate is a marker of oxygen deficiency, lipids of tissue necrosis and myoinositol of granulation tissue (gliosis).

#### Indication of MRS:

- differential diagnosis of low-grade and high-grade tumors
- monitoring under radio-chemotherapy
- differentiation of recurrent tumor from secondary necrosis due to therapy

### Susceptibility-Weighted Imaging (SWI)

SWI is a modified 3D gradient-echo technique which exploits the susceptibility differences between tissues and uses the phase image to detect these differences. The magnitude and phase data are combined to produce an enhanced contrast magnitude image which is exquisitely sensitive to products of blood-deteriora-

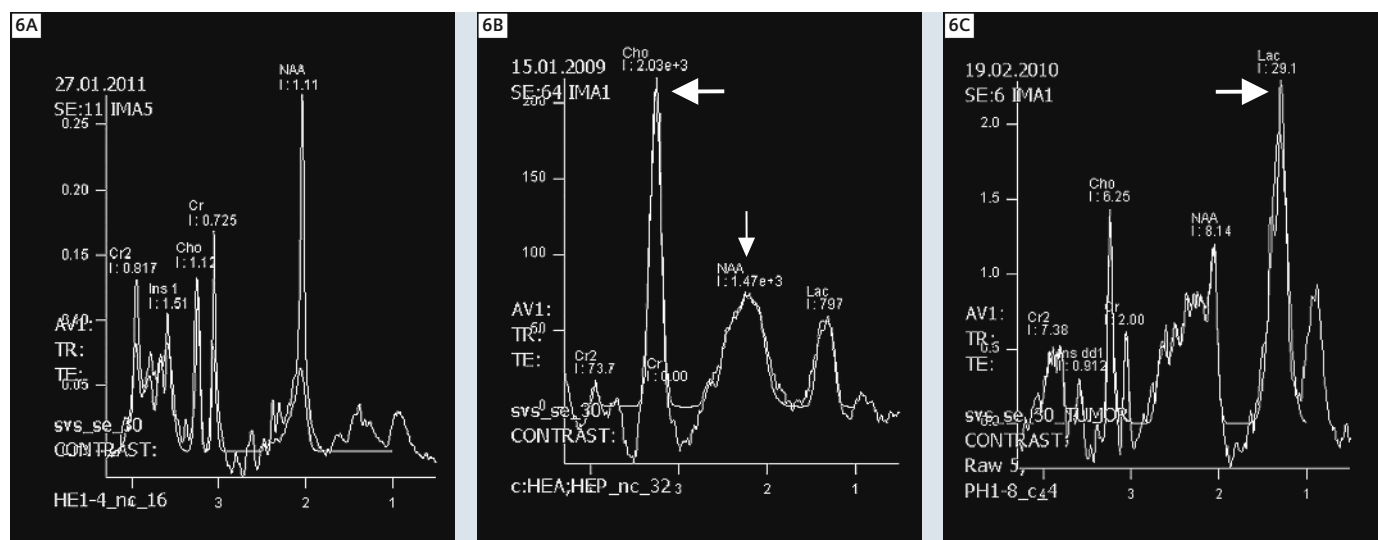
tion (DeoxyHB, MetHB and Hemosiderin) (Fig. 7 A–D).

Iron depositions can be the result of an untreated high blood pressure and accompanied by a gliosis could be a sign of a brain damage. Residual blood after a stroke, amyloid angiopathy or brain injury can be easily detected with gradient-echo sequences, such as SWI or T2\*.

#### Indications of SWI:

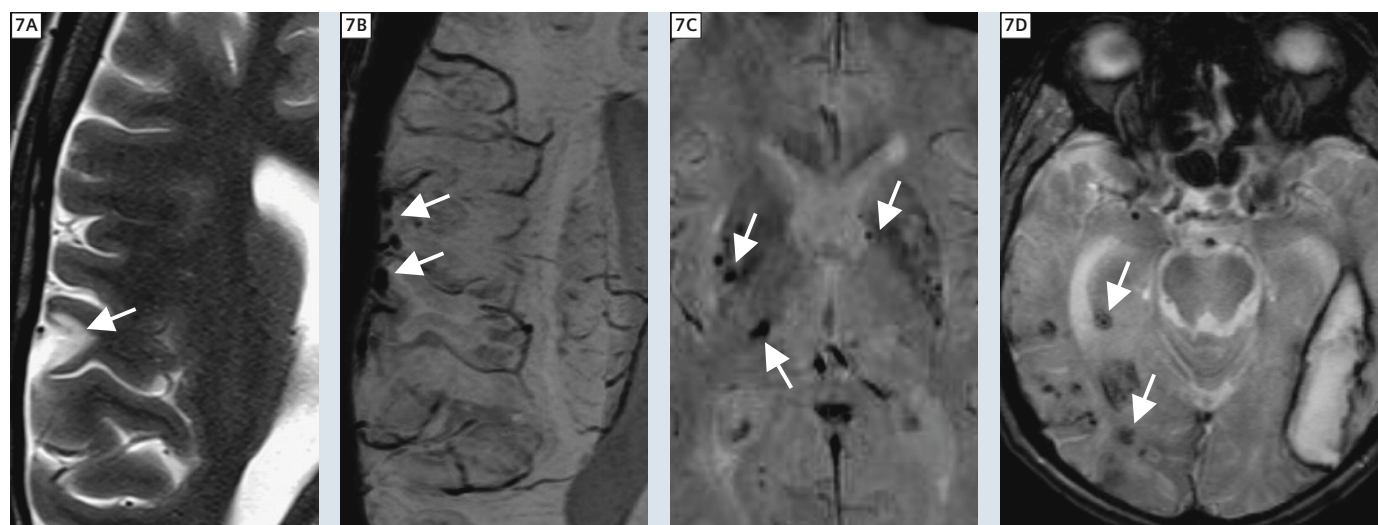
- micro-bleedings in hypertension and vascular dementia
- superficial bleedings in amyloid angiopathy
- hemorrhagic contusion and diffuse axonal injury after brain trauma
- iron deposition in neurodegenerative diseases

## MR Spectroscopy: tumor progression vs. pseudoprogression



**6** (6A) Normal spectrum. (6B) Spectrum of an Oligodendroglioma with high Cholin as a marker of a high proliferation-rate (thick arrow) and with low NAA as a marker of lost neuronal integrity (thin arrow). (6C) Spectrum of a therapy-induced necrosis with low Cholin and NAA and with high Lactate as a sign of oxygen deficiency (thick arrow).

## Iron deposition after trauma, in hypertension and in amyloid angiopathy



**7** (7A) Circumscribed cortical gliosis (arrow) after brain injury without visible micro-bleeding on the T2-weighted image. (7B) Same patient with the same localization with well visible micro-bleedings (arrows) on SWI. (7C) Hypertensive small micro-bleedings in the basal ganglia and in the thalamus. (7D) Amyloid angiopathy with a large intraparenchymal bleeding on the left and with multiple superficial micro-bleedings on the right (arrows).

## Advanced imaging in cerebrovascular diseases and vascular lesions

Contrast enhanced MR Angiography (MRA) is a well established complementary examination to Doppler sonography and in most cases replacement for digi-

tal subtraction angiography by producing high-quality static images.

### Time resolved MR Angiography

The latest MRA technique is time resolved or 4D MRA with a time resolution of <0.7 s. This method is capable

of capturing the dynamic filling of vessels, thus demonstrating the arterial, capillary and the venous phase of the cerebral circulation, similar to digital subtraction angiography (DSA). Hemodynamic changes caused by arterial stenoses and occlusions can be well

detected and dural arteriovenous fistulas (Figs. 8A, B) or arteriovenous malformations can be easily diagnosed. 4D MRA can contribute to the preoperative evaluation and characterization of a tumor by its degree of vascularization (Figs. 9A–F).

Indication of 4D MR Angiography

- hemodynamic changes due to an arterial stenosis or occlusion
- dural arteriovenous fistulas
- vascular malformations of the brain, face or neck

### Advanced MR imaging of inflammatory demyelinating diseases of the central nervous system

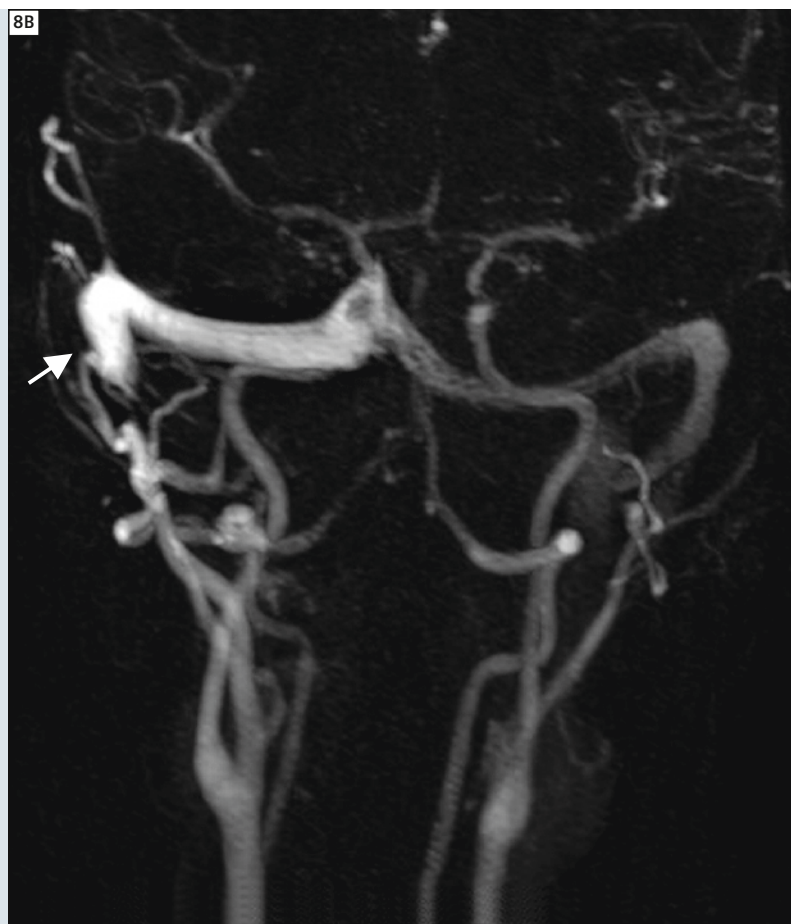
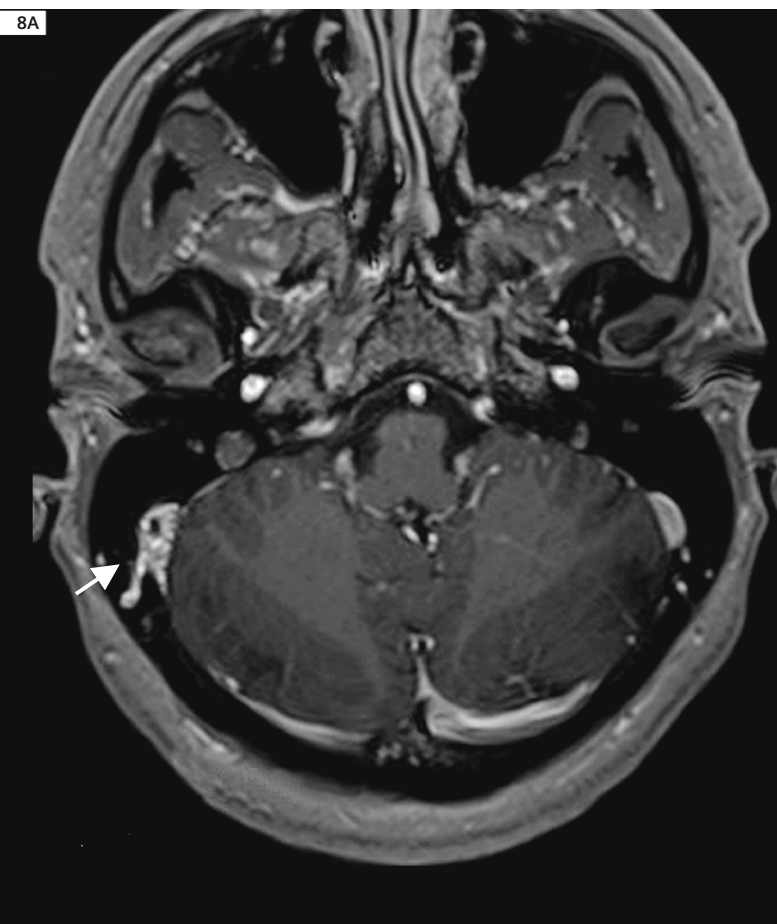
Advanced MR techniques have revolutionized the recognition and characterization of white matter disease. MR imaging is required to depict the presence and location of inflammatory lesions within the optic nerve, the brain and spinal cord. The morphology and distribution of lesions along the ventricular lining and perimedullary veins, in juxtacortical and infratentorial location may permit a tentative diagnosis. The acuity of lesions is assessed based on

the presence of contrast enhancement or by alterations in the composition of neurometabolites in MR spectroscopy when large and unusual lesions or diffuse white matter changes are present. Follow-up examinations by high resolution MR sequences are of major importance to depict 'dissemination in time'.

### 3D Fluid-Attenuated Inversion Recovery Sequence (FLAIR SPACE)

provides a higher spatial resolution with 0.8 to 1 mm isotropic slices and inherent contrast resolution in comparison to T2-weighted (Fig. 10A) and proton den-

## 4D MRA of a dural arteriovenous fistula – high temporal resolution



**8** (8A) Contrast enhanced MRI shows a filling defect of the right sigmoid sinus (arrow). (8B) The 4D MRA depicts the arterial filling of the sinus as sign of a dural arteriovenous fistula (arrow) with origin from the branches of the external carotid artery.

sity-weighted images (Fig. 10B) and 2D standard FLAIR sequences. Higher resolution is beneficial due to better recognition of small demyelinating lesions on the initial examination: This holds particularly true in locations such as the brainstem, at the temporal horns, corpus callosum and in juxta- and cortical location. On follow-up examinations, isotropic 3D multiplanar reconstructions facilitate comparison and increase sensitivity to recognize new lesions. High inherent contrast allows to better differentiate cortical and juxta-cortical lesions (Fig. 10C) similar to the 3D DIR sequence. Furthermore 3D FLAIR

permits to differentiate acute and old lesions and to distinguish demyelination from perilesional edema and concomitant neurodegeneration of white matter tracts.

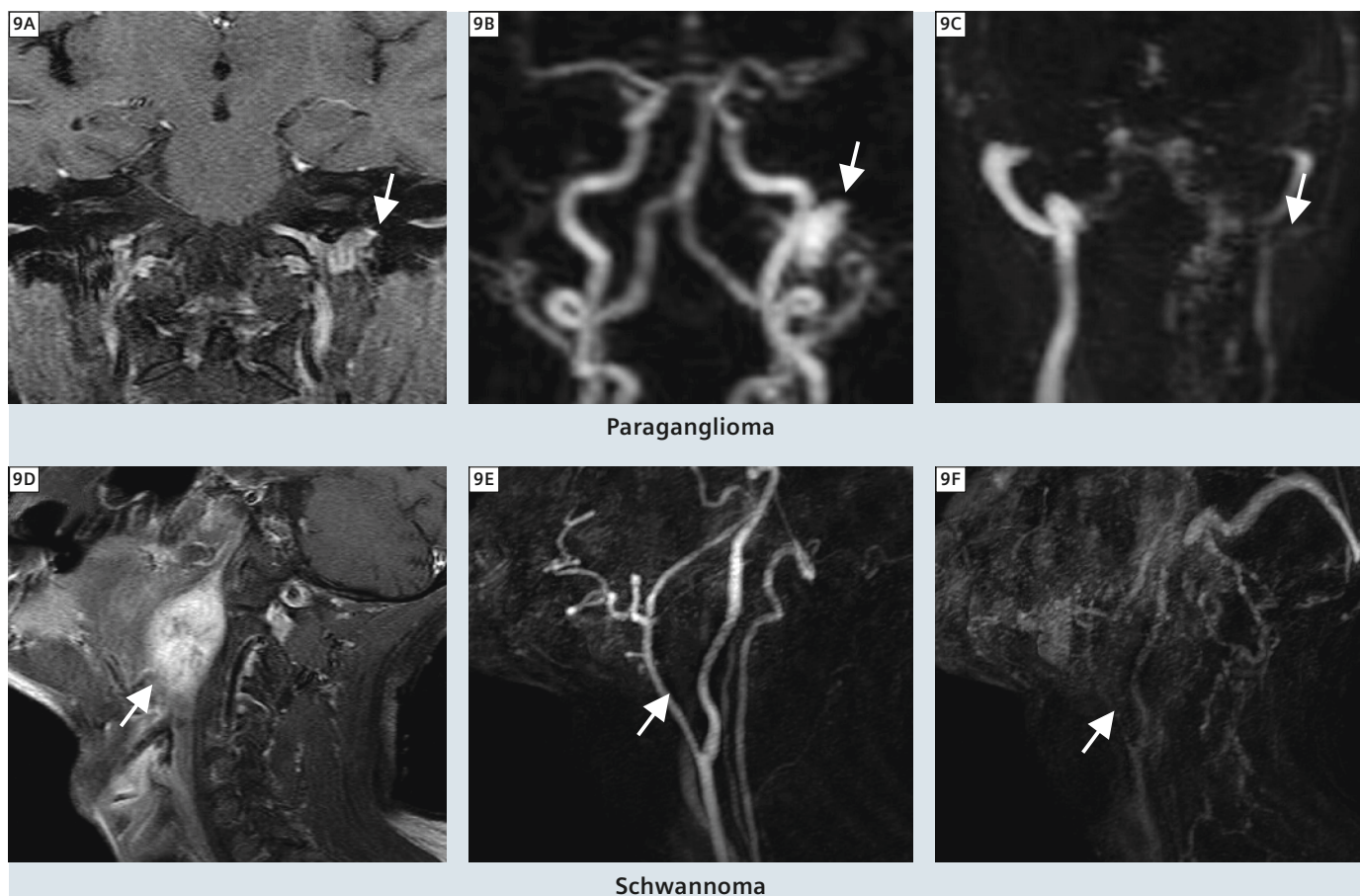
### 3D T1 MPRAGE sequence

provides isotropic resolution (0.8 to 1 mm) and thus sensitivity in recognition of small contrast enhancing lesions. High accuracy in detecting focal axonal destruction requires reassessment of the current concept of the frequency and distribution of 'dark holes' which are a common finding with this new sequence.

### 3D Double Inversion-Recovery (DIR) sequence

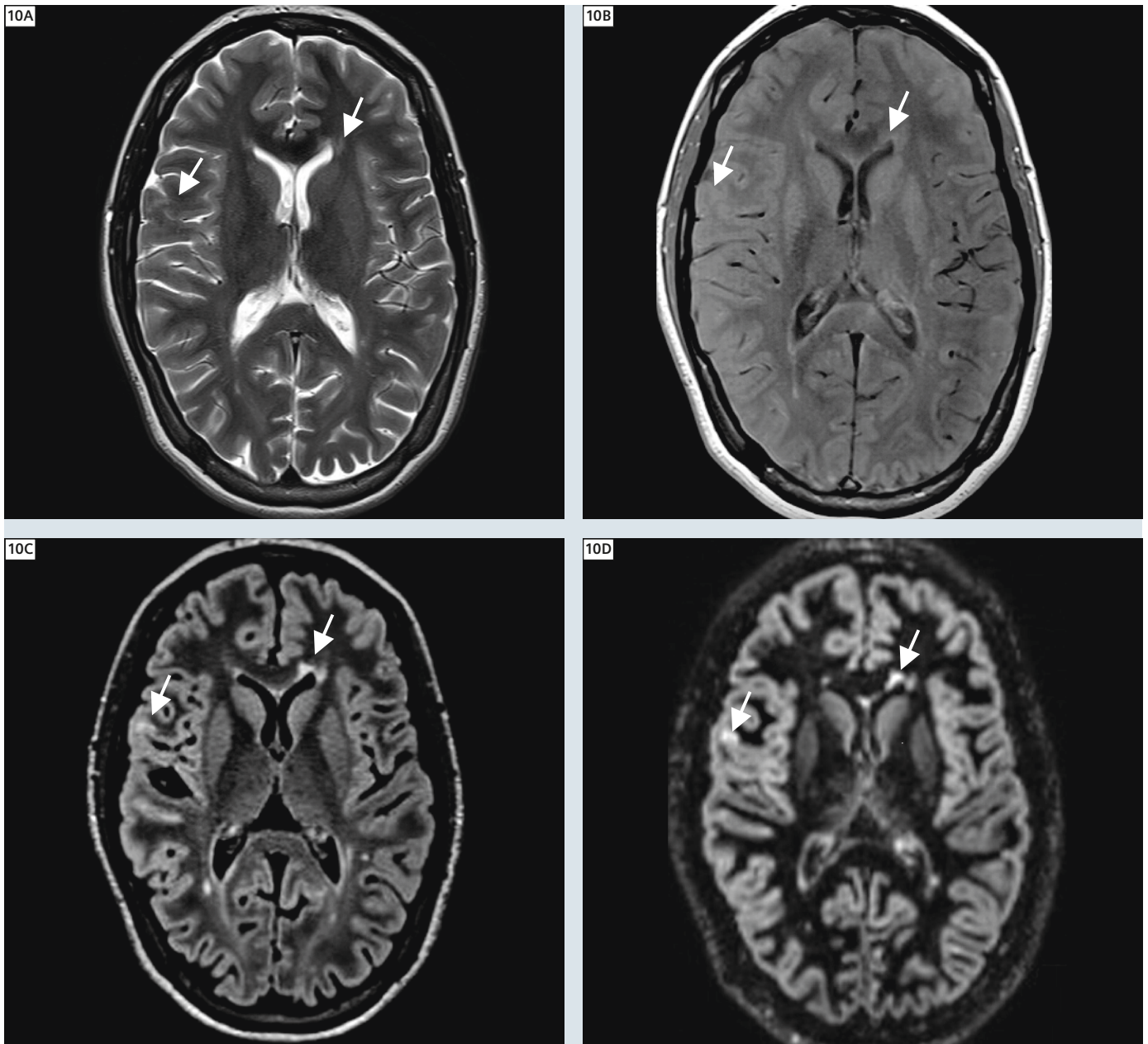
is characterized by a high sensitivity to depict cortical (Fig. 10D) and deep grey matter involvement due to high signal of the lesions relative to the low white and grey matter signal intensity. 3D SPACE DIR sequence is equivalent to 3D FLAIR SPACE to depict white matter infra- and supratentorial lesions. The sequence appears slightly superior to recognize focal and generalized cortical grey matter volume loss in the vicinity of subcortical lesions and as a sign of neurodegeneration respectively.

## 4D MRA for demonstrating tumor perfusion: diagnostic and preoperative information



**9** The similar location, morphology and signal intensity of a paraganglioma (glomus tumor) and neurinoma (arrows: **9A, C**) makes the differentiation sometimes challenging. The 4D MRA however, demonstrates the difference clearly: a paraganglioma shows an early and strong tumor filling (**9B**), and early washout in the venous phase (**9C**) whereas a vagal neurinoma (**9D**) exhibits no macroscopic vascularization in the arterial (**9E**) and venous (**9F**) phase.

## New sequences: increased sensitivity to gray and white matter involvement by demyelination



**10** Axial T2w (10A) and PD images (10B) hardly allow recognition of demyelinating lesions indicated by arrows within the forceps minor of the corpus callosum and in intracortical location within the subcentral gyrus. Images are acquired with 3.5 mm contiguous slices. Improved delineation of the corresponding lesions and significant more demyelinating plaques in the 3D FLAIR (10C) und 3D SPACE DIR sequence (10D) acquired at 1.0 and 1 mm slice thickness respectively.

Inflammatory demyelinating disease: new 3D sequences yield higher diagnostic accuracy, improved clinical and imaging correlation, and more precise follow-up assessment.

### Contact

Prof. Bernhard Schuknecht, M.D.  
Diagnostic, Vascular and  
Interventional Neuroradiology  
Medizinisch Radiologisches Institut MRI Zürich

Bahnhofplatz 3  
8001 Zürich  
Switzerland  
image-solution@ggaweb.ch

**ESMRMB**

European Society for Magnetic Resonance in Medicine and Biology



Further information  
and registration online  
[www.esmrmmb.org](http://www.esmrmmb.org)

## 2013 Lectures on Magnetic Resonance

Educational courses, exercises, and practical demonstrations on MR physics and engineering

**NEW!**

**RF coils: Design and build your own**  
*May 28–30, Berlin/DE*

**Acquisition strategies for hyperpolarised spin systems: Spectral, spatial and temporal**  
*August 25–27, Lyngby/DK*

**Create your own echo: How to generate, calculate and manipulate echoes**  
*September 2–4, Munich/DE*

**Resting state fMRI – basic concepts, methods & applications**  
*September 2–4, Vienna/AT*

**Clinical MR spectroscopy**  
*September 12–14, Nijmegen/NL*

**NEW!**

**Inverse imaging, sparse sampling, compressed sensing, and more**  
*September 16–18, Freiburg/DE*

**NEW!**

**Simultaneous multi-slice/multiband imaging**  
*September 19–21, Essen/DE*

**Small animal MR imaging**  
*October 10–12, Münster/DE*

**Diffusion: What it means and how to measure it**  
*October 12–14, Split/HR*

**Advanced methods for acquisition and analysis of fMRI data**  
*November 20–22, Tübingen/DE*

**RF pulses: Design and applications**  
*November 27–29, Tübingen/DE*

**NEW!**

**MRI simulation for sequence development, protocol optimisation, and education**  
*December 2–4, Bonn/DE*

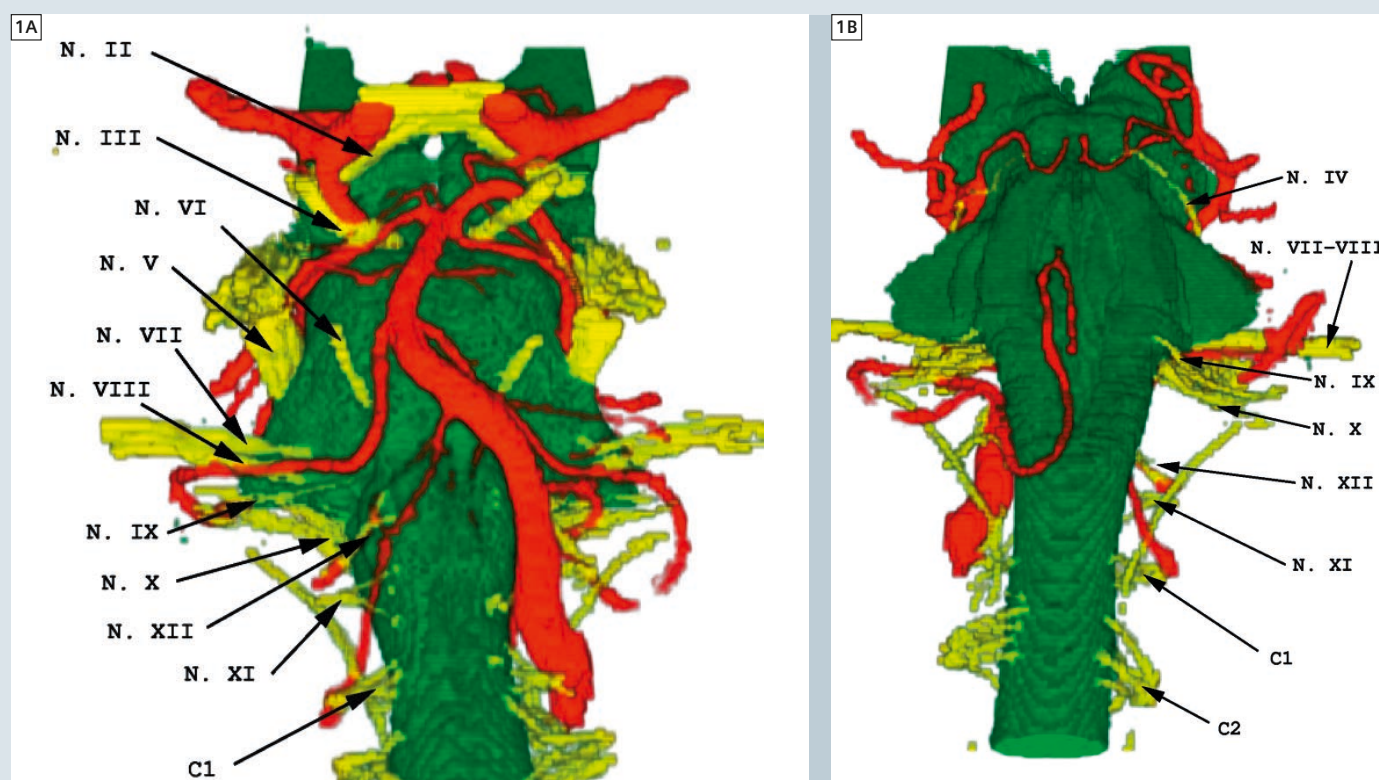
**RF simulation for MR systems: Coil design and safety**  
*December 12–14, Utrecht/NL*

# Imaging of Diseases of the Cranial Nerves: Tips and Tricks

Bernd F. Tomandl<sup>1</sup>; Norbert Sommer<sup>2</sup>; Patrick J. Egan<sup>1</sup>; Tibor C. Mitrovics<sup>1</sup>

<sup>1</sup>Dpt. of Radiology and Neuroradiology, Christophsbad Hospital, Göppingen, Germany

<sup>2</sup>Dpt. of Neurology, Christophsbad Hospital, Göppingen, Germany



**1** Frontal (1A) and rear (1B) view of the brain stem show the origin of the cranial nerves and their relation to surrounding arteries. The pictures were created from MR data. Figure courtesy of K. E. W. Eberhardt, Werneck, Germany and Peter Hastreiter, Erlangen, Germany.

## Introduction

The intention of this article is to alert readers to common problems and pitfalls concerning magnetic resonance imaging (MRI) for pathologies of cranial nerves. It also provides an introduction to helpful sequences and post processing techniques. There are numerous reports about imaging of the cranial nerves that show the capabilities of sub-millimeter heavily T2-weighted images, like the CISS or balanced FFE-sequences

for the visualisation of the anatomy of the cranial nerves in the living body [1]. However, these sequences will only show the course of the cranial nerves within the basal cisterns, and whilst this is helpful in clinically-suspected cases of neurovascular compression symptoms [2, 3], in most other cases more information is needed to find the cause of cranial nerve palsy. To familiarise the reader with cranial nerve imaging,

examples of the normal anatomy as well as typical pathological cases are shown in this article. Most images were acquired with a 1.5T MAGNETOM Avanto (Siemens Healthcare, Erlangen, Germany). All cited references are available online for free.

## Anatomy and MR sequences

Imaging of diseases of the cranial nerves requires good knowledge of the course

**Table 1: Course and function of the cranial nerves (CN).**

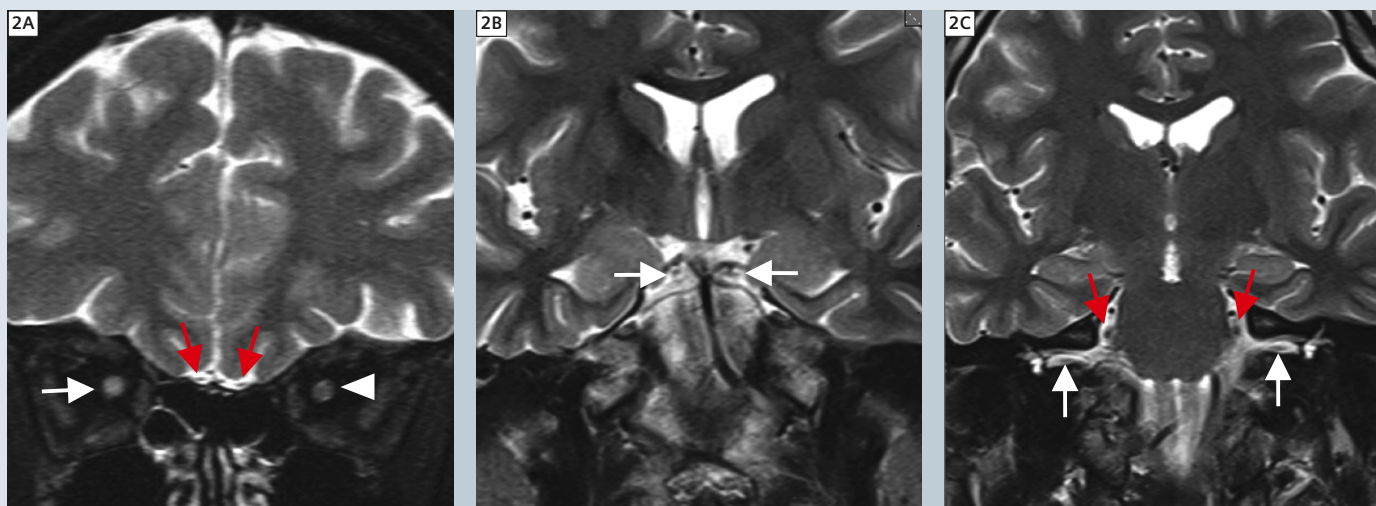
CN	Name	Course and Function
I	Olfactory nerves	Part of the brain. Responsible for the sense of smell. They run in the anterior base of the skull; their fibres exit the skull through the cribriform plate. These nerves are frequently injured in skull-base fractures.
II	Optic nerves	Part of the brain; surrounded by CSF and the dura. Responsible for the sense of vision. Frequent diseases affecting the optic nerves include multiple sclerosis and pituitary adenomas, as well as meningiomas and gliomas of the optic nerves.
III IV VI	Oculomotor nerves Trochlear nerves Abducens nerves	Responsible for eye movement. The relatively large oculomotor nerves also control pupillary constriction. While CN III and VI are easily identified on CISS images, the trochlear nerve – being the only one of the cranial nerves to leave the brain stem at its back below the quadrigeminal plate – is often difficult to find due to its tiny size [11]. The course of the abducens nerves is interesting. They leave the brain stem below the pons, enter a duplication of the dura at the clivus (Dorello's canal), and finally enter the cavernous sinus after crossing the petrosphenoidal ligament (Gruber's ligament). Imaging of an affliction of an abducens nerve should therefore include contrast-enhanced T1w images of the clivus with fat saturation. Acute palsy of the oculomotor nerve is frequently (15%) related to an intracranial aneurysm of the internal carotid artery at the origin of the Pcom.
V	Trigeminal nerves	They divide into three branches: the V1 (ophthalmic), V2 (maxillary) and V3 (mandibular) branch. They leave the skull through the superior orbital fissure (V1), the foramen rotundum (V2) and the foramen ovale (V3). They transmit sensations from the face, scalp and teeth, including chewing. Neurovascular compression of the nerve at the entrance zone to the brain stem may result in trigeminal neuralgia.
VII VIII	Facial nerves Vestibulocochlear nerves	The facial and vestibulocochlear nerves both enter the internal auditory meatus. The facial nerves are responsible for the sensation of taste from the anterior 2/3 of the tongue as well as the motoric innervation of face muscles. Acoustic schwannomas and meningiomas are frequent pathologic findings affecting these nerves.
IX X XI	Glossopharyngeal nerves Vagus nerves Accessory nerves	The glossopharyngeal, vagus and accessory nerves leave the skull through the jugular foramen. CN IX is also responsible for involuntary blood-pressure reflexes, cardiac and respiratory sensing, contraction of the pharynx and the swallowing reflex. Some of these signals overlap with CN X, which is more involved in reflexes and vital functions. They can be involved in skull-base tumors or dissections of the carotid artery.
XII	Hypoglossal nerves	The hypoglossal nerves exit the skull through the hypoglossal foramen. They control the movement of the tongue by innervating three of the four muscles. The fourth muscle is under the control of CN X.

Parts of table 1 are courtesy of Alicia Mae Prater, <http://suite101.com/article/the-cranial-nerves-a105837>.

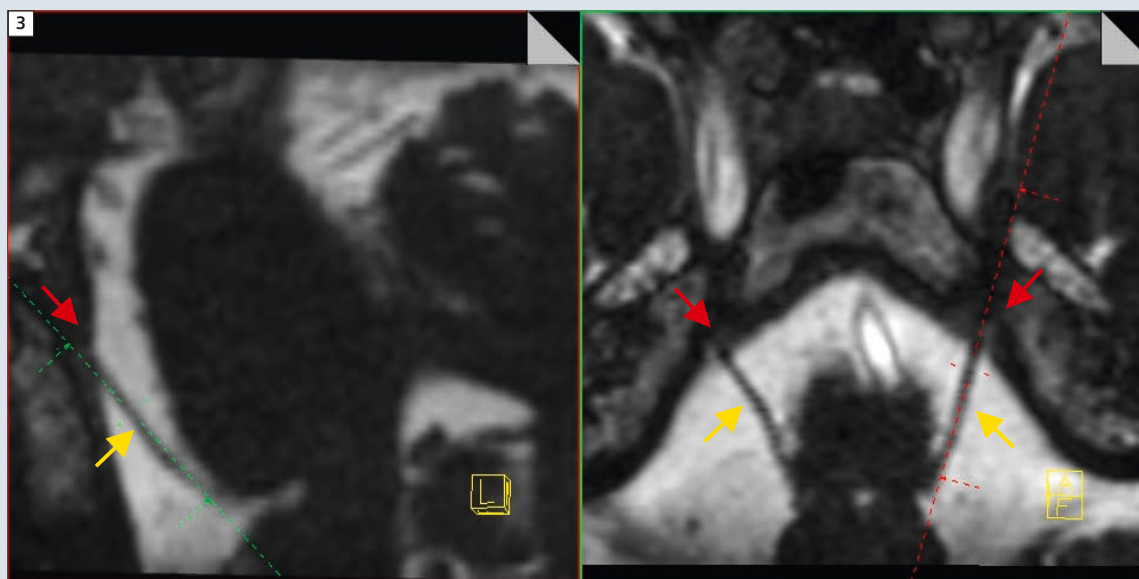
of the particular involved cranial nerve. An overview of the cranial nerves is given in table 1 and figure 1. A more interactive and entertaining introduction to cranial nerve anatomy and function is given by Barbara Liang on the wisc-online site (<http://www.wisc-online.com/Objects/ViewObject.aspx?ID=AP11504>). Large cranial nerves are visible even on standard MR images: The ophthalmic, optical, trigeminal, oculomotoric as well

as the facial and vestibulocochlear nerves can be readily identified on 4 mm T2w images (Fig. 2). The smaller nerves are more difficult to see and thin section images are required. As an example how the anatomic course of a cranial nerve influences the choice of MR sequences, the course of the sixth cranial nerves (abducens nerves) is as follows: The nerves leave the brain stem below the pons, enter a duplication of the dura at

the clivus (Dorello's canal), and finally enter the cavernous sinus after crossing the petrosphenoidal ligament (Gruber's ligament) [4]. While CISS-images will only show the intracisternal course of the nerve (Fig. 3), other sequences are needed to exclude an infarction in the pons or a tumor along the course of the nerve. Imaging of an acute affliction of an abducens nerve should therefore always include diffusion-weighted



**2** 4 mm T2w TSE MRI. Some cranial nerves are always visible: **(2A)** T2w TSE with fat saturation in a patient with multiple sclerosis. Hyperintense right optic nerve indicating optic neuritis (white arrow). The left optic nerve is normal (arrowhead). In addition the olfactory nerves are visible (red arrows). **(2B)** The oculomotor nerves (arrows) crossing the space between the posterior cerebral artery and the superior cerebellar artery. **(2C)** The trigeminal nerves at their origin (red arrows) and the facial and vestibulocochlear nerves within the internal acoustic canal are clearly visible (white arrows).



**3** Multiplanar reformations from 0.7 mm CISS images in oblique sagittal and coronal planes show the intracisternal course of the abducens nerves (yellow arrows) and the origin of Dorello's canal (red arrows).

images (DWI) of the pons and (if no infarction is visible) contrast-enhanced T1w images of the clivus (sagittal plane) and cavernous sinus (coronal plane) with fat saturation [5]. Time-of-Flight (TOF) MR angiography (MRA) can be helpful to detect aneurysms in the cavernous sinus. Always remember that this technique is not sufficient to exclude intracranial aneurysms [6]. Often T1-weighted 3D-sequences after

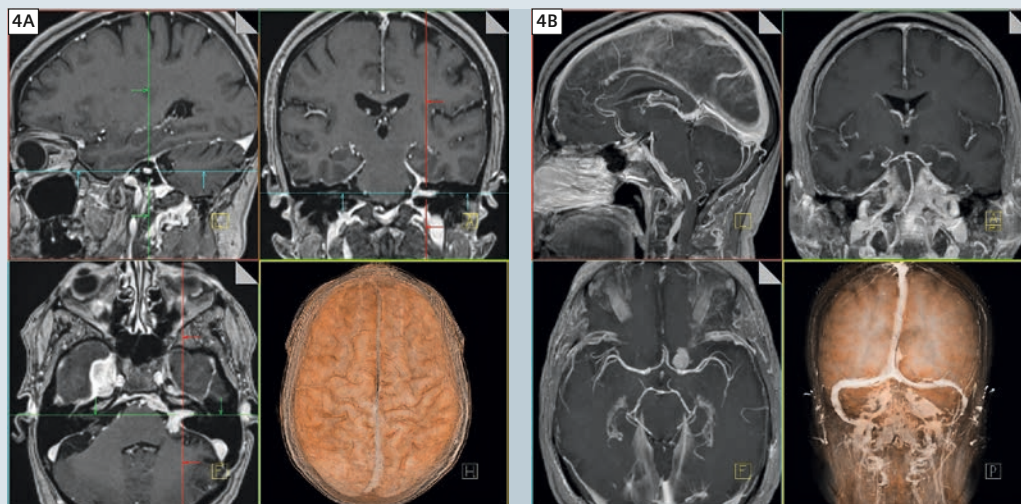
administration of gadolinium (e.g. Magnetization Prepared Rapid Gradient Echo (MPRAGE)) are very helpful as they allow for intensive post processing of the data (Fig. 4) [7].

### Post processing

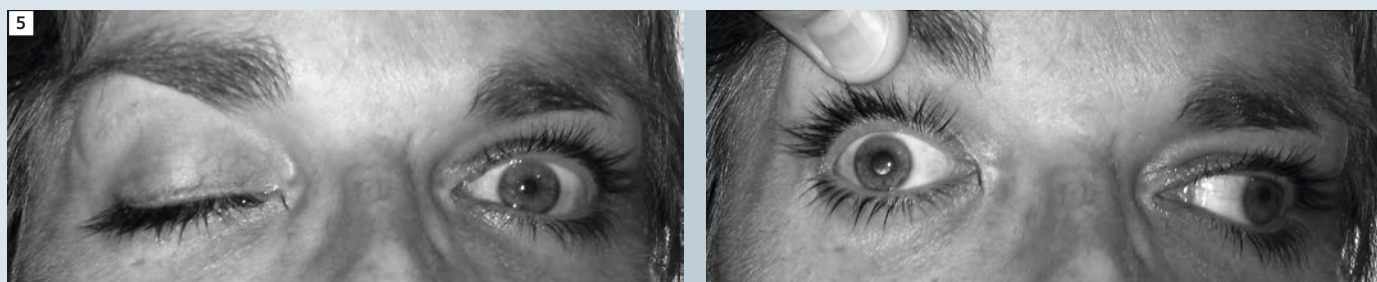
Usually the cranial nerves follow an oblique course through the basal cisterns. Therefore 3D post processing with multiplanar reconstructions (MPR) and/

or volume rendering is often helpful to get a clearer delineation of the course of a specific cranial nerve and its vicinity. The following case report will make that more clear:

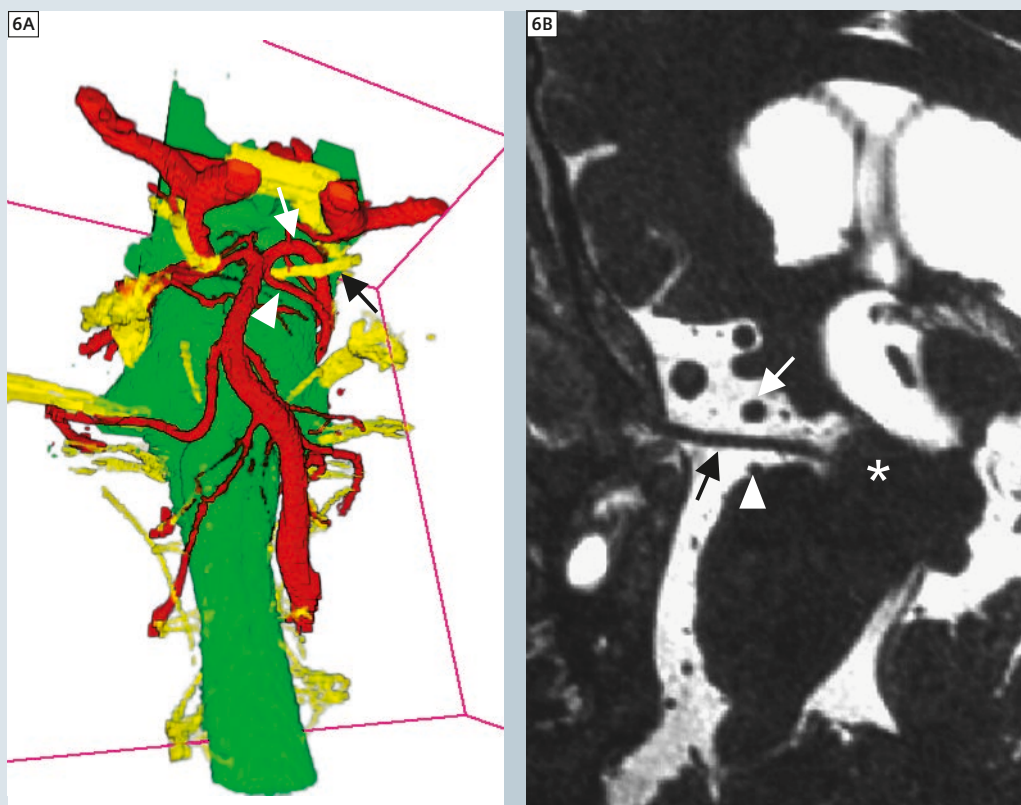
A 46-year-old woman attended her physician after she developed acute ptosis and double vision especially when looking to the left side (Fig. 5). Clinical examination revealed an oculomotor palsy. The normal anatomy of the third



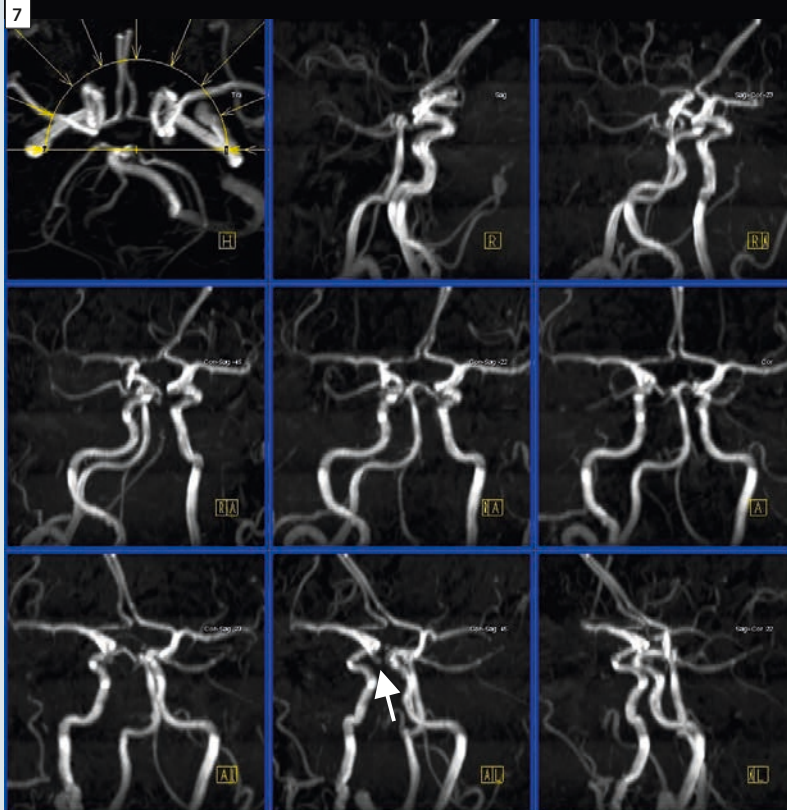
**4** T1w MPRAGE after intravenous administration of Gadolinium-DTPA in a patient with multiple meningiomas and an assumed acoustic schwannoma. **(4A)** MPR in three orthogonal planes allows for optimal delineation of the tumor within the internal acoustic canal. In addition a volume rendered image shows the brain surface. **(4B)** Thin section MIP images (15 mm) and low opacity volume rendering allow good delineation of both the large intracranial arteries and veins.



**5** Acute right oculomotor palsy in a 46-year-old woman.



**6** Intracranial course of the left oculomotor nerve (black arrow) demonstrated on a volume rendered image **(6A)** of the brainstem and an oblique sagittal view from 0.7 mm CISS data **(6B)**. The nerve (black arrow) leaves the midbrain (\*) between the posterior cerebral artery (white arrow) and the superior cerebellar artery (white arrowhead). After crossing the basal cisterns it enters the cavernous sinus.

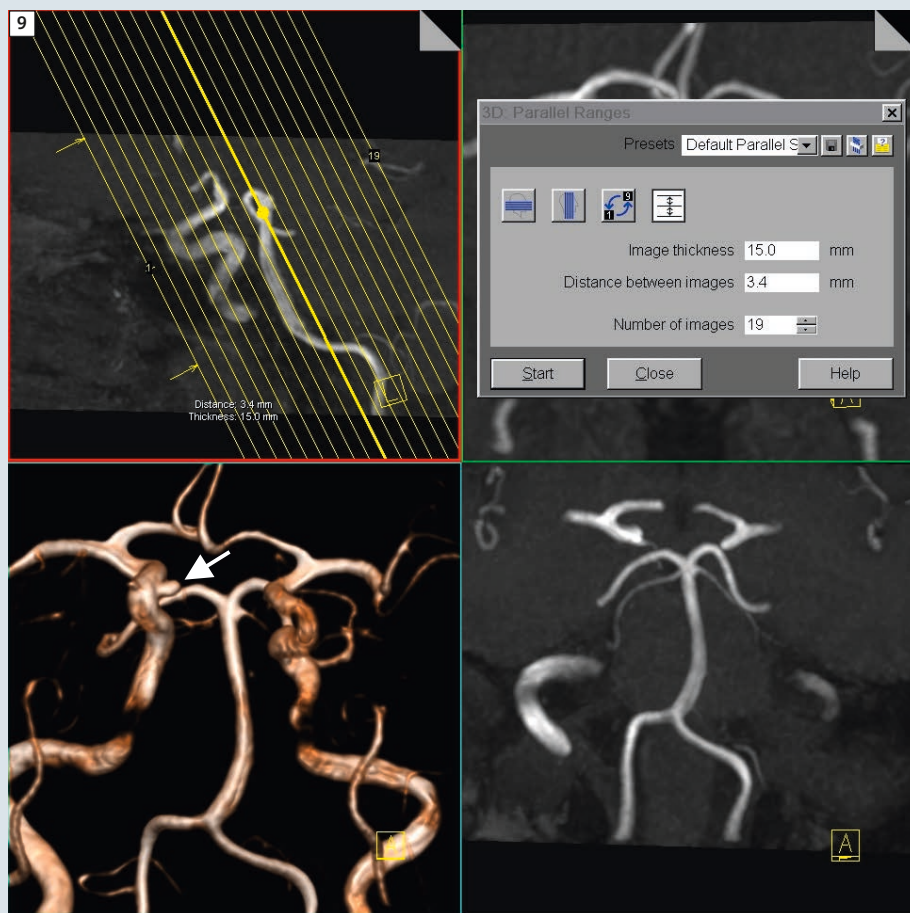


**7** 180° MIP of the whole volume of TOF-MRA. It is very difficult to detect the small aneurysm of the internal carotid artery (arrow).



**8** Thin section (15 mm) MIP images in three orthogonal and a volume-rendered image from a right rear lateral view clearly shows the 3 mm aneurysm of the intracranial internal carotid artery at the origin of the posterior communicating artery.

cranial nerve is shown in figure 6. MRI was performed including DWI and TOF-MRA without result. As the oculomotor palsy did not improve within 4 weeks the patient was sent to our hospital. She brought her images on a CD and we reviewed the images including post processing of the TOF-MRA that was done on a Siemens MultiModality workplace (Leonardo). While it was very difficult to see the lesion on the initially produced maximum intensity projection (MIP) reconstructions that included the whole volume data (Fig. 7) it was rather easy to detect the aneurysm on 15 mm thin MIP images in 3 planes and even easier on volume rendered images (Fig. 8). This is a good example why whole-volume MIP imaging is not very helpful if we want to see more than just the big arteries [8]. Of course it is mandatory to review the source images before any kind of 3D-imaging is done [9]. In our hospital we use routinely thin section MIPs of 15 mm section thickness in sagittal axial and oblique coronal planes where the coronal plane is reconstructed parallel to the basilar artery to get a clear visualization of the 2 vertebral arteries and the basilar artery and its branches (Fig. 9). Using this type of reconstruction makes it easy to delineate aneurysms in the vicinity of the cranial nerves. It is important to know that about 15% of acute oculomotor palsy cases are caused by intracranial aneurysms that are usually located at the distal intracranial internal carotid artery at the origin of the posterior communicating artery [10]. The course of the nerve roughly parallels the course of the posterior communicating artery (Fig. 6). It is very important to perform the MRA with high quality in these patients. We must be aware that TOF-MRA cannot exclude an aneurysm because slow flow within the aneurysm may lead to non-visualisation within the flow sensitive sequences so that other imaging modalities like contrast-enhanced MRA, CTA or even DSA are sometimes necessary.



**9** Oblique coronal thin MIP reformations (15 mm section thickness) are done parallel to the basilar artery to get a free view on the vertebral arteries and the basilar artery and its branches. The volume rendered image shows a small probably intracavernous aneurysm of the internal carotid artery (arrow).

## Summary

Before performing MRI of a patient with cranial nerve palsy make sure that you know the course of the particular cranial nerves. Use thin section CISS-sequences to see the intracisternal course of the nerves. Use fat suppressed T1w images after contrast administration to visualize pathology within the skull base. Use 3D MPRAGE for a variety of reconstructions. Don't rely on whole-volume MIP images from TOF-MRA. Routinely use the excellent post-processing tools that come with all Siemens scanners, such as MPR, thin section MIPs and volume rendering. This will ensure that you will not miss important findings.

### Contact

Prof. Dr. Bernd F. Tomandl, M.D.  
Department of Radiology and Neuroradiology  
Christophsbad Hospital  
Faurndauerstr. 6–28  
73033 Göppingen  
Germany  
Phone: +49 7161 601 9389  
Fax: +49 7161 601 9332  
bernd.tomandl@christophsbad.de  
web: www.christophsbad.de

The statements by Siemens' customers described herein are based on results that were achieved in the customer's unique setting. Since there is no "typical" hospital and many variables exist (e.g., hospital size, case mix, level of IT adoption) there can be no guarantee that other customers will achieve the same results.

### References

- Sheth, S., Branstetter, B.F.t., and Escott, E.J.: 'Appearance of normal cranial nerves on steady-state free precession MR images', *Radiographics* : a review publication of the Radiological Society of North America, Inc, 2009, 29, (4), pp. 1045-1055.
- Gaul, C., Hastreiter, P., Duncker, A., and Naraghi, R.: 'Diagnosis and neurosurgical treatment of glossopharyngeal neuralgia: clinical findings and 3-D visualization of neurovascular compression in 19 consecutive patients', *The journal of headache and pain*, 2011, 12, (5), pp. 527-534.
- Lang, E., Naraghi, R., Tanrikulu, L., Hastreiter, P., Fahlbusch, R., Neundorfer, B., and Troscher-Weber, R.: 'Neurovascular relationship at the trigeminal root entry zone in persistent idiopathic facial pain: findings from MRI 3D visualisation', *Journal of neurology, neurosurgery, and psychiatry*, 2005, 76, (11), pp. 1506-1509.
- Ono, K., Arai, H., Endo, T., Tsunoda, A., Sato, K., Sakai, T., and Makita, J.: 'Detailed MR imaging anatomy of the abducent nerve: evagination of CSF into Dorello canal', *AJNR. American journal of neuroradiology*, 2004, 25, (4), pp. 623-626.
- Mitsuya, K., Nakasu, Y., Horiguchi, S., Harada, H., Nishimura, T., Yuen, S., Asakura, K., and Endo, M.: 'Metastatic skull tumors: MRI features and a new conventional classification', *Journal of neuro-oncology*, 2011, 104, (1), pp. 239-245.
- Tomycz, L., Bansal, N.K., Hawley, C.R., Goddard, T.L., Ayad, M.J., and Mericle, R.A.: "Real-world" comparison of non-invasive imaging to conventional catheter angiography in the diagnosis of cerebral aneurysms', *Surgical neurology international*, 2011, 2, pp. 134.
- Lettau, M., Sartor, K., Heiland, S., and Hahnel, S.: '3T high-spatial-resolution contrast-enhanced MR angiography of the intracranial venous system with parallel imaging', *AJNR. American journal of neuroradiology*, 2009, 30, (1), pp. 185-187.
- Runck, F., Steiner, R.P., Bautz, W.A., and Lell, M.M.: 'MR imaging: influence of imaging technique and postprocessing on measurement of internal carotid artery stenosis', *AJNR. American journal of neuroradiology*, 2008, 29, (9), pp. 1736-1742.
- Tomandl, B.F., Kostner, N.C., Schemperschofe, M., Huk, W.J., Strauss, C., Anker, L., and Hastreiter, P.: 'CT angiography of intracranial aneurysms: a focus on postprocessing', *Radiographics* : a review publication of the Radiological Society of North America, Inc, 2004, 24, (3), pp. 637-655.
- Nam, K.H., Choi, C.H., Lee, J.I., Ko, J.G., Lee, T.H., and Lee, S.W.: 'Unruptured Intracranial Aneurysms with Oculomotor Nerve Palsy: Clinical Outcome between Surgical Clipping and Coil Embolization', *Journal of Korean Neurosurgical Society*, 2010, 48, (2), pp. 109-114.
- Yousry, I., Moriggl, B., Dieterich, M., Naidich, T.P., Schmid, U.D., and Yousry, T.A.: 'MR anatomy of the proximal cisternal segment of the trochlear nerve: neurovascular relationships and landmarks', *Radiology*, 2002, 223, (1), pp. 31-38.

# 3T DTI in Patients with Glaucoma. New Approaches for Data Analysis & Clinical Implications

Tobias Engelhorn<sup>1</sup>; Georg Michelson<sup>2</sup>; Joachim Hornegger<sup>3</sup>; Arnd Doerfler<sup>1</sup>

<sup>1</sup>Department of Neuroradiology, University Erlangen-Nuremberg, Germany, <sup>2</sup>Department of Ophthalmology, University Erlangen-Nuremberg, Germany, <sup>3</sup>Department of Computer Science, University Erlangen-Germany, Germany

## Background

Glaucoma is responsible for approximately 10% of cases of blindness throughout the world and thus the third leading cause of blindness with over 8 million cases each year [1]. Glaucoma is considered a nervous system-based degenerative disease that is only partially influenced by ocular factors [2]. Moreover, neuronal degeneration involving all parts of the central visual pathways was documented at autopsy in patients with advanced glaucoma and severe visual field loss in both eyes [3]. Central neuronal degeneration can be assessed non-invasively using diffusion tensor imaging (DTI). To assess the optical pathways, DTI can exclusively depict the optic nerve (3<sup>rd</sup> neuron) and optic radiation (4<sup>th</sup> neuron) [4–6]. In addition, subtle changes can be assessed by calculation of fractional anisotropy (FA), which measures the orientation coherence of diffusion and provides information about axonal integrity [7]. The aim of the study presented was to evaluate whether 3T DTI with volumetric analysis of the optical pathway and calculation of diffusion coefficients can assess the (early) spread of glaucomatous damage within the central nervous system and to determine whether DTI-derived changes correlate with disease severity determined by established ophthalmological tests in patients with glaucoma. In addition, user-independent fast and robust assessment, new automatic segmentation approaches and a framework for a voxel-based morphometric analysis of the optic radiation were developed [8–14] and will be described.

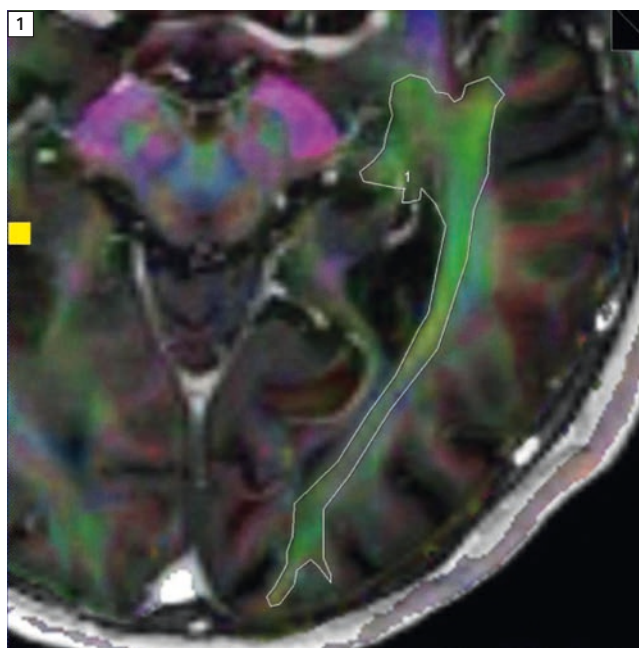
## Methods

The Clinical Investigation Ethics Committee of the University of Erlangen-Nuremberg approved the study protocol. Fifty patients (18 men, 32 women; mean age  $52.2 \pm 12.6$  and  $60.0 \pm 16.9$  years, respectively) diagnosed with damage of the optic nerve head or visual disturbance, were randomly selected for magnetic resonance imaging (MRI) and subsequent DTI. Fifty age-matched patients without glaucoma undergoing MRI because of headaches, dizziness, or stenosis of the nasolacrimal duct served as controls (22 men, 28 women; mean age  $54.0 \pm 14.2$  and  $61.4 \pm 15.1$  years, respectively). In these patients, increased intraocular pressure (IOP), optic nerve head atrophy or visual disturbances were excluded by an ophthalmological

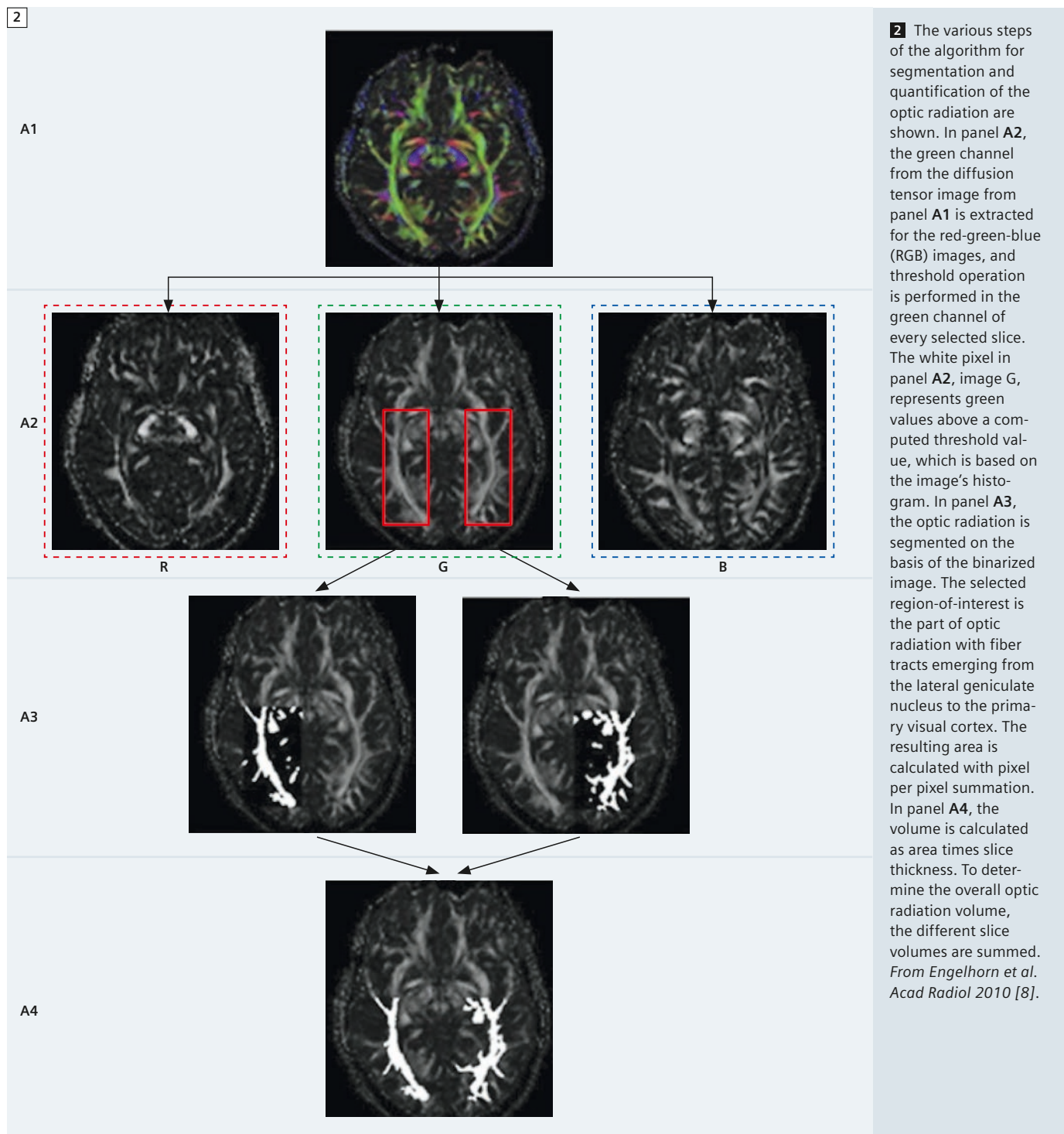
examination. Available additional examinations were referred to for evaluation, including Heidelberg Retinal Tomography, automated perimetry, spatial-temporal contrast sensitivity (frequency doubling test), nonmydriatic fundus images and optical coherence tomography (OCT) with measuring of the retinal nerve fiber layer (RNFL) thickness in glaucoma patients and controls.

## Magnetic resonance imaging

MRI was performed using a 3T high-field scanner (MAGNETOM Trio with Tim; Siemens Healthcare AG, Erlangen, Germany) with a gradient field strength up to 45 mT/m (72 mT/m effective). Anatomic data were obtained in a T1-weighted three-dimensional magne-



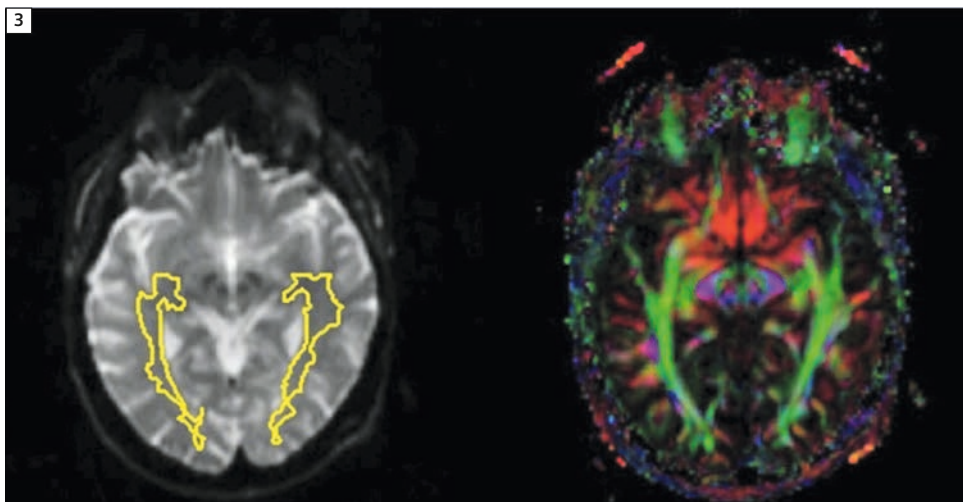
**1** For manual volumetric assessment of the optic radiation (4<sup>th</sup> neuron), the DTI sequence was fused with a high-resolution anatomical T1w MPRAGE sequence using Siemens-built-in software (Neuro 3D card). Exemplarily, the left lateral geniculate nucleus (LGN) with the optic radiation straight to the optic cortex are outlined.



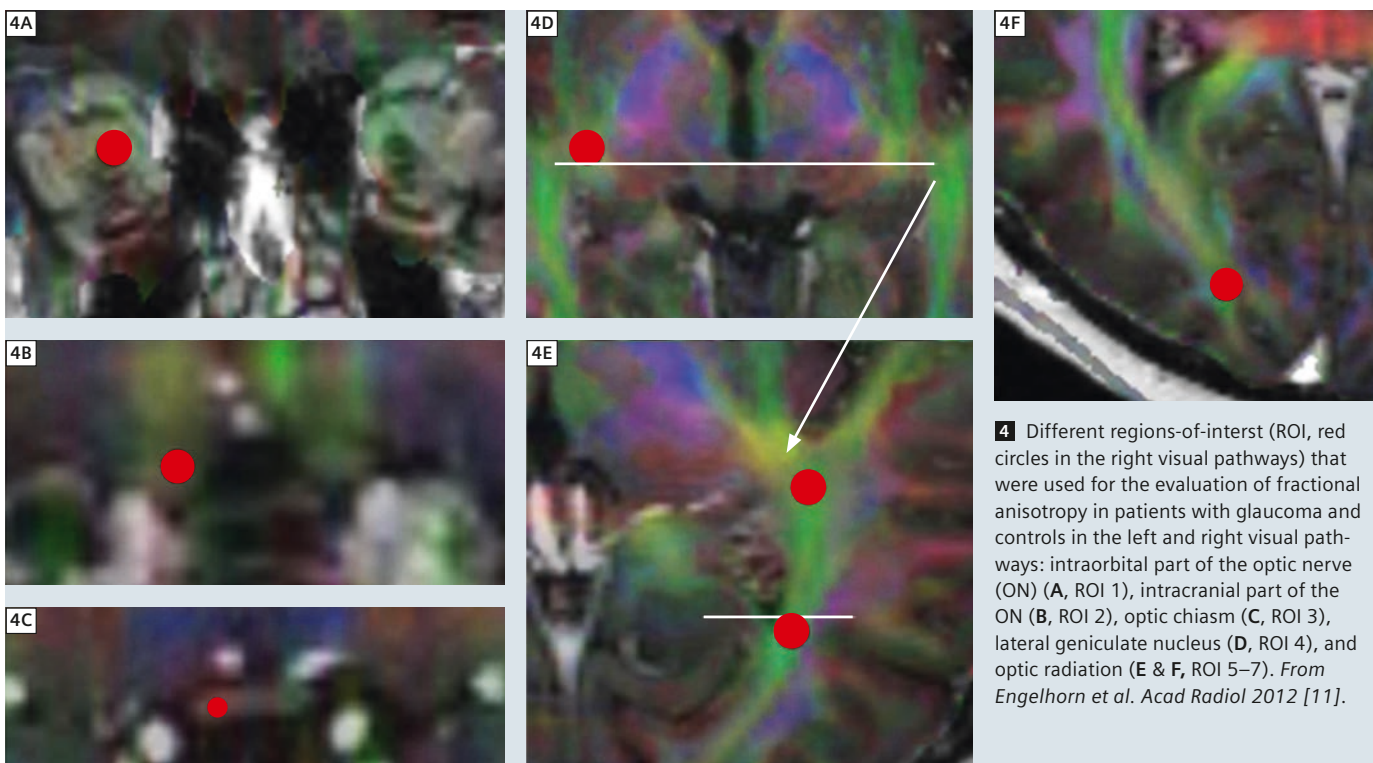
tization-prepared rapid gradient-echo sequence (MPRAGE, TR 900 ms; TE 3 ms; FOV 23 x 23 cm; acquisition matrix size 512 x 256 reconstructed to 512 x 512; reconstructed axial plans with 1.2 mm slice thickness). DTI was performed in the axial plane

with 4 mm slice thickness and no inter-slice separation using a single-shot, spin-echo, echoplanar imaging diffusion tensor sequence covering the whole visual pathway (TR 3400 ms; TE 93 ms; FOV 23 x 23 cm; acquisition matrix size 256 x 256; number of signal averages,

7; partial Fourier acquisition 60%). Diffusion weighting with a maximal  $b$ -factor of 1000 s/mm<sup>2</sup> was carried out along 15 icosahedral directions complemented by one scan with  $b = 0$ . Data sets were automatically corrected for imaging distortions and coregistered



**3** Sample-automated segmentation of the optic radiation on an axial brain slice. The left side shows the segmented optic radiation on a non-diffusion-weighted image ( $b=0$ ). The corresponding diffusion direction color-coded image weighted with FA is shown on the right side. The structure of the part of the visual pathway representing the main fiber bundle of the optic radiation and the LGN is clearly captured. From El-Rafei et al. *Magn Reson Imaging* 2011 [10].



**4** Different regions-of-interest (ROI, red circles in the right visual pathways) that were used for the evaluation of fractional anisotropy in patients with glaucoma and controls in the left and right visual pathways: intraorbital part of the optic nerve (ON) (A, ROI 1), intracranial part of the ON (B, ROI 2), optic chiasm (C, ROI 3), lateral geniculate nucleus (D, ROI 4), and optic radiation (E & F, ROI 5–7). From Engelhorn et al. *Acad Radiol* 2012 [11].

in reference to T1-weighted MPRAGE images. These and further calculations, such as determining the independent elements of the diffusion tensor, deriving the corresponding eigenvalues and eigenvectors, and reconstructing and volume rendering fibers, were performed using dedicated software (Neuro 3D; Siemens Healthcare AG).

### Data analysis & postprocessing

For manual segmentation by two experienced neuroradiologists (T.E. and A.D.)

and quantification of the optic radiation, the seed regions for the tracking algorithm were selected on the coregistered T1-weighted images that were overlaid on the DTI data (Fig. 1). As a start region, an area consisting of approximately 12 to 18 voxels was chosen covering the LGN [5]. Therewith, fiber tracts emerging from the LGN into the primary visual cortex were investigated. The resulting fiber pathways were evaluated visually for integrity and accuracy of the reconstructed fibers (i.e. the course on the

coregistered anatomic T1-weighted data was compared to the known anatomy of the visual pathway). In addition, volume rendering of the LGN and fiber tracts was performed by outlining the fourth neurons on each DTI slice by hand to calculate rarefaction.

### Automated segmentation of the optic fibers

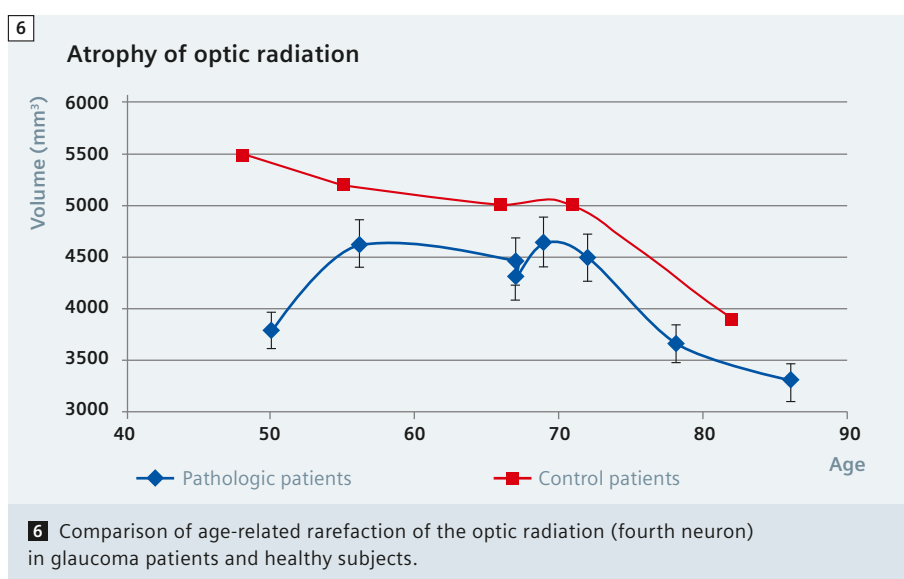
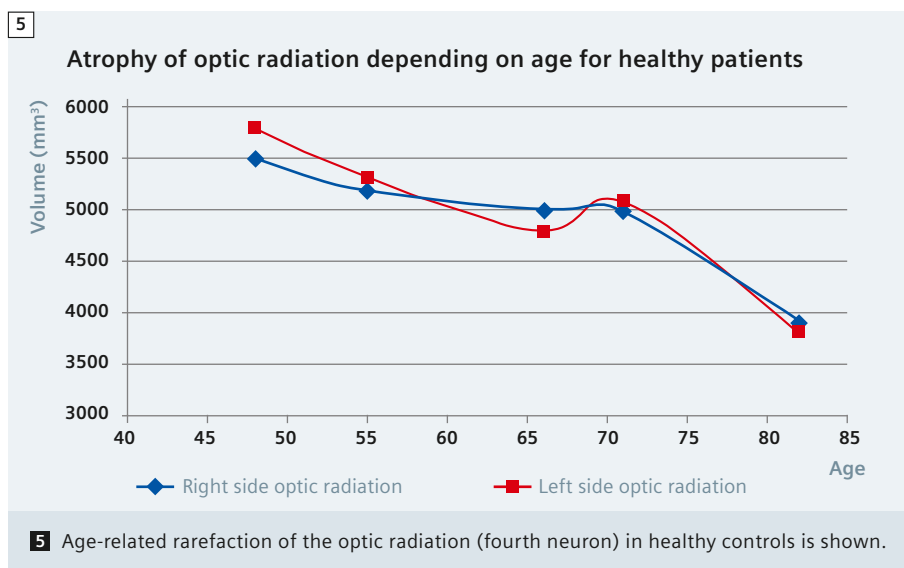
For automated segmentation and quantification of the optic radiation, a Mathcad-based software program<sup>1</sup>

(Parametric Technology Corporation, Needham, MA, USA) was developed (Figs. 2, 3). The program selects slices in which optical radiation is present by making use of the pattern recognition, head organ dimension (i.e. before actual image processing), location of the optic radiation in relation to the head size, and area of the largest green concentration (horizontal direction) as a starting point. Furthermore, the region-of-interest is selected for both sides. The green channel is extracted for the red-green-blue image and threshold operation in the green channel of every selected image. The white pixel represents green values above a computed threshold value, which is based on the image's histogram. The optic radiation is segmented on the basis of the binarized image. The resulting area is calculated with a simple pixel per pixel summation. In the next step, the volume is calculated as area times slice thickness. To receive the overall optic radiation volume, the different slice volumes are summed.

### Qualitative analysis of the optic fibers using diffusion coefficients

For qualitative assessment of the optic fibres, calculation of fractional anisotropy (FA) and radial diffusivity (RD) maps was performed with a dedicated software package (Neuro 3D; Siemens Healthcare AG). Regions of interest (ROIs) of approximately 9 mm<sup>2</sup> (range, 6–12 mm<sup>2</sup>) were depicted on the FA maps superimposed over the T1-weighted three-dimensional MPRAGE sequence described above. The following ipsilateral and contralateral ROIs were used for evaluation of FA (Fig. 4):

ROI 1: the intraorbital part of the optic nerve directly after the eyeball  
 ROI 2: the intracranial part of the optic nerve directly before the optic chiasm  
 ROI 3: the lateral part of the optic chiasm  
 ROI 4: the lateral geniculate nucleus (LGN)  
 ROI 5: the optic radiation directly after the LGN  
 ROI 6: the optic radiation at the level of the posterior horn of the lateral ventricle  
 ROI 7: the optic radiation directly before its cortical spread



Statistical analyses were performed using PASW<sup>1</sup> release 18.0 (SPSS, Inc, Chicago, IL, USA).

### Results

The automated segmentation and quantification of the optic radiation was feasible in all patients and controls. The evaluation matched 94% with manual evaluation for all patients and Cronbach's  $\alpha$  was > 0.81 for calculation of the manually and semiautomatically derived volumes. The mean evaluation time of semiautomatic segmentation including the time for data transfer was significantly shorter (38 minutes) compared to manual segmentation (91 minutes).

As result of DTI, age-related atrophy of up to 30% of the optic radiation was detected in healthy patients (Fig. 5) and there was high correlation between a decrease in the volume of the fourth neuron of both sides with increasing age ( $r = 0.82$ ) (Fig. 5).

44% of glaucoma patients had at least a slight rarefaction of the optic radiation, i.e. averaged rendered volume was < 85% compared to controls. In these patients, the averaged rendered volume of the optic radiation of both sides was reduced to  $67 \pm 16\%$  compared to controls (Fig. 6).

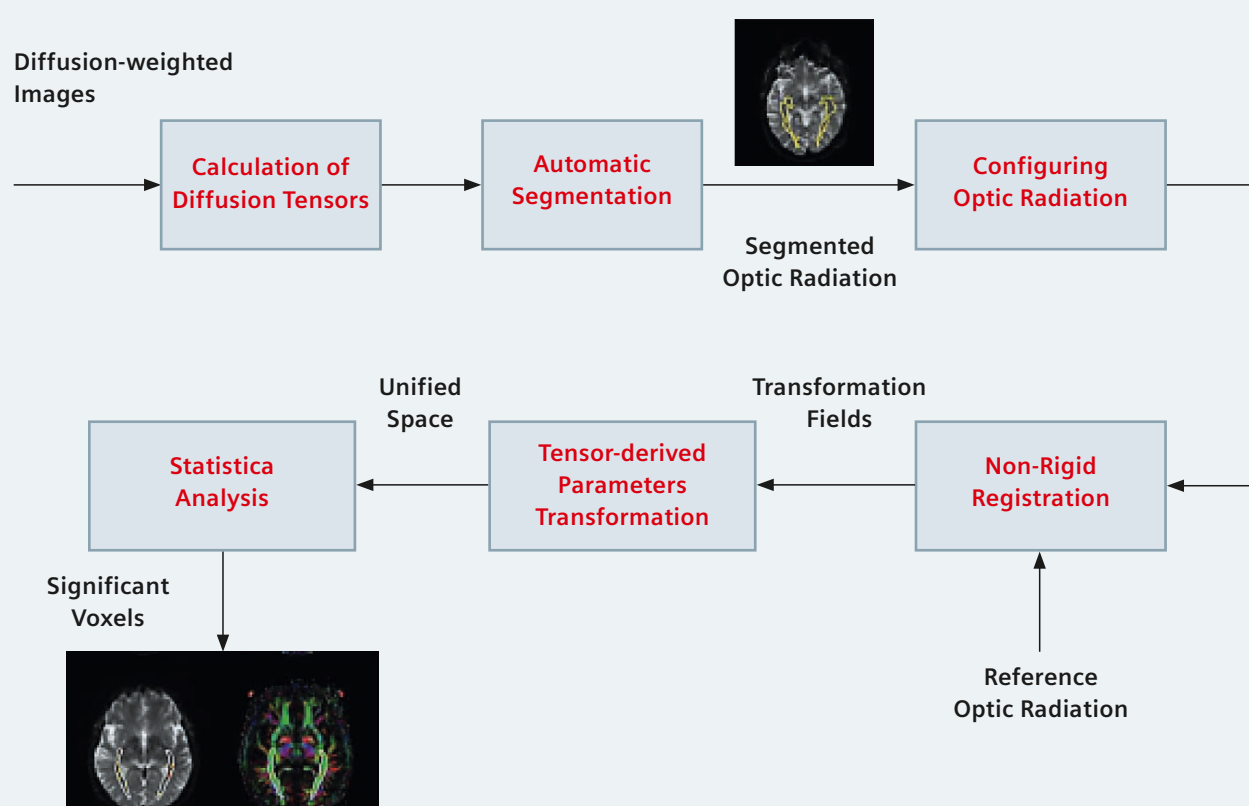
Measurement of FA in ipsilateral and contralateral ROIs was feasible in all test

Table 1

Localization	FA	
	Patients with Glaucoma	Controls
ROI 1	$0.36 \pm 0.11$	$0.42 \pm 0.13$
ROI 2	$0.48 \pm 0.15^*$	$0.66 \pm 0.12$
ROI 3	$0.32 \pm 0.16$	$0.35 \pm 0.17$
ROI 4	$0.21 \pm 0.09$	$0.24 \pm 0.07$
ROI 5	$0.40 \pm 0.16^*$	$0.57 \pm 0.13$
ROI 6	$0.48 \pm 0.17$	$0.64 \pm 0.11$
ROI 7	$0.44 \pm 0.22^*$	$0.53 \pm 0.20$

7 FA: fractional anisotropy; ROI = region-of-interest. \*Significantly lower FA values compared to controls (p-value < 0.05). From Engelhorn et al. Acad Radiol 2012 [11].

8



8 Schematic of the analysis framework according to El-Rafei et al. (6). The system analyzes the diffusion tensor images of the optic radiation to produce localization maps showing regions with significant differences between glaucoma and control groups. The schematic illustrates the different steps including optic radiation identification and configuration, registration and statistical analysis. From El-Rafei et al. Magn Reson Imaging 2011 [10].

subjects. Mean evaluation time was 32 minutes per patient. Cronbach's  $\alpha$  at the 95% confidence interval for FA was 0.990 (right side) and 0.886 (left side). In controls, there was high correlation between a decrease in FA of both sides with increasing age ( $r = 0.78$ ). The overall percentage change in FA in control subjects between 45 and 83 years of age was  $33.7 \pm 10.7\%$ . This difference was significant ( $P < 0.05$ ). Right-side and left-side FA measurements in controls and glaucoma patients were similar and differed only in small ranges up to 5%. Hence, the measurements for both sides were averaged and are displayed in Figure 7.

FA was significantly reduced in the intracranial part of the optic nerve (3<sup>rd</sup> neuron of the visual pathways) and in all three sections of the optic radiation (4<sup>th</sup> neuron of the visual pathways), thus in all sections with a more or less straight axonal direction. In contrast, there was no significant decrease (but a slight tendency toward a decrease) in FA in the intraorbital optic nerve, the optic chiasm, and the LGN. The explanation for this finding is most likely the crossing of axons in the optic chiasm and the reconnection of axons in the LGN, resulting in a change of the straight axonal direction with subsequent decrease in FA [4, 15], whereby ineluctably, movement of the eyeball subsequently results in movement of the intraorbital optic nerve, downgrading the quality of FA analysis in this section of the visual pathways by motion artifacts. This limitation could be overcome with retrobulbar anesthesia if needed.

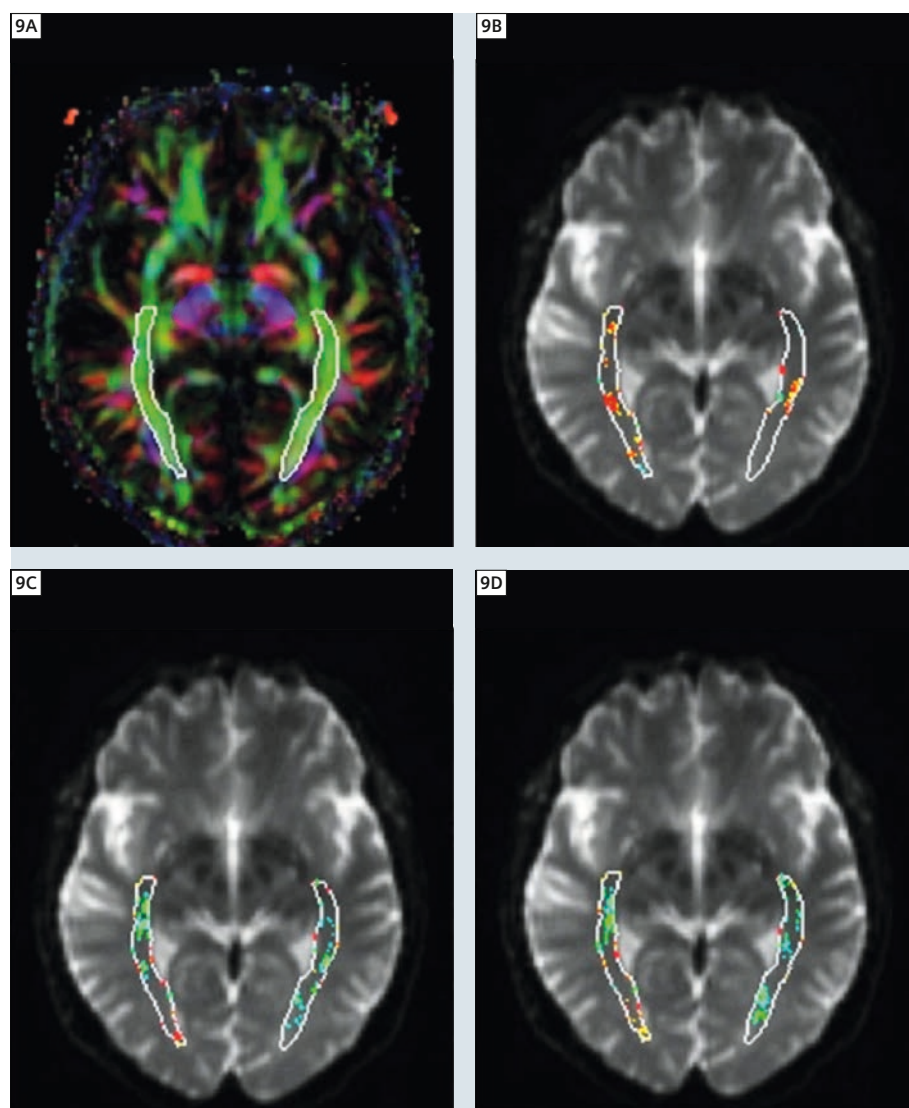
In addition, we could establish a framework for automatic voxel-based morphometric analysis of the optic radiation using DTI (Figs. 8, 9) that can be also used in other forms of neurodegenerative brain disease: glaucoma patients have increased radial diffusivity (RD) and mean diffusivity (MD) significant voxels with a main concentration in the proximal part of the optic radiation. The proposed analysis provides a robust framework to capture the significant local changes of the optic radiation due to glaucoma.

### Correlation between MRI and ophthalmic examination

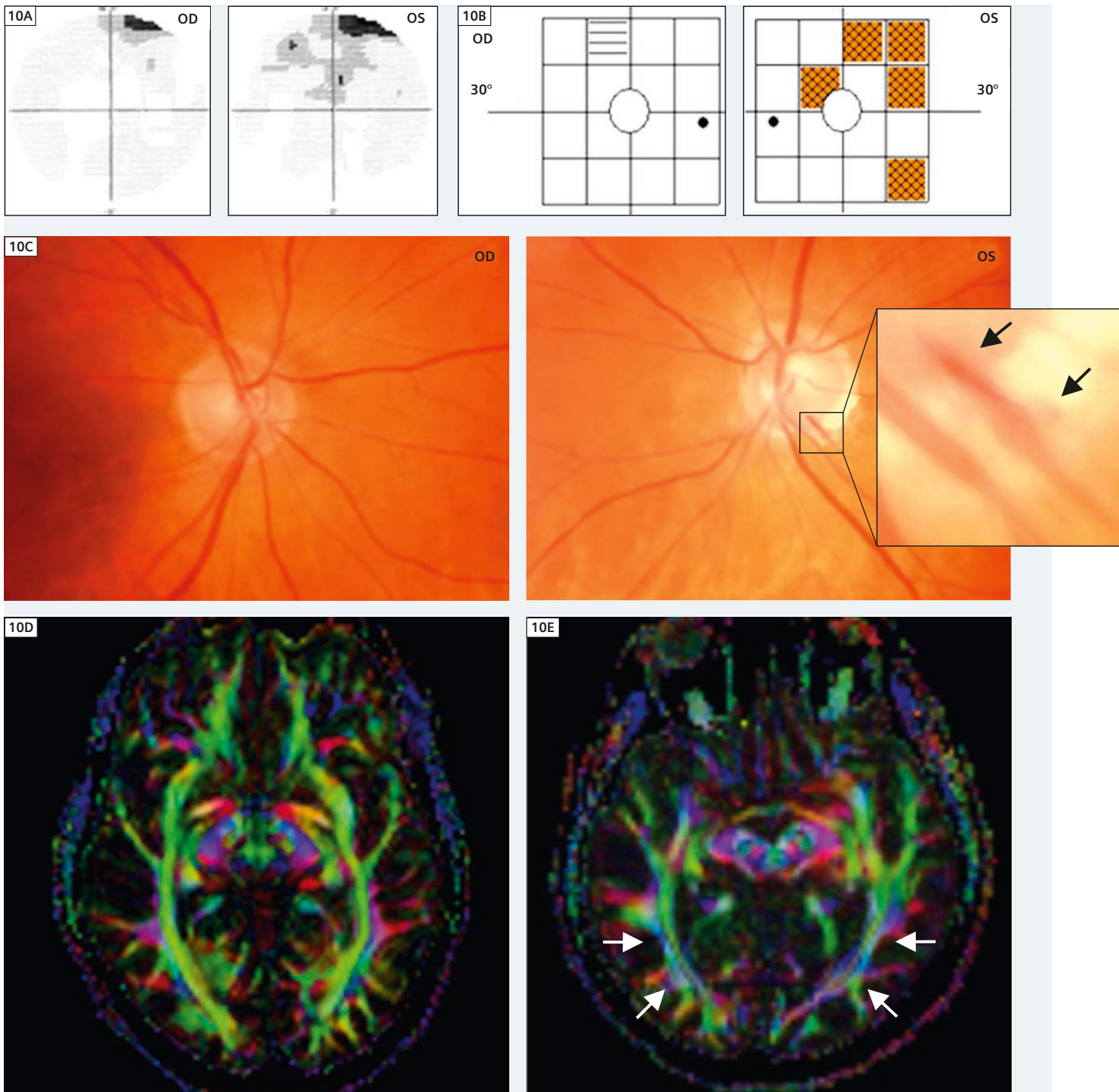
Correlations were found for the presence/absence of rarefied optic radiation and the stage of optic nerve atrophy (Fig. 10). One-tailed analysis of data revealed a correlation of the stage of optic nerve atrophy with the presence of rarefied optic radiation (Kendall tau-b = 0.272;  $P < 0.05$ ). The homonymous visual field defect scores were related to the corresponding rarefaction

of the optic radiation ( $P < 0.05$ ).

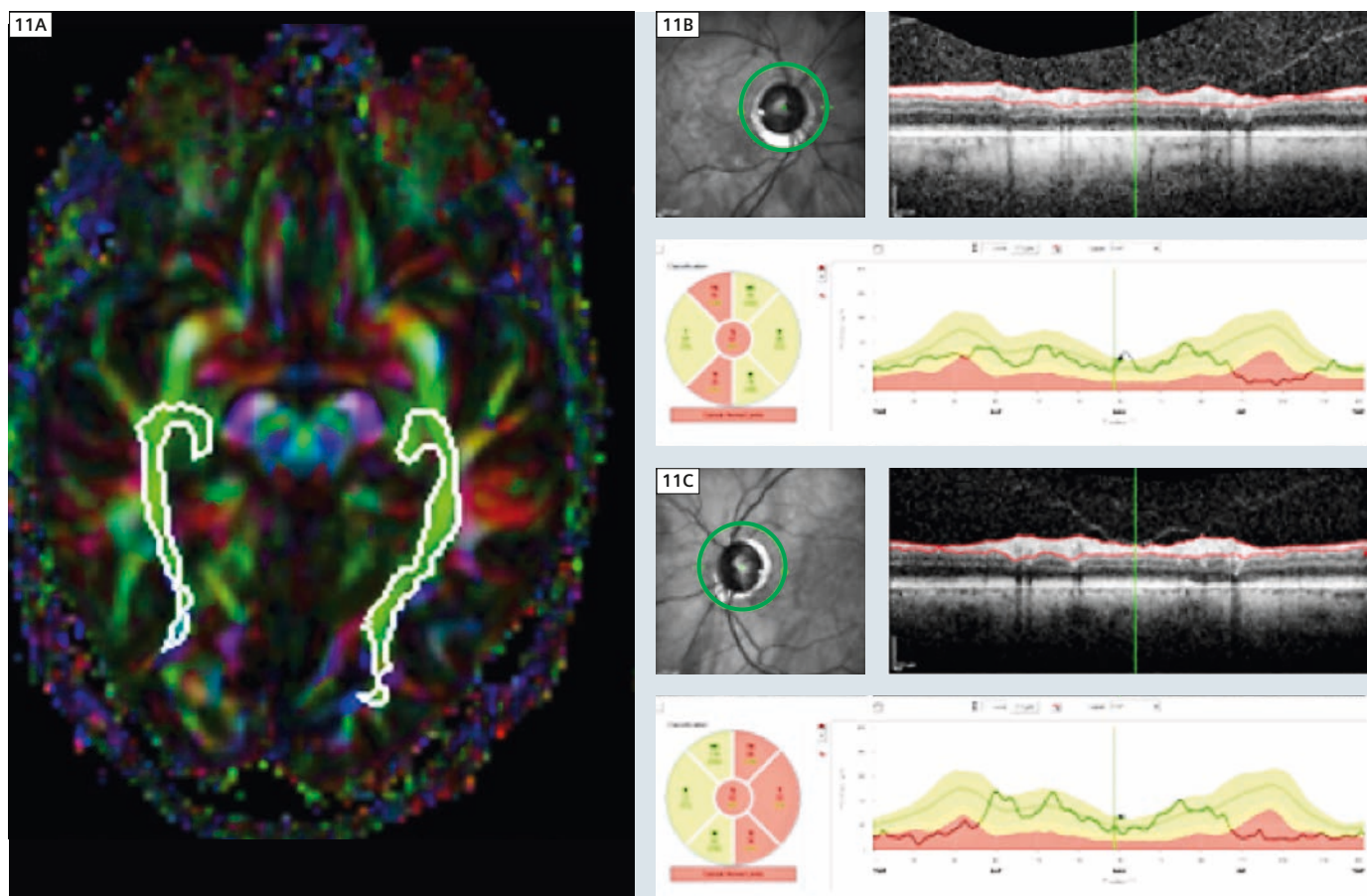
Analogously to volumetric analysis, there was high correlation between decrease in FA measured and the extent of optic nerve atrophy and spatiotemporal contrast sensitivity of the retina ( $r > 0.81$ ). Aside, there was high correlation between atrophy of the retinal fiber layer measured with optical coherence tomography (Fig. 11) and a decrease in FA and an increase in RD (Fig. 12).



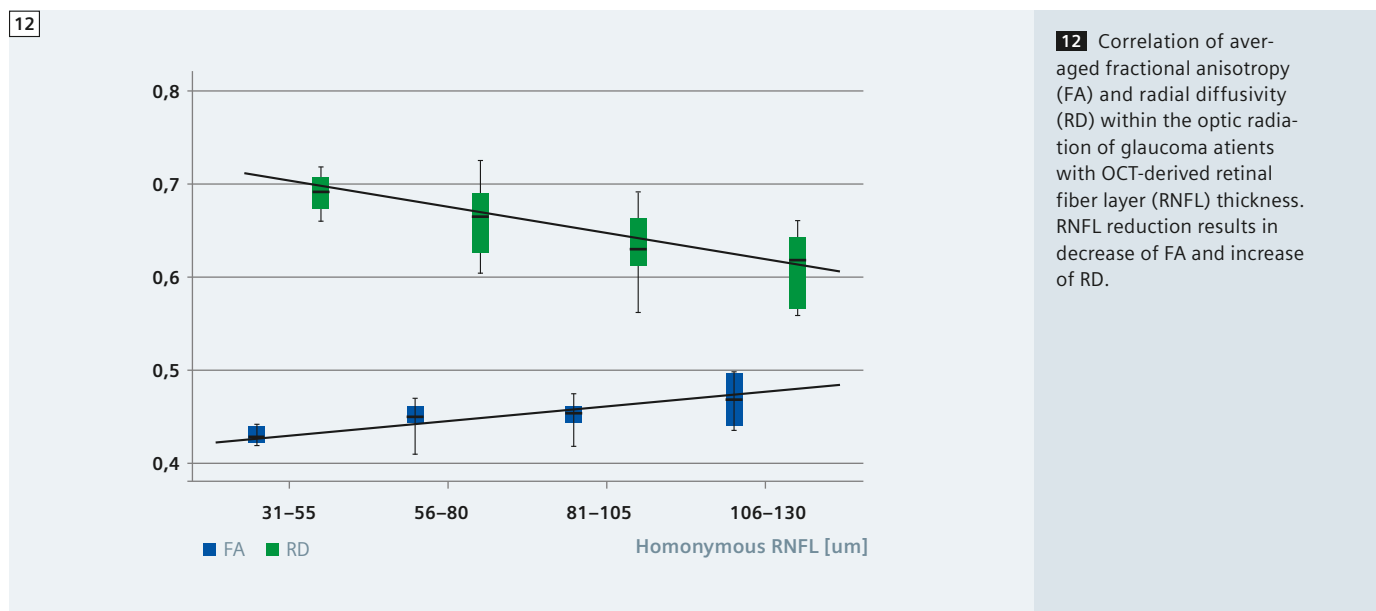
**9** Optic radiation of the reference subject (9A) and the significant optic radiation voxels based on the analysis of fractional anisotropy (9B), radial diffusivity (9C) and mean diffusivity (9D) in the presence of glaucoma (6). The significant regions are marked and the color code is as follows: red, control group's mean value greater than glaucoma group's mean value with  $p$ -value  $< 0.05$ ; yellow, control group's mean value greater than glaucoma group's mean value with  $p$ -value  $< 0.05$ ; green, control group's mean value less than glaucoma group's mean value with  $p$ -value  $< 0.05$ ; cyan, control group's mean value less than glaucoma group's mean value with  $p$ -value  $< 0.05$ . From El-Rafei et al. *Magn Reson Imaging* 2011 [10].



**10** 68-year-old female patient, OD/OS with primary open angle glaucoma, in OS a parapapillary bleeding of the optic nerve head. **(10A)** In both eyes (OS [left] > OD [right]) the automated perimeter showed predominantly superior visual field defects due to a loss of axons of the 3<sup>rd</sup> neuron. **(10B)** The frequency doubling test indicated impaired spatial-temporal contrast sensitivity primarily in OS in the superior and temporal area as well as nasal near the center. **(10C)** Typical signs of glaucomatous optic nerve atrophy were recorded by a non-mydratic fundus camera that is in OS a small rim area, smaller inferior rim than temporal and a parapapillary bleeding (arrows). **(10D)** DTI shows intact optic radiation in a healthy 67-year-old woman without any visual disturbances. **(10E)** DTI reveals significant rarefaction of the optic radiation compared to the age-matched control (arrows). DTI, diffusion tensor imaging; OD, right eye; OS, left eye. From Engelhorn et al. *Acad Radiol* 2011 [9].



**11** 49-year-old male patient with primary open angle glaucoma and significant reduction of optic radiation (**11A**). Optical coherence tomography (OCT) demonstrates correlating reduction of retinal nerve fiber layer (RNFL) of both eyes, i.e. the 1<sup>st</sup> and 2<sup>nd</sup> neurons of the optic pathways (**11B, C**).



**12** Correlation of averaged fractional anisotropy (FA) and radial diffusivity (RD) within the optic radiation of glaucoma patients with OCT-derived retinal fiber layer (RNFL) thickness. RNFL reduction results in decrease of FA and increase of RD.

## Conclusion and clinical implications

Using DTI at 3 Tesla, the intracranial optic fibers were assessed *in vivo* non-invasively by volumetric analysis and by calculation of diffusion coefficients within the optic nerve and the optic radiation.

Based on volumetric analysis, we could demonstrate that

- 1) there is ongoing physiological atrophy of the optic radiation with increasing age and
- 2) that there is significant pronounced atrophy of the optic radiation in glaucoma patients with
- 3) good correlation to the extent of optic nerve atrophy whereas morphological MRI sequences do not show pathological findings.

Aside, FA measurement in different sections of the visual pathways is feasible, and

- 4) there is also significant physiological decrease in FA with increasing age;
- 5) compared to age-matched controls, FA is significantly decreased in the intracranial part of the optic nerve and in the optic radiation in glaucoma patients; and
- 6) there is a high correlation between the decrease in FA and the severity of optic nerve atrophy and retinal impairment. In contrast to volumetric analysis, there is a significant change in FA even at the very early stage of glaucoma.

Hence, DTI with calculation of diffusion coefficients is a sensitive tool for early diagnosis of glaucoma and therapy monitoring. In addition

- 7) the approach for automatic segmentation of the optic radiation and analyzing diffusion coefficients seems to be robust and is clearly faster compared to manual segmentation.

<sup>1</sup>Mathcad and PASW are not Siemens Healthcare products. Siemens bears no responsibility for these products including, but not limited to, its regulatory status.

### References

- 1 Quigley HA, Broman AT. The number of people with glaucoma worldwide in 2010 and 2020. *Br J Ophthalmol* 2006; 86:63–70.
- 2 Gupta N, Yuecel YH. What changes can we expect in the brain of glaucoma patients? *Surv Ophthalmol* 2007; 52:S122–S126.
- 3 Gupta N, Ang LC, Noel de Tilly L, et al. Human glaucoma and neural degeneration in intracranial optic nerve, lateral geniculate nucleus, and visual cortex. *Br J Ophthalmol* 2006; 90:674–678.
- 4 Staempfli P, Riemmueller A, Reischauer C, et al. Reconstruction of the human visual system based on DTI fiber tracking. *J Magn Reson Imaging* 2007; 26:886–893.
- 5 Taoka T, Sakamoto M, Iwasaki S, et al. Diffusion tensor imaging in cases with visual field defect after anterior temporal lobectomy. *AJNR Am J Neuroradiol* 2005; 26:797–803.
- 6 Shimony JS, Burton H, Epstein AA, et al. Diffusion tensor imaging reveals white matter reorganization in early blind humans. *Cereb Cortex* 2006; 16:1653–1661.
- 7 Basser PJ, Mattiello J, LeBihan D. MR diffusion tensor spectroscopy and imaging. *Biophys J* 1994; 66:259–267.
- 8 Engelhorn T, Haider S, Michelson G, Doerfler A. A new semi-quantitative approach for analysing 3T diffusion tensor imaging of optic fibres and its clinical evaluation in glaucoma. *Acad Radiol* 2010; 17:1313–1316.
- 9 Engelhorn T, Michelson G, Waerntges S, Struffert T, Haider S, Doerfler A. Diffusion tensor imaging detects rarefaction of optic radiation in glaucoma patients. *Acad Radiol* 2011; 18:764–769.
- 10 El-Rafei A, Engelhorn T, Wärrntges S, Dörfler A, Hornegger J, Michelson G. A framework for voxel-based morphometric analysis of the optic radiation using diffusion tensor imaging in glaucoma. *Magn Reson Imaging* 2011; 29:1076–1087.
- 11 Engelhorn T, Michelson G, Waerntges S, Hempel S, El-Rafei A, Struffert T, Doerfler A. A New Approach to Assess Intracranial White Matter Abnormalities in Glaucoma Patients Changes of Fractional Anisotropy Detected by 3T Diffusion Tensor Imaging. *Acad Radiol* 2012; 19:485–488.
- 12 Michelson G, Wärrntges S, Engelhorn T, El-Rafei A, Hornegger J, Dörfler A. Integrity/Demyelination of the optic radiation, morphology of the papilla, and contrast sensitivity in glaucoma patients. *Klin Monbl Augenheilkd* 2012; 229:143–148.
- 13 Michelson G, Engelhorn T, Wärrntges S, El Rafei A, Hornegger J, Doerfler A. DTI parameters of axonal integrity and demyelination of the optic radiation correlate with glaucoma indices. *Graefes Arch Clin Exp Ophthalmol* 2013; 251:243–253.
- 14 Engelhorn T, Michelson G, Waerntges S, Otto M, El-Rafei A, Struffert T, Doerfler A. Changes of radial diffusivity and fractional anisotropy in the optic nerve and optic radiation of glaucoma patients. *TSWJ* 2012 April [Epub ahead of print]
- 15 Hsu JL, Leemans A, Bai CH, et al. Gender differences and age-related white matter changes of the human brain: a diffusion tensor imaging study. *Neuroimage* 2008; 39:566–577.

### Contact

Prof. Tobias Engelhorn, M.D.  
Department of Neuroradiology  
University Hospital Erlangen  
Schwabachanlage 6  
D-91054 Erlangen  
Germany  
Phone: +49-9131-8544824  
Fax: +49-9131-8536179  
tobias.engelhorn@uk-erlangen.de

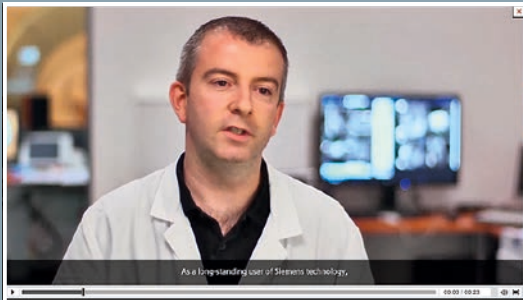
# What's your favorite Dot Feature?

Dot (Day optimizing throughput) is the most comprehensive MRI workflow solution, and it helps take the complexity out of MRI. Dot has now established itself in the field and our customers have told us what they like best about Dot:



“Within our environment, we just could not provide a cardiac MRI service without the Cardiac Dot Engine.”

**Dr. Russell Bull, MRCP, FRCR**  
Consultant Radiologist  
*Royal Bournemouth Hospital, Bournemouth, UK*



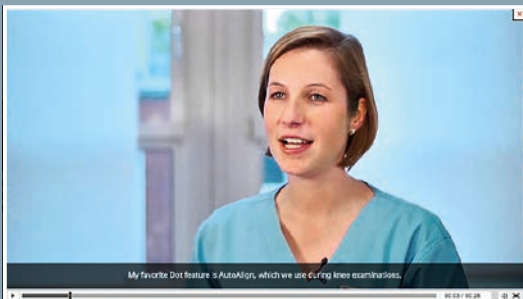
“The Dot Decisions functionality in Abdomen Dot has enabled us to schematize and simplify these protocols. With Dot, we can now ensure our examinations are far more reproducible and of excellent quality.”

**Arnaud Lambert**  
Technologist  
*Imagerie Médicale Saint Marie, Osny, France*



“Cardiac Dot (Engine) allows us to obtain automatic positioning of the main slices necessary to evaluate cardiac function with a high degree of reproducibility.”

**Professor Philippe Cluzel, MD, PhD**  
*Service de Radiologie Polyvalente Diagnostique et Interventionnelle Hôpital Pitié-Salpêtrière, Paris, France*



“AutoAlign is helpful especially for colleagues who rarely perform knee examinations because the slices are positioned automatically, which saves a lot of time. Furthermore, our knee examinations have become reproducible.”

**Linda Willeke**  
Technologist  
*St. Franziskus Hospital, Münster, Germany*

Experience a Dot workflow yourself and hear from more customers at

**[www.siemens.com/Dot](http://www.siemens.com/Dot)**

Dot is now available for 3T MAGNETOM Skyra and MAGNETOM Verio and for 1.5T MAGNETOM Aera and MAGNETOM Avanto.

Visit our site  
optimized for  
tablets and  
smartphones



# Case Study:

## Murray Valley Encephalitis (MVE)

Jan Neal

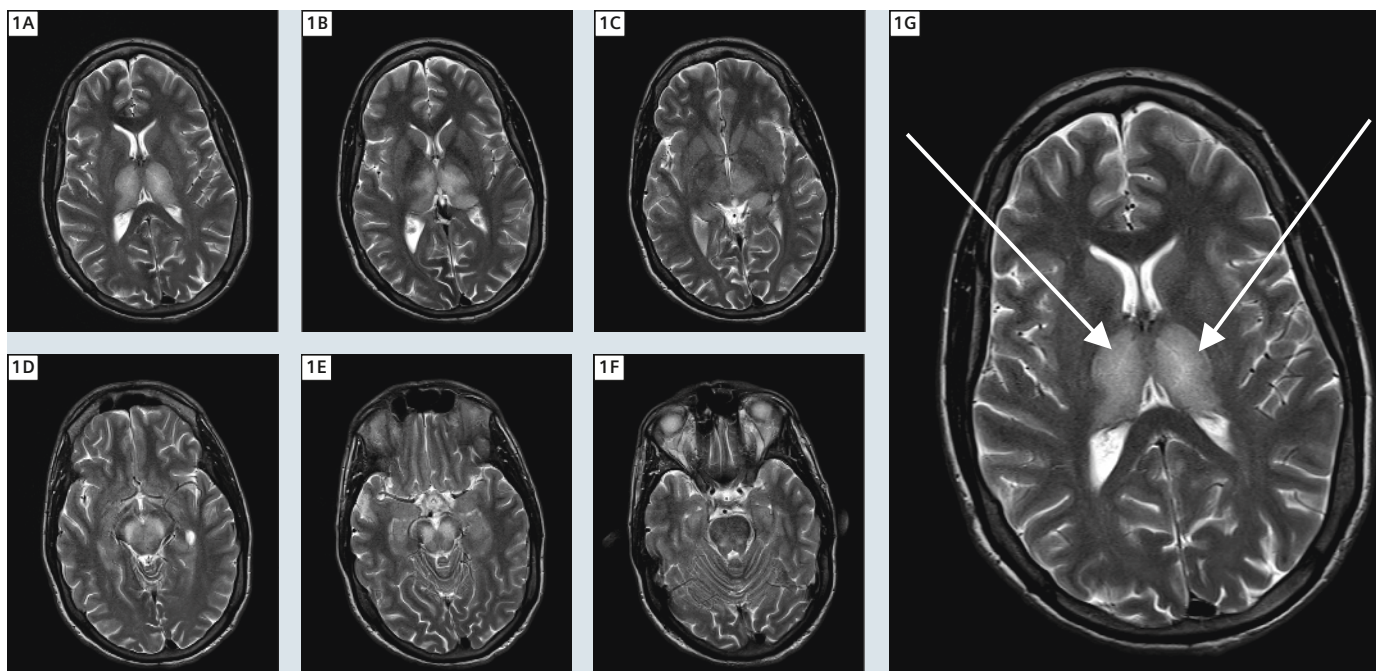
Benson Radiology, Adelaide, Australia

### Introduction

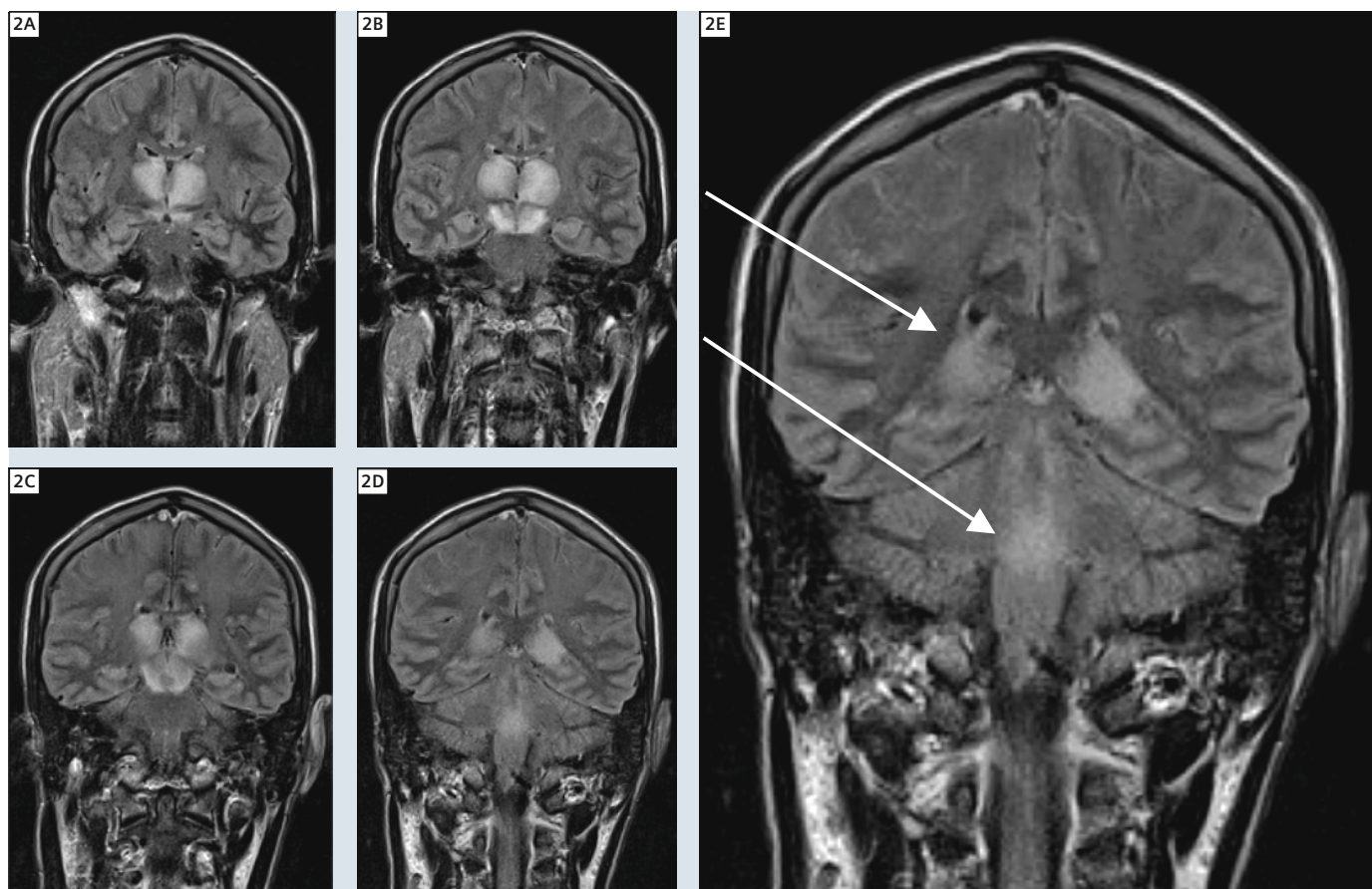
Murray Valley Encephalitis (MVE) is caused by infection with a flavivirus belonging to the Japanese encephalitis (JE) antigenic complex, which also includes St. Louis encephalitis (StLE) and West Nile (WN) virus. The MVE virus occurs in Australia, New Guinea, and probably islands in the eastern part of Indonesia [1]. MVE virus is believed to be maintained in a natural cycle involving water birds and *Culex annulirostris* mosquitos. The natural transmission cycle of the JE group involves infection of a mosquito vector alternating with viral amplification in a variety of

vertebrae hosts. Human disease is incidental to this cycle. Only one in 1,000 to 2,000 infections results in clinical illness resembling JE [1]. They are neurotropic viruses, which cause illness with headache, fever, vomiting followed by drowsiness, mental confusion and in severe cases there may be hyperactive reflexes, spastic paresis, seizures, coma and death. These viruses are becoming increasingly important globally as their geographic ranges steadily increase [2]. MR imaging (MRI) is more sensitive than computed tomography (CT) for detecting

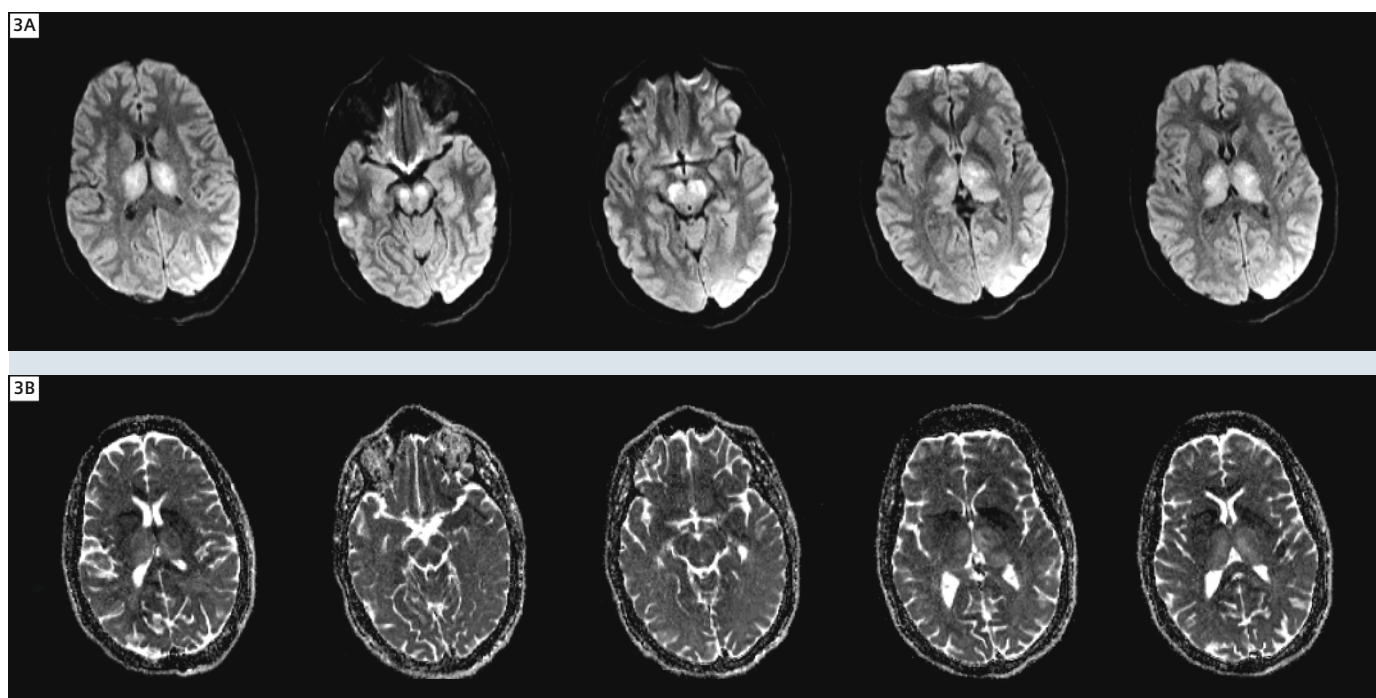
MVE-associated abnormalities such as changes in the thalamus, basal ganglia, midbrain, pons and medulla. When clinically correlated these changes can be specific to JE but not very sensitive. Mortality among hospitalized patients is about 20–30%. About half of the survivors have residual neurological deficits [2]. There is no vaccine for MVE virus. Prevention relies on mosquito control and avoidance of mosquito bites. There have been no human cases of MVE infection in South Australia for over 30 years.



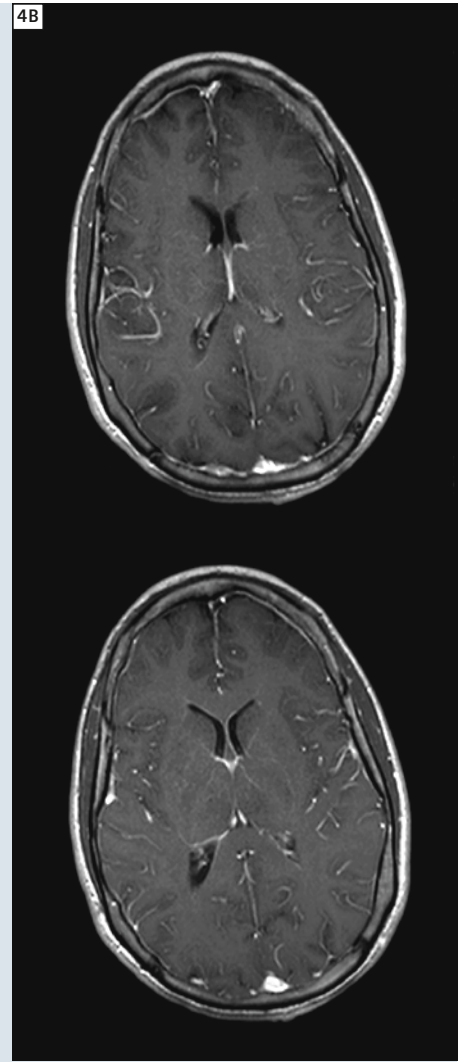
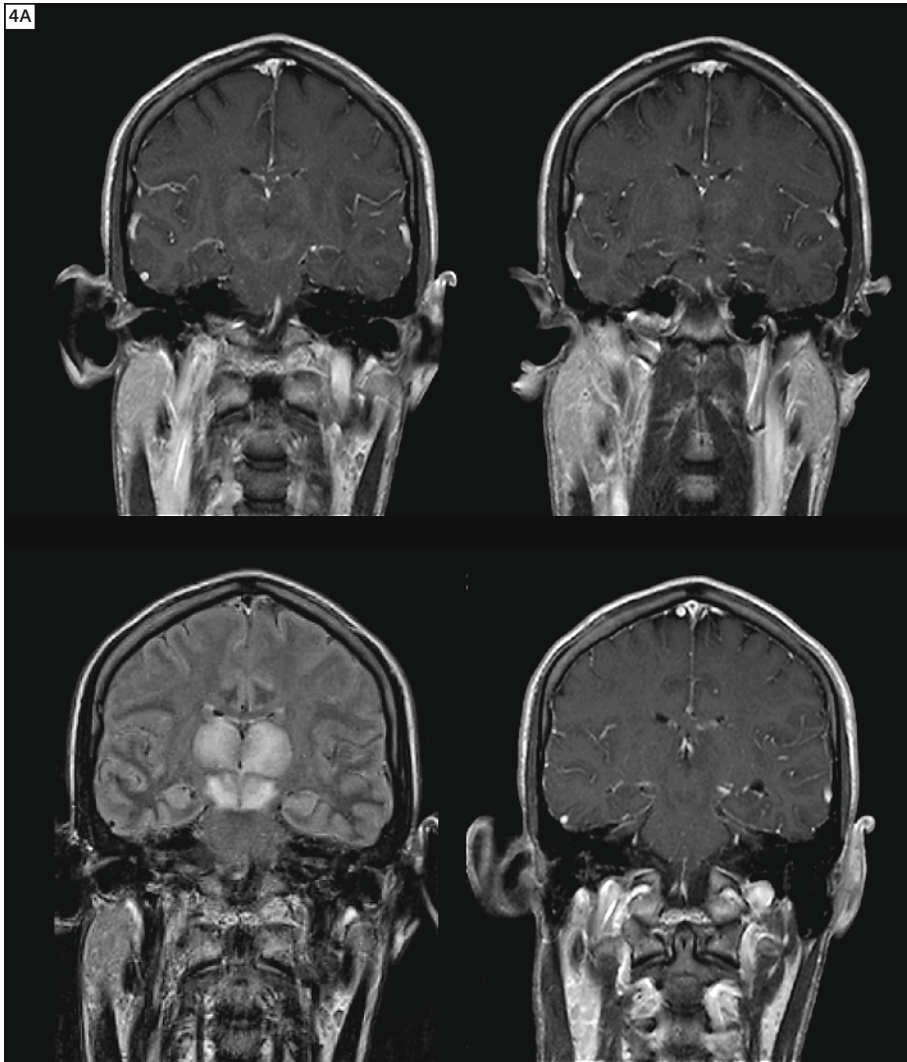
**1** T2-weighted axial images. Abnormal bilateral and symmetric hyperintense signal to central deep grey matter structures including the thalami, substantia nigra, dorsal midbrain and pons.



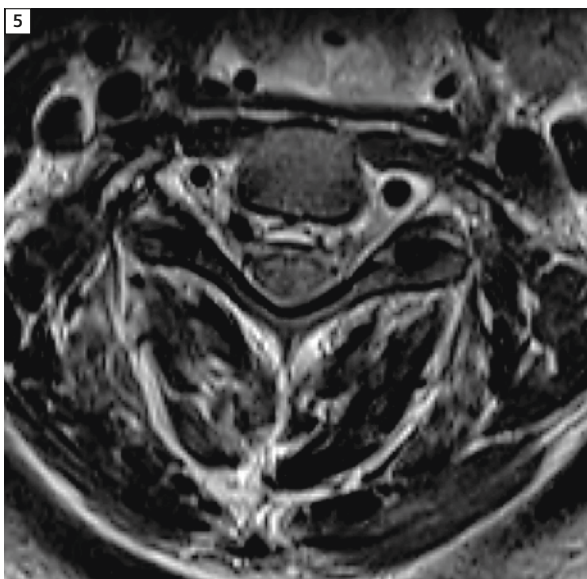
**2** FLAIR coronal images showing abnormal hyperintense signal as seen in Figure 1. T1w images show corresponding hypointense signal.



**3** Diffusion b1000 trace images (3A) and ADC images (3B). These images do not show restricted diffusion. Therefore this is not an acute infarct.



**4** Post contrast imaging, T1w coronal (3<sup>rd</sup> image is a T2w coronal showing the enhancement not evident post contrast) (4A) and T1w axial (4B) showing no enhancement. Pattern, lack of enhancement and the clinical picture do not suggest tumor.



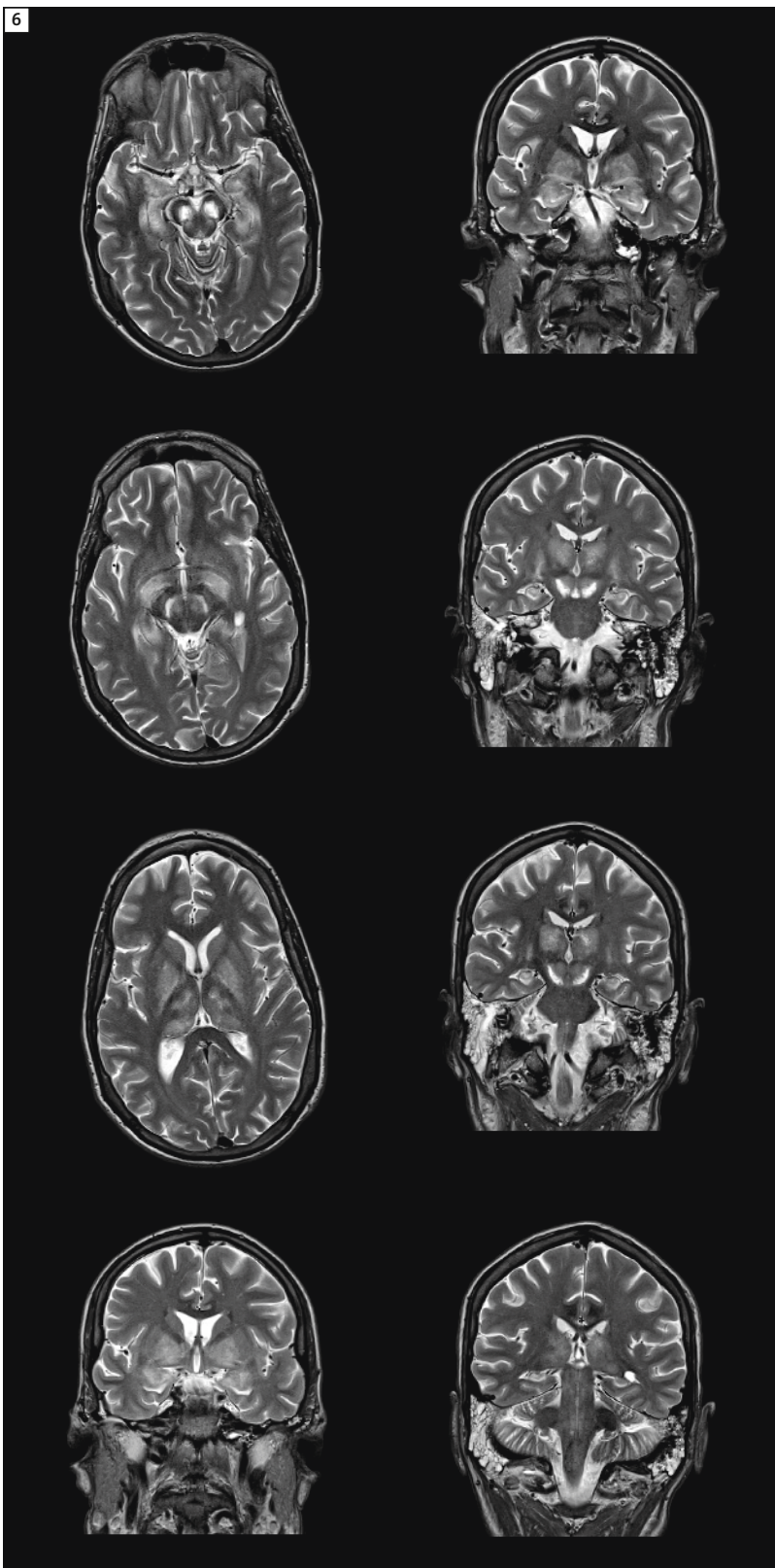
**5** T2w axial image of the cervical spine shows subtle high signal changes involving the anterior portion of the cervical cord.

## Patient history

A 26-year-old male was admitted to intensive care unit with respiratory failure. MRI head is requested.

## Sequence details

MRI examination was performed on a Siemens 1.5T MAGNETOM Avanto system, using the head coil. Standard pre and post contrast sequences were acquired. Pre contrast PD/T2-weighted axial, T1w axial, T1w sagittal, FLAIR coronal, diffusion-weighted scans, MR venography and post contrast T1w axial and coronal images were acquired.



**6** After 5 weeks the patient remained ventilated with no signs of neurological improvement. Repeat MRI Brain and c. spine performed. This showed no improvement, there has, in fact, been significant progression of gross abnormal signal intensity with new involvement of the globus pallidus and medial temp lobe.

## Imaging findings

MRI of the brain showed grossly abnormal appearances of the thalami, substantia nigra and dorsal aspect of the brainstem. Given the lack of restricted diffusion and no enhancement a tumor or Herpes Simplex virus (HSV) encephalitis were ruled out. Remainder of the brain was normal. Differential diagnosis would include metabolic processes (osmotic myelinolysis). Correlating to the patient's clinical history it was not felt likely in this case. So an underlying infective aetiology particularly flavivirus infection such as MVE is favored. [3]

## Conclusion

MRI is an excellent clinical tool to aid in the diagnosis of MVE. The classic MR appearance of this virus can assist in expediting the diagnosis. Blood testing must be done in interstate laboratories and can take some time for results to be returned.

## References

- 1 Mackenzie JS, Lindsay MD, Coelen RJ, et al. Arboviruses causing human disease in the Australasian zoogeographic region. *Arch Virol* 1994; 136:447.
- 2 Einsiedel L, Kat E, Ravindran J, et al. MR Findings in Murray Valley Encephalitis. *AJNR Am J Neuro-radiol* 24:1379-1382, August 2003.
- 3 From the radiology report by Dr. S. Knox, Consultant Radiologist, Benson Radiology.



## Contact

Jan Neal, Grad Dip MRT  
Benson Radiology  
Adelaide  
South Australia  
jan.neal@bensonradiology.com.au

# Neuroimaging of Stroke.

## The Complementary Roles of CT and MRI

Karl-Olof Lövblad; Vitor Mendes Pereira

*Hôpitaux Universitaires de Genève, Department of Diagnostic and Interventional Neuroradiology, Geneva, Switzerland*

### Abstract

Cerebral ischemia or stroke is now considered a treatable medical emergency. This has created the need for powerful diagnostic tools for its determination with accuracy. Computed tomography (CT) and Magnetic resonance imaging (MRI) have known great technological improvements that have paralleled the clinical successes with treatment modalities. While overall equivalent, both techniques have their pros and cons and tend to be more and more accepted as complimentary techniques that may be used either alone or sequentially depending on the question that is being asked. This paper deals with their use alone and in combination for the diagnosis.

### Introduction

Cerebral ischemia and its resultant pathology, stroke, is one of the leading causes of morbidity and mortality in industrialized countries. This is in part

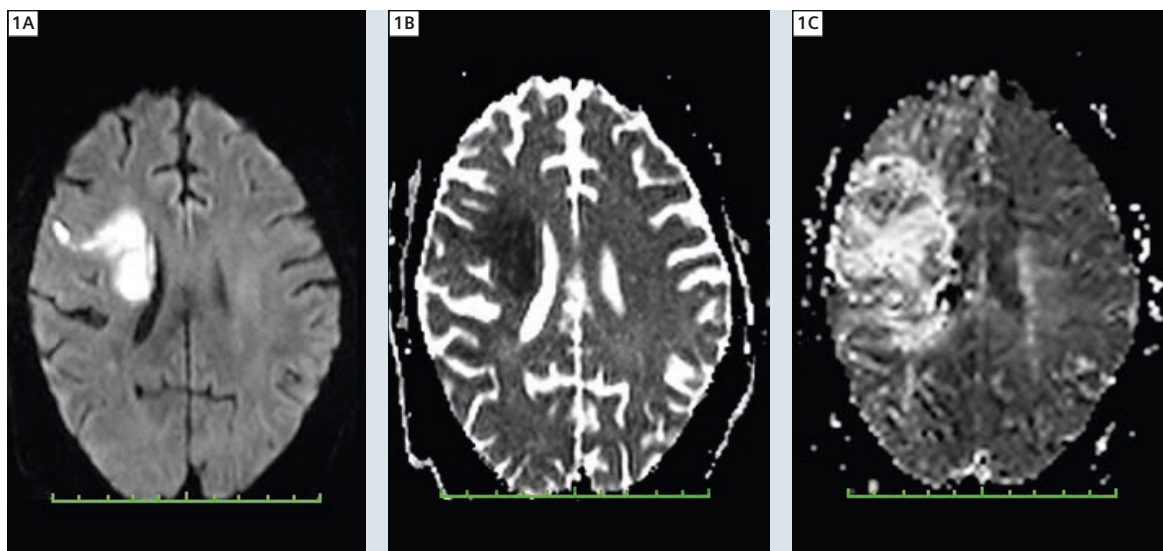
due to the fact that it shares common causes with cardiovascular diseases such as arteriosclerosis among others. While stroke was for a long time considered an untreatable entity for which there was no treatment and where the only outcome at best was a long and difficult period in rehabilitation, over the last two decades, parallel advances in both therapies and imaging have provided the clinician with new options when confronted with these patients.

The main objective when confronted with a patient who has acute signs referable to a possible stroke is to exclude another possible pathology that could cause identical symptoms [1].

In the emergency situation, imaging has to perform many roles while being short and not interfering with the time window: it has to exclude another pathology (primarily hemorrhage), detect ischemia, demonstrate occlusion, show

hypoperfusion and eventual penumbra and finally determine hemorrhagic risk and eventual outcome.

Since its introduction in the 70's, computed tomography has always played an important role in the management of patients with neurological diseases [2, 3]. Initially for patients with acute symptoms it was mainly used to exclude a very clear cause of neurological dysfunction such as cerebral hemorrhage. However, as knowledge and experience with the use of CT has increased, it has proved itself to be a very powerful tool in experienced hands (or eyes) [4]: one can see early signs of loss of differentiation between white and grey matter as well as signs of sulcal effacement that will eventually precede hypodensity; hypodensity will correspond to the accumulation and increase in water content in the tissue. Frank hypodensity when encompassing more than 33% of the MCA territory



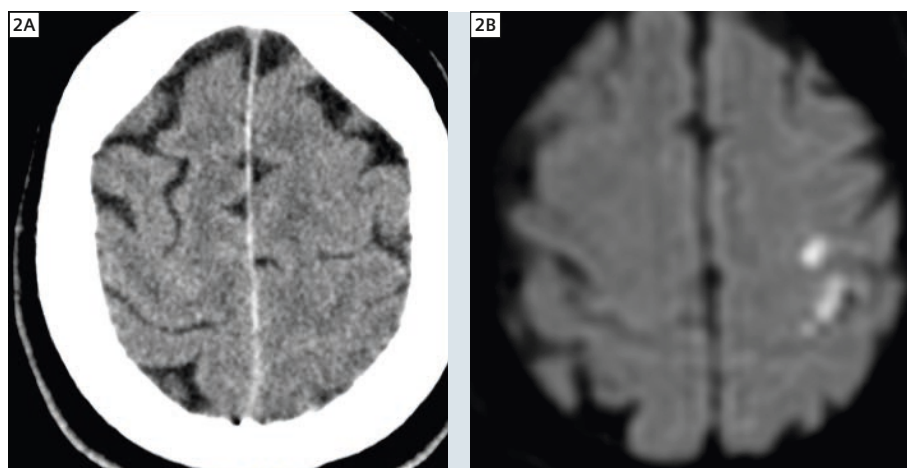
**1** Patient with left-sided weakness: there is a right-sided hyperintensity on the DWI image corresponding to ischemia (1A) along with a decrease in the ADC (1B), as well as hypoperfusion (1C). The difference between the diffusion lesion and the perfusion area corresponds to the penumbra.

was found to be a contra-indication to the administration of thrombolysis since there was a subsequent increase in mortality [5].

After the publication of the initial NINDS thrombolysis trial [6], as well as the ECAS trial [7], intravenous thrombolysis slowly became accepted as a standard of care for patients with acute stroke. It had the main drawback that therapy was initially considered to be effective only 3 hours after symptom onset (considered to be the 'therapeutic window'). This had two impacts. The first was to look for a way of not just diagnosing but of certifying that one was treating a patient with acute stroke: thus began a new era for neuroimaging to become a marker for acute stroke. The second was to search for more effective drugs and to try to expand the therapeutic window. Recent evaluation of thrombolysis data has shown that for rTPA at least the therapeutic window is now 4.5 hours [8]. Also there is mounting evidence that mechanical non pharmacological may be performed with improved outcomes [9].

## The imaging revolution

During the 90's the first real revolution was the clinical implementation of echoplanar imaging capable scanners [10] that would thus allow diffusion [11] and perfusion imaging [12] techniques to move into the clinical arena. This led to the capacity of performing whole brain datasets demonstrating both diffusion lesion and perfusion deficit [13] (Fig. 1). Diffusion imaging relies on the capacity of a diffusion sequence to demonstrate changes in water distribution between the intra- and extra-cellular compartments that may occur in stroke [14]: on the so-called diffusion-weighted images (DWI) this is associated with a signal increase that can be quantified by assessing the maps of the apparent diffusion coefficient (ADC) that are usually generated at the same time. Initially this led to great enthusiasm due to the high sensitivity [15] and specificity of DWI for stroke and it was even hoped that it might constitute the first step towards the equivalent of an ECG for cerebral ischemia [16]. A very simple MR protocol consists of



**2** Patient with right-sided weakness. The CT shows possible sulcal effacement in the left frontal lobe (2A). The diffusion image shows without doubt that there are many small hyperintense lesions (2B).

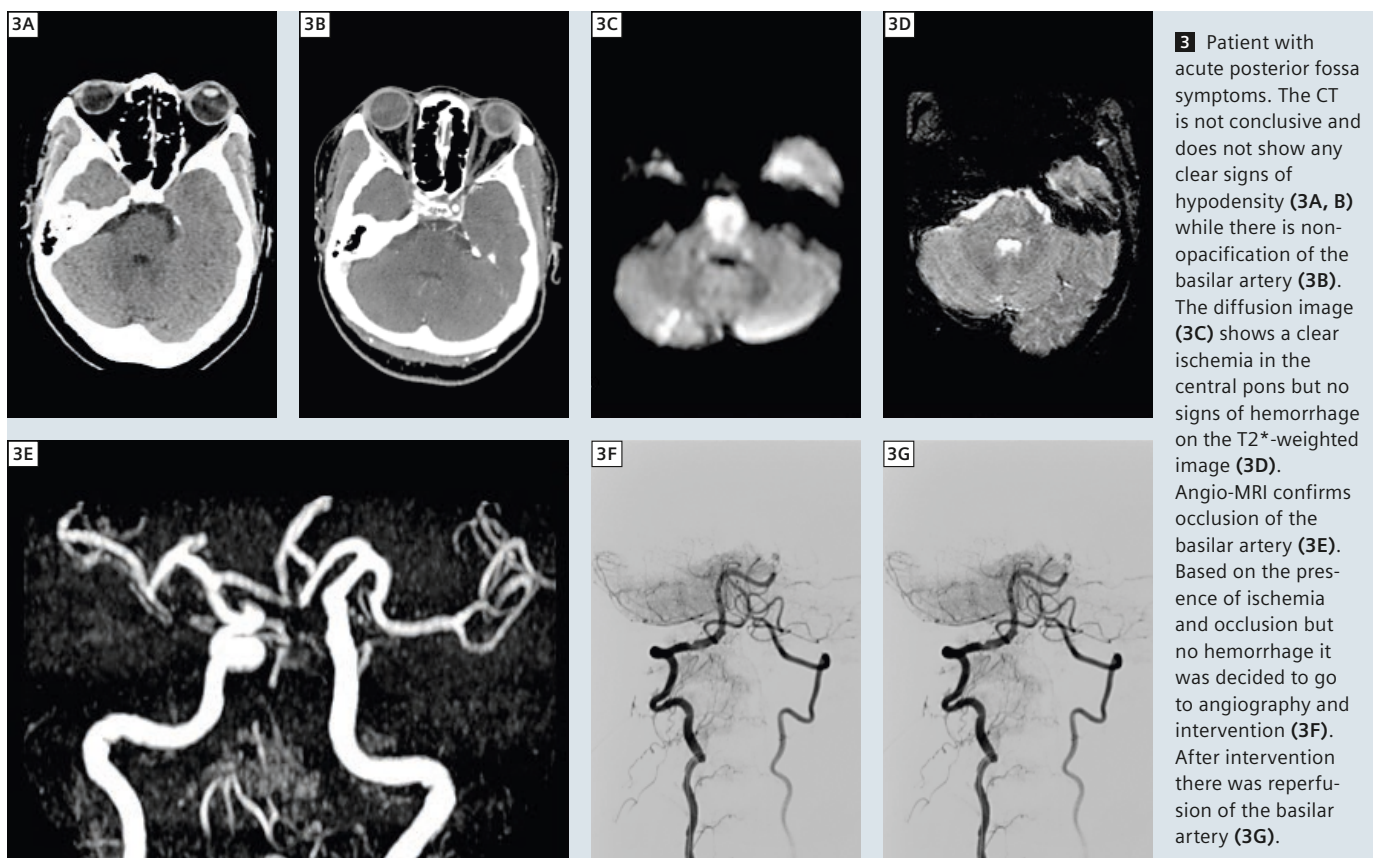
a T2-weighted image, a T2\*-weighted image a Time-of-flight (TOF) MR angiography (MRA) sequence and the diffusion and perfusion sequences, all of which can be done in 20 minutes or less. Computed tomography had also made some advances since its debut with the development of spiral scanning [16]. While this was initially applied to do examinations of the chest and abdomen, it set the standard for future potential uses in imaging of the neck vessels. Here it was the additional development of multi-slice scanners that allowed one to cover larger and larger areas in shorter times, thus enabling both implement accurate angio-CT of the head and neck vessels as well a brain CT perfusion imaging [17].

Due to a certain facility of use, CT became the leading technique. Indeed, along with some difficulties in its use (magnetic fields, claustrophobia, many sequences), MRI was also considered more difficult to read when it came to the detection of hemorrhage in inexperienced hands. Also, since its use is slightly less time consuming, it has been widely adopted for screening patients with acute stroke that are enrolled in clinical trials or even in clinical routine of thrombolysis protocols.

However, magnetic resonance imaging, due to its capacity to provide a better visual delineation of acute and especially

small infarcts [18] (Fig. 2), has become a preferred tool for drug trial where very often an accurate assessment of ischemic lesion volume is absolutely necessary in order to assess drug safety and efficacy [19].

After years of debate and controversy, it has finally been established that MRI can demonstrate hemorrhage probably as well as CT and is better at demonstrating ischemic lesions with DWI (Fig. 2). The penumbra concept, which has evolved substantially from its initial description, has been a cause of some controversy. Indeed, it was first a situation in which neuronal dysfunction was caused by decreased blood flow and thus cellular damage [20]. Since it was somewhat unclear in its scope and exact definition the area was called the penumbra. From this initial description of this entity, the clinical concept has evolved towards an imaging-driven one where the penumbra is seen as an area of hemodynamically impaired brain and not one of synaptic dysfunction. However since it is the hemodynamics that are at its basis, both kinds of penumbra – overall, or at least from a clinical point-of-view – can be considered the same in order to have a working hypothesis towards implementation of treatment. It is for this reason also that one prefers to speak about tissue at risk and not just about penumbra.



Initially the MR penumbra concept was based on a simple visual subtraction between the hypoperfused area and the smaller central initial DWI lesion. While rather imprecise and probably inexact, it provided the clinicians with an initially functioning model to use to monitor disease and interventions.

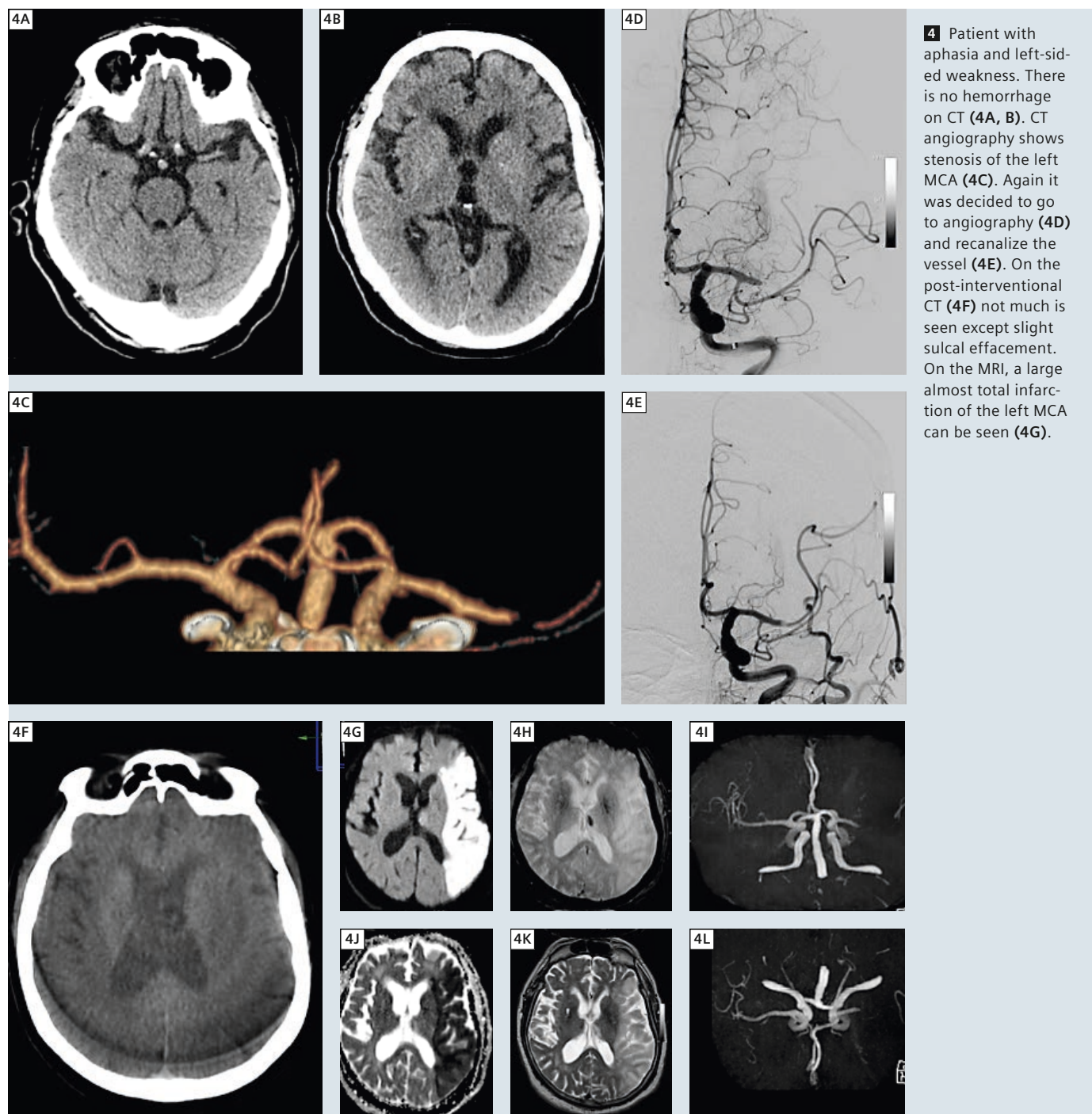
When considering the ischemic brain, one point that has always been considered elusive, at least with CT and MRI, has been the capacity to detect collateral flow. Indeed, since from a physiological point-of-view, a drop in blood flow is very quickly followed by neuronal death, perfusion is maintained at least by a collateral system of present. This is an observation that is very often made by interventional neuroradiologists, and an area where planar (CT and MRI) imaging has failed somewhat. However it is becoming increasingly evident that at least a partial image of collateral flow can be seen on post-contrast CT images where very often dilated collateral vessels will appear or on MRI where arterial

spin labeling (ASL) seems to be able to demonstrate at least in some instances the presence of collateral circulation. This may be especially relevant in cases that arrive at the hospital beyond the therapeutic window: indeed, in any case, based on imaging there may still be a potential tissue at risk, or little signs of secondary hemorrhage so that these patients may indeed benefit from the use of a non-pharmacological intervention. The typical case will be a patient arriving with symptoms after 5 hours where intravenous rTPA is thus contraindicated but where MRI reveals only a small lesion with a surrounding hypoperfusion: this candidate may be amenable to clot extraction and/or stenting based on imaging findings.

### The strengths of CT and MRI

A strength of magnetic resonance imaging is clearly its capacity to demonstrate even small lesions that will be often invisible or only visible to the trained eye.

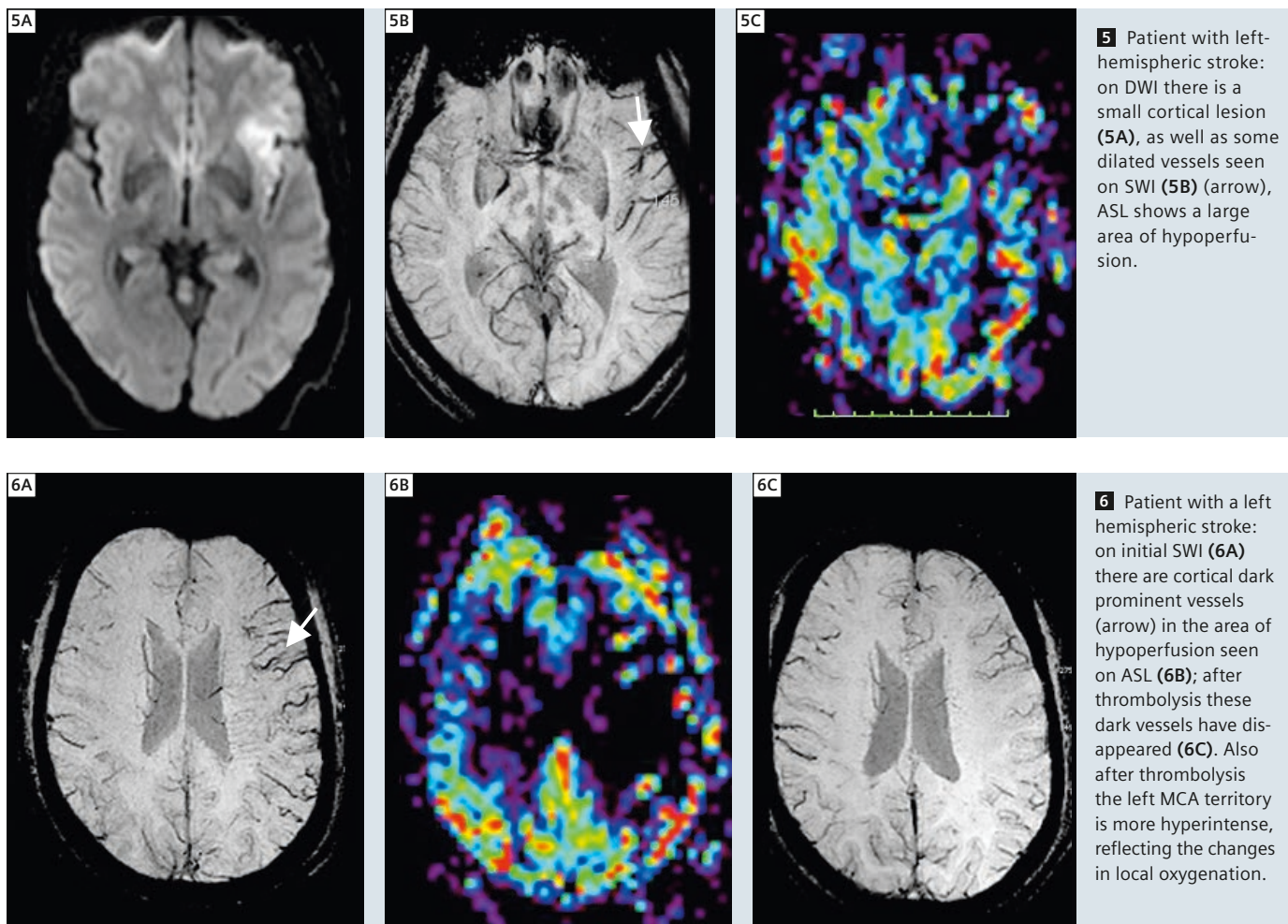
Magnetic resonance provides whole brain coverage with both diffusion and perfusion sequences; additional techniques such as ASL and susceptibility-weighted imaging (SWI) can provide unique information on the ischemic brain. Very often MRI can provide a diagnostic result in patients where the initial CT is not conclusive (Fig. 3). MRI also remains non-ionizing, which is of prime importance if one considers patients that require frequent follow-ups. This is why, even in patients who have had an initial CT, MRI is to be preferred for follow-up: on the second day DWI will be able to demonstrate the exact extent of the lesion and thus allow one to obtain a better delineation of the final lesion extent (Fig. 4). As already explained, arterial spin labeling is a technique using labeled blood as an endogenous tracer: this has been shown to produce images of cerebral blood flow but also shown able – at least in part – to obtain images containing information about collateral flow [21] (Fig. 5); this could be of advantage



in cases of strokes again beyond the therapeutic window and where the outcome could be improved by some kind of treatment. SWI, due to its inherently strong T2\* weighting, could help to demonstrate the well known venous stasis that is present in severe cases of stroke [22]; it can also demonstrate small bleeds better, and there have been

some instances where it has been shown to demonstrate changes referable to the altered oxygenation in these tissues [23] (Fig. 6). The use of higher fields such as 3T has enabled an improvement in perfusion techniques and the implementation of SWI and ASL clinically [24]. In addition, new high-resolution angiography techniques should allow one to

investigate the vessels both intra- and extracranially (Figs. 7 and 8). A CT is very often more accessible since there is no need to screen often unconscious or uncooperative patients for metallic implants; the room can also be entered more quickly by an emergency team that does not have to remove pens, scissors and wallets from their pockets



before placing the patient on the table. Also, until recently the gantries of CT scanners gave the team a better view of the often unstable and sometimes intubated patients so that they could be monitored more safely during the examination.

The typical situation where CT and MRI are both going to be necessary are the cases of less acute situations, where an initial CT and CT angiography (CTA) shows a lesion maybe not amenable to thrombolysis but which necessitates a more thorough work-up because of the underlying disease. This is the case in carotid disease, where patients either present with a stroke or with stroke-like symptoms. The initial CT may initially be normal despite the patient having certain clinical signs of acute stroke: in these cases going to MRI can be very helpful. This will be the case for small

cortical lesions. It will typically be the case in patients with severe carotid stenosis, where CT has often been done since CTA will provide the best delineation of vascular calcification, but where MRI can provide two additional findings: the demonstration of small ischemic emboli in the brain and local demonstration of the presence of plaque hemorrhage (Figs. 9 and 10).

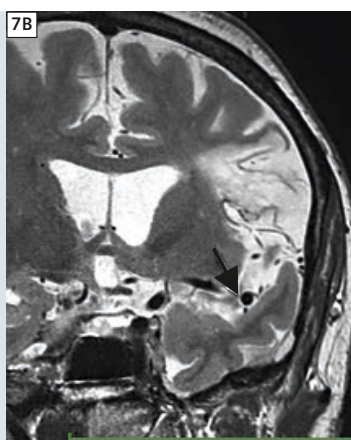
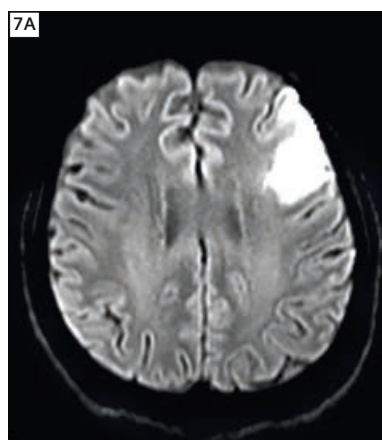
### Future perspectives

Whenever one considers the etiologies of stroke, local carotid plaque vulnerability is going to be a key factor. Thus, the idea of performing any kind of 'molecular' imaging that would allow to determine which plaque is more 'active' and more prone to eventually seed emboli is very seductive. This could be done either by MRI using either SPIO contrast materials, or even by conventional contrast

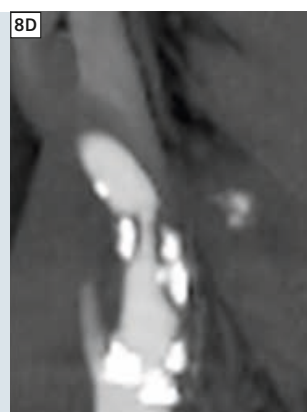
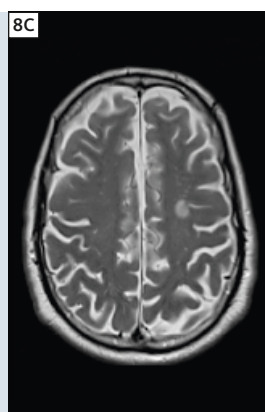
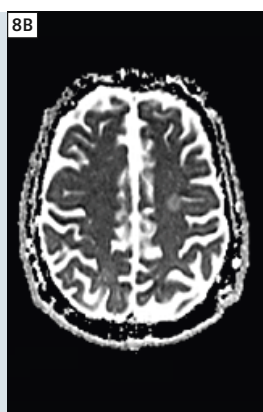
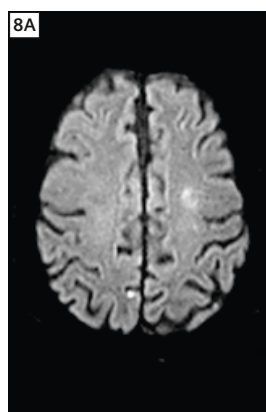
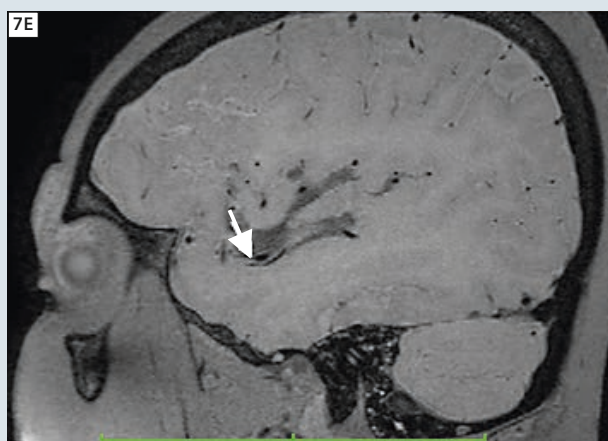
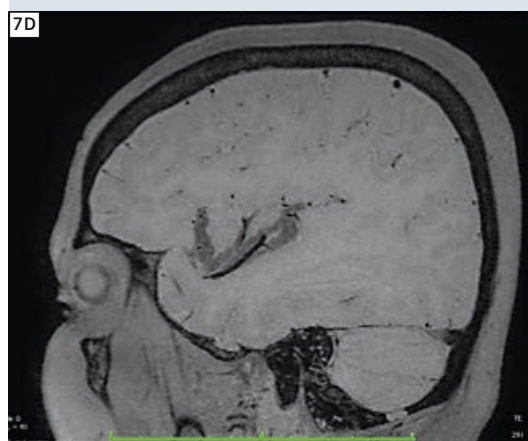
media or some combination of a nuclear medicine technique with a radiological method (CT or MRI) to produce combined hybrid imaging.

### Conclusions

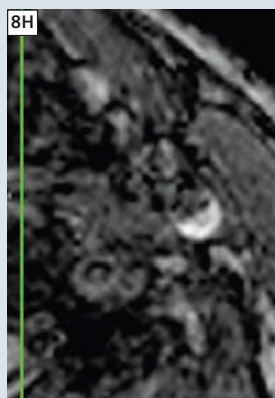
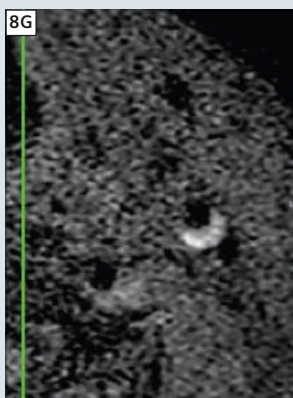
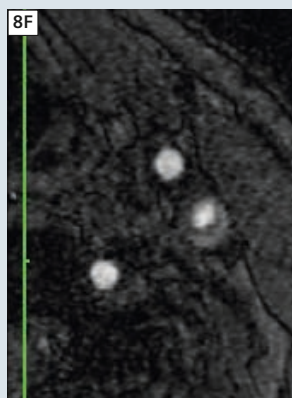
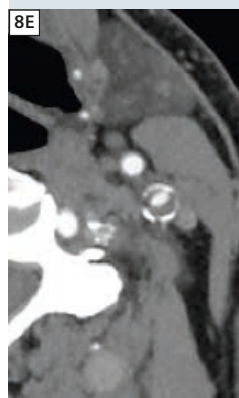
From a radiological point of view we are now at a crossroads where we deploy two advanced techniques, CT and MRI. These techniques are equally useful since they have complementary pros and cons: MRI is more sensitive to ischemia, but CT can more clearly demonstrate hemorrhage; CT angiography may provide a more correct lumino-graphic effect and demonstrate plaque calcification better. Both techniques can be utilized in first intention with almost comparable results, but this depends often on local logistics. However, in complex vascular situations it becomes increasingly clear that one needs both

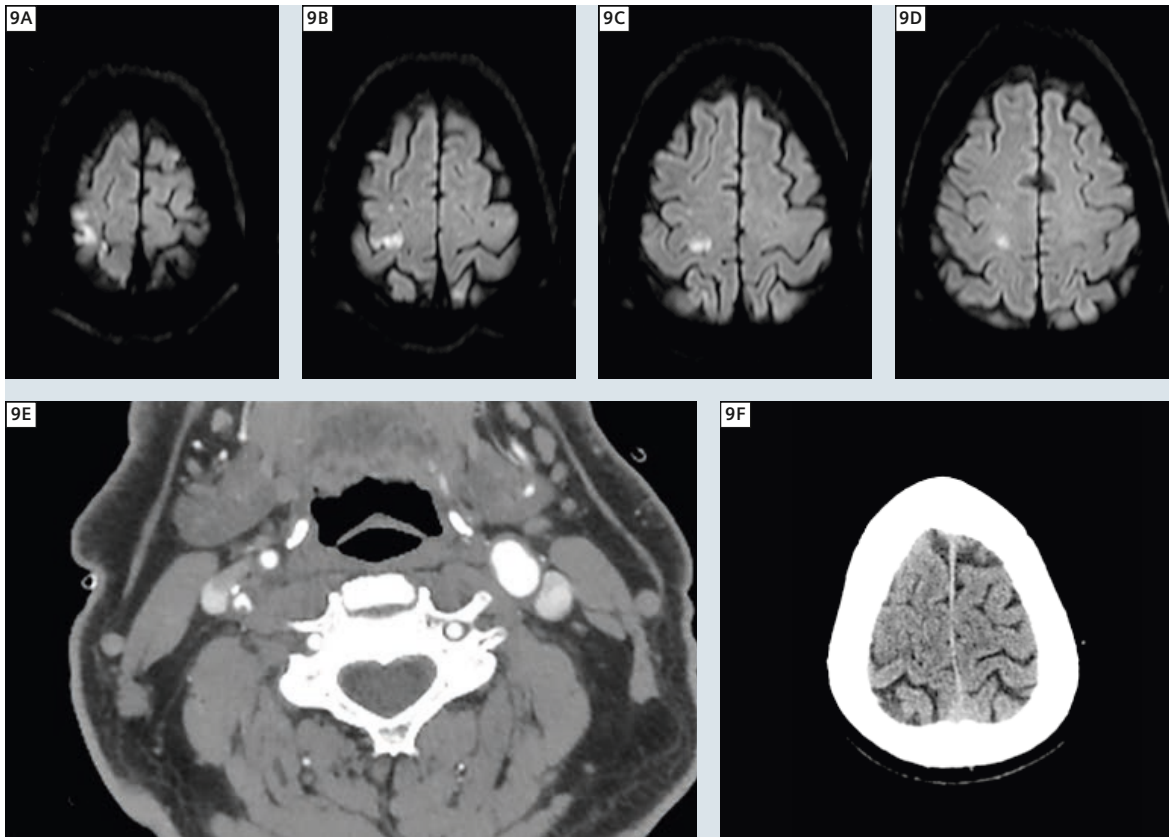


**7** Patient with an intracranial stenosis and a frontal opercular infarction on the left. The DWI image shows a left frontal lesion (7A) and the high resolution MRA images show the stenosis (arrows).

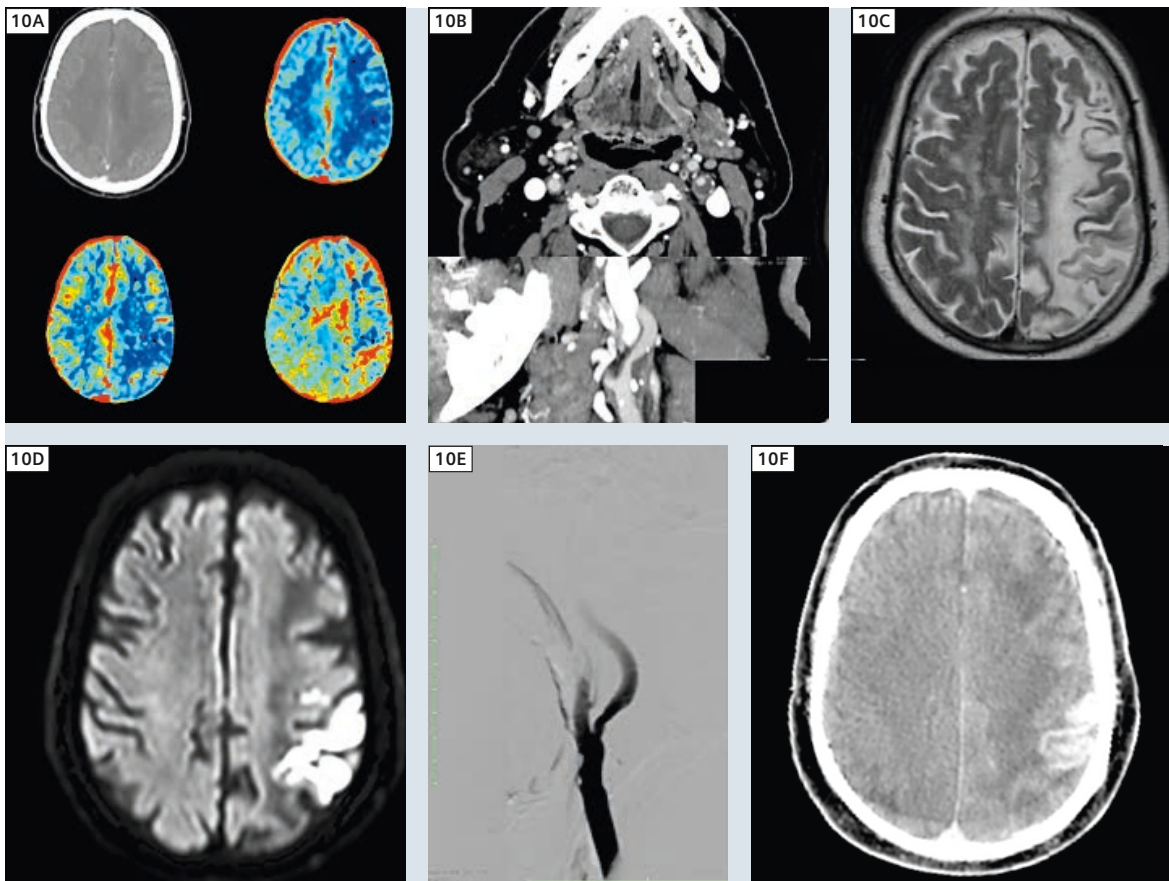


**8** Patient with a tight stenosis of the left ICA, as well as cortical lesions (8A–C). The carotid artery is calcified on CTA (8D, E) and on MRI there is a hemorrhage visible in the plaque (8F–H).





**9** Patient with a high-grade carotid stenosis on the right, seen on CTA. On the diffusion images one can clearly see the many ischemic cortical lesions (**9A–D**) that can only be seen retrospectively as a slight cortical swelling on the CT (**9F**).



**10** Patient with acute stroke. There is hypoperfusion on the perfusion CT but not clearly any new lesion visible (**10A**). On T2 there are extensive alterations in the brain parenchyma (**10C**). On DWI one can see that there is a recent ischemic cortical area that explains the new symptoms (**10D**). Angiography revealed a carotid stenosis (**10E**) and CT after angiography showed luxury perfusion in the ischemic territory with contrast accumulation but no blood (**10F**).

the information from the CT, which can better exclude hemorrhage and demonstrate vascular calcifications, and from the MRI, which has an inherently higher contrast to demonstrate small cortical lesions that will explain the patient's status.

Magnetic resonance is also mandatory for follow-up examinations: not only does it allow one to determine exact lesion extent, but it will also help determine prognosis based on this finding. Indeed, it has been demonstrated that both acute and late ischemic lesion volumes do correlate with clinical status and outcome [25].

The progresses and improvements in imaging that have been made in the last two decades have been enormous and have allowed us not just to improve diagnostic quality but also to gain insights into the disease processes that are ongoing so that therapy can be planned optimally and the follow-up can be as precise as possible. Thus, any stroke service should not rely on only CT or only MRI but use both in an optimized and optimal way in order to improve patient outcomes and safety.

## References

- Adams HP Jr, del Zoppo G, Alberts MJ, Bhatt DL, Brass L, Furlan A, Grubb RL, Higashida RT, Jauch EC, Kidwell C, Lyden PD, Morgenstern LB, Qureshi AI, Rosenwasser RH, Scott PA, Wijdicks EF; American Heart Association; American Stroke Association Stroke Council; Clinical Cardiology Council; Cardiovascular Radiology and Intervention Council; Atherosclerotic Peripheral Vascular Disease and Quality of Care Outcomes in Research Interdisciplinary Working Groups. Guidelines for the early management of adults with ischemic stroke: a guideline from the American Heart Association/American Stroke Association Stroke Council, Clinical Cardiology Council, Cardiovascular Radiology and Intervention Council, and the Atherosclerotic Peripheral Vascular Disease and Quality of Care Outcomes in Research Interdisciplinary Working Groups: the American Academy of Neurology affirms the value of this guideline as an educational tool for neurologists. *Stroke* 2007; 38(5):1655-711.
- Lövlblad KO, Baird AE. Computed tomography in acute ischemic stroke. *Neuroradiology*. 2010 Mar;52(3):175-87.
- Lövlblad KO, Baird AE. Actual diagnostic approach to the acute stroke patient. *Eur Radiol*. 2006 Jun;16(6):1253-69.
- von Kummer R, Holle R, Gizyska U, Hofmann E, Jansen O, Petersen D, Schumacher M, Sartor K. Interobserver agreement in assessing early CT signs of middle cerebral artery infarction. *AJNR Am J Neuroradiol*. 1996 Oct;17(9):1743-8.
- von Kummer R, Allen KL, Holle R, Bozzao L, Bastianello S, Manelfe C, Bluhmki E, Ringleb P, Meier DH, Hacke W. Acute stroke: usefulness of early CT findings before thrombolytic therapy. *Radiology*. 1997 Nov;205(2):327-33.
- The NINDS rt-PA stroke study group. Tissue plasminogen activator for acute ischemic stroke. *N Engl J Med* 1995; 333:1581-1587.
- Hacke W, Kaste M, Fieschi C, Toni D, Lesaffre E, von Kummer R, Boysen G, Bluhmki E, Höxter G, Mahagne MH, et al. Intravenous thrombolysis with recombinant tissue plasminogen activator for acute hemispheric stroke. The European Cooperative Acute Stroke Study (ECASS). *JAMA*. 1995 Oct 4;274(13):1017-25.
- Hacke W, Kaste M, Bluhmki E, Brozman M, Dávalos A, Guidetti D, Larrue V, Lees KR, Medeghri Z, Machnig T, Schneider D, von Kummer R, Wahlgren N, Toni D; ECASS Investigators (2008) Thrombolysis with alteplase 3 to 4.5 hours after acute ischemic stroke. *N Engl J Med* 25;359(13):1317-29.
- Dávalos A, Pereira VM, Chapot R, Bonafé A, Andersson T, Gralla J; Solitaire Group. Retrospective multicenter study of Solitaire FR for revascularization in the treatment of acute ischemic stroke. *Stroke*. 2012 Oct;43(10):2699-705.
- Edelman RR, Wielopolski P, Schmitt F. Echo-planar MR imaging. *Radiology*. 1994 Sep;192(3):600-12.
- Le Bihan D, Breton E, Lallemand D, Grenier P, Cabanis E, Laval-Jeantet M. MR imaging of intravoxel incoherent motions: application to diffusion and perfusion in neurologic disorders. *Radiology*. 1986 Nov;161(2):401-7.
- Rosen BR, Belliveau JW, Vevea JM, Brady TJ. Perfusion imaging with NMR contrast agents. *Magn Reson Med*. 1990 May;14(2):249-65.
- Sorensen AG, Buonanno FS, Gonzalez RG, Schwamm LH, Lev MH, Huang-Hellinger FR, Reese TG, Weisskoff RM, Davis TL, Suwanwela N, Can U, Moreira JA, Copen WA, Look RB, Finklestein SP, Rosen BR, Koroshetz WJ. Hyperacute stroke: evaluation with combined multisection diffusion-weighted and hemodynamically weighted echo-planar MR imaging. *Radiology*. 1996 May;199(2):391-401.
- Warach S, Chien D, Li W, Ronthal M, Edelman RR. Fast magnetic resonance diffusion-weighted imaging of acute human stroke. *Neurology*. 1992 Sep;42(9):1717-23.
- Lövlblad KO, Laubach HJ, Baird AE, Curtin F, Schlaug G, Edelman RR, Warach S. Clinical experience with diffusion-weighted MR in patients with acute stroke. *AJNR Am J Neuroradiol*. 1998 Jun-Jul;19(6):1061-6.
- Koroshetz WJ, Gonzalez G. Diffusion-weighted MRI: an ECG for brain attack? *Ann Neurol* 1997;41:565-566.
- Kalender WA, Seissler W, Klotz E, Vock P. Spiral volumetric CT with single-breath-hold technique, continuous transport, and continuous scanner rotation. *Radiology*. 1990 Jul;176(1):181-3.
- Wintermark M, Bogousslavsky J. Imaging of acute ischemic brain injury: the return of computed tomography. *Curr Opin Neurol*. 2003 Feb; 16(1):59-63.
- Chalela JA, Kidwell CS, Nentwich LM, Luby M, Butman JA, Demchuk AM, Hill MD, Patronas N, Latour L, Warach S. Magnetic resonance imaging and computed tomography in emergency assessment of patients with suspected acute stroke: a prospective comparison. *Lancet*. 2007 Jan 27;369(9558):293-8.
- Lövlblad KO, Baird AE, Schlaug G, Benfield A, Siewert B, Voetsch B, Connor A, Burzynski C, Edelman RR, Warach S. Ischemic lesion volumes in acute stroke by diffusion-weighted magnetic resonance imaging correlate with clinical outcome. *Ann Neurol*. 1997 Aug;42(2):164-70.
- Astrup J, Siesjö BK, Symon L. Thresholds in cerebral ischemia - the ischemic penumbra. *Stroke*. 1981 Nov-Dec;12(6):723-5.
- Altrichter S, Kulcsar Z, Jägersberg M, Federspiel A, Viallon M, Schaller K, Rüfenacht DA, Lövlblad KO. Arterial spin labeling shows cortical collateral flow in the endovascular treatment of vasospasm after post-traumatic subarachnoid hemorrhage. *J Neuroradiol*. 2009 Jun;36(3):158-61.
- Hermier M, Nighoghossian N, Derex L, Wiart M, Nemoz C, Berthezène Y, Froment JC. Hypointense leptomeningeal vessels at T2\*-weighted MRI in acute ischemic stroke. *Neurology*. 2005 Aug 23;65(4):652-3.
- Viallon M, Altrichter S, Pereira VM, Nguyen D, Sekoranta L, Federspiel A, Kulcsar Z, Sztajzel R, Ouared R, Bonvin C, Pfeuffer J, Lövlblad KO. Combined use of pulsed arterial spin-labeling and susceptibility-weighted imaging in stroke at 3T. *Eur Neurol*. 2010;64(5):286-96.
- Lövlblad KO, Haller S, Pereira VM. Stroke: high-field magnetic resonance imaging. *Neuroimaging Clin N Am*. 2012 May;22(2):191-205.
- Lövlblad KO, Baird AE, Schlaug G, Benfield A, Siewert B, Voetsch B, Connor A, Burzynski C, Edelman RR, Warach S. Ischemic lesion volumes in acute stroke by diffusion-weighted magnetic resonance imaging correlate with clinical outcome. *Ann Neurol*. 1997 Aug;42(2):164-70.

## Contact

Karl-Olof Lövlblad, M.D.  
Hôpitaux Universitaires de Genève  
Department of Diagnostic and  
Interventional Neuroradiology  
Department of Medical Imaging and  
Information Technology  
4 rue Gabrielle-Perret-Gentil  
1211 Geneva  
Switzerland  
Phone: +41 22 372 70 33  
Fax: +41 22 372 70 72  
karl-olof.lovlblad@hcuge.ch

# Implication of Brain Susceptibility-Weighted Imaging

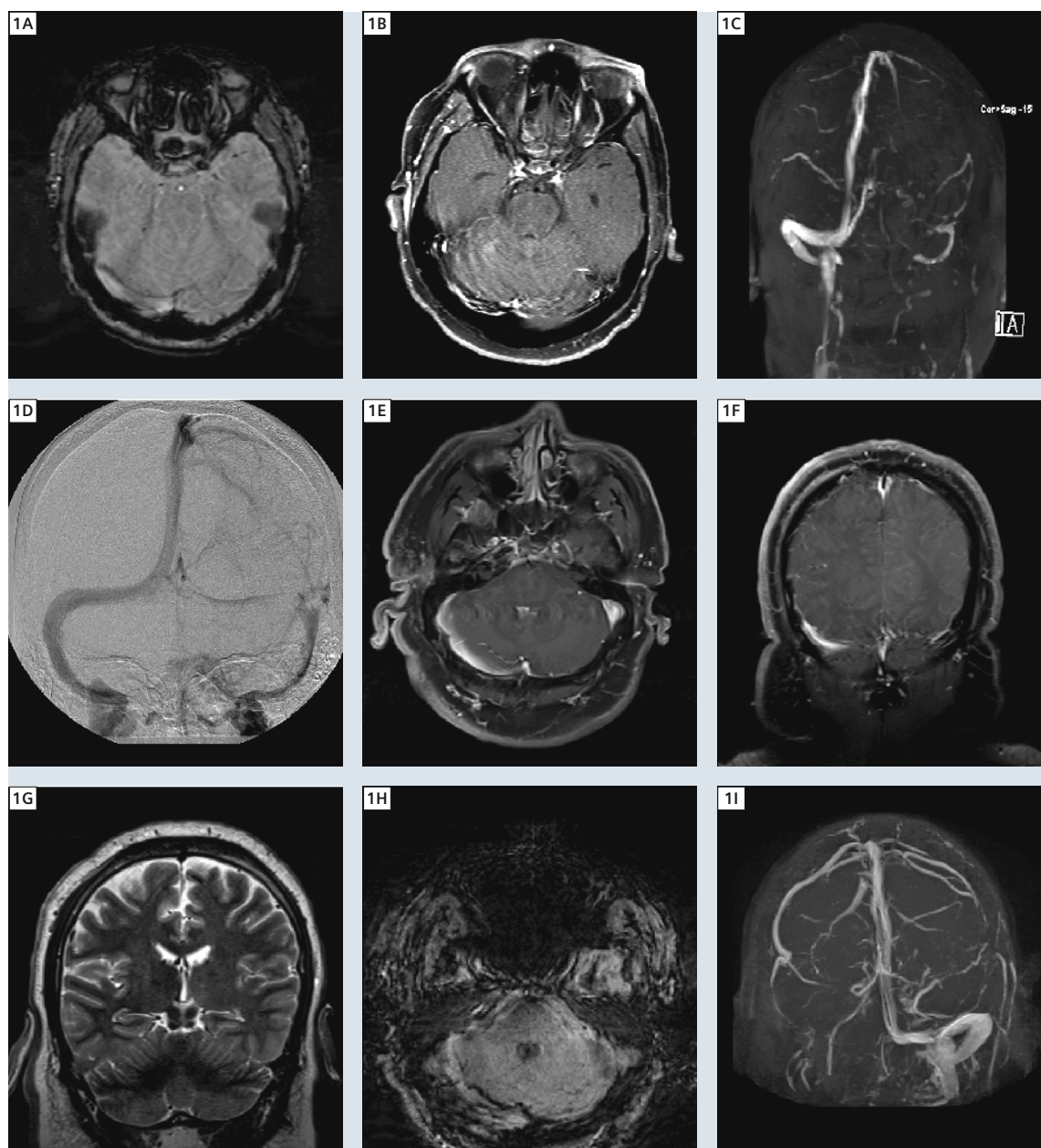
Yu-Kun Tsui<sup>1,3</sup>; Fong Y Tsai<sup>1,2</sup>; Chi-Yuan Chen<sup>1</sup>; Kwo-Whei Lee<sup>4</sup>

<sup>1</sup>Imaging Research Center, Taipei Medical University, Taipei, Taiwan.

<sup>2</sup>University California Irvine Medical Center, Orange, Ca. USA.

<sup>3</sup>Chi-Mei Medical Center, Tainan, Taiwan.

<sup>4</sup>Chang-Hua Christian Hospital, Chang-Hua, Taiwan.



**1** (1A) SWI showed no high signal at left transverse sinus and (1B) no contrast in the left transverse sinus is seen on contrast enhanced MRI. (1C) MR venography showed poor visualization of left dural sinus, it cannot distinguish between atresia or thrombosis.

(1D) Venous phase of DSA confirmed left transverse sinus thrombosis as seen in SWI.

(1E, F) In another case contrast-enhanced T1-weighted MRI showed contrast-enhanced right transverse sinus.

(1G) Coronal T2-weighted MRI showed iso-intensity signal in right sinus and (1H) low signal on SWI, these two findings are compatible with chronic thrombosis and confirmed by (1I) venous phase of DSA.

## Introduction

Susceptibility-weighted imaging (SWI) is an MR imaging technique sensitive to magnetic susceptibility effects. It uses both magnitude and phase information from a high-spatial resolution three-dimensional GRE pulse sequence [1–3]. While phase post processing accentuates the magnetic properties of different substances, SWI is sensitive in detecting intravenous deoxygenated blood as well as extravascular blood products. It was originally referred to as high-resolution blood oxygen level-dependent (BOLD) venography [2, 4], but due to its broader application in detecting other diamagnetic or paramagnetic substances including iron, calcification, deoxygenated hemoglobin content etc., it is now referred to as SWI [1, 5]. SWI has been used in studies of vascular pathologies, trauma, arteriovenous malformation, tumor, multiple sclerosis, stroke, and other brain disease [6, 7]. The clinical application of SWI has been demonstrated in both adult and pediatric populations<sup>1</sup> [8, 9].

The principles of SWI have been extensively described by Reichenbach and Haacke et al. [1, 10]. The sensitivity to susceptibility effects is maximized by using a long-TE high-resolution fully flow-compensated three-dimensional GRE sequence with filtered phase information in each voxel both to enhance the contrast in magnitude images and to add the susceptibility differences between tissues as a new source of information [1, 10–12]. After the imaging acquisition, the final processed SWI magnitude images are obtained after merging magnitude and phase images [10]. Due to combining both magnitude and phase information, the final processed SWI magnitude images can provide a benefit in detecting signal-intensity changes arising from both T2 and susceptibility differences between tissues. The processed SWI magnitude images can further generate into thick minIP images to demonstrate vascula-

ture, tortuous structures, and the continuity of vessels or lesions across slices. In processed SWI magnitude images, deoxyhemoglobin (deoxy-Hb), being paramagnetic with four unpaired electrons, generates magnetic fields that additively combine with the external magnetic field [2, 13], and presents as an intrinsic contrast agent appearing hypointensity in venous structure. On the other hand, arteries are hyperintense because of time-of-flight effects and lack of T2\* effect [10, 14]. Therefore, the use of SWI in distinct and simultaneous evaluation of the arterial and venous systems of brain and related vascular pathologies is conceivable and possible and the application of SWI has been widely expanded [7, 15, 16, 31–36].

## Vascular malformations

Several types of vascular malformations with slow or venous flow have been shown to be better visualized with SWI, including developmental venous anomaly (DVA), cerebral cavernous malformation (CCM), telangiectasia and Sturge-Weber Syndrome (SWS) [5, 6, 9]. SWI not only offers improved sensitivity but can also depict vascular structures that are invisible on conventional T2\* GRE images.

### DVA

DVA is the most common type of vascular malformation. DVA consists of radially arranged venous complexes converging to a centrally located venous trunk, which drains the normal brain parenchyma [17]. SWI can demonstrate the whole structure clearly and has been proven to provide better detection of venous structures than conventional T2\* imaging. However, please note that in some DVA lesions with relatively higher blood flow, no obvious medullary veins of DVA may be shown on SWI [18].

### CCM

CCM comprises 5%–13% of all the central nervous system vascular malformations [19]. CCM lesions can be detected in routine MR imaging when they have calcification or have previously bled. However, if CCM lesions are intact and have not bled, they may be almost invisible

except for a faint or ill-defined nonspecific blush of enhancement after contrast administration. In addition, lack of flow-related signal intensity makes CCM undetectable using conventional MR angiographic techniques. Because of the possibility of blood stagnation phenomenon and chronic microhemorrhages, CCM lesions contain deoxy-Hb or hemosiderin and become very dark, thus easily detected on SWI, especially in the case of tiny lesions. The high degree of SWI sensitivity in assigning the number of CCM lesions is significantly superior to that of T2-weighted fast spin echo and GRE sequences [20].

## Telangiectasia

Telangiectasia is a low-flow vascular malformation with low signal intensity on SWI and is typically small, ranging from several millimeters to 2 cm in size [21]. Telangiectasia lesions are mostly found in the pons, but are less well imaged with conventional MR sequences [22]. They may occur sporadically or may be associated with syndromes (e.g., hereditary hemorrhagic telangiectasia) or may occur as a result of endothelial injury, such as radiation-induced vascular injury, particularly in children who have received cranial irradiation [9]. SWI is a useful adjunct to conventional MR imaging in diagnosing telangiectasia.

## Sturge-Weber syndrome (SWS)

SWS is a neurocutaneous disorder characterized by cutaneous angioma, glaucoma, and leptomeningeal venous angiomatosis. The leptomeningeal angiomatosis is associated with loss of normal cortical venous drainage results in abnormal venous drainage through the deep venous system, which may lead to progressive venous stasis and chronic hypoxia. The typical imaging findings include cerebral hemiatrophy and cortical 'tram-track' calcification resulting from chronic venous ischemia. The pial angioma is often easily seen with contrast-enhanced imaging. SWI can detect microstructural changes in cortex and white matter, as well as deep venous collaterals in children with SWS, and may be useful to objectively assess

<sup>1</sup>MR scanning has not been established as safe for imaging fetuses and infants under two years of age. The responsible physician must evaluate the benefit of the MRI examination in comparison to other imaging procedures.

microstructural abnormalities at an early stage of SWS when interventions have the best chance to prevent irreversible neurocognitive sequelae [23].

### **Vascular pathologies with arteriovenous shunting**

As previously mentioned in this article, venous structure are hypointense due to the presence of deoxyhemoglobin and arteries appear hyperintense due to time-of-flight effects and lack of T2\* effect in processed SWI images. Therefore, abnormal hyperintense signal within the veins in processed SWI images may indicate the presence of lesion with high-flow arteriovenous shunting, such as arteriovenous malformation (AVM) and dural arteriovenous fistula (DAVF) [15, 16]. The accuracy of the SWI sequence in the detection of arteriovenous shunting can be further improved by performing post-contrast SWI studies [24].

### **Arteriovenous malformation (AVM)**

AVM is a congenital vascular malformation that results in abnormal direct arteriovenous shunt. Imaging studies, including MR and intra-arterial digital subtraction angiography (DSA), are essential to identify and define exactly the different vascular components before embarking on therapy such as surgery, embolization, or radiosurgery. The use of SWI may be beneficial in the visualization and delineation of very small AVM lesions without hemorrhages and may help to detect these lesions at an early stage prior to bleeding [25]. SWI is also accurate for the detection of arteriovenous shunting in AVM lesions and may offer a noninvasive alternative to angiography in screening for, or follow-up of, treated lesions [15].

### **Dural arteriovenous fistula (DAVF)**

The clinical features of DAVF range from headache, vertigo, or tinnitus to neurologic deficits or a life-threatening intracranial hemorrhage [26]. However, the clinical and neuroradiologic diagnosis of DAVF may be challenging. In processed

SWI images, abnormally increased signal intensity in venous structures can result from high flow and rapid shunting of oxygenated blood via fistula. Due to the ability of SWI to detect and delineate intravascular deoxygenated blood and venous structures, as well as prominence of venous vasculature due to the prolonged passage time of intracranial blood, venous engorgement, and possible venous congestion caused by DAVF, can also be identified by SWI [16, 27]. The use of SWI may be helpful in early diagnosis and prompt treatment in DAVF.

### **Cerebral venous sinus thrombosis**

Cerebral venous sinus thrombosis (CVST) is an unusual condition which is difficult to diagnose due to its variable modes of onset and wide spectrum of symptoms and signs [28]. In the present series, the major female predominance, age of onset, frequency of various onset and different clinical manifestation are those classically reported [29]. CVST usually presents nonspecific lesions, including hemorrhage, edema or infarction. Because of its sensitivity to susceptibility effects, SWI is of additional diagnostic value for clot detection in CVST in conjunction with conventional MR sequences and MRV, particularly in the acute phase of thrombosis and in cortical CVST [30]. Because of the ability to detect signal-intensity changes coming from both T2 and susceptibility differences between tissues, processed SWI images can demonstrate not only the CVST, but also the extent of parenchymal edema and even hemorrhage that can occur after venous thrombosis leading to infarction. Furthermore, in some cases with chronic CVST, SWI should be incorporated in the evaluation of chronic occluded dural sinuses which often misleads as patent sinuses due to the enhancement in post-contrast images.

### **Stroke**

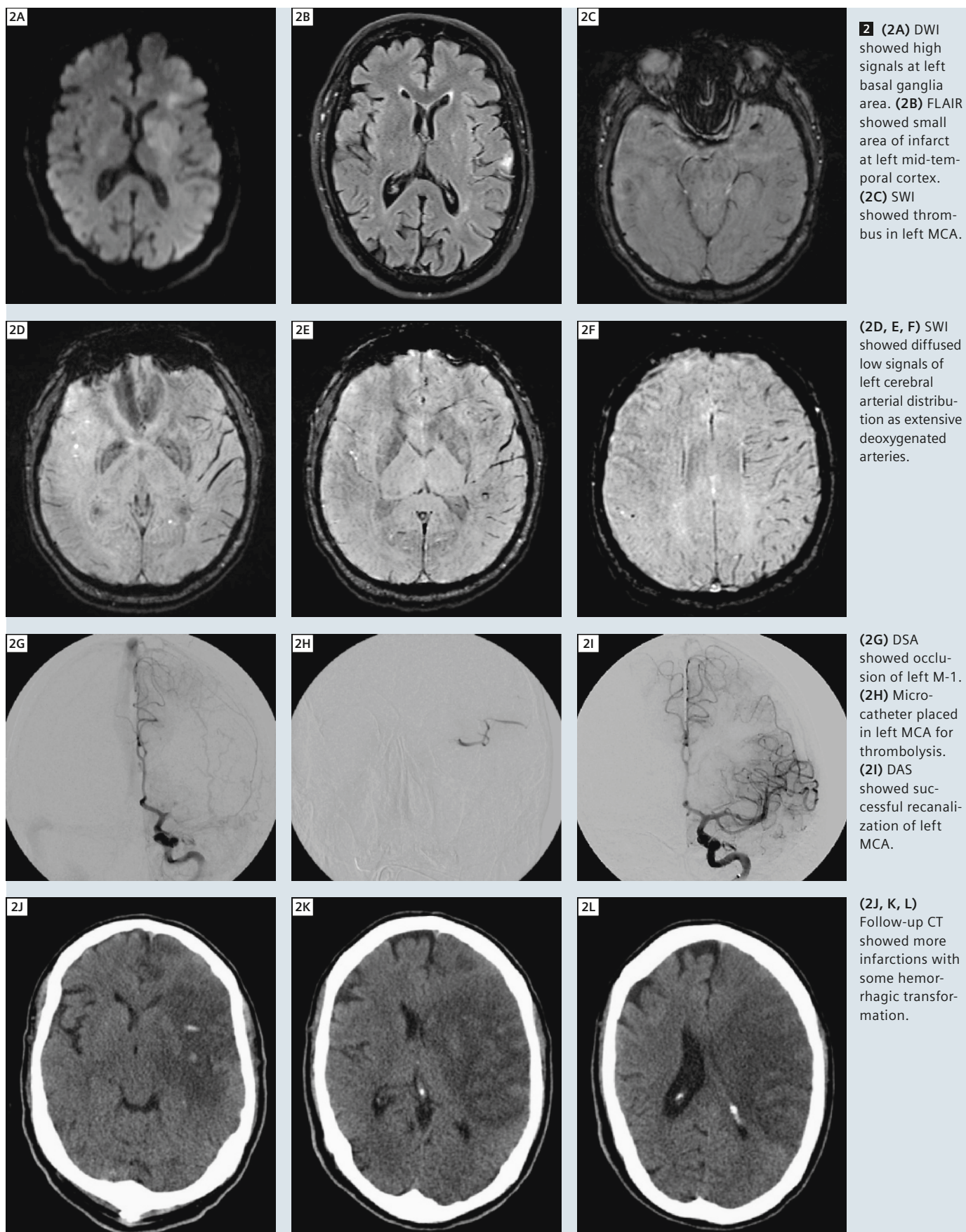
Acute infarction with or without hemorrhage occurs due to thromboembolism, arterial stenosis or other entity. Acute thromboembolism accumulates high intracellular deoxy-Hb, which causes

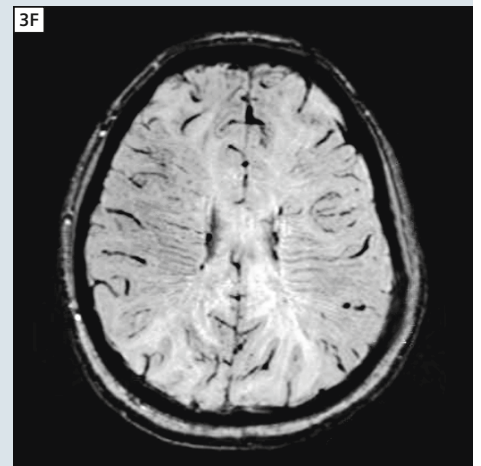
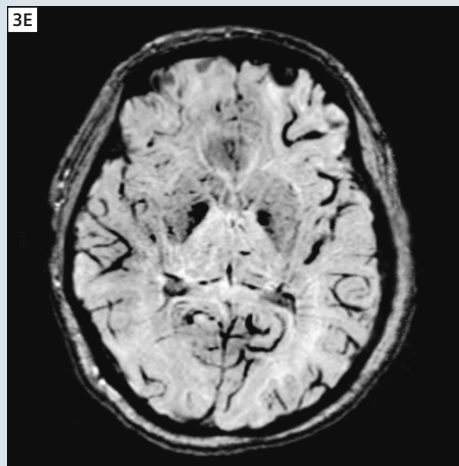
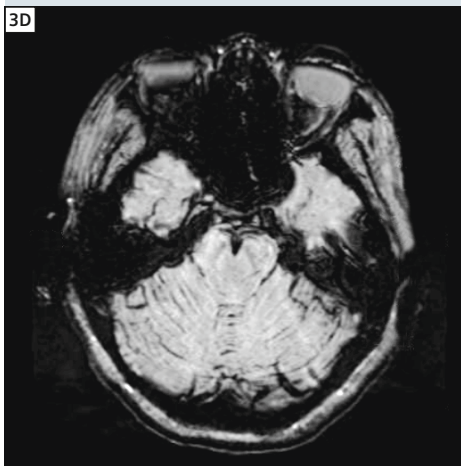
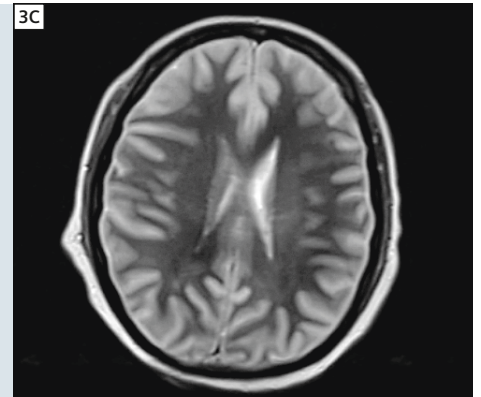
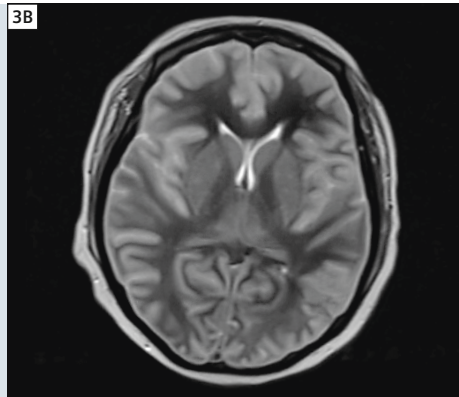
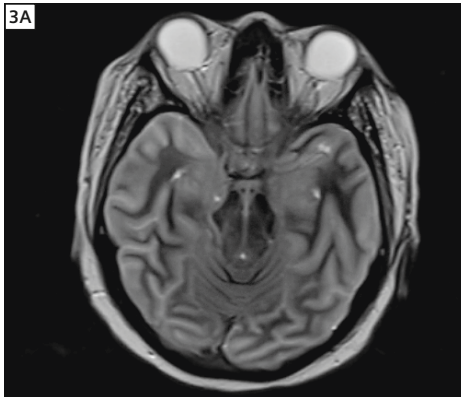
T2\* shortening secondary to paramagnetic susceptibility differences making the thromboembolism visible on SWI. SWI can also add information about the acute stroke in detecting acute hemorrhage and in detecting cerebral amyloid angiopathy (CAA) with micro- or macro-hemorrhages. Therefore, SWI is useful in the assessment of acute stroke.

The ability of SWI to detect hemorrhages may influence the subsequent treatment decision making for patients with acute stroke. To differentiate microbleeds and calcification in the infarct area, an analysis of phase image may be helpful. The susceptibility effects due to blood clots and blood stasis with deoxy-Hb detected in SWI can help locate the intra-arterial thromboembolism [31]. This may be useful in planning various treatment options and in assessing the extent of infarct [32].

In addition to its usefulness in the assessment of acute infarct, SWI also has the potential to predict stroke evolution. SWI can provide comparable information on mean transit time (MTT) and is an alternative to perfusion-weighted imaging (PWI) for the assessment of ischemic penumbra. The mismatch between SWI and diffusion-weighted imaging (DWI) can be a marker for ischemic penumbra and a predictor of stroke evolution [33]. The detection of deoxygenated blood and deep medullary veins in infarct region by SWI offers the possibility to assess tissue viability [9]. Because of the ability to demonstrate the abnormal visibility of transcerebral or deep medullary veins, SWI also has potential to evaluate the possibility of further hemorrhagic transformation in acute stroke patients treated by intravenous thrombolysis [34]. Therefore, SWI may be useful to select acute ischemic stroke patients for endovascular therapy. Further investigation may validate these implications of SWI for acute stroke.

There are two essences of imaging studies for acute stroke: speed and accuracy. Modified MR imaging including DWI, SWI and FLAIR, may be useful for acute stroke. However, the image acquisition may take too long for examining acute stroke patients due to motion from agi-





**3** (3A–C) T2-weighted MRI showed diffuse cerebral edema, optic nerve sheath swelling and transtentorial herniations, however, those findings cannot confirm imaging evidence of brain death.

(3D–F) SWI showed extensive deoxygenated intracranial arteries and veins it indicates no intracranial circulation.

(3G) CT angiography confirmed no intracranial circulation as imaging evidence of brain death and compatible with the findings of SWI.

tation and mental status changes. In our study, by adjusting the parameters of SWI including phase resolution, voxel size, matrix size and partial Fourier, reasonable diagnostic quality of SWI images can be obtained with shorter scanning time to 2 minutes and 14 seconds (with base resolution to  $150 \times 192$  with voxel size of  $1.5 \times 1.2 \times 2.0$  mm and phase resolution 70%). This change can facilitate the application of SWI for acute stroke patients.

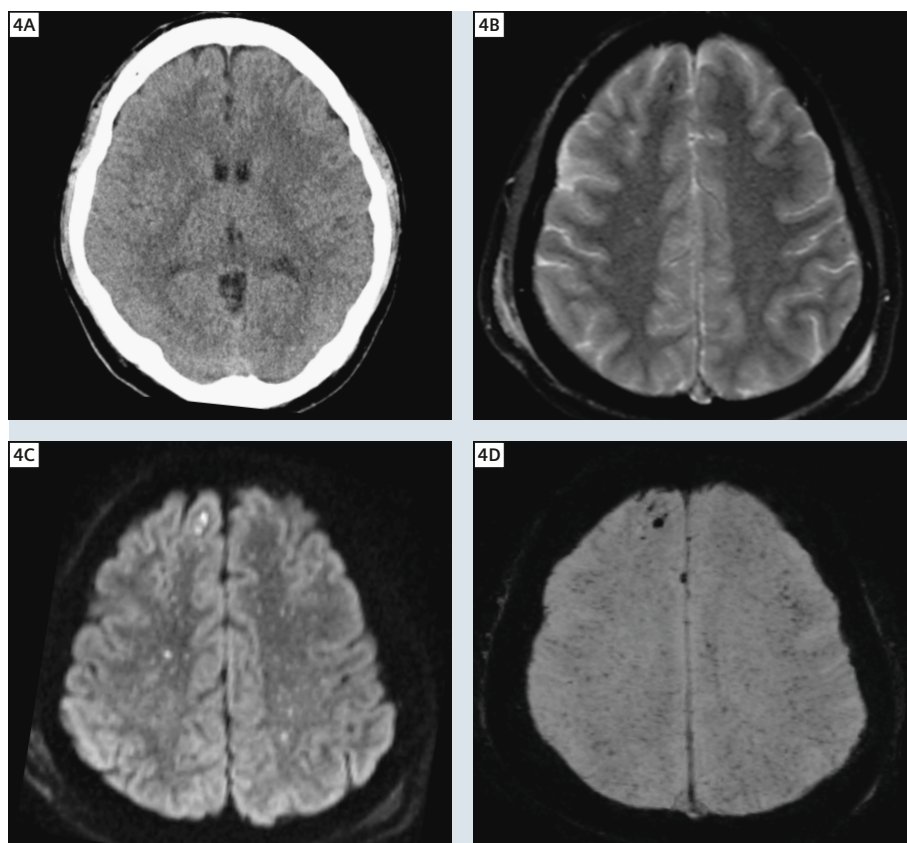
Mismatch PWI/DWI may indicate potential presence of penumbra, however, it cannot identify irreversible brain damage from ischemic stroke. Diffused deoxygenated middle cerebral artery on SWI indicates irreversible brain tissue with extensive oxygen extraction from severe ischemia. Recanalization was achieved, but the patient had progressive infarction (Figs. 2G–I). When imaging, SWI should incorporate evaluation for thrombolytic therapy to avoid complication and reduce the use of interventions in patients with very poor prognosis [33–35].

## Brain death

In the case of patient with brain death, SWI show all intracranial vessels, including arteries and veins, as hypointensity and prominent cortical and deep cerebral veins. This change could reflect a combination of increased oxygen extraction, arterial and venous stasis, and/or possible venous dilation secondary to release substances after cell death. This finding most likely indicates a higher level of intravascular deoxygenated blood and diffuse hypoxia-ischemia change due to stopped blood flow with blood stasis, and may correspond to conventional angiographic and nuclear medicine imaging findings [36]. This initial experience of detecting prominent hypointense signals in intracranial arteries on SWI in patients with brain death may indicate absence of intracranial arterial circulation and thus may enable definitive diagnosis of brain death [36].

## Trauma

**Traumatic brain injury (TBI)** is a major cause of morbidity, mortality and lost years of productive life throughout the



**4** (4A) Non-contrast brain CT appeared normal. (4B) Axial GRE MRI showed several tiny microhemorrhages. (4C) Axial DWI MRI showed more microinfarctions and/or microhemorrhages. (4D) SWI showed numerous diffuse microhemorrhages resulting from vascular injury due to the toxic effect of local free fatty acid release or microinfarctions.

world [37]. CT is the primary imaging modality for the assessment of TBI. However, TBI patients with **diffuse axonal injury (DAI)** often exhibit tiny or punctuate hemorrhages in the deep subcortical white matter and are not routinely depicted by brain CT or conventional MR imaging sequences. SWI is 3–6 times more sensitive than conventional T2\*-weighted gradient-echo (T2\*GE) sequence in detecting DAI hemorrhages [38], especially for lesions in the brain-stem [6]. Furthermore, other traumatic intracranial hemorrhages can also be shown in SWI to establish the degree of injury more accurately.

**Fat embolism syndrome (FES)** is an uncommon but serious complication of traumatic injury and is frequently diagnostically challenging because first assessment by brain CT is usually normal. FES includes a triad: hypoxia, neurologic abnormalities, and petechial skin rashes

[39]. In the brain, FES causes microinfarcts, vasogenic edema, and petechiae [40]. Conventional MR imaging has been reported to effectively visualize microinfarcts and vasogenic edema in FES in brain, but SWI can show diffuse microhemorrhages resulting from vascular injury due to toxic effect of local free fatty acids release or microinfarctions, which cannot be detected by other MR sequences. In a case of DAI, the abnormal neurological features appear immediately post injury, whereas in FES neurologic abnormalities appear generally after orthopedic intervention or hours after trauma [41].

## Other implications for SWI

**Assessment of brain tumor.** The advances of MR imaging have provided diagnostic, staging, morphologic, metabolic and functional information of brain tumor. The development of SWI

improves the ability to evaluate not only internal vascular architecture and hemorrhages, but also intratumoral calcification, which may not be detected in other MR sequences. These internal findings may be useful for diagnosis, differential diagnosis, and staging of brain tumors [42]. SWI can also be used in identifying the hemorrhagic change or telangiectasia which occurs after radiation therapy [9]. SWI may assist to differentiate primary or secondary lesions by a deep medullary vein inside of tumor. It may be an important tool to diagnose the type of tumor.

### Assessment of multiple sclerosis

Although the mechanism of iron accumulation in brain tissue is not yet clear, however, this phenomenon is observed in many neurodegenerative and inflammatory diseases, including multiple sclerosis (MS).

Local accumulation of iron due to disruption of the blood-brain barrier and accumulation of iron-rich macrophages is found in MS brains [43]. SWI can indicate the lesions that may not be seen in conventional MR sequences because of its sensitivity in detecting iron deposition. Furthermore, because of the ability to present cerebral venous architecture, SWI can show the veins draining the MS lesions and also can help to diagnose chronic cerebrospinal venous insufficiency (CCSVI) in MS patients [44, 45].

### Venous hypertension

Pseudotumor cerebri (PTC), or idiopathic intracranial hypertension, is a syndrome associated with multiple clinical conditions. The elevation of intracranial venous pressure may be a universal mechanism in PTC with different etiologies [46, 47]. This elevated venous pres-

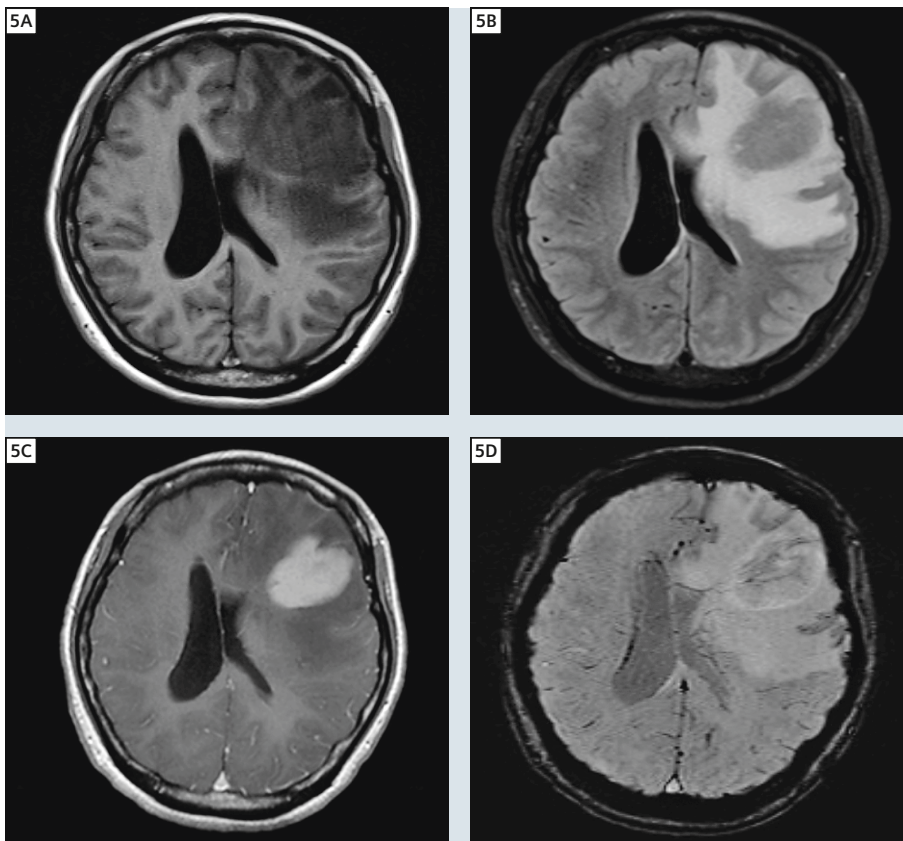
sure leads to elevation in CSF and intracranial pressure by resisting CSF absorption [47]. Sometimes these high pressures appear to be secondary to central venous hypertension but more often they seem to be the result of lesions obstructing cerebral venous outflow. The diagnosis of idiopathic intracranial hypertension is essentially one of exclusion of known causes of raised intracranial pressure [48]. CVST, in particular, must be excluded before idiopathic intracranial hypertension can be diagnosed [49]. In patients with the appropriate clinical phenotype of intracranial hypertension, SWI with conventional MR sequences can help to exclude the possibility of intracranial hypertension caused by CVST or other intracranial abnormality [7].

### Hyperperfusion syndrome

Cerebral hyperperfusion syndrome (CHS) is characterized by ipsilateral headache, hypertension, seizures, and focal neurological deficits after carotid endarterectomy, carotid stenting, extra-cranial-intracranial bypass, or other revascularization procedures [50]. Intracranial hemorrhage will develop in up to 40% of these patients and has 36% mortality. The incidence of the syndrome varies, reflecting the range of mild to severe (intracranial hemorrhage) symptoms. MR imaging abnormalities include white-matter edema, focal infarction, and local or more overt hemorrhage. The hypersignal intensities along the involved cerebral hemisphere on SWI are suggestive of increased oxygenation and hyperperfusion. The possibility that SWI demonstrates increased oxygenated blood and perfusion in the areas of CHS may provide a rapid and convenient method to diagnose CHS [7]. Further investigation and study correlated with perfusion-weighted MR imaging, single-photon emission computed tomography (SPECT), or positron emission tomography (PET) are necessary to confirm the utility of SWI in detecting CHS.

### Conclusion

The use of SWI to detect hemorrhage and vascular architecture has been documented and discussed in many studies.

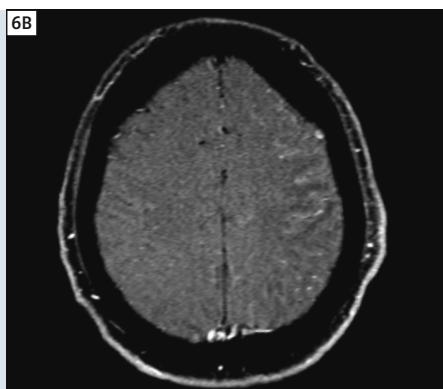


**5** (5A) T1-weighted MRI showed low signal mass at left frontal lobe. (5B) Proton T2-weighted MRI showed tumor with extensive edema. (5C) Contrast enhanced T1-weighted MRI showed a solid enhancement tumor. (5D) SWI showed medullary veins located transversely through the tumor.

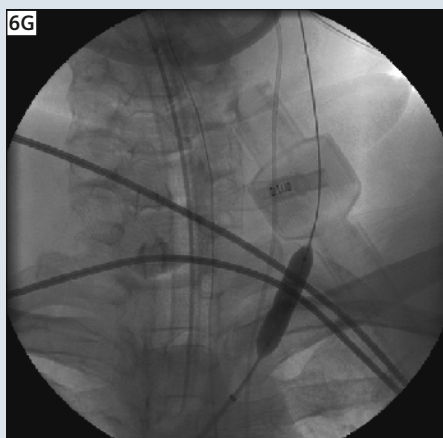
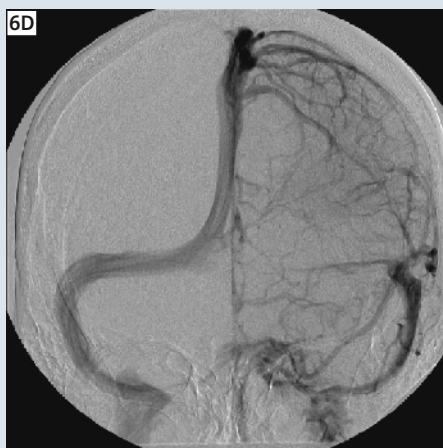
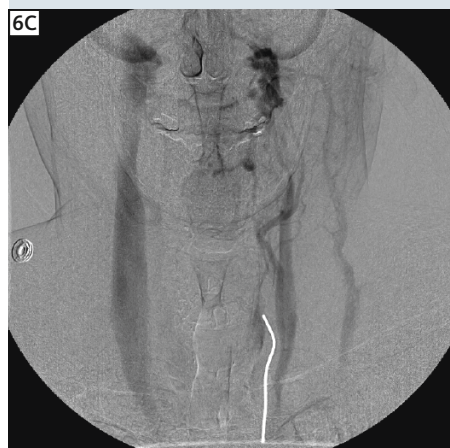
SWI is useful in the improvement and provision of additional diagnostic information for intracranial diseases. SWI may expand to many other implications for brain pathology. Thus SWI should be a routine component of MRI studies of all cerebral disorders.

#### References

- 1 Haacke EM, Xu Y, Cheng YC, et al. Susceptibility weighted imaging (SWI). *Magnetic resonance in medicine : official journal of the Society of Magnetic Resonance in Medicine / Society of Magnetic Resonance in Medicine* 2004;52:612-618.
- 2 Reichenbach JR, Haacke EM. High-resolution BOLD venographic imaging: a window into brain function. *NMR in biomedicine* 2001;14:453-467.
- 3 Reichenbach JR, Jonetz-Mentzel L, Fitzek C, et al. High-resolution blood oxygen-level dependent MR venography (HRBV): a new technique. *Neuroradiology* 2001;43:364-369.
- 4 Lee BC, Vo KD, Kido DK, et al. MR high-resolution blood oxygenation level-dependent venography of occult (low-flow) vascular lesions. *AJNR American journal of neuroradiology* 1999;20:1239-1242.
- 5 Sehgal V, Delproposto Z, Haacke EM, et al. Clinical applications of neuroimaging with susceptibility-weighted imaging. *Journal of magnetic resonance imaging : JMRI* 2005;22:439-450.
- 6 Mittal S, Wu Z, Neelavalli J, et al. Susceptibility-weighted imaging: technical aspects and clinical applications, part 2. *AJNR American journal of neuroradiology* 2009;30:232-252.
- 7 Tsui YK, Tsai FY, Hasso AN, et al. Susceptibility-weighted imaging for differential diagnosis of cerebral vascular pathology: a pictorial review. *Journal of the neurological sciences* 2009;287:7-16.
- 8 Meoded A, Poretti A, Northington FJ, et al. Susceptibility weighted imaging of the neonatal brain. *Clinical radiology* 2012;67:793-801.
- 9 Tong KA, Ashwal S, Obenaus A, et al. Susceptibility-weighted MR imaging: a review of clinical applications in children. *AJNR American journal of neuroradiology* 2008;29:9-17.



**6** (6A, B) SWI showed high signals along left cerebral veins. (6C) showed left jugular vein stenosis. (6D) Venous phase of DSA showed left transverse sinus thrombosis. (6E) Venous pressure was still very high after thrombolysis and angioplasty of left jugular vein. (6F) showed stenosis was also seen at distal left jugular vein. (6G) Balloon angioplasty was performed. (6H) Partial dilatation of left distal jugular vein.



- 10 Haacke EM, Mittal S, Wu Z, et al. Susceptibility-weighted imaging: technical aspects and clinical applications, part 1. *AJNR American journal of neuroradiology* 2009;30:19-30.
- 11 Rauscher A, Sedlacik J, Barth M, et al. Magnetic susceptibility-weighted MR phase imaging of the human brain. *AJNR American journal of neuroradiology* 2005;26:736-742.
- 12 Rauscher A, Sedlacik J, Deistung A, et al. Susceptibility weighted imaging: data acquisition, image reconstruction and clinical applications. *Zeitschrift für medizinische Physik* 2006;16:240-250.
- 13 Thomas B, Somasundaram S, Thamburaj K, et al. Clinical applications of susceptibility weighted MR imaging of the brain – a pictorial review. *Neuroradiology* 2008;50:105-116.
- 14 Barnes SR, Haacke EM. Susceptibility-weighted imaging: clinical angiographic applications. *Magnetic resonance imaging clinics of North America* 2009;17:47-61.
- 15 Jagadeesan BD, Delgado Almandoz JE, Moran CJ, et al. Accuracy of susceptibility-weighted imaging for the detection of arteriovenous shunting in vascular malformations of the brain. *Stroke; a journal of cerebral circulation* 2011;42:87-92.
- 16 Letourneau-Guillon L, Krings T. Simultaneous arteriovenous shunting and venous congestion identification in dural arteriovenous fistulas using susceptibility-weighted imaging: initial experience. *AJNR American journal of neuroradiology* 2012;33:301-307.
- 17 Abe T, Singer RJ, Marks MP, et al. Coexistence of occult vascular malformations and developmental venous anomalies in the central nervous system: MR evaluation. *AJNR American journal of neuroradiology* 1998;19:51-57.
- 18 Fushimi Y, Miki Y, Togashi K, et al. A developmental venous anomaly presenting atypical findings on susceptibility-weighted imaging. *AJNR American journal of neuroradiology* 2008;29:E56.
- 19 Labauge P, Brunereau L, Levy C, et al. The natural history of familial cerebral cavernomas: a retrospective MRI study of 40 patients. *Neuroradiology* 2000;42:327-332.
- 20 de Souza JM, Domingues RC, Cruz LC, Jr., et al. Susceptibility-weighted imaging for the evaluation of patients with familial cerebral cavernous malformations: a comparison with t2-weighted fast spin-echo and gradient-echo sequences. *AJNR American journal of neuroradiology* 2008;29:154-158.
- 21 Lee RR, Becher MW, Benson ML, et al. Brain capillary telangiectasia: MR imaging appearance and clinicopathologic findings. *Radiology* 1997;205:797-805.
- 22 Yoshida Y, Terae S, Kudo K, et al. Capillary telangiectasia of the brain stem diagnosed by susceptibility-weighted imaging. *Journal of computer assisted tomography* 2006;30:980-982.
- 23 Juhasz C, Haacke EM, Hu J, et al. Multimodality imaging of cortical and white matter abnormalities in Sturge-Weber syndrome. *AJNR American journal of neuroradiology* 2007;28:900-906.
- 24 Jagadeesan BD, Delgado Almandoz JE, Benzinger TL, et al. Postcontrast susceptibility-weighted imaging: a novel technique for the detection of arteriovenous shunting in vascular malformations of the brain. *Stroke; a journal of cerebral circulation* 2011;42:3127-3131.
- 25 Essig M, Reichenbach JR, Schad LR, et al. High-resolution MR venography of cerebral arteriovenous malformations. *Magnetic resonance imaging* 1999;17:1417-1425.
- 26 Kwon BJ, Han MH, Kang HS, et al. MR imaging findings of intracranial dural arteriovenous fistulas: relations with venous drainage patterns. *AJNR American journal of neuroradiology* 2005;26:2500-2507.
- 27 Saini J, Thomas B, Bodhey NK, et al. Susceptibility-weighted imaging in cranial dural arteriovenous fistulas. *AJNR American journal of neuroradiology* 2009;30:E6.
- 28 Bousser MG, Chiras J, Bories J, et al. Cerebral venous thrombosis--a review of 38 cases. *Stroke; a journal of cerebral circulation* 1985;16:199-213.
- 29 Tsai FY, Wang AM, Matovich VB, et al. MR staging of acute dural sinus thrombosis: correlation with venous pressure measurements and implications for treatment and prognosis. *AJNR American journal of neuroradiology* 1995;16:1021-1029.
- 30 Idbaih A, Boukobza M, Crassard I, et al. MRI of clot in cerebral venous thrombosis: high diagnostic value of susceptibility-weighted images. *Stroke; a journal of cerebral circulation* 2006;37:991-995.
- 31 Mamlouk MD, Tsai FY, Drachman D, et al. Cerebral Thromboembolism: Value of Susceptibility weighted Imaging (SWI) in the initial diagnosis of acute infarction. *NRJ Digital* 2012;2:86-97.
- 32 Rovira A, Orellana P, Alvarez-Sabin J, et al. Hyperacute ischemic stroke: middle cerebral artery susceptibility sign at echo-planar gradient-echo MR imaging. *Radiology* 2004;232:466-473.
- 33 Kao HW, Tsai FY, Hasso AN. Predicting stroke evolution: comparison of susceptibility-weighted MR imaging with MR perfusion. *European radiology* 2012;22:1397-1403.
- 34 Hermier M, Nighoghossian N, Derex L, et al. Hypointense transcerebral veins at T2\*-weighted MRI: a marker of hemorrhagic transformation risk in patients treated with intravenous tissue plasminogen activator. *Journal of cerebral blood flow and metabolism : official journal of the International Society of Cerebral Blood Flow and Metabolism* 2003;23:1362-1370.
- 35 Tsai FY, Kao HW, Tsui YK, Chen CY. Identifying irreversible brain tissue damage and penumbra. presented at 8<sup>th</sup> World Stroke Congress Oct 10-13<sup>th</sup>, Beasilia, Brazil.
- 36 Tsai FY, Lee KW, Kao HW, et al. Susceptibility-Weighted Imaging, an additional tool to Diagnose Brain Death: Initial Experience. *NRJ Digital* 2012;2:000-000.
- 37 Brown AW, Elovic EP, Kothari S, et al. Congenital and acquired brain injury. 1. Epidemiology, pathophysiology, prognostication, innovative treatments, and prevention. *Archives of physical medicine and rehabilitation* 2008;89:S3-8.
- 38 Babikian T, Freier MC, Tong KA, et al. Susceptibility weighted imaging: neuropsychologic outcome and pediatric head injury. *Pediatric neurology* 2005;33:184-194.
- 39 Johnson MJ, Lucas GL. Fat embolism syndrome. *Orthopedics* 1996;19:41-48; discussion 48-49.
- 40 Zaitzu Y, Terae S, Kudo K, et al. Susceptibility-weighted imaging of cerebral fat embolism. *Journal of computer assisted tomography* 2010;34:107-112.
- 41 Kumar S, Gupta V, Aggarwal S, et al. Fat embolism syndrome mimicker of diffuse axonal injury on magnetic resonance imaging. *Neurology India* 2012;60:100-102.
- 42 Sehgal V, Delproposto Z, Haddad D, et al. Susceptibility-weighted imaging to visualize blood products and improve tumor contrast in the study of brain masses. *Journal of magnetic resonance imaging : JMIR* 2006;24:41-51.
- 43 Craelius W, Migdal MW, Luessenhop CP, et al. Iron deposits surrounding multiple sclerosis plaques. *Archives of pathology & laboratory medicine* 1982;106:397-399.
- 44 Singh AV, Zamboni P. Anomalous venous blood flow and iron deposition in multiple sclerosis. *Journal of cerebral blood flow and metabolism : official journal of the International Society of Cerebral Blood Flow and Metabolism* 2009;29:1867-1878.
- 45 Zivadinov R, Schirda C, Dwyer MG, et al. Chronic cerebrospinal venous insufficiency and iron deposition on susceptibility-weighted imaging in patients with multiple sclerosis: a pilot case-control study. *International angiology : a journal of the International Union of Angiology* 2010;29:158-175.
- 46 King JO, Mitchell PJ, Thomson KR, et al. Cerebral venography and manometry in idiopathic intracranial hypertension. *Neurology* 1995;45:2224-2228.
- 47 Karahalios DG, Rekeate HL, Khayata MH, et al. Elevated intracranial venous pressure as a universal mechanism in pseudotumor cerebri of varying etiologies. *Neurology* 1996;46:198-202.
- 48 Sussman JD, Sarkies N, Pickard JD. Benign intracranial hypertension. Pseudotumour cerebri: idiopathic intracranial hypertension. *Advances and technical standards in neurosurgery* 1998;24:261-305.
- 49 Bioussé V, Ameri A, Bousser MG. Isolated intracranial hypertension as the only sign of cerebral venous thrombosis. *Neurology* 1999;53:1537-1542.
- 50 van Mook WN, Rennenberg RJ, Schurink GW, et al. Cerebral hyperperfusion syndrome. *Lancet neurology* 2005;4:877-888.
- 51 Tsai FY, Lee KW, Kao HW, Chen CY. Susceptibility-Weighted Imaging: an additional tool to diagnosis of brain death: initial experience. *The Neuro-radiology J.* 2012;2:733-736.
- 52 Tsai FY, Shi YY, Chan WP, Tsai PH, Chung HW. Practical Aspects of Shortening Acquisition Time in Brain MR Susceptibility-Weighted Imaging. *The Neuroradiology J.* 2012;2:613-620.

#### Contact

Fong Y Tsai, M.D., FACR  
Imaging Research Center  
Taipei Medical University  
250 Wu-Xing Street  
Taipei, 11031  
Taiwan  
ftsai@uci.edu or ftsai@tmu.edu.tw

# Pseudoprogression and Pseudoresponse: Imaging Challenges in the Assessment of Post Treatment Glioma

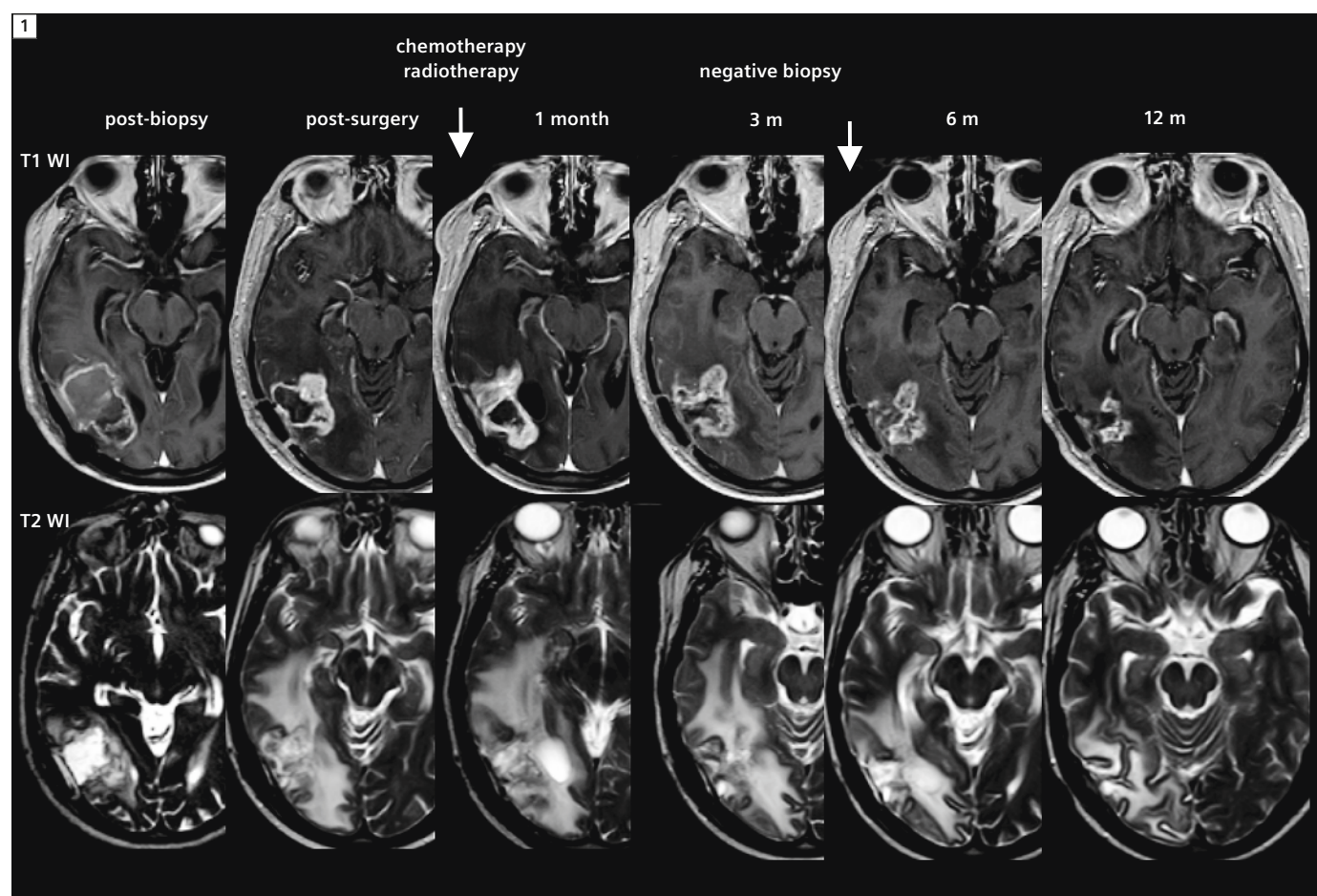
L. Celso Hygino Cruz Jr.; Nina Ventura

*Clínica de Diagnóstico por Imagem (CDPI, DASA), Rio de Janeiro, Brazil*

Glioblastoma multiforme is the most common primary malignant type of brain neoplasm in adults and is associated with a dismal prognosis. The current standard of care is surgical resection followed by radiation therapy

(RT) and concomitant and adjuvant temozolomide (TMZ) chemotherapy [1]. Bevacizumab, an anti-vascular endothelial growth factor (VEGF) agent, has been recently approved for recurrent glioblastoma.

With the standardization of treatment around surgery/RT/TMZ and the current use of bevacizumab, certain patterns that were not previously noticed are beginning to emerge. These changes in magnetic resonance (MR) imaging can



**1 Pseudoprogression.** 59-year-old male, GBM treated with surgery followed by chemotherapy and radiotherapy. Just one month after finishing the treatment the lesion increased in size. The chemotherapy was continued and the lesion decreased in the follow-up exams.

have an impact on individual patient care and on clinical trials of new therapies (alguma referencia).

### Pseudoprogression

Pseudoprogression is a subacute treatment-related reaction, usually associated with asymptomatic patients [2]. Shortly after completion of RT, predominantly within the first 3 months, patients with high-grade brain tumors can present with an increase in contrast-enhancing lesion size, mimicking tumor progression, followed by subsequent improvement or stabilization without any further treatment [3, 4].

### Pseudoresponse

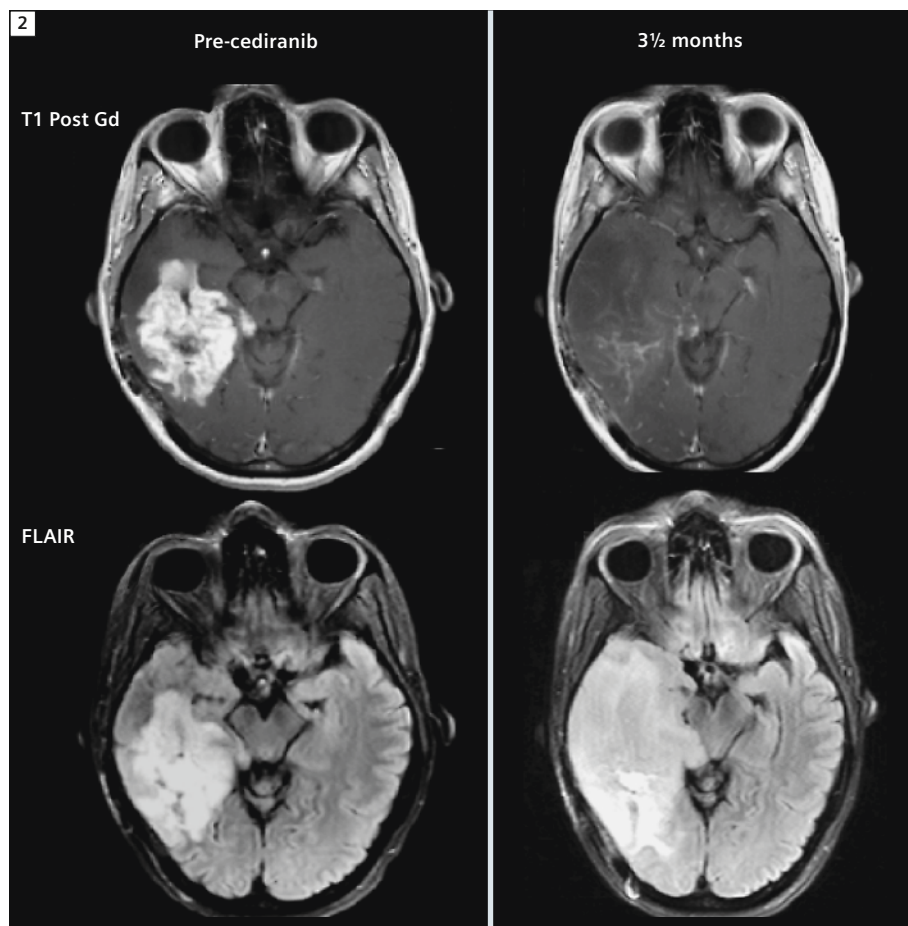
Pseudoresponse is a rapid decrease in contrast enhancement observed in recent high-grade glioma treatment trials after administration of antiangiogenic agents such as bevacizumab and cediranib, a VEGF receptor tyrosine kinase inhibitor [5]. These agents produce a high response rate and 6-month progression-free survival, but with rather modest effects on overall survival.

### Mcdonald Criteria

The Macdonald Criteria [6] are currently the most widely used guideline for assessing response to therapy in patients with high-grade gliomas. According to the Macdonald Criteria, tumor progression is considered to have occurred when an increase of 25% in the size of the contrast-enhancing lesion is observed. There are important limitations to these criteria, since they address only the contrast-enhancing component of the tumor, which is nonspecific and may not always be considered a true surrogate of tumor response.

### Pathophysiology

Pseudoprogression is found to correspond to gliosis and reactive radiation-induced changes without evidence of viable tumor [6]. It may represent an exaggerated response to effective therapy, involving early changes to the vascular endothelium and the blood-brain barrier (BBB), causing new or increased contrast enhancement on MR imaging examina-



**2 Pseudoresponse.** An enhancing expansive lesion is demonstrated after treatment failure with concomitant radio and chemotherapy. After initiation of antioangiogenic treatment, a marked decrease in the enhancing portion of the lesion is seen. However, a clear expansion of the lesion can be seen

tions. Most importantly, some studies have found an association between the incidence of pseudoprogression and increased survival; perhaps pseudoprogression represents an active 'inflammatory' response against the tumor [4]. The early decrease in contrast enhancement seen in pseudoresponse suggests a change in vascular permeability, with a 'normalization' of the BBB, rather than a true tumor reduction, as being the underlying cause of the improvement [7]. Normalization of the BBB and subsequent reduction in the vasogenic edema can result in an improvement of symptoms [8, 9].

### O6-Methylguanine DNA MGMT promoter

The methylation status of the methyltransferase (MGMT) promoter has been

shown to be a potent prognostic factor in patients with GBM; cells that are deficient in MGMT have shown an increased sensitivity to TMZ. Furthermore, MGMT promoter status may predict pseudoprogression in ~90% of patients with methylated glioblastoma [10], due to higher sensitivity to treatment [4] and an approximately 60% probability of early true tumor progression was observed in unmethylated MGMT promoter tumors [11]. Thus, we can speculate that methylated MGMT may be a good indicator of therapeutic response and better prognosis, as an increased overall survival rate has been observed in these patients.

## Advanced MR imaging techniques

No single imaging technique has been validated to recognize and adequately establish a diagnosis of pseudoprogression [12] and the diagnosis should depend on follow-up scans until an improved method is established.

Dynamic susceptibility-weighted contrast-enhanced perfusion MR imaging (DSC) is a surrogate marker for angiogenesis and has been used to assess brain tumor treatment response with high sensitivity for distinguishing residual/recurrent neoplasm from radiation brain injury [13–15].

Permeability DSC is also a potential new tool for differential diagnosis between pseudoprogression and true tumor progression. Although no prospective study

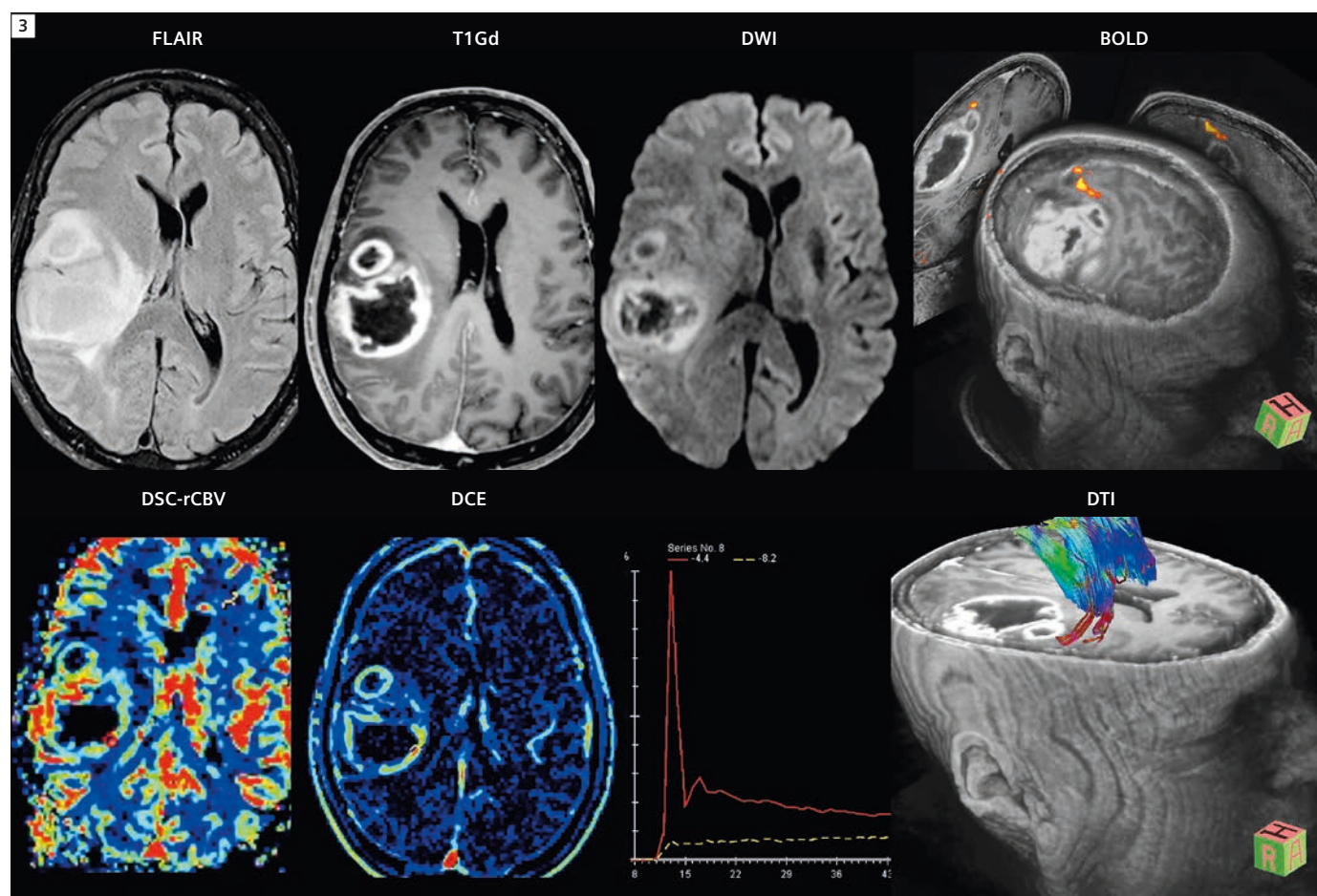
has examined this hypothesis, preliminary results with this new technique seem very promising, and a number of clinical trials are underway to better delineate the performance of all of the above techniques.

Other techniques, such as MR spectroscopy, diffusion-weighted imaging (DWI) and diffusion tensor imaging (DTI) have been assessed to differentiate tumor progression and/or residual tumor from necrosis [11, 16]. In short, none of them provides sufficient information for differential diagnosis between pseudoprogression and true tumor progression.

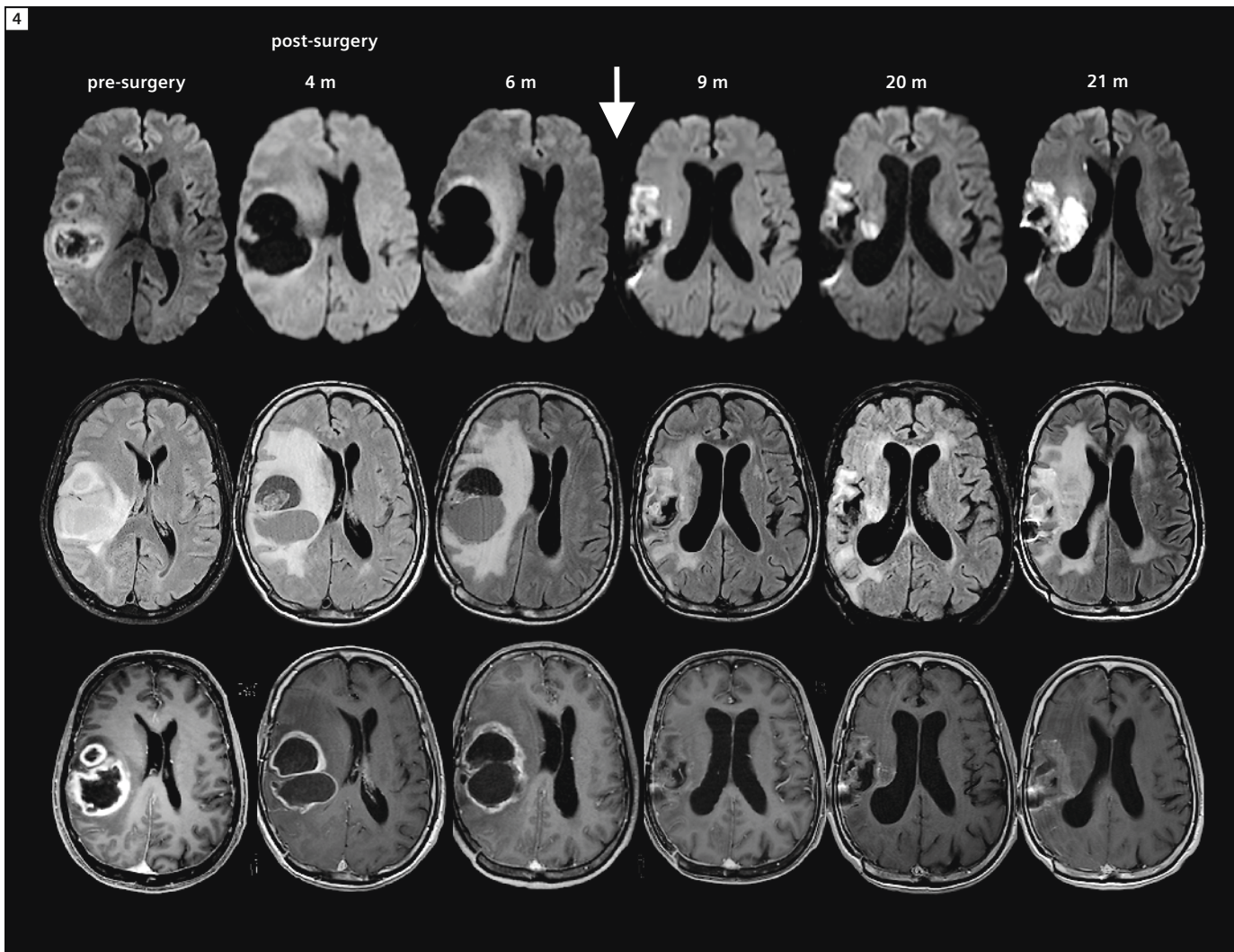
## Management

Pseudoprogression may influence the clinical recommendation to continue with adjuvant chemotherapy rather than the

change to a second-line therapy for recurrence [17]. Currently, the only method of distinguishing pseudoprogression and early progression of disease is to perform follow-up examinations of the patients, since conventional MR imaging is unable to differentiate them and alternative techniques have not yet been validated in prospective trials [4, 11]. Analysis with follow-up conventional MR imaging examinations allows such a distinction because the changes related to pseudoprogression decrease in size. If a post chemoradiotherapy follow-up MR imaging examination demonstrates complete or partial response or stable disease (i.e. smaller or stable tumor enhancement), maintenance of chemotherapy is typically continued. When enlargement occurs, then the treating



**3** 58-year-old male, GBM. In the first MR exam, an expansive necrotic lesion is demonstrated, with areas of restricted diffusion, hyperperfusion and high permeability. Presurgical planning could also be made by using functional MRI analysis using BOLD and tractography sequences to demonstrate the relationship with eloquent areas.



**4** After failure of the concomitant radio and chemotherapy, second line treatment with antiangiogenic drug was indicated. Just after the initiation of anti-VEGF therapy, a reduction in the contrast enhancing area was seen. Besides a continuing reduction in the enhancing portion of the lesion, an expansion is observed in the FLAIR sequence. However, diffusion images demonstrate an area of restricted diffusion, which may correspond to areas of tumor dissemination, and which may lead to new areas of contrast enhancement.

physician does face a dilemma. If pseudoprogession is suspected, perhaps based on MGMT status and/or very early changes in imaging features in the first months post treatment, ongoing chemotherapy with TMZ might be continued, with close monitoring. In clinically symptomatic patients, more options must be considered, including cessation of therapy, addition of anti-VEGF treatment, or even surgery, since identical symptoms can be observed in patients with true tumor progression and patients with pseudoprogession [8].

## Conclusion

Pseudoprogession and pseudoresponse are abnormalities that have been described following high-grade tumor treatment, and remarkably both appear to be associated with future favorable patient outcome. Both phenomena appear to be best diagnosed through follow-up scans because no established method of imaging is yet capable of yielding a definitive diagnosis of true tumor versus enhancement changes due to other reasons. DSC and other methods appear promising but require further testing in the multi-center setting.

## Contact

L. Celso Hygino Cruz Jr.  
Clínica de Diagnóstico por Imagem  
(CDPI,DASA)  
Centro Médico Barrashopping  
Av das Americas 466, SI 325  
Rio de Janeiro  
Brazil  
celsohygino@hotmail.com

## References

- 1 Hygino da Cruz LC Jr, Rodriguez I, Domingues RC, Gasparetto EL, Sorensen AG. Pseudoprogression and pseudoresponse: imaging challenges in the assessment of posttreatment glioma. *AJNR Am J Neuroradiol*. 2011 Dec;32(11):1978-85.
- 2 Taal W, Brandsma D, de Bruin HG, et al. Incidence of early pseudo-progression in cohort of malignant glioma patients treated with chemoradiation with temozolomide. *Cancer* 2008;113:405-10.
- 3 de Wit MC, de Bruin HG, Eijkenboom W, et al. Immediate post-radiotherapy changes in malignant glioma can mimic tumor progression. *Neurology* 2004;63:535-37.
- 4 Brandsma D, Stalpers L, Taal W, et al. Clinical features, mechanisms, and management of pseudoprogression in malignant glioma. *Lancet Oncol* 2008;9:453-61.
- 5 Batchelor TT, Sorensen AG, di Tomaso E, et al. AZD2171, a pan-VEGF receptor tyrosine kinase inhibitor, normalizes tumor vasculature and alleviates edema in glioblastoma patients. *Cancer Cell* 2007;11:83-95.
- 6 Macdonald DR, Cascino T, Schold SJ, et al. Response criteria for phase II studies of supratentorial malignant glioma. *J Clin Oncol* 1990;8:1277-80.
- 7 Gerstner ER, Duda DG, di Tomaso E, et al. VEGF inhibitors in the treatment of cerebral edema in patients with brain cancer. *Nat Rev Clin Oncol* 2009;6:229-36.
- 8 Brandsma D, van den Bent MJ. Pseudoprogression and pseudoresponse in the treatment of gliomas. *Curr Opin Neurol* 2009;22:633-38.
- 9 Clarke JL, Chang S. Pseudoprogression and pseudoresponse: challenges in brain tumor imaging. *Curr Neurol Neurosci Rep* 2009;9:241-46.
- 10 Brandes AA, Tosoni A, Franceschi E, et al. Recurrence pattern after temozolomide concomitant with and adjuvant to radiotherapy in newly diagnosed patients with glioblastoma: correlation with MGMT promoter methylation status. *J Clin Oncol* 2009;27:1275-79.
- 11 Brandes AA, Franceschi E, Tosoni A, et al. MGMT promoter methylation status can predict the incidence and outcome of pseudoprogression after concomitant radiochemotherapy in newly diagnosed glioblastoma patients. *J Clin Oncol* 2008;26:2192-97.
- 12 Chaski C, Neyns B, Michotte A, et al. Pseudoprogression after radiotherapy with concurrent temozolomide for high-grade glioma: clinical observations and working recommendations. *Surg Neurol* 2009;72:423-28.
- 13 Mangla R, Singh G, Ziegelitz D, et al. Changes in relative cerebral blood volume 1 month after radiation-temozolomide therapy can help predict overall survival in patients with glioblastoma. *Radiology* 2010;256:575-84.
- 14 Tsien C, Galba n CJ, Chenevert TL, et al. Parametric response map as an imaging biomarker to distinguish progression from pseudoprogression in high-grade glioma. *J Clin Oncol* 2010;28:2293-99.
- 15 Gahramanov S, Raslan AM, Muldoon LL, et al. Potential for differentiation of pseudoprogression from true tumor progression with dynamic susceptibility-weighted contrasted-enhanced magnetic resonance imaging using ferumoxytol vs. gadoteridol: a pilot study. *Int J Radiat Oncol Biol Phys* 2011;79:514-23.
- 16 Sundgren PC, Fan X, Weybright P, et al. Differentiation of recurrent brain tumor versus radiation injury using diffusion tensor imaging in patients with new contrast enhancing lesions. *Magn Reson Imaging* 2006;24:1131-42.
- 17 Sanghera P, Perry J, Sahgal A, et al. Pseudoprogression following chemoradiotherapy for glioblastoma multiforme. *Can J Neurol Sci* 2010;37:36-42.

*We are looking forward to hearing from you.*

[www.siemens.com/flash-survey](http://www.siemens.com/flash-survey)



Please take a moment to complete a brief reader survey.

Your feedback will help us to produce a high-quality publication that matches your needs and serves as a resource for achieving your clinical, operational and financial goals. We value your feedback.

# Imaging and Spectroscopy at 9.4 Tesla: First Results on Patients and Volunteers

R. Pohmann<sup>1</sup>; G. Shajan<sup>1</sup>; J. Hoffmann<sup>1</sup>; J. Budde<sup>1</sup>; G. Hagberg<sup>1,2</sup>; O. Bieri<sup>3</sup>; S. Bisdas<sup>4</sup>; U. Ernemann<sup>4</sup>; M. Weigel<sup>5</sup>; Ph. Ehses<sup>1,2</sup>; J. Hennig<sup>5</sup>; G. Chadzynski<sup>1,2</sup>; K. Scheffler<sup>1,2</sup>

<sup>1</sup>MRC Department, MPI for Biological Cybernetics, Tübingen, Germany

<sup>2</sup>Dept. Biomedical Magnetic Resonance, University of Tübingen, Tübingen, Germany

<sup>3</sup>Division of Radiological Physics, Department of Radiology, University of Basel Hospital, Basel, Switzerland

<sup>4</sup>Dept. of Neuroradiology, University of Tübingen, Tübingen, Germany

<sup>5</sup>Department of Radiology Medical Physics, University Medical Center Freiburg, Freiburg, Germany

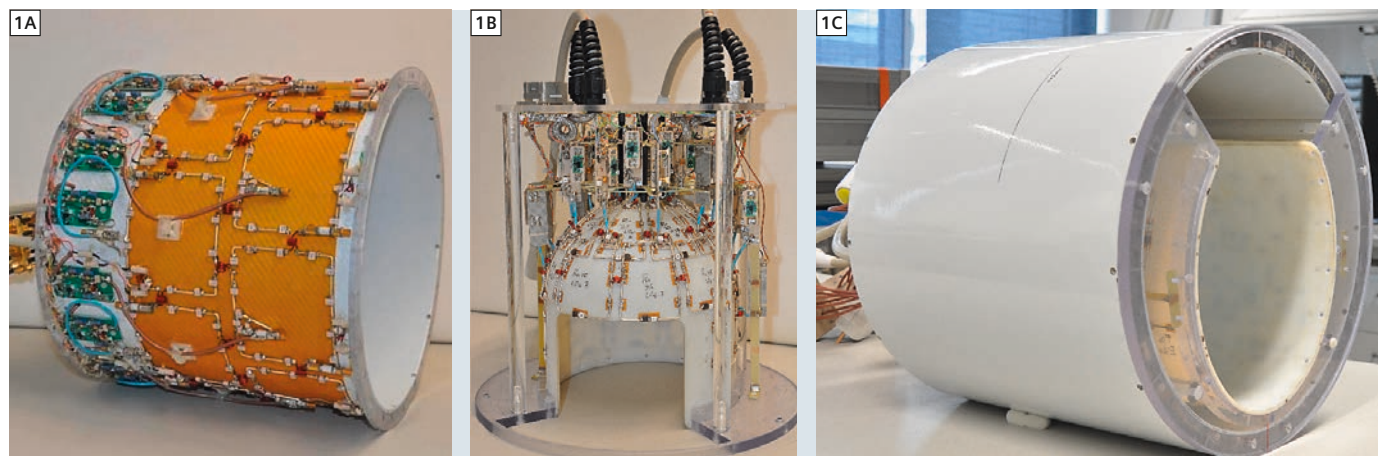
## Introduction

9.4 Tesla<sup>8</sup> (T) is currently the highest field strength to have been successfully used for imaging and spectroscopy in humans, and the Max Planck Institute for Biological Cybernetics in Tübingen is probably the first site to have enrolled patients for an ethically-approved study of brain tumors in November 2012. Since 2008 when the first human MR

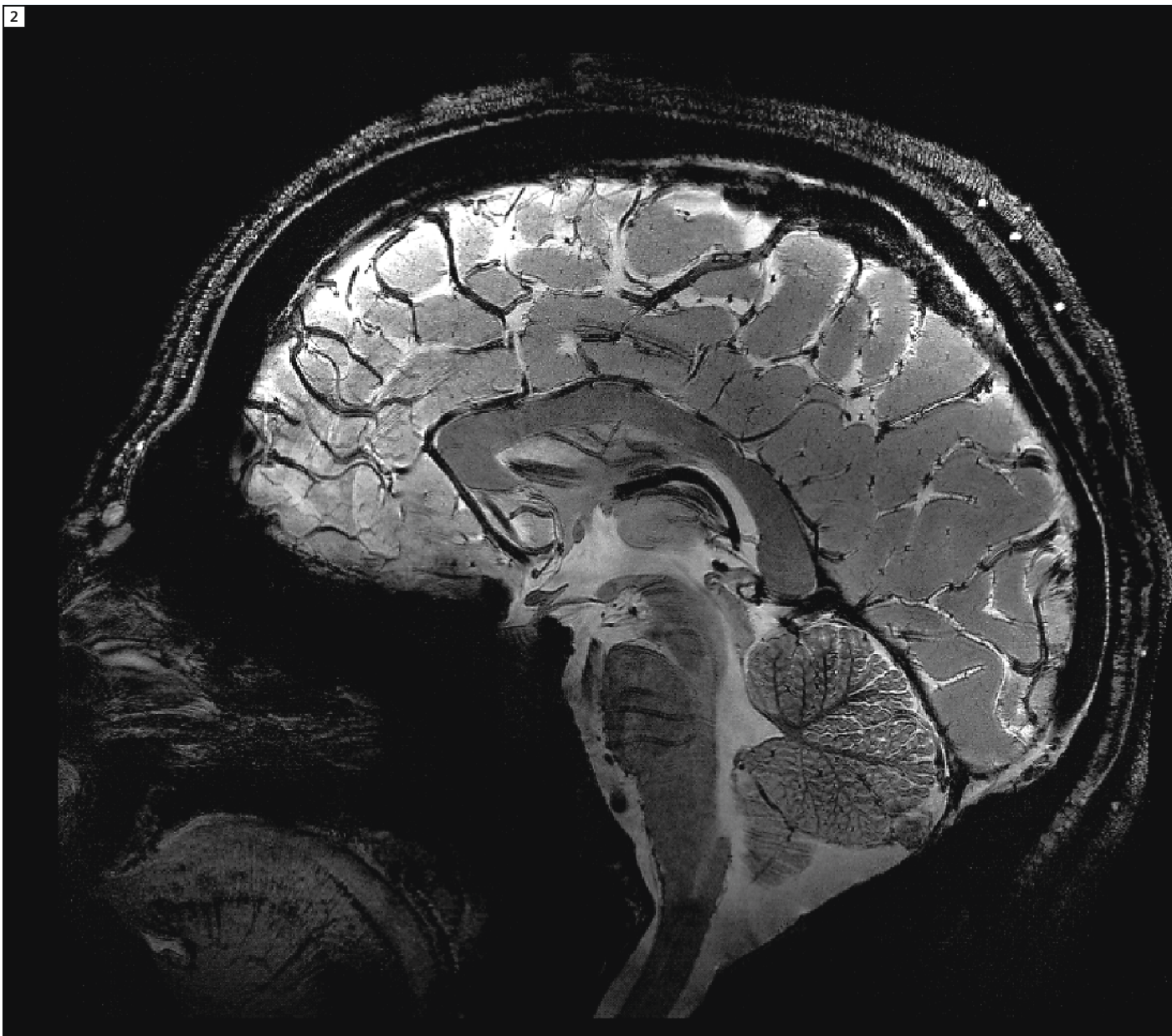
imaging (MRI) / MR spectroscopy (MRS) measurements at 9.4T began in Tübingen, 261 healthy subjects have volunteered to participate.

The big step from 3T to 7T has clearly shown the advantages and problems at very high fields. Most prominent are challenges related to the transmitted radio frequency (RF) field in terms of

specific absorption rate (SAR) and transmit homogeneity, as well as increased susceptibility effects. The next step from 7T to 9.4T is somewhat smaller and, accordingly, further increased RF inhomogeneity and susceptibility variations have been observed, although these are qualitatively similar to those effects reported at 7T. So far, in our experience



**1** (1A) Photograph of the transmit array hardware. Integrated TR switches with preamplifiers enable the coil to be used in the transceive mode as well. (1B) Photograph of the 31-channel receive-only array. (1C) Final RF configuration with the receive array assembled inside the transmit array.



**2** A non-intensity corrected sagittal gradient echo image demonstrating whole brain coverage at 9.4T. Transmit phases of the 16 transmit elements were optimized for this slice. An in plane resolution of 280  $\mu\text{m}$  with a slice thickness of 1 mm was obtained within 5 min, 33 s (TR 400 ms, TE 14 ms, nominal flip angle 30°).

the most striking differences between 7T and 9.4T are the even shorter RF wave length and the significantly increased susceptibility effects. The short wave length and thus locally very confined excitation patterns actually increase the flexibility and effectiveness of parallel transmit techniques and lead us to the design of transmit arrays with 16 independent loops. The sensitivity to

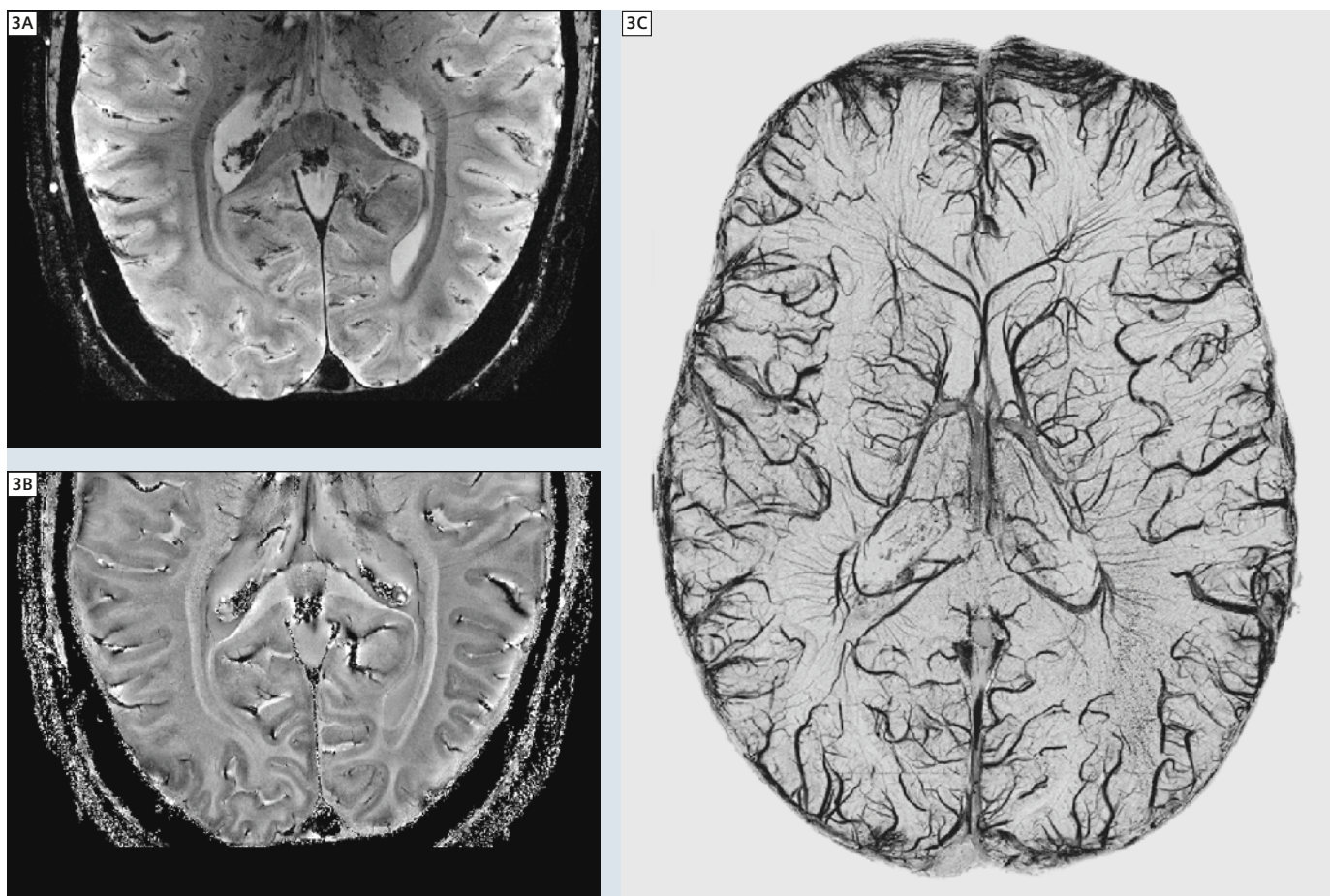
local susceptibility changes is also highly increased, as demonstrated in T2\*-weighted BOLD experiments, and effects related to orientational anisotropy become clearly visible.

In this report we show examples of different imaging techniques and spectroscopy that has been measured during the last two years at 9.4T. The goal was to test the feasibility of basic imaging

sequences, such as gradient echoes, and to apply advanced techniques like TrueFISP and hyperechoes with reduced SAR. Quantitative comparisons of signal strength, relaxation times and contrast can be found in the referenced papers.

### Dedicated RF coils for 9.4T

In addition to the static magnetic field strength ( $B_0$ ), RF coil performance is a



**3** T2\*-weighted magnitude (3A) and phase (3B) image of the same slice through the brain of a volunteer, acquired at 9.4T. (3C) Susceptibility-weighted image from a different volunteer. This image was acquired with a 16-channel microstrip transceiver coil and a spatial resolution of  $0.175 \times 0.175 \times 1.3 \text{ mm}^3$ .

dominant factor in determining the sensitivity of an MR experiment. The principal RF engineering challenge at high  $B_0$  field is to achieve homogeneous excitation across the volume of interest. As the wavelength in tissue approaches sample dimensions, constructive and destructive interference of the electromagnetic field causes field concentration, but also signal voids, resulting in an inhomogeneous MR image [1]. At 9.4T, even in human brain MRI, severe field dropouts appear in the lower temporal lobe and cerebellum if the coil is driven in the conventional circularly polarized (CP) mode, making it a challenging task to achieve whole-brain excitation. While the traveling wave approach is able to extend the imaged volume into the lower regions of the

brain with often acceptable homogeneity [2], static and dynamic RF shimming approaches are the most promising techniques to mitigate the  $B_1^+$  field inhomogeneities. They require an array of transmit elements with the possibility to individually control the amplitude and phase of the current to each of these coil elements. An additional degree of freedom can be obtained by arranging the transmit elements in multiple rows to extend the longitudinal coverage and more importantly, to correct the inhomogeneities in all three directions [3]. While transceiver coils, which combine multi-channel transmit and receive in the same array elements, are a popular design for ultra-high field applications [4], both signal-to-noise ratio (SNR) and parallel imaging performance can be

improved by using a separate array of receive coil detectors that closely follows the contours of the anatomy [5]. Parallel imaging benefits particularly from the shorter wavelength at ultra-high field strength because of reduced inductive coupling to the farther coil elements, resulting in distinct coil sensitivities and hence effective sensitivity encoding [6]. Our approach for human brain imaging at 9.4T combines separate transmit and receive arrays to maximize the receive sensitivity together with the ability to modulate the transmit field in three dimensions.

The transmit coil consists of 16 elements arranged in two rows of eight elements each [3]. The lower row elements are rotated by  $22.5^\circ$  with respect to the upper row and all adjacent coil elements

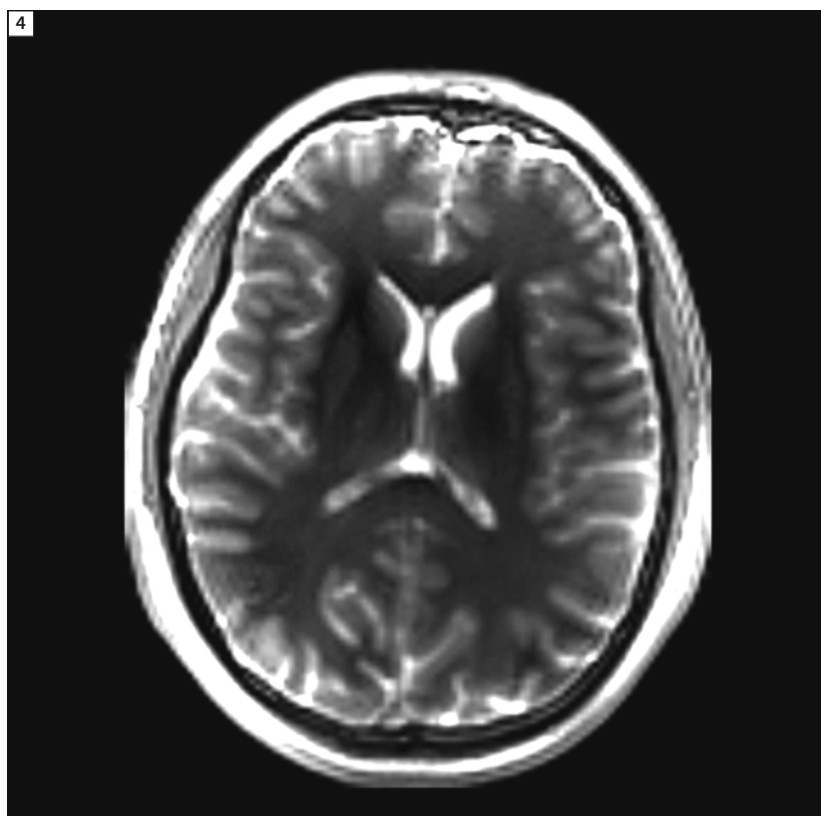
are inductively decoupled. For reception, 31 elements are arranged symmetrically in 4 rows on a close-fitting helmet for maximum sensitivity. A combination of inductive decoupling and geometric overlap is used to minimize the inductive coupling between the coil elements [7]. The transmit and receive arrays and the final setup are shown in Figure 1. Unlike for the closely-coupled transmitter arrays, subject-specific adjustments of the transmit array are not required. Furthermore, the RF circuitry and low noise preamplifiers required for the receive elements are closely packed in the coil housing, thus providing a simple and fast setup, comparable to clinical routine examinations. Due to the dual row design of the transmit array, the entire brain, including the cerebellum, can be imaged. This is demonstrated in the sagittal image in Figure 2, for which slice selective static phase shimming was applied to optimize the transmit phase.

### High-resolution GRE, TrueFISP and susceptibility-weighted imaging

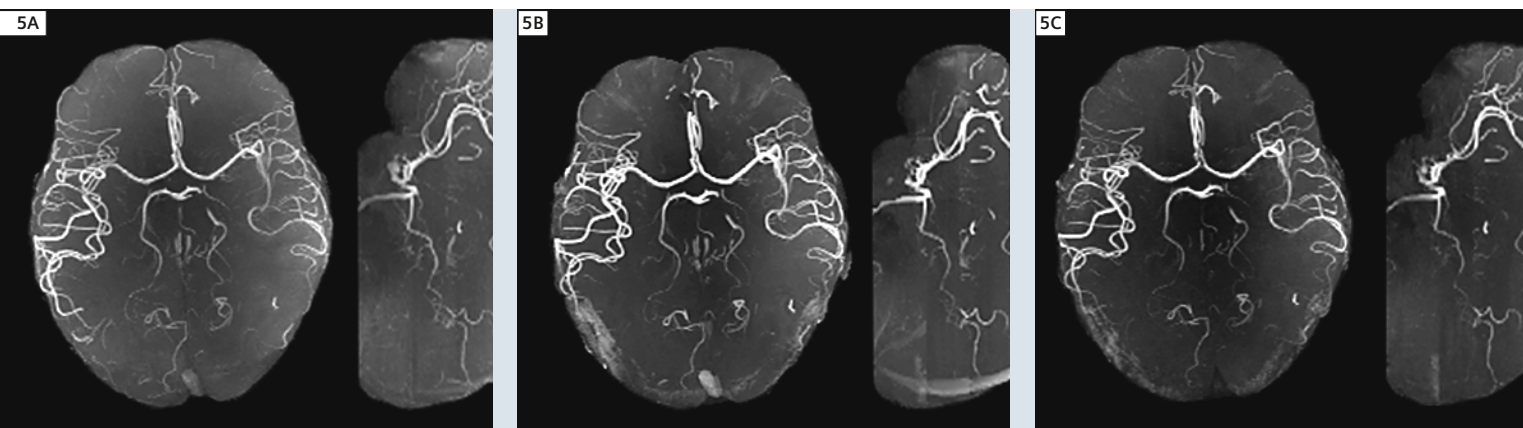
Due to the high sensitivity towards variations in the magnetic susceptibility at 9.4T, improved and even novel contrast mechanisms can be achieved. The pulse sequences required to exploit these advantages are based on gradient-echo techniques and are relatively insensitive towards SAR limitations and inhomogeneities of the transmit field. T2\*-weighted images (Fig. 3A) already show excellent image contrast and can replace T1 or T2-weighted imaging techniques that suffer from serious SAR-limitations and B<sub>1</sub>-dependent contrast variations in many applications. In addition, these techniques allow for fast acquisition with parameters that are optimized for maximum SNR. Thus, using flip angles close to the Ernst-angle and carefully adjusting bandwidth and echo time makes it possible to reach high spatial resolutions in acceptable scan times. The image in Fig. 3A was acquired with a voxel volume of 40 nl (voxel size 0.2 × 0.2 × 1 mm<sup>3</sup>, echo time 20 ms,

repetition time 28 ms, 21 slices) within around 15 min, using the above described combination of a 16-channel transmit and a 31-channel receive array. Even higher contrast-to-noise ratio can be reached by using the image phase as completely B<sub>1</sub>-independent contrast parameter. Phase images (Fig. 3B) show good contrast between gray and white matter, but are also able to depict intracortical structures or oriented fibers. In addition, phase imaging at high fields is used to detect changes in iron or myelin content [8, 9]. At 9.4T, the high sensitivity of phase imaging makes voxel sizes below 20 nl feasible within reasonable scan times of around 20 minutes. Finally, magnitude and phase information are combined in susceptibility-weighted imaging (SWI, Fig. 3C) to specifically emphasize susceptibility

variations as in venous blood. In a comparison to images acquired at 3T, an SNR gain of almost a factor of nine was found [10]. In addition, the high sensitivity towards susceptibility variations made it possible to distinguish venous structures at a considerably smaller size. These data show that anatomical imaging with high resolutions, great contrast and high image quality is possible at 9.4T without the limitations due to SAR or B<sub>1</sub>-inhomogeneity. Modulations of the magnetic susceptibility, especially, can be detected with high accuracy with simple gradient echo sequences at 9.4T. Additionally, the strong susceptibility effect can help to improve the spatial specificity of spin-echo EPI-based functional MRI studies [11]. Successful balanced SSFP imaging is commonly hampered by its prominent



**4** Axial sample image from an isotropic 3D whole brain balanced SSFP scan acquired at 9.4T (other scan parameters were: 1.5 mm isotropic, 144 × 144 × 96 matrix, TR 1.6 ms, TE 0.6ms, BW 1825 Hz/Pixel, flip angle ~10°, TA 9.5 sec.).



**5** Maximum Intensity Projections across 40 mm for axial (left) and sagittal multi-slab 3D ToF data sets acquired with FA/TE: **(5A)** 14°/4.55 ms; **(5B)** 24°/4.55 ms; **(5C)** 24°/10ms, all from a healthy volunteer.

sensitivity to local frequency offsets (off-resonances) that may lead to pronounced signal voids, typically appearing as dark bands in the image. Since the major cause of such local off-resonances are susceptibility-related frequency shifts that are expected to scale linearly with the main magnetic field, successful banding artifact reduction becomes a key issue at ultra-high field MRI with balanced SSFP.

Here, we demonstrate *in vivo* balanced SSFP imaging of human brain at 9.4T. Signal voids with balanced SSFP become apparent for frequency offsets close to about  $1/(2TR)$  or  $-1/(2TR)$  or multiple thereof, where TR is the repetition time of the balanced SSFP imaging protocol. As a result, the appearance of banding artifacts with balanced SSFP is directly related to its repetition time and can thus be mitigated by a reduction by ultra-fast imaging, typically associated with a TR close to about 1 ms. For a TR  $\sim 1.6$  ms (see Fig. 4), banding artifacts are expected for local frequency offsets as far as about  $\pm 300$  Hz, and artifact-free balanced SSFP imaging becomes available and can be demonstrated even at ultra-high fields. SAR constraints that become more severe at ultra-high fields and the exceptional short TR used with ultra-fast imaging limit the maximum flip angle for balanced SSFP imaging for

*in vivo* applications to about  $10^\circ$ . For the typical low  $T2/T1 \ll 1$  for tissues and with respect to an estimated  $T2/T1 \sim 1/30$  for brain tissue at 9.4T, however, optimal balanced SSFP imaging becomes shifted towards the low flip angle regime ( $\sim 20^\circ$ ), approaching the limits set by SAR. Moreover, for balanced SSFP only a marginal contrast is expected between normal appearing gray and white matter tissue due to the highly similar  $T2/T1$ , being in contrast to the experimental results, as shown in Fig. 4. Similar to what was observed at low fields, the appearance of a prominent contrast between gray and white matter is likely due to magnetization transfer effects.

### Time-of-flight imaging in patients and volunteers

Time-of-flight (ToF) angiography aims to visualize the cerebral arteries and relies on the in-flow effect: continuous excitation suppresses the local signal while in-flowing blood remains unsuppressed and strongly contributes to the final image contrast. The most popular approach is selective 3D excitation of a slab with limited extent. The image contrast is determined by the slab thickness, the velocity of the blood flow across the slab and by the sequence repetition time, TR. The goal is to avoid saturation

of the flowing blood, allowing it to cross the entire slab within just one or a few TR times.

ToF angiography at ultra-high magnetic field strengths benefits from long tissue  $T1$  times that lead to improved background suppression. However, SAR restrictions impose severe limits on the reduction of tissue signal that may be achieved, and the suppression of signals in the cerebral veins, obtained by additional pulses, also becomes challenging. At 7T, the use of VERSE (variable-rate selective excitation, [12]) pulses has proven beneficial to attain both goals: a high signal contrast in arteries only within SAR limits [13, 14]. VERSE consists of a shaped RF pulse applied together with a time-varying gradient. In order to reduce SAR without excessive time penalty, pulse segments with high RF power are prolonged in time, while segments with low power requirements are shortened. The excitation bandwidth of VERSE is therefore effectively varied from segment to segment, making it sensitive to off-resonance effects, such as chemical shift differences and  $B_0$  inhomogeneities. Since such effects tend to increase with the magnetic field strength, we decided to use the TONE RF pulse with a 100% flat top shape for excitation rather than VERSE. The sole modification of the standard clinical

*syngo* MR B15 sequence was to allow a variable duration of the excitation pulse. Slab-wise imaging (2.4 cm axial FOV) with a 3D gradient echo sequence, a TR of 20 ms, a GRAPPA factor of 4 and 32 reference lines, and an in-plane voxel size of  $0.5 \times 0.5$  mm with a slice thickness of 0.4 mm was used. The echo time (3.8; 4.55; 10 ms), flip-angle (FA 15–36°) and the duration of the excitation pulse (1024–4096  $\mu$ s) were varied. The acquisition time for each slab was between 1 ½–3 ½ min.

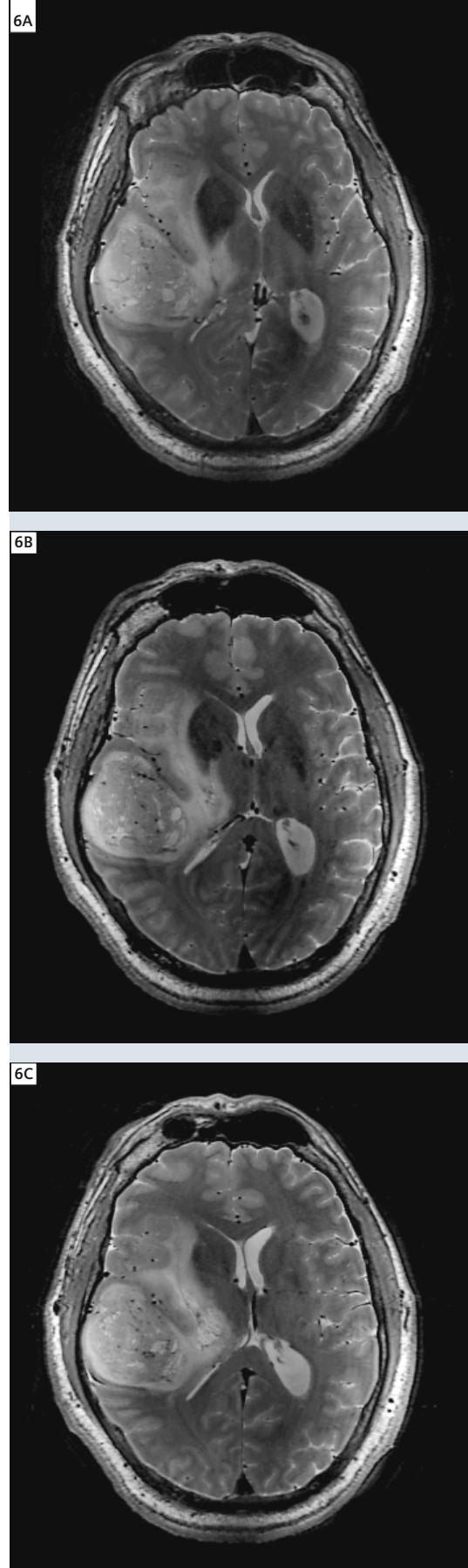
Post-processing consisted of removing the scalp signal originating from the subcutaneous fat using BET (Brain Extraction Tool, FSL<sup>5</sup>), and intensity correction, obtained after thresholding out the angiographic information and fitting the background signal with a 2<sup>nd</sup> order polynomial. Maximum Intensity Projections were performed across 40 mm. We found that a reasonable flip angle at 9.4T is 20–30° to optimize the signal for blood that remains within the slab for about 5 excitations.

The improved contrast-to-background ratio that we expected was not achieved with the standard TONE pulse due to SAR restrictions. Even in the absence of pulses for the suppression of venous blood or magnetization transfer, we came close to the SAR limits (95–99%) with low flip angles of 14–16°. Under these conditions, the venous signal was prominent and the image contrast was poor (Fig. 5A). By increasing the duration of the RF pulses, the flip angle could be increased to 24°–32°, yielding an improved image contrast (Fig. 5B). Nevertheless there was no room for additional venous suppression pulses, not even by the reduced flip angle approach that has been successfully introduced at 7T [15]. At 9.4T, not only the T1 but also the T2 relaxation times are changed. The T2 in arterial blood is similar to tissue (about 40 ms) while in venous blood it is substantially shorter (5–9 ms dependent on the fractional oxyhemoglobin content [16]). In line with these observations we found that increasing the TE from 4.5 to 10 ms was sufficient to suppress the

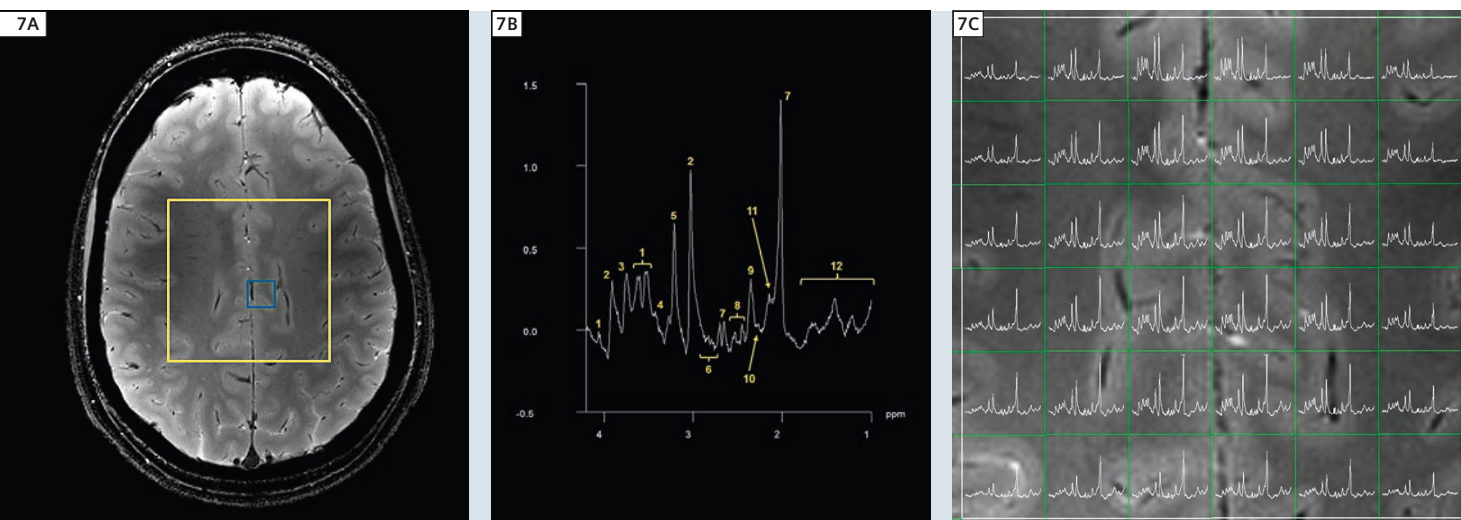
venous blood in the sagittal sinus without substantially compromising the visibility of the arteries (Fig. 5C).

## Hyperecho imaging

Turbo spin echo (TSE, RARE, FSE) sequences [17] find widespread application in clinical routine MRI, the main reason being that they combine the diagnostically relevant T2 contrast with the robust signal behavior of spin echo refocusing. T2 contrast is highly sensitive to a broad variety of pathologies such as inflammation and is an indispensable tool for examination of various pathologies of the CNS. Spin echo refocusing facilitates a relative insensitivity to susceptibility and field inhomogeneity, i.e.  $B_0$  effects. Additionally, TSE sequences produce a high amount of stimulated echo contributions that are T1-weighted. Since  $T1 \gg T2$  for most biological tissues, particularly at ultra-high fields, these stimulated echo contributions partially counterbalance the signal loss from refocusing flip angles deviating from 180° due to  $B_1$  variations. All in all, these reasons seem to make TSE sequences the ideal technique for clinical imaging at (ultra-)high fields. However, a major drawback is the high RF power deposition caused by the multiple refocusing RF pulses, which can lead to severe tissue heating. Thus, the RF power deposition, usually quantified in terms of SAR has to be strictly limited. Since SAR increases quadratically with field strength, the same image acquired at 9.4T requires almost ten times the SAR as at 3T. Therefore, the fast multiple refocusing of magnetization with high turbo factors in modern TSE sequences severely hampers their use at ultra-high fields. Common ways of mitigating SAR problems include reducing the number of slices, shortening the echo train via a smaller turbo factor, increasing the repetition time TR, changing the shape of the RF pulses (e.g. using a Gaussian shaped pulse) and increasing the duration of the RF pulses. No matter which (combination of) option(s) is chosen, some compromise has to be made in



**6** Three out of five slices from the hyperTSE experiment performed at 9.4T in Tübingen.



**7** Localizer (7A), single spectrum (7B) and all the spectra within the VOI (7C) acquired from the brain of a healthy volunteer. Localizations of VOI and single spectrum were marked with yellow and blue squares respectively.

terms of SNR, acquisition time, volume coverage and image quality. Another effective means to reduce SAR is to lower the refocusing flip angle in a TSE sequence. However, for conventional TSE sequences with constant refocusing flip angles, this method results in lower SNR and changes the contrast of the resulting images, particularly in case of the vast flip angle reductions that are necessary for TSE imaging at 9.4T. Methods that employ variable instead of constant refocusing flip angles along the TSE train have been introduced in order to allow SAR reductions while maintaining a T2-like contrast and high SNR. These novel TSE sequences are usually referred to as hyperTSE-, Hyperecho-TSE-, and smooth transitions between pseudo steady states (TRAPS)-sequences [18, 19, 20, 21]. Generally, high signal for the echoes encoded for the center of *k*-space is maintained, thus, warranting a high SNR for the reconstructed image. The signal in the peripheral parts of *k*-space may be reduced slightly due to lower flip angles; however, strong stimulated echo contributions still maintain sufficient signal levels at ultra-high fields due to  $T_1 \gg T_2$ , as mentioned above.

Whereas the Hyperecho-scheme makes use of symmetry relations between the flip angles to reinstate the full signal at some given point of time (echo) within the TSE train [18], TRAPS allows an almost free variation of refocusing flip angles along the TSE train after a preparation of magnetization close to the so-called static pseudo steady state (SPSS) [19, 22, 23]. In the SPSS, the echo intensity always stays close to the optimal value that can be reached for a given flip angle. Any loss of coherence would lead to signal fluctuations and inevitable signal loss, resulting in image artifacts. Since the variation of signal in *k*-space directly influences the point spread function (PSF), flip angle variations can also be used to improve the PSF. Thus, TRAPS, which offers the unique possibility to vary flip angles in a flexible way in hyperTSE sequences, allows both considerable SAR savings as well as the optimization of image properties for TSE [19, 20, 21, 24]. A great emphasis in TRAPS lies on the flip angle train, which has to be properly adapted to any changes of the protocol settings that influence the timing or the view ordering / reordering of the TSE sequence. 'Unwise variations' can lead to

suboptimal image and SAR properties.

Basically, there are two recipes to calculate suitable flip angles for TRAPS:

1. Setting the flip angles directly via some support points defined by functions, etc. This AUTO-TRAPS approach has the advantage that the flip angle courses can be adapted in a flexible way to consider protocol changes made by the user, and the AUTO-TRAPS recipe allows a quite direct control of SAR [21].
2. More sophisticated refocusing flip angle schemes can be obtained by calculating the flip angles from a predefined signal course or echo intensity course along the echo train [24]. This method has the advantage that dedicated image properties can be set via the predefined signal course [24]. However, there is no unique solution for the flip angles and it is more complex to adapt the settings to any protocol changes made by the user.

For our proof of concept study at 9.4T, a flexible AUTO-TRAPS approach was used [21]. The TRAPS based flip angle method was implemented in a self-made TSE sequence within the IDEA platform *syngo* MR B15. A T2-weighted TSE protocol with the following parameters was

set up: FOV  $220 \times 175 \text{ mm}^2$ , 5 slices with 1 mm slice distance, voxel size  $0.58 \times 0.58 \times 1.0 \text{ mm}^3$ , turbo factor 17, TE 48 ms, TR 8.94 s. Due to additional T1-weighted stimulated echo contributions, hyperTSE sequences (as all low flip angle TSE sequences) show a reduced T2 contrast compared to a TSE  $180^\circ$  sequence at a given echo time. In order to compensate for this effect, TE was increased from the originally desired value [20]. Here, please note that T2 relaxation times are considerably shorter at 9.4T than at 3T or even 1.5T. Thus, a comparatively low TE already gives a substantial T2 contrast. The used hyperTSE protocol demonstrated a relative SAR of 33.7%, i.e. a SAR saving of 66.3% compared to a conventional TSE sequence. This allowed the acquisition of 5 slices instead of only 1. Fig. 6 shows the first hyperTSE images from a patient at 9.4T. The used AUTO-TRAPS based hyperTSE demonstrates very good imaging behavior and suggests that hyperTSE sequences are highly suitable for acquiring ultrahigh resolution images at 9.4T that offer promising diagnostic value.

### Proton spectroscopy in patients and volunteers

Chemical shift imaging (CSI) data were collected with a Stimulated Acquisition Mode sequence (STEAM) with the following parameters: TE 20 ms; TR 2000 ms; TM 11 ms; FOV  $160 \times 160 \text{ mm}^2$ ; volume of interest (VOI)  $60 \times 60 \times 10 \text{ mm}^3$  and  $40 \times 40 \times 10 \text{ mm}^3$  (volunteer and patient respectively); voxel size  $10 \text{ mm}^3$  isotropic; spectral bandwidth 4000 Hz. In order to keep the reference voltage below the hardware limits, the  $90^\circ$  h-sinc RF pulses (sinc pulses with 4 side lobes) within the standard STEAM sequence had to be replaced by  $90^\circ$  hermite pulses. Additionally, their RF bandwidth has been increased to 3100 Hz. This allowed minimizing the influence of chemical shift displacement. In order to determine the reference voltage necessary for the STEAM sequence, CSI acqui-

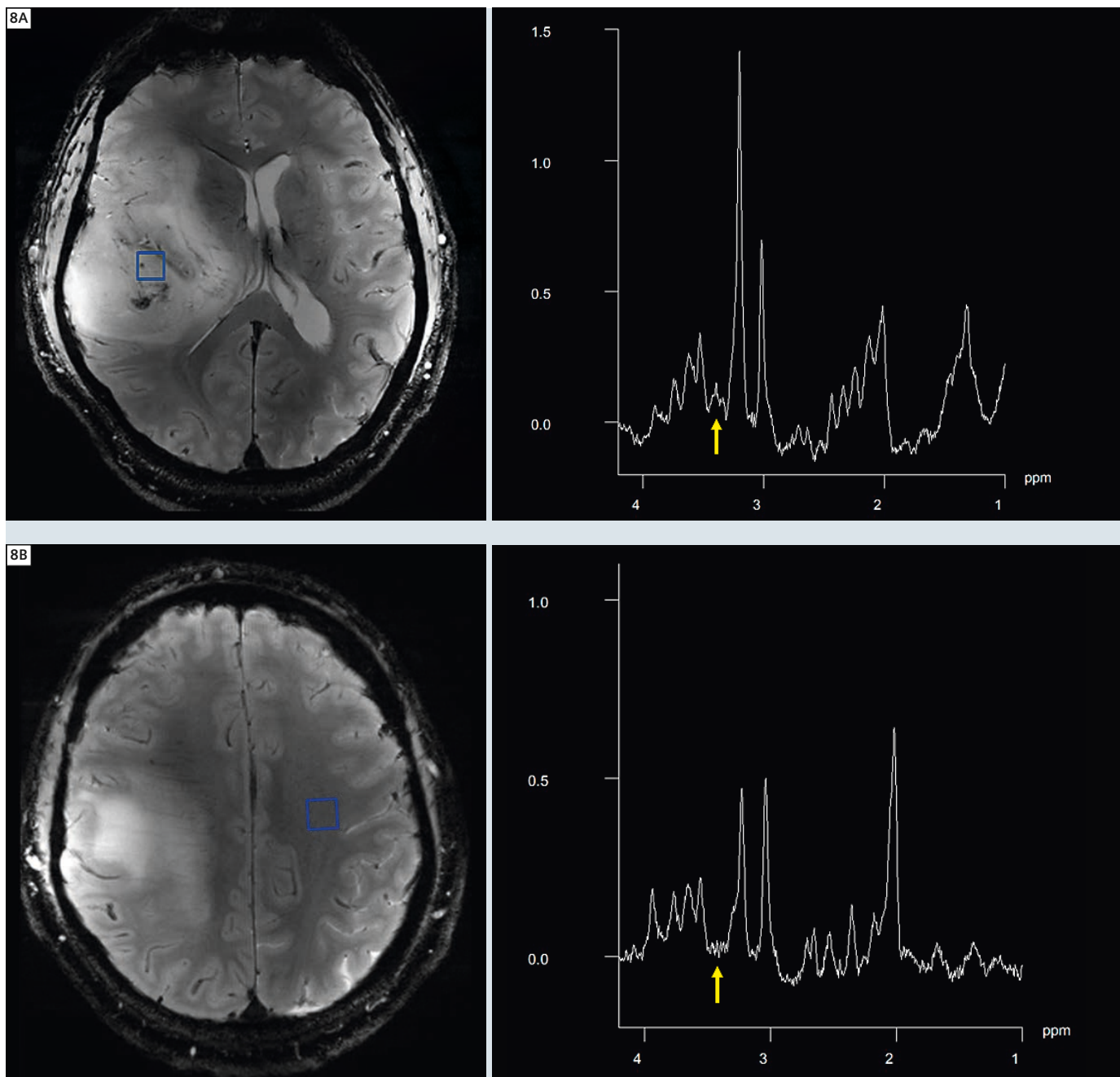
sition was preceded by an Actual Flip angle Mapping (AFI) scan [25, 26]. Figure 7 shows spectra acquired from a healthy volunteer (31 years old). In this case, an 8-channel transmit coil combined with a 24-channel receive array was used for data acquisition. Here, the spectra were acquired from a superior region of the human brain. The VOI (yellow square, Fig. 7A) was placed in the axial plane, parallel to the line between the anterior and posterior commissures (ac-pc line). A typical spectrum from healthy brain tissue (localization within the VOI marked with blue square) is presented in Fig. 7B. The following brain metabolites have been identified: myo-Inositol (Ins, marked with 1), methylene ( $\text{CH}_2$ ) and methyl groups ( $\text{CH}_3$ ) of creatine and phosphocreatine (Cr and PCr, #2), overlapped peaks of glutamine and glutamate (Gln and Glu, #3), taurine (Tau, #4), choline containing compounds (tCho, #5), aspartate (Asp, #6), N-acetylaspertate (NAA, #7), Gln (#8), Glu (#9),  $\gamma$ -Aminobutyric acid (GABA, #10), N-acetylaspertylglutamate (NAAG, #11) and macromolecules (#12). Improved spectral resolution and SNR make it possible to differentiate between metabolites which are typically overlapped at lower field strengths, particularly the resonances between  $\sim 4$  and  $\sim 3.2$  ppm, and  $\sim 2.9$  and  $2.1$  ppm (Ins, Glu, Gln, GABA, NAA and NAAG). Those findings are in agreement with results described in previous studies [27, 28]. Analysis of the spectra acquired from the entire VOI (Fig. 7C) shows that the spectra from the central  $4 \times 4$  voxel region have excellent quality. Specialized sequences [29, 30] and parallel transmit techniques [31] will further improve the spectra by reducing the chemical shift displacement, which is still significant for some of the peaks (tCho, Cr and NAA), as well the dependence of the signal amplitude on the spatially inhomogeneous transmit field. Spectra acquired from the brain of a 43-year-old patient with clinically confirmed oligodendroglioma are shown in

Fig. 8A. MR scanning showed the presence of an extended tumorous mass in the right hemisphere, pressing on the cerebral midline that was deviated towards the left hemisphere. In the antero-posterior direction the tumor extended from the frontal to the parietal lobe, and in the cranio-caudal direction from the hand area in the primary motor cortex, across the lateral fissure into the temporal cortex. The tumor texture was heterogenous and showed calcifications, confirmed by CT scans, indicating an oligodendroglioma.

Here all the CSI data were collected with a 16-channel transmit coil combined with a 31-channel receiving helmet. Spectra were collected at two different locations: within the lesion (Fig. 8A), and contralaterally, in healthy tissue (Fig. 8B). Analysis of the acquired spectra revealed a strong decrease in the signal of NAA and an increase in signals of tCho, Glu, Gln, and Ins within the lesion (Fig. 8A) compared to the contralateral side (Fig. 8B). Observations made here are in agreement with the previous clinical studies performed at lower magnetic fields (1.5 and 3T) [28, 29]. Furthermore, our results suggest an increase in signals of Tau and scyllo-inositol (Scyllo) within the tumor tissue (Figs. 8A and 8B, marked with yellow arrow). According to the latest research those play an important role in distinction between different tumor types or grades [32, 33] and may serve as prognostic markers [34]. However, the accurate detection of Scyllo and Tau with  $^1\text{H}$  MRS at lower magnetic field strengths could be difficult as they are strongly overlapped with the neighboring resonances of tCho and Ins.

### Summary

Although inhomogeneity in  $B_1$  and  $B_0$  is further increased at 9.4T compared to 7T resulting variations in signal strength across the image is acceptable and comparable to 7T. We currently investigate the possible gain in SNR going from 3T to 7T and to 9.4T, and preliminary results indicate the expected linear



**8** Localizer and single spectrum acquired from the lesion (**8A**) and from the contralateral side (**8B**). Blue squares denote the localization of the spectra whereas the yellow arrows indicate the position of Tau and Scyllo.

increase. However, a solid comparison is quite difficult due to very different coil geometries and technologies used at these different field strengths. Macroscopic homogeneous  $B_1$  and  $B_0$  fields are the prerequisite for the study of microscopic susceptibility changes within tissue, which are significantly enhanced at ultra-high fields. Thus, one

of the most important steps in the near future in our lab will be the implementation and application of parallel transmit concepts and corresponding RF coil technology, as well as systems to improve and control  $B_0$  homogeneity such as dynamic shimming with high-order shim inserts.

## Acknowledgement

Dr. Mathias Nittka, Siemens Healthcare, Erlangen.

<sup>§</sup>The 7T and 9.4T systems are investigational devices. The products mentioned herein are still under development and not commercially available yet. Their future availability cannot be ensured.

<sup>§</sup>Brain Extraction Tool, FSL is not a Siemens Healthcare Product. Siemens bears no responsibility for this product including, but not limited to, its regulatory status.

## References:

- 1 Van de Moortele PF, Akgun C, Adriany G, Moeller S, Ritter J, Collins CM, Smith MB, Vaughan JT and Ugurbil K. B. Destructive Interferences and Spatial Phase Patterns at 7T with a Head Transceiver Array Coil. *Magn Reson Med* 2005; 54:1503-1518.
- 2 Hoffmann J, Shajan G, Budde J, Scheffler K, Pohmann R: Human Brain Imaging at 9.4 Tesla Combining a Tunable Patch Antenna for Transmission. *Magn. Reson. Med.*, ePub ahead. DOI: 10.1002/mrm.24367 (2012).
- 3 Shajan G, Hoffmann J, Scheffler K, and Pohmann R. A 16-Element Dual-row Transmit Coil Array for 3D RF Shimming at 9.4T. In: *Proceedings of the 20th Annual Meeting of ISMRM, Melbourne, 2012*, p 308.
- 4 Shajan G, Hoffmann J, Budde J, Adriany G, Ugurbil K, Pohmann R: Design and Evaluation of an RF Front-End for 9.4 T Human MRI. *Magn. Reson. Med.* 66, 594-602 (2011).
- 5 Wiggins GC, Triantafyllou C, Potthast A, Reykowski A, Nittka M and Wald LL. 32-Channel 3 Tesla Receive-Only Phased Array Head Coil with Soccer-Ball Element Geometry. *Magn Reson Med* 2006; 56:216-223.
- 6 Wiesinger F, Van de Moortele PF, Adriany G, Zanche ND, Ugurbil K and Pruessmann KP. Potential and feasibility of parallel MRI at high field. *NMR Biomed* 2006; 19:368-378.
- 7 Shajan G, Hoffmann J, Scheffler K and Pohmann R. A 31-Element Receive Array for Human Brain Imaging at 9.4 T. No. 351, *Proceedings of the 2012 ESMRMB Annual Meeting*.
- 8 G. A. Lodygensky, J. P. Marques, R. Maddage, E. Perroud, S. V. Sizonenko, P. S. Hüppi, R. Gruetter: *In vivo assessment of myelination by phase imaging at high magnetic field*. *Neuroimage* 59, 1979-1987 (2012).
- 9 M. Fukunaga, T.Q. Li, P. van Gelderen, J.A. de Zwart, K. Shmueli, B. Yao, J. Lee, D. Maric, M.A. Aronova, G. Zhang, R.D. Leapman, J.F. Schenck, H. Merkle, J.H. Duyn: *Layer-specific variation of iron content in cerebral cortex as a source of MRI contrast*. *Proc. Natl. Acad. Sci. USA* 107, 3834-3839 (2010).
- 10 J. Budde, G. Shajan, J. Hoffmann, K. Ugurbil, R. Pohmann: *Human Imaging at 9.4 T Using  $T_2^*$ , Phase- and Susceptibility-Weighted Contrast*. *Magnetic Resonance in Medicine* 65, 544-550 (2011).
- 11 Budde J, Shajan G, Zaitsev M, Scheffler K, Pohmann R: Functional MRI in human subjects with gradient-echo and spin-echo EPI at 9.4 T. *Magn. Reson. Med.*, in press (2013).
- 12 Conolly D, Nishimura D, Macovski A, Glover G. Variable-rate selective excitation. *J Magn Reson* 1988;78:440-477.
- 13 Schmitter S, Bock M, Johst S, Auerbach EJ, Ugurbil K, Van de Moortele PF. Contrast enhancement in TOF cerebral angiography at 7 T using saturation and MT pulses under SAR constraints: impact of VERSE and sparse pulses. *Magn Reson Med* 2012;68(1):188-197.
- 14 Cerebral TOF Angiography at 7T: Pushing the Limits to Reap the Benefits of Ultra-High Field Imaging, Issue 49 of *MAGNETOM Flash* · 1/2012 · [www.siemens.com/magnetom-world](http://www.siemens.com/magnetom-world) by: Schmitter S, Wu X, Pfeuffer J, Hamm M, Ugurbil K, Van de Moortele PF.
- 15 Johst S, Wrede KH, Ladd ME, Maderwald S. Time-of-Flight magnetic resonance angiography at 7 T using venous saturation pulses with reduced flip angles. *Invest Radiol* 2012;47: 445-450.
- 16 Lee S-P, Silva AC, Ugurbil K, Kim SG. Diffusion-weighted spin-echo fMRI at 9.4T: Microvascular/Tissue contribution to BOLD signal changes. *Magn Reson Med* 1999;42:919-928.
- 17 Hennig J, Nauwerth A, et Friedburg H: RARE imaging: a fast imaging method for clinical MR, *Magn Reson Med* 1986; 3: 823-833.
- 18 Hennig J and Scheffler K, Hyperechoes, *Magn Reson Med* 2001; 46:6-12.
- 19 Hennig J, Weigel M, Scheffler K. Multiecho sequences with variable refocusing flip angles: Optimization of signal behavior using smooth transitions between pseudo steady states (TRAPS). *Magn Reson Med* 49: 527-535 (2003).
- 20 Weigel M and Hennig J. Contrast Behavior and Relaxation Effects of Conventional and Hyper-echo-Turbo Spin Echo Sequences at 1.5T and 3T. *Magn Reson Med* 55: 826-835 (2006).
- 21 Weigel M and Hennig J. Development and Optimization of T2 weighted Methods with Reduced RF Power Deposition (Hypercho-TSE) for Magnetic Resonance Imaging. *Z Med Phys* 18: 151-161 (2008).
- 22 Alsop DC. The sensitivity of low flip angle RARE imaging. *Magn Reson Med.* 1997; 37:176-84.
- 23 Hennig J, Scheffler K, Easy Improvement of Signal-to-Noise in RARE sequences with Low Refocusing Flip Angles *Magn Reson Med.* 2000; 983-985.
- 24 Hennig J, Weigel M, Scheffler K. Calculation of Flip Angles for Echo Trains With Predefined Amplitudes With the Extended Phase Graph (EPG)-Algorithm: Principles and Applications to Hypercho and TRAPS Sequences. *Magn Reson Med* 51: 68-80 (2004).
- 25 Yarnykh VL. Optimal radiofrequency and gradient spoiling for improved accuracy of T1 and B1 measurements using fast steady-state techniques. *Magn Reson Med*, 2010; 57(1):192-200.
- 26 Pohmann R, Scheffler K. A theoretical and experimental comparison of different techniques for B1 mapping at very high fields. *NMR Biomed*, 2012; e-pub ahead of print.
- 27 Avdievich NI, Pan JW, Baehring JM, Spencer DD, Hetherington HP. Short echo spectroscopic imaging of the human brain at 7T using transceiver arrays. *Magn Reson Med* 2009; 62:17-25.
- 28 Deelchand DK, Van de Moortele PF, Adriany G, Iltis I, Andersen P, Strupp JP, Vaughan T, Ugurbil K, Henry PG. in vivo  $^1\text{H}$  NMR spectroscopy of the human brain at 9.4 T: initial results. *J Magn Reson* 2010; 206:74-80.
- 29 Henning A, Fuchs A, Murdoch JB, Boesinger P. Slice-selective FID acquisition, localized by outer volume suppression (FIDLOWS) for  $^1\text{H}$  MRSI of the human brain at 7 T with minimal signal loss. *NMR Biomed* 2009; 22:683-696.
- 30 Boer VO, van Lier ALHMMW, Hoogduin JM, Wijnen JP, Luijten PR, Klomp DWJ. 7-T  $^1\text{H}$  MRS with adiabatic refocusing at short TE using radiofrequency focusing with a dual-channel volume transmit coil. *NMR Biomed* 2011; 24(10):1038-1046.
- 31 Hetherington HP, Avdievich NI, Kuznetsov AM, Pan JW. RF shimming for spectroscopic localization in the human brain at 7T. *Magn Reson Med* 2010; 63:9-19.
- 32 Rijpkema M, Schuurin J, van der Meulen Y, van der Graaf M, Bernsen H, Boerman R, van der Kogel A, Heerschap A. Characterization of oligodendrogliomas using short echo time  $^1\text{H}$  MR spectroscopic imaging. *NMR Biomed*, 2003; 16:12-18.
- 33 Chawla S, Oleaga L, Wang S, Krejza J, Wolf RL, Woo JH, O'Rourke DM, Judy KD, Grady MS, Melhem ER, Poptani H. Role of proton magnetic resonance spectroscopy in differentiating oligodendrogliomas from astrocytomas. *J Neuroimaging*, 2010; 20:3-8.
- 34 Wilson M, Cummins CL, MacPherson L, Sun Y, Natarajan K, Grundy RG, Arvanitis TN, Kauppinen RA, Peet AC. Magnetic resonance spectroscopy metabolite profiles predict survival in pediatric brain tumors. *Eur J Cancer*, 2013; 49:457-464.

**Contact**

Professor Klaus Scheffler, Ph.D.  
MRC Department  
Max Planck Institute for Biological Cybernetics  
Department of Biomedical Magnetic Resonance  
Center for Integrative Neuroscience,  
CIN University of Tübingen  
Spemannstr. 41  
72076 Tübingen  
Germany  
Phone: +49 (0)7071 601-700/701  
Fax: +49 (0)7071 601-702  
[klaus.scheffler@tuebingen.mpg.de](mailto:klaus.scheffler@tuebingen.mpg.de)

# Improved Echo Planar Diffusion-Weighted imaging of the Head and Neck using *syngo* ZOOMit

Philipp Riffel, Henrik J. Michaely

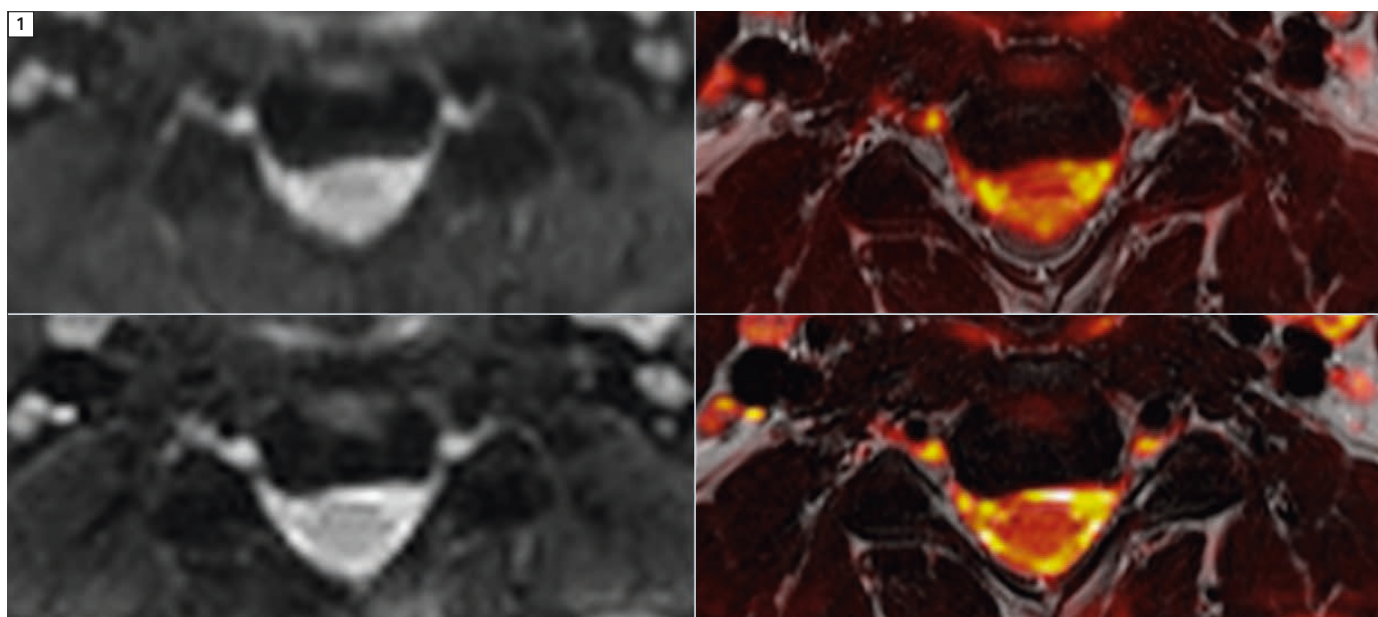
*Institute of Clinical Radiology and Nuclear Medicine, University Medical Center Mannheim, University of Heidelberg, Germany*

## DWI as a cancer biomarker

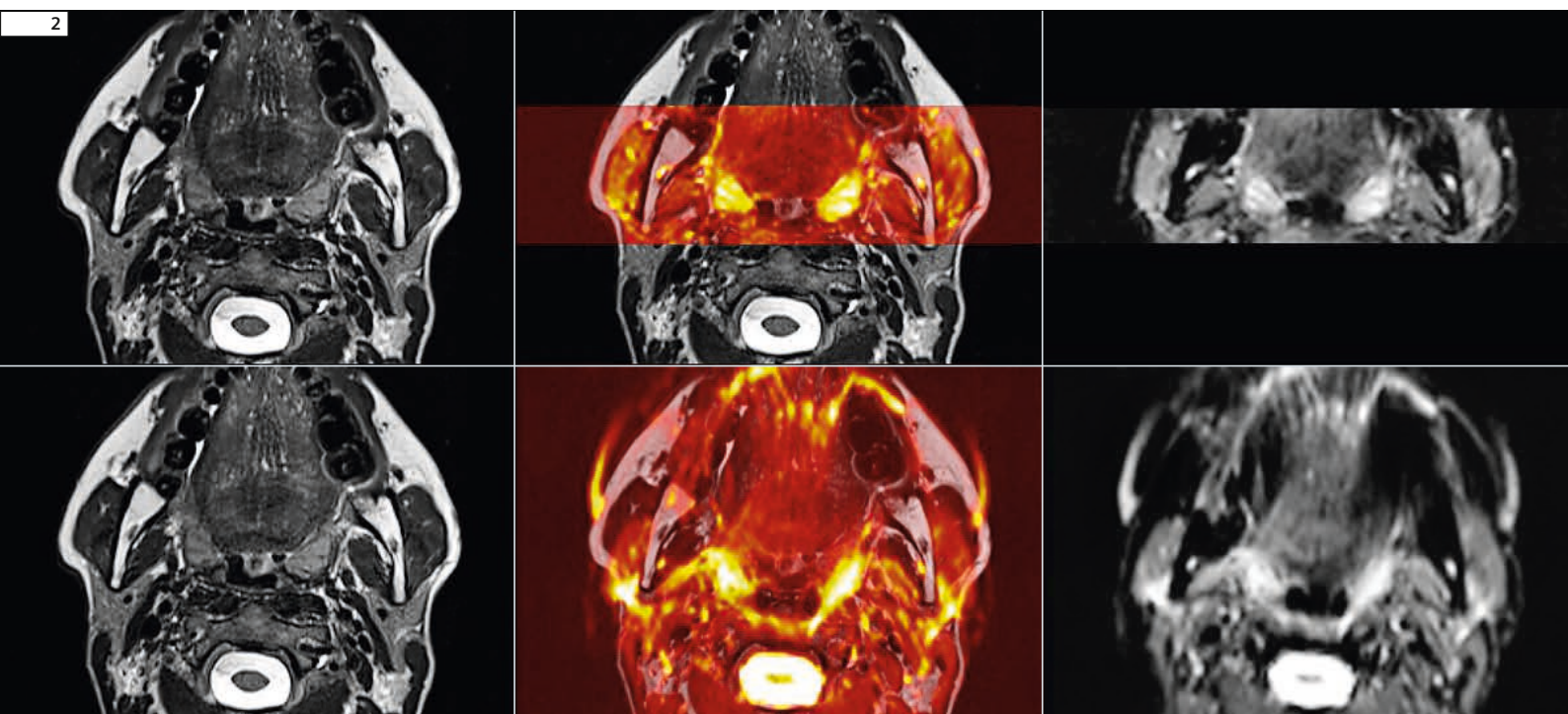
Echo-planar imaging (EPI) is a single-shot MR imaging (MRI) technique based on the rapid acquisition of a train of sign-alternating gradient echoes [1]. EPI sequences offer high signal-to-noise ratio (SNR) and imaging speed (volume coverage) which render them attractive for functional neuroimaging and diffusion-weighted magnetic resonance imaging (DWI). Imaging biomarkers are important tools for the detection and characterization of cancers as well as for

monitoring the response to therapy. DWI is rapidly gaining popularity for the assessment of oncologic and non-oncologic pathologies. DWI depends on the microscopic motion of water. This motion, called Brownian motion, is due to thermal agitation and is highly influenced by the cellular environment of water. Thus, findings on DWI could be an early harbinger of biologic abnormality [2]. Once a technique primarily used in neuroradiology, diffusion-weighted

MRI is already being incorporated into general oncologic imaging practice because of its many clinical advantages. Recently, Padhani and Koh have alluded to the promising future of DWI as a cancer biomarker in tumor staging with an improved tissue characterization (differentiating benign from malignant lesions), in monitoring response to chemotherapeutic agents, and in differentiating post-therapeutic changes from residual active tumor [2].



**1** Fused images of T2 TSE with corresponding conventional diffusion-weighted (top row) and zoomed diffusion-weighted images (bottom row). The conventional images show a significant displacement between the diffusion-weighted images and the corresponding morphology. The zoomed diffusion-weighted images enable exact correlation between DW images and anatomy.



**2** Zoomed diffusion-weighted images (top row) show a better correlation with T2 TSE compared to conventional diffusion-weighted images (bottom row). The improved image quality is especially obvious in areas prone to artifacts such as the tongue and hard palate.

## EPI-DWI in the head and neck

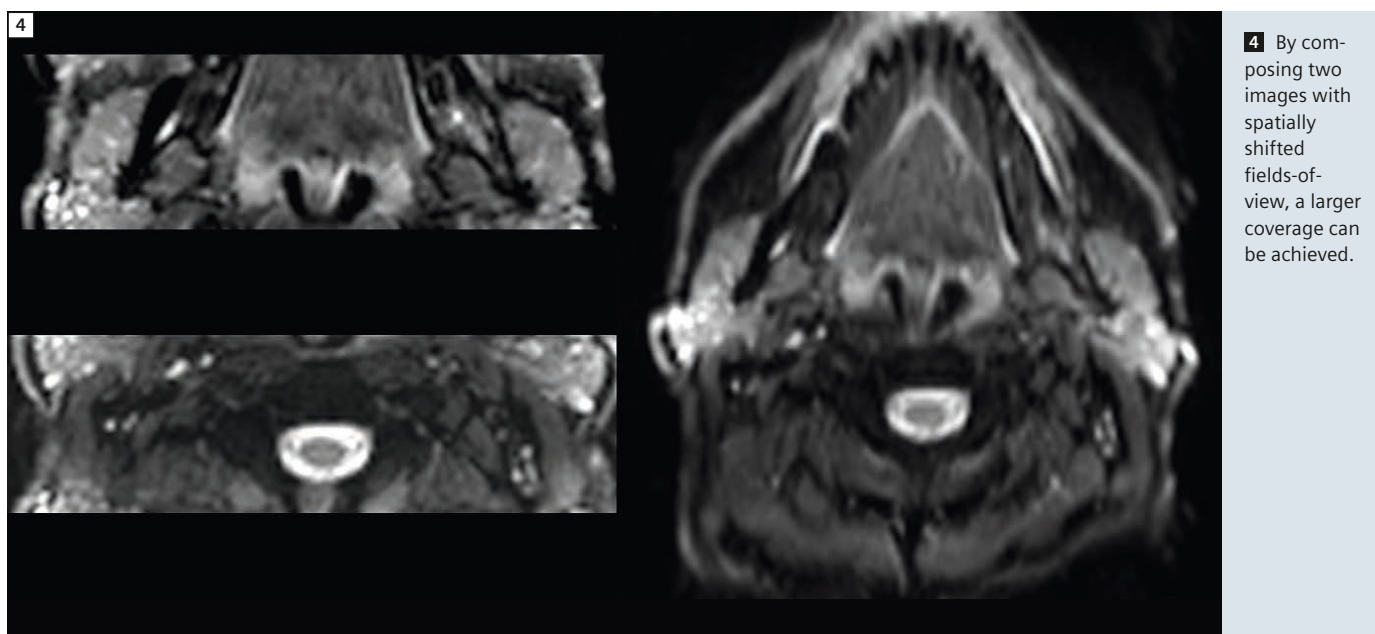
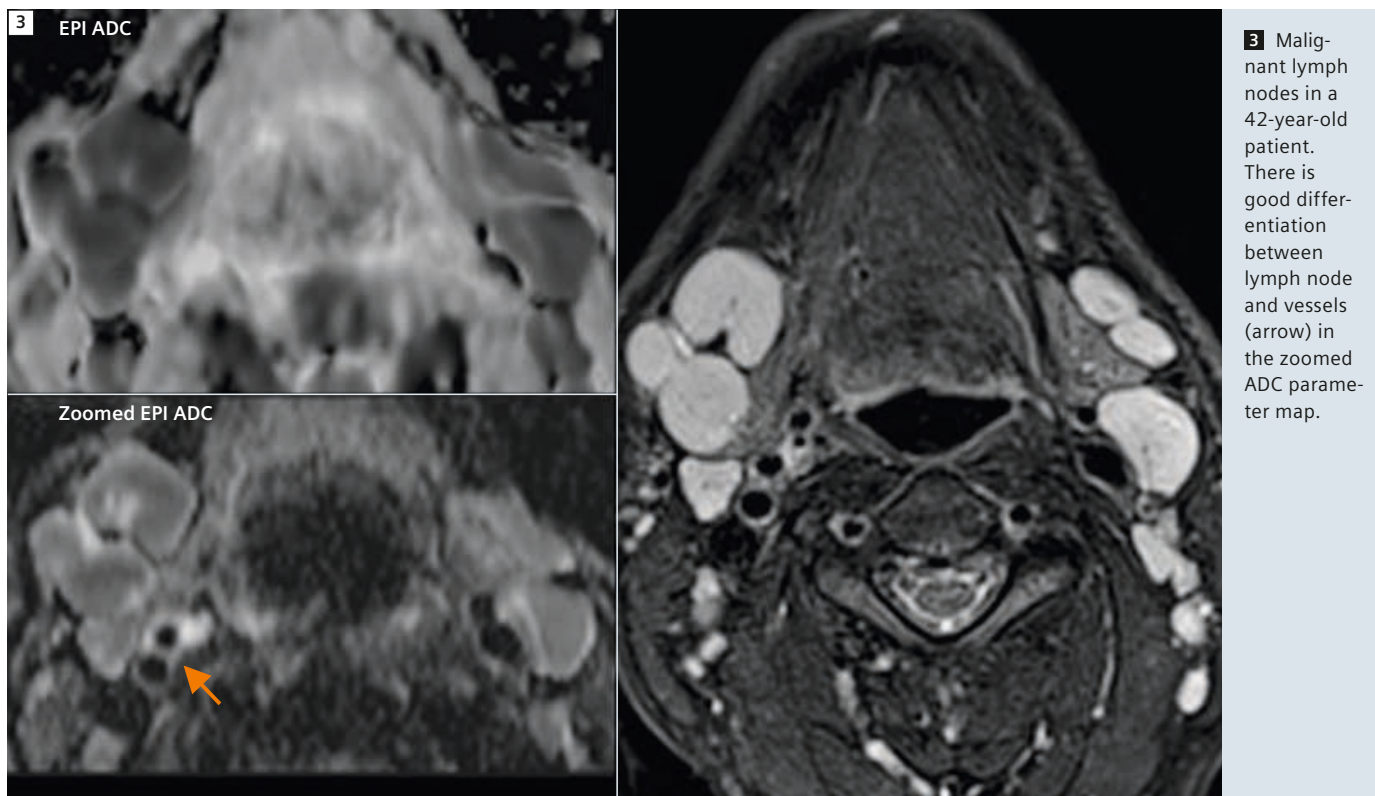
DWI is potentially useful in the evaluation of head and neck lesions [3, 4] and ADC measurements have suggested that this imaging method may be useful for their characterization [4]. Although results of initial studies were both challenging and promising, one drawback was the technical difficulty in assessing diffusion by echo-planar DW imaging. Applications of EPI may be affected by inherent problems, such as ghosting artifacts, as well as by geometric distortions and signal losses caused by chemical shift and susceptibility differences. These effects degrade the achievable image quality and limit the spatial resolution. This is especially valid for the head and neck area. Due to the presence of dental work, as well as adjacent air and bone, it may be difficult to obtain precise ADC measurements in lesions located in these regions. Therefore in the majority of studies only lesions larger than 1 cm were evaluated. Currently the

determination of accurate ADC values in smaller tumors and lymph nodes seems to be unreliable [3-5]. Therefore, DWI techniques that are less sensitive to susceptibility artifacts are mandatory for the evaluation of head and neck lesions.

## Solution approaches

Physically, the above mentioned artifacts are caused by phase distortions, which increase with longer echo time and mimic the encoding of spatial information during image reconstruction. Therefore, fundamental to overcoming these limitations is the use of shorter echo trains [6]. There are several possibilities for reducing these artifacts and conventional DWI has seen many improvements. Latest developments include, for example, read-out segmented EPI [7]. In combination with navigator-based phase corrections and re-acquisition, read-out segmented EPI can effectively reduce susceptibility artifacts [8] and is now commercially available as *syngo* RESOLVE.

Nevertheless, this approach may increase acquisition time and is best applied in the imaging of non-moving organs. A complementary way of decreasing the echo train is to reduce the field-of-view (FOV) along the phase-encoding dimension of the image while simultaneously avoiding image aliasing. First attempts used spin-echo and stimulated-echo EPI sequences with orthogonal RF pulses to excite an inner-volume FOV and then reduce the number of  $k$ -space lines required for image reconstruction [9]. A major drawback of these techniques is the restricted volume coverage due to neighboring sections becoming presaturated by one of the RF excitations [6]. With the clinical availability of parallel RF transmit coils and the potential to utilize its spatial information in an array during RF transmission, it is now possible to move beyond the uniform slice-select excitation and to generate spatially-tailored RF pulses. Two-dimensional spatially-selective RF excitation pulses for



single-shot echo-planar imaging combined with reduced FOV – i.e. zooming – in the phase-encoding direction leads to a decreased number of acquisition *k*-space lines and significantly shortens the length of the EPI echo train [6, 10]. The numerically calculated two-dimen-

sional RF pulse provides, in addition, superior flip angle homogeneity, since it is optimized using the  $B_1$  field information of the two independent RF channels. To summarize, zoomed imaging provides largely improved homogeneity with decreased distortion artifacts, opening

new clinical applications. We have investigated the applicability of zoomed diffusion imaging of the neck, to examine its potential for reduced susceptibility artifacts in regions close to major air cavities and the associated clinical relevance.

## Initial results of zoomed DWI in the head and neck

All examinations were performed on a 3T whole-body MR system (MAGNETOM Skyra, Siemens Healthcare, Erlangen, Germany) equipped with a two-channel fully dynamic parallel transmit array, termed TimTX TrueShape. The excitation of the standard diffusion-weighted EPI sequence was extended by the two-dimensional spatially-selective RF pulse using an echo-planar transmit trajectory. We found that *syngo* ZOOMit bears considerable potential for overcoming some of the inherent limitations of conventional EPI techniques. In particular, for a reduced FOV, zoomed DWI allows for improved image quality in terms of markedly reduced susceptibility artifacts. Zoomed images allows for an excellent correlation between the zoomed DW images and the morphological T2 TSE images (Fig. 1). This is especially obvious in regions prone to artifacts, e.g. in the tongue or the hard palate (Fig. 2). As head and neck squamous cell carcinomas (HNSCC) are often located in those

anatomical distributions, zoomed imaging could potentially improve diagnostic accuracy in the assessment of cancers in early stage in those areas.

Additionally, due to the improved image quality with less distortions, zoomed images provide perfect delineation of cervical lymph nodes and an exact co-registration with morphological images. Figure 3 shows images of a patient with malignant lymph nodes. While the malignant lymph nodes could also be seen on the conventional diffusion-weighted images, the differentiation between lymph node and vessels could only be achieved with zoomed DWI. Due to the reduced distortion artifacts, the external carotid artery delivers a sharply delineated flow void, which allowed the radiologist to absolve the vessel of tumor infiltration.

The achieved improvements in image quality originate from both the shorter echo train (at a given TE) and the possible reduction of the TE. On the other hand, the improved image quality is at the expense of a smaller FOV and a lower SNR due to the decreased number of

acquired echoes. To cover a larger FOV several images of spatially shifted fields-of-view may be composed (Fig. 4).

## Conclusions

These initial data are encouraging as they demonstrate that zoomed imaging (*syngo* ZOOMit) may be a very robust method for DW imaging of challenging areas such as the head and neck, enabling more reliable imaging, particularly in areas close to major air cavities. With improved correlation with anatomy, zoomed DWI may assist in the detection and assessment of early cancers in regions where the application of conventional DWI may have been limited. Such developments are crucial, especially given the need to counteract the much more pronounced susceptibility problems in high-field MRI systems at 3T and beyond.

## References

- 1 Mansfield, P. & Maudsley, A.A. Medical imaging by NMR. *Br J Radiol* 50, 188-194 (1977).
- 2 Padhani, A.R., et al. Diffusion-weighted magnetic resonance imaging as a cancer biomarker: consensus and recommendations. *Neoplasia* 11, 102-125 (2009).
- 3 Wang, J., et al. Head and neck lesions: characterization with diffusion-weighted echo-planar MR imaging. *Radiology* 220, 621-630 (2001).
- 4 Sumi, M., et al. Discrimination of metastatic cervical lymph nodes with diffusion-weighted MR imaging in patients with head and neck cancer. *AJNR Am J Neuroradiol* 24, 1627-1634 (2003).
- 5 Holzapfel, K., et al. Value of diffusion-weighted MR imaging in the differentiation between benign and malignant cervical lymph nodes. *Eur J Radiol* 72, 381-387 (2009).
- 6 Rieseberg, S., Frahm, J. & Finsterbusch, J. Two-dimensional spatially-selective RF excitation pulses in echo-planar imaging. *Magn Reson Med* 47, 1186-1193 (2002).
- 7 Morelli, J., et al. Clinical evaluation of single-shot and readout-segmented diffusion-weighted imaging in stroke patients at 3 T. *Acta Radiol* (2013).
- 8 Morelli, J.N., et al. Echo planar diffusion-weighted imaging: possibilities and considerations with 12- and 32-channel head coils. *J Clin Imaging Sci* 2, 31 (2012).
- 9 Turner, R., von Kienlin, M., Moonen, C.T. & van Zijl, P.C. Single-shot localized echo-planar imaging (STEAM-EPI) at 4.7 tesla. *Magn Reson Med* 14, 401-408 (1990).
- 10 Pfeuffer, J., et al. Zoomed functional imaging in the human brain at 7 Tesla with simultaneous high spatial and high temporal resolution. *Neuroimage* 17, 272-286 (2002).

## Contact

Philipp Riffel, M.D.  
Institute of Clinical Radiology  
and Nuclear Medicine  
University Medical Center Mannheim  
Medical Faculty Mannheim –  
University Heidelberg  
Theodor-Kutzer-Ufer 1-3  
68167 Mannheim  
Germany  
Phone: +49 621 383 2067  
Fax: +49 621 383 3817  
philipp.riffel@umm.de

# Sodium ( $^{23}\text{Na}$ )-Imaging as Therapy Monitoring in Oncology – Future Prospects

Stefan Haneder, M.D.<sup>1</sup>; Stefan O. Schoenberg, M.D.<sup>1</sup>; Simon Konstandin, Ph.D.<sup>2</sup>; Lothar R. Schad, Ph.D.<sup>2</sup>

<sup>1</sup>Institute of Clinical Radiology and Nuclear Medicine, University Medical Center Mannheim, Heidelberg University, Mannheim, Germany

<sup>2</sup>Computer-Assisted Clinical Medicine, Heidelberg University, Mannheim, Germany

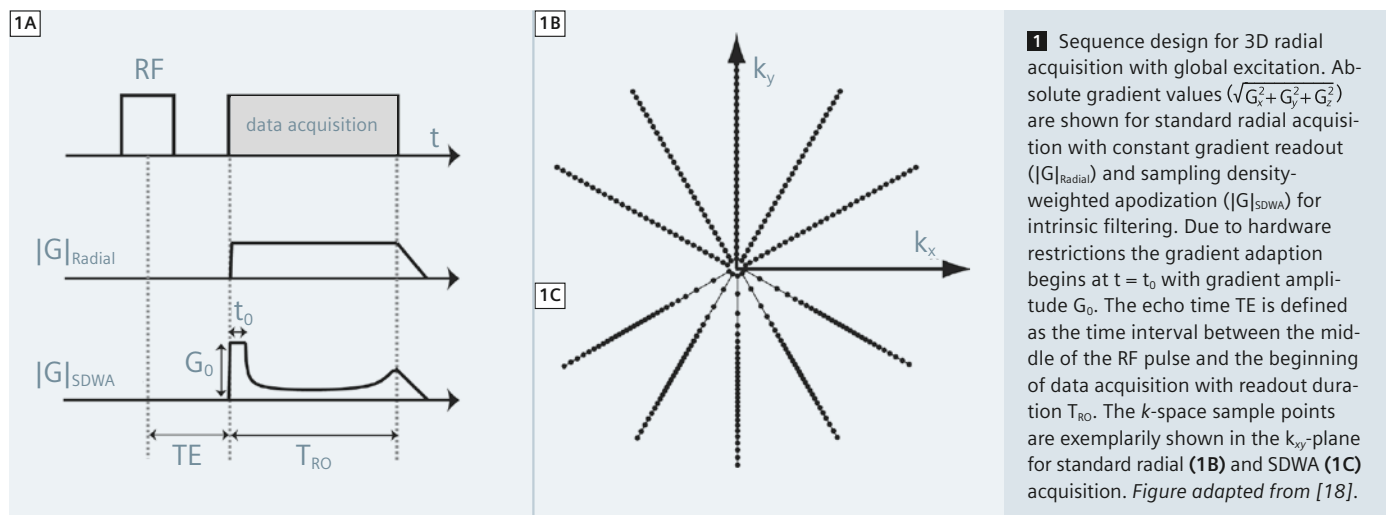
## Introduction

**“Form follows function” – Louis Sullivan, 1896**

Whilst this concept was originally applied to modern architecture, it could well become a highly appropriate maxim for future imaging and therapy concepts. Magnetic resonance imaging (MRI) has continually developed into a powerful, widely used diagnostic tool and offers the opportunity to expand traditional imaging concepts based on morphological information. In the future, the pure morphology will remain a central component of multimodal imaging, but will be flanked increasingly by functional approaches reaching far beyond the current imaging standards. In oncological therapy follow-up the drawback of relying on pure morphology is widely known, resulting, for example, from delayed morphological reflection of

tumor regression. Consequently, the RECIST Working Group addressed this point in the context of the new RECIST 1.1 criteria [1]: „A key question considered by the RECIST Working Group in developing RECIST 1.1 was whether it was appropriate to move from anatomic unidimensional assessment of tumour burden to either volumetric anatomical assessment or to **functional assessment with PET or MRI**. It was concluded that, at present, there is not sufficient standardisation or evidence to abandon anatomical assessment of tumour burden. The only exception to this is in the use of FDG-PET imaging as an adjunct to determination of progression. [...]” This statement contains several basic implications for future MR strategies of therapy control. **First**, the internal radi-

ology benchmark of functional MR sequences seems to be nuclear medicine approaches, already fixed in guidelines as PERCIST 1.0 [2]. **Second**, further multicenter, international studies are required to obtain reliable data for (functional) MR approaches. **Third** – not explicitly, but indirectly – the radiology community should not abandon the assessment of new functional approaches and should try to implement them in clinical settings. The arsenal of current functional MR imaging approaches includes diffusion-weighted imaging (DWI), diffusion tensor imaging (DTI), arterial spin labeling (ASL), blood-oxygenation level dependent imaging (BOLD) and sodium ( $^{23}\text{Na}$ )-imaging. DWI [3] should be emphasized as a kind of paradigm shifting technique. Since the 1990s DWI has been performed for intracranial diseases and has contrib-



uted to the detection of early stroke. But in recent years the number of studies has increased substantially, evaluating this method in detection and characterization of lesions, especially in the field of oncology and the possibility of (early) tumor treatment response [4-8]. This remarkable success story cannot (yet) be applied to  $^{23}\text{Na}$  imaging, but we are witnessing continuous development.

### Physiological and technical basics

$^{23}\text{Na}$  ions play a fundamental role in human life and can be traced – similar to protons ( $^1\text{H}$ ) – ubiquitarily in the human body. Fluxes of  $^{23}\text{Na}$  ions in cells and across cell membranes are central part of many processes of cell activity. Up to 70% of the energy from adenosine triphosphate (ATP) hydrolysis is used for the  $\text{Na}^+\text{-K}^+\text{-ATPase}$ , which pumps three  $\text{Na}^+$  ions out of the cell while two  $\text{K}^+$  ions vice versa [9]. An extracellular concentration of  $\approx 145$  mM and an intracellular concentration of  $\approx 12\text{--}20$  mM (10) are maintained in healthy tissue by this pump mechanism, which leads to a mean tissue sodium concentration (TSC) of about 50 mM. Pathologic changes such as tissue injury, edema, or necrosis result in a degradation of  $\text{Na}^+\text{-K}^+\text{-ATPase}$  and hence in an increase in TSC from 50 mM up to 145 mM in case of cell burst [11].

From an electro-physiological point-of-view, some physical characteristics of  $^{23}\text{Na}$  hamper the simple application for MR imaging. The sodium nucleus has a spin of  $3/2$  and is therefore subject to quadrupolar relaxation resulting in a biexponential  $T_2$  decay with relaxation times of  $T_{2f}^* 0.5\text{--}8$  ms and  $T_{2s}^* 15\text{--}30$  ms for the fast and slow component, respectively [12]. Additionally, sodium MRI suffers from low *in vivo* concentration with a weak gyromagnetic ratio of only  $1/4$  of that for  $^1\text{H}$  resulting in an approximately 10-fold lower MR sensitivity compared to  $^1\text{H}$  MRI with about 10,000-fold less signal. Consequently, signal-to-noise ratio (SNR)-efficient acquisition strategies with short echo times such as the radial scheme [13] are required. Many MR sequences were recently developed to acquire the

k-space homogeneously yielding higher SNR: twisted projection imaging (TPI) [14], 3D cones [15], density-adapted projection reconstruction [16, 17]. Since filtering is usually applied to sodium images as a post-processing step, sampling density-weighted apodization (SDWA) with intrinsic filtering [18, 19] is preferred when using short readout durations (Fig. 1). Anisotropic 3D imaging sequences using cones [20] or twisted projection imaging [21] were recently developed for applications where anisotropic resolutions are needed (e.g., cartilage).

The technical developments of acquisition strategies and sequence design over the last decade were accompanied by MR hardware improvements. The trend to higher field strengths and stronger gradient systems was continued and led not only to a routine use of 3T MR scanners in patient care but to a growing number of 7T whole-body-MR installations worldwide. The electro-physiological characteristics of  $^{23}\text{Na}$  predestine the implementation of higher field strengths. Complementary progression can be stated for coil design. Meanwhile multi-channel  $^{23}\text{Na}$  coils are commercially available and experimental new designs – as a double-tuned two-port surface resonator for  $^{23}\text{Na}$ - and  $^1\text{H}$ -imaging [22, 23] – have been introduced.

### Oncologic therapy monitoring using $^{23}\text{Na}$ MRI – quo vadis?

Taking into account the above-described technical developments over the last few years, a kind of renaissance of  $^{23}\text{Na}$ -MRI and the determination of tissue sodium content (TSC) can be stated. Feasibility of  $^{23}\text{Na}$ -MRI for *in vivo* imaging of physiological conditions has been demonstrated in various parts of the human body, e.g. kidney [24-26], cartilage and musculoskeletal in general [12, 27-29], brain [30, 31] heart [32-34] and prostate [35]. Initial translation from physiology to pathophysiology was correspondingly addressed in a broad spectrum of organs and different pathologies. The possibility of imaging of transplanted kidneys [36] and detection of renal changes after 3 dimensional con-

formal radiotherapy in a long-term follow-up in patients after gastric cancer [37], has been shown. In musculoskeletal imaging, for example, different cartilage repair approaches in the knee were evaluated with  $^{23}\text{Na}$ -MRI at 7T [38-40] and presented marked differences in comparison to native cartilage. Increased sodium concentrations were found in different brain tumors relative to normal brain structures [41, 42]. An up to threefold increase in TSC can be observed in human stroke [43] allowing monitoring of the progression of stroke pathophysiology [44, 45]. Surprising results revealed a study about relapsing-remitting multiple sclerosis at early and advanced stage. TSC was increased inside demyelinating lesions in both groups of patients, but TSC accumulation dramatically increases in the advanced stage, especially in the normal-appearing brain tissues, concomitant with disability [46]. Furthermore,  $^{23}\text{Na}$ -MRI provides a non-invasive solution to distinguish viable from nonviable myocardial tissue after myocardial infarction in an animal model [47] and in humans [48, 49]. TSC measurements have shown an increased signal mainly in nonviable myocardium after infarction due to loss of cell membrane integrity. Despite the never-ending discussion of necessity of separating intra- and extracellular  $^{23}\text{Na}$  components, TSC offers a unique tool for measuring tissue viability noninvasively. The pathophysiology phenomena in almost all acute pathologies (stroke, myocardial infarction) are mainly based on the idea of changing  $^{23}\text{Na}$  environments e.g. due to the loss of cell membrane integrity and the following adjustment of intra- and extracellular  $^{23}\text{Na}$  concentrations. Laymon et al. [50] described that cell membrane depolarization preceding the large degree of cell division in neoplastic tissue leads to an increase in the intracellular sodium concentration (ISC) and a concomitant rise in the total TSC. In human brain tumors, Ouwerkerk and co-workers showed that measured  $^{23}\text{Na}$  changes within the tumors cannot only be attributed to alterations in  $^{23}\text{Na}$  relaxation time, e.g. in the presence of surrounding edema, but reflect

real intrinsic changes of Na<sup>+</sup>-K<sup>+</sup>-pump function [41]. This research group concluded in the same work as prospect to therapy monitoring:

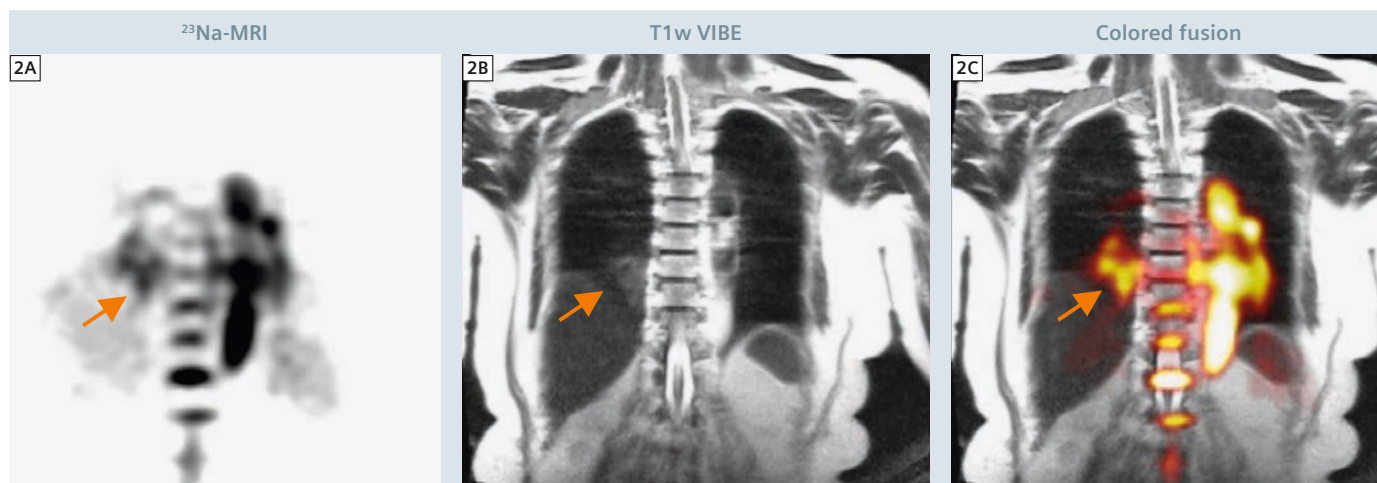
“Therapies that alter tumor ion homeostasis or affect or destroy tumor cell membrane integrity are likely to generate changes that are observable with <sup>23</sup>Na MR imaging and sodium concentration measurements. With these measurements, changes can be observed much earlier than the effects of anatomic remodeling.”

This idea of using <sup>23</sup>Na as surrogate parameter for oncology therapy control is therefore not new and was among others also addressed by Thulborn et al. [42] in the field of management of brain tumors. The ability to quantify early effects of tumor therapeutic response using non-invasive <sup>23</sup>Na-MR imaging approaches would have a major impact in clinical oncology. To date, clinical studies assessing these predicted potentials are missing, but first data, mainly derived from different animal models, apart from several tumor entities, have been published.

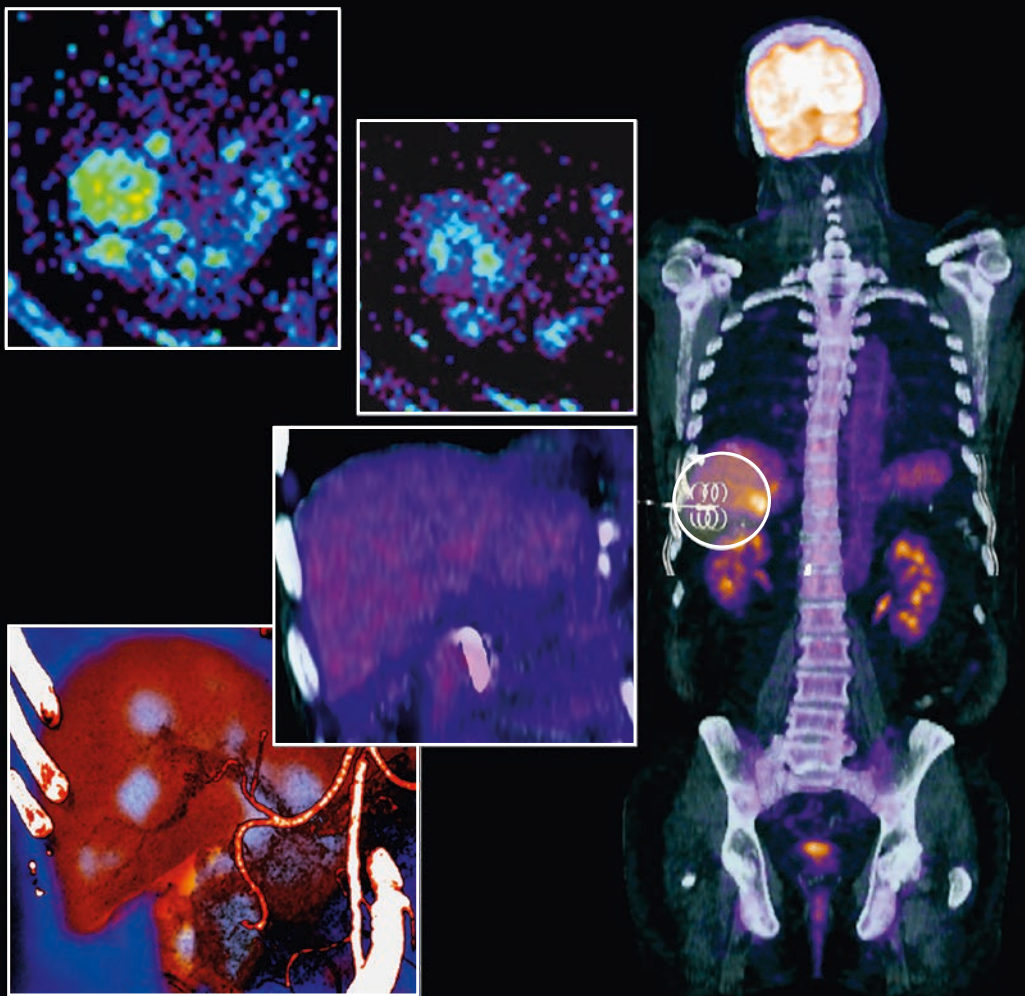
In 2000, Kline et al. [51] detected significantly increased <sup>23</sup>Na signal in mouse xenograft tumors propagated from human prostate cancer cell lines, 24h after administration of antineoplastics compared to baseline. Histopathological

correlation of explanted tumors confirmed that chemotherapy reduced proliferation, inversely correlated with <sup>23</sup>Na MRI response on a tumor-to-tumor basis. A logical development was the combination with another functional MR approach. Babsky et al. [52] performed <sup>23</sup>Na-MRI and DWI in a mice model with subcutaneously-implanted radiation-induced fibrosarcoma (RIF-1) before, and daily for 3 days after, chemotherapy treatment. In contrast to the control group, *in vivo* MRI experiments showed an increase in both <sup>23</sup>Na and apparent diffusion coefficient (ADC) in treated tumors, correlating to histological confirmed decreased cell density. After chemotherapy a chemical analysis showed an increased relative extracellular space and [Na<sup>+</sup>] concentration in treated tumors. Sharma and co-workers [53] evaluated at 4.23T the association between *in vivo* intracellular <sup>23</sup>Na MRI intensities, immuno-biomarkers and histopathological features respectively, to monitor the early tumor response to chemotherapy using a rat xenograft breast tumor model. They concluded that intracellular <sup>23</sup>Na MRI intensities possibly indicate chemosensitivity response *in vivo* associated with apoptosis and different pre-malignant features within 24 hours of exposure of cancer cells to anti-neoplastic Taxotere drug.

Schepkin et al. [54] compared <sup>23</sup>Na and DWI for their ability to detect early cellular changes in rats with subcutaneous 9L gliosarcomas treated with chemotherapy. Both imaging modalities were able to detect early changes (2 days post-treatment) in tumor cellularity continuing to evolve to a maximum after 8 days. Subsequent tumor shrinkage followed the functional parameters. The authors concluded that therapeutically-induced changes in <sup>23</sup>Na and DWI were found to have similar dynamic and spatial changes and detect similar early cellular changes after treatment. The same research group demonstrated the sensitivity and applicability of <sup>23</sup>Na and DWI as tools for dynamic assessment of tumor response to therapy [55]. They detected in a 9L rat gliosarcoma model, a correlation between tumor <sup>23</sup>Na and DWI to gauge tumor response to therapy with varying doses of chemotherapy. In summary, all animal studies confirmed the possibility to detect tumor changes with <sup>23</sup>Na imaging after oncologic therapy as correlation of treatment success. But the really astonishing finding of these preclinical studies is the indication that <sup>23</sup>Na MRI could develop into an early predictor of therapy response within the first 24h. If these results were to be affirmed in human studies, it could lead to a major medical



**2** Image examples, including (2A) <sup>23</sup>Na-MRI, (2B) morphological T2w HASTE (Half fourier-Acquired Single shot Turbo spin Echo) and (2C) a colored fusion of both sequences, of a 66-year-old male patient with lung cancer (stage IV adenocarcinoma). The lung cancer in the right lower lobe is marked with an arrow. Courtesy of PD Dr. Thomas Henzler, University Medical Center Mannheim, Heidelberg University, Germany



**3** Potential multimodal treatment planning combining different currently available functional approaches such as DWI and  $^{18}\text{F}$ -FDG-PET-CT supporting the need for further MRI techniques such as  $^{23}\text{Na}$ -MRI [59].

and economical impact on oncological therapy control and generate an early imaging tool for personalized therapy control.

One of the first *in vivo* translation into human pathologies in oncology treatment monitoring was reported by Henzler et al. [56], who showed the feasibility of  $^{23}\text{Na}$ -MRI in patients with lung cancer (Fig. 2). In this feasibility study, three patients with stage IV adenocarcinoma of the lung were enrolled and multimodal examined. Data were available of  $^{23}\text{Na}$ - and non-contrast enhanced  $^1\text{H}$ -MRI, CT and  $^{18}\text{F}$ -FDG-PET-CT. One of the three included patients was chemo-naïve and examined before and after the initiation of combination therapy. Fusion of  $^{23}\text{Na}$ -MR images with  $^1\text{H}$ -MRI, CT and FDG-PET-CT was feasible in all patients and showed differences in solid and necrotic tumor areas. Between

the two exams the signal intensity of the tumor as well as the ratio of signal intensity between the tumor and the CSF slightly increased indicating early therapy induced changes within the tumor. The authors concluded that  $^{23}\text{Na}$ -MRI is feasible in patients with lung cancer and could provide valuable functional molecular information regarding tumor viability, and potentially a treatment response.

A second example was recently published by Layman et al. [50] from the University of Pittsburgh. This research group aimed in their feasibility study to implement and compare [ $^{18}\text{F}$ ]-fluorothymidine ( $^{18}\text{F}$ -FLT) positron emission tomography (PET),  $^{23}\text{Na}$  and morphological MRI at 3T in patients with glioblastoma multiforme. Two patients underwent repetitive scans at baseline (before therapy), at an early and a late follow-up

time point after beginning therapy. Both functional methods were registered to the morphological MRI and calculated on a voxel-wise basis to address the heterogeneity of tumor physiology. Both –  $^{18}\text{F}$ -FLT PET and  $^{23}\text{Na}$ -MRI – independently presented changes of the tumor tissue varying in different regions, as a function of scan time point. But these initial results indicate that the two functional modalities may provide complementary information regarding tumor progression and response. The authors stated that, unlike  $^{18}\text{F}$ -FLT uptake, changes in sodium concentration occur without limitations from the state of the blood brain barrier. But the final value of  $^{23}\text{Na}$  MRI in these patients and the possibility to discriminate tumor progression from pseudoprogression requires additional patient data and outcome control. Undoubtedly  $^{23}\text{Na}$  MRI is an auspicious

functional technique, for which the pre-clinical animal and first *in vivo* human data show a huge potential in the field of oncology treatment. However, this technique clearly still requires a special and sophisticated technical setup, which up to now is only available in a select number of research centers worldwide.

### Integrated concepts of functional therapy +/- monitoring\*

The great challenge for the coming years is to translate this additional diagnostic information into a more effective, less invasive therapy for the patient with fewer side effects and at the same time higher cost-effectiveness rendering it more affordable for the general health care system. This implies that imaging is specific for the mechanism of the disease and the target of the therapy on one hand and provides a complete picture of the systemic spread and thus the stage of the disease on the other. For this, the critical gap between modern molecular histopathology, molecular imaging and image-guided, minimally-invasive therapy has to be bridged and the results transferred from basic science into clinical routine. This challenge cannot be comprehensively addressed by a single research group, but requires the close interaction of scientists from multiple disciplines of medical imaging and from different types of academic institutions as well as industry in close proximity on a medical university campus. Currently, industry on campus (IOC) initiatives such as the one from the German Federal Ministry of Research in Germany are specifically designed to facilitate this type of interdisciplinary, patient-focused research on a single campus in a long-term private-public partnership. As an example, the initiative 'Mannheim Molecular Intervention Environment (M<sup>2</sup>OLIE)' aims at developing a closed-loop treatment process in oligometastatic patients spanning from personalized molecular imaging to target-specific minimally-invasive multimodal therapy. Patients with a previously treated oncologic disease and de novo development of a few metastases are the fastest growing group of cancer

patients. With dedicated multimodal minimally-invasive therapies a stabilization of the disease can be potentially achieved with survival times almost similar to those in cured patients. The key to a precise elimination of these metastases is the detailed tumor characterization, as current studies have shown that the individual tumor cell clones of each lesion substantially differ from each other [57].

The key to a successful implementation of these techniques is the seamless integration of the entire diagnostic information into a single comprehensive therapeutic modality. Within the last 5 years substantial innovations have been brought into clinical routine by a close cooperation between industry, scientists and clinicians: state-of-the art robot-assisted X-ray systems offer much higher degrees of freedom for placement of needles and catheters and at the same time allow for image-guided control of the intervention by use of rotating flat panels. New algorithms for dose reduction such as compressed sensing will enable time-resolved 4D imaging with a fraction of currently applied radiation doses [58]. New molecular contrast mechanisms in MRI such as <sup>23</sup>Na imaging, as described above, could play a key role in this comprehensive setting since images from 4D CT, functional MRI and PET data can be fused using current advances in software and provide information for the interventionist on blood flow and metabolism of the tumor in real-time (Fig. 3).

\*Adapted from [59].

### Conclusion

Taking into account the three basic implications deduced in the introduction, <sup>23</sup>Na-MRI undeniably has still a long way to go. But – also undeniably – <sup>23</sup>Na-MRI clearly shows promise as an outstanding new approach for measuring tissue viability non-invasively. And its full potential is by no means exhausted. This technique can develop into a non-invasive avenue of therapy monitoring for a variety of diseases, particularly, but not solely, in oncological settings.

### Acknowledgment

We thank PD Dr. Thomas Henzler, University Medical Center Mannheim, Heidelberg University for providing Figure 2.

#### References

- 1 Eisenhauer EA, Therasse P, Bogaerts J, et al. New response evaluation criteria in solid tumours: revised RECIST guideline (version 1.1). *Eur J Cancer*. 2009;45(2):228-47.
- 2 Wahl RL, Jacene H, Kasamon Y, Lodge MA. From RECIST to PERCIST: Evolving Considerations for PET response criteria in solid tumors. *J Nucl Med*. 2009;50 Suppl 1:122S-50S.
- 3 Le Bihan D, Breton E, Lallemand D, Aubin ML, Vignaud J, Laval-Jeantet M. Separation of diffusion and perfusion in intravoxel incoherent motion MR imaging. *Radiology*. 1988;168(2): 497-505.
- 4 Koh DM, Collins DJ. Diffusion-weighted MRI in the body: applications and challenges in oncology. *AJR American journal of roentgenology*. 2007;188(6):1622-35.
- 5 Taouli B, Koh DM. Diffusion-weighted MR imaging of the liver. *Radiology*. 2010;254(1):47-66.
- 6 Desouza NM, Reinsberg SA, Scurr ED, Brewster JM, Payne GS. Magnetic resonance imaging in prostate cancer: the value of apparent diffusion coefficients for identifying malignant nodules. *Br J Radiol*. 2007;80(950):90-5.
- 7 Sinha S, Lucas-Quesada FA, Sinha U, DeBruhl N, Bassett LW. In vivo diffusion-weighted MRI of the breast: potential for lesion characterization. *Journal of magnetic resonance imaging : JMRI*. 2002;15(6):693-704.
- 8 Kwee TC, Takahara T, Ochiai R, et al. Whole-body diffusion-weighted magnetic resonance imaging. *European journal of radiology*. 2009;70(3): 409-17.
- 9 Silbernagl S, Despopoulos A. *Color Atlas of Physiology*. New York.: Thieme, 2003.
- 10 Hilal S, Ra J, Oh C, Mun I, Einstein S, Roschmann P. Sodium imaging. . In: Stark D, Bradley W, eds. *Magnetic resonance imaging*. St. Louis 1988; p. 715–29.
- 11 Boada FE, LaVerde G, Jungreis C, Nemoto E, Tanase C, Hancu I. Loss of cell ion homeostasis and cell viability in the brain: what sodium MRI can tell us. *Curr Top Dev Biol*. 2005;70:77-101.
- 12 Constantinides CD, Gillen JS, Boada FE, Pomper MG, Bottomley PA. Human skeletal muscle: sodium MR imaging and quantification-potential applications in exercise and disease. *Radiology*. 2000;216(2):559-68.
- 13 Lauterbur P. Image formation by induced local interactions: examples employing nuclear magnetic resonance. *Nature*. 1973;242(5394):190–1.
- 14 Boada FE, Shen GX, Chang SY, Thulborn KR. Spectrally weighted twisted projection imaging: reducing T2 signal attenuation effects in fast three-dimensional sodium imaging. *Magn Reson Med*. 1997;38(6):1022-8.
- 15 Gurney PT, Hargreaves BA, Nishimura DG. Design and analysis of a practical 3D cones trajectory. *Magn Reson Med*. 2006;55(3):575-82.
- 16 Nagel AM, Laun FB, Weber MA, Matthies C, Semmler W, Schad LR. Sodium MRI using a

- density-adapted 3D radial acquisition technique. *Magn Reson Med*. 2009;62(6):1565-73.
- 17 Konstandin S, Nagel AM, Heiler PM, Schad LR. Two-dimensional radial acquisition technique with density adaption in sodium MRI. *Magn Reson Med*. 2011;65(4):1090-6.
  - 18 Konstandin S, Nagel AM. Performance of sampling density-weighted and postfiltered density-adapted projection reconstruction in sodium magnetic resonance imaging. *Magn Reson Med*. 2013;69(2):495-502.
  - 19 Stobbe R, Beaulieu C. Advantage of sampling density weighted apodization over postacquisition filtering apodization for sodium MRI of the human brain. *Magn Reson Med*. 2008;60(4):981-6.
  - 20 Staroswiecki E, Bangerter NK, Gurney PT, Grafendorfer T, Gold GE, Hargreaves BA. In vivo sodium imaging of human patellar cartilage with a 3D cones sequence at 3 T and 7 T. *Journal of magnetic resonance imaging : JMIR*. 2010;32(2):446-51.
  - 21 Watts A, Stobbe RW, Beaulieu C. Signal-to-noise optimization for sodium MRI of the human knee at 4.7 Tesla using steady state. *Magn Reson Med*. 2011;66(3):697-705.
  - 22 Wetterling F, Hogler M, Molkenhuth U, et al. The design of a double-tuned two-port surface resonator and its application to in vivo hydrogen- and sodium-MRI. *J Magn Reson*. 2012;217:10-8.
  - 23 Wetterling F, Corteville DM, Kalayciyan R, et al. Whole body sodium MRI at 3T using an asymmetric birdcage resonator and short echo time sequence: first images of a male volunteer. *Phys Med Biol*. 2012;57(14):4555-67.
  - 24 Haneder S, Konstandin S, Morelli JN, et al. Quantitative and Qualitative <sup>23</sup>Na MR Imaging of the Human Kidneys at 3 T: Before and after a Water Load. *Radiology*. 2011;260(3):857-65.
  - 25 Maril N, Rosen Y, Reynolds GH, Ivanishev A, Ngo L, Lenkinski RE. Sodium MRI of the human kidney at 3 Tesla. *Magn Reson Med*. 2006;56(6):1229-34.
  - 26 Haneder S, Kettner P, Konstandin S, et al. Quantitative in vivo <sup>23</sup>Na MR-Imaging of the healthy human kidney: determination of physiological ranges at 3.0T with comparison to DWI and BOLD. *Magma*. 2013; in press; DOI 10.1007/s10334-013-0369-4.
  - 27 Trattnig S, Zbyn S, Schmitt B, et al. Advanced MR methods at ultra-high field (7 Tesla) for clinical musculoskeletal applications. *European radiology*. 2012;22(11):2338-46.
  - 28 Noebauer-Huhmann IM, Juras V, Pfirrmann CW, et al. Sodium Imaging of the Lumbar Intervertebral Disk at 7 T: Correlation with T2 Mapping and Modified Pfirrmann Score at 3 T – Preliminary Results. *Radiology*. 2012.
  - 29 Borthakur A, Shapiro EM, Akella SV, Gougoutas A, Kneeland JB, Reddy R. Quantifying sodium in the human wrist in vivo by using MR imaging. *Radiology*. 2002;224(2):598-602.
  - 30 Clayton DB, Lenkinski RE. MR imaging of sodium in the human brain with a fast three-dimensional gradient-recalled-echo sequence at 4 T. *Acad Radiol*. 2003;10(4):358-65.
  - 31 Kohler S, Preibisch C, Nittka M, Haase A. Fast three-dimensional sodium imaging of human brain. *Magma*. 2001;13(2):63-9.
  - 32 Jerecic R, Bock M, Nelles-Vallespin S, Wacker C, Bauer W, Schad LR. ECG-gated <sup>23</sup>Na-MRI of the human heart using a 3D-radial projection technique with ultra-short echo times. *Magma*. 2004;16(6):297-302.
  - 33 Konstandin S, Schad LR. Two-dimensional radial sodium heart MRI using variable-rate selective excitation and retrospective electrocardiogram gating with golden angle increments. *Magn Reson Med*. 2012. doi: 10.1002/mrm.24523
  - 34 Greiser A, Haase A, von Kienlin M. Improved cardiac sodium MR imaging by density-weighted phase-encoding. *Journal of magnetic resonance imaging : JMIR*. 2005;21(1):78-81.
  - 35 Hausmann D, Konstandin S, Wetterling F, et al. Apparent Diffusion Coefficient and Sodium Concentration Measurements in Human Prostate Tissue via Hydrogen-1 and Sodium-23 Magnetic Resonance Imaging in a Clinical Setting at 3 T. *Investigative radiology*. 2012.
  - 36 Rosen Y, Lenkinski RE. Sodium MRI of a human transplanted kidney. *Acad Radiol*. 2009;16(7):886-9.
  - 37 Haneder S, Michael HJ, Schoenberg SO, et al. Assessment of renal function after conformal radiotherapy and intensity-modulated radiotherapy by functional (1)H-MRI and (23)Na-MRI. *Strahlenther Onkol*. 2012;188(12):1146-54.
  - 38 Trattnig S, Welsch GH, Juras V, et al. <sup>23</sup>Na MR imaging at 7 T after knee matrix-associated autologous chondrocyte transplantation preliminary results. *Radiology*. 2010;257(1):175-84.
  - 39 Zbyn S, Stelzener D, Welsch GH, et al. Evaluation of native hyaline cartilage and repair tissue after two cartilage repair surgery techniques with <sup>23</sup>Na MR imaging at 7 T: initial experience. *Osteoarthritis Cartilage*. 2012;20(8):837-45.
  - 40 Juras V, Zbyn S, Pressl C, et al. Sodium MR imaging of Achilles tendinopathy at 7 T: preliminary results. *Radiology*. 2012;262(1):199-205.
  - 41 Ouwerkerk R, Bleich KB, Gillen JS, Pomper MG, Bottomley PA. Tissue sodium concentration in human brain tumors as measured with <sup>23</sup>Na MR imaging. *Radiology*. 2003;227(2):529-37.
  - 42 Thulborn KR, Lu A, Atkinson IC, Damen F, Villano JL. Quantitative sodium MR imaging and sodium bioscales for the management of brain tumors. *Neuroimaging Clin N Am*. 2009;19(4):615-24.
  - 43 Maudsley AA, Hilal SK. Biological aspects of sodium-23 imaging. *Br Med Bull*. 1984;40(2):165-6.
  - 44 Thulborn KR, Davis D, Snyder J, Yonas H, Kassam A. Sodium MR imaging of acute and subacute stroke for assessment of tissue viability. *Neuroimaging Clin N Am*. 2005;15(3):639-53, xi-xii.
  - 45 Thulborn KR, Gindin TS, Davis D, Erb P. Comprehensive MR imaging protocol for stroke management: tissue sodium concentration as a measure of tissue viability in nonhuman primate studies and in clinical studies. *Radiology*. 1999;213(1):156-66.
  - 46 Zaaraoui W, Konstandin S, Audoin B, et al. Distribution of brain sodium accumulation correlates with disability in multiple sclerosis: a cross-sectional <sup>23</sup>Na MR imaging study. *Radiology*. 2012;264(3):859-67.
  - 47 Rochitte CE, Kim RJ, Hillenbrand HB, Chen EL, Lima JA. Microvascular integrity and the time course of myocardial sodium accumulation after acute infarction. *Circ Res*. 2000;87(8):648-55.
  - 48 Ouwerkerk R, Bottomley PA, Solaiyappan M, et al. Tissue sodium concentration in myocardial infarction in humans: a quantitative <sup>23</sup>Na MR imaging study. *Radiology*. 2008;248(1):88-96.
  - 49 Sandstede JJ, Hillenbrand H, Beer M, et al. Time course of <sup>23</sup>Na signal intensity after myocardial infarction in humans. *Magn Reson Med*. 2004;52(3):545-51.
  - 50 Laymon CM, Oborski MJ, Lee VK, et al. Combined imaging biomarkers for therapy evaluation in glioblastoma multiforme: correlating sodium MRI and F-18 FLT PET on a voxel-wise basis. *Magn Reson Imaging*. 2012;30(9):1268-78.
  - 51 Kline RP, Wu EX, Petrylak DP, et al. Rapid in vivo monitoring of chemotherapeutic response using weighted sodium magnetic resonance imaging. *Clin Cancer Res*. 2000;6(6):2146-56.
  - 52 Babsky AM, Hekmatyar SK, Zhang H, Solomon JL, Bansal N. Application of <sup>23</sup>Na MRI to monitor chemotherapeutic response in RIF-1 tumors. *Neoplasia*. 2005;7(7):658-66.
  - 53 Sharma R, Kline RP, Wu EX, Katz JK. Rapid in vivo Taxotere quantitative chemosensitivity response by 4.23 Tesla sodium MRI and histo-immunostaining features in N-Methyl-N-Nitrosourea induced breast tumors in rats. *Cancer Cell Int*. 2005;5:26.
  - 54 Schepkin VD, Chenevert TL, Kuszpit K, et al. Sodium and proton diffusion MRI as biomarkers for early therapeutic response in subcutaneous tumors. *Magn Reson Imaging*. 2006;24(3):273-8.
  - 55 Schepkin VD, Lee KC, Kuszpit K, et al. Proton and sodium MRI assessment of emerging tumor chemotherapeutic resistance. *NMR Biomed*. 2006;19(8):1035-42.
  - 56 Henzler T, Konstandin S, Schmid-Bindert G, et al. Imaging of tumor viability in lung cancer: initial results using <sup>23</sup>Na-MRI. *Rofo*. 2012;184(4):340-4.
  - 57 Gerlinger M, Rowan AJ, Horswell S, et al. Intra-tumor heterogeneity and branched evolution revealed by multiregion sequencing. *N Engl J Med*. 2012;366(10):883-92.
  - 58 Kuntz J, Gupta R, Schonberg SO, Semmler W, Kachelriess M, Bartling S. Real-time X-ray-based 4D image guidance of minimally invasive interventions. *European radiology*. 2013.
  - 59 Schonberg SO, Wangler B. From molecular imaging markers to personalized image-guided therapy. *Zeitschrift für medizinische Physik*. 2013.

#### Contact

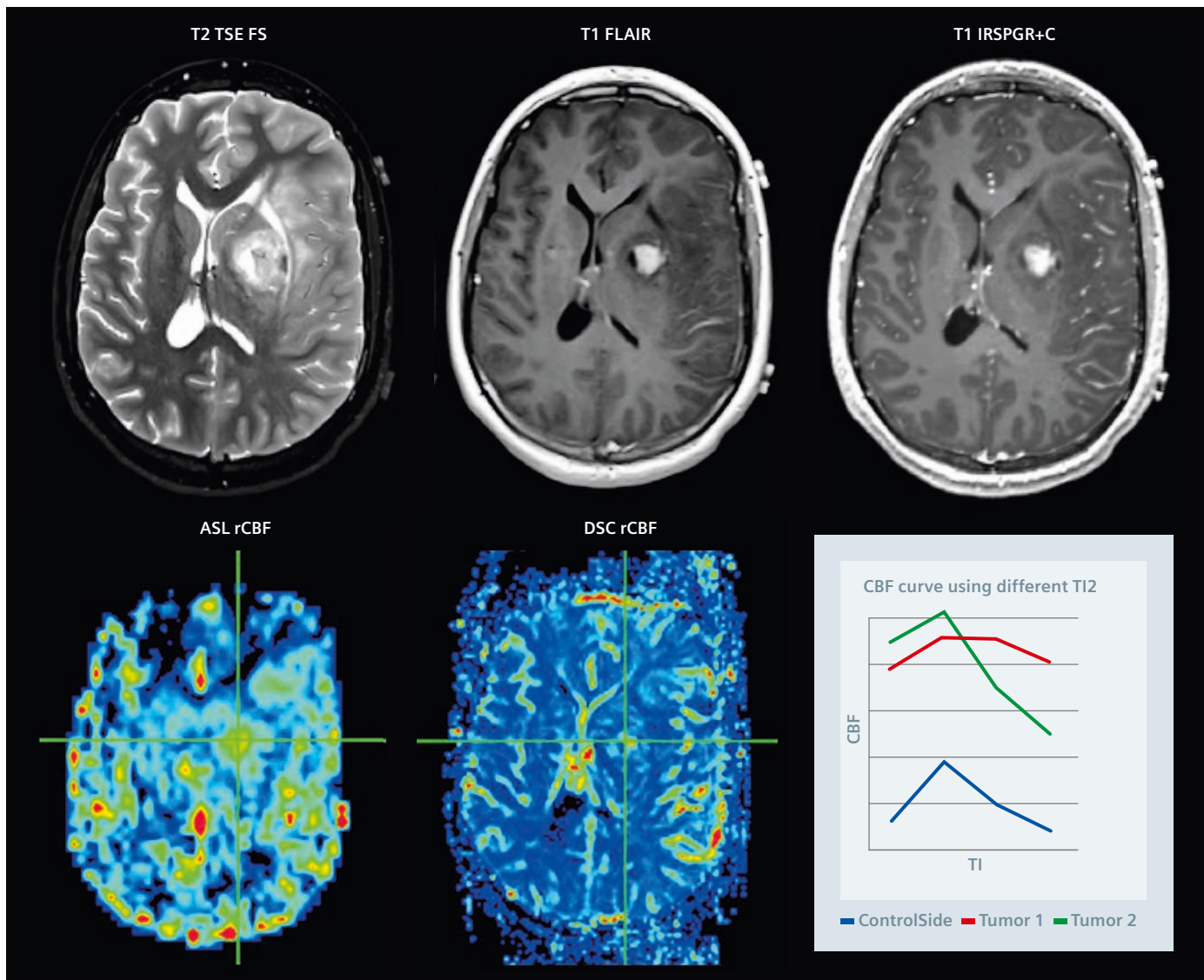
Stefan Haneder, M.D.  
 Institute of Clinical Radiology  
 and Nuclear Medicine  
 University Medical Center Mannheim  
 Heidelberg University  
 Theodor-Kutzer-Ufer 1–3  
 68167 Mannheim  
 Germany  
 Phone: +49/621/383 2067  
 Fax: +49/621/383 1910  
 stefan.haneder@umm.de

# A novel 2D Pulsed Arterial Spin Labeling Protocol for Pediatric Cases with Brain Tumor

Yang Wang, M.D.<sup>1</sup>; Chang Y. Ho, M.D.<sup>1</sup>; Josef Pfeuffer, Ph.D.<sup>2</sup>

<sup>1</sup>Center for Neuroimaging, Department of Radiology and Imaging Sciences, Indiana University School of Medicine, Indianapolis, IN, USA

<sup>2</sup>Siemens Healthcare, MR Applications Development, Erlangen, Germany



**1** rCBF curve using different TI allows assessment of the rCBF considering pathological alteration in regional arterial transit time.

## Introduction

Arterial spin labeling (ASL) is a non-invasive MRI technique that does not rely on ionizing radiation for measuring regional cerebral blood flow (rCBF). ASL can be applied as an attractive alternative method for measuring perfusion in pediatric<sup>#</sup> brain tumor patients where it is desirable to minimize the use of ionizing radiation and Gd-based contrast agents. Compared with conventional dynamic susceptibility contrast (DSC) techniques, ASL can be quantitative enabling the measurement of global hypo- or hyper-perfusion as well as absolute perfusion changes in longitudinal studies. However, to date ASL has not been widely utilized in clinical practice.

Quantification of rCBF using ASL perfusion MRI requires several experimental and physiological parameters to be properly accounted for. Variable bolus transit time and post-labeling delay are two confounding factors that may compromise the quantitative accuracy of perfusion estimates [3]. While the widely used PICORE Q2TIPS method of pulsed ASL (PASL) with a fixed temporal width tagging bolus enables quantitative estimates of rCBF from measurements taken at a single inversion time (TI), one of the key assumptions of Q2TIPS is that TI is sufficiently long for the trailing edge of the tagged bolus to have reached the imaging voxel [4]. Empirical observations suggest that transit time can be altered in different physiological and/or pathological conditions [1, 3, 5]. Therefore, we have developed a new PASL protocol<sup>§</sup> that fits the single compartment model to multiple TI acquisitions to reduce artifacts caused by spatially variable bolus transit times<sup>§</sup>.

## Theory

PASL uses an inversion pulse and a tag saturation module to define the temporal duration of the tag (e.g. QUIPSS or Q2TIPS methods) [8], where a single compartment model can be used to estimate rCBF [2].

$$\begin{aligned} \Delta M &= 0 & Tl_2 < t_A \\ \Delta M &= 2fM_0\alpha(Tl_2 - Tl_1)e^{-\left(\frac{t}{Tl_b}\right)} & t_A < Tl_2 < t_A + Tl_1 \\ \Delta M &= 2fM_0\alpha Tl_1e^{-\left(\frac{t}{Tl_b}\right)} & t_A + Tl_1 < Tl_2 \end{aligned}$$

In this model  $\Delta M$  is the signal difference between label and control images,  $Tl_2$  is the total inversion time between the label pulse and the readout of the proximal slice,  $Tl_1$  is bolus cut off time (also defines bolus duration),  $t_A$  is the arterial transit time (ATT) referring to the time it takes the arterial blood to travel from the labeling site to the capillaries in the issue being imaged,  $Tl_b$  is the longitudinal relaxation time of blood,  $\alpha$  is the inversion efficiency and  $M_0$  is the acquired map of equilibrium magnetization of arterial blood. This model assumes no exchange of labeled blood water into the tissue. Using this model, the rCBF map can be calculated using equation (1) [7], where  $\lambda$  = blood/tissue water partition coefficient,  $\tau$  = bolus cut off time (also defines bolus duration).

$$f = \frac{\lambda \Delta M}{2\alpha M_0 \tau \exp(-Tl_2/Tl_b)} \quad (1)$$

In this model as proposed by Buxton et al. [2], different slices are measured at different inversion times  $Tl_2^{SLICE}$  due to the acquisition duration of a slice using 2D fast imaging methods like EPI, so that rCBF estimates that account for different  $Tl_2^{SLICE}$  can be made by applying an inverted factor  $\Delta M^{CORRECTED} = \Delta M \cdot \exp(\Delta Tl_2^{SLICE} / Tl_b)$ , which normalizes the different  $Tl_2^{SLICE}$  for different slices to the first slice with  $Tl_2^{SLICE-1}$ . In line with the shape of PASL kinetic curves shown by Gallichan et al. [3], after a transit time  $\Delta t$ , the first inverted blood spins of the bolus arrive at the slice. During the time  $(\Delta t + \tau)$ , the bolus accumulates in the slice and give the increase in perfusion signal  $\Delta M$  according the function  $\Delta M \sim t \cdot \exp(-t/Tl_1')$ . At the time  $(\Delta t + \tau)$ , the perfusion signal  $\Delta M$  reaches a maximum. After the time  $(\Delta t + \tau)$  the perfusion signal  $\Delta M$  undergoes longitudinal relaxation modeled with an effective relaxation time  $Tl_1'$  according the function  $\Delta M \sim \exp(-t/Tl_1')$ .  $Tl_1'$  is a function of  $Tl_1$  in tissue and blood. This approach minimizes bias in rCBF values if the bolus arrives in time in all regions of the slice with minimal temporal dispersion. In brain regions with altered bolus transit times due to pathology or biological differences, the bolus transit times are

larger than  $(Tl_2^{SLICE} - \tau)$ , then the standard model calculation will underestimate the true rCBF.

In this study, we introduce a novel protocol to acquire two consecutive PASL scans with identical parameters, one in ascending and another in descending slice order. Each slice now has two average perfusion maps with different  $Tl_2^{SLICE}$  times. The two maps and corresponding  $Tl_2^{SLICE}$  can be interpolated, e.g. an average  $Tl_2^{compensated} = (Tl_2^{SLICE-1,1} + Tl_2^{SLICE-1,2}) / 2$  is assumed. Then, all slices have the same average  $Tl_2$ , while signal-to-noise ratio (SNR) per unit time is preserved. No further assumptions, as in the standard model, are required, because all maps for different slices are quantified with  $Tl_2^{average}$ . This approach minimizes bias in rCBF estimates if the bolus arrival time varies between brain regions. In addition, a model validity map can be calculated from the rCBF maps at different  $Tl_2^{SLICE}$ : the experimental signal difference at different  $Tl_2^{SLICE}$  is set in ratio (A / B) to the theoretical model:  $\Delta M(Tl_2^{SLICE-1,1}) / \Delta M(Tl_2^{SLICE-1,2}) = :A$  compared to  $\exp(-(Tl_2^{SLICE-1,1} - Tl_2^{SLICE-1,2}) / Tl_1') = :B$ .

Moreover, we collected data using four different inversion times ( $Tl_2$ ) with a fixed bolus cut off time ( $Tl_1$ ), then fitted those four different datasets with the theoretical perfusion curve of the single compartment model, in order to estimate rCBF and regional ATT [3].

## Methods

PASL data were acquired using PICORE Q2TIPS sequence on a 3T MRI scanner (MAGNETOM Verio, A Tim System, Siemens Healthcare, Germany). A 32-channel head receive coil was used to increase SNR. Scan parameters: 16 slices, 5 mm thickness, dist. factor 20%, matrix  $64 \times 64$ , field-of-view (FOV) 24 cm, 6/8 partial Fourier, BW 2298 Hz/Px, TR 3000 ms, TE 13 ms,  $Tl_1$  700 ms, four different  $Tl_2$  (1200 ms, 1500 ms, 1800 ms, 2100 ms) were applied twice with one scan in ascending and another one in descending slice order, each scan with 32 acq. pairs plus one  $M_0$  image, total scan time of the protocol about 11 min. Inline 3D Prospective Acquisition

Correction (PACE) was used during all PASL scans to minimize head motion artifacts [6]. In post-processing, perfusion-weighted images were calculated for each T12 acquisition and combined from two scans with different slice order. Then four different perfusion-weighted images were fitted into the single compartment model to estimate ATT and rCBF, as described elsewhere [1, 3].

## Case report

A 16-year-old male presented with slurred speech and blurred vision. MR morphological imaging shows a heterogeneously enhancing tumor centered in the left putamen with a final pathologic diagnosis of primitive neuroectodermal tumor (PNET). Both PASL and DSC perfusion are concordant in demonstrating regional increased CBF within the tumor, consistent with a high grade neoplasm. Using our novel PASL protocol, we were able to generate different rCBF maps at different TI, and more precisely

assessed the rCBF, considering the pathological alteration in regional ATT (Fig. 1).

## Conclusion

The development of a robust, quantitative ASL protocol is critical for estimation of CBF in research and clinical applications. A number of studies have measured multiple TI times for the same slices and demonstrated in healthy human brain that the model provides unbiased rCBF estimates in some regions, but in other regions considerable bolus dispersion and latency have been observed [3]. Moreover, acquisition of multiple TI will considerably increase the exam time and might not be feasible in some clinical applications. In this report, a novel PASL multiple-TI protocol is introduced using a 32-channel coil to preserve SNR at clinically acceptable measurement durations. Brain tumors remain the second most common tumor in the pediatric age group after leukemia. It is well known

that malignant brain tumors typically cause neoangiogenesis due to increased metabolic demand, resulting in an increase in rCBF. By developing a robust, quantifiable ASL protocol tumor grading – and therefore clinical management – can be more accurately accomplished without the use of gadolinium injection. The novel PASL multiple-TI method enables us to more accurately estimate rCBF in pediatric tumor cases at clinically acceptable examination time. Future research is needed to determine whether this method may be useful for doctors in making treatment decisions and monitoring patients' response to treatment.

**Acknowledgements:** We gratefully acknowledge Drs. Laura M. Parkes and Helen Beaumont (Centre for Imaging Sciences & Biomedical Imaging Institute, University of Manchester, UK) for assistance with data analysis.

## References

- 1 Bokkers, R. P., J. P. Bremmer, B. N. van Berckel, A. A. Lammertsma, J. Hendrikse, J. P. Pluim, L. J. Kappelle, R. Boellaard and C. J. Klijn (2010). "Arterial spin labeling perfusion MRI at multiple delay times: a correlative study with H(2)(15)O positron emission tomography in patients with symptomatic carotid artery occlusion." *J Cereb Blood Flow Metab* 30(1): 222-229.
- 2 Buxton, R. B., L. R. Frank, E. C. Wong, B. Siewert, S. Warach and R. R. Edelman (1998). "A general kinetic model for quantitative perfusion imaging with arterial spin labeling." *Magn Reson Med* 40(3): 383-396.
- 3 Gallichan, D. and P. Jezzard (2009). "Variation in the shape of pulsed arterial spin labeling kinetic curves across the healthy human brain and its implications for CBF quantification." *Magn Reson Med* 61(3): 686-695.
- 4 Luh, W. M., E. C. Wong, P. A. Bandettini and J. S. Hyde (1999). "QUIPSS II with thin-slice T11 periodic saturation: a method for improving accuracy of quantitative perfusion imaging using pulsed arterial spin labeling." *Magn Reson Med* 41(6): 1246-1254.
- 5 MacIntosh, B. J., N. Filippini, M. A. Chappell, M. W. Woolrich, C. E. Mackay and P. Jezzard (2010). "Assessment of arterial arrival times derived from multiple inversion time pulsed arterial spin labeling MRI." *Magn Reson Med* 63(3): 641-647.
- 6 Thesen, S., O. Heid, E. Mueller and L. R. Schad (2000). "Prospective acquisition correction for head motion with image-based tracking for real-time fMRI." *Magnetic Resonance in Medicine* 44(3): 457-465.
- 7 Wang, J., D. J. Licht, G. H. Jahng, C. S. Liu, J. T. Rubin, J. Haselgrove, R. A. Zimmerman and J. A. Detre (2003). "Pediatric perfusion imaging using pulsed arterial spin labeling." *J Magn Reson Imaging* 18(4): 404-413.
- 8 Wong, E. C., R. B. Buxton and L. R. Frank (1998). "Quantitative imaging of perfusion using a single subtraction (QUIPSS and QUIPSS II)." *Magn Reson Med* 39(5): 702-708.

## Contact

Yang Wang, M.D.  
Center for Neuroimaging  
Department of Radiology  
and Imaging Sciences  
Indiana University School of Medicine  
355 W. 16th Street, GH Suite 4100  
Indianapolis, IN 46202-7176  
USA  
Phone: +1 (317) 963-7506  
Fax: +1 (317) 963-7547  
ywang1@iupui.edu

\*MR scanning has not been established as safe for imaging fetuses and infants under two years of age. The responsible physician must evaluate the benefit of the MRI examination in comparison to other imaging procedures.

†WIP – Works in progress: The new PASL protocol is currently under development; it is not for sale in the U.S. Its future availability cannot be ensured.

\*Patent US 2010/0141254 A1 by J. Pfeuffer using this technique was filed on Oct 22, 2009.

# Try them on your system

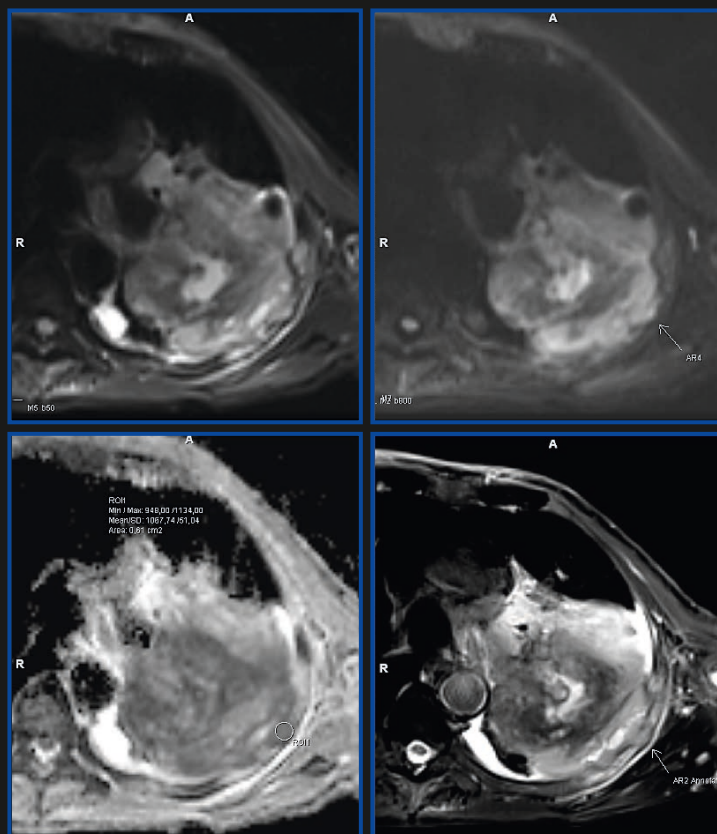
Trial licenses for some of the applications featured in this issue of MAGNETOM Flash are available free of charge for a period of 90 days.

For further details, product overviews, image galleries, step-by-step videos, case studies and general requirements visit us at:

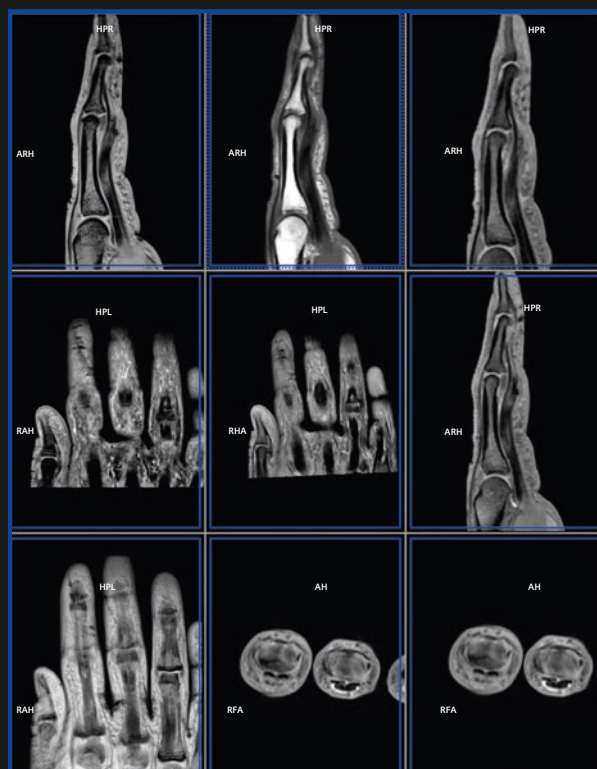
[www.siemens.com/discoverMR](http://www.siemens.com/discoverMR)

Direct link for USA: [www.siemens.com/WebShop](http://www.siemens.com/WebShop)

Direct link for UK: [www.siemens.com.uk/mrwebshop](http://www.siemens.com.uk/mrwebshop)



syngo BLADE,  
(page 87)



Trauma case (page 84)

## High SNR and excellent iPAT performance for fast and high quality imaging

- Imaging the whole hand and wrist in a single measurement
- Comfortable patient positioning with arms on the side
- Fast and easy patient preparation with SlideConnect technology



16-channel  
Hand/Wrist coil

Discover our extensive coil portfolio for musculoskeletal MRI: [www.siemens.com/redefine-MRI-with-coils](http://www.siemens.com/redefine-MRI-with-coils)

# MAGNETOM Aera – Combining Throughput and Highest Quality MRI in an Optimized Clinical Workflow

Johan Dehem, M.D.

VZW Jan Yperman, Ieper, Belgium

We have been using the 1.5T MAGNETOM Aera for a year now and it is perhaps time to reflect on how the system is performing in a busy environment. My experiences with the MAGNETOM Aera are summarized in this article. Compared to our earlier 1.5T MAGNETOM Symphony a Tim system, MAGNETOM Aera's new RF system – Tim 4G – introduces signal increase that is used to scan at higher resolution than before whilst keeping the same acquisition time or can be combined with parallel imaging for higher speed.

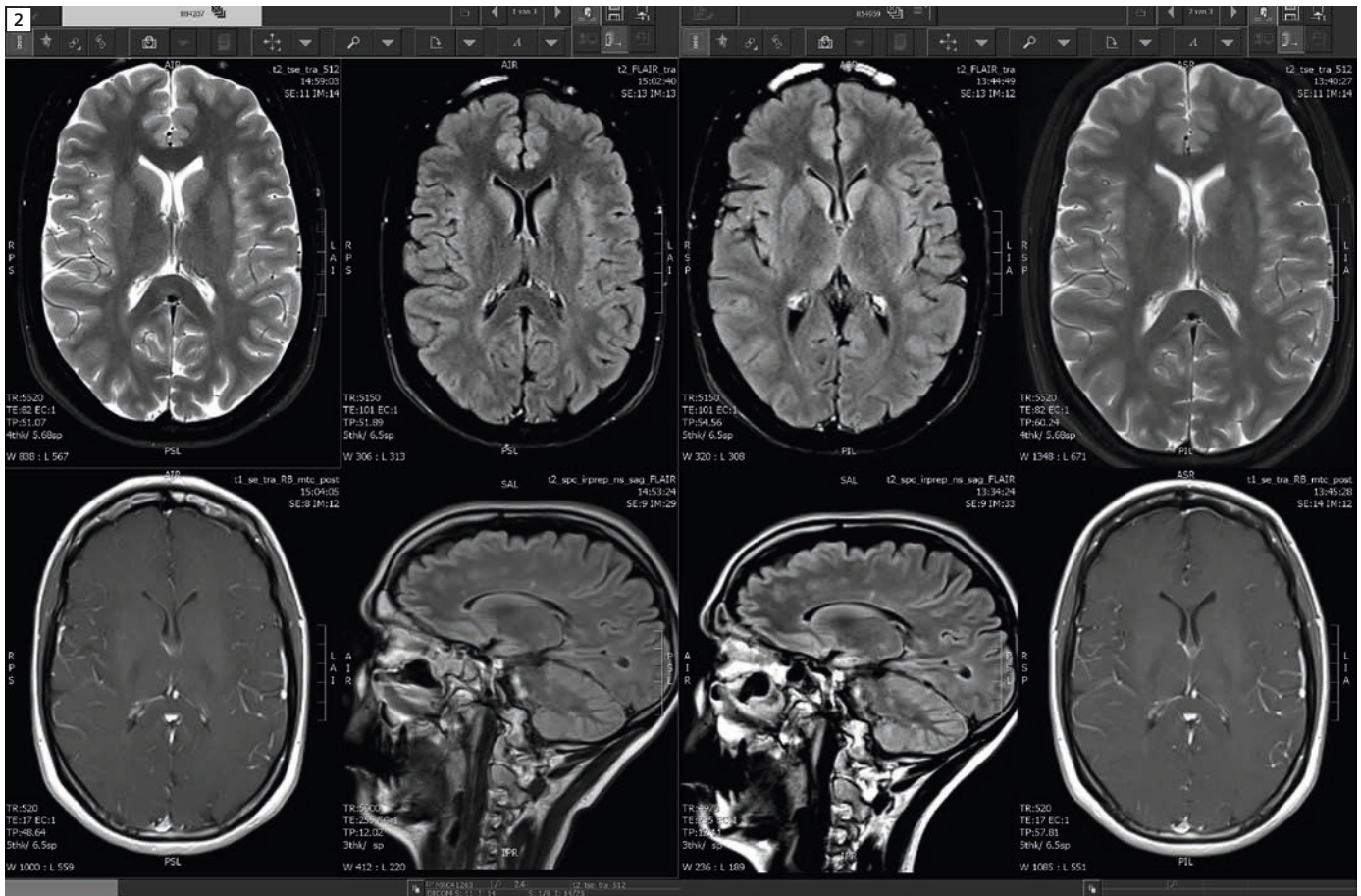
## Section 1: fast brain imaging with Tim 4G and Dot

In our center we use eight sequences for brain evaluation in a 20-minute time slot that includes getting the patient in and out of the MRI suite. Figure 1 shows the details of the brain protocol we follow. The Brain Dot Engine helps us to acquire all brain examinations with consistent accurate coverage from the foramen magnum up to the vertex and from left to right or anteroposterior without fault, which is possible irrespective of the experience level of the operators. Moreover, Brain Dot Engine starts with an AutoAlign 3D localizer which is mapped to the Tailarach space, and as a result sequence planning is automated according to the reference space independent of patient positioning / habitus. This is especially convenient in follow-up examinations, such as in this case of demyelinating disease or tumor, resulting in a more reliable and comfortable comparison of the examinations at different time points (Fig. 2).



**1** Sequence details of our 20-minute brain evaluation:

1. T2\*w EPI, 23 slices, 5 mm in 9.7 sec, 0.9 x 0.9 x 5 (FOV 185 x 220, matrix 216 x 256) res
2. T1w sag SE, 4 mm slices in 2:09 min, 0.7 x 0.7 x 4 (FOV 290 x 223, matrix 246 x 320) res
3. T2w ax TSE, 25 slices, 4 mm in 01:34 min, 0.5 x 0.5 x 4 (FOV 171 x 221, matrix 256 x 384)
4. T2w FLAIR, 23 slices, 5 mm in 32 sec x 2 0.8 x 0.8 x 5 (FOV 211 x 211, matrix 205 x 256)
5. DWI EPI b500, b500, b1000, 69 slices in 1:30 min (1.2 x 1.2 x 5, FOV 216 x 231, matrix 174 x 188)
6. 3D TOF 3 slabs, 116 slices in 2:44 min, 0.4 x 0.4 x 0.5 mm isotropic (FOV 141 x 181, matrix 376 x 512)
7. T1w cor TSE, 22 4 mm slices in 1:34 min, 0.8 x 0.8 x 4 (FOV 174 x 200, matrix 213 x 256)
8. T1w ax SE 22 4 mm slices in 2:34 min, 0.9 x 0.9 x 5 (FOV 174 x 200, matrix 213 x 256)



**2** Follow-up examination at different time-points in demyelinating disease. Even the small lesions are comparable since anatomy is depicted consistently, independent of operator and patient positions even on a different PACS system and on the viewing system of the referring physician.

## Section 2: 16-channel MSK coils

The new RF system enables the use of 16-channel MSK coils like the Shoulder, Foot/Ankle and Hand/Wrist coils. The new wrist coil gives abundant signal and superb detail. The wrist coil has grown, in fact, to a 16-channel hand-wrist coil (Fig. 3), which is quite convenient for both the patient and the operators and helps faster setup times. Many patients have combined hand/wrist pathology and symptoms, and extended coverage is a huge benefit. Since it is easy to position the hand in the Hand/Wrist coil, examining the fingers has become very straightforward. Figure 4 shows a young butcher who suffered from a deep wound in the index finger. You still can notice the susceptibility artifacts on the coronal STIR and GRE (Figs. 4D, E). One week later the

young man can no longer flex the distal interphalangeal joint (DIP) of the index finger. MRI nicely depicts the torn deep flexor retracted to the proximal phalanx in the tendon sheet (Figs. 4H, I). All these images have an in-plane resolution of 0.5 mm, a slice thickness of 2.3 mm or less and scanning times of 1.30 min or less thanks to the higher signal from the high-channel coil.

Since this coil is so successful for fingers, it could also be used for toes. This is the flexibility with Tim.

Figure 5 shows images of a middle-aged man, who suffers from a “tingling pain sensation” in the forefoot intermetatarsal space III-IV and numb feeling in digit IV. A T2 hyperintense, T1 hypointense dumbbell shaped lesion bulging between the metatarsal heads III-IV is clearly demonstrated (Figs. 5A, B, C) confirming the clinical suspicion of Morton neuroma.



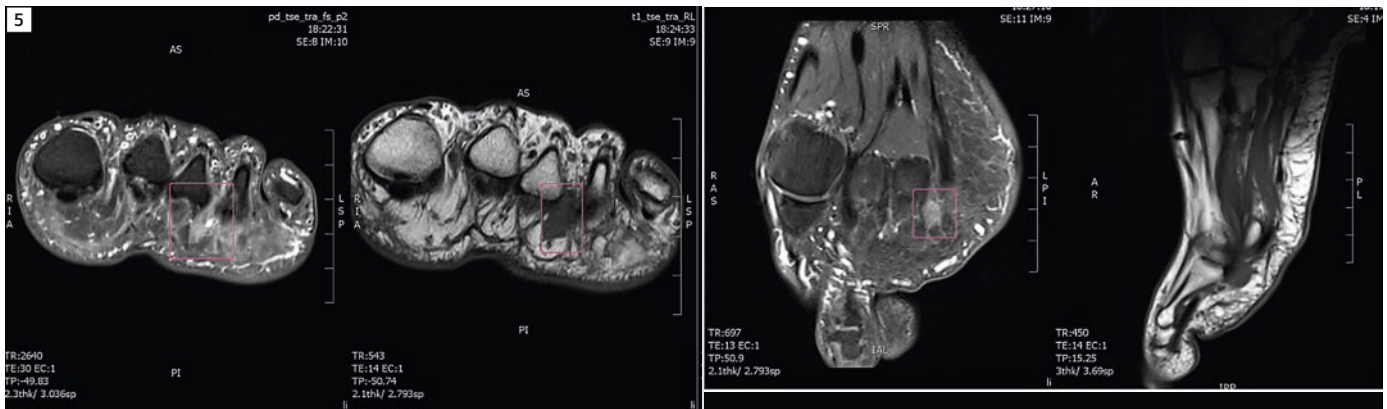
**3** 16-channel Hand/Wrist coil.

## Section 3: reduction of susceptibility artifacts caused by metal

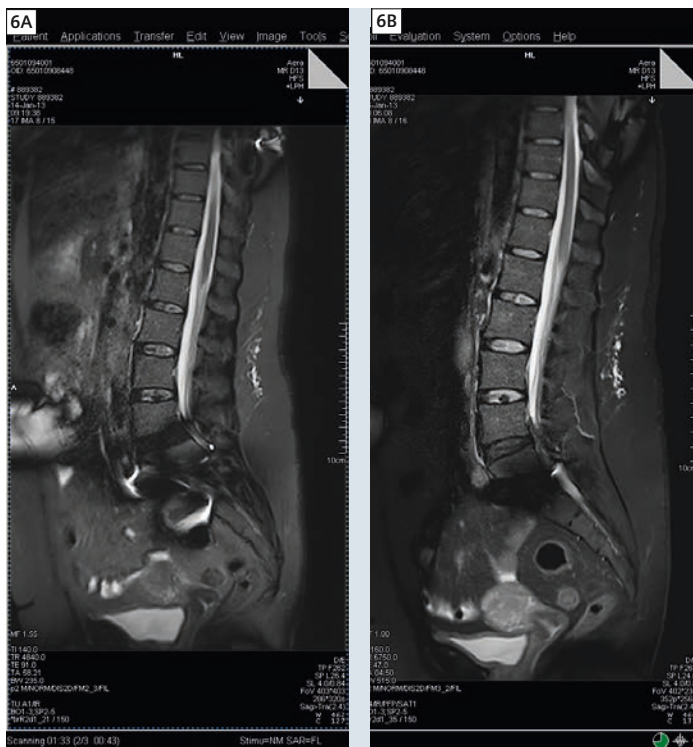
MRI is challenging in the presence of metal. MAGNETOM Aera came equipped with syngo WARP with high bandwidth TSE and TSE STIR protocols and an



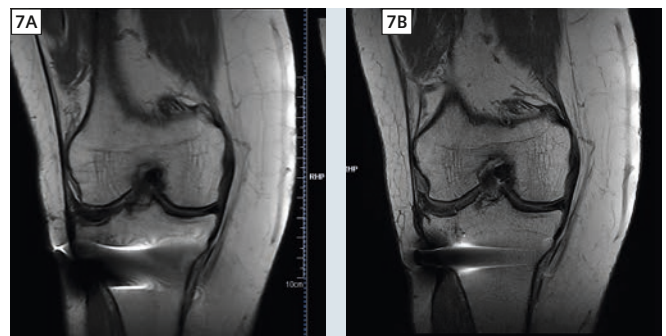
4 Superb details in a case of trauma to index finger in 1:30 min per sequence.



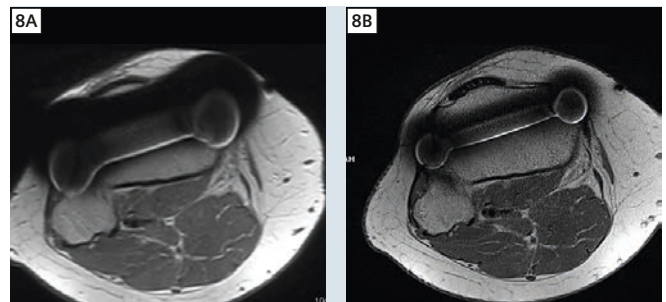
**5** Toe imaging using the 16-channel Hand/Wrist coil. Excellent image quality showing Morton neuroma between the metatarsal heads III and IV.



**6** T2w TIR versus T2w TIR WARP demonstrates dramatic improvement in image quality with the disc L5-S1 showing up on the WARP images only (Fig. 6B).



**7** T1-weighted coronal imaging degraded by artifacts (7A). T1 VAT WARP does the job (7B).



**8** Proton density-weighted axial image largely degraded (8A). PD VAT WARP nicely demonstrates the material and recovers the distortion (8B).

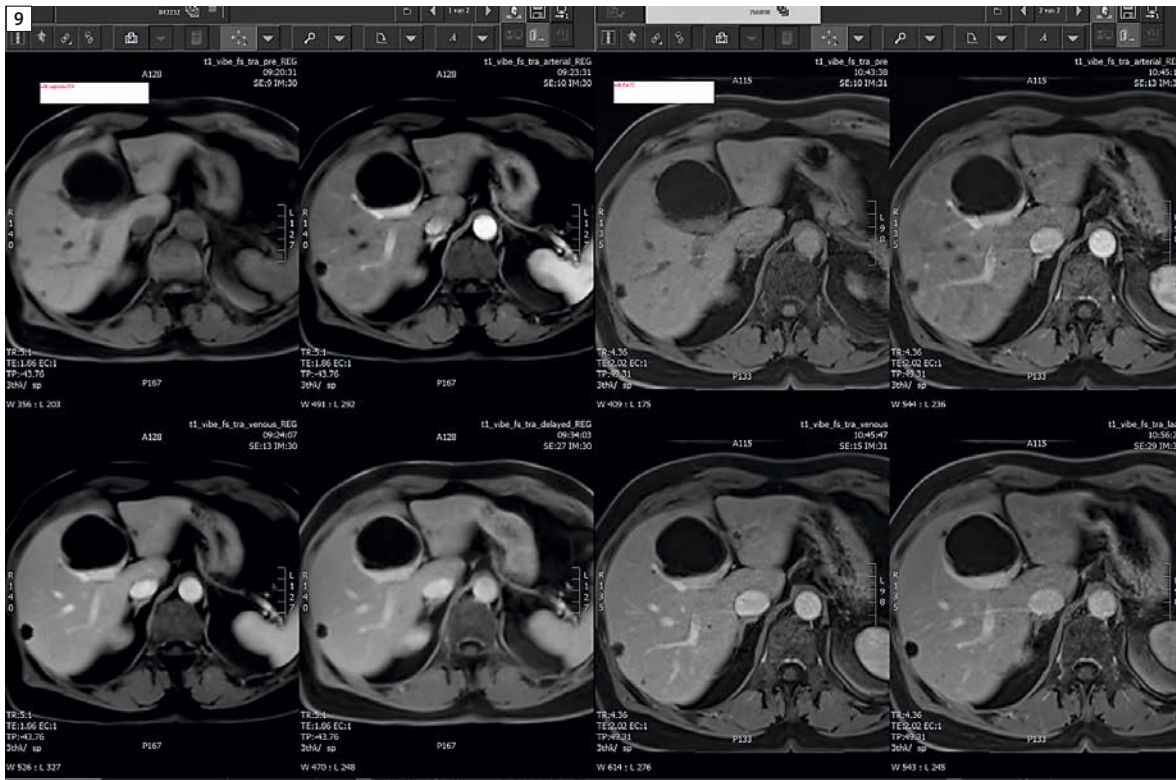
optional VAT (View Angle Tilting) technique. In Figures 6–8 I share some examples of real day-to-day cases. Figures 7 and 8 show images of a female patient who has had osteosynthesis for tibial plateau fracture following a skiing accident 20 years ago. She had an MRI of the knee, after another skiing accident. WARP helped reduce susceptibility artifacts for better image quality and confidence in diagnosis.

## Section 4: faster imaging with CAIPIRINHA

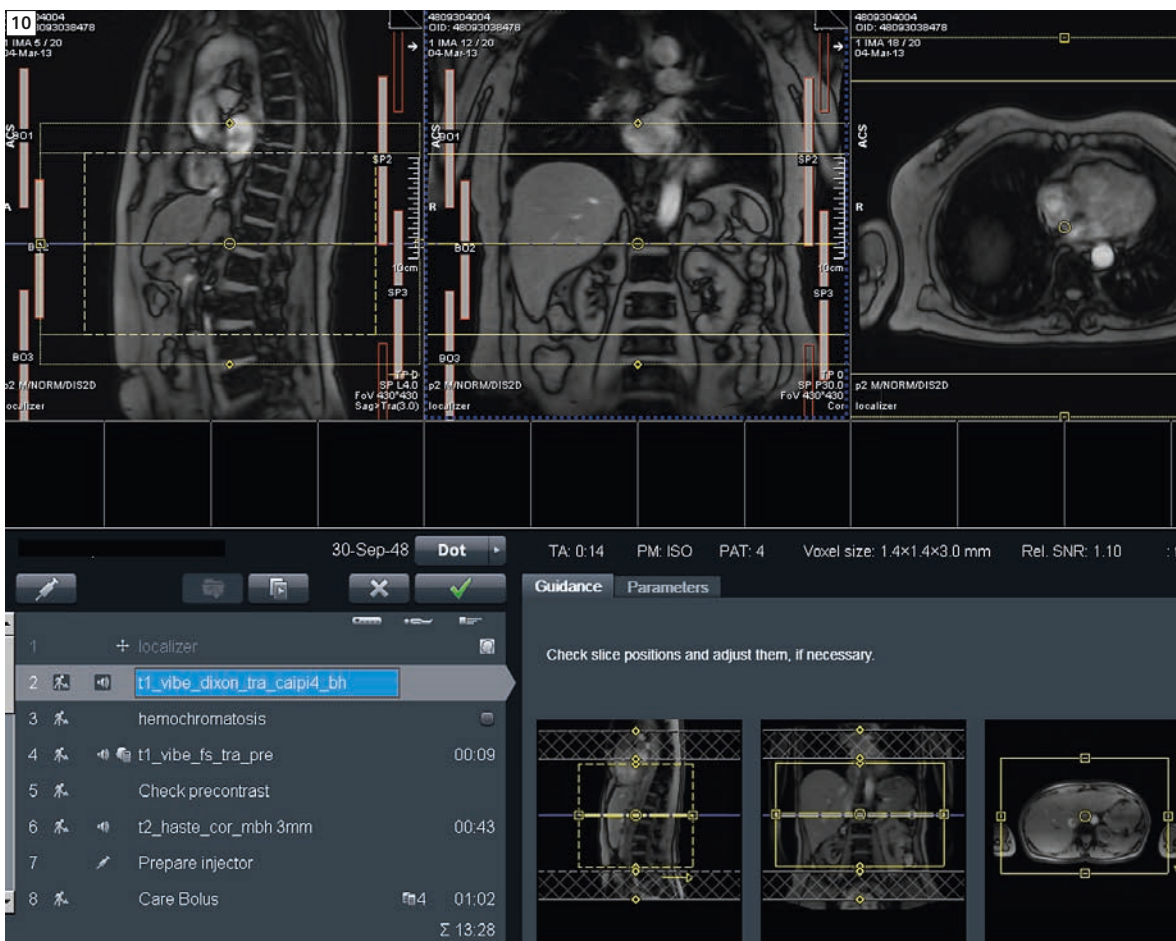
CAIPIRINHA (Controlled Aliasing in Parallel Imaging Results in Higher Acceleration) is a new parallel imaging technique from Siemens.

The new RF system and high channel coils (Body 18) provide the signal that is needed, whilst the parallel imaging with fourfold acceleration with CAIPIRINHA

offers the speed required to maintain short breath-holds even at large coverage in the z-direction and thin slices. The short breath-holds are a real game changer especially in the case of elderly patients, but even young and fit patients benefit. No trade-off between thick slice / large coverage or thin slice / partial coverage is necessary: we always scan full coverage with thin slices. Examination of the abdo-



**9** CAIPIRINHA PAT4 in 10 sec compared to PAT2 in 21 sec with same slice thickness and in-plane resolution.



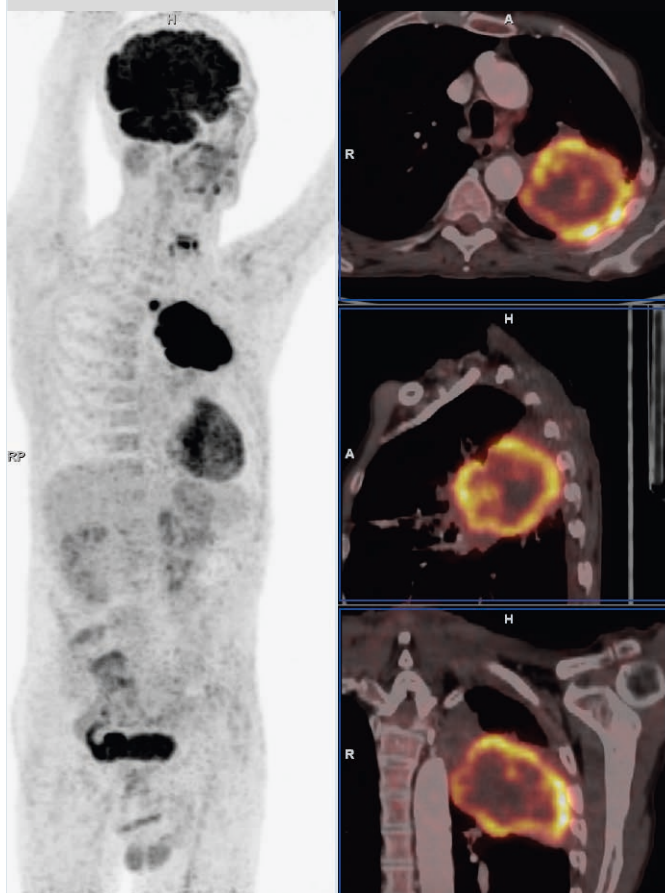
**10** With CAIPIRINHA no trade-off between thick slice / large coverage or thin slice / partial coverage is necessary: we always scan full coverage with thin slices. The coverage is well seen in this screenshot (yellow dotted box top left, or yellow bold box top middle).

men and thorax benefits greatly from the Aera system. It all fits perfectly together. Here are some examples.

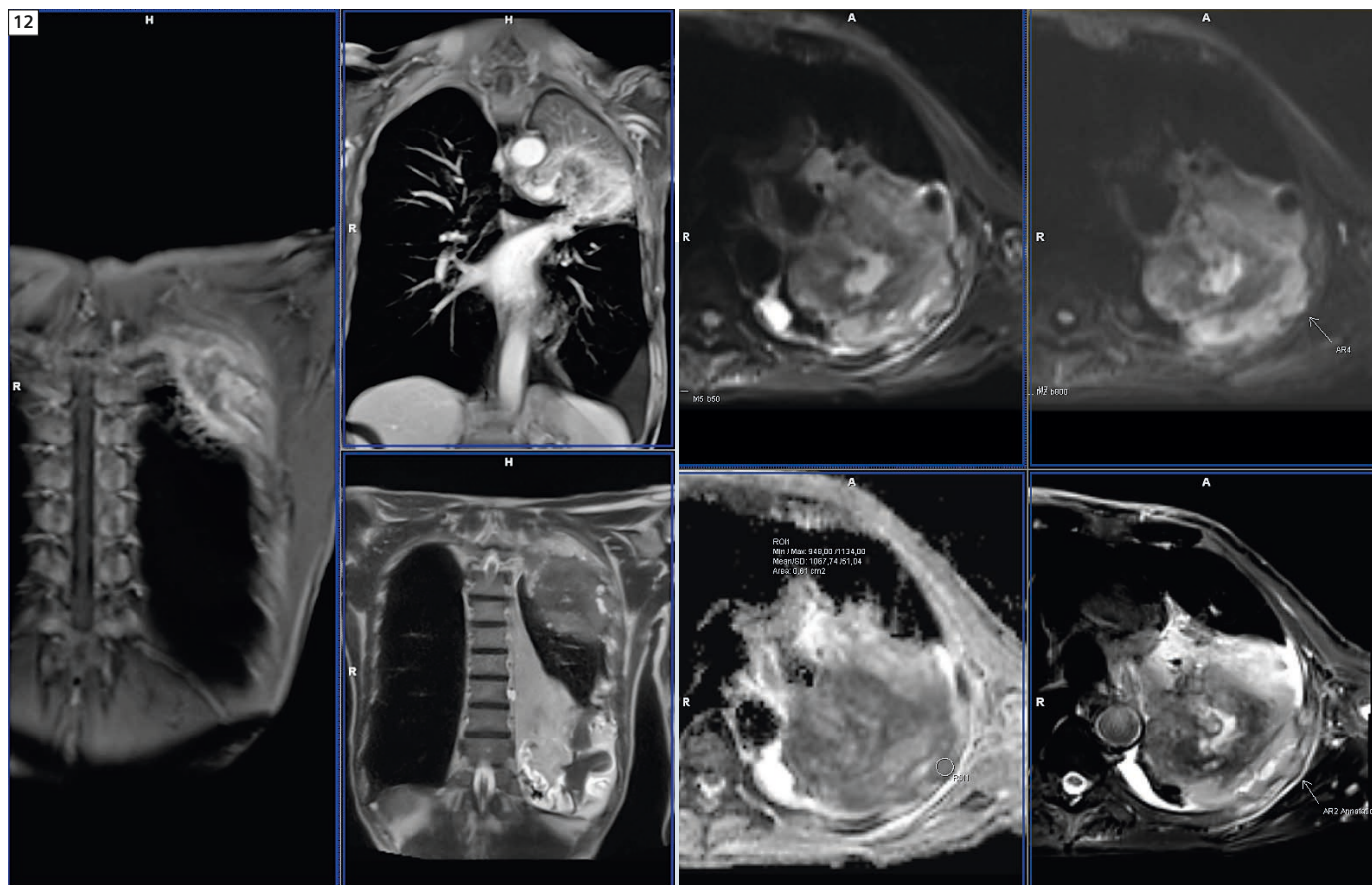
More signal in less scanning time!

Figure 9 demonstrates how, in a liver examination in the same patient examined with CAIPi4, the images with a breath-hold of 10 sec have more signal than the same images (same slice thickness and in-plane resolution) with iPAT2 and 21 sec breath-hold.

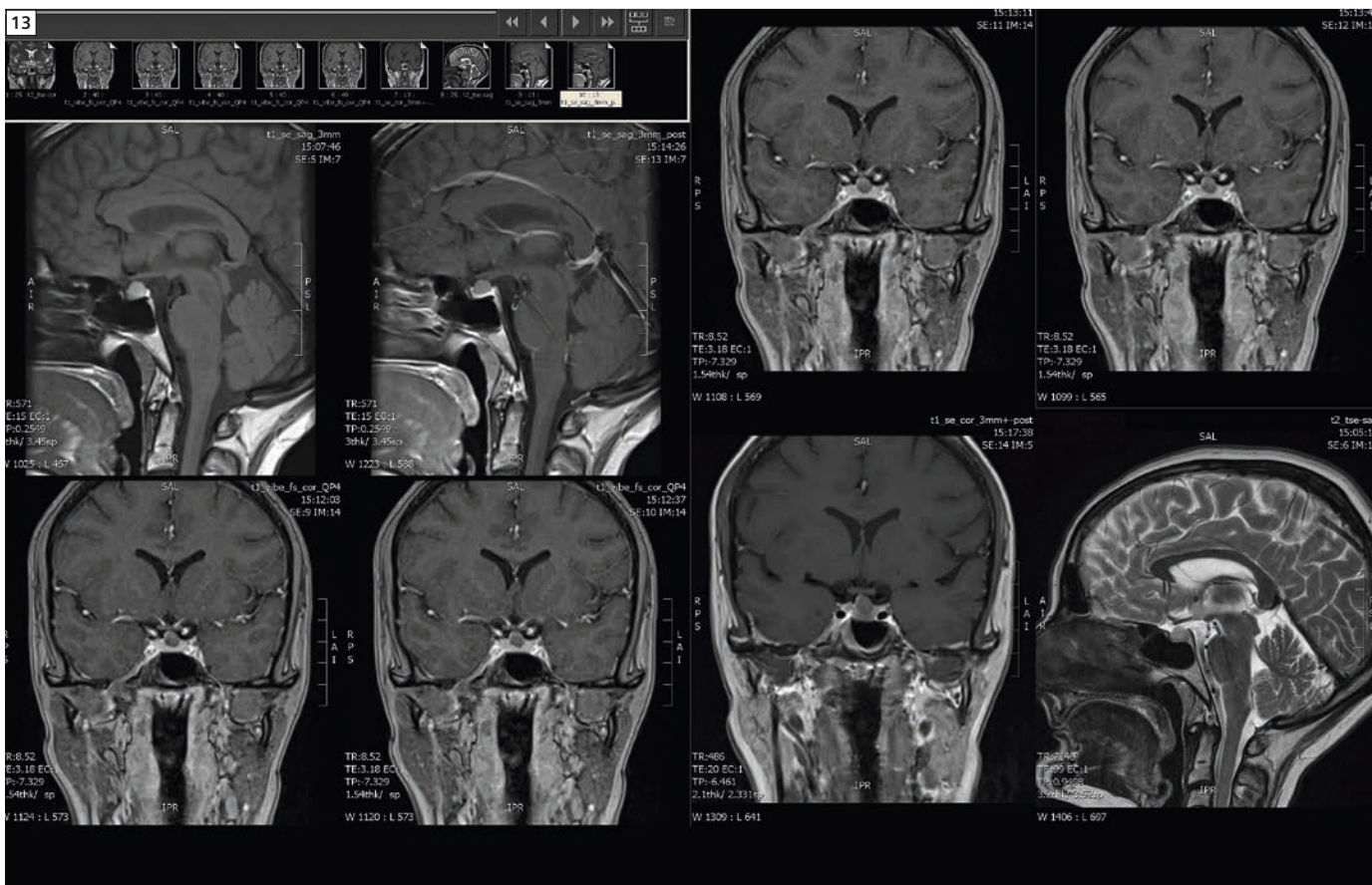
MRI examination of the thorax – although more rare – follows the same rules as the abdomen: sequences should be fast enough for the patient to cooperate. Figure 11 gives an example of a metastatic lung carcinoma where PET-CT was not able to exclude or confirm chest wall invasion. MRI was ordered and it turned out to be quite an easy job on MRI, having the short breath-hold CAIPiR-INHA PAT 4 VIBE sequences. Even this patient, who clearly is in a bad condition,



**11** A case of a metastatic lung carcinoma where PET-CT was not able to exclude or confirm chest wall invasion.



**12** CAIPiRINHA PAT4 VIBE post-contrast coronal showing the tumor (arrow) and lateral and dorsal chest wall invasion (small arrows). Axial T2w BLADE and free breathing DWI show the chest wall invasion with actual rib invasion.



**13** Coronal dynamic sella imaging with CAIPI PAT4 VIBE in 34 seconds.

14 AAShoulder_Scout		
2	t1_tse_fs-dixon_ax	01:48
3	t2_tse_cor-blade-fs	01:08
4	t2_dess-3D-tra	02:41
5	t1_tse_fs-dixon_sag	01:54
6	t1_vibe_dixon_caipi4	01:41
7	MPR planning ...	
8	t2_tse_tra-blade-fs	00:58
		Σ 11:08

**14** Screenshot showing 1.41 min CAIPI VIBE Dixon for 3D shoulder imaging. High SNR due to the 16-channel MSK coils allows us to use these fast sequences.

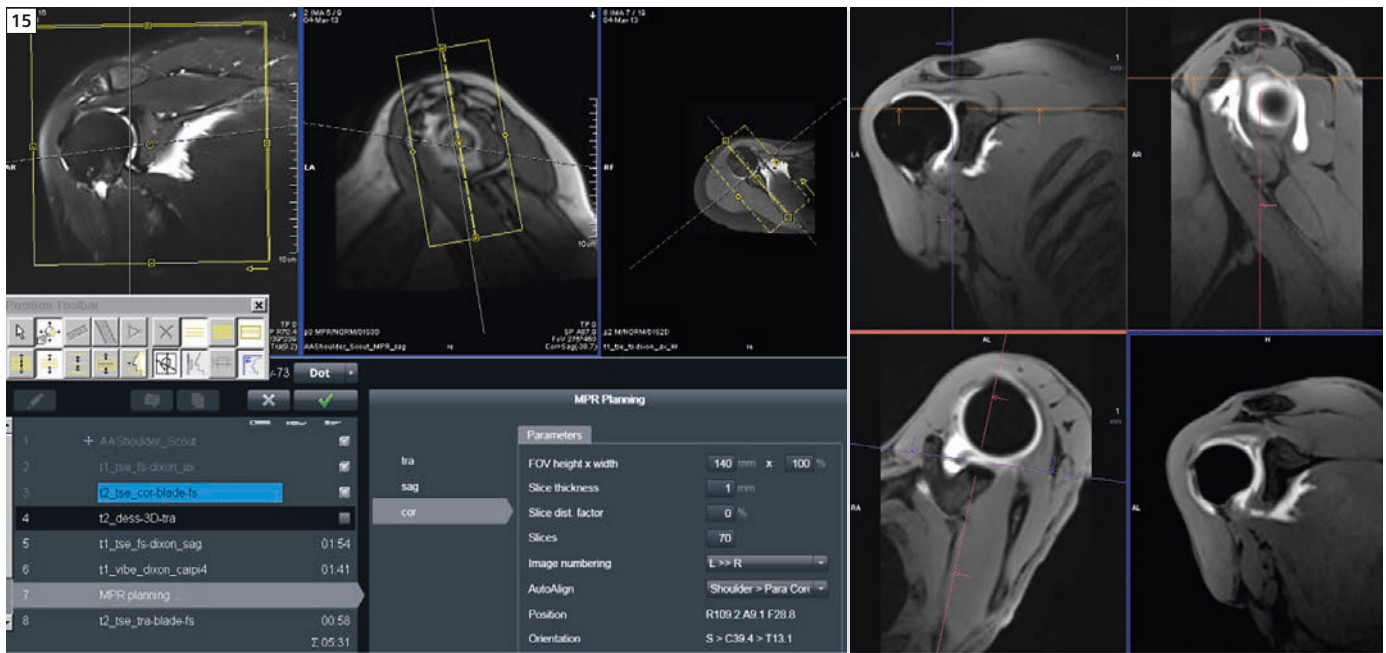
cooperated and tolerated the exam well. Invasion in the lateral and dorsal chest wall is readily depicted in both axial and coronal enhanced images. Axial T2w BLADE and free breathing diffusion-weighted imaging (DWI) confirm the chest wall invasion with actual rib invasion and the malignant nature is clearly translated in low ADC values of the lesion (Fig. 12). Maybe we don't have the fancy colors, like PET does, but

we do have the diagnosis! CAIPIRINHA can be used in other regions, too. Figure 13 shows images of a female patient who underwent a brain scan in search of a (post-traumatic?) cause of the headaches. A small mass in the sella was incidentally found. Coronal dynamic VIBE imaging provides a means to assess the perfusion of the sella and pick up smaller lesions e.g. adenomas as demonstrated in this examination. The VIBE sequence is

pimped using CAIPIRINHA with 4-fold acceleration, providing 40 high res 1.5 mm slice thickness images every 34 seconds, and dramatically improving detection rate. The acquisition speed makes it possible to complete this examination within the same 20-minute time slot. At our center, shoulder examination is mostly done after arthrogram. This can cause some discomfort and the fast scanning of patients is the best option to avoid movement artifacts. *syngo* BLADE helps reduce motion artifacts. However CAIPIRINHA is a huge benefit here. We acquire a 3D VIBE Dixon fatsat with CAIPI PAT4 in 1:41 min. The screenshot in Figure 14 shows the details of our shoulder protocol.

## Section 5: the Large Joint Dot Engine for shoulder imaging

The AutoAlign tool in the Dot Engine helps technologists to plan more quickly and accurately, with reduced operator-depen



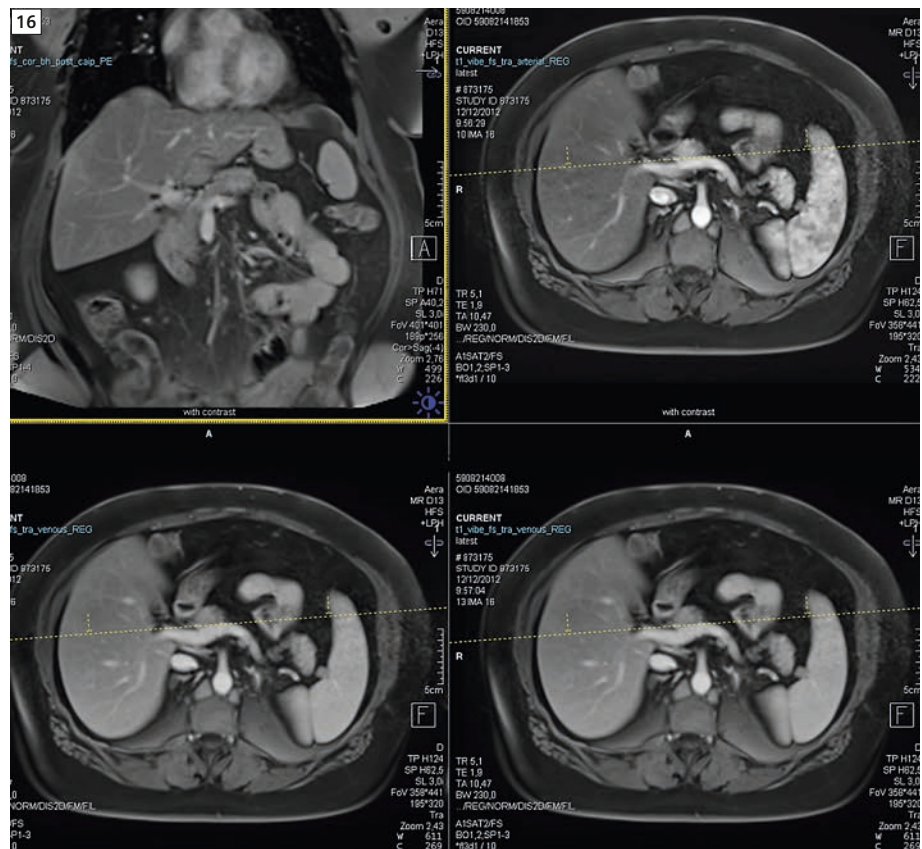
15 Shoulder Dot screenshot showing Inline MPR planning and VIBE CIAP1 reformats.

dent variation. Figure 15 shows the sequences used and a total exam time of 11:08 minutes.

Two 3D blocks are scanned: 3D VIBE Dixon fatsat with CAIPI PAT4 (1:41 min) and 3D DESS fatsat (2:41 min) are acquired. These are reconstructed in axial, paracoronar and parasagittal planes inline, rather than in post-processing, thanks to the Inline MPR function of Dot. While still planning the sequences, the technologist already plans the multi-planar reconstruction so that the MPRs are available for reporting without delay as depicted. This produces an incremental benefit in workflow.

## Section 6: liver imaging with Abdomen Dot Engine

Dot has many smart tools that help improve efficiency, consistency, reproducibility and throughput. AutoAlign is one tool I mentioned above in Brain Dot. The Abdomen Dot Engine actually provides several operator-independent tools: with AutoAlign for liver, and AutoCoverage, you always have the complete anatomy covered, ensuring good quality images with fewer incidences requiring repeat scans. This is a significant benefit of Dot and it holds true when we image obese patients, too.



16 Excellent image quality, fat suppression and coverage in an obese patient in 10.7 sec (breath-hold).

MAGNETOM Aera's 70 cm open bore enables some larger patients to fit for the first time in their lives inside an MRI machine. But even if we did manage to fit such a patient inside the previous MRI scanner, we still ran into the problems of too much noise and of breath-holds that were too long to cover all the phase encoding steps needed in an obese patient. The increased signal available on the Aera tackles the noise problem and the CAIPIRINHA technique gives you a fourfold parallel imaging factor (without additional noise) resulting in acceptable breath-hold times (10.7 sec) even in large patients. Again, it all fits perfectly together!

Abdomen Dot enables easier, faster and more consequent – less operator-dependent – sequence planning and execution with AutoCommand tools where breath-hold commands are given by the system in a language the patient understands. The Abdomen Dot features ABLE (add-in for Automatic Breath-hold Liver Exams) where the system actually triggers on bolus arrival to ensure a pure arterial phase even in cirrhotic liver patients where timing of the bolus could be a

challenge for less experienced technologists (Fig. 17).

Non-rigid liver registration of dynamic VIBE series is an automatic step done within the ABLE function to save all phases registered in the database, which enables faster and more accurate reading and reporting.

Different contrast scans (b50 – b800 DWI and ADC map & T2w BLADE) can be in similar anatomical positions as close as possible to the multi-phase dynamic scans due to smart AutoCoverage functionality in Abdomen Dot. The example of a cirrhotic liver in Figure 18 will clearly illustrate the efficiency in reading.

This holds true within the scope of a single examination but becomes even more important when comparing examinations at different time points (Fig. 19). Having imaged and sent the images to the PACS in registered series turns out to be of great benefit for reading and reporting in follow-up examinations. This registration process allows for synchronized scrolling up and down simultaneously in the registered series even in a bare bone viewing system used by, for example, the referring physician. Figure 19 shows how convenient it was to reevaluate the liver on MRI in a case

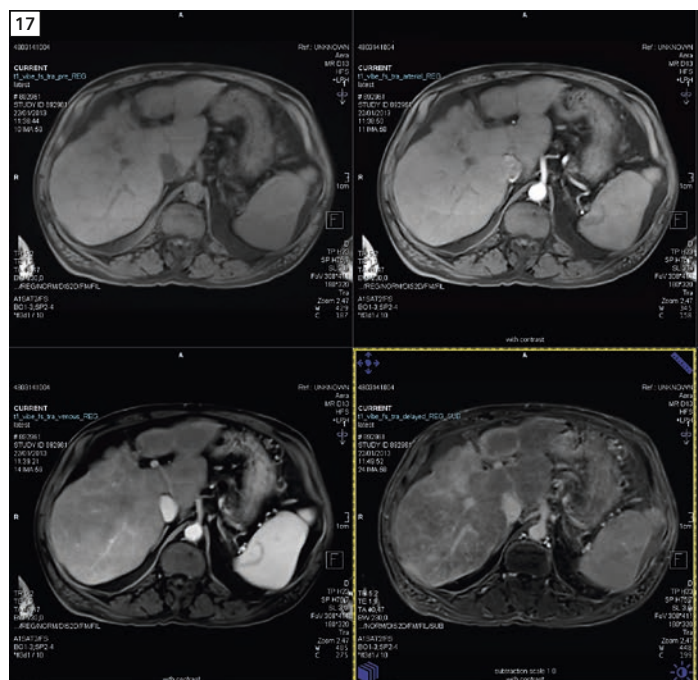
of invasive adenocarcinoma of the sigmoid colon. Comparing exams from 2011 and 2013 even on a bare bone viewing system: the Dot registration provides all the synchronization that is needed.

## Section 7: excellent images in the head/neck region

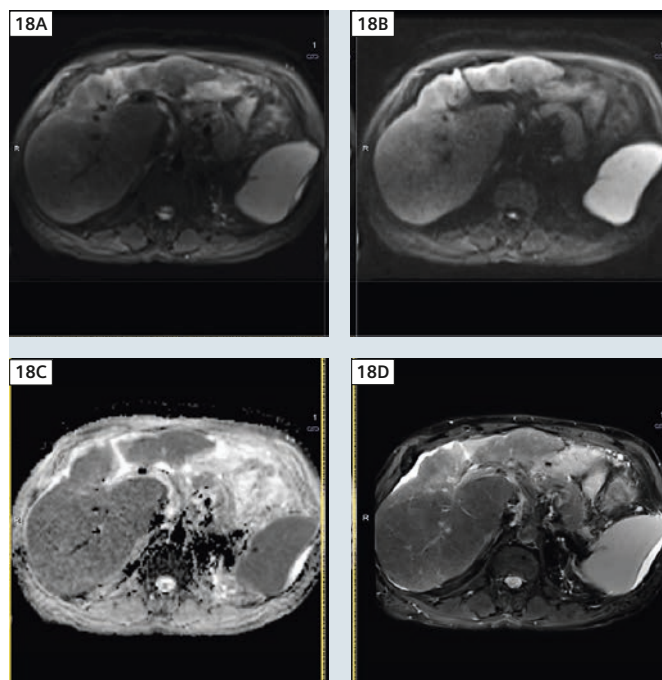
Whereas in the old days fatsat could be problematic in the cervicothoracic region, TSE Dixon really assists with impeccable fatsat images and having the T2w or T1w TSE images for free.

Figure 20 gives a nice example of metastatic melanoma after gadolinium enhancement: no artifacts in the base of the neck! DWI has also improved due to the gradient power enabling short TE thus minimizing artifacts.

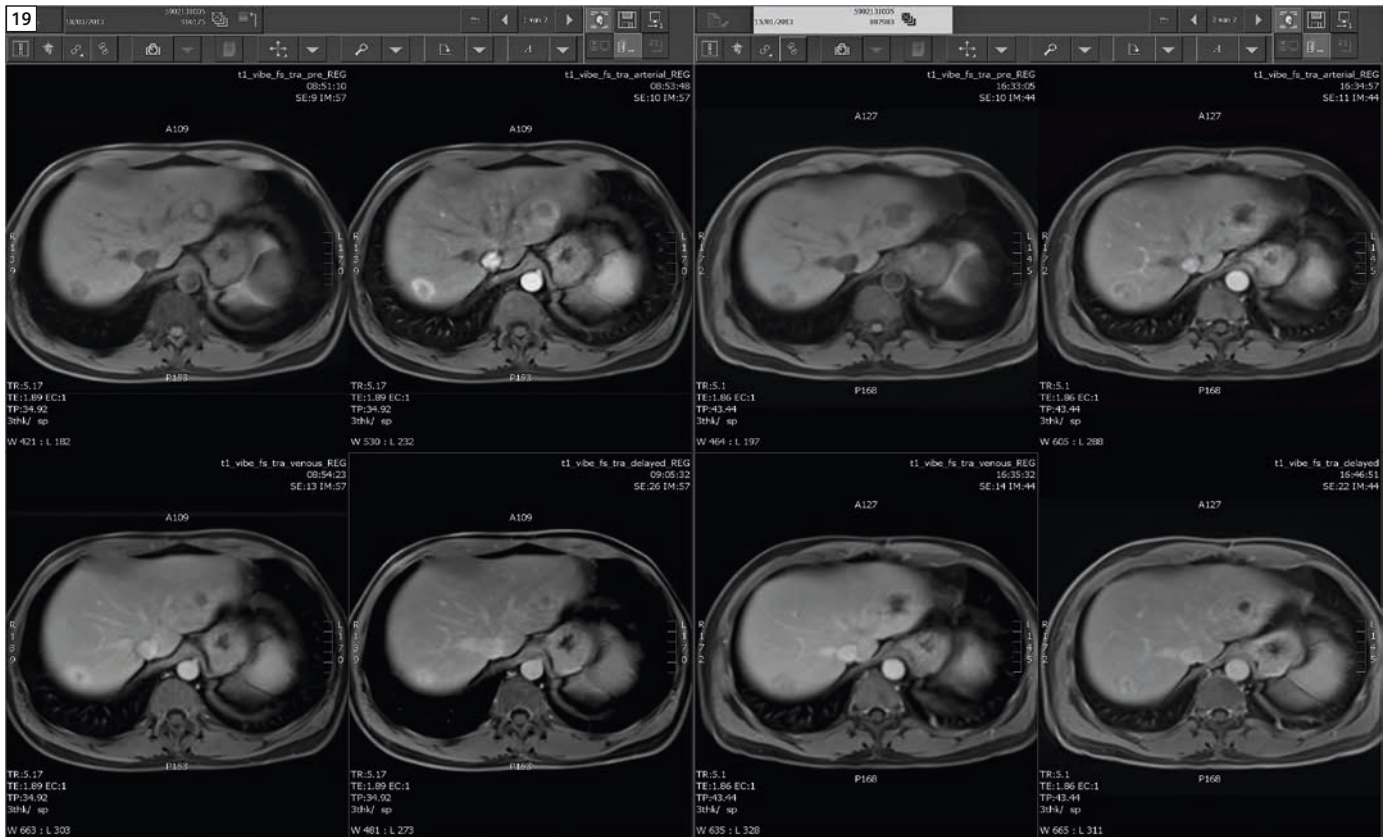
The next two examples of DWI in the neck highlight the importance of ADC maps. High signal on the high *b*-value DWI and low ADC value confirm the malignant nature of the metastatic melanoma. DWI can help in determining the nature of lesions, such as in the small benign mixed tumor (BMT) of the right parotid gland with high ADC value depicted in Figure 22.



**17** Abdomen Dot ABLE technique helps ensure accurate dynamic liver phases even in cirrhotic livers.



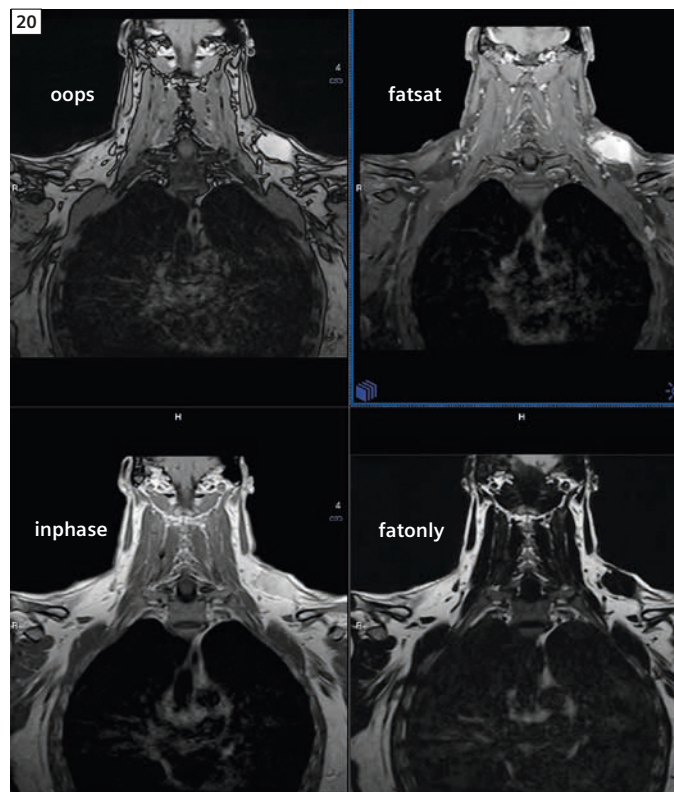
**18** (18A) VIBE, (18B) DWI, (18C) ADC map and (18D) T2w BLADE all at almost similar slice positions. This helps in faster and more accurate reading and reporting.



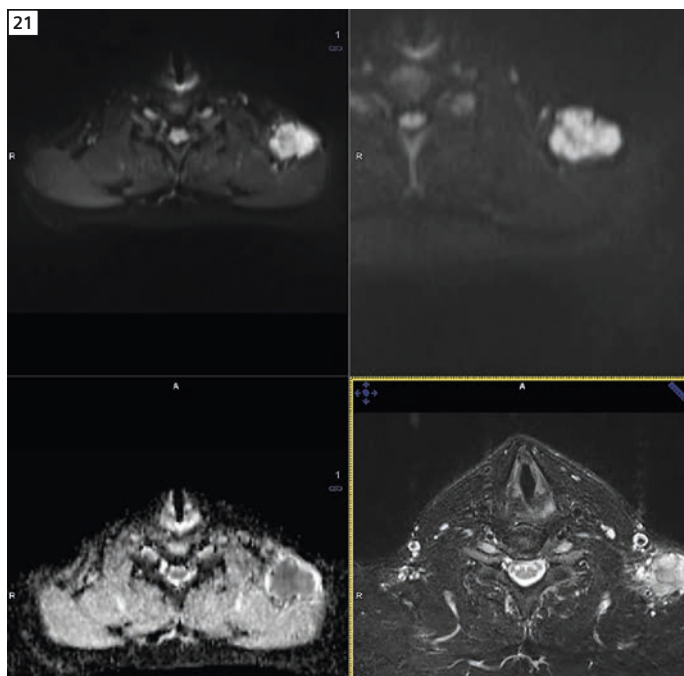
19 Shows the relevance of liver registration and synchronized viewing for efficiency.

## Section 8: leveraging *syngo.via*

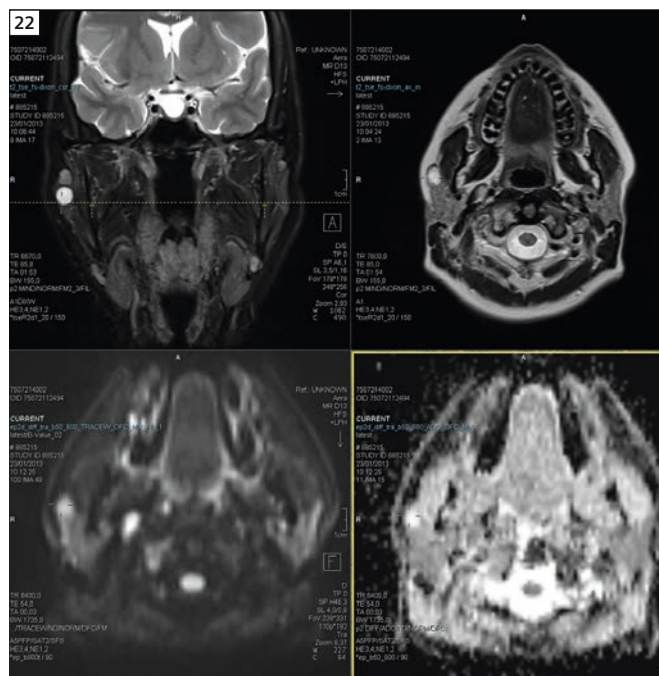
Presenting the roadmap to vascular surgeons has been made easier and better with *syngo.via*. The MIP and composing functionality helps us to integrate three 4D datasets for angiography of the aorta and lower limbs into one dataset and to present the roadmap to the vascular surgeons – something that we do in every case. Cardiac evaluation is done on *syngo.via* and, again, instead of having to leave my reporting system to go to the workstation, I simply push the *syngo.via* button and do my evaluations. Another area where I use *syngo.via* is for volume calculations. Volume calculating helps me out with every acoustic neuroma and for prostate (benign prostate hypertrophy). The inline registration in the Dot engines really helps with the multi timepoint follow up of 90% of cases: it gives me the series synchronized and sends them in that registered way to my non-intelligent, bare bone viewing station (the reporting



20 TSE Dixon showing In-phase, Out-of-phase, fat and water coronal in a case of meta-static melanoma post-contrast.)



**21** CAIPIRINHA, axial, DWI, ADC map and Fatsat T2w axial?? Showing low ADC (arrow) metastatic melanoma.



**22** Coronal T2w TSE, T2w axial showing hyperintense lesion. DWI and ADC map with high ADC (arrow) help confirm benign mixed tumor diagnosis.

system). This synchronization-registration assists in most of the brain and abdomen cases. *syngo.via* helps in reading difficult cases, where I like to compare, for example, not only the registered axial slices but also coronal slices, the free breathing DWI and other contrasts. When this is required, I simply push the *syngo.via* button on my viewing station and get my patient opened up in *syngo.via*. It makes reading and reporting not only faster but also more accurate.

## Conclusion

The new RF, high-channel coils, gain in SNR, faster techniques like CAIPIRINHA, new metal implant imaging possibilities, Dot features and *syngo.via* all are a perfect fit and the MAGNETOM Aera truly combines throughput and highest quality MR imaging in an optimized clinical workflow.

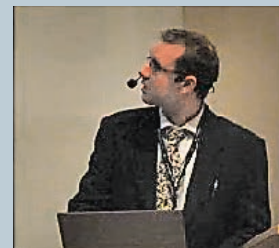
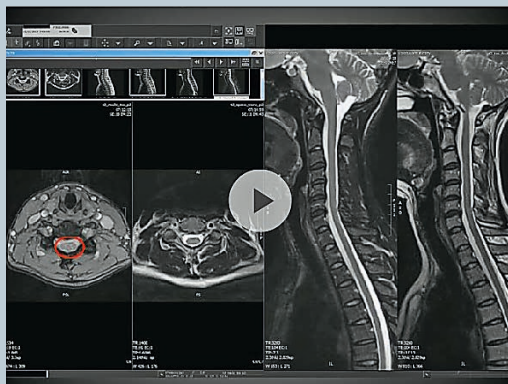
## Contact

Johan Dehem, M.D.  
VZW Jan Yperman  
Ieper  
Belgium  
johan.dehem@gmail.com

## Further information

Visit us at  
[www.siemens.com/magnetom-world](http://www.siemens.com/magnetom-world)  
to listen to Dr. Dehem's talk on **Highest Quality Imaging in an Optimized Clinical Workflow** given during the lunch symposium at the 15<sup>th</sup> International MRI Symposium MR 2013 in Garmisch-Partenkirchen, Germany.

Go to  
[www.siemens.com/magnetom-world](http://www.siemens.com/magnetom-world)  
> Clinical Corner > Clinical Talks

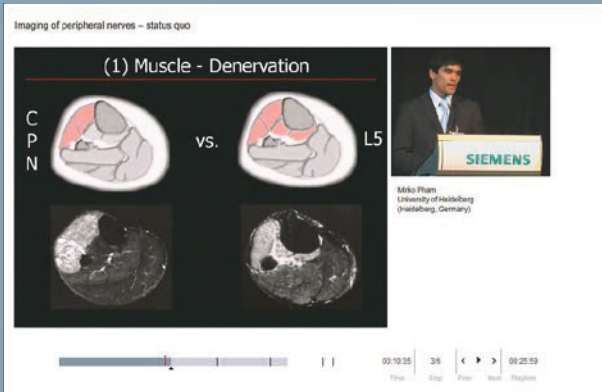


Johan Dehem, M.D.  
VZW Jan Yperman  
(Ieper, Belgium)

# Relevant clinical information at your fingertips

From technology to clinical applications, you will find all the latest news on Siemens MR at

[www.siemens.com/magnetom-world](http://www.siemens.com/magnetom-world)



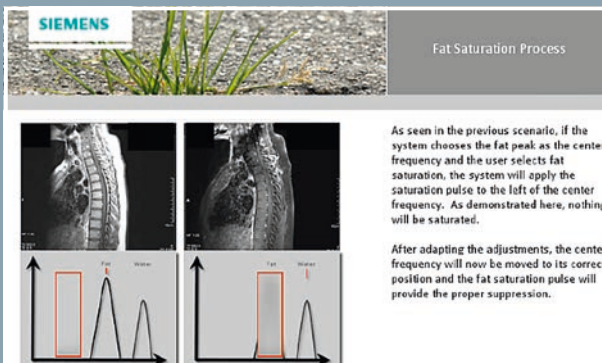
Don't miss the talks of international experts on Magnetic Resonance Imaging.

Go to  
Education > e-trainings & Presentations



The centerpiece of the MAGNETOM World Internet platform consists of our users' clinical results. Here you will find case reports and clinical methods.

Go to  
Clinical Corner > Case Studies



Just a mouse click away you will find application videos and useful tips allowing you to optimize your daily MR examinations.

Go to  
Clinical Corner > Application Tips

For the whole range of clinical MR information visit us at

[www.siemens.com/magnetom-world](http://www.siemens.com/magnetom-world)

# Initial Experience with Whole-Body Diffusion-Weighted Imaging in Oncological and Non-Oncological Patients

Marcos Vieira Godinho, M.D.<sup>1</sup>; Romulo Varella de Oliveira, M.D.<sup>1</sup>; Clarissa Canella, M.D., MSc<sup>1</sup>; Flavia Costa, M.D., MSc<sup>1</sup>; Thomas Doring, MSc<sup>1</sup>; Ralph Strecker, Ph.D.<sup>2</sup>; Romeu Cortes Domingues, M.D.<sup>1</sup>; Leonardo Kayat Bittencourt, M.D., MSc<sup>1</sup>

<sup>1</sup>*Clínica de Diagnóstico por Imagem, Rio de Janeiro, Brazil*

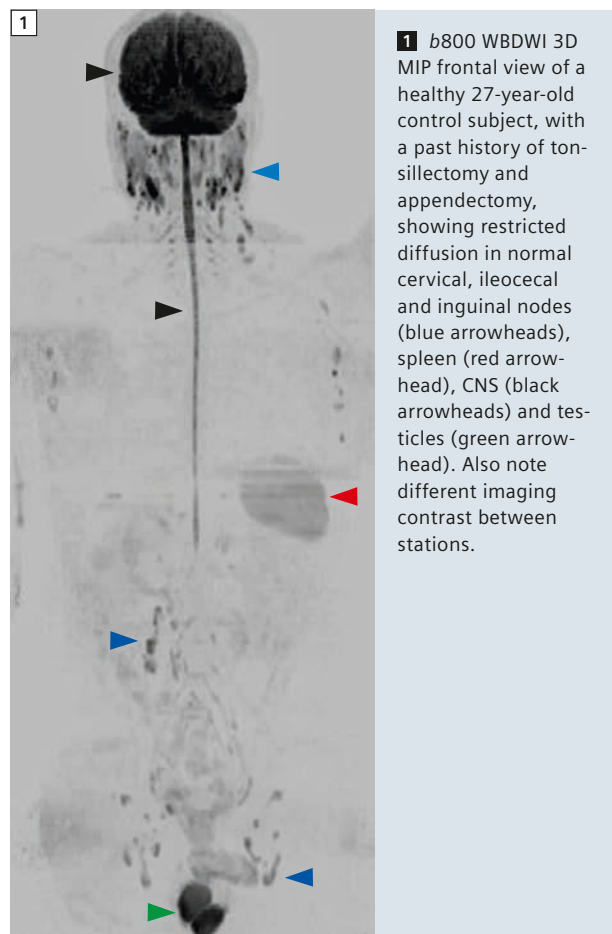
<sup>2</sup>*Siemens Healthcare, São Paulo, Brazil*

## Background

Initially used as a diagnostic tool for acute stroke, over recent years diffusion-weighted imaging (DWI) has developed a growing role in the diagnosis and follow-up of diseases not only in extra-cranial pathologies, but also as a study of the whole body in systemic diseases,

providing a steady increase of indications for the technique. With a growing elderly population worldwide and the highest incidence of oncologic illnesses, use of whole-body diffusion-weighted imaging (WBDWI) in this setting is evolving.

We initially used WBDWI for the already established indication in oncological patients with breast, prostate, gastrointestinal, hematological and other cancers, and then also decided to investigate its use in patients with auto-immune, inflammatory and infectious diseases.



The purpose of this article is to describe our examination technique, imaging protocols, interpretation of imaging findings and initial experience with oncological and non-oncological diseases, as well as the limitations of the study.

## Methods

Since September 2011 we have recruited patients with oncological disease undergoing diagnostic or follow-up exams in our clinic with findings in conventional MRI suggestive of metastases, as well as patients with auto-immune or inflammatory systemic diseases and those with imaging findings that could be differential diagnosis for metastatic disease. In some cases the purpose was the staging of the disease before initial treatment, in other cases we did the follow-up of patients during therapy.

WBDWI was performed on a 1.5T clinical scanner (MAGNETOM Aera, Siemens Healthcare, Erlangen, Germany) recently installed in our center using two 18-channel body phase array coils together with the combined 20-channel Head/Neck coil. Patients were examined in supine position and four stations of axial free-breathing DWI with short tau inversion recovery (STIR) fat suppression were obtained using the following parameters: echo time (TE) 79 ms, repetition time (TR) 19000 ms, inversion time (TI) 180 ms,  $b$ -values 0 and 800 s/mm<sup>2</sup>, read-out bandwidth 1502 Hz/pixel, 5 averages, field-of-view (FOV) 400 mm, slice thickness (SL) 5 mm, matrix size 128 × 128, voxel size 3.1 × 3.1 × 5.0 mm<sup>3</sup>, acquisition time per station 7.17 min. The protocol also included four stations of axial T1-weighted (T1w) VIBE in- and opposed-phase images (TR 7.01 ms /TE1 2.38 ms /TE2 4.76 ms, FOV 450 mm, SL 5 mm, matrix 512 × 512, voxel size 0.9 × 0.9 × 5 mm<sup>3</sup>) and axial T2-weighted (T2w) HASTE images with fat suppression STIR (TR 600 ms /TE 81 ms, FOV 420 mm, SL 5 mm, matrix size 256 × 256, voxel size 1.6 × 1.6 × 5 mm<sup>3</sup>). Head, neck, chest, abdomen, pelvis and proximal thighs were studied. The four stations were composed inline, after the last station was acquired. No contrast media was administered and total duration of

each exam was about 60 minutes.

So far, we have performed 4 exams with healthy controls, 9 exams with actual oncological patients (1 breast cancer, 1 small cell cancer with unknown primary site, 3 prostate cancers, 2 gastrointestinal neuroendocrine cancers, 1 plasmacytoma, 1 lymphoma) and 4 exams with non-oncological cases (1 prostatitis, 1 dermatopolymyositis, 1 spondyloarthritis, 1 chronic recurrent multifocal osteomyelitis).

## Imaging findings

Our objective was to look for findings based on the principle that some neoplasms and their metastases have restricted diffusion because of their hypercellular nature. Inflammatory/infectious illnesses may also have foci of restricted diffusion along the body because some of them may produce abscesses. We always tried to detect lesions and to characterize their distribution. In other patients we also analyzed  $b_0$  images looking for the T2 shine-through effect, as explained further below.

For interpretation of WBDWI we used 'raw' data with inverted gray scale in  $b_0$  and  $b_{800}$  images, so lesions with restricted diffusion appeared as black foci in a white background (Figs. 4B and 6). In some cases, we also obtained the calculated  $b_{1400}$  images, improving the specificity of the findings, as in this case only lesions with real restricted diffusion were seen. Apparent Diffusion Coefficient (ADC) Maps were obtained for all patients and ADC values were measured. We also did three-dimensional maximum intensity projection (3D MIP) reconstructions using the Siemens composer tool in all cases and used T1w and STIR images for anatomical reference and fusion with WBDWI.

## Control subjects

Before initiating the study with patients, we studied healthy subjects to test and adjust the protocols, to understand normal findings in the exams, considering the presence of imaging artifacts, problems with misregistration and intrinsic limitations of the study.

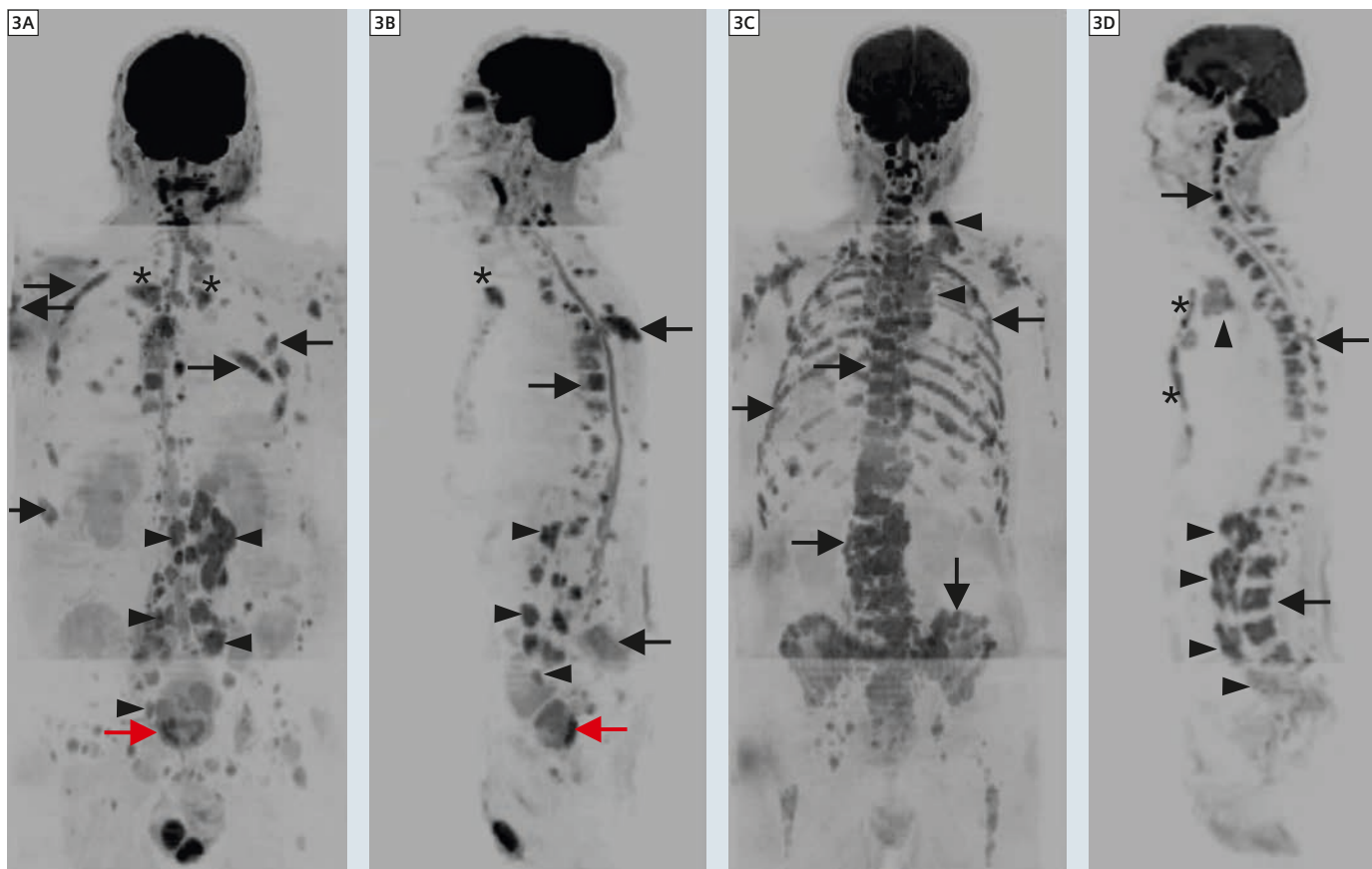
Normal brain tissue, spine, spleen and testicles had restricted diffusion, notably the latter. Even in control cases, small lymph nodes free of disease appeared with restricted diffusion, mainly in the neck, a finding which we consider as a limitation of the study (Fig. 1).

In some patients a mismatch between the head/neck and the thorax station, was observed. A problem most prominently visible in the 'broken spine' in sagittal MPR images and described by other authors before [1]. We also observed in some cases spatial variations in image intensity between the different stations which impaired the image interpretation of MPR images. It is worth to mention here that both the broken spine artifact and inhomogeneous signal can be corrected by using the new Diffusion Mode for Composing in software version syngo MR D13A.

We did not study the whole arms, because an increase in the size of the FOV would have been necessary, which could have reduced the resolution of the images.

## Oncological patients

One of the most prominent features of the WBDWI were the study of metastatic bone disease, which was well depicted in most of the oncologic patients studied, with examples of all types of distribution (Figs. 2, 3 and 5–9), some confirmed by biopsy. In one patient with breast cancer the findings of bone scintigraphy were similar to that of WBDWI. In one of the patients (small cell cancer with unknown origin) when we compared the results of PET-CT scan with WBDWI, the last one showed a greater number of bone metastases (Figs. 7–9). The performance of WBDWI was even better in the case of diffuse bone marrow involvement when we analyzed it side by side with T1w in- and opposed-phase images and with fusion of both, to help in the differentiation of the lymphomatous infiltrate from hyperplastic red bone marrow (which could also present as black foci in the inverted gray scale of WBDWI), as there was no signal reduction in T1w opposed-phase compared with T1w in-phase images (Fig. 8). The reduced ADC values obtained in the lymphoma-



**3** Two different patients with prostate cancer. Frontal (**3A**) and lateral views (**3B**) of *b800* WBDWI 3D MIP of a 79-year-old male, recent diagnosis of prostate cancer during investigation of bone lesions: multiple bone metastases (black arrows), including lesions in the clavicles (asterisks) and enlarged pelvic and retroperitoneal lymph nodes (arrowheads). Also note markedly restricted diffusion in the prostate (red arrows). Frontal (**3C**) and lateral views (**3D**) of *b800* WBDWI 3D MIP of an 84-year-old male, diagnosis of recurrent metastatic prostate cancer after prostatectomy: there are diffuse bone lesions (arrows) including metastases in the sternum (asterisk) and multiple enlarged pelvic and retroperitoneal lymph nodes as well as mediastinal and supraclavicular nodes (arrowheads), these last ones less common, characterizing advanced disease.

tous lesions also helped us to distinguish both.

Other kinds of metastatic spread could be shown, and enlarged lymph nodes were noted in patients with lymphoma, small cell and prostate cancers, the first one with disseminated nodal disease (Figs. 7 and 9), the second one with mediastinal nodal disease (Fig. 5) and the last ones with retroperitoneal spread (Fig. 3), corroborating the natural history of the diseases. One patient with relapsing prostate cancer had also enlarged mediastinal, axillary and supraclavicular lymph nodes, an uncommon finding most seen in advanced disease (Figs. 3C and 3D). However, the depiction of enlarged lymph nodes was not homogeneous along the body, because the performance of WBDWI to show

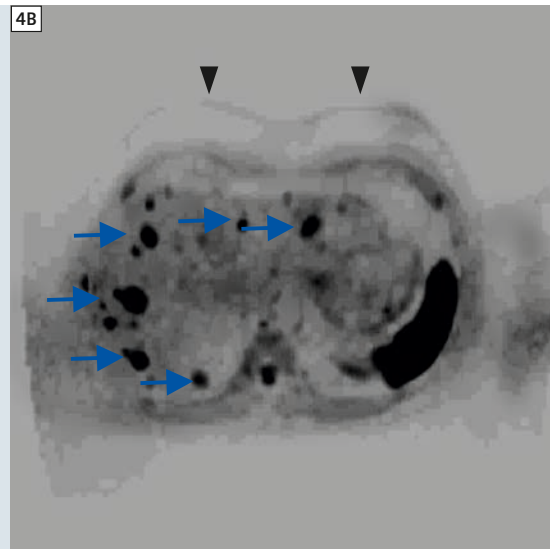
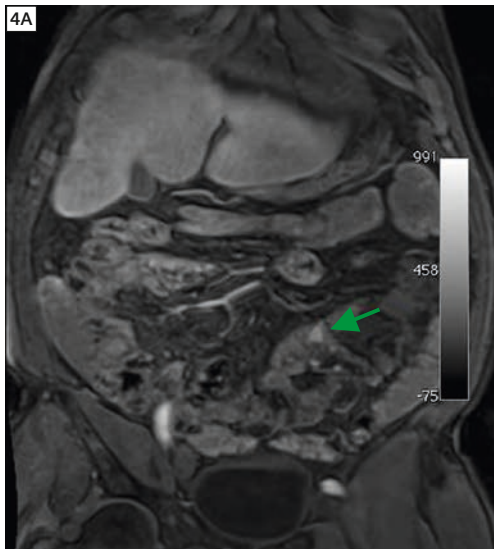
metastatic lymph nodes in the mediastinum were worse in comparison with cervical, axillary, retroperitoneal and pelvic nodal spread, probably because of respiratory and cardiac motion artifacts and pulsation artifacts from thoracic arteries. In the patient with small cell cancer PET-CT showed more mediastinal disease than the WBDWI.

In one specific case, the patient came to our institution with shoulder pain and was submitted to MRI of the shoulder, showing lesions suspected for bone metastases. The study was complemented with WBDWI that showed much more bone lesions as well as retroperitoneal and pelvic nodal disease. The pattern and combination of bone and nodal disease, together with a mass with restricted diffusion infiltrating the pros-

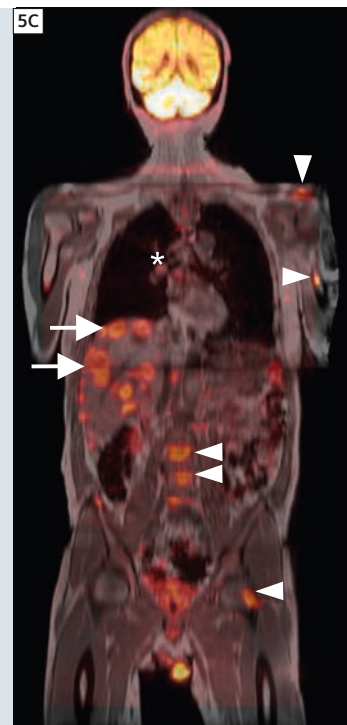
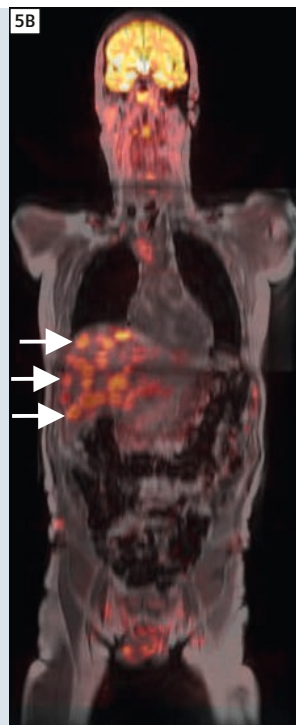
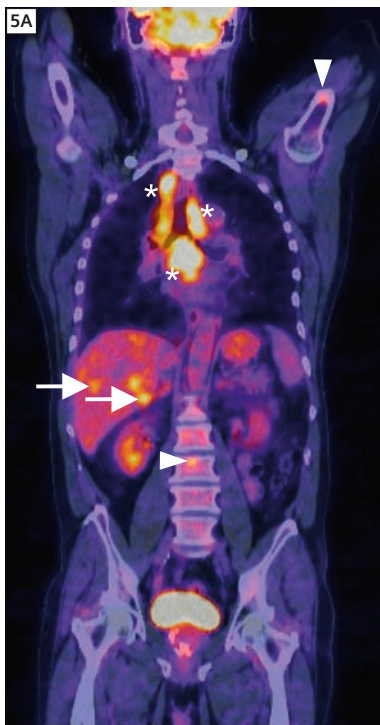
tate suggested the diagnosis of metastatic prostate cancer, confirmed by biopsy (Figs. 3A and 3B).

The detection of visceral metastases, mainly liver metastatic lesions, could be well done in 3 patients (1 small cell cancer and 2 neuroendocrine gastrointestinal tumors had multiple liver metastases), also showing us the natural history of the diseases. In the patient with small cell cancer most of the liver lesions had central necrosis without restriction of diffusion and a peripheral region of restricted diffusion (Fig. 5). No lesion was found in the central nervous system in any of the patients in WBDWI neither in other imaging sequences.

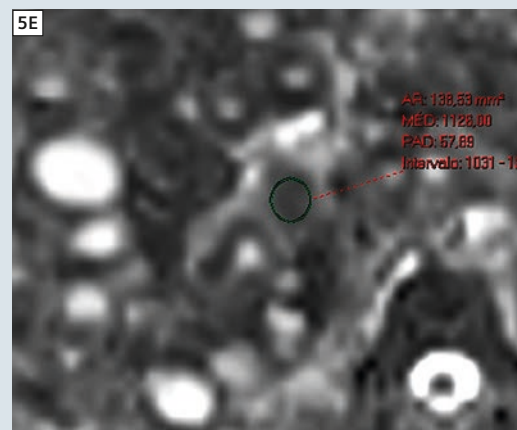
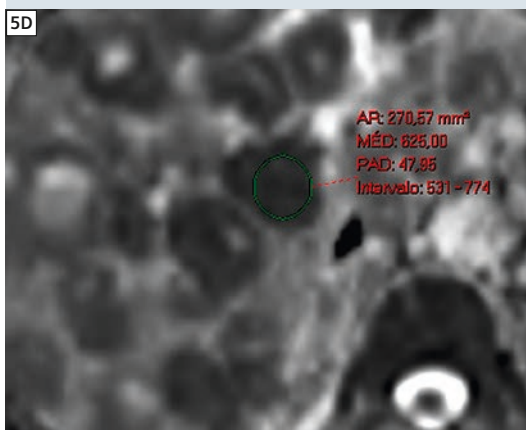
The patient with plasmacytoma was accompanied during the treatment (one DWI before and one after the beginning

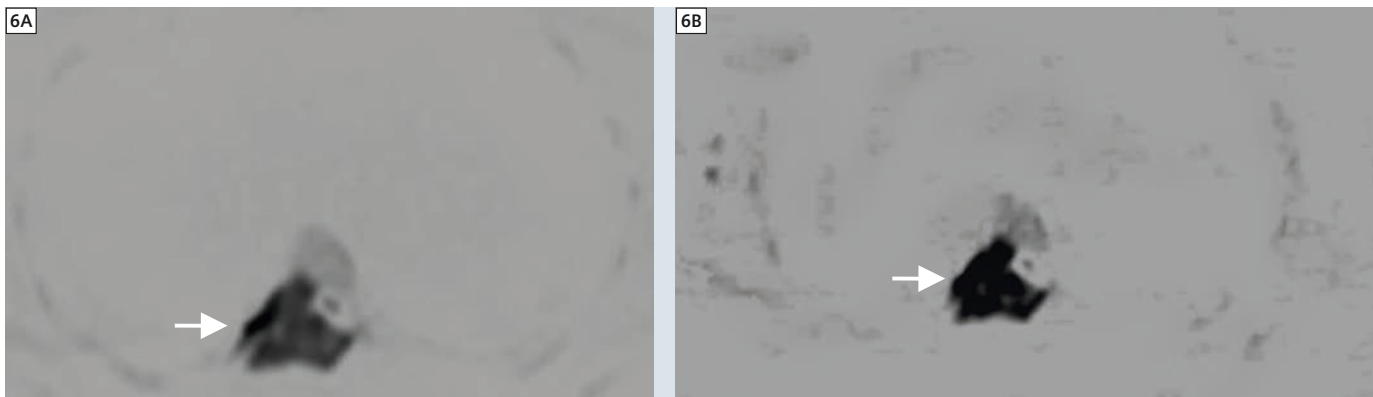


**4** 70-year-old male, carcinoid tumor of small bowel. Magnetic resonance enterography (4A): small bowel lesion with contrast enhancement (green arrow). Axial b800 image (4B): multiple liver metastases (blue arrows). The primary site was not well depicted in this case.

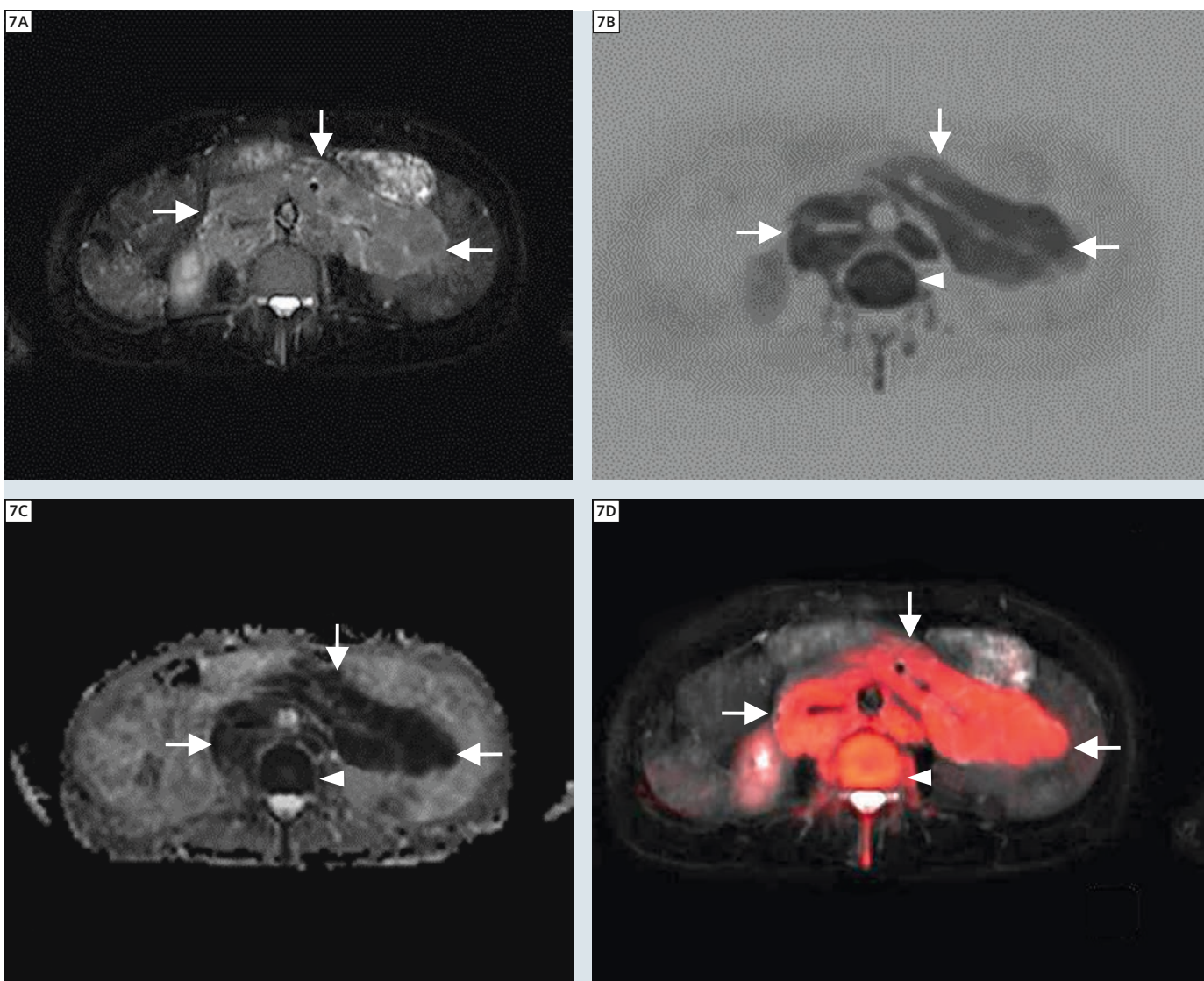


**5** 67-year-old male, investigating weight loss in the last six months. Biopsy of mediastinal enlarged lymph node has shown small cell cancer. No primary site was discovered. Reconstruction of PET-CT in coronal plane (5A) showing fluorodeoxyglucose uptake in liver (arrows) and bone lesions (arrowheads) and in enlarged mediastinal lymph nodes (asterisks). Fused T1w in-phase and b800 DWI coronal images (5B and 5C): liver lesions with markedly restricted diffusion some with central necrosis (arrows), bone metastases (arrowheads) and mediastinal enlarged lymph nodes (asterisks). Bone lesions were better depicted in WBDWI, but comparison was compromised because WBDWI was done two months after PET-CT. Comparison between ADC values of one liver lesion in the first (5D) and second DWI (5E) two months after treatment: increasing ADC value of the lesion in follow-up image. Also note there are more areas of cystic/necrotic degeneration along the liver after initial treatment.

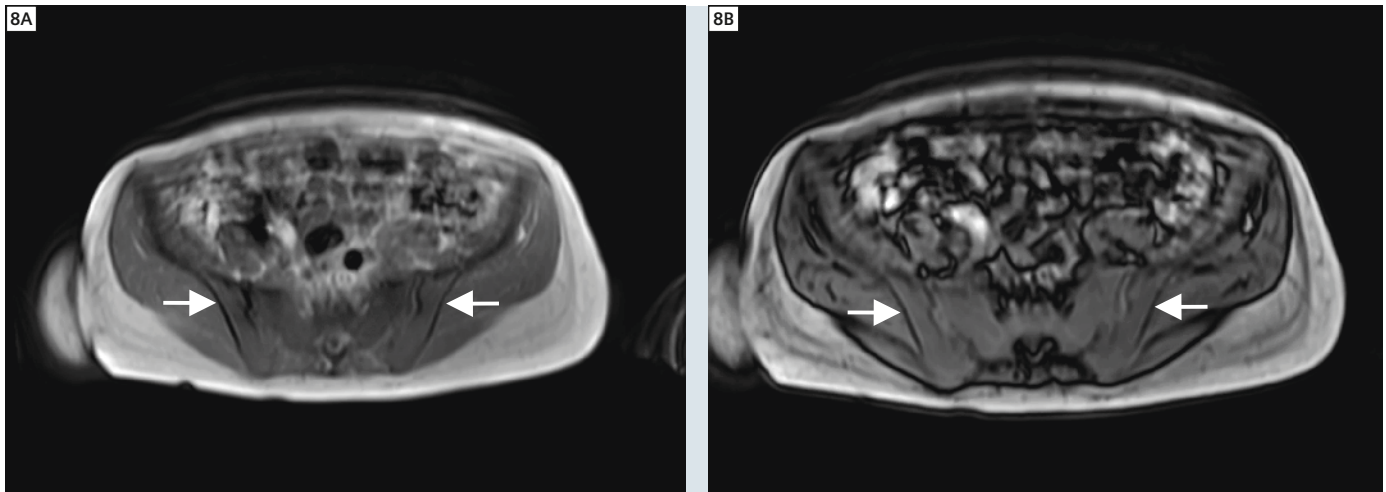




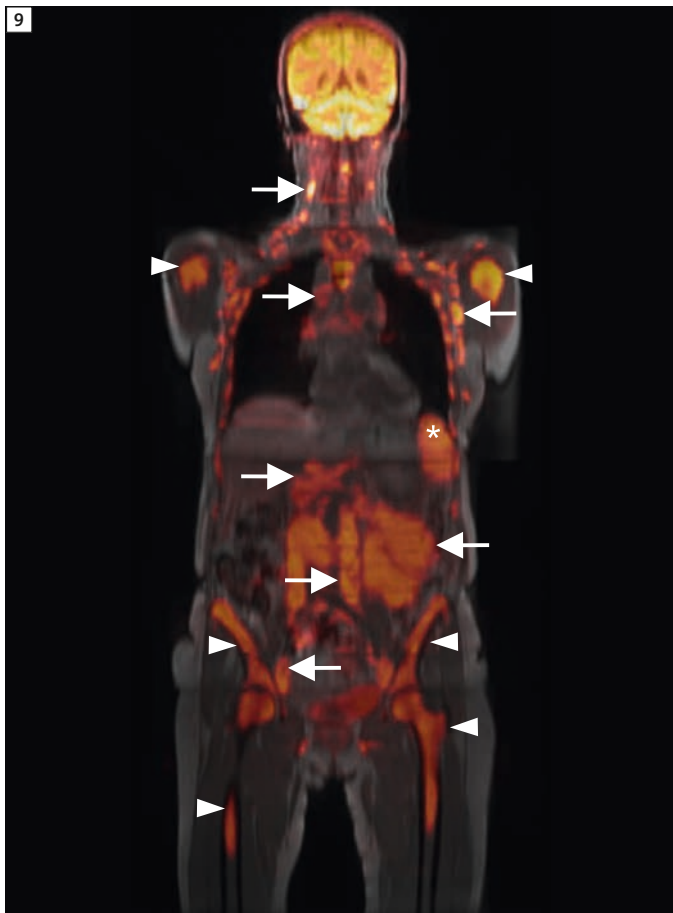
**6** 46-year-old female, dorsal thoracic pain. Axial  $b800$  image (**6A**) and calculated  $b1400$  image (**6B**) showing expansive lesion with markedly restricted diffusion in dorsal vertebral body (arrows). Biopsy revealed plasmacytoma.



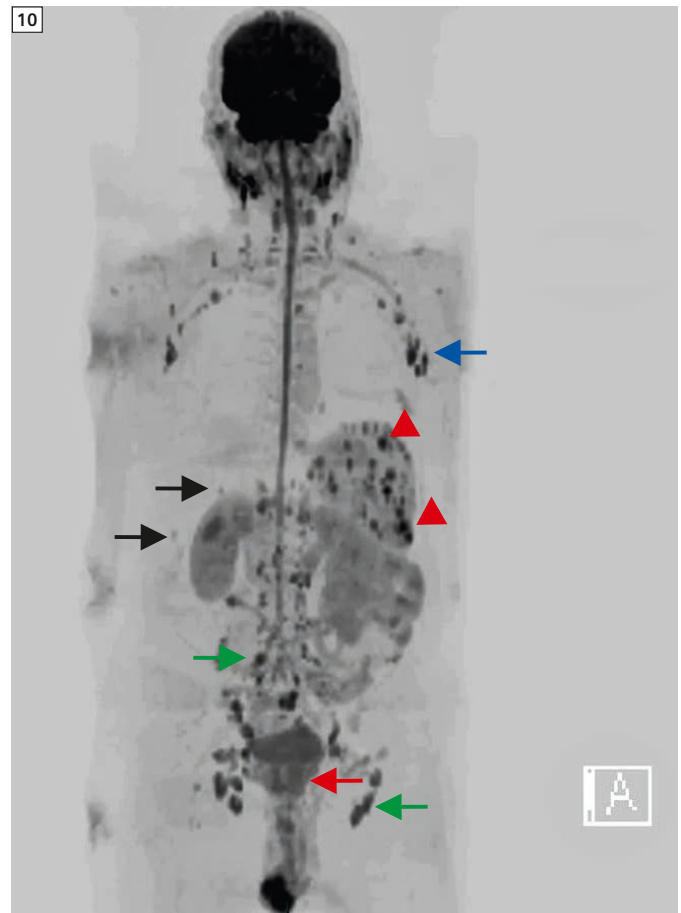
**7** WBDWI of a 66-year-old female with recurrent lymphoma, presenting with diffuse enlarged lymph nodes and bone marrow infiltration. STIR (**7A**),  $b800$  DWI (**7B**), ADC map (**7C**) and fused STIR and  $b800$  DWI (**7D**), showing conglomerate of retroperitoneal and mesenteric lymph node masses (arrows) and restricted diffusion in the bone marrow of a lumbar vertebra (arrowhead).



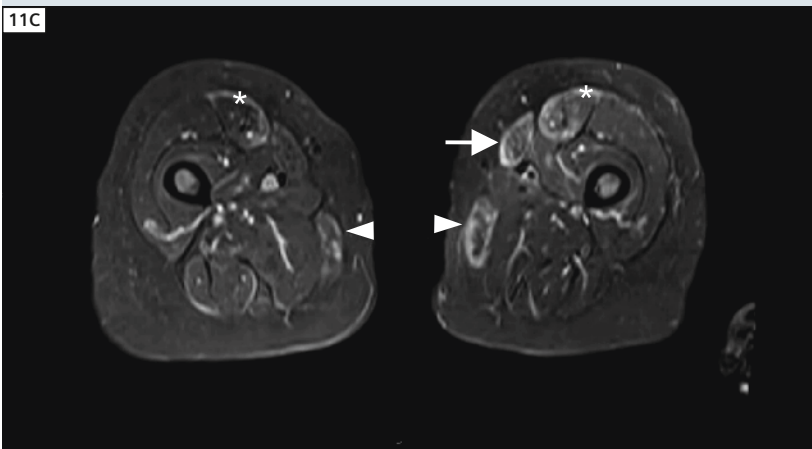
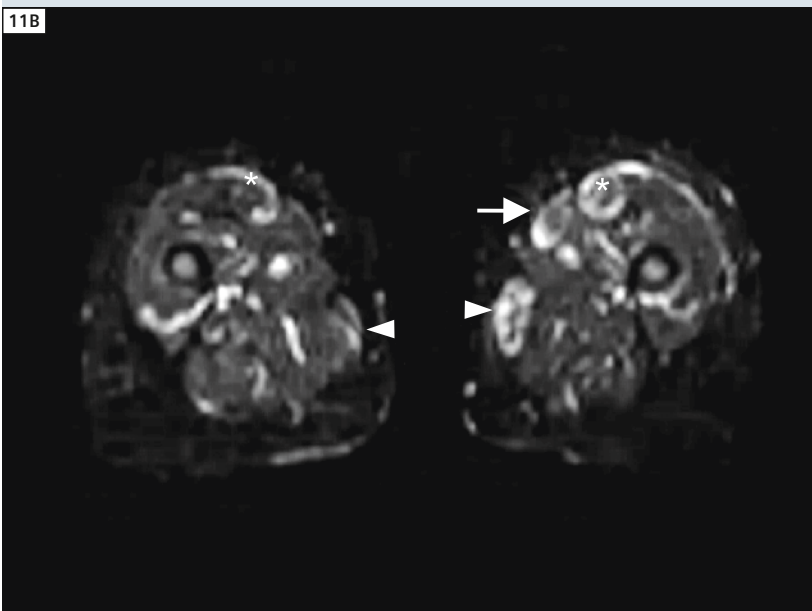
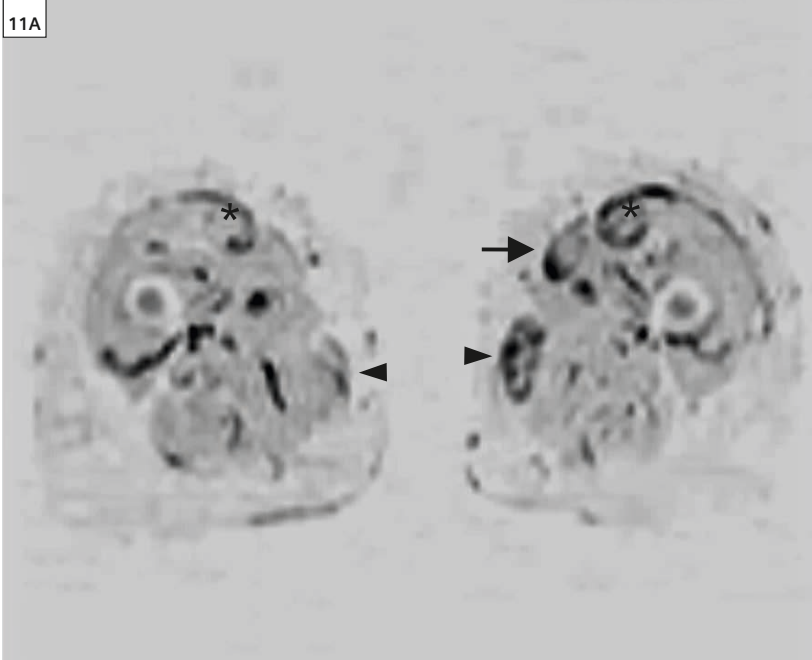
**8** T1w in-phase (**8A**) and T1w opposed-phase (**8B**) of the bony pelvis in axial plane (same patient as in figure 7), showing diffuse bone marrow hypointensity, without signal reduction in T1w opposed-phase images, indicating tumoral infiltration instead of red marrow hyperplasia (confirmed by bone marrow biopsy).



**9** Fused T1w in-phase and b800 DWI coronal images (same patient as in figure 7), showing diffuse bone marrow infiltration (arrowheads), conglomerate of retroperitoneal and mesenteric lymph node masses, and enlarged cervical, axillary, mediastinal, hepatic hilum, mesenteric, retroperitoneal, common iliac and external iliac lymph nodes (arrows). Note the spleen in left hypochondrium (asterisk).



**10** 62-year-old male, HIV+, fever and malaise with prior negative prostate biopsy. 3D reconstruction from WBDWI showing prostatitis with slightly restricted diffusion in prostate (red arrow), associated with two tiny liver abscesses (black arrows), enlarged lymph nodes (green arrows) and multiple spleen abscesses with markedly restricted diffusion (red arrowheads).



**11** 39-year-old female, diagnosis of dermatopolymyositis four months ago, treatment with corticosteroids, decreasing serum levels of muscle enzymes. Axial  $b_0$  images with inverted gray scale (**11A**) and standard gray scale (**11B**) and STIR images (**11C**): edema in rectus femoris bilaterally (asterisks), left sartorius (arrow) and gracilis muscles (arrowheads) and in their respective aponeuroses.

of the treatment), where an increase of the ADC of the bone lesions was observed after two months of the first session of radiotherapy, with a subsequent improvement in the clinical symptoms. One of the patients with small cell tumor with unknown primary site was also followed up (one DWI before and one after the beginning of the treatment) and showed an increase in the ADC values in bone and liver lesions after one week of the second cycle of chemotherapy, also accompanied by clinical improvement (Fig. 5). Unlike other authors, we didn't use histogram analysis of the ADC values [2].

### WBDWI beyond oncological applications

During the study a patient presented at our institution with fever and malaise investigating liver, splenic and nodal lesions one month after a negative biopsy for prostate cancer. He was submitted to a conventional MRI of the abdomen and pelvis and we complemented the exam with WBDWI. There were multiple lesions suggested of abscesses with central region presenting hypointense signal in T1w and hyperintense signal in STIR images with markedly restricted diffusion in the liver and notably in the spleen. We could also note axillary lymph nodes, as well as pelvic and retroperitoneal enlarged lymph nodes, the latter with apparent central areas of abscess formation on conventional images. There were also foci with slightly restricted diffusion in the prostate (Fig. 10). The type and pattern of distribution of the lesions suggested the diagnosis of prostatitis with septic foci to lymph nodes and solid viscera, which was confirmed by laboratory exams. Adequate antibiotics were administered and there was clinical improvement of the patient initially. During the investigation of prostatitis it was also discovered the patient was HIV positive with Acquired Immunodeficiency Syndrome, which could have helped in the spread of the septic disease.

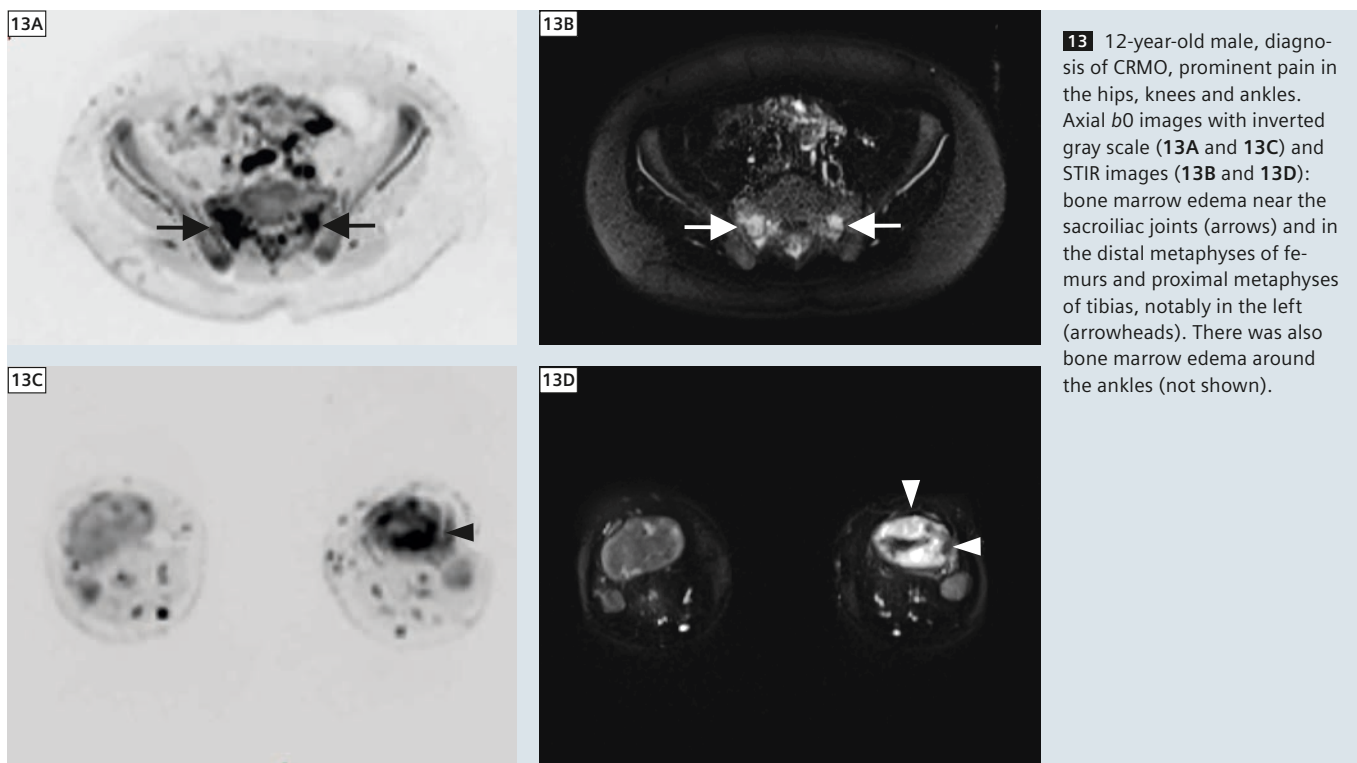
In rheumatic patients, we mostly used the T2 shine-through effect of WBDWI in the interpretation of images. The patient with dermatopolymyositis had decreas-



ing serum titles of muscle enzymes and had edema predominantly in rectus femoris, sartorius and gracilis muscles and their aponeuroses in the thighs (Fig. 11). In the patient with spondyloarthritis, enthesitis near the spinous processes of lumbar spine and in interspinous ligaments could be well depicted (Fig. 12),

a finding described in the literature [3]. Chronic recurrent multifocal osteomyelitis (CRMO) is an autoinflammatory disorder of children and young adults that is characterized by non-bacterial osteomyelitis presenting with multifocal bone pain secondary to sterile osseous inflammation, with a relapsing and remitting

course. In the study of the patient with CRMO we also included in the protocol a station for the distal thighs and legs. This patient had marked bilateral edema in metaphyses around the ankles and the knees adjacent to the growth plate, this last one being the most common location of the disease in the tubular



bones according to the literature [4], and prominent edema in the sacrum near the sacroiliac joints, a finding less common (Fig. 13). In rheumatic diseases, *b0* images had a similar performance in comparison with STIR images to detect muscle and bone marrow edema, as well as in the detection of enthesopathy. The *b800* images were not helpful in these cases, because the lesions had no real restricted diffusion.

## Conclusion

WBDWI may play an important role in the near future for the detection of visceral and mostly bone metastases from many types of cancer. The method is also promising in the demonstration of a visual notion of the disease as a whole in some auto-immune and inflammatory illnesses, probably helping in the assessment of their severity. One of our colleagues is studying a larger number of patients with chronic recurrent multifocal osteomyelitis (CRMO)

using WBDWI, so that we soon may have more answers about the advantages and disadvantages of WBDWI in these cases. We have not studied other possible indications of WBDWI, for example the assessment of bone marrow features in patients with other hematological non-neoplastic conditions, such as sickle cell disease and thalassemia, which is certainly a large field to be explored. Our center is not an academic institution and we didn't enroll patients in a randomized and double-blind fashion. So far, the exact role of WBDWI in the oncological and non-oncological setting and its sensitivity, specificity and accuracy in comparison with other exams (e.g. bone scintigraphy, PET-CT, PET-MR) must be accessed by large clinical trials.

## References

- 1 Koh DM, Blackledge M, Padhani AR, Takahara T, Kwee TC, Leach MO, Collins DJ. Whole-Body Diffusion-Weighted MRI: Tips, Tricks, and Pitfalls. *AJR*. 2012 Aug; 199:252-262.
- 2 Padhani AR, Koh DM, Collins DJ. Whole-Body Diffusion-weighted MR Imaging in Cancer: Current Status and Research Directions. *Radiology*. 2011 Dec; 261(3): 700-718.
- 3 Hermann KGA, Althoff CE, Schneider U, Zühlsdorf S, Lembcke A, Hamm B, Bollow M. Spinal Changes in Patients with Spondyloarthritis: Comparison of MR Imaging and Radiographic Appearances. *RadioGraphics*. 2005; 25:559-570.
- 4 Khanna G, Sato TSP, Ferguson P. Imaging of Chronic Recurrent Multifocal Osteomyelitis. *RadioGraphics*. 2009; 29:1159-1177.



Marcos Vieira  
Godinho



Leonardo Kayat  
Bittencourt

## Contact

Marcos Godinho  
Clínica de Diagnóstico por Imagem  
Rio de Janeiro  
Brazil  
mgodinho25@yahoo.com.br

**Save the Date**

# Heidelberg Summer School

## Musculoskeletal Cross Sectional Imaging 2013

**July 5<sup>th</sup> / 6<sup>th</sup> 2013**  
**Heidelberg, Germany**

The Heidelberg Summer School offers advanced learning opportunities and promotes the academic exchange of knowledge, ideas, and experiences by bringing together physicians and professional staff from all over the world. Excellent speakers will cover a wide range of medical, physical, and technical topics in musculoskeletal imaging. All lectures are in English.

### Course director

Marc-André Weber, M.D., M.Sc.

Professor of Radiology, Section Head Musculoskeletal Radiology at the University Hospital Heidelberg

### CME Accreditation

The symposium will be accredited by the 'Landesärztekammer Baden-Württemberg' with CME credits (category A).

Also, the symposium is accredited for 1 category 3 credit point for the ESSR diploma by the European Society of Musculoskeletal Radiology.

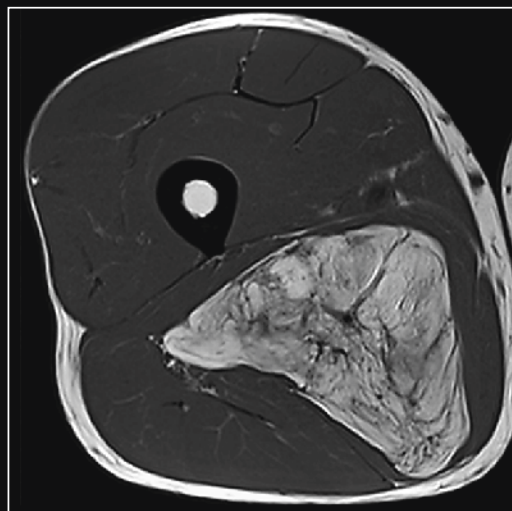
### Registration

Mrs. Marianne Krebs, Secretary of the Section Musculoskeletal Radiology

Marianne.Krebs@med.uni-heidelberg.de

**For further information please visit:**

[www.heidelbergsummerschool.de](http://www.heidelbergsummerschool.de)



# Parallel Transmission and its Clinical Implementation: Enabling new Clinical Imaging Paradigms

Fernando Boada<sup>1</sup>; Tim Shepherd<sup>1</sup>; Andrew Rosenkrantz<sup>1</sup>; Eric E. Sigmund<sup>1</sup>; Jorgen Fütterer<sup>2</sup>; Hersh Chandarana<sup>1</sup>; Mari Hagiwara<sup>1</sup>; Henry Rusinek<sup>1</sup>; Artem Mikheev<sup>1</sup>; Mary Bruno<sup>1</sup>; Christian Geppert<sup>3</sup>; Christopher Glielmi<sup>3</sup>; Josef Pfeuffer<sup>3</sup>

<sup>1</sup>Department of Radiology NYU Langone Medical Center, New York, NY, USA

<sup>2</sup>Department of Radiology, Radboud University Nijmegen Medical Centre, Nijmegen, The Netherlands

<sup>3</sup>Siemens Healthcare

## Introduction

The use of multiple and independent receive channels to accelerate MR data acquisition has enabled numerous clinical applications that are now part of the standard clinical workflow at state-of-the-art imaging centers. Parallel transmission (pTX) was, likewise, introduced as a means to enable and improve the use of extended RF excitations schemes such as multidimensional spatially-selective excitation, which, although conceptually powerful, were previously rendered impractical due to their long RF pulse durations.

The 3T MAGNETOM Skyra is the first clinical system to feature a parallel transmission architecture capable of enabling applications beyond B<sub>1</sub> shimming. This revolutionary capability allows enhancing the performance and reliability of several imaging sequences that are essential for advanced clinical applications. These enhancements are particularly significant at 3T, where B<sub>1</sub> field inhomogeneity can be problematic over large fields-of-view (FOV). We present several examples where the role of this technology demonstrates clinical benefits by enabling previously impractical imaging paradigms and/or improving the performance of existing ones.

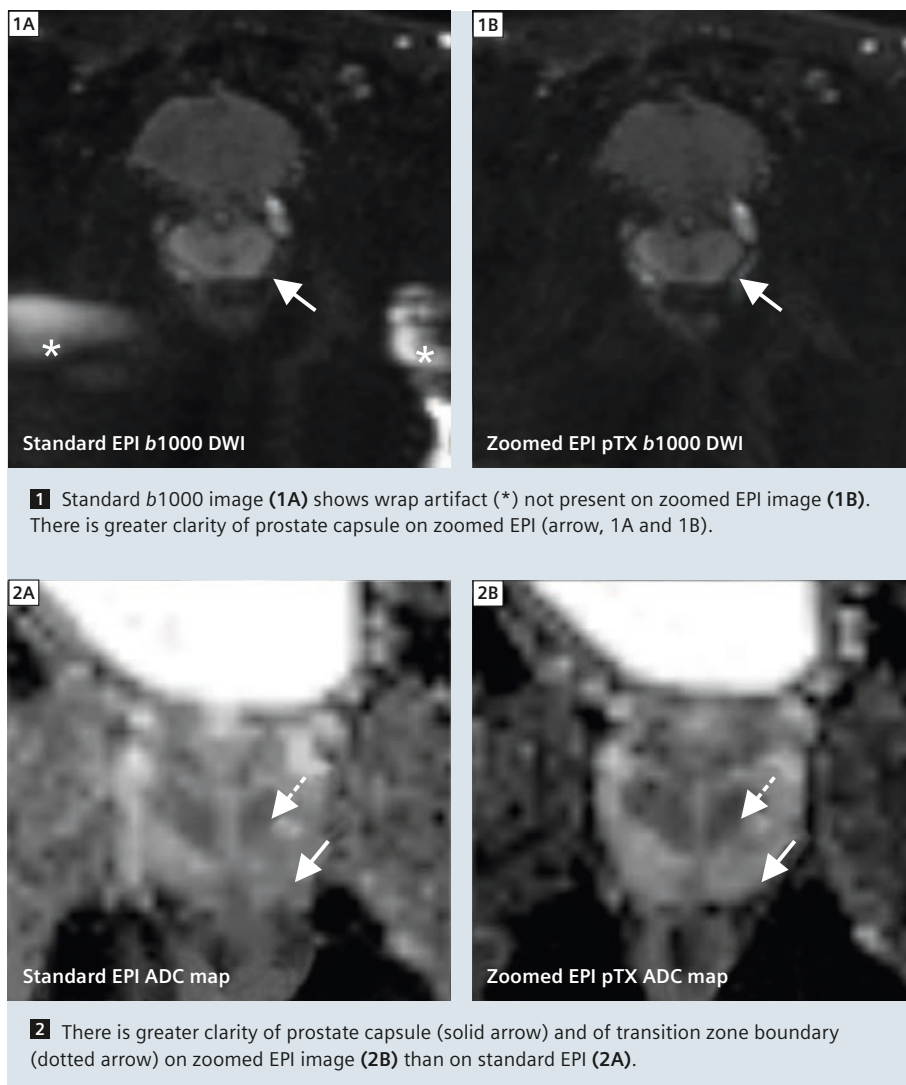


**Table 1: Comparison of standard and zoomed DWI.**

Feature	Standard EPI	Zoomed EPI
<i>b1000 s/mm<sup>2</sup> images</i>		
Absence of ghosting artifact	3.8 ± 0.4	4.3 ± 0.5
Absence of wrap artifact	3.7 ± 0.8	4.7 ± 0.5
Clarity of prostate capsule	4.0 ± 0.0	4.8 ± 0.4
Clarity of peri-urethral region	3.5 ± 0.5	4.2 ± 1.0
Overall image quality	3.7 ± 0.5	4.0 ± 0.6
<i>ADC maps</i>		
Reduced distortion of prostate	3.5 ± 0.5	3.8 ± 0.4
Clarity of transition zone boundary	3.2 ± 0.8	3.5 ± 0.4
Clarity of prostate capsule	3.2 ± 0.4	3.8 ± 0.4
Overall image quality	3.2 ± 0.4	3.7 ± 0.5
ADC (x 10 <sup>-3</sup> mm <sup>2</sup> /s)	1.34 ± 0.3	1.41 ± 0.8

## Prostate imaging

Diffusion-weighted imaging (DWI) is a critical sequence for prostate cancer detection and localization, but often suffers from spatial-distortion EPI artifacts related to the field inhomogeneity induced by the neighboring air spaces; these challenges can be more problematic at 3T. In this challenging imaging scenario, 2D-selective zoomed EPI in conjunction with a more homogeneous localized (B<sub>1</sub>-shimmed) RF excitation can be particularly helpful. The impact of zoomed EPI on image quality of prostate DWI at 3T was assessed in six volunteers who underwent prostate MRI using an 18-channel body matrix receive coil. Scans included a single-shot EPI DWI sequence (*b*-values 50, 500, and 1000 s/mm<sup>2</sup>) performed with a regular sinc pulse ('Standard') and with the advanced 2D spatially selective RF pulse ('ZOOMit') combined with a reduced FOV approach (zoomed EPI). The *b*1000 images and ADC maps were assessed for various image quality measures on a scale from 1 to 5 (5 = highest image quality). Also, peripheral zone (PZ) ADC and estimated signal-to-noise (eSNR: determined as mean/SD of PZ) on *b*1000 images were measured. These measures were compared between standard and zoomed EPI.

Compared with standard EPI, zoomed EPI *b*1000 images showed improvements in ghosting, wraparound artifacts, clarity of prostate capsule, and clarity of peri-urethral region (Fig. 1, Table 1). By contrast, zoomed EPI ADC maps showed improvements in clarity of prostate capsule and overall image quality (Fig. 2). eSNR was nearly identical between standard and zoomed EPI *b*1000 images. The prostate showed a small increase in mean ADC on zoomed EPI images (mean increase 0.07 x 10<sup>-3</sup> mm<sup>2</sup>/s). However, ADC reproducibility between standard and zoomed EPI DWI remained high (mean coefficient of variability of ADC (4.4 ± 4.0)%, range 0.3 to 11.0%).

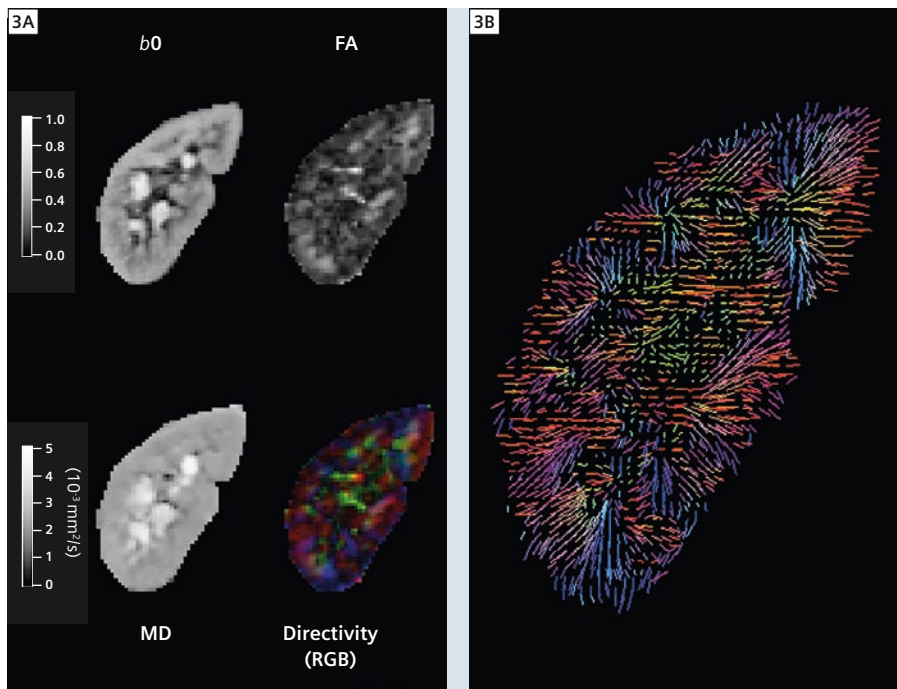
This preliminary assessment showed improvements in numerous measures relating to artifacts and anatomic clarity

## Skyra pTX architecture

The Skyra pTX system builds upon the existing clinical MAGNETOM Skyra platform, namely, a 3T magnet with a 70 cm patient bore diameter and parallel RF excitation via two fully independent, phase-coherent RF channels (TimTX TrueShape). The two pTX RF channels allow extended dynamic RF excitation schemes using a two-channel RF body coil. State-of-the-art imaging gradients (45 mT/m peak amplitude, 200 mT/m/s slew rate) and a full complement of Tim 4G multi-channel receive coils round out the hardware configuration of the system. The scanner operates under software version *syngo* MR D13C providing full access to further new technologies such as Dot,

*syngo* REVEAL etc. While there are pTX features that can be applied during the adjustments (patient-specific B<sub>1</sub>-shimming, volume-selective B<sub>1</sub>-shimming), we have focused on the improved sequences and applications which provide new features with pTX. This includes 2D-selective RF pulses with an echo-planar TX trajectory that excite a selective volume (so-called 'inner-volume') and allows to reduce the FOV in the phase direction [1, 2] for zoomed echo planar imaging (EPI) (*syngo* ZOOMit).

<sup>§</sup> Firevoxel and Igor Pro are not Siemens Healthcare products. Siemens bears no responsibility for these products including, but not limited to, their regulatory status.



**3** Kidney Zoomed-EPI DTI images.

**(3A)** Images obtained with  $b_0$  sec/mm<sup>2</sup>, fractional anisotropy (FA) map, mean diffusivity (MD) map, and direction-encoded color map. Medullary anisotropy is evident in the FA map. **(3B)** Color-coded primary diffusion eigenvectors display radial pattern of medullary tubules.

when applying 2D-selective zoomed EPI with for prostate DWI at 3T. While the FOV was held fixed to ensure comparability between the sequences, the use of a smaller FOV is easily achieved with zoomed EPI and currently under investigation. Nonetheless, even without this adjustment, zoomed DW-EPI using 2-channel pTX has potential to improve image quality for DWI of the prostate at 3T.

## Renal imaging

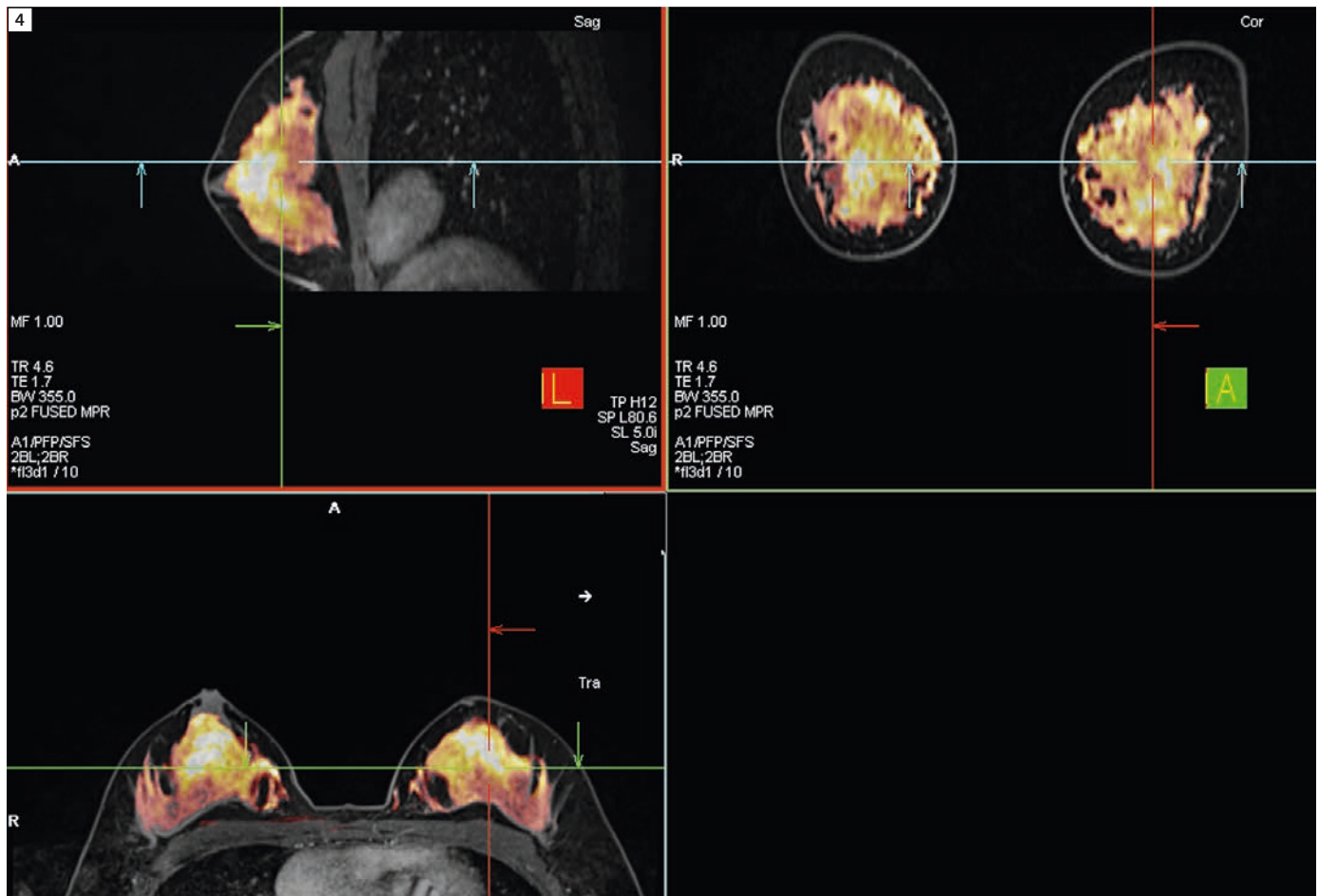
Diffusion-tensor imaging (DTI) uses multiple diffusion sensitizing directions to evaluate anisotropic microstructure and is a promising imaging technique for the functional assessment of kidneys. Microstructure is a key factor in renal physiology, where cortex contains randomly oriented structures, while medulla holds more aligned vessel and tubular networks. Kidney DTI has shown that renal medulla has inherently higher fractional anisotropy (FA) in comparison with the isotropic cortex [2-4]. However, kidney

DTI using single-shot spin-echo EPI typically suffers from imaging artifacts such as field-inhomogeneity-related distortions, and low spatial resolution due to the matrix size and long echo trains required for abdominal imaging. In this context, shortening the echo train length could reduce the aforementioned distortions. To achieve the same level of spatial resolution, while keeping a shorter echo train length, the imaging FOV must be reduced along the phase direction by the same factor used to shorten the echo train length. Zoomed EPI achieves such a goal through the use of 2D-selective RF excitation. Four consecutive healthy volunteers without any history of renal disease (three males, one female; mean age 28 (24-30 years); non-fasting conditions) were imaged on the Skyra pTX system. Free-breathing single-shot 2D-selective zoomed EPI DW images were acquired with reduced FOV in the left-right direction with the following parameters: 10-14 coronal slices, slice thickness

4 mm, no gap; FOV of 83 x 400 mm; 64 x 308 acquisition matrix, 1.3 mm resolution, TR 4000 ms; TE 65 ms; six diffusion directions; monopolar diffusion gradients; two  $b$ -values ( $b_0$  and  $b_{500}$  s/mm<sup>2</sup>); parallel imaging (GRAPPA) factor of two and scan time 5:28 min. An additional saturation band was applied to suppress signal from the left side of the body extending slightly beyond the stop-band. Right kidney images were co-registered by using a two-dimensional rigid body transform algorithm, and MR images at the same  $b$ -value and direction were then averaged by using locally developed software (Firevoxel<sup>®</sup>). DT processing was performed with custom software written in Igor Pro<sup>®</sup> (Wavemetrics, Portland, OR, USA). Parametric maps were generated of DTI eigenvalues  $\lambda_i$  and eigenvectors, mean diffusivity (MD) and fractional anisotropy (FA). The ZOOMit DTI technique allowed for high quality diffusion images of the kidney with reduced blurring and distortion (Fig. 3) compared to full FOV EPI DTI. Medullary anisotropy and radial orientation pattern was evident in all volunteers (e.g. Fig. 3). The medullary / cortical MD and FA values were  $2.04 \pm 0.14$  /  $2.21 \pm 0.12$   $\mu\text{m}^2/\text{ms}$ , and  $0.34 \pm 0.08$  /  $0.13 \pm 0.04$ , respectively, consistent with literature [3-5]. MD showed significantly higher, and FA significantly lower, cortical than medullary values. ZOOMit DTI may be valuable for clinical assessment of kidney pathology, particularly for applications closely scrutinizing cortico-medullary differentiation.

## Breast imaging

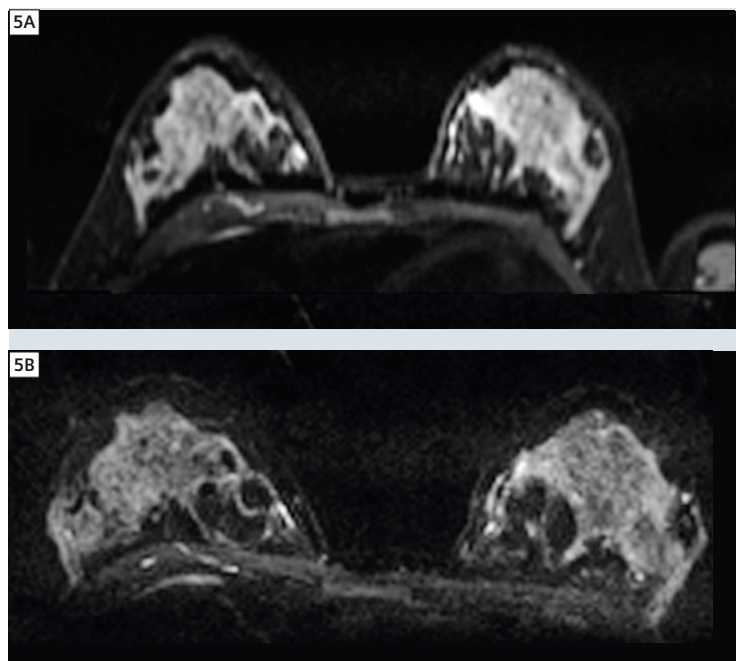
Diffusion-weighted imaging (DWI) of the breast is increasingly used for the differential diagnosis and treatment response monitoring of breast cancer. Conventional EPI techniques are prone to characteristic artifacts, such as susceptibility artifacts, image blurring and spatial distortion resulting from gradient non-linearity and eddy currents. Thus, there can be a significant mismatch in lesion appearance and position between morphologic sequences and EPI which can potentially affect the diagnostic accuracy. In addition, the strong demand



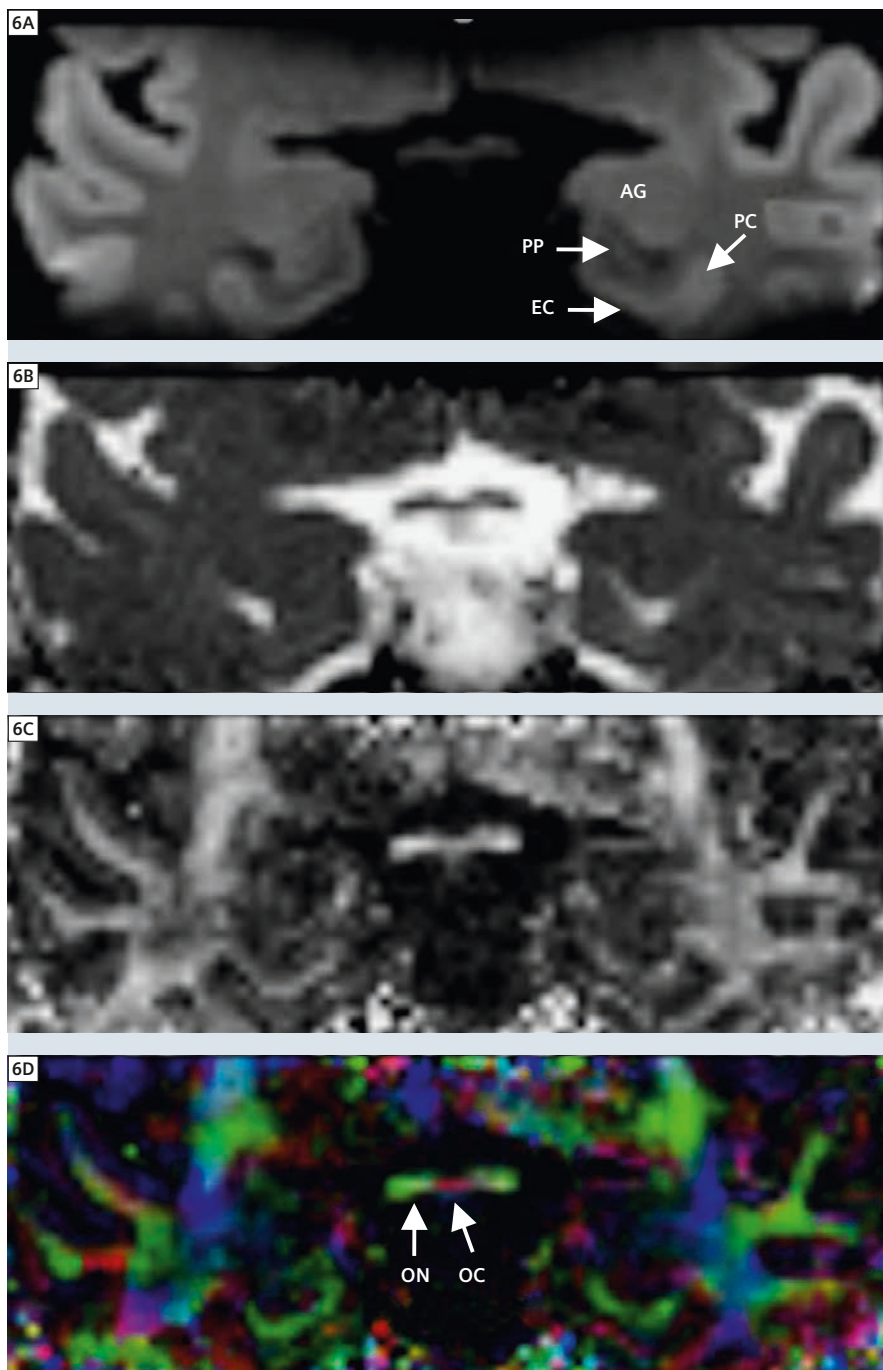
4 T1-weighted VIBE fused with a diffusion-weighted (b400) dataset.

on the gradient system limits the spatial resolution to only moderate in-plane resolution around  $1.8 \times 1.8 \text{ mm}^2$  or even coarser. Thus spatially-selective excitation with EPI ZOOMit was applied to a) mitigate the spatial distortion by shortening the phase encode burden and the echo train length and b) to allow the user to restrict the acquisition volume to the breast alone resulting in a higher spatial resolution.

3 healthy subjects were scanned using a 4-channel combined (biopsy and diagnostic) breast coil. For comparison, in both protocols 24 axial slices were acquired with three b-values in 3-scan trace mode with GRAPPA factor of 2. The nominal in-plane resolution was  $1.8 \times 1.8 \text{ mm}^2$  vs  $1.3 \times 1.3 \text{ mm}^2$  for zoomed EPI where the FOV could be reduced from 332 to 260 mm as well as the



5 Standard DW-EPI (5A) and zoomed EPI (5B).



**6** 1.2 mm in-plane resolution reduced FOV diffusion tensor images of the medial temporal lobes using the *syngo* ZOOMit application with single-shot EPI (top to bottom: diffusion trace, ADC, FA and color orientation map). This particular coronal slice at the level of the uncus and amygdala (AG) demonstrates distortion-free quantitative diffusion in several regions affected by early Alzheimer's disease including the perirhinal cortex (PC), entorhinal cortex (EC) and perforate pathway (PP) in the subjacent white matter. Without the reduced number of phase encoding steps enabled by ZOOMit, these structures are often severely distorted by susceptibility generated from air spaces in the subjacent temporal bone.

matrix slightly increased (192 x 78 to 200 x 78). Both protocols were set up for comparable acquisition times, 3:53 min ('standard') and 3:39 min (ZOOMit). Figure 4 shows an overlay of a T1-weighted VIBE with a diffusion-weighted ( $b400$ ) dataset in multi-planar reconstruction to illustrate the excellent co-registration and resolution. In Figure 5 the comparison between standard DW-EPI (top) with the described ZOOMit DWI protocol (bottom) is shown. There is a clear improvement regarding resolution and distortion, in this example the reduced SNR however is obvious as well. This is due to two reasons, first due to increased echo time with a longer RF pulse; but secondly also a *higher resolution* protocol was acquired. In signal-starved situations, such as fatty breasts higher averaging might still be advised. Clinically, the higher spatial resolution allows the more accurate DWI evaluation of enhancing foci and small non-mass enhancement on MRI. ZOOMit DWI shows potential to mitigate spatial distortions commonly observed in standard EPI. Further developments and investigations are anticipated to balance SNR and spatial resolution, as well as a quantitative comparison including measured ADC and reduction of artifacts. The preliminary data suggest that using ZOOMit DWI can enable higher spatial resolution in breast applications at reduced distortions when supported by sufficient SNR.

### Medial Temporal lobe imaging

The hippocampus and entorhinal cortex form a critical neuronal circuit for declarative memory formation that is often altered by different pathologies, including Alzheimer's disease. Unfortunately, standard single-shot EPI DTI fails to properly characterize the medial temporal lobe structures and their functional connectivity due to geometric distortions from subjacent temporal bone airspaces. In this setting, the 2D-selective RF excitation approach using a Skyra pTX system can be used to overcome these distortions at 3T and, therefore, quantify

diffusion tensor properties for specific medial temporal lobe structures. To evaluate the role of ZOOMit EPI in this setting, five healthy human volunteers were imaged using the 20-channel head/neck receive coil. Single-shot EPI diffusion-weighted images with fat saturation were obtained (TR 2200 ms, TE 83 ms, NEX 15, acquisition time 8 min, 10 gradient directions,  $b800 \text{ s/mm}^2$ ) using ZOOMit EPI. The protocol used a  $13.3 \times 4.4 \text{ cm}$  FOV (read x-phase axes) with 1.5 mm in-plane resolution ( $90 \times 30$  image matrix). 18 contiguous 3 mm thick oblique coronal slices were obtained orthogonal to the long axis of the temporal lobe with the most posterior slice prescribed tangential to the vertical portion of the hippocampal tail. ZOOMit DW images had acceptable signal-to-noise ( $6.6 \pm 1.1 @ b800 \text{ s/mm}^2$ ) and significantly reduced geometric distortions from subjacent temporal bone airspaces compared to full FOV acquisitions. Diffusion-weighted images resolved specific components of the medial temporal lobes such as the entorhinal cortex (EC), perforant pathway white matter (PP), hippocampal head,

**Table 2: Quantitative diffusion values using zoomed diffusion.**

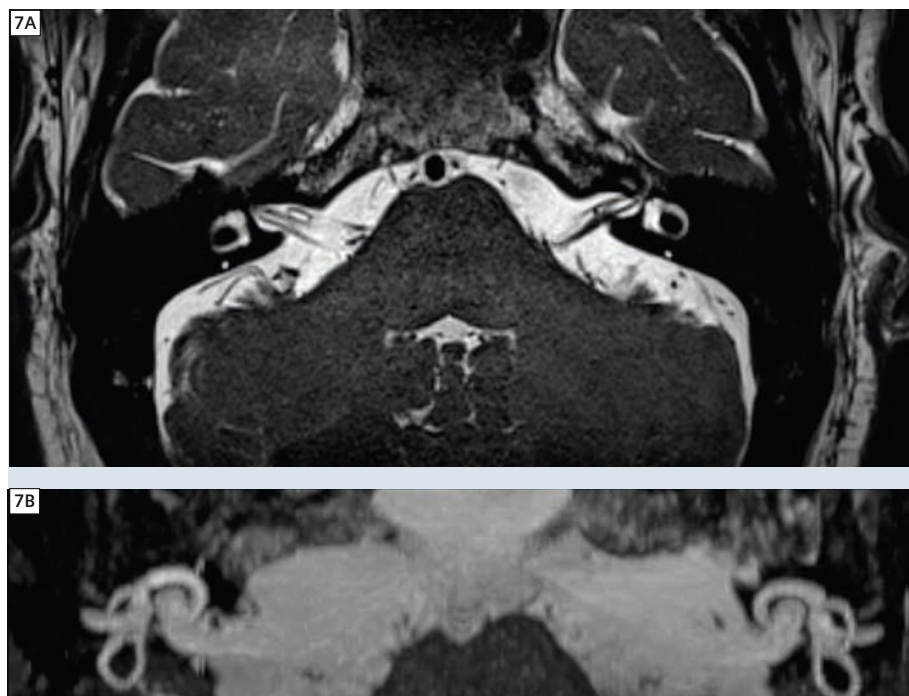
Region	Mean diffusivity ( $\times 10^{-3} \text{ mm}^2/\text{s}$ )	Fractional Anisotropy
CA1	$0.82 \pm 0.04$	$0.25 \pm 0.06$
DG	$0.86 \pm 0.06$	$0.27 \pm 0.06$
ERC	$0.77 \pm 0.08$	$0.32 \pm 0.07$
PP	$0.81 \pm 0.07$	$0.40 \pm 0.08$

subiculum, dentate gyrus (DG), molecular and neuronal layers of the hippocampus (CA1). Quantitative data (Table 2) was consistent with prior DTI parameter values from human hippocampus autopsy samples [5]. Color fiber orientation maps demonstrated coherence from CA1 neuron apical dendrites as previously shown [5] and data may allow tractography of the perforant pathway between the entorhinal cortex and hip-

pocampus. The central portion of the color fiber orientation map (Fig. 6) also demonstrates the midline optic chiasm (OC, red) and paired, anterior coursing optic nerves (ON, green, 4.5 mm diameter). This is a nice illustration of the capability for ZOOMit diffusion to also achieve sufficient resolution to accurately measure diffusion parameters in cranial nerves. Similar results have been observed for the trigeminal nerves and may provide improved diagnosis/monitoring for trigeminal neuralgia.

### ZOOMit SPACE

Similarly to ZOOMit EPI, SPACE with reduced FOV using ZOOMit can increase acquisition efficiency enabling improved spatial resolution or T2-weighting for a given scan duration. For example, ZOOMit SPACE was acquired using the 20-channel head/neck receive coil to visualize the internal auditory canal (IAC) in a patient with Meniere's disease (axial orientation, TR 1000 ms, TE 125 ms, 2 averages, echo train length of 54,  $160 \times 80 \text{ mm}$  FOV,  $2 \times 2 \times 0.5 \text{ mm}$  resolution, flip angle 100 degrees, BW: 255 Hz/Px, acquisition time 2:31 min). The acquisition time in this case was approx. 50% shorter than with the non-zoomed reference protocol. As shown in Figure 7, this case shows clear anatomical features including cochlear and vestibular nerves, as well as posterior and lateral semi-circu-



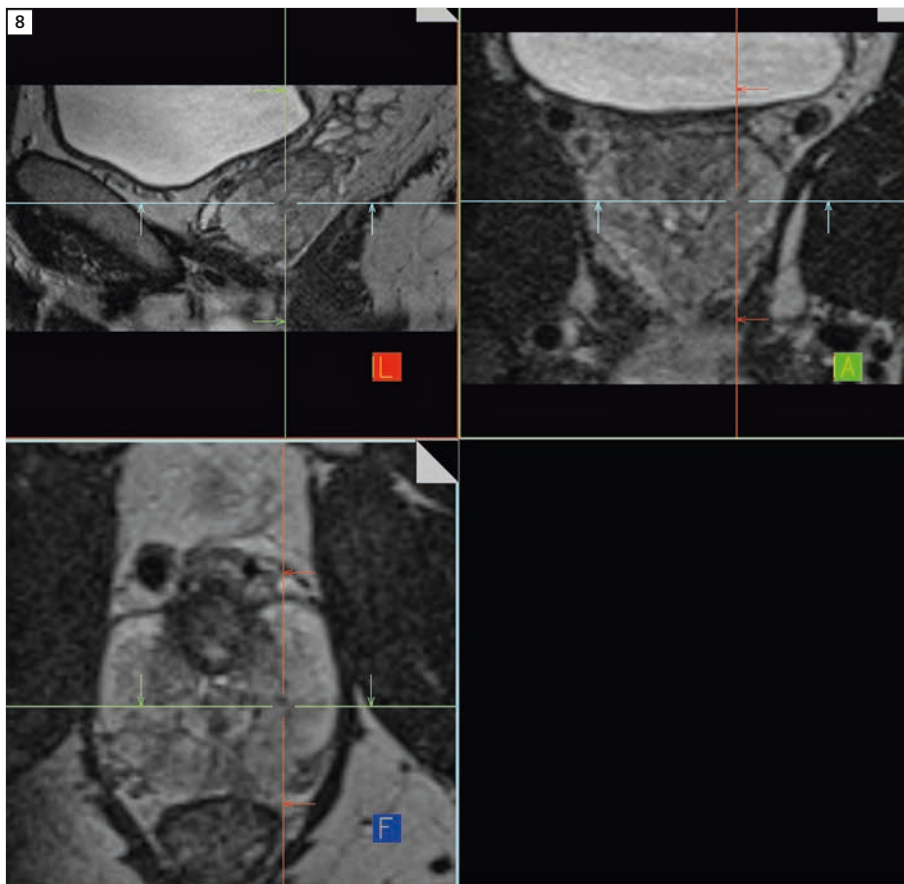
**7** Zoomed T2-weighted SPACE of the IAC (7A) and thin maximum intensity projection (7B).

lar canals in an axial slice (top) and thin maximum intensity projection (bottom). Another application is depicted in Figure 8 using ZOOMit SPACE in the prostate. This example was acquired using a combination of the body-18 and spine coil elements. TR 2000 ms, TE 99 ms, echo train length of 57 and 600 Hz/pixel at 320 x 160 matrix and 72 slices; using a 230 x 115 FOV this resulted in a voxel size of 0.7 x 0.8 x 1 mm at a total acquisition time of 7:15 min providing the capabilities of reformatting the data in any orientation.

## Conclusions

The results shown clearly demonstrate that 2D-selective RF excitation on a 2-channel pTX system enables zoomed EPI acquisitions on 3T scanners that can significantly reduce the limitations imposed by spatial distortions due to field inhomogeneity. Together with the inherent ability to simultaneously improve excitation inhomogeneity while providing effective reduced FOV implementations, the TimTX TrueShape clinical platform is ideally suited to fully capitalize on a wide range of improved imaging approaches that require a practical and fully integrated multi-channel transmission platform. These approaches have been previously demonstrated to be of significant value in similarly challenging imaging settings, albeit at the expense of requiring a complex hardware set up due to the lack of commercially available, fully-integrated, multi-channel transmission platforms. The introduction of the clinical Skyra TimTX TrueShape platform is poised to have a significant impact on the clinical implementation of such powerful imaging tools.

For further scientific details of the above shown studies, please refer to Proc ISMRM 2013 abstract numbers (#): #3390 (prostate), #1554 (kidney), #1739 (breast), #3021 (neuro).



8 Zoomed T2-weighted SPACE of the prostate (MPR).

## References

- 1 Rieseberg S, Frahm J, Finsterbusch J. Two-dimensional spatially-selective RF excitation pulses in echo-planar imaging. *Magn Reson Med*. 2002 Jun;47(6):1186-93.
- 2 Schneider R et al. Evaluation of 2D RF echo planar pulse designs for parallel transmission. *Proc ISMRM 2012* #3459.
- 3 Ries M, et al. Diffusion tensor MRI of the human kidney. *JMRI* 2001;14(1):42-49.
- 4 Notohamiprodjo M et al. Diffusion tensor imaging of the kidney with parallel imaging: Initial clinical experience. *Invest Radiol* 2008;43(10):677-685.
- 5 Sigmund EE et al. Intravoxel incoherent motion and diffusion-tensor imaging in renal tissue under hydration and furosemide flow challenges. *Radiology* 2012;263(3):758-769.
- 6 Shepherd TM et al. diffusion tensor microscopy indicates the cytoarchitectural basis for diffusion Anisotropy in the human hippocampus. *AJNR* 2007;28:958-964.

## Contact

Fernando Boada  
Department of Radiology  
NYU Langone Medical Center  
660 1<sup>st</sup> Avenue  
New York, NY 10016  
USA  
fernando.boada@nyumc.org

# Liver Imaging Today

Tobias Heye, M.D.<sup>1</sup>; Mustafa R. Bashir, M.D.<sup>2</sup>

<sup>1</sup>Department of Radiology, University Hospital Basel, Switzerland

<sup>2</sup>Department of Radiology, Duke University Medical Center, NC, USA

## Introduction

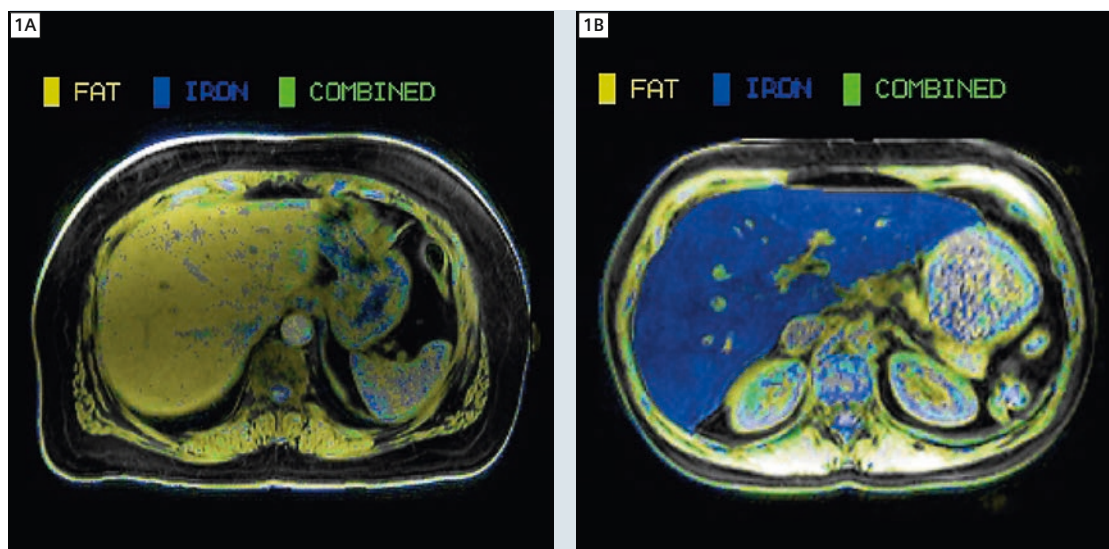
Liver disease is a global burden with a growing incidence and prevalence. The World Health Organization recently estimated that there are 800,000 cirrhosis-related deaths per year world-wide [1]. Chronic liver disease has a great impact on public health care costs with therapeutic options ranging from antiviral treatment for viral hepatitis to orthotopic liver transplant for end stage cirrhosis. A variety of pathogens, which can be toxic, viral, metabolic or autoimmune in nature, can induce fibrosis which may progress to cirrhosis if the disease is not detected and treated. An estimated 150 million people world-wide are chronically infected with hepatitis C virus, approximately 350,000 people die due to hepatitis C related liver disease [2]. Liver fibrosis may be reversible at an early stage, which indicates the

importance of screening and detection of liver disease. Many forms of liver fibrosis and cirrhosis especially secondary to viral hepatitis increase the risk for the development of liver cancer, namely hepatocellular carcinoma.

Non-alcoholic steatohepatitis is emerging as a major pathway into chronic liver disease and is closely related to other metabolic disease entities such as diabetes and morbid obesity. The incidence and prevalence of these diseases has risen steadily over recent years.

In a clinical context, liver disease is often reflected by a combination of several contributing factors, fibrosis, hepatic steatosis and iron overload, each with different forms of manifestations. Although these diseases are considered 'diffuse', actual hepatic parenchymal involvement by any of these can be

irregular and patchy, leaving other parenchymal areas unaffected. Clinical management of patients with diffuse liver disease requires tools to accurately detect and classify the various forms of liver disease. Even with decades of experience in imaging, liver biopsy and the histological workup of the specimens have traditionally been the reference standard in the characterization of liver disease [3]. However, biopsy is prone to sampling errors if less affected parenchyma is sampled and may not reflect the true disease severity and distribution in a particular organ due to the variance in the heterogeneous pattern of histological changes on a macroscopic scale [4, 5]. Biopsy, associated with the risks of an invasive procedure, is employed for disease detection and staging, but periodically repeated biopsy is not a practical

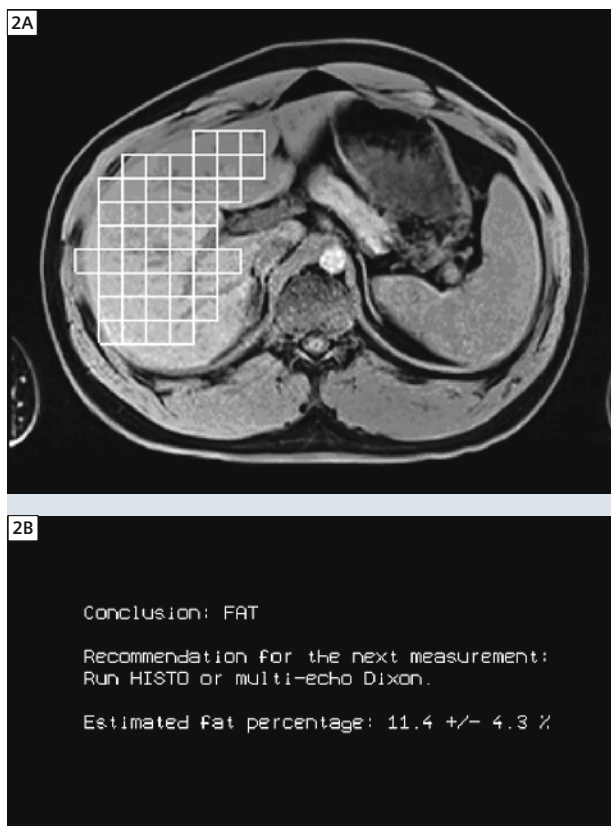


**1** Results of the Screening Dixon technique which produces color coded maps to visualize the distribution of detected abnormal metabolites in two different clinical examples. **(1A)** A patient with diffuse hepatic steatosis as indicated by the yellow hue. **(1B)** A patient with diffuse iron overload as marked by blue overlay to the affected liver.

method for disease monitoring. Additionally, given its attendant risks and costs, biopsy is only performed in patients in whom liver disease is strongly suspected, and is not suitable for evaluating those patients with only mild or questionable symptoms. Thus, there has been great interest in non-invasive methods to assess diffuse liver disease, and imaging modalities, in particular magnetic resonance imaging (MRI), have evolved as potential tools to measure certain biomarkers.

Liver MRI offers a variety of methods to detect and quantify parenchymal changes which occur in chronic liver disease [6, 7]. In contrast to liver biopsy, liver MRI allows for assessment and evaluation of the entire liver volume by means of quantitative measurements and color coded maps which reflect the geographical disease distribution. Quantification of excessive fat and iron deposition was shown to be accurate as demonstrated by many studies in the literature [8, 9]. The characterization of focal liver lesions and determination of treatment options for hepatocellular carcinoma is a well-established clinical application of liver MRI, and this use will grow as the prevalence of chronic liver disease increases [10]. The detection and accurate classification of liver fibrosis and cirrhosis remains challenging, despite the usefulness of liver MRI in the aforementioned scenarios [7].

While liver MRI may soon provide a comprehensive evaluation of liver disease it is a complex technique requiring highly trained personnel, cooperative patients and optimized scanning conditions to produce diagnostic images acceptable for clinical interpretation. MRI must compete with other imaging modalities, sonography and computed tomography (CT) in categories such as availability, cost, acquisition time, robustness, reproducibility, patient acceptance, and comfort. In particular, it has been advocated that MRI needs to close the gap in acquisition time compared to CT; simultaneously methods should be employed to stan-

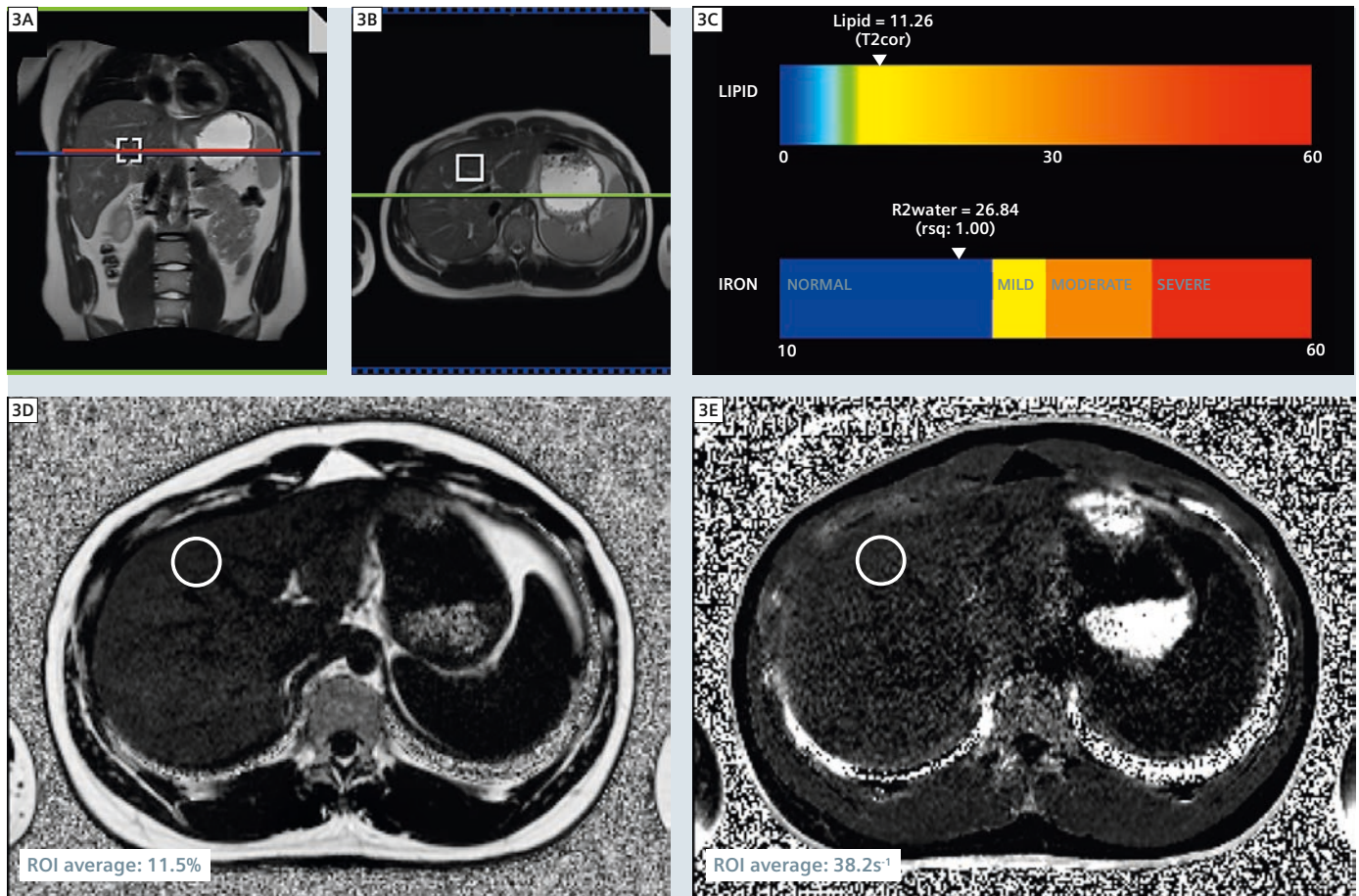


**2** Example of the Screening Dixon segmentation algorithm which identifies large portions of the liver and the automated conclusion given by the dual signal intensity ratio calculation (In-phase/ Opposed-phase and Fat-Only/Water-Only data sets) in a volunteer. **(2A)** Segmentation result, **(2B)** automated conclusion.

dardize the image acquisition workflow, improve reproducibility of a quantitative imaging protocol, and reduce the time spent performing redundant data acquisition or preparatory steps [11]. However, in terms of diagnostic performance, lack of ionizing radiation compared with CT, and the variety of tissue contrasts available, MRI has several clear advantages. In the following article we will discuss new methods which address MRI related issues like artifacts and breathing motion while improving image quality and spatial resolution, offer fast automated screening techniques for the detection of parenchymal changes, and optimize the imaging workflow to decrease overall acquisition time.

## Liver imaging

A modern liver imaging protocol must accomplish at least two main goals. The presence of diffuse liver disease, fat, iron deposition and possibly fibrosis/cirrhosis should be detected and ideally quantified, even if not expected at the time that the examination is initiated. Additionally, focal hepatic lesions, in particular in the setting of cirrhosis, must be characterized to allow for classification into benign entities, such as simple cysts, hemangiomas, focal nodular hyperplasias (FNH) or adenomas versus malignant hepatic tumors like hepatocellular carcinoma, cholangiocarcinoma or metastatic disease. These tasks must be accomplished within a reasonable amount of time without compromise in image quality or obtainable information. A number of methodologies have become recently available which provide automated diagnosis of diffuse liver disease, higher spatial resolution imaging, and automated workflows.



**3** Quantification results from the same volunteer as in Fig. 2. **Top:** HISTO (3A, B) voxel positioning, (3C) quantification results in a graphical norm range display. **Bottom:** Multi-echo Dixon (3D) fat percentage map, (3E)  $R_2^*$  map.

## Screening Dixon

Fat and water separation can be realized by 3D In- and Opposed-Phase T1-weighted data acquisition with two-point Dixon reconstruction. This 3D gradient-echo imaging sequence produces four sets of images with In-/Opposed-Phase, Water-Only and Fat-Only depiction. The Water-Only image set can further be employed as a standard pre-contrast fat-suppressed sequence, one of the standard in a liver MRI protocol with contrast material application [12]. The two-point Dixon method offers visual, qualitative assessment of hepatic steatosis but the acquired data allow for a semi-quantitative estimation of fat deposition as well as iron overload [13, 14]. This pulse sequence provides two essential image sets (In- and Opposed-Phase and

pre-contrast T1) in a single breath-hold. The Screening Dixon method represents a two-point Dixon technique with an additional liver sampling algorithm that automatically segments large portions of the liver. Within a large volume of the segmented liver, dual signal intensity ratios from In-phase/Opposed-phase and Fat-Only/Water-Only data sets are calculated by the algorithm to produce an assessment regarding the presence of diffuse liver disease. The result of the algorithm (normal, fat, iron, or combined disease) can be coupled with a recommendation to perform a dedicated quantitative sequence for the detected abnormal metabolite (e.g. iron quantification sequence) [13, 15]. Hence, the Screening Dixon technique offers an automated approach to diffuse liver disease but simultaneously allows

for a quantitative MRI protocol tailored to the individual patient. Instead of performing a time consuming all-in-one MR imaging protocol that comprises any type of quantification, the Screening Dixon methods stratifies protocol steps in a way that only essential quantitative sequences are acquired, potentially reducing overall acquisition time compared with an exam which performs quantification unnecessarily (Figs. 1, 2). Notably, although this method can provide estimates of proton density fat fraction (PDFF) and  $R_2^*$  (a surrogate for iron concentration), these are not corrected for a variety of potentially confounding factors, and should be confirmed by a dedicated quantification sequence when abnormal. Even so, this algorithm performs well for the task of detecting diffuse steatosis/siderosis [16].

## Fat and iron quantification

$R2^*$  and PDFF can be quantified in two different ways. Multi-echo, T2 corrected, single breath-hold spectroscopy (HISTO) gives highly reproducible values from a single voxel [17]. Multi-echo 3D gradient echo (VIBE) imaging, with Dixon reconstruction and correction for  $T2^*$  as well as the multi-spectral nature of fat, allows quantification with good spatial resolution [18].

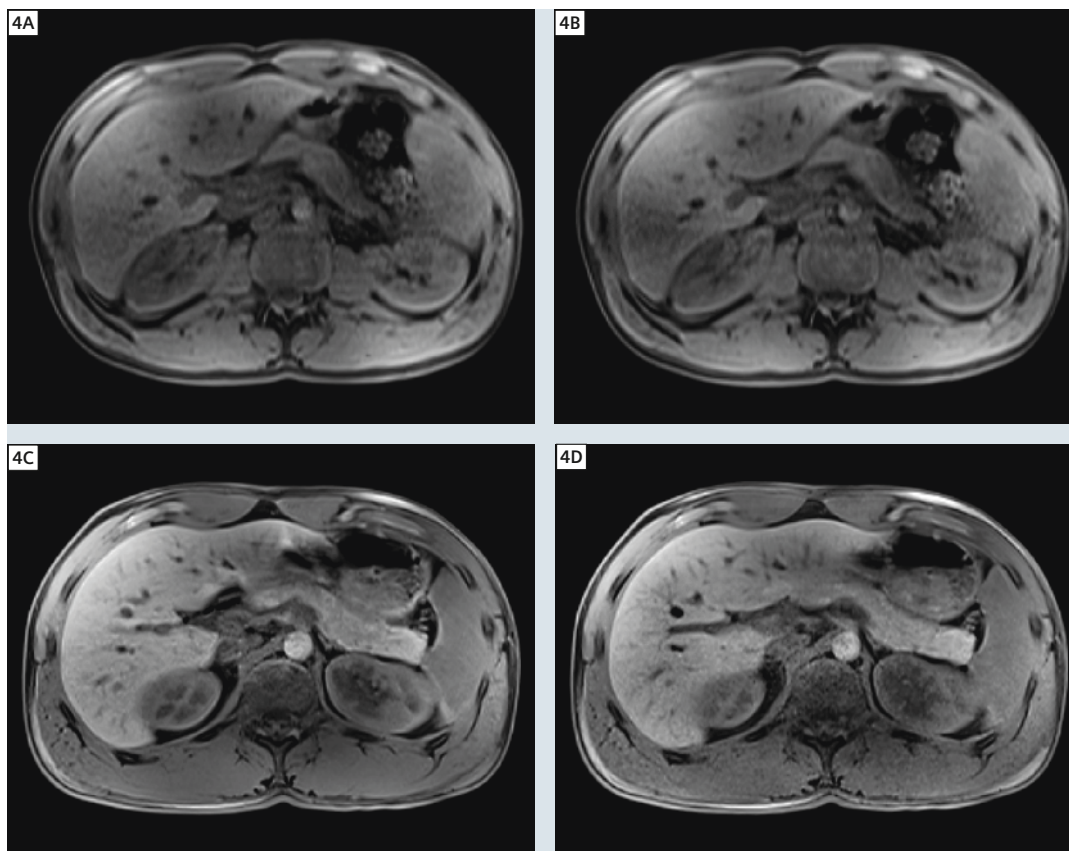
Figure 3 shows quantification results from the same volunteer as in Fig. 2. The results are consistent and support the initial Screening Dixon estimation.

## CAIPIRHINA

There are two distinct time points within a contrast enhanced liver MRI protocol which are crucial in the acquisition of diagnostic images. Hepatic arterial phase imaging is the mainstay in the detection of hepatocellular carcinoma [18]. Here, accurate timing is important [22]. The

images may be acquired as a multi-arterial phase to improve temporal resolution [17]. A 'late phase', whether the vascular equilibrium phase obtained with extracellular contrast agents or the hepatocyte phase obtained with hepatobiliary agents, can differentiate lesions based on their contrast retention behavior. For both elements within a liver MRI protocol, a compromise must be made between achievable image resolution and acquisition time. This conflict is even more challenging for single breath-hold/multiple arterial phase imaging. The duration of a breath-hold remains the limiting factor in contrast enhanced liver imaging, and a sequence must balance the two factors; sufficient spatial resolution within a reasonable acquisition time. The evolution of parallel imaging techniques has allowed multiple acquisitions within the arterial phase time window to reliably capture the late hepatic arterial phase, a critical image for hepatocellular carcinoma imaging. However, 20-25 sec-

ond breath-holds remain challenging for some patients. Hepatobiliary phase imaging is ideally done using high spatial resolution to utilize the diagnostic information derived from hepatocyte specific contrast agent for all liver abnormalities, in particular for smaller otherwise indeterminate lesions (> 1 cm lesion diameter). Although the time window for the hepatobiliary phase is wider compared to arterial phase imaging, the achievable spatial resolution is similarly limited by the duration of a breath-hold which may be even shorter at the end of an examination due to developing fatigue of the patient. Patients with impaired or poor breath-holding capabilities may render any breath-hold sequence acquisition non-diagnostic if the acquisition time exceeds their capabilities. Further increasing standard parallel imaging acceleration, however, decreases the signal-to-noise ratio (SNR) and induces image artifacts.



**4** Comparison of standard VIBE acquisition with iPAT acceleration to acceleration with CAIPIRHINA and higher-order acceleration factors in a volunteer without intravenous contrast. Please note how acquisition time and/or spatial resolution can be modulated by incorporating CAIPIRHINA.

Triple phase imaging, slice thickness 5 mm, matrix  $256 \times 128$ :

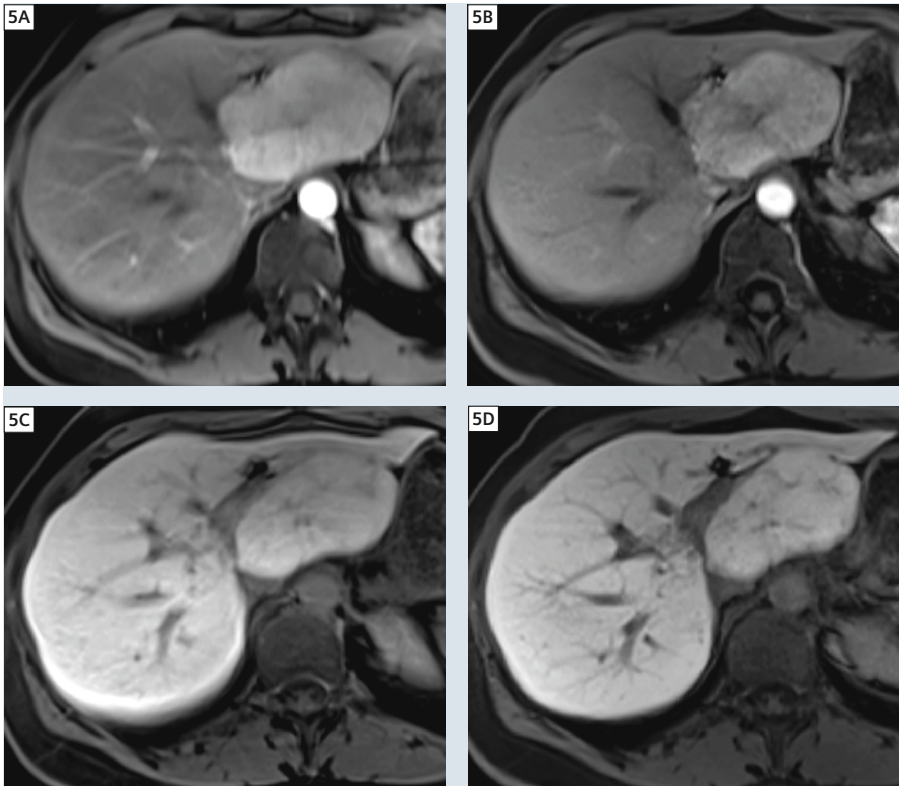
**(4A)** iPAT, acceleration factor 2: acquisition time 28 seconds for three phases.

**(4B)** CAIPIRHINA, acceleration factor  $2 \times 3$ : acquisition time 11 seconds for three phases.

Single phase imaging, slice thickness 3 mm, matrix  $320 \times 195$ :

**(4C)** iPAT, acceleration factor 2: acquisition time 20 seconds.

**(4D)** CAIPIRHINA, acceleration factor  $2 \times 2$ : acquisition time 13 seconds.



**5 Triple arterial phase imaging:**

(5A) iPAT, acceleration factor 2: matrix  $256 \times 115$ , spatial resolution  $1.3 \times 2.8 \times 5$  mm, acquisition time 29 seconds for three phases.

(5B) CAIPIRINHA, acceleration factor  $2 \times 2$ : matrix  $256 \times 156$ , spatial resolution  $1.3 \times 1.8 \times 5$  mm, acquisition time 26 seconds for three phases.

**Hepatobiliary phase imaging:**

(5C) iPAT, acceleration factor 2: matrix  $256 \times 192$ , spatial resolution  $1.3 \times 1.8 \times 4$  mm, acquisition time 22 seconds.

(5D) CAIPIRINHA, acceleration factor  $2 \times 3$ : matrix  $288 \times 216$ , spatial resolution  $1.2 \times 1.6 \times 4$  mm, acquisition time 12 seconds.

Two examinations utilizing iPAT and CAIPIRINHA acceleration and gadoxetate disodium in a patient with a focal liver lesion characterized as focal nodular hyperplasia (FNH) based on arterial and hepatobiliary phase imaging. Comparison between standard iPAT and CAIPIRINHA acquisition reveals improved contrast, sharpness and detail based on increased spatial resolution. Acquisition time was also decreased in the hepatobiliary phase (5D), eliminating the breathing motion artifacts seen in (5C).

CAIPIRINHA (Controlled Aliasing in Parallel Imaging Results in Higher Acceleration), a new parallel imaging technique differs in the  $k$ -space sampling pattern compared to standard acceleration techniques and is more efficient in using the coil sensitivities [21]. Undersampling is performed in both the phase and partition directions, allowing for a higher acquisition matrix and improved image resolution. This provides dramatic improvements in spatial resolution for the same breath-hold times, and can be optimized to provide a combination of high

spatial resolution and reduced breath-hold duration (Figs. 4, 5).

### Workflow – Abdomen Dot Engine

MRI data acquisition is time consuming, and the considerably longer examination times (compared to CT) must be justified by added benefits to patient care. Total examination time is composed of time spent acquiring image data and time spent performing a variety of setup tasks, including patient positioning and pulse sequence preparation. In liver MRI, prepa-

ratory tasks have been shown to consume more time than image acquisition, as such there is substantial opportunity for improvement in addressing the efficiency of performing these tasks [19]. This leads to operator dependent workflow, inconsistent image quality, and prolonged examination times. Additional patient specific factors further influence the achievable image quality and overall examination time, for example patients vary in their breath-holding capabilities and may fatigue throughout an examination. Adjustment of the imaging strategy, breath-hold versus free breathing, triggered imaging versus a shortened, fast imaging protocol may be necessary to accommodate individual differences. Additionally, many of the pulse sequence preparatory tasks are redundant and therefore offer opportunities for automation or a guided standardized setup. The current MRI acquisition workflow can be rendered more efficient thus reducing overall room time.

The Abdomen Dot Engine is an approach that incorporates various strategies to optimize and standardize a complex abdominal MRI protocol. It allows for automatic detection and positioning of an individualized field-of-view (FOV) based on localizer images, can stratify a protocol into patient specific breathing capabilities and provides tools such as automatic bolus timing for dynamic scanning [20]. A liver MRI protocol, for example can be standardized and partitioned into its typical elements (pre-contrast, multiple arterial, portal venous, and equilibrium phases), so that key settings such as delay times between each element can be configured by the user through an interface that offers an overview of all protocol steps (Fig. 6). A standardized and guided workflow for MRI examinations is needed to release the operator from redundant tasks, such as defining patient-specific sequence parameters, and allowing him or her to focus on global protocol strategies. Furthermore, the consistency of image quality across studies may be improved, and the risk of rescanning a sequence or the entire protocol may be reduced, increasing the robustness of the modal-



**6** Example of the Abdomen Dot Engine user interface showing the guidance view that allows global planning of delay times within a dynamic contrast enhanced liver MRI protocol.

ity. Additionally, multiple scan types which differ by only a few minor components (e.g., with or without MR Cholangiopancreatography (MRCP), with or without diffusion-weighted imaging) can be combined into a single, efficient protocol with a few key decision points, reducing redundancy and allowing for simpler base protocol maintenance and modification when necessary.

## Summary

MRI examinations face serious competition compared to sonography and CT when categories such as robustness, acquisition time, patient comfort and

health care costs are considered. An abundance of information may be acquired through high resolution imaging and dedicated quantitative MRI sequences, but images and measurements should be reproducible and reliable in their diagnostic value. The redundancy of preparatory steps for the operator within an MRI protocol is an opportunity for more efficient and less time consuming imaging. In addition, the image acquisition process can be improved by means of faster imaging at higher resolution with the implementation of new parallel imaging acceleration techniques, to reduce the risk of motion

in patients with limited breath-hold capabilities. Intelligent imaging protocols, which self-optimize during the course of the examination or use initial pulse sequences to tailor subsequent sequence selection, can provide faster and more efficient examinations, which include quantitative data when appropriate. Combining all of the described improvements may equip liver MRI examinations with sufficient tools to remain unique in delivering disease specific quantitative data while expanding their diagnostic value.

## References

- 1 The global burden of disease: 2004 update. World Health Organization, 2004.
- 2 Hepatitis C. Fact sheet N°164: World Health Organization, July 2012.
- 3 Angelucci E, Brittenham GM, McLaren CE, et al. Hepatic iron concentration and total body iron stores in thalassemia major. *The New England journal of medicine*. 2000;343(5):327-31.
- 4 Rockey DC, Caldwell SH, Goodman ZD, Nelson RC, Smith AD, American Association for the Study of Liver D. Liver biopsy. *Hepatology*. 2009;49(3):1017-44.
- 5 Villeneuve JP, Bilodeau M, Lepage R, Cote J, Lefebvre M. Variability in hepatic iron concentration measurement from needle-biopsy specimens. *J Hepatol*. 1996;25(2):172-7.
- 6 Boll DT, Merkle EM. Diffuse liver disease: strategies for hepatic CT and MR imaging. *Radiographics*. 2009;29(6):1591-614.
- 7 Bonekamp S, Kamel I, Solga S, Clark J. Can imaging modalities diagnose and stage hepatic fibrosis and cirrhosis accurately? *J Hepatol*. 2009;50(1):17-35.
- 8 Meisamy S, Hines CD, Hamilton G, et al. Quantification of hepatic steatosis with T1-independent, T2-corrected MR imaging with spectral modeling of fat: blinded comparison with MR spectroscopy. *Radiology*. 2011;258(3):767-75.
- 9 Yokoo T, Shieh-morteza M, Hamilton G, et al. Estimation of hepatic proton-density fat fraction by using MR imaging at 3.0 T. *Radiology*. 2011;258(3):749-59.
- 10 Cruite I, Schroeder M, Merkle EM, Sirlin CB. Gadoxetate disodium-enhanced MRI of the liver: part 2, protocol optimization and lesion appearance in the cirrhotic liver. *AJR American journal of roentgenology*. 2010;195(1):29-41.
- 11 Bashir MR, Dale BM, Gupta RT, Horvath JJ, Boll DT, Merkle EM. Gradient shimming during magnetic resonance imaging of the liver: comparison of a standard protocol versus a novel reduced protocol. *Investigative radiology*. 2012;47(9):524-9.
- 12 Ringe KI, Husarik DB, Sirlin CB, Merkle EM. Gadoxetate disodium-enhanced MRI of the liver: part 1, protocol optimization and lesion appearance in the noncirrhotic liver. *AJR American journal of roentgenology*. 2010;195(1):13-28.
- 13 Bashir MR, Merkle EM, Smith AD, Boll DT. Hepatic MR imaging for in vivo differentiation of steatosis, iron deposition and combined storage disorder: single-ratio in/opposed phase analysis vs. dual-ratio Dixon discrimination. *European journal of radiology*. 2012;81(2):e101-9.
- 14 Boll DT, Marin D, Redmon GM, Zink SI, Merkle EM. Pilot study assessing differentiation of steatosis hepatitis, hepatic iron overload, and combined disease using two-point dixon MRI at 3 T: in vitro and in vivo results of a 2D decomposition technique. *AJR American journal of roentgenology*. 2010;194(4):964-71.
- 15 Bashir MR, Dale BM, Merkle EM, Boll DT. Automated liver sampling using a gradient dual-echo Dixon-based technique. *Magnetic resonance in medicine : official journal of the Society of Magnetic Resonance in Medicine / Society of Magnetic Resonance in Medicine*. 2012;67(5):1469-77.
- 16 Bashir MR, Zhong X, Dale BM, Gupta RT, Boll DT, Merkle EM. Automated patient-tailored "Screening" of the liver for diffuse steatosis and iron overload using MRI. *Am J Roentgenol*; in press.
- 17 Pineda N, Sharma P, Xu Q, et al. Measurement of Hepatic Lipid: High-Speed T2-Corrected Multi-echo Acquisition at 1H MR Spectroscopy – A Rapid and Accurate Technique. *Radiology* 2009, 252(2):568-76.
- 18 Zhong X, Nickel MD, Kannengiesser SAR, Dale B, Kiefer B, Bashir M. Fat and Iron Quantification Using a Multi-Step Adaptive Fitting Approach with Multi-Echo GRE Imaging. *Proc. Intl. Soc. Magn. Reson. Med* 2013, 21:401.
- 19 Willatt JM, Hussain HK, Adusumilli S, Marrero JA. MR Imaging of hepatocellular carcinoma in the cirrhotic liver: challenges and controversies. *Radiology*. 2008;247(2):311-30.
- 20 Mori K, Yoshioka H, Takahashi N, et al. Triple arterial phase dynamic MRI with sensitivity encoding for hypervascular hepatocellular carcinoma: comparison of the diagnostic accuracy among the early, middle, late, and whole triple arterial phase imaging. *AJR Am J Roentgenol*. 2005;184(1):63-9.
- 21 Roth CJ, Boll DT, Wall LK, Merkle EM. Evaluation of MRI acquisition workflow with lean six sigma method: case study of liver and knee examinations. *AJR American journal of roentgenology*. 2010;195(2):W150-6.
- 22 Martin DR, Sharma P, Kitajima H. Challenges and Clinical Value of Automated and Patient-Specific Dynamically Timed Contrast-Enhanced Liver MRI Examination. *MAGNETOM Flash* 2009; 3:40-5.
- 23 Breuer FA, Blaimer M, Mueller MF, et al. Controlled aliasing in volumetric parallel imaging (2D CAIPRINHA). *Magn Reson Med* 2006, 55, 549-56.
- 24 Riffel P, Attenberger UI, Kannengiesser S, Nickel M, Arndt C, Meyer M, Schoenberg SO, Michaely HJ. Highly Accelerated T1-Weighted Abdominal Imaging Using 2-Dimensional Controlled Aliasing in Parallel Imaging Results in Higher Acceleration: A Comparison With Generalized Autocalibrating Partially Parallel Acquisitions Parallel Imaging. *Investigative Radiology* 2013; in press; DOI 10.1097/RLI.0b013e31828654ff.

## Contact

Tobias Heye  
University Hospital Basel  
Department of Radiology  
Petersgraben 4  
CH-4031 Basel  
Switzerland  
Phone: +41 (0)61 328 6324  
tobias.heye@usb.ch

# Faster Abdominal MRI Examinations by Limiting Table Movement

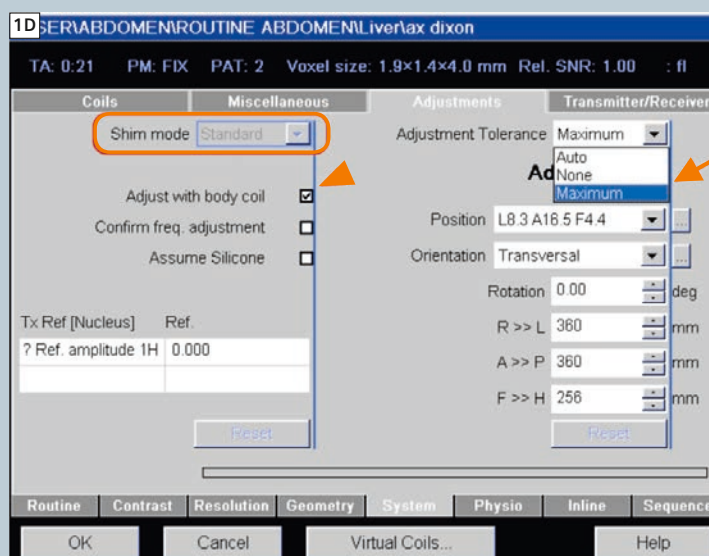
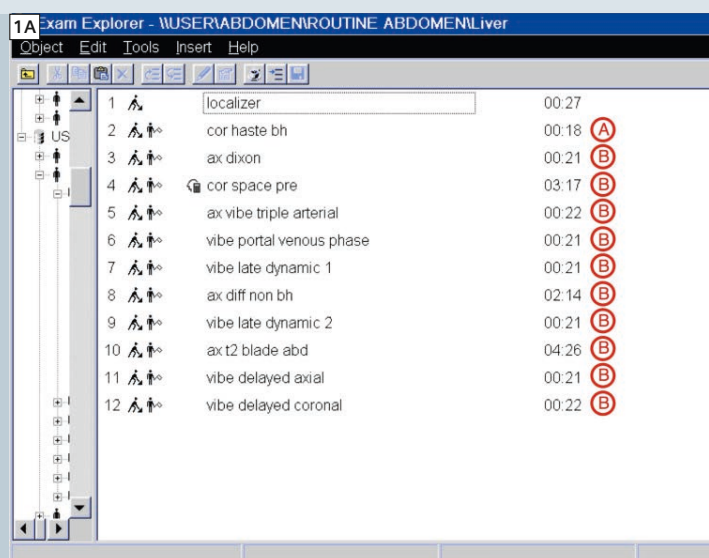
Mustafa Rifaat Bashir<sup>1</sup>; Brian Marshall Dale<sup>2</sup>; Wilhelm Horger<sup>3</sup>;  
Daniel Tobias Boll<sup>1</sup>; Elmar Max Merkle<sup>1</sup>

<sup>1</sup>Radiology, Duke University Medical Center, Durham, NC, USA

<sup>2</sup>Siemens Healthcare, Cary, NC, USA

<sup>3</sup>Siemens Healthcare, Erlangen, Germany

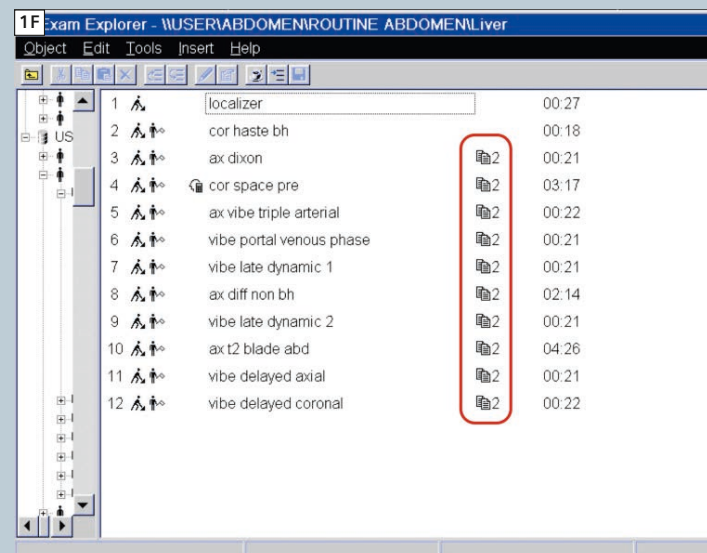
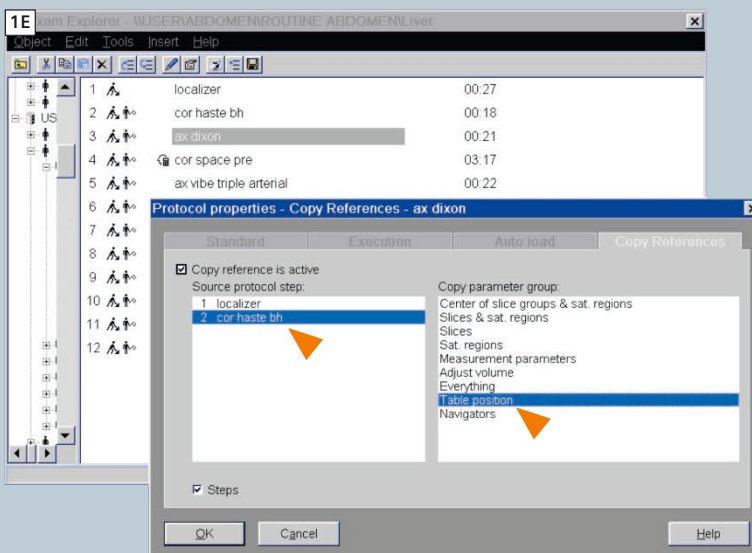
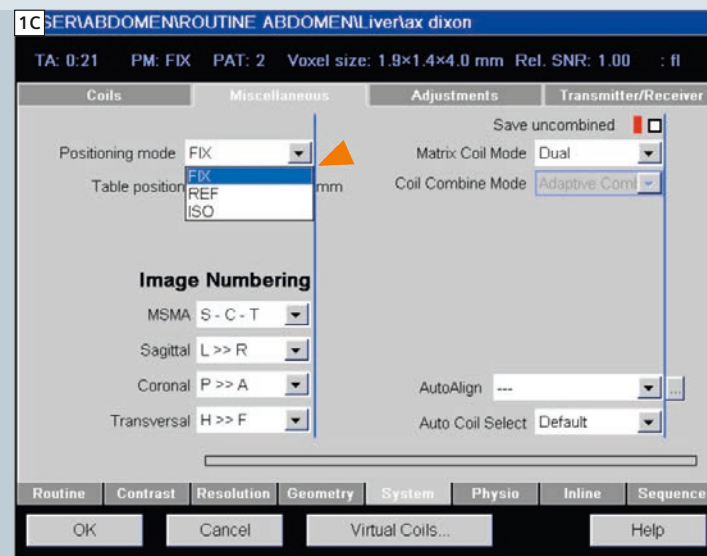
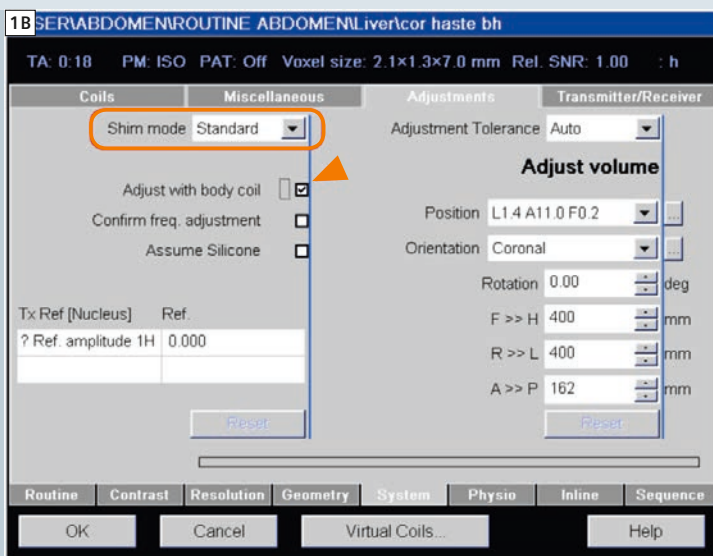
**1** How to create a minimized shimming protocol. Modifications will be made to pulse sequences following the initial localizers (**1A**). For the second sequence in the scan protocol, 'Shim mode' is set to 'Standard', and 'Adjust with body coil' is selected (**1B**). For the third and subsequent sequences, 'Positioning mode' is set to 'FIX' (**1C**). 'Shim mode' is set to 'Standard', 'Adjust with body coil' is selected, and 'Adjustment Tolerance' is set to 'Maximum' (**1D**). Finally, for the third sequence, a reference is created to the table position of the second sequence (**1E**). The same reference is created for all subsequent sequences (**1F**).

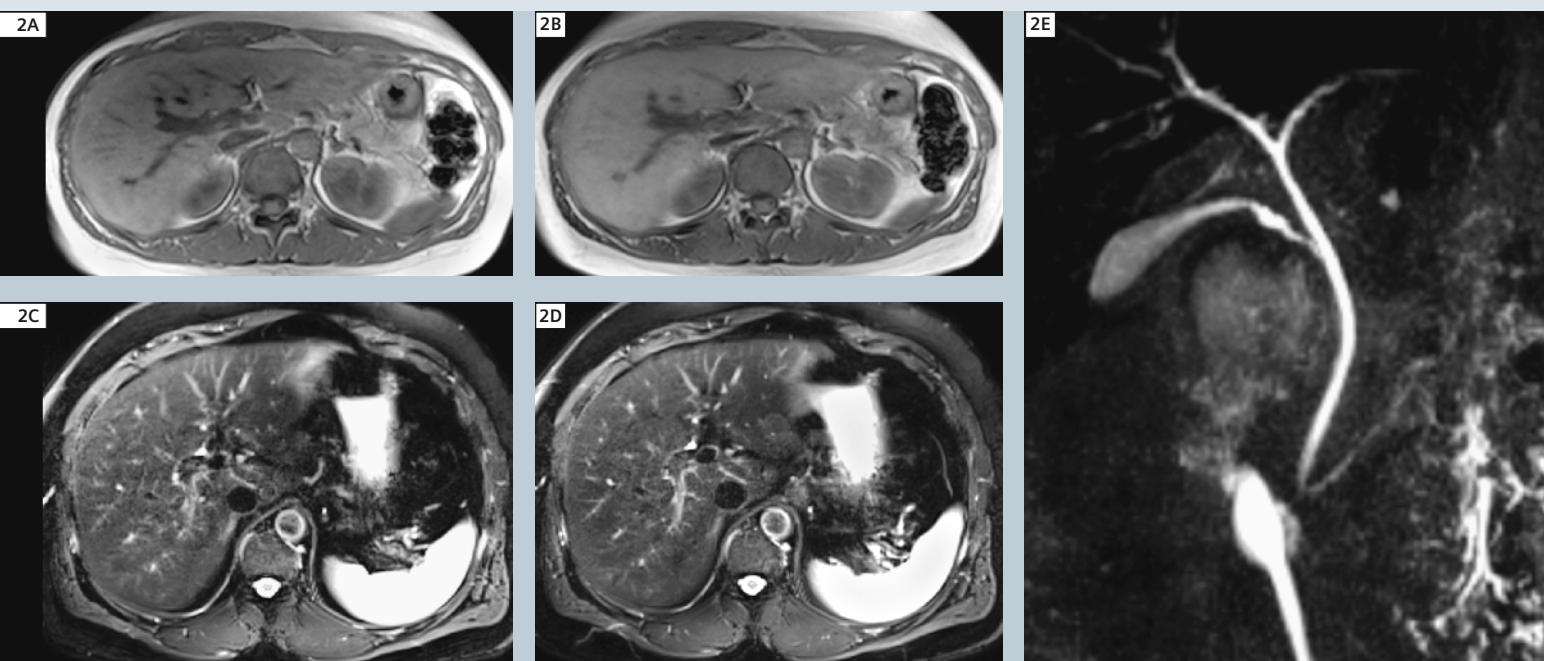


Hepatic magnetic resonance imaging (MRI) is widely used for a variety of indications, including characterization of focal lesions, detection of diffuse liver disease, as well as evaluation for hepatocellular carcinoma in patients with chronic hepatitis or cirrhosis [1-8]. One of the main criticisms of hepatic MRI is scan time, both in terms of length and variability. In a small prospective study at a single center, table times in contrast-enhanced MRI of the liver were shown to vary from 19 up to 58 minutes, even when examinations were performed by an experienced technologist [9]. In a detailed analysis of MRI scanner

activity during various imaging examinations, we observed that the number of adjustments performed by the scanner prior to initiating a pulse sequence was higher when imaging the liver as compared to the knee [10]. These adjustments take time, with the acquisition of shim data alone taking up to 20 s per pulse sequence. The need to acquire new adjustment data is dictated, in part, by table movement, after which field homogeneity in the scan volume must be measured, and additional adjustments made as needed. This increases the time that the MRI system spends preparing to scan but not actually acquiring image data [10].

A more recent study showed that a scan protocol in which the table moves only once during the examination achieves significant total scan time savings by obviating the need to gather new adjustment data during the course of the examination [11]. For every step in which the table moves and new shim data is acquired, this protocol change reduces the time spent collecting prescan adjustment data by approximately 30 s. In that study, a reduction in total examination time of up to 20% was observed in a non-contrast liver MRI/MRCP protocol, with no observable change in image quality.





## Methods

Automated algorithms to minimize table movement have already been incorporated into MAGNETOM MRI systems under *syngo* MR D11 and later software versions. Under earlier software versions, a few simple steps can be performed to convert a standard MRI protocol into a minimized shimming protocol, in order to realize the time savings previously described. These changes can all be made via the Exam Explorer (Fig. 1A).

### Pulse Sequence #1 – localizer

The first pulse sequence of an examination is a localizer, typically utilizing either a three-plane TrueFISP or HASTE technique. At the MRI console, under the 'Sequence' card, the Shim is set to 'None' (typically the default value), and precalibrated prescan data is used with no need to acquire new prescan data. No additional modification of this sequence is required.

### Pulse Sequence #2 – first and only table move

Using the image data from the localizer sequence, the image volume for Pulse Sequence #2 is prescribed. This volume should be centered on the area of interest and rather large, covering the volume of interest for the entire examination; at our

institution, we typically use a coronal HASTE sequence for this purpose. The prescan data acquired in this step, including shim data, will be carried forward for the remainder of the examination. The following modifications are made to this pulse sequence:

1. In the 'System' card, under the 'Adjustments' tab, set 'Shim mode' to 'Standard'. Check the 'Adjust with body coil' box (Fig. 1B).

### Pulse Sequences #3 and higher – no further table movements

For all subsequent pulse sequences, table movement is disallowed, and prescan adjustment data from Pulse Sequence #2 is carried forward, so that as little time as possible is spent acquiring new adjustment data. The following modifications are made:

1. In the 'System' card, under the 'Miscellaneous' tab, set 'Position mode' to 'FIX' (Fig. 1C).
2. In the 'System' card, under the 'Adjustments' tab: set 'Shim mode' to 'Standard'; select 'Adjust with body coil'; and set 'Adjustment Tolerance' to 'Maximum' (Fig. 1D).
3. From the Exam Explorer, right-click on the sequence and select 'Properties'.

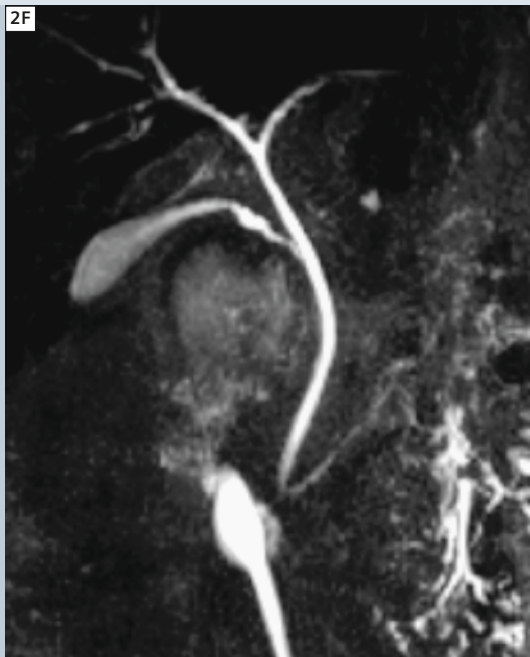
Under the 'Copy References' tab, check the 'Copy reference is active' box, then select Pulse Sequence #2 in the left-hand window and 'Table position' in the right-hand window (Fig. 1E). In combination with step #2 above, this ensures that the MRI system table will not move when progressing to later pulse sequences in the examination, despite different prescriptions for the imaging volume.

4. Repeat steps 1–4 for all subsequent sequences (Figure 1F).

## Discussion

Preparatory adjustments made by an MRI system are essential to realize excellent image quality. In particular, adequate shimming is necessary to ensure magnetic field homogeneity. Shimming is a process whereby the main magnetic field ( $B_0$ ) is fine-tuned to compensate for field fluctuations and inhomogeneities introduced by the presence of the human body within the scanner. These adjustments are applied specifically to a volume within the bore of the magnet (based on the anticipated imaging volume), attempting to optimize magnetic field homogeneity within that volume while sacrificing field homogeneity outside of the volume.

2F



**2** Comparison of image quality between conventional (2A, 2C, and 2E) and minimized shimming (2B, 2D, and 2F) protocols in three different subjects. Note similar tissue contrast fat, suppression, image sharpness, and overall image quality.

A scanning protocol which prohibits table movement can reduce total table time by removing the need to repeatedly acquire adjustment data, particularly time-consuming shim data, throughout the course of the examination. Even though placing the liver at isocenter during an inspiratory breath-hold means that it would be located, on average, cranial to isocenter during free breathing sequences, the above study observed no differences in image quality in any type of pulse sequence. Note we do not suggest that patient- and position-specific shimming is unnecessary, but rather that if patient position can be maintained during the examination and adequate initial adjustment data is acquired, table movement during the examination and much of the additional adjustment data may be unnecessary. This holds true for both typical quantitative and qualitative abdominal MRI applications (Fig. 2). In addition, it may be possible to achieve the same time savings by any protocol which prevents table movement, for example a protocol where the image volumes of all pulse sequences are centered in the same location.

An overall workflow analysis of abdominal MRI acquisitions shows that shortening data acquisition times can reduce over-

all imaging time [10]. This is likely to be of greatest benefit in examinations where the large majority of table time is spent acquiring image data, e.g. musculoskeletal and brain examinations [10]. However, much less attention has been directed to other events which contribute to total imaging time, including time spent preparing the patient for imaging as well as scanner preparation, such as image prescription and prescan adjustments. In abdominal MRI, where preparatory activities take up a large proportion of total table time, reducing the prescan time represents an important opportunity to reduce total table time substantially [10]. Since this methodology is independent of the particular details of the imaging protocol, it could be applied to a variety of routine clinical and novel imaging techniques. In conclusion, any MRI protocol can be easily modified to minimize the time spent collecting prescan adjustment data. In certain scenarios, such modifications can reduce total scan time by as much as 20% with no sacrifice in image quality.

## References

- 1 Kukuk GM, Gieseke J, Weber S, et al. Focal liver lesions at 3.0 T: lesion detectability and image quality with T2-weighted imaging by using conventional and dual-source parallel radiofrequency transmission. *Radiology* 2011 May;259(2):421-8.
- 2 Purysko AS, Remer EM, Veniero JC. Focal liver lesion detection and characterization with GD-EOB-DTPA. *Clin Radiol* 2011 Jul;66(7):673-84.
- 3 Bashir MR, Merkle EM, Smith AD, Boll DT. Hepatic MR imaging for in vivo differentiation of steatosis, iron deposition and combined storage disorder: Single-ratio in/opposed phase analysis vs. dual-ratio Dixon discrimination. *Eur J Radiol* 2011 Feb 15.
- 4 Meisamy S, Hines CD, Hamilton G, et al. Quantification of hepatic steatosis with T1-independent, T2-corrected MR imaging with spectral modeling of fat: blinded comparison with MR spectroscopy. *Radiology* 2011 Mar;258(3):767-75.
- 5 Hankins JS, McCarville MB, Loeffler RB, et al. R2\* magnetic resonance imaging of the liver in patients with iron overload. *Blood* 2009 May 14;113(20):4853-5.
- 6 Carneiro AA, Fernandes JP, de Araujo DB, et al. Liver iron concentration evaluated by two magnetic methods: magnetic resonance imaging and magnetic susceptibility. *Magn Reson Med* 2005 Jul;54(1):122-8.
- 7 Marin D, Di Martino M, Guerrisi A, et al. Hepatocellular carcinoma in patients with cirrhosis: qualitative comparison of gadobenate dimeglumine-enhanced MR imaging and multiphase 64-section CT. *Radiology* 2009 Apr;251(1):85-95.
- 8 Kim TK, Lee KH, Jang HJ, et al. Analysis of gadobenate dimeglumine-enhanced MR findings for characterizing small (1–2-cm) hepatic nodules in patients at high risk for hepatocellular carcinoma. *Radiology* 2011 Jun;259(3):730-8.
- 9 Roth CJ, Boll DT, Chea YW, Wall LK, Merkle EM. Implementation of graphic user interface screen capture solution for workflow assessment of abdominal MR examinations valuable tool to analyze discrepancies in expected and experienced MR table time. *Acad Radiol* 2009 Oct;16(10):1286-91.
- 10 Roth CJ, Boll DT, Wall LK, Merkle EM. Evaluation of MRI acquisition workflow with lean six sigma method: case study of liver and knee examinations. *AJR Am J Roentgenol* 2010 Aug;195(2):W150-6.
- 11 Bashir MR, Dale BM, Gupta RT, Horvath JJ, Boll DT, Merkle EM. Gradient shimming during magnetic resonance imaging of the liver: comparison of a standard protocol versus a novel reduced protocol. *Invest Radiol*. 2012 Sep;47(9):524-9.

## Contact

Mustafa Rifaat Bashir, M.D.  
Duke University Medical Center 3808  
Durham, NC 27710  
USA  
Phone: +1 919 684 7663  
mustafa.bashir@duke.edu

# Bandwidth in MRI?

Joachim Graessner, Dipl.-Ing.

Siemens Healthcare, Hamburg, Germany

Questions about the term 'bandwidth' are most frequently asked during MR trainings and discussions regarding MR parameters and image quality. This article is intended to clarify the meaning of bandwidth in MRI, to show dependencies with other MR parameters,

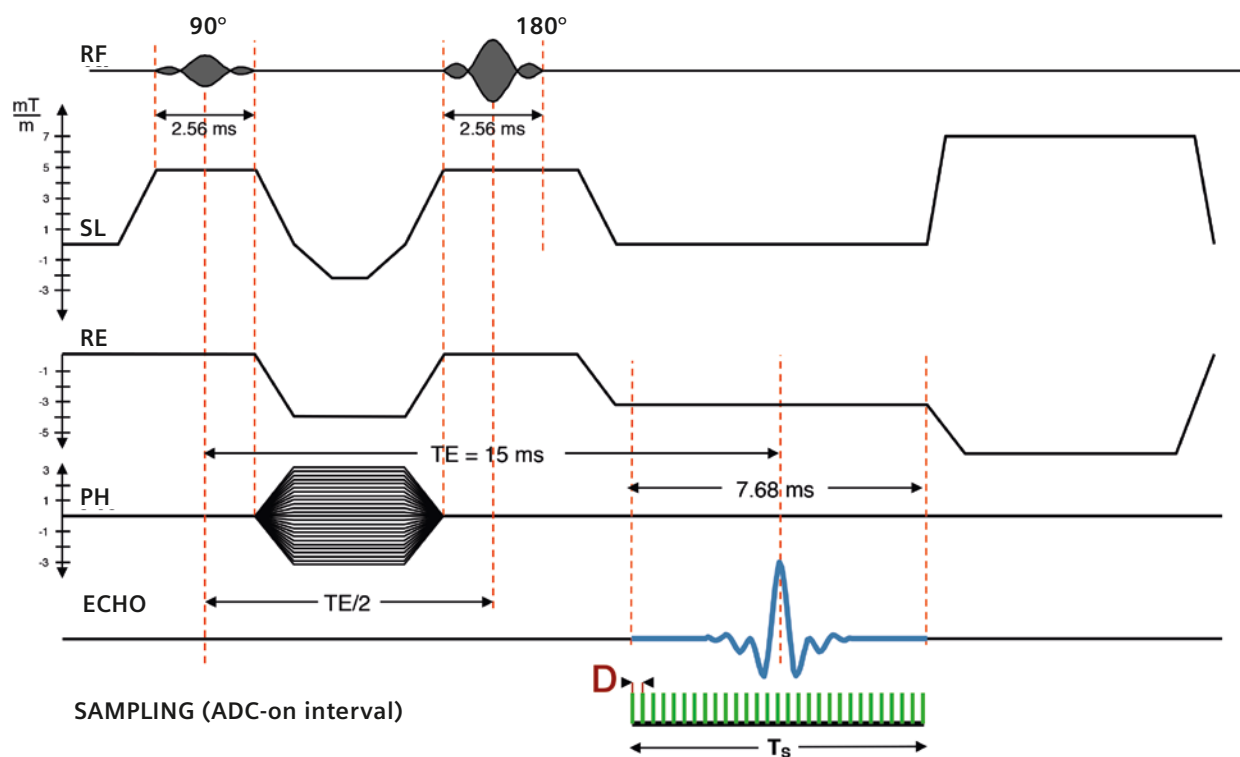
and to give hints for daily routine work and protocol optimization. The bandwidth occurs twice in the course of an MR sequence (Fig.1): during transmission describing properties of the radiofrequency (RF) pulses and during reception of the MR signal.

## Transmission phase

During transmission you have to apply RF pulses which contain a certain range of frequencies, i.e., bandwidth, to excite a discrete slice thickness or volume while a local gradient is on as well. The bandwidth typically lies in the range of a

1

se\_15b130 Sequence Timing Diagram



1 Sequence timing for se15\_b130.

few kilohertz (kHz). The syngo user interface offers three types of pulses for most sequences in the Sequence parameter card, part 2: Low SAR, Normal, and Fast (Fig. 2).

Pros and Cons for RF pulse types with timing examples:

#### Low SAR (3.84 ms)

- Longer RF pulse with good slice profile
- Reduced SAR values (lower amplitude)
- Less crosstalk between slice; narrower gaps tolerated
- Longer minimum TEs and TRs

#### Normal (2.56 ms)

- Normal RF pulse with good slice profile
- Optimized SAR behavior

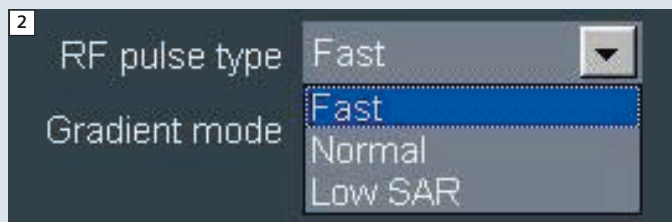
#### Fast (1.28 ms)

- Shorter RF pulse, with a compromised slice profile
- Higher SAR compared to the other modes (higher amplitude)
- Shorter echo spacing (ES)
- Opportunity for shorter TEs and TRs
- Fewer susceptibility artifacts

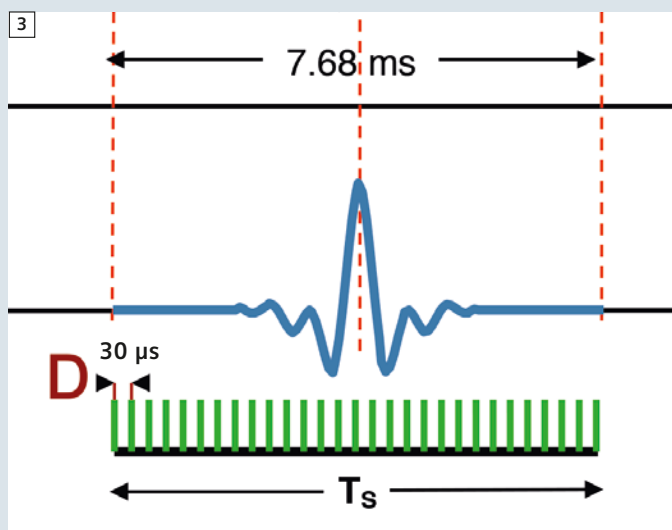
The 'Fast' mode is mainly applied in sequences where measurement speed and short echo spacing (ES) – the time from one echo to the next echo – is essential for good image quality: HASTE, EPI, TrueFISP, and TurboFlash. These modes can be combined with up to three gradient modes: Whisper, Normal and Fast. The gradient modes influence the slew rate of the gradient pulses, or the steepness of the ramps from zero to full gradient strength and back. The trade-off for faster sequence timing with shorter TEs and TRs usually results in more noise and a higher potential for peripheral stimulation.

### Reception phase

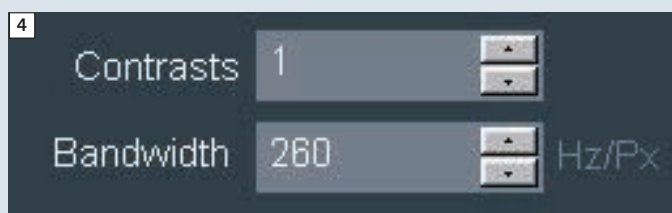
When the echo signal appears, a read-out gradient is switched on and the analog-digital-converter (ADC) samples this signal. The gradient encodes different rows of frequencies into signal; the time-amplitude integral defines the measured field-of-view (FOV). The ADC is virtually asking the echo-signal (e.g., every 30 microsecond ( $\mu$ s)) how high its



**2** RF pulse types.



**3** Sampling time  $T_s$  and dwell time  $D$ .



**4** Bandwidth in the syngo user interface.

amplitude is and writes these values in a digital fashion into the memory of the image computer. This time is called the dwell time  $D$ . For a 256 base matrix this process has to be repeated 256 times. The whole sample period  $T_s$  will be in this example (Fig. 3):

$$T_s = 256 \times 30 \mu s = 7.680 \text{ ms}$$

$$T_s = N \times D \text{ with } N = \text{matrix in read}$$

The frequency content of this sampled signal is the reciprocal of the dwell time:

$$f = 1/D.$$

In the above example it is roughly 33 kHz.

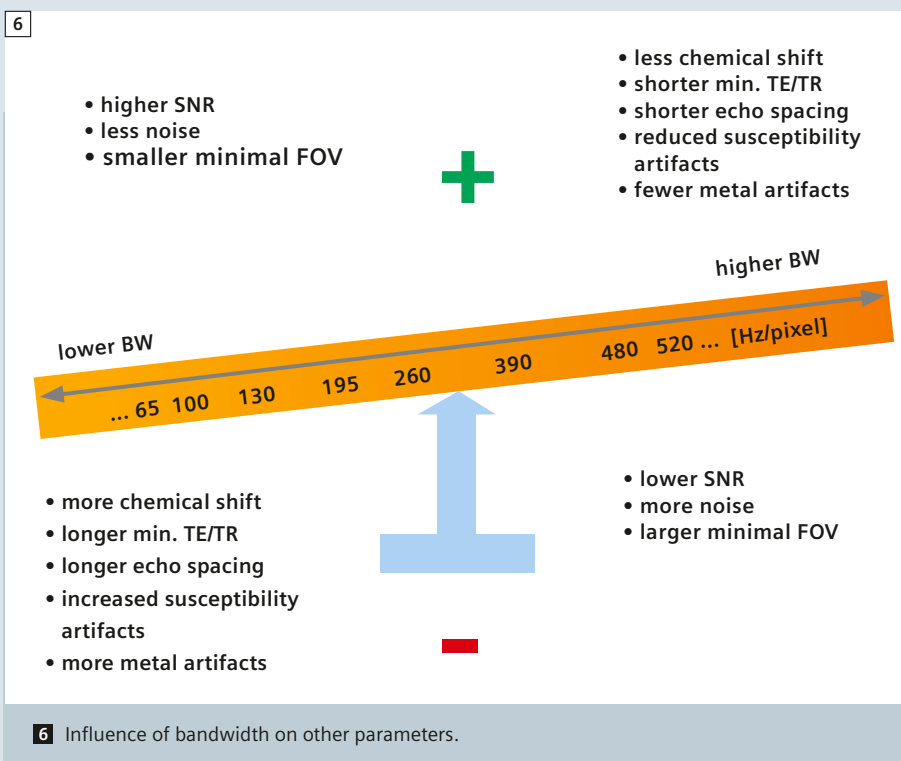
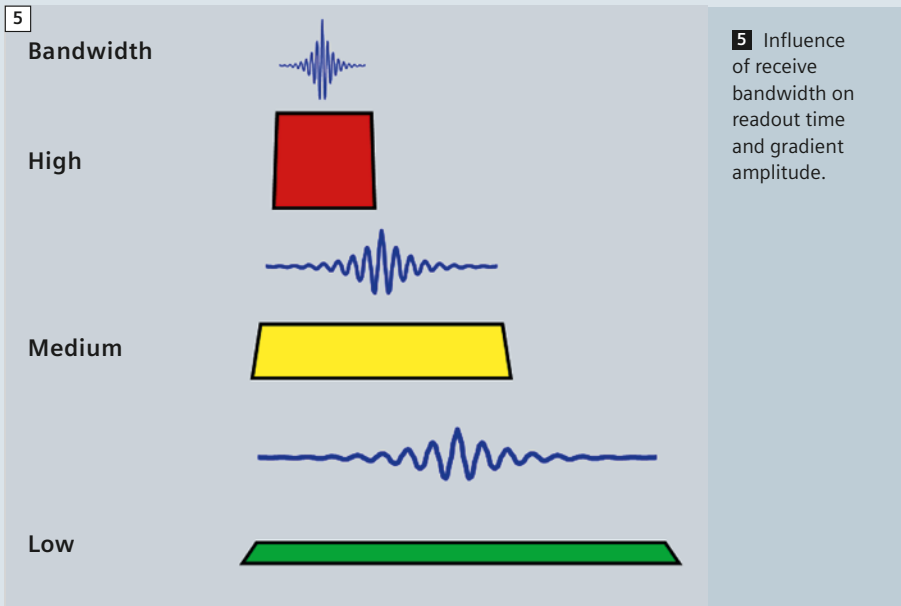
The magic term bandwidth (BW) is the reciprocal of the total sampling time  $T_s$  and has the unit of Hz/pixel:

$$\text{Bandwidth: } BW = 1/T_s \text{ [Hz/pixel]}$$

The parameter 'Bandwidth' is found on the Sequence parameter card, part 1 (Fig. 4).

The bandwidth describes in a simplified manner which frequency range from our analyzed echo signal is transferred into one pixel:

1. lower left pixel: 0-130 Hz
2. lower left pixel 130-260 Hz and so forth. If you continue this fill-up task to the last pixel of a 256 matrix you end up with 33 kHz in the lower right pixel.



Increasing the bandwidth reduces the sampling time  $T_s$  and shortens the sequence timing, allowing shorter TE and TR values and vice versa (Fig. 5). The disadvantage of a higher bandwidth is the larger amount of noise which is sampled due to larger frequency range.

This translates into a lower signal-to-noise-ratio (SNR). A slightly bumpy analogy is a motorway, where you have a speed limit and the number of cars per hour is limited. If you increase the speed limit, more cars will pass per hour and the noise for the neighbors rises as well.

On the positive side we have the shorter echo spacing (ES) which delivers less blurring in the images. The lipid signal in turbo spin echo protocols is also influenced by the echo spacing and the turbo factor (TF) [1]; the shorter the ES and the higher the TF, the brighter the fat in TSE protocols. The larger readout (RE) gradient amplitude needed for a high BW protocol increases the minimally adjustable FOV (Fig. 6). Furthermore, high bandwidth protocols play an important role in metal artifact reduced scanning. Shorter optimized excitation pulses combined with short readout intervals and short ES enables fewer distortions due to conditional implants. This feature is enhanced with optimized protocols which use WARP and VAT (view angle tilting) [2–4].

Last but not least, the chemical shift between water and fat gets smaller with high BW and larger with lower BW. This feature is of less importance for fatsat protocols. Fat resonates at an approximately 3.3 ppm lower frequency than water. Although commonly excited in the first part of a sequence, fat and water from the same physical place answer with different frequencies. In the above mentioned sorting process of frequency ranges into pixels we have to face a missorting. Fat will always appear shifted to lower frequencies by a certain amount of pixel in the readout direction. The only exception is the EPI sequence where we have a very strong chemical shift artifact in the phase encoding direction (PH) due to the long sampling period producing echoes. This very long sampling period in the order of >40 ms or more translates into a quite low bandwidth (<25 Hz/pixel). Fatsat is therefore mandatory for EPI measurements.

The chemical shift in readout direction is indicated as a mouse-over tooltip on the bandwidth field in the Sequence parameter card, part 1 (Fig. 7).

As one can see, chemical shift is not a big issue at low field strengths (Table 1). It is getting important at 1.5T and above for the range of practical bandwidth of a few hundreds Hz/pixel. But with the rise of the magnetic field the resolution typically goes up as well, keeping the abso-

lute chemical shift in millimeters reasonably low. A protocol at 3T with a bandwidth of 195 Hz/pixel and an inplane resolution of 0.3 mm creates an absolute chemical shift of less than 0.7 mm. Figure 8 demonstrates in an exaggerated way the artificial movement of the intervertebral discs (orange) towards the upper vertebrae or the spinal cord depending on the chosen readout direction and bandwidth option. The low bandwidth examples should be avoided in daily routine, although one may gain SNR and shorter scan time with lower bandwidth protocols.

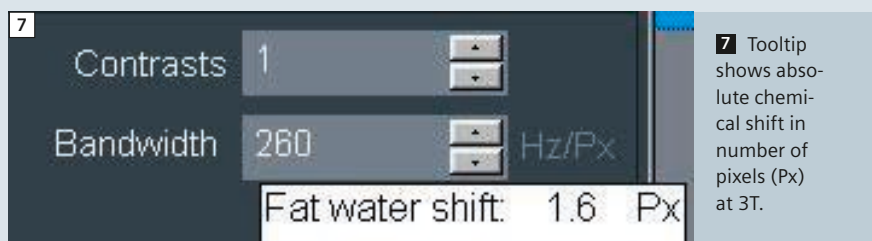


Table 2 shows the effects of optimizing a TSE protocol with respect to change of bandwidth and resolution for a 1.5T scanner. Identical SNR is the border condition for these four examples. TE was kept in the mid thirty ms range. The

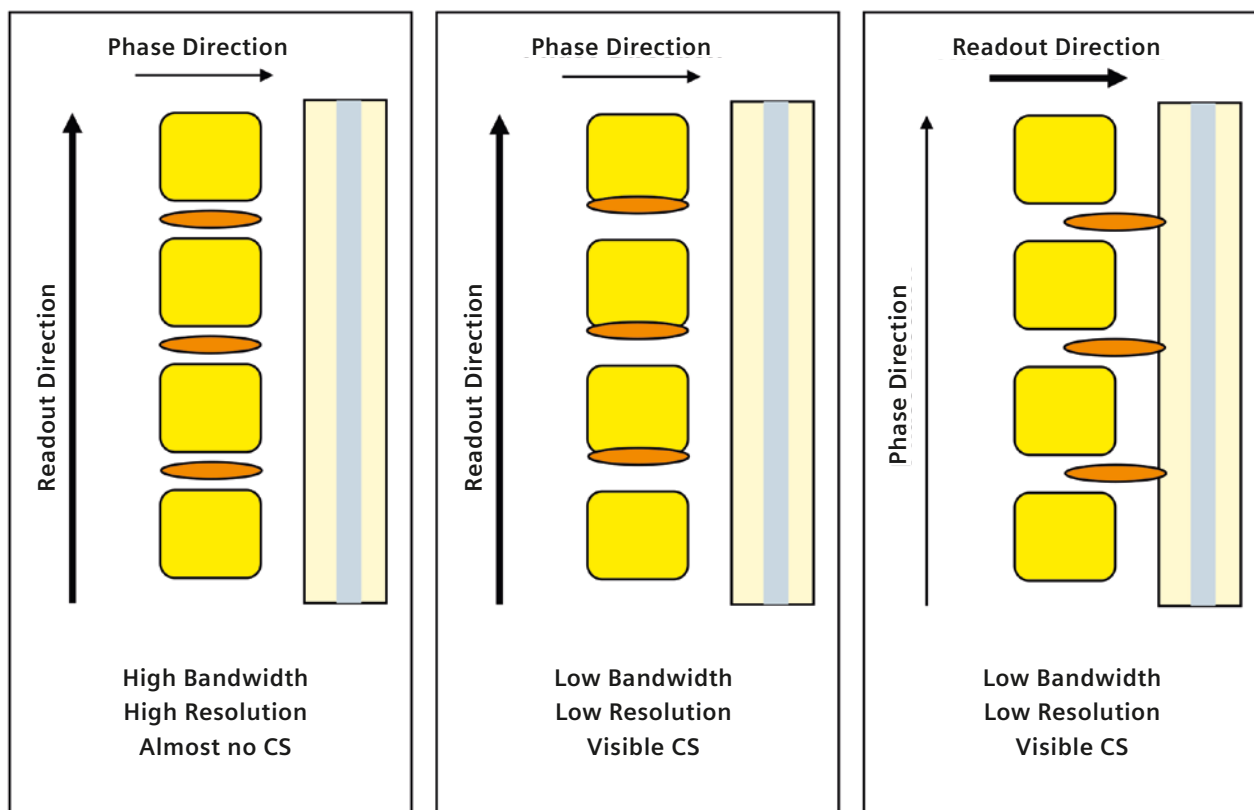
penalty for better resolution is usually longer measurement time. Personal taste and application dictates the parameters chosen. Starting with protocol B, one can speed up the scan by halving the bandwidth to

**Table 1: Absolute pixel shift for different field strengths.**

Bandwidth*	Readout time	Chemical Shift* 0.35T	Chemical Shift* 1T	Chemical Shift* 1.5T	Chemical Shift* 3T	Chemical Shift* 7T	Relative SNR change*
[Hz/pixel]	[ms]	[pixel]	[pixel]	[pixel]	[pixel]	[pixel]	[%]
3000	0.330	0.017	0.05	0.075	0.15	0.3	-79
2000	0.500	0.025	0.07	0.1	0.2	0.5	-74
1000	1.000	0.05	0.1	0.2	0.4	1.0	-64
520	1.920	0.09	0.3	0.4	0.8	1.9	-50
480	2.080	0.1	0.3	0.4	0.9	2.1	-48
390	2.560	0.13	0.35	0.5	1.1	2.5	-42
260	3.840	0.2	0.5	0.8	1.6	3.8	-29
195	5.120	0.25	0.7	1.1	2.2	5.1	-18
<b>130</b>	<b>7.680</b>	<b>0.4</b>	<b>1.1</b>	<b>1.6</b>	<b>3.2</b>	<b>7.6</b>	<b>0</b>
100	1.000	0.5	1.4	2.1	4.2	9.9	14
78	12.280	0.6	1.8	2.7	5.4	12.7	29
65	15.380	0.8	2.1	3.2	6.4	15.2	41
50	20.000	1.0	2.8	4.2	8.4	19.8	61

\*Rounded values for convenience.

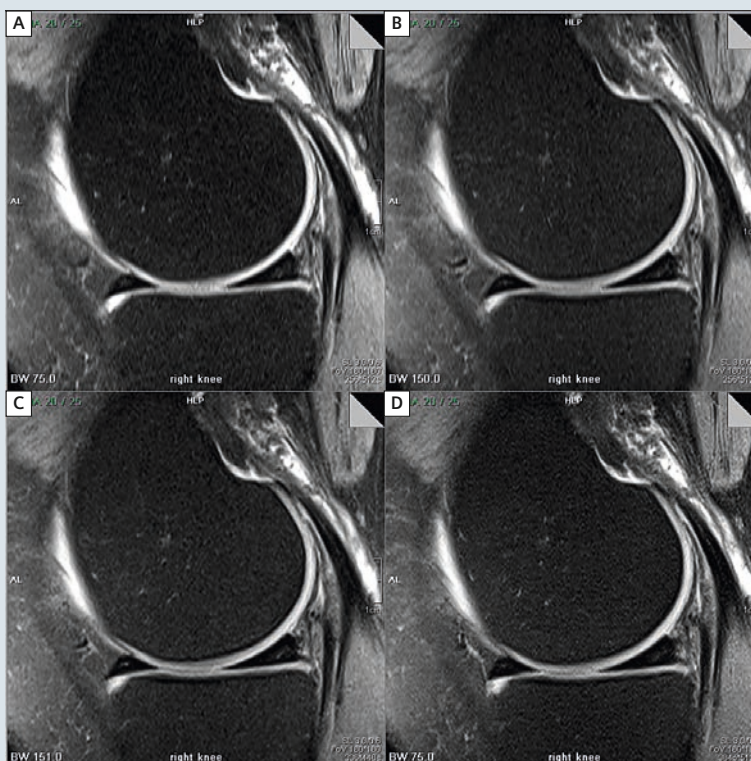
8



8 Chemical shift (CS) on an example sagittal spine.

compensate for the SNR loss coming from the reduction of acquisitions. An increase of the inplane resolution in protocol C and D results in an obvious prolongation of the scan time which could be kept tolerable when reducing the bandwidth. In example D partial Fourier, i.e., reducing the measured turbofactor, allows a TR minimization for an acceptable scan time. One could save further time in this example by a decrease of phase oversampling, which was chosen 100% for a phase encoding in head-feet direction to minimize flow artifacts from the arteries; a slight increase of the FOV, e.g., to 200 mm, could compensate for this SNR reducing step though sacrificing some hundreds of a mm inplane resolution.

On a 3T system one should at least increase the bandwidth by 50% and save time by adjusting the other parameters. The higher signal of 3T supports this measure.



9 Image examples for table 2.

**Table 2: Protocol optimization.**

Knee sagittal, 25 slices, FOV 180 mm, 3 mm, matrix 512 x 256, TF 7, weak Fatsat, 100% Phase OS, iPAT 2, 15-channel coil, identical SNR.

#	Parameter	Bandwidth	Matrix	Resolution	Scantime	TR	TE	Echo-spacing	Averages	partial Fourier	rel. SNR
	Unit	[Hz/pixel]	-	mm <sup>2</sup>	min:s	ms	ms	ms	-	-	-
A	low BW normal Resolution*	75	256 x 512	$0.7 \times 0.35 =$ <b>0.245</b>	2:46	4020	36	17.8	1	off	1
B	high BW normal Resolution*	150	256 x 512	$0.7 \times 0.35 =$ <b>0.245</b>	3:32	2770	34	11.2	2	off	1
C	high BW higher Resolution	150	336 x 448	$0.54 \times 0.4 =$ <b>0.216</b>	<b>4:43</b>	2870	34	11.7	2	off	1
D	low BW higher Resolution*	75	384 x 512	$0.47 \times 0.35 =$ <b>0.165</b>	<b>6:04</b>	3240	37	18.7	2	on	1

\* In Accordance to the German MR Guidelines (BÄ)

## Further reading

1. Magnets, Spins and Resonances; Siemens 2003.
2. Magnets, Flow and Artifacts; Siemens 2004.
3. The Physics of Clinical MR Taught Through Images: Runge, Nitz, Schmeets; Thieme 2008.
4. MRI the Basics: Hashemi, Bradley, Lisanti; LWW 2010.

5. Handbook of MRI Sequences: Bernstein, King, Zhou; Elsevier 2004.
6. MRI from Picture to Proton: McRobbie, Moore, Graves, Prince; Cambridge 2007. Especially recommended for the German speaking community:
7. Praxiskurs MRT: Nitz, Runge; Thieme 2011.
8. MRT-Guide für MTRA/RT: Nitz; Thieme 2012.

## References

- 1 Piraino D, Hardy PA, Schils JP, Richmond BJ, Tkach JA, Belhobek GH. (1993). Fast Spin-Echo Imaging of the Knee: Factors Influencing Contrast. JMIR 3:835-842.
- 2 Ulbrich EJ, Sutter R, Ranieri FA, Nittka M, Pfirrmann CW (2012). STIR Sequence With Increased Receiver Bandwidth of the Inversion Pulse for Reduction of Metallic Artifacts. AJR 199: 735-742.
- 3 Sutter R, Ulbrich EJ, Jellus V, Nittka M, Pfirrmann CWA (2012). Reduction of Metal Artifacts in Patients with Total Hip Arthroplasty with Slice-encoding Metal Artifact Correction and View-Angle Tilting MR Imaging. Radiology 265: 204-214.
- 4 Koch KM, Hargreaves BA, Butts Pauly K, Chen W, Gold GE, King KF (2010). Magnetic Resonance Imaging Near Metal Implants. JMIR 32: 773-787.

## Helpful links



The Impact of Bandwidth on MR Image Quality: Chen Lin, 2012.  
<http://www.indiana.edu/~mri/seminars/slides/The%20Impact%20of%20Bandwidth%20on%20MRI%20Image%20Quality%20CL20120324.pdf>



Metal Artifact Reduction in MRI – High Bandwidth Techniques, SEMAC, and VAT: Val Runge, 2013.  
[http://www.clinicalmri.com/pdf/Garmisch/2\\_Garmisch\\_2013\\_Metal\\_artifact\\_reduction.pdf](http://www.clinicalmri.com/pdf/Garmisch/2_Garmisch_2013_Metal_artifact_reduction.pdf)

## Contact

Joachim Graessner, Dipl.Ing.  
 Siemens AG Healthcare  
 GER H IM BM MR  
 Lindenplatz 2  
 20099 Hamburg  
 Germany  
[joachim.graessner@siemens.com](mailto:joachim.graessner@siemens.com)

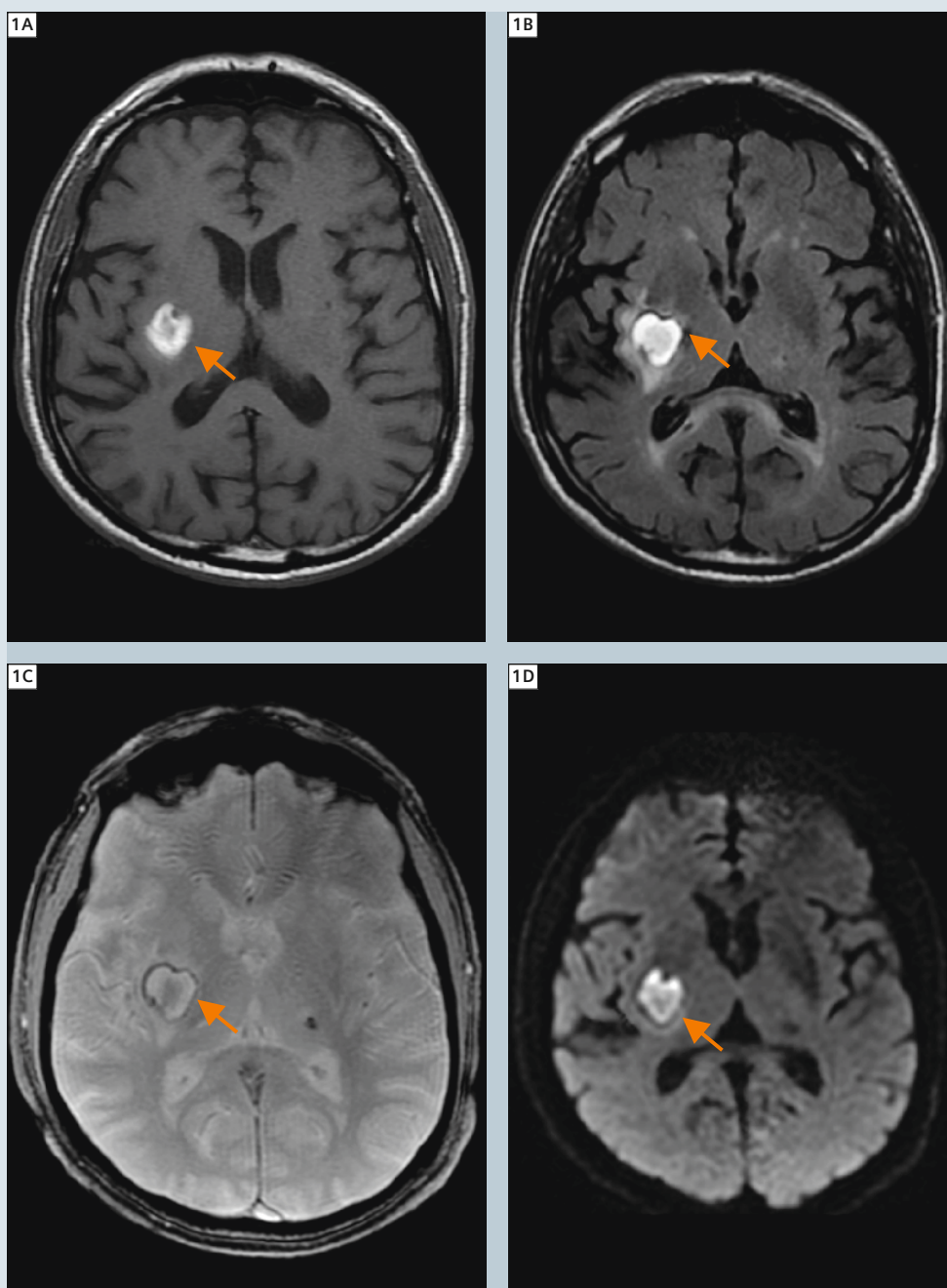
# Indications for 24 Hours/7 Days Emergency MRI

Marc-André Weber, M.D., M.Sc.; Jürgen Biederer, M.D.

Heidelberg University Hospital, Diagnostic and Interventional Radiology, Heidelberg, Germany

## Introduction

For many years MR imaging (MRI) has been considered a second-line procedure required for further diagnostic work-up after first-line imaging with x-ray, ultrasound or even computed tomography (CT) in the emergency room. However, the increasing performance of modern MR equipment and sequence design have broadened the range of indications, now making MRI the first-line imaging modality of choice for a number of clinical conditions. This is most obvious in neurovascular emergencies, but it also applies to a number of other indications. More and more, an 'emergency MRI' is being requested at night or during weekends. In most cases, the decision whether to perform it is taken according to the particular circumstances, such as the availability of sufficiently skilled staff and radiological expertise. The aim of this article is to suggest stratification criteria and to provide a list of clinical situations that might justify the performance of an MRI scan during night or weekend shifts based on the clinical relevance, i.e. immediate consequences. Conditions that do not require direct therapeutic intervention should not trigger an MRI scan outside the regular schedules. The limitation to only a small number of indications improves clinical decision-making and facilitates the preparation and training of the staff for these situations. The following suggestions have been developed at University Hospital Heidelberg in cooperation between the Department of Diagnostic and Interventional Radiology (Head: Hans-Ulrich Kauczor, M.D.), the Orthopedics and Trauma Surgery Clinic, the Spinal Cord Injury Center, the Vascular Surgery Clinic, the Department of Anesthesiology, and the Center

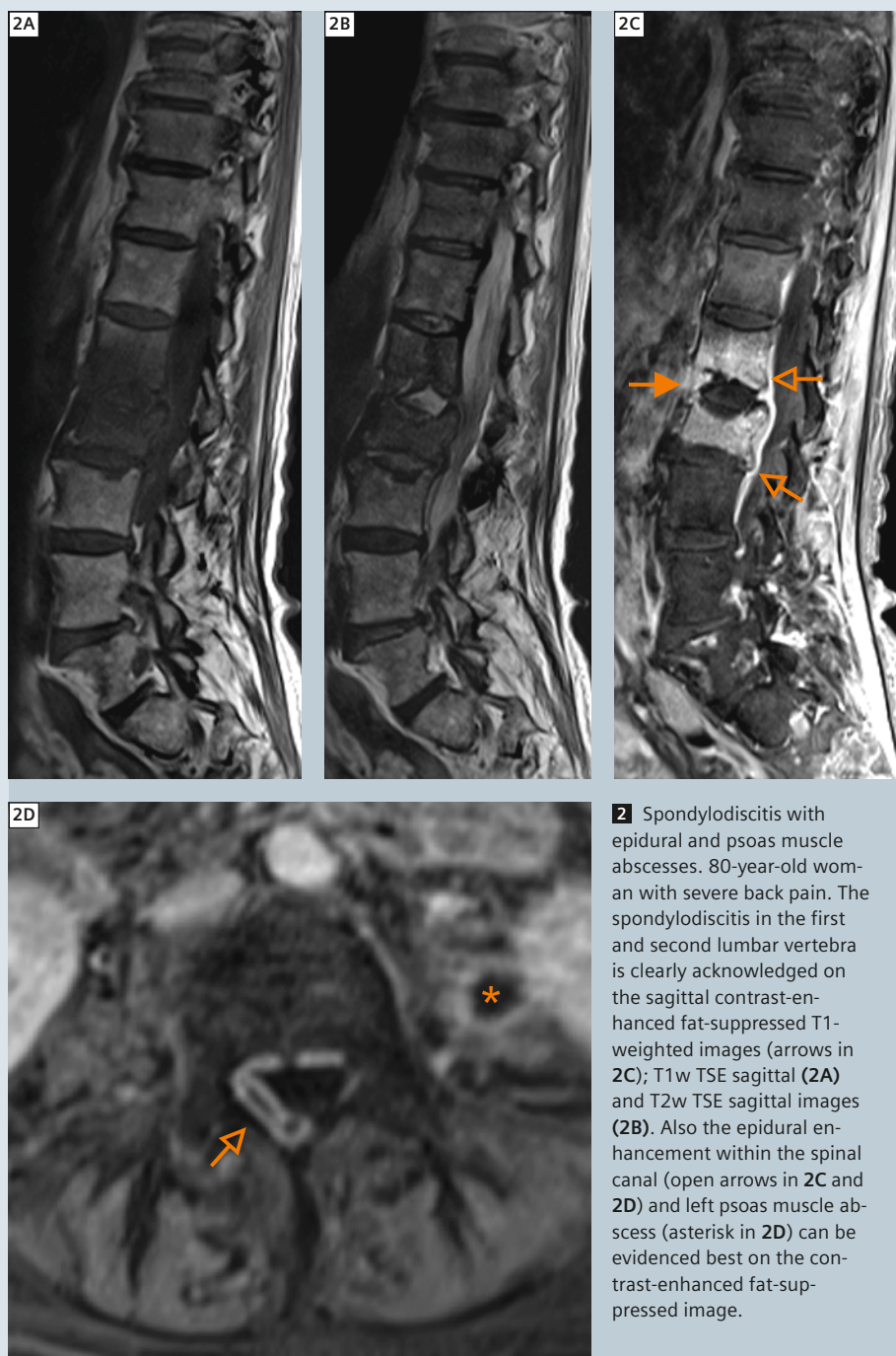


**1** Intracranial hemorrhage in the right basal ganglia with small perifocal edema (arrows). 74-year-old man presenting with left sided hemiparesis since waking up 6 hours before. (1A) Axial unenhanced T1w, (1B) axial FLAIR, (1C) axial T2\*w, (1D) axial diffusion-weighted image (b-value of 1000 s/mm<sup>2</sup>).

for Pediatric and Adolescent Medicine. Of course, the following suggestions are subject to ongoing discussion and refinement. The Department of Diagnostic and Interventional Radiology is the central service provider at the University Hospital Heidelberg in the field of diagnostic general radiological imaging and interventions. More than 91,000 examinations in out-patients and more than 71,000 in in-patients are performed annually, covering all indications and organ systems, with more than 210,000 imaging procedures every year. It should be noted that the following suggestions have been developed for a general radiological department. Dedicated neuroradiological departments may therefore develop additional suggestions regarding brain imaging.

### List of indications for emergency MRI at the Department of Diagnostic and Interventional Radiology in Heidelberg

The list of indications differentiates between emergencies requiring immediate MRI (Category A, urgent care required as soon as possible day and night) and urgent cases with high priority but no need for immediate intervention (Category B, to be performed within 12 hours, e.g. next day). It was also considered important to define a third category (Category C) for situations that do not require an immediate MRI scan since equally diagnostic alternatives are available. Although such examinations may sometimes be urgently requested, it is strongly recommended to resist and to preserve the resources of the emergency MRI staff. This list represents the current stage of management and is intended to be regularly updated.

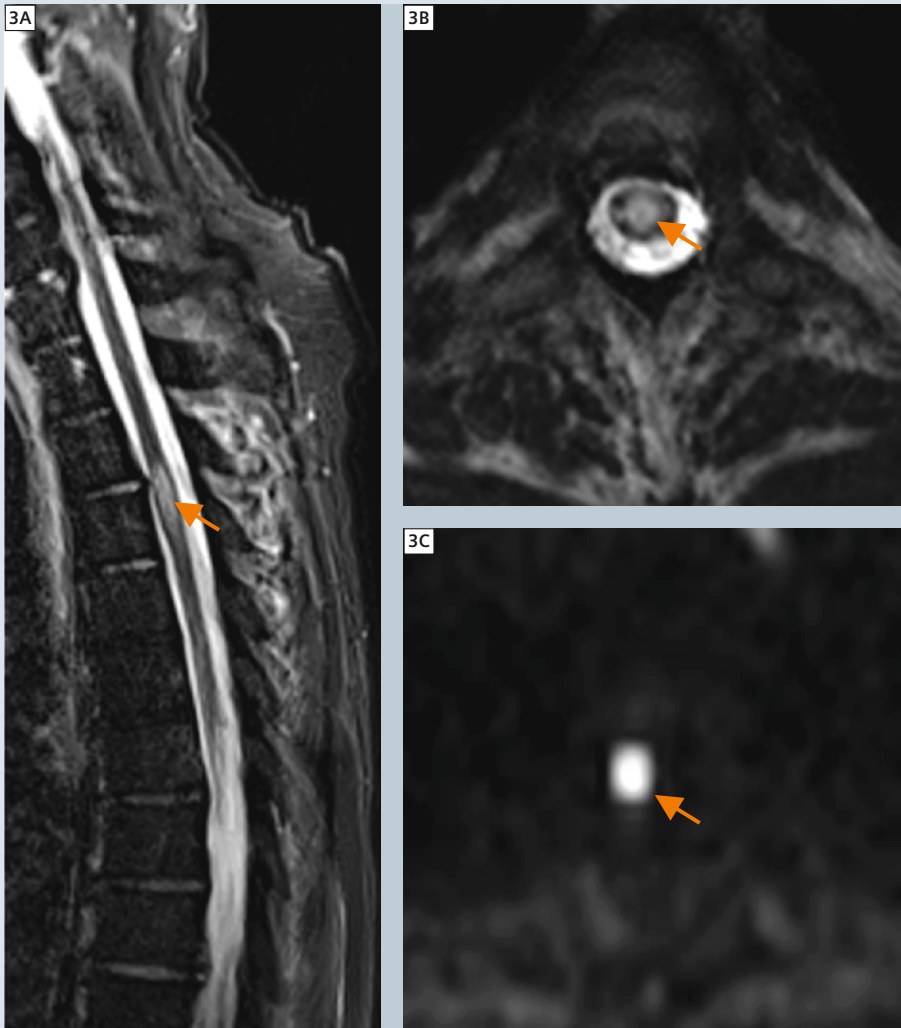


**2** Spondylodiscitis with epidural and psoas muscle abscesses. 80-year-old woman with severe back pain. The spondylodiscitis in the first and second lumbar vertebra is clearly acknowledged on the sagittal contrast-enhanced fat-suppressed T1-weighted images (arrows in 2C); T1w TSE sagittal (2A) and T2w TSE sagittal images (2B). Also the epidural enhancement within the spinal canal (open arrows in 2C and 2D) and left psoas muscle abscess (asterisk in 2D) can be evidenced best on the contrast-enhanced fat-suppressed image.

### Category A Indications for an immediate emergency MRI

1. Cerebral and neurovascular emergencies (Fig. 1; e.g. acute cerebral ischemia or herniation syndromes in children): minimal protocol: T2-weighted TSE, dark-fluid imaging, diffusion-weighted imaging (DWI), time-of-flight (TOF) angiography, NO routine intra-venous (i.v.)-contrast medium administration.

2. Acute traumatic and non-traumatic syndromes with paraplegia and apparent neurologic deficits (such as paresis, sensory disturbances, disturbances in bladder or rectum function) that raise suspicion of a lesion of the myelon or the cauda equina. Examples include: Clinically suspected spondylodiscitis with epidural abscesses (Fig. 2; clinical relevance: immediate surgery indicated for epidural abscesses); acute spinalis



**3** Spinalis anterior syndrome. 53-year-old man with acute paraplegia at level Th5 after surgical endovascular repair on an aortic dissection Stanford type B. At level of third thoracic vertebra there is swelling of the myelon with edema (arrows) on T2-weighted images (3A: STIR sagittal, 3B: T2w SPACE) and restricted diffusion on the image with a  $b$ -value of 1000 s/mm<sup>2</sup> (arrow in 3C).

anterior syndrome (Fig. 3); suspicion of epidural hematoma following spinal anesthesia or spinal surgery; suspected spinal cord contusion; clinical relevance: surgical decompression if edema of the spinal cord is detected). **Minimal protocol:** T2w TSE fat-saturated sagittal, T1w SE sagittal, T2w TSE transversal (non-fat-saturated) findings-centered. Optional: Diffusion-weighted imaging in case of suspected spinal ischemia. In case of suspected epidural abscess MRI with i.v.-contrast medium required.

3. Strong clinical suspicion of septic arthritis (Fig. 4; clinical relevance: early joint lavage to prevent chondrolysis indicated). MRI with i.v.-contrast medium required.
4. Strong clinical suspicion of osteomyelitis in children. MRI with i.v.-contrast medium required.
5. Acute pulmonary artery embolism in pregnant women or very young patients (Fig. 5; pulmonary artery embolism protocol based on free breathing TrueFISP images. I.v.-contrast-enhanced TWIST per-

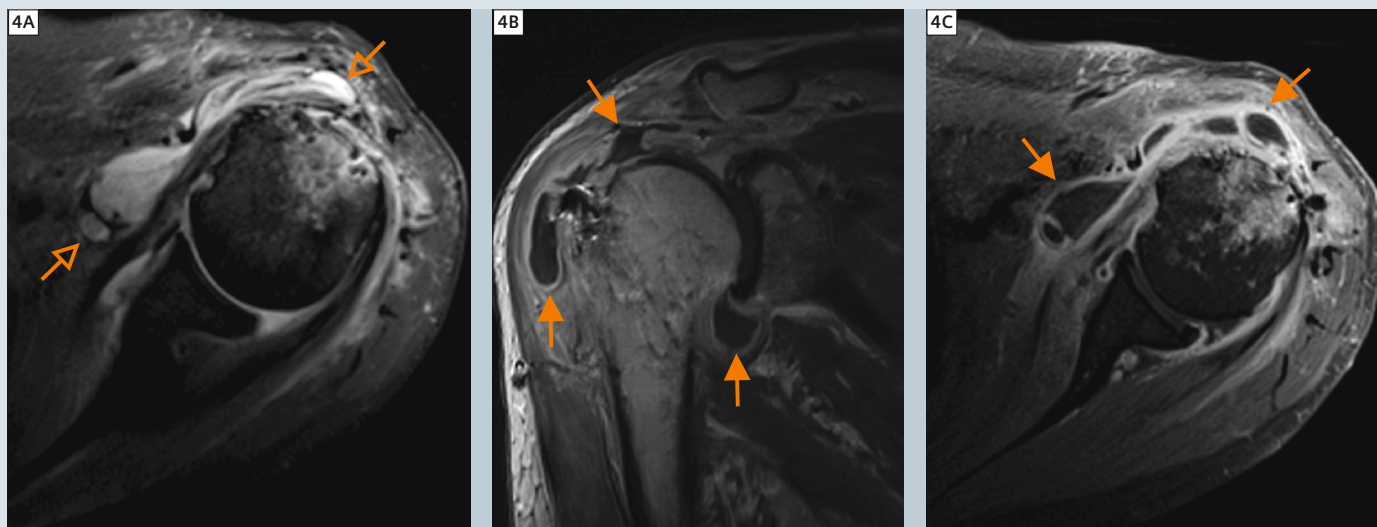
fusion and high spatial resolution MR angiography (MRA) only to be used, if exclusion of small peripheral emboli would be clinically relevant).

### Category B Indications for an MRI within 12 hours include:

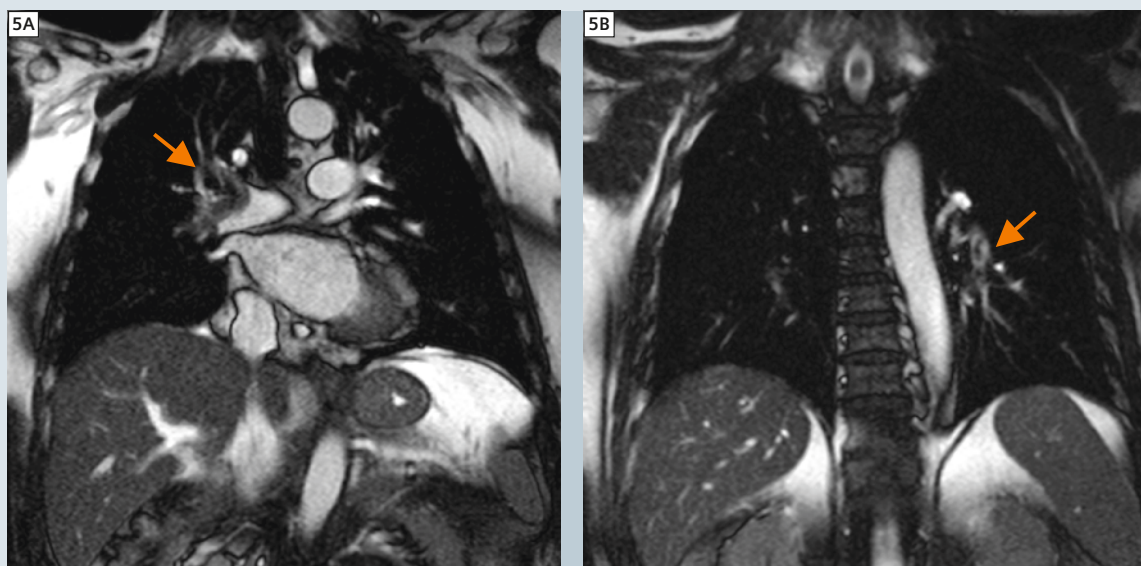
1. Spinal emergencies without neurological symptoms, e.g. to exclude spondylodiscitis or a ligamentous affection following a trauma of the spine, suspicion of a discoligamentous injury according to CT findings (use standard spine MR protocols).
2. In conventional radiography inconclusive findings or suspicion of occult fractures to prevent exposure to radiation in CT (especially in childhood).

### Category C Indications that do NOT justify an emergency MRI (=> e.g. CT as alternative emergency modality or MRI the next working day):

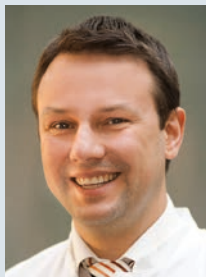
1. Run-off MRA for arteriosclerosis or acute occlusion of the lower limb (CT angiography as an alternative).
2. Suspicion or follow-up of intracranial hemorrhage (CT as an alternative) unless classified as neurovascular emergency according to Category A 1.
3. Suspicion of cerebral metastasis (CT with contrast medium as an alternative).
4. Urgent MRI requests due to organizational issues of the referring clinical partner or because of the patient's wish.



**4** Septic arthritis of the shoulder joint in a 69-year-old man following shoulder arthroscopy and supraspinatus muscle refixation. The joint effusion is appreciated on the axial T2-weighted fat-saturated images (open arrows in **4A**). The strong synovialitis (arrows) is clearly evidenced on the contrast-enhanced coronal (**4B**) and axial (**4C**) MR images (**4B** without and **4C** with fat saturation).

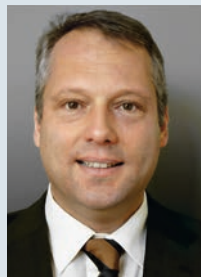


**5** Acute pulmonary embolism in both pulmonary arteries shown on T1/T2-weighted coronal TrueFISP images (arrows; this examination was obtained in a 64-year-old patient with renal insufficiency and suspected pulmonary embolism, being referred for non-contrast-enhanced MRI).



#### Contact

Marc-André Weber, M.D., M.Sc.  
Professor of Radiology  
Heidelberg University Hospital  
Diagnostic and Interventional Radiology  
Im Neuenheimer Feld 110  
69120 Heidelberg  
Germany  
MarcAndre.Weber@med.uni-heidelberg.de



#### Contact

Jürgen Biederer, M.D.  
Professor of Radiology  
Heidelberg University Hospital  
Diagnostic and Interventional Radiology  
Im Neuenheimer Feld 110  
69120 Heidelberg  
Germany  
Juergen.Biederer@med.uni-heidelberg.de

# Musculoskeletal Imaging at 3T with Simultaneous Use of Multipurpose Loop Coils

Elena Ferrer<sup>1</sup>; Rafael Coronado Santos<sup>2</sup>

<sup>1</sup>Radiology Department, Clínica Creu Blanca, Barcelona, Spain,

<sup>2</sup>Imaging & Therapy Division, Siemens S.A. Healthcare Sector, Madrid, Spain

## Introduction

The goal of this paper is to show how the simultaneous use of multipurpose Loop Coils in magnetic resonance imaging (MRI) enables high-resolution musculoskeletal (MSK) studies with an increased level of contrast and specificity for assessing muscles, tendons, ligaments, joints, cartilage, etc and how this imaging procedure helps to obtain accurate clinical diagnoses.

In the following sections we present six different daily patient routine examinations carried out at Clínica Creu Blanca, a leading Spanish institution in Sports Medicine MRI (Fig. 1).

## Material and methods

All MRI exams shown in this article were performed at 3 Tesla open bore system with TrueForm technology (MAGNETOM Verio, Siemens Healthcare, Germany), equipped with 32-channel (Tim [102 × 32] configuration) in combination with multipurpose Loop Coils and Flex Coil interfaces.

Loop Coils come in three sizes (Fig. 2), Large (11 cm diameter), Medium (7 cm diameter) and Small (4 cm diameter). They are iPAT-compatible (integrated Parallel Acquisition Technique) in combination with other coils and can be combined with any coil and the lower part of the 32-channel Head Coil (Table 1). The Flex Coil Interface is not permanently mounted and therefore allows flexible coil positioning.

The imaging protocols include axial, coronal and sagittal Proton Density-weighted (PD) Turbo Spin Echo (TSE) sequences with and without Fat Saturation (Fat Sat) and T1-weighted TSE.



1 Clínica Creu Blanca (Barcelona, Spain)

## Patient and coil positioning

Correct patient positioning and the selection of right loop coils for the region-of-interest have a huge influence on image quality (e.g. to avoid coil filling-factor). In addition, we have to make sure that the patient is positioned comfortably to make

the scan bearable and to reduce the risk of patient movements. The following six examinations – as performed at Clínica Creu Blanca's daily routine – explain how we do it and the results that can be achieved.

**Table 1: Flex Coil Interface and Loop Coils: main characteristics**

Flex Coil Interface			
General	<ul style="list-style-type: none"><li>• Integrated for low-noise preamplifiers</li><li>• Allows flexible coil positioning</li><li>• Only one interface necessary for all loop coils</li><li>• Several Flex Coil Interfaces can be used simultaneously</li></ul>		
Loop Coils			
	Loop Coil, large	Loop Coil, medium	Loop Coil, small
General	<ul style="list-style-type: none"><li>• No coil tuning</li><li>• iPAT-compatible in combination with other coils</li></ul>	<ul style="list-style-type: none"><li>• No coil tuning</li><li>• iPAT-compatible in combination with other coils</li></ul>	<ul style="list-style-type: none"><li>• No coil tuning</li><li>• iPAT-compatible in combination with other coils</li></ul>
Applications	Examination of upper or lower extremities (e.g. shoulder, axilla)	Examination of inner ear, wrist and fingers, pediatric examinations <sup>§</sup>	Examination of small structures near the surface (e.g. joints of fingers and toes, wrist, skin, temporomandibular joints (TMJ))
Can be combined with	Any coil and the lower part of the 32-channel Head Coil	Any coil and the lower part of the 32-channel Head Coil	Any coil and the lower part of the 32-channel Head Coil
Cannot be combined with	The complete 32-channel Head Coil and the complete 32-channel Body Coil	The complete 32-channel Head Coil and the complete 32-channel Body Coil	The complete 32-channel Head Coil and the complete 32-channel Body Coil
Weight	225 g	175 g	200 g
Diameter	110 mm	70 mm	4 mm

<sup>§</sup> MR scanning has not been established as safe for imaging fetuses and infants under two years of age. The responsible physician must evaluate the benefit of the MRI examination in comparison to other imaging procedures.



**2** (2A) Loop Coils (11, 7 and 4 cm diameter). (2B) 4 cm Loop Coil and a Flex Coil Interface.

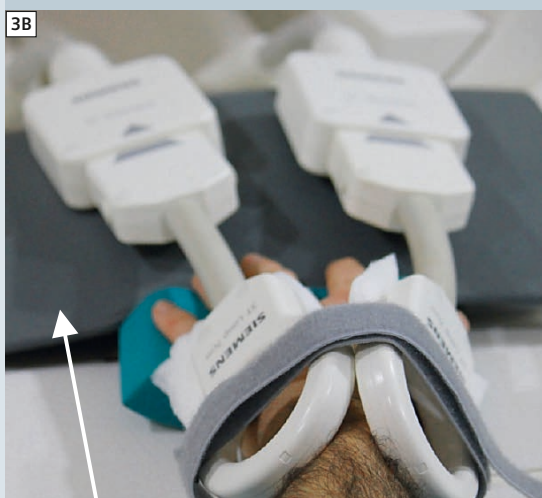
### Carpals examination

This examination was performed using three Flex Coil Interfaces and three 7 cm Loop Coils (Fig. 3). The obtained images are depicted in Figure 4.



7 cm diameter Loop Coil

Flex Coil Interface



Flat pad



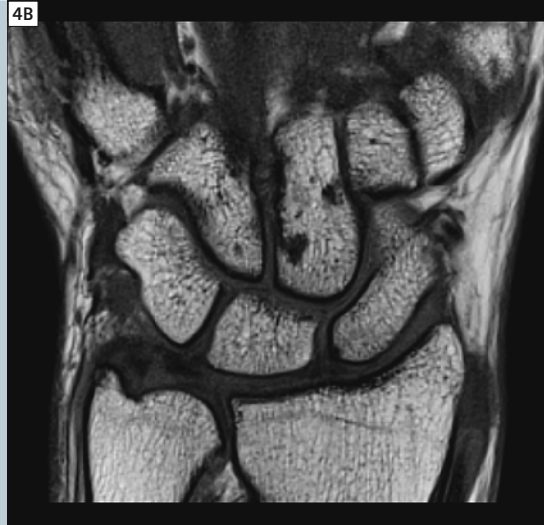
Cables should not be crossed otherwise there will be a signal error when a three plane localizer is launched.



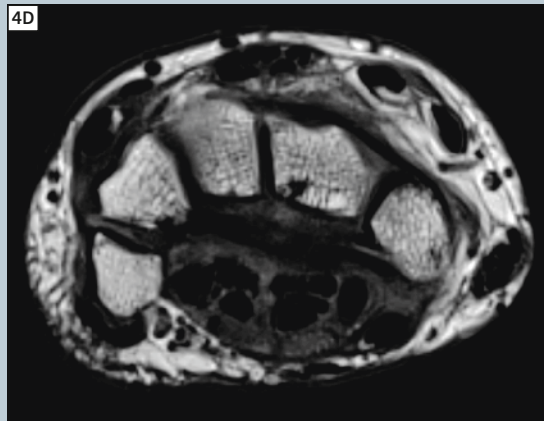
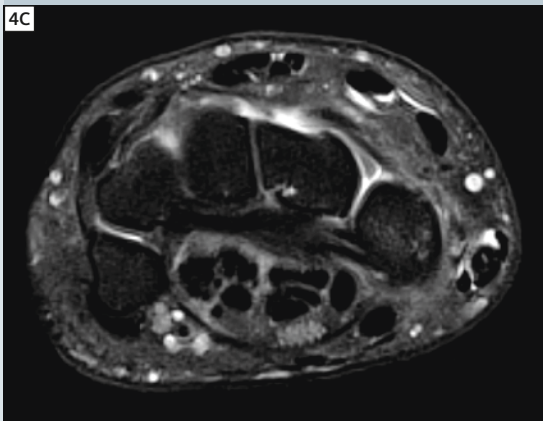
Pad located under the forearm



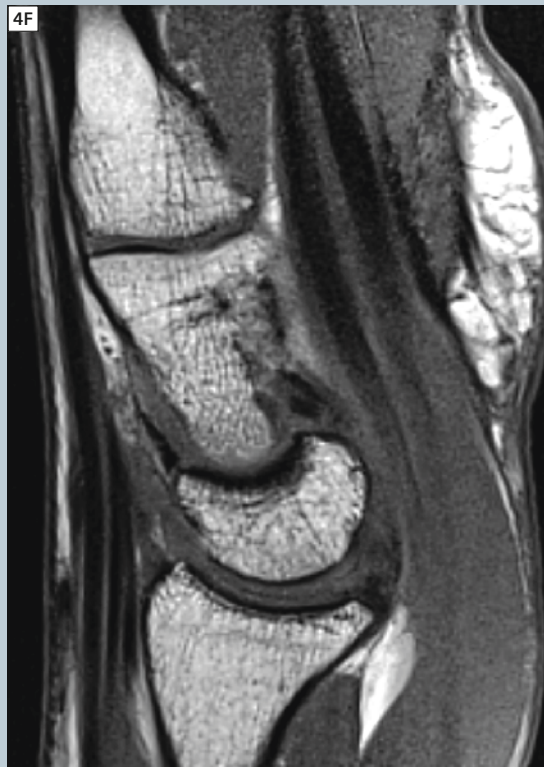
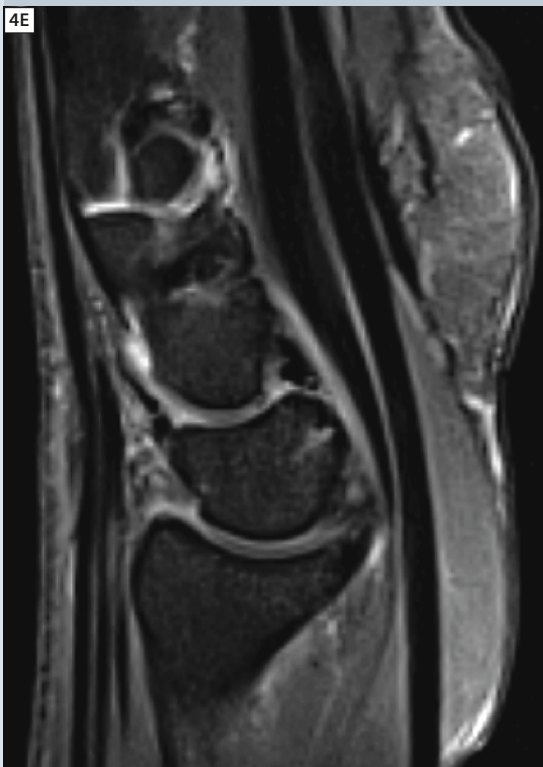
**3** Patient and coil positioning for carpals examination.



**4** (4A) Coronal PD Turbo Spin Echo (TSE) Fat Sat, TR 3500 ms, TE 44 ms, Slice thickness (SL) 1.7 mm, in-plane resolution  $0.4 \times 0.4 \text{ mm}^2$ , matrix  $192 \times 192 \text{ px}^2$ . (4B) Coronal T1w TSE, TR 1290 ms, TE 12 ms, SL 1.7 mm, in-plane resolution  $0.3 \times 0.3 \text{ mm}^2$ , matrix  $320 \times 320$ .



(4C) Axial PD TSE Fat Sat, TR 4400 ms, TE 47 ms, SL 2 mm, in-plane resolution  $0.3 \times 0.3 \text{ mm}^2$ , matrix  $256 \times 256 \text{ px}^2$ . (4D) Axial PD TSE, TR 2400 ms, TE 34 ms, SL 2 mm, in-plane resolution  $0.3 \times 0.3 \text{ mm}^2$ , matrix  $256 \times 256 \text{ px}^2$ .



(4E) Sagittal PD TSE Fat Sat, TR 4100 ms, TE 44 ms, SL 1.8 mm in-plane resolution  $0.4 \times 0.4 \text{ mm}^2$ , matrix  $192 \times 192 \text{ px}^2$ . (4F) Sagittal T1w TSE, TR 1000 ms, TE 12 ms, SL 1.8 mm, in-plane resolution  $0.3 \times 0.3 \text{ mm}^2$ , matrix  $320 \times 320 \text{ px}^2$ .

## Thumb metacarpals examination

This examination was performed using two Flex Coil Interfaces and two 4 cm Loop Coils (Fig. 5). The obtained images are depicted in Figure 6.



Flex Coil Interfaces are separated by a cushion

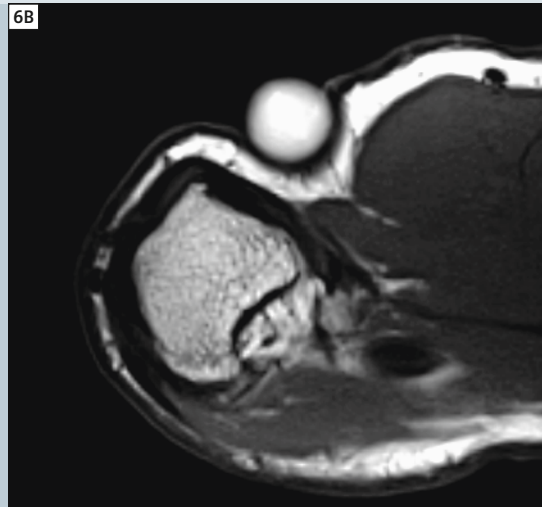
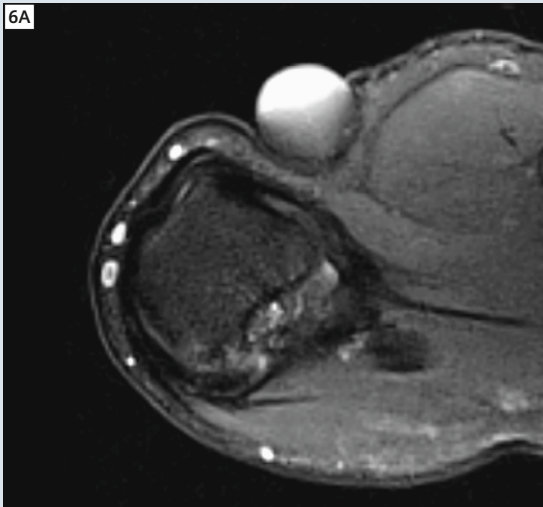


Cables are not crossed and Flex Interface cables don't make loops

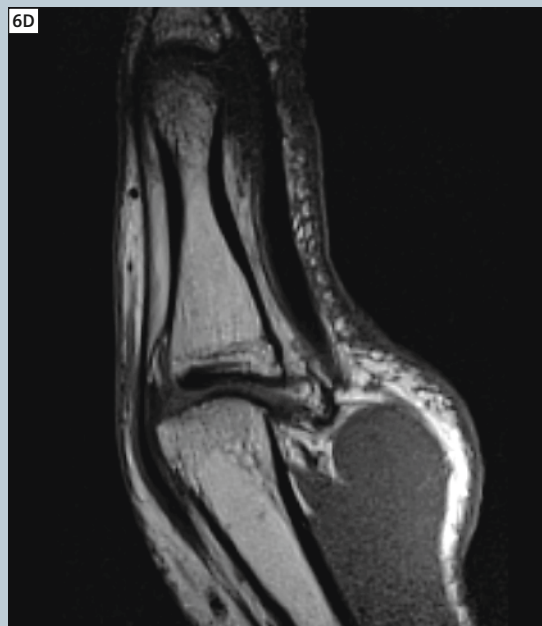


The forearm is immobilized by a strap

**5** Patient and coil positioning for thumb metacarpals examination.



**6** (6A) Axial PD TSE Fat Sat, TR 5200 ms, TE 47 ms, SL 2 mm, in-plane resolution  $0.3 \times 0.3 \text{ mm}^2$ , matrix  $256 \times 256 \text{ px}^2$ .  
(6B) PD TSE, TR 3000 ms, TE 35 ms, SL 2 mm, in-plane resolution  $0.3 \times 0.3 \text{ mm}^2$ , matrix  $256 \times 256 \text{ px}^2$ .



(6C) Sagittal PD TSE Fat Sat, TR 4100 ms, TE 44 ms, SL 1 mm, in-plane resolution  $0.4 \times 0.4 \text{ mm}^2$ , matrix  $192 \times 192 \text{ px}^2$ .  
(6D) Sagittal T1w TSE, TR 810 ms, TE 12 ms, SL 1 mm, in-plane resolution  $0.3 \times 0.3 \text{ mm}^2$ , matrix  $256 \times 256 \text{ px}^2$ .



(6E) Coronal PD TSE Fat Sat, TR 3500 ms, TE 44 ms, SL 1.2 mm, in-plane resolution  $0.4 \times 0.4 \text{ mm}^2$ , matrix  $192 \times 192 \text{ px}^2$ .  
(6F) Coronal T1w TSE, TR 650 ms, TE 12 ms, SL 1.2 mm, in-plane resolution  $0.3 \times 0.3 \text{ mm}^2$ , matrix  $256 \times 256 \text{ px}^2$ .

## Ankle examination

This examination was performed using three Flex Coil Interfaces and three 7 cm Loop Coils (Fig. 7). The obtained images are depicted in Figure 8.



U-shape cushion to place the feet and fix the ankle with a strap.



U-shape cushion to place the feet and fix the ankle with a strap.



The triangular leg pad should be placed to increase patient comfort and to avoid lumbar lordosis.



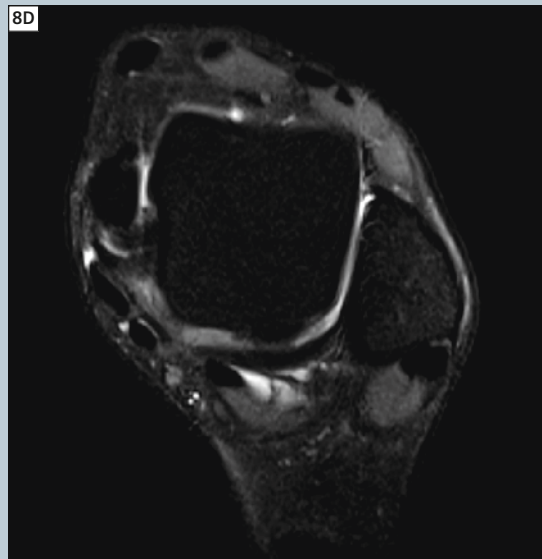
Flex Interface Coils are separated by flat pads and a couple of straps are used to immobilize the ankle.



**7** Patient and coil positioning for ankle examinations.



**8** (8A) Sagittal PD TSE Fat Sat, TR 5200 ms, TE 52 ms, SL 2.5 mm, in-plane resolution  $0.4 \times 0.4 \text{ mm}^2$ , matrix  $320 \times 320 \text{ px}^2$ . (8B) Sagittal T1w TSE, TR 719 ms, TE 10 ms, SL 2.5 mm, in-plane resolution  $0.4 \times 0.4 \text{ mm}^2$ , matrix  $320 \times 320 \text{ px}^2$ .



(8C) Axial PD TSE, TR 4140 ms, TE 44 ms, SL 1.8 mm, in-plane resolution  $0.3 \times 0.3 \text{ mm}^2$ , matrix  $384 \times 384 \text{ px}^2$ . (8D) Axial PD TSE Fat Sat, TR 8710 ms, TE 40 ms, SL 1.8 mm, in-plane resolution  $0.4 \times 0.4 \text{ mm}^2$ , matrix  $320 \times 320 \text{ px}^2$ .



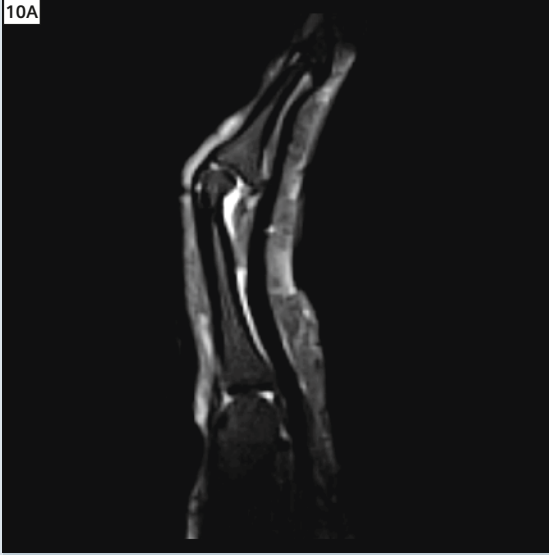
(8E) Coronal T1w TSE, TR 719 ms, TE 12 ms, SL 2 mm, in-plane resolution  $0.3 \times 0.3 \text{ mm}^2$ , matrix  $320 \times 320 \text{ px}^2$ . (8F) Coronal PD TSE Fat Sat, TR 5400 ms, TE 50 ms, SL 2 mm, in-plane resolution  $0.3 \times 0.3 \text{ mm}^2$ , matrix  $320 \times 320 \text{ px}^2$ .

## Metacarpals or fingers examination

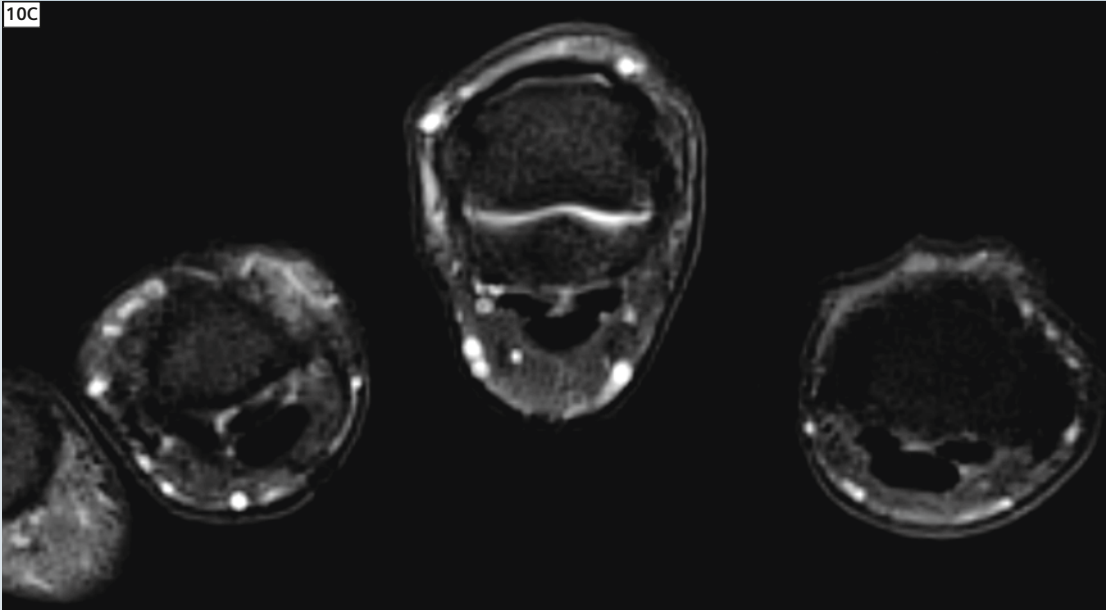
This examination was performed using two Flex Coil Interfaces and two 7 cm Loop Coils (Fig. 9). The obtained images are depicted in Figure 10.



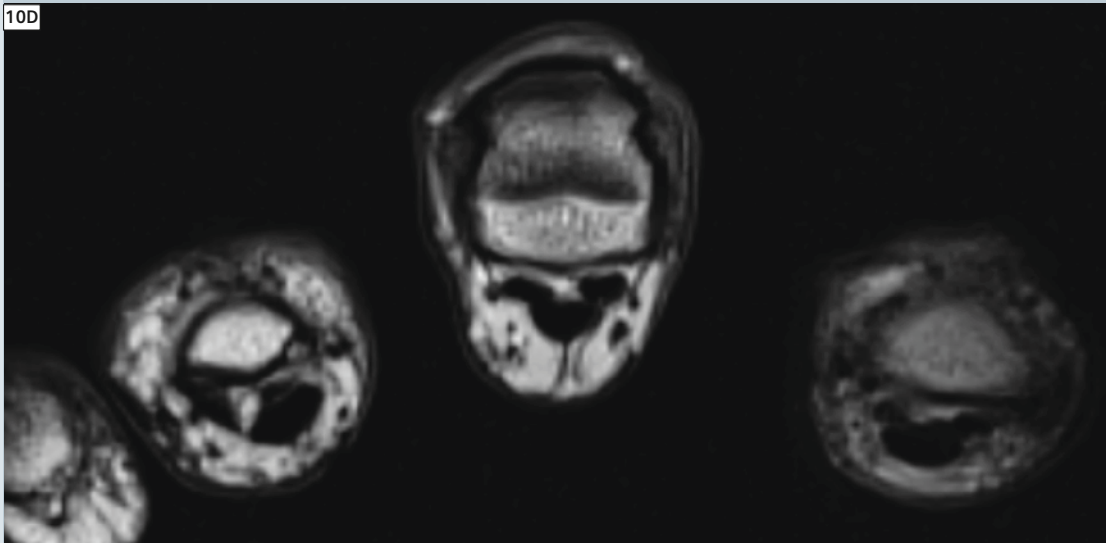
9 Patient and coil positioning for metacarpals or fingers examination.

**10A****10B**

**10** **(10A)** Sagittal PD TSE Fat Sat, TR 4100 ms, TE 44 ms, SL 1.3 mm, in-plane resolution  $0.5 \times 0.5 \text{ mm}^2$ , matrix  $192 \times 192 \text{ px}^2$ . **(10B)** Sagittal T1w TSE, TR 1000 ms, TE 12 ms, SL 1.3 mm, in-plane resolution  $0.3 \times 0.3 \text{ mm}^2$ , matrix  $320 \times 320 \text{ px}^2$ .

**10C**

**(10C)** Axial PD TSE Fat Sat, TR 5600 ms, TE 52 ms, SL 2.5 mm, in-plane resolution  $0.3 \times 0.3 \text{ mm}^2$ , matrix  $256 \times 256 \text{ px}^2$ .

**10D**

**(10D)** Axial PD TSE, TR 3000 ms, TE 34 ms, SL 2.5 mm, in-plane resolution  $0.3 \times 0.3 \text{ mm}^2$ , matrix  $256 \times 256 \text{ px}^2$ .

## Distal inter-phalangeal examination

This examination was performed using two Flex Coil Interfaces and two 4 cm Loop Coils (Fig. 11). The obtained images are depicted in Figure 12.



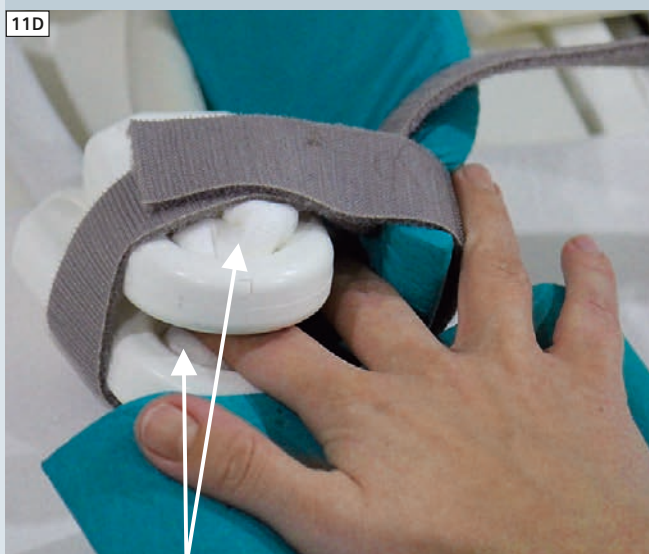
Gauze



Gauze to improve patient comfort and acquisition.



The phalanx is placed in the center of the loop coil.



Gauze

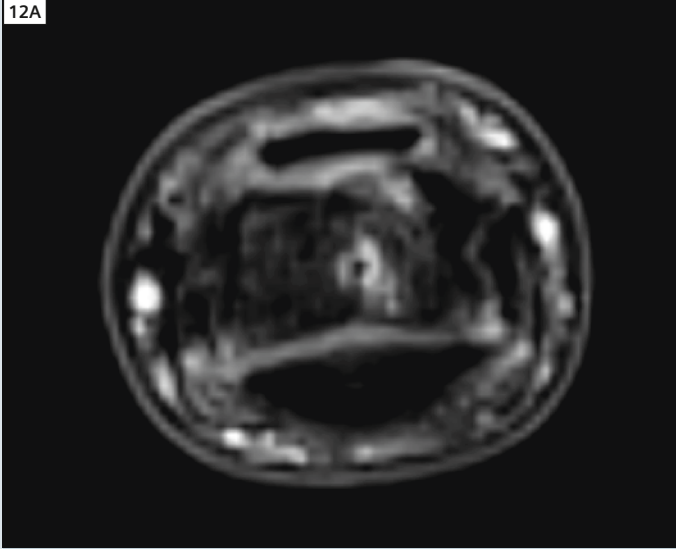


Cushion between the two Flex Coil Interfaces.

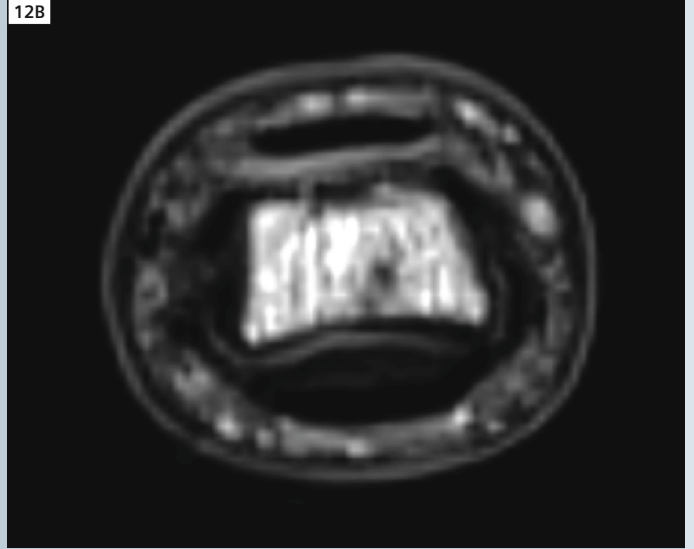
Loop Coils

**11** Patient and coil positioning for distal inter-phalangeal examinations.

12A



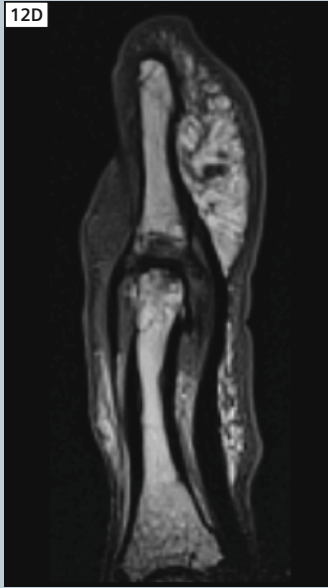
12B



12C



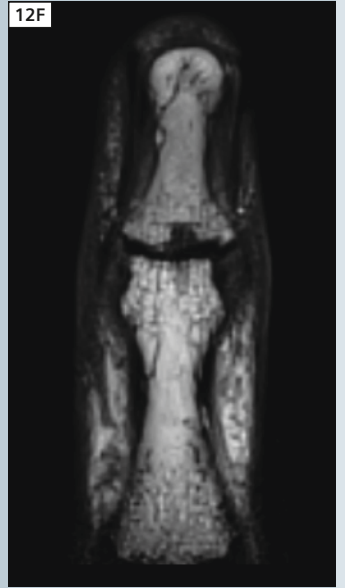
12D



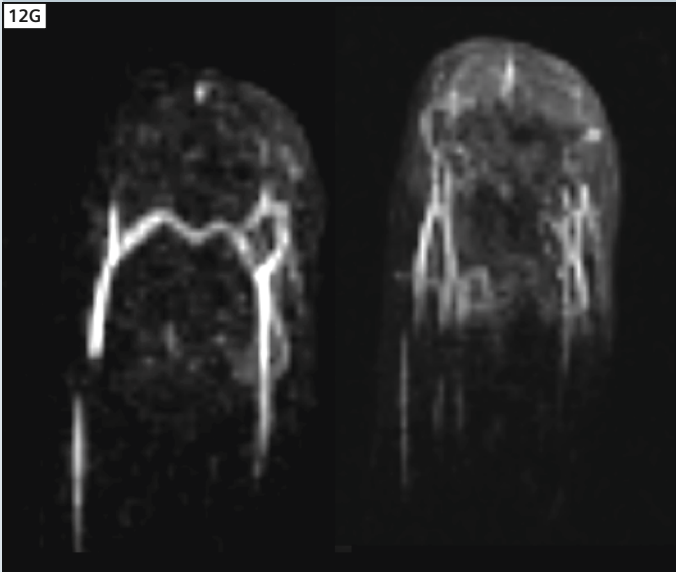
12E



12F



12G



**12 (12A)** Axial PD TSE Fat Sat, TR 5200 ms, TE 47 ms, SL 2 mm, in-plane resolution  $0.3 \times 0.3 \text{ mm}^2$ , matrix  $256 \times 256 \text{ px}^2$ .

**(12B)** Axial PD TSE, TR 3000 ms, TE 35 ms, SL 2 mm, in-plane resolution  $0.3 \times 0.3 \text{ mm}^2$ , matrix  $256 \times 256 \text{ px}^2$ .

**(12C)** Sagittal PD TSE Fat Sat, TR 4100 ms, TE 44 ms, SL 1 mm, in-plane resolution  $0.4 \times 0.4 \text{ mm}^2$ , matrix  $192 \times 192 \text{ px}^2$ .

**(12D)** Sagittal T1w TSE, TR 810 ms, TE 12 ms, SL 1 mm, in-plane resolution  $0.3 \times 0.3 \text{ mm}^2$ , matrix  $256 \times 256 \text{ px}^2$ .

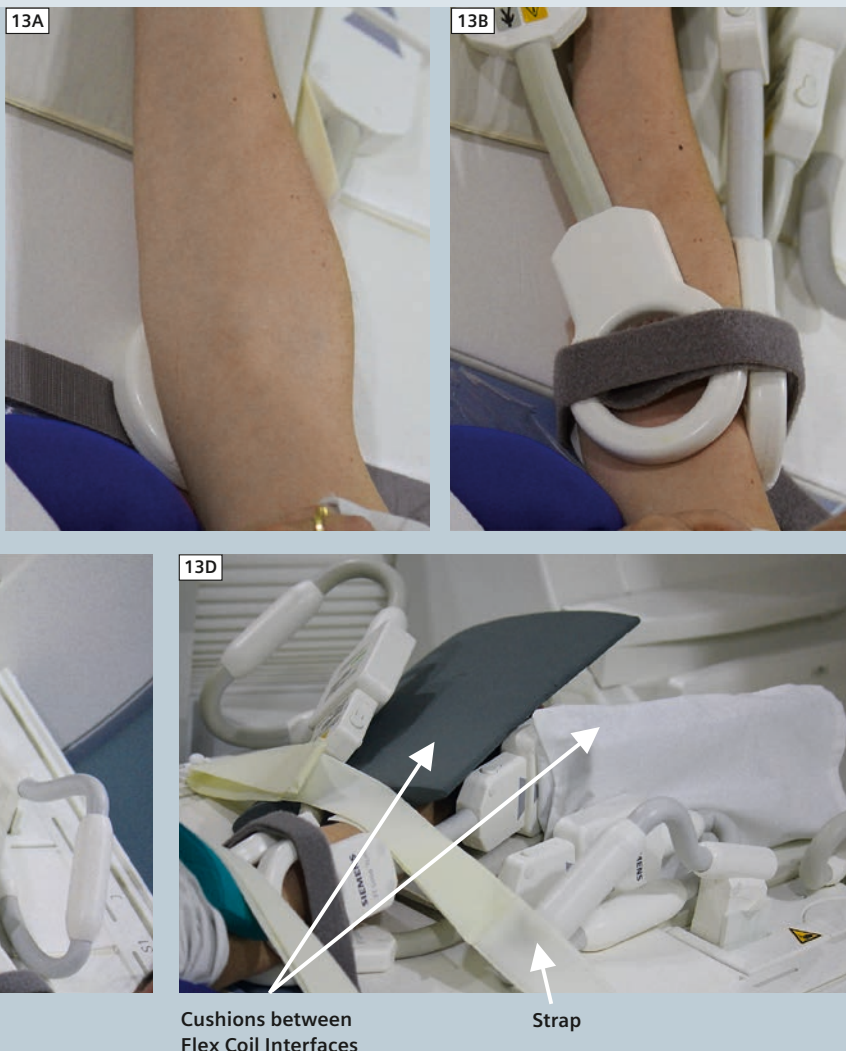
**(12E)** Coronal PD TSE Fat Sat, TR 3500 ms, TE 44 ms, SL 1.2 mm, in-plane resolution  $0.4 \times 0.4 \text{ mm}^2$ , matrix  $192 \times 192 \text{ px}^2$ .

**(12F)** Coronal T1w TSE, TR 650 ms, TE 12 ms, SL 1.2 mm, in-plane resolution  $0.3 \times 0.3 \text{ mm}^2$ , matrix  $192 \times 192 \text{ px}^2$ .

**(12G)** This figure shows an angiography of a finger whose third phalange was amputated: coronal FLASH 3D post contrast, TR 1.5 ms, TE 3.82 ms, SL 0.7 mm, in-plane resolution  $0.7 \times 0.7 \text{ mm}$ , matrix  $192 \times 174 \text{ px}^2$ .

## Elbow examination

This examination was performed using three Flex Coil Interfaces and three 7 cm Loop Coils (Fig. 13). The obtained images are depicted in Figure 14.



**13** Patient and coil positioning for elbow examinations.

## Conclusion

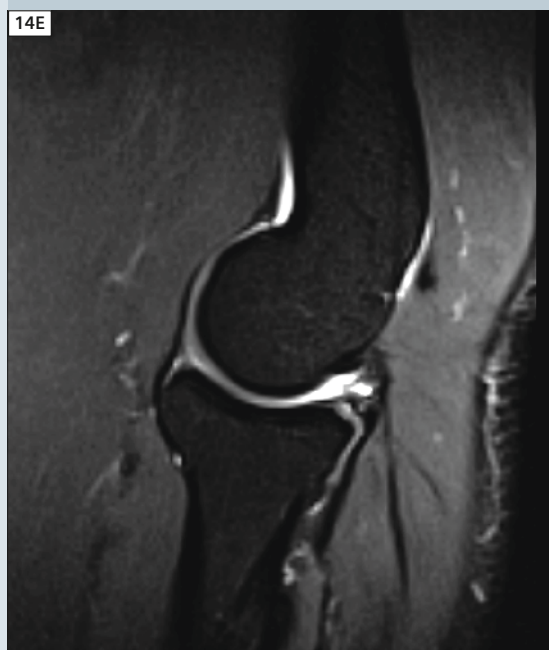
High-resolution MSK imaging can be acquired using a 3T magnetic field (MAGNETOM Verio) and a combination of multipurpose Loop Coils. It does not claim to replace dedicated MSK coils (e.g. knee coil, hand coil) but it might represent an alternative method for institutions whose number of MSK studies is scarce and/or that are not concerned about reducing MSK examination times and/or increasing patient throughput but that want to achieve similar levels of diagnostic accuracy as dedicated coils [1–6].

### References

- 1 Biochemical Imaging, Tallal C. Mamisch, Timothy Hughes. MAGNETOM Flash 1/2007, p 6-7.
- 2 High-Resolution (Fast) Imaging, Tallal C. Mamisch, Timothy Hughes. MAGNETOM Flash 1/2007, p. 8-9.
- 3 Application Hints for MR Orthopedic Imaging: The Knee Examination, Steve Rigsby. MAGNETOM Flash 1/2007, p. 48-49.
- 4 MRI in Inflammatory Arthritis, Marius Horger. MAGNETOM Flash 1/2009, p. 54-58.
- 5 Musculoskeletal MRI in Sports Medicine, Heinz-Peter Schlemmer et al. MAGNETOM Flash 1/2010, p. 88-98.
- 6 Chondral Fracture of the Talar Dome and Siastasis of the Os Trigonum. Anna K. Chacko, Charles P. Ho. MAGNETOM Flash 1/2011, p. 63-65.

### Contact

Elena Ferrer  
Clínica Creu Blanca  
P. Reina Elisenda 17  
08034 Barcelona  
Spain  
Phone +34 932 522 522  
elferre@creu-blanca.es



**14** (14A) Axial PD TSE Fat Sat, TR 4400 ms, TE 47 ms, SL 2 mm, in-plane resolution  $0.5 \times 0.5 \text{ mm}^2$ , matrix  $256 \times 256 \text{ px}^2$ . (14B) Axial PD TSE, TR 2700 ms, TE 41 ms, SL 2 mm, in-plane resolution  $0.4 \times 0.4 \text{ mm}^2$ , matrix  $320 \times 320 \text{ px}^2$ .

(14C) Coronal PD TSE Fat Sat, TR 5000 ms, TE 44 ms, SL 1.8 mm, in-plane resolution  $0.5 \times 0.5 \text{ mm}^2$ , matrix  $192 \times 192 \text{ px}^2$ . (14D) Coronal T1w TSE, TR 1000 ms, TE 12 ms, SL 1.8 mm, in-plane resolution  $0.3 \times 0.3 \text{ mm}^2$ , matrix  $320 \times 320 \text{ px}^2$ .

(14E) Sagittal PD TSE Fat Sat, TR 4800 ms, TE 41 ms, SL 2 mm, in-plane resolution  $0.5 \times 0.5 \text{ mm}^2$ , matrix  $192 \times 192 \text{ px}^2$ . (14F) Sagittal T1w TSE, TR 1000 ms, TE 12 ms, SL 2 mm, in-plane resolution  $0.3 \times 0.3 \text{ mm}^2$ , matrix  $320 \times 320 \text{ px}^2$ .

# Automated Morphological Knee Cartilage Analysis of 3D MRI at 3T

Jurgen Fripp, Ph.D.<sup>1</sup>; Erin Lucas, M.Sc.<sup>2</sup>; Craig Engstrom, Ph.D.<sup>3</sup>; Shekhar S. Chandra, Ph.D.<sup>1</sup>; Rachel Surowiec, M.Sc.<sup>2</sup>; Robert Evans M.Sc.<sup>5</sup>; Sharon Balamoody, M.D.<sup>5</sup>; Raphael Schwarz, Ph.D.<sup>4</sup>; Lars Lauer, Ph.D.<sup>4</sup>; Richard J. Hodgson BM, Ph.D.<sup>5</sup>; Charles Ho, Ph.D.<sup>2</sup>; Stuart Crozier, Ph.D.<sup>6</sup>.

<sup>1</sup>The Australian E-Health Research Centre, CSIRO ICT Centre, Brisbane, Australia

<sup>2</sup>Steadman Philippon Research Institute, Vail, Colorado, USA

<sup>3</sup>School of Human Movement Studies, University of Queensland, Brisbane, Australia

<sup>4</sup>Siemens Healthcare, Erlangen, Germany

<sup>5</sup>Leeds Musculoskeletal Biomedical Research Unit, Leeds, University of Leeds, Leeds, UK

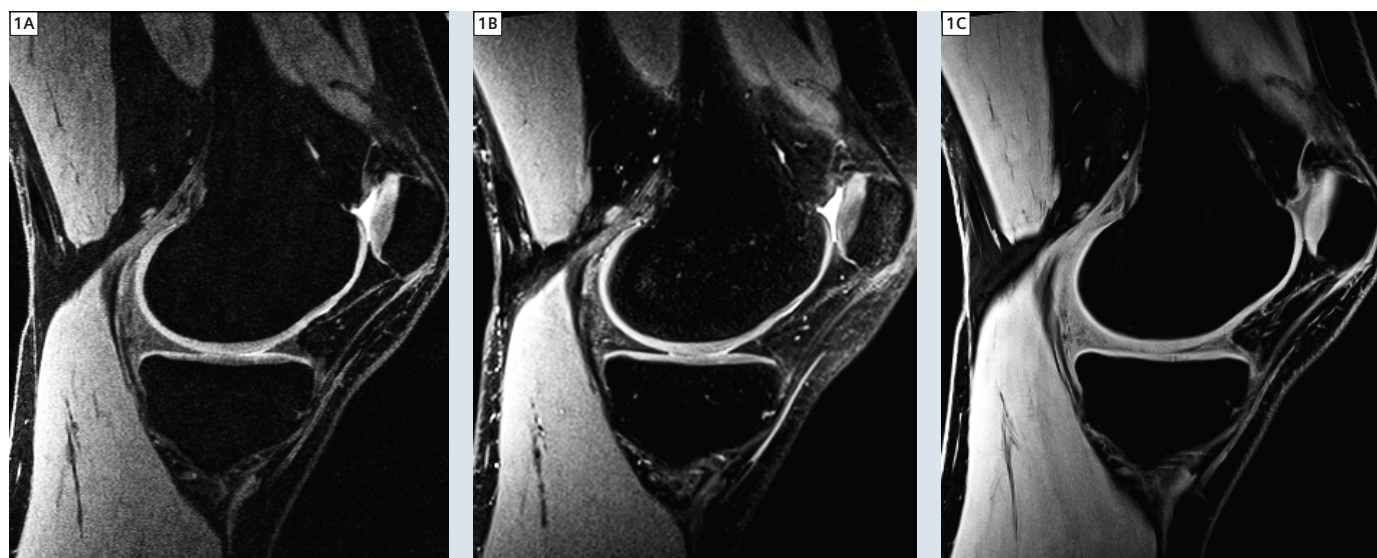
<sup>6</sup>School of Information Technology & Electrical Engineering, University of Queensland, Brisbane, Australia.

## Introduction

Quantitative magnetic resonance (MR) imaging including morphological and biochemical measurements have shown promise for detecting early cartilage changes [1, 2]. Morphological measures (volume, thickness, surface area and curvature) can be derived from MR images and have been shown to vary with osteoarthritis (OA) [2, 3]. As biochemical changes occur before gross tissue loss, improved sensitivity for early OA detection requires using quantitative cartilage mapping techniques such as T2, T2\*,

T1rho, dGEMERIC\*, Sodium and CEST [4]. Although quantitative MR has been used extensively in research, it is still not commonly used clinically for multiple reasons, mostly related to limited validation of reproducibility and the time required to perform analyses. Extracting accurate and reproducible quantitative cartilage measures from MR images has been the focus of significant research but remains an open problem [5]. In recent studies, it has been found that different research groups can obtain

notably different morphometric results, reflecting subtle variations in regional definitions of anatomy, methods and calculation techniques [6]. A desired direction (although difficult to achieve), is to standardize and automate processes for quantitative cartilage analyses which would improve reproducibility and post-processing time necessary for clinical application. An important aspect of this process would include automated segmentation and standardizing the sequences used for acquisition.



**1** Visual comparison of all sequences acquired for representative subject; **(1A)** Sagittal T2w DESS (TR 16.3 ms; TE 4.72 ms; flip angle 25°), **(1B)** Sagittal PDw SPACE (1200 ms; 32 ms; 120°), **(1C)** Sagittal T1w VIBE (20 ms; 5.74 ms; 12°).

In recent years several different approaches have been developed to perform automated segmentation of articular cartilage from MR images [7–11]. A primary limitation of previous work has been limited validation of accuracy especially on pathological cohorts and different scanning sequences. Gradient echo sequences such as DESS and FLASH have most commonly been used for morphologic measurements because they provide relatively homogeneous cartilage signal and excellent delineation of the cartilage-bone interface [12–16]. Spin echo sequences have more clinical value due to their larger dynamic range and signal contrast resolution within the cartilage, other soft tissue and bone, although this makes segmentation more challenging. Scan times for the sequence chosen for segmentation must also be considered. Ideally, the scans used for quantitative cartilage segmentation and analyses would also be readily used for clinical diagnosis since patient scan time is limited.

In this article we will review the performance of a new automated segmentation algorithm for the knee cartilages. An aim of this work is to evaluate the accuracy and reproducibility of this automated approach when the scheme is

applied to scans from asymptomatic volunteers acquired at 3T with different 3D MR sequences (T2w DESS, T1w VIBE and PDw SPACE), different coils (8 and 15-channel knee coils), and test re-test (3 scans of the same subject/s repositioned between scans). Additionally, initial results will be presented with scans from pathological subjects imaged using PDw SPACE.

## Method

### Data sets:

#### Asymptomatic subjects:

##### 3D sequence comparison

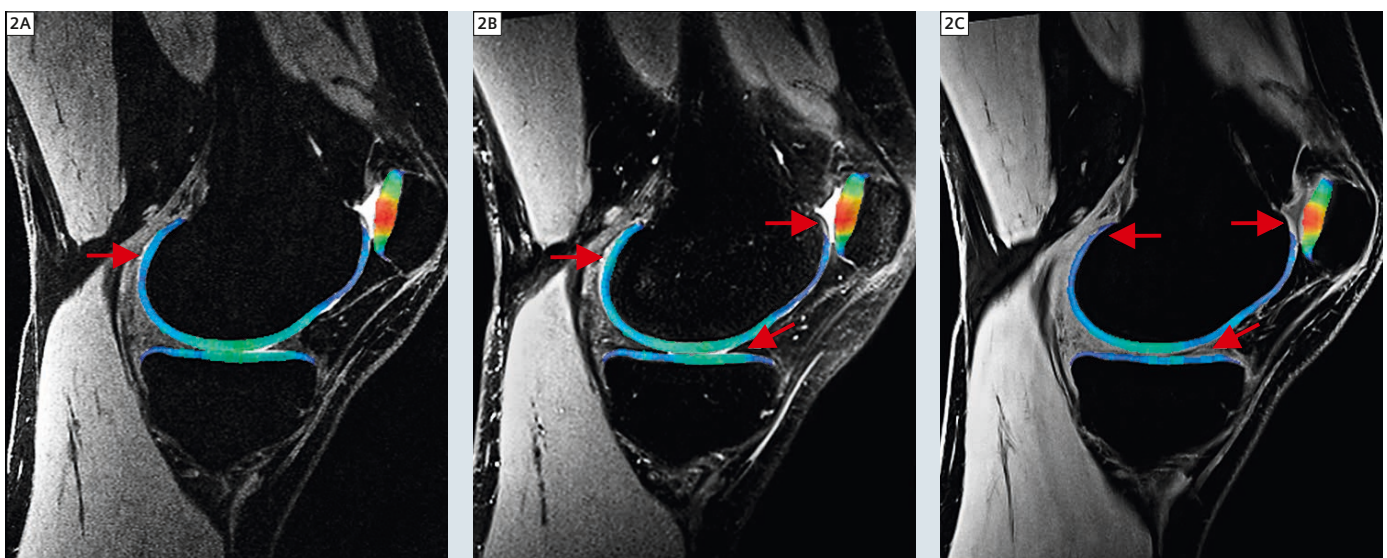
MR imaging of the knee joint was performed on 10 healthy volunteers (3 males and 7 females; aged 23 to 45 years, mass 50–90 kg). Informed consent was obtained and the medical research ethics committee of the University of Queensland approved the current study. All images were acquired at the University of Queensland on a 3T MR scanner (MAGNETOM Trio, Siemens Healthcare, Erlangen, Germany) using an 8-channel transmit-receive knee coil. The knee for each subject was imaged using three 3D MR sequences; T2w DESS, T1w VIBE and PDw SPACE. A slice from each scan sequence of one subject can be seen in figure 1, illustrating the difference in

image contrast, especially at the bone-cartilage and cartilage-synovial interfaces. The scanning parameters are given in table 1.

The articular cartilage in each DESS image was manually segmented on every sagittal slice in the volume by a musculoskeletal expert using the ROI plugin in ImageJ [17] taking on average 2 hours. Segmentations for other MR sequences were obtained by independently co-registering the sub images within a bounding box around the manual DESS segmentation (dilated by 7 mm) for each cartilage plate (implemented using ITK [18]). The segmentation masks were not adjusted to match the sequence.

### Test re-test

MR imaging was performed on 16 healthy volunteers (5 males and 11 females; aged 23 to 52). Informed consent was obtained and the local research ethics committee approved the current study. All images were acquired and anonymized at the Leeds Musculoskeletal Biomedical Research Unit on a 3T MR scanner (MAGNETOM Verio, Siemens Healthcare, Erlangen, Germany) using 8 and 15-channel transmit-receive knee coils. The knee for each subject



**2** Visual comparison of automated segmentation results (colormap represents thickness streamlines). Arrows point to several focal errors. These slices correspond to those presented in figure 1.

**Table 1: MR sequence parameters used in this study, from the University of Queensland (UQ), University of Leeds (UL) and the Steadman Philippon Research Institute (SPRI).**

Sequence	DESS	DESS	VIBE	SPACE	SPACE
SITE	UL	UQ	UQ	UQ	SPRI
N	16	10	10	10	3
Acquisition time	11:10	9:44	10:14	08:40	04:46
Phase encoding direction	AP	AP	AP (RL, N=3)	AP	AP
Number of slices	160	160	80	176	176
Slice thickness (mm)	0.70	0.70	1.50	0.60	0.70
Slice spacing (mm)	0.36 x 0.36	0.36 x 0.46	0.31 x 0.31	0.49 x 0.49	0.60 x 0.60
Image matrix	384 x 384	384 x 312	512 x 512	320 x 320	256 x 256
Phase encoding steps	308	250	512	294	151
Fat suppression	WE	WE	WE	SPAIR	SPAIR
GRAPPA factor/ref lines	NA	NA	NA	2/24	2/24
Number of averages	1	1	1	1.4	1
Slice resolution	80%	80%	100%	91.88%	100%
Slice oversampling	0%	10%	0%	0%	0%
Phase resolution	100%	81%	100%	100%	100%
Phase oversampling	0%	10%	0%	0%	0%
Turbo factor/echo spacing/ echo train	1/0/0	1/0/0	1/0/0	53/-/-	84/4.98/284
Repetition time (TR) ms	16.3	16.3	20	1200	1200
Echo time (TE) ms	4.72	4.72	5.65	32	45
Flip angle	25	25	12	PdVar	PdVar
Bandwidth (Hz/pixel)	352	352	130	539	425

WE = water excitation

**Table 2: Computational efficiency of our approach.**

<b>CPU clock speed:</b>	3.2 GHz	<b>OS</b>	Windows7
<b>Machine CPU count:</b>	4	<b>Compiler</b>	VisualStudio10
<b>Machine memory:</b>	8 GB	<b>Libraries</b>	ITK 3.20, VTK 5.6

	DESS	SPACE	VIBE
<b>Image dimensions</b>	384 x 312 x 160	320 x 320 x 176	512 x 512 x 80
<b>Multi-threaded</b>	2	2	2
<b>Total segmentation time (min)</b>	4.6	3.9	4.1
<b>Peak memory used:</b>	1.5 GB	1.2 GB	1.6 GB

was imaged using a DESS sequence with parameters outlined in table 1, and involved, scanning twice with the 8-channel coil and once with a 15-channel coil. The subject was taken off the table and repositioned between each scan. The articular cartilage in the first 8-channel coil DESS images was manually segmented on every fourth sagittal slice from the original MR by a trained radiographer then reviewed and adjusted where necessary by a musculoskeletal radiologist with experience of cartilage segmentation using Analyze 10.

#### Pathological case studies

For qualitative evaluation of the automated segmentation performance with clinical scans, automated segmentation from three patient scans obtained pre-operatively were qualitatively assessed. All images were acquired and anonymized at the Steadman Clinic on a 3T MR scanner (MAGNETOM Verio, Siemens Healthcare, Erlangen, Germany) for this study by the Steadman Philippon Research Institute (SPRI) with approval from the Vail Valley Medical Center Internal Review Board. The knee for each patient was imaged using a 15-channel

knee coil with the SPACE sequence with parameters outlined in table 1. Subject 1 was a patient with excessive synovial fluid and synovitis in the joint space. Subject 2 was a patient with extensive cartilage damage. Cartilage damage was graded arthroscopically using the International Cartilage Repair Society (ICRS) grading system. The femoral cartilage lesions included grade 4 on the medial femoral condyle, grade 2 on the lateral femoral condyle, and grade 2 in the central trochlea. The tibial cartilage lesions included grade 3 on the posterior lateral tibial plateau. Grades 2 and 3 patellar lesions were also present. Subject 3 was a patient with moderate cartilage damage. The femoral cartilage damage included grade 2 damage to the lateral femoral condyle. The damage to the tibial cartilage included diffuse grade 1 damage to the lateral plateau, and grade 3 damage to the anterior lateral plateau. The patella cartilage had grades 2 and 3 damage.

#### Analysis:

##### MRI automatic segmentation

The MR images from each subject were automatically segmented using an

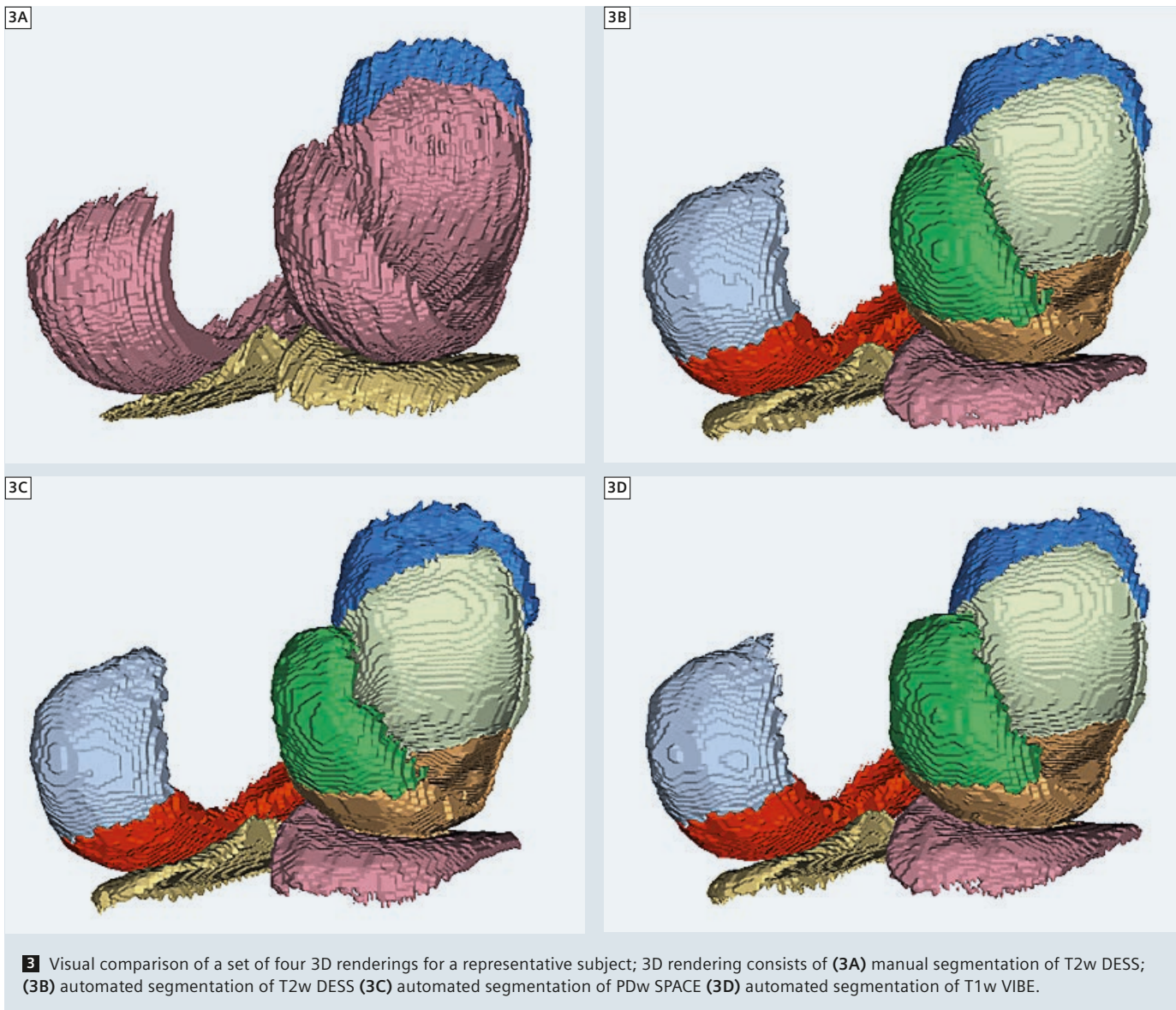
improved version of a recently published 3D shape model based scheme [11]. The improvements primarily consist of optimization and tradeoffs for speed (total computation time 4 to 5 minutes), multi-sequence performance and some changes to better handle MR artifacts (particularly bias-fields) and pathologies such as synovitis.

The basic scheme consists of four stages 1) preprocessing, 2) atlas alignment 3) bone segmentation and 4) cartilage segmentation.

**1) Preprocessing:** Noise on raw MR images was reduced with a median filter implemented in ITK [18].

**2) Atlas alignment:** An average MR atlas image was affinely registered to the subject. The obtained transform was used to propagate the bone atlas surface into the preprocessed image and then estimate pose and shape parameters. The atlas surface was partitioned into 8 regions (patella, medial and lateral tibial, medial and lateral femoral condyle, medial and lateral central femoral and femoral trochlea).

**3) Bone segmentation:** The bone (femur, tibia and patella) is segmented



using an adaptive threshold shape based segmentation scheme described in Fripp et al. [19]. This technique was improved by including robust regional thresholds to handle signal attenuation commonly found in the femoral-patella region, as well as aliasing artefacts that can cover the patella bone.

**4) Cartilage segmentation:** The cartilage segmentation scheme is based on the technique described in Fripp et al. [11, 19]. This technique was improved by including the aforementioned robust regional cartilage statistics, and secondly an explicit synovial fluid segmentation was performed.

Starting from the bone segmentation, a statistical model extracts the bone-cartilage interface (BCI). The thickness based cartilage segmentation is performed iteratively driven locally by local edges and estimated tissue probabilities within each region. Initially it assumes that all bright tissue is cartilage, and uses a statistical model to constrain the estimated cartilage thickness. Possible synovial fluid patches are then detected as non cartilage tissues with high signal intensity. If found, the 'synovial fluid' tissue probabilities are then combined with the other tissue probabilities and local edge information to estimate the local thickness

which is statistically constrained. At each iteration tissue and edge properties are re-estimated, local areas that definitely have no cartilage are disabled, and local thickness is estimated within a reduce search space to refine the cartilage segmentation.

#### Validation of automatic segmentation

The extent of spatial overlap between the manual segmentations (A) and automatic cartilage segmentations (B) were evaluated for the femoral, tibial, and patellar cartilage using the Dice similarity index (DSI) [20]. The DSI ranges from 0 (no overlap in segmenta-

**Table 3: Average and standard deviation of the validation measures comparing automatic and manual segmentations for each cartilage plate and MR sequence in the University of Queensland**

Cartilage	Site	Sequence	N	DSI	Median DSI	Vol. RD (%)	R
Patellar	UL	DESS	16	82.74±6.11	85.15	11.58±11.06	0.95
	UQ	DESS	10	83.44±4.65	84.61	9.11±6.1	0.98
	UQ	SPACE	10	79.77±4.46	80.74	10.49±10.75	0.90
	UQ	VIBE	10	82.57±5.53	84.10	7.98±20.16	0.76
Tibial	UL	DESS	16	83.3±1.68	82.97	4±5.83	0.98
	UQ	DESS	10	80.47±2.23	81.48	12.39±8.73	0.97
	UQ	SPACE	10	79.08±3	79.46	-5.06±9.26	0.97
	UQ	VIBE	10	78.14±3.05	78.85	15.26±10.85	0.94
Femoral	UL	DESS	16	82.64±2.85	82.18	-1.51±7.31	0.94
	UQ	DESS	10	83.87±2.04	83.88	1.79±6.27	0.93
	UQ	SPACE	10	80.14±2.72	80.09	2.71±5.28	0.91
	UQ	VIBE	10	80.76±2.73	81.30	4.46±9.21	0.88

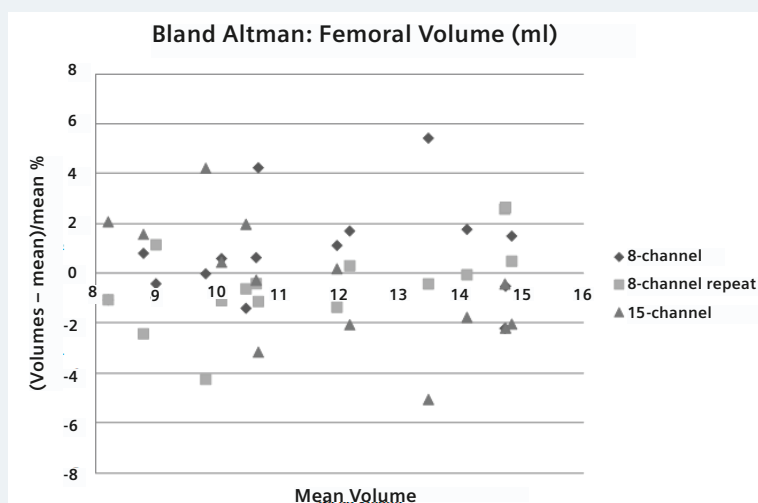
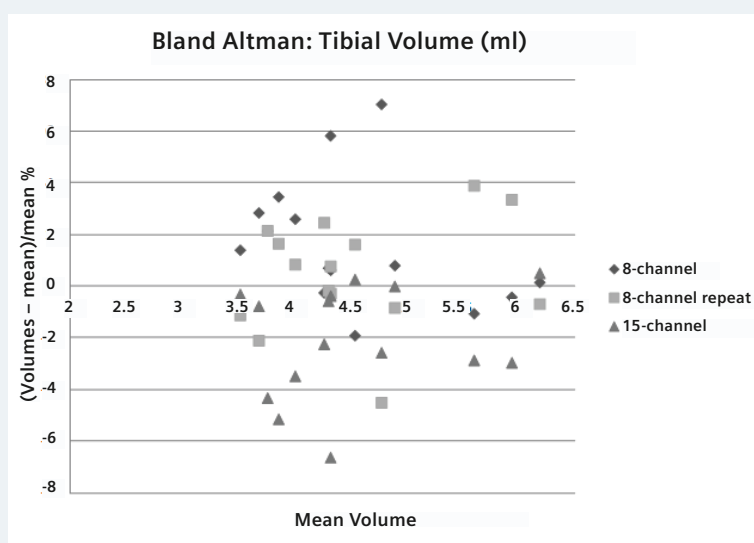
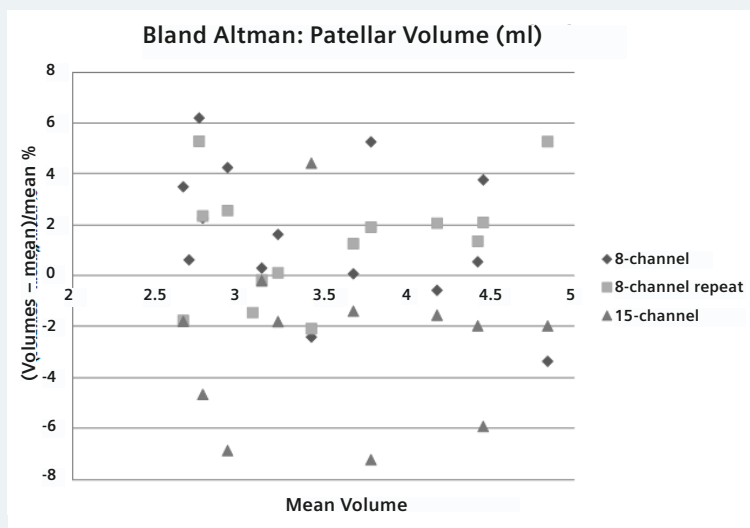
tions) to 100 (perfect agreement) when expressed as percentages. Volume measures were calculated to compare the results with the automatic (A) and manual (or re-test) (B) segmentation. For each cartilage region the volume,  $V$ , was calculated as the number of labeled voxels multiplied by the voxel dimensions. The reproducibility between cartilage measurement was assessed by calculating the Pearson's correlation coefficient ( $R$ ), Bland-Altman plots, and the percentage relative difference between the volume measurements ( $\text{Vol.RD} = 100 \times |V_a - V_b| / V_b$ ).

## Results

### Asymptomatic subjects: 3D sequence comparison

The results of the segmentation on each sequence for a representative subject can be seen in figures 2 and 3, whose computational efficiency is outlined in table 2. Overall, the segmentation of the DESS appears qualitatively to have the highest accuracy, likely due to the good contrast-to-noise at both the cartilage-bone and cartilage-synovial fluid interfaces. The VIBE sequence was reasonably accurate, although the larger slice thickness and lower cartilage-synovial contrast, especially when imaged coro-

nally resulted in mis-segmentation in the patellar-femoral and tibial-femoral cartilage regions. Although the cartilage tissue is inhomogeneous and the bone-cartilage interface can be indistinct, the *syngo* SPACE sequence generally worked well, and due to the good cartilage-synovial contrast overall its precision was similar to the VIBE. A summary of the quantitative validation for all datasets is provided in table 3. It can be seen that the DESS sequence obtained the highest and most consistent DSI in all cartilage regions (80–84%), while the VIBE (78–83%) and SPACE (79–80%) obtained fairly accurate



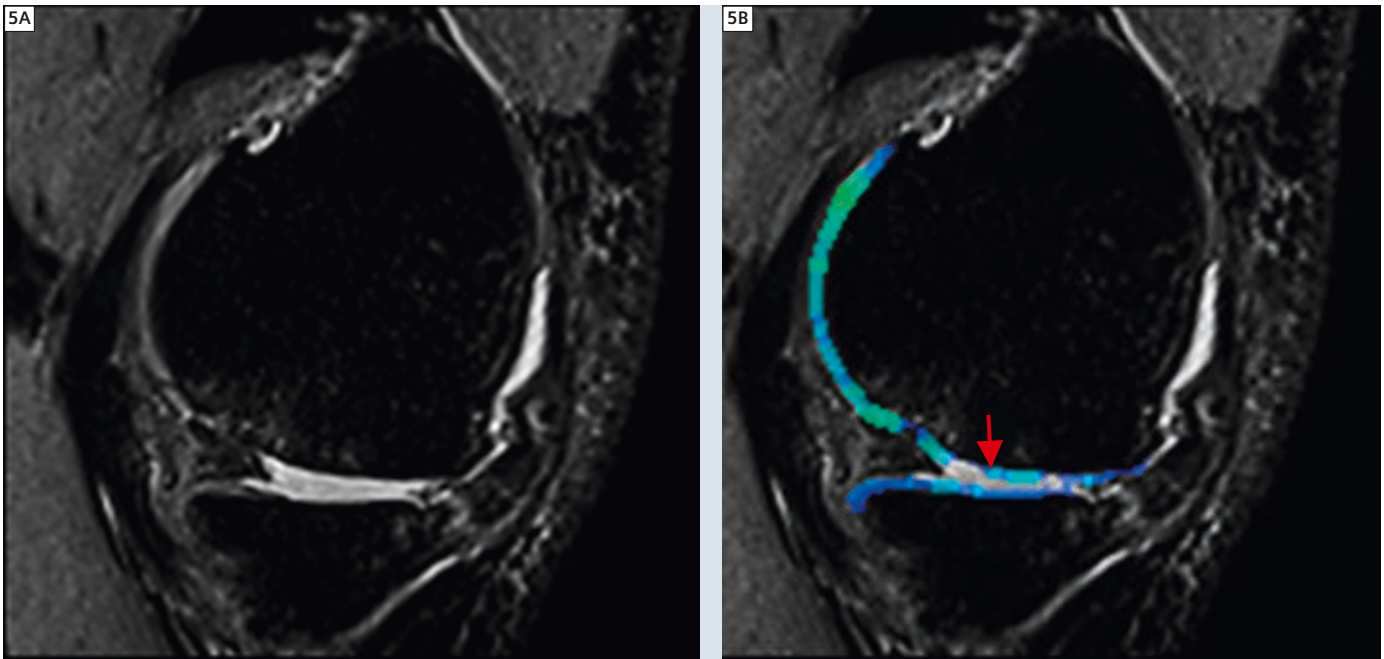
and consistent results. The manual DESS volumes and those calculated automatically for the DESS ( $R = 0.93$ – $0.98$  in both UQ and UL datasets), VIBE ( $R = 0.76$ – $0.94$ ) and SPACE ( $R = 0.91$ – $0.97$ ) were strongly correlated (Table 3). As the manual volumes were calculated on the DESS, there could be a bias towards the DESS, resulting in improved accuracy and stronger correlations. To fairly compare the sequences, manual segmentations of the SPACE and VIBE sequences should be performed.

In this study no gross segmentation errors were observed. The most common segmentation errors were focal errors, particularly at the cartilage interfaces (patella-femoral and femoral-tibial) as well as towards the ends of the cartilage regions (top of patellar, edges of the tibial). In a few cases, the cartilage signal drops in the inter-chondylar notch, sometimes resulted in mis-segmentation of cartilage as bone. In most scans, a non-uniform signal attenuation around the patella-femoral region was observed, which made detection of and separation of cartilage-synovial fluid more difficult (especially for VIBE) and increasing the amount of mis-segmentation in a few cases.

#### Asymptomatic subjects: test re-test and different coils

Bland-Altman plots of the (patellar, tibial and femoral) cartilage volume from the three scans of all 16 subjects can be seen in figure 4, and had an average coefficient of variation of (4.7, 2.7, 2.2)%. The automated volumetric analysis of the repeated scans with the 8-channel coil showed strong correlation ( $R = 0.97$ ,  $0.97$ ,  $0.99$ ), with all but four (of 48) cartilage plates having an absolute volume difference of less than 3%, three of these were patellar (4.2–5.5%) and one tibial (5.5%). Comparing the volume estimated automatically from the 8-channel and 15-channel coils also showed strong correlation ( $R = 0.96$ ,  $0.98$ ,  $0.99$ ), however, the volume estimated from the 8-channel coil appears

**4** Bland-Altman plot comparing automatic cartilage volume obtained for the (top) patella and (middle) tibial (bottom) femoral cartilages.



**5** Auto-segmentation results from Subject 1. Arrow points to mis-segmentation of tibial femoral intersection.

systemically larger than that of the 15-channel coil in all cartilage plates (between 0.67–5.5%). Manual analysis is required to determine if this bias is due to actual MR imaging differences or simply a bias in the segmentation algorithm due to subtle changes in the image contrast or other effects.

#### Case studies: pathological cases

Figures 5 to 8 show the SPACE sequence with overlaid automated segmentation contour for each subject (1, 2, 2 and 3 respectively).

The segmentation results for subject 1 were excellent and the excessive joint fluid and synovitis did not appear to have a significant effect on the segmentation. There were some segmentation errors where the superficial femoral and tibia cartilage was under-segmented at the medial tibial femoral interface (Fig. 5). There was also some under-segmentation of the medial patellar cartilage. Subject 2 had more severe cartilage damage and there were some segmen-

tation errors. Figure 6 shows an ICRS grade 4 lesion on the medial femoral condyle and a resulting segmentation error. The segmentation performed well on an ICRS grade 2 lesion to the lateral femoral condyle, shown in figure 7. Again under-segmentation errors were noticed at the tibial femoral interface. The trochlea also exhibited under-segmentation.

The segmentation for Subject 3 was excellent. The ICRS grade 2 cartilage lesion on the patella was well segmented as shown in figure 8, although there was some over-segmentation of the patella into the synovial fluid.

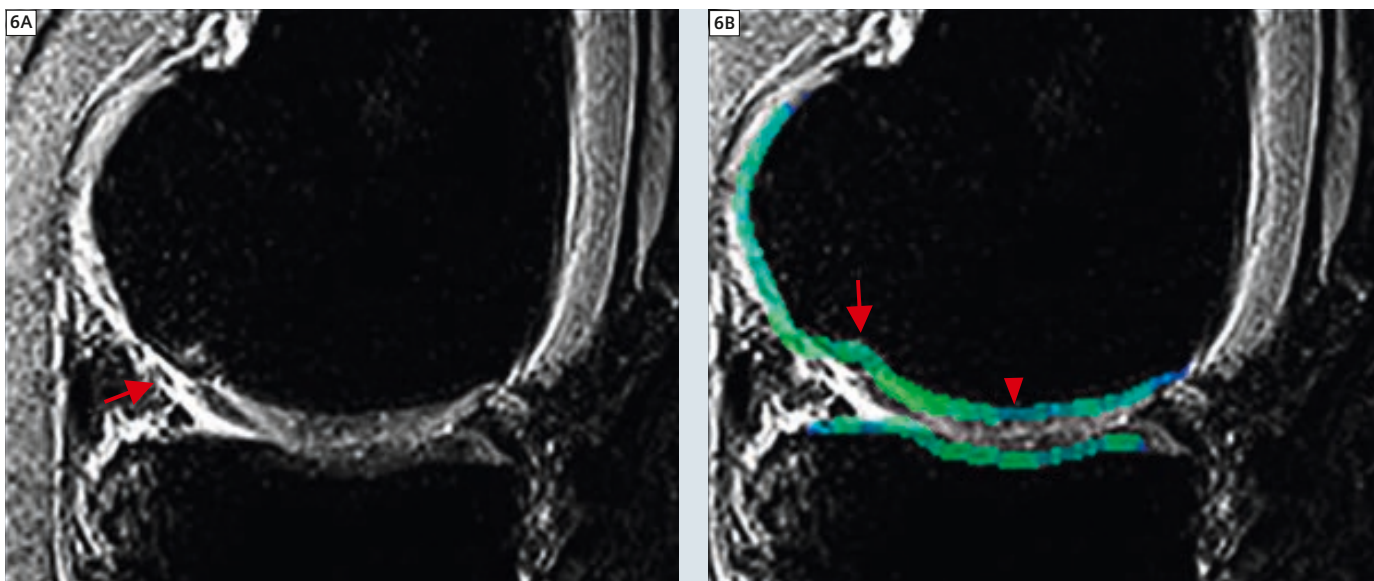
#### Discussion

The purpose of this paper was to assess the accuracy and repeatability of a novel automated cartilage segmentation routine.

The automatic segmentation of the DESS sequence had the highest correlation with the manual segmentations defined originally on the DESS. The

SPACE and VIBE had lower correlation and precision, making the detection of very subtle longitudinal changes more challenging. These results were not surprising, with VIBE having poor cartilage-synovial and muscle contrast, while SPACE has a less homogeneous cartilage appearance and the bone-cartilage interface (BCI) is less well defined [21]. However, as SPACE allows more accurate detection and grading of cartilage lesions and other internal cartilage changes compared to gradient echo techniques and thus has more clinical value [22, 23]. The scan time for SPACE is significantly faster than the other sequences, even if parallel imaging was enabled.

The shape and thickness based segmentation scheme was performed directly on the 3D scans and the results did not show any critical problems due to image contrast, resolution, sectioning or planar choice. In general the areas that cause the most errors and variability are at low contrast interfaces, particularly carti-



**6** Auto-segmentation results from Subject 2. Segmentation error was noticed at location of an ICRS grade 4 cartilage lesion on the femoral condyle (see arrow head) and at the tibial femoral interface (see arrow).

lage-cartilage. Strong signal inhomogeneity was observed to cause some focal mis-segmentation, particularly by cartilage being mis-identified as synovial fluid. Although the quantitative analysis for the coronal VIBE images was reasonable, errors due to partial voluming artifacts were observed in the patellar and femoral chondyles. For reproducible automated analysis using our technique a higher slice resolution would be recommended.

The automatic segmentation on the DESS sequence was found to have high same day reproducibility when repositioned and using two different knee coils. Manual segmentations of all scans is required to determine whether the subtle difference between 8 and 15-channel knee cartilage volumes is introduced by the coils or from some bias in the segmentation algorithm induced by subtle changes in signal/contrast or other effects.

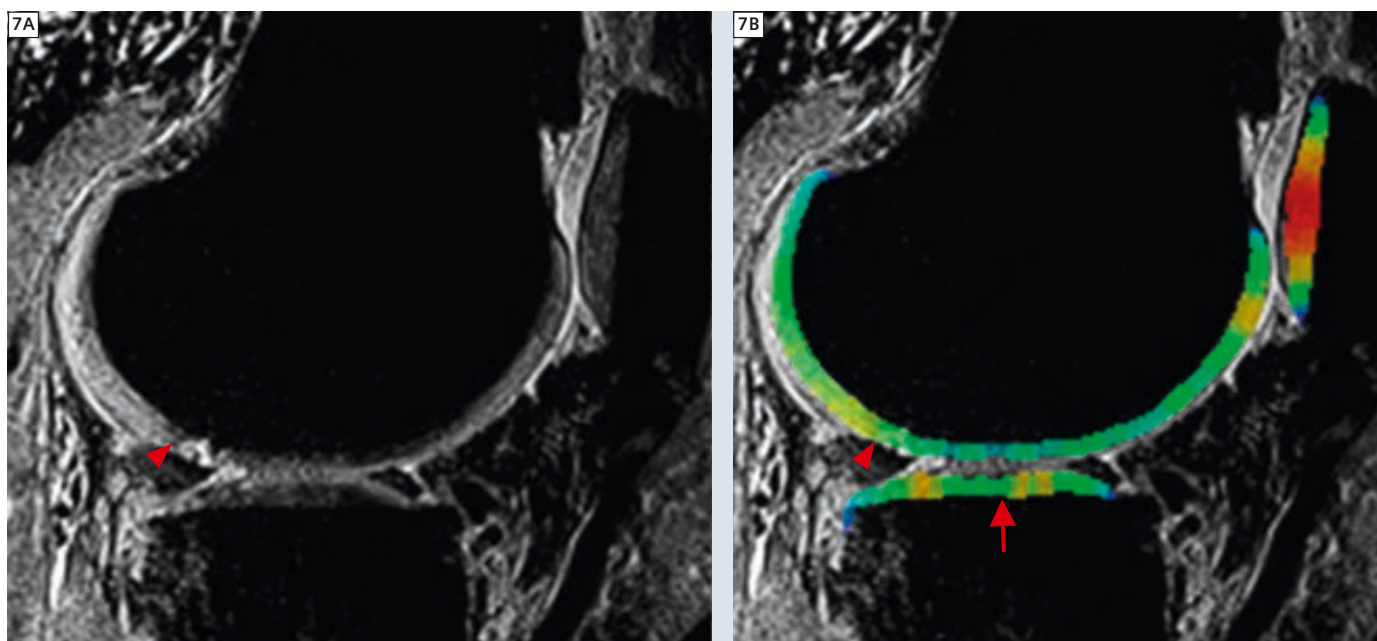
The initial results on the pathological

scans showed promise for use of the auto-segmentation routinely with patients. Areas with segmentation errors included the interface between the tibial and femoral cartilage, the superior tibial cartilage, and the medial patella. Excessive joint fluid and synovitis did not appear to affect the segmentation results. The subject with the most severe cartilage damage had the least successful segmentation results which may indicate that current segmentation regime is limited to less severe cases.

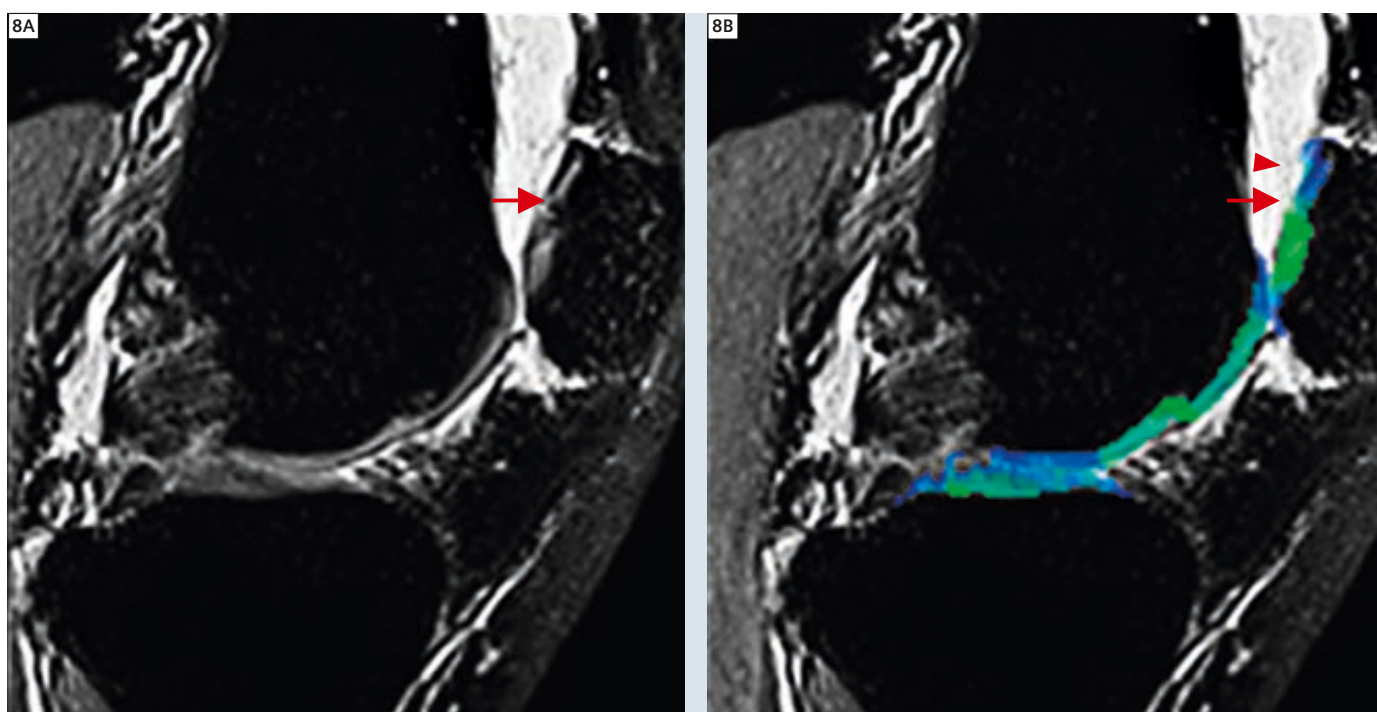
Segmentation processing time is very important for routine clinical use, the current algorithm is fast enough (< 5 minutes) to be run while other images are being scanned, allowing results to be available for assessment by radiologists at the end of the MRI session. Further validation using different image contrasts, resolutions, field strengths and coils as well as pathologic scans is required, especially to investigate any biases that could occur.

Although, the initial case reports show promise with pathologic cases further quantitative comparison on a larger dataset between manual and automated segmentation is required.

There are several clinical applications of automated cartilage segmentation. Manual segmentation is too time intensive and cannot be implemented into the routine clinical sessions. Automated cartilage segmentation allows for quantitative assessment of the morphological and biochemical state of the cartilage. Morphological cartilage data can be used for treatment planning and can be tracked over time to determine progression or healing of cartilage damage. Additionally, cartilage segmentations can be registered to biochemical sequences such as T2 and T1-mapping which have been shown to be more sensitive to early cartilage degeneration before morphological measurements.



**7** Auto-segmentation results from Subject 2. Good segmentation results were noticed at location of an ICRS grade 2 cartilage lesion on the femoral condyle (see arrow head). The superficial tibial cartilage is under-segmented (see arrow).



**8** Auto-segmentation results from Subject 3. Good segmentation results were noticed at location of an ICRS grade 2 cartilage lesion on the patella (see arrow). There was some over-segmentation of the patella into the synovial fluid (see arrow head).

## Conclusion

The accuracy and reproducibility of automatic cartilage segmentation and subsequent volume measures obtained from T2w DESS, T1w VIBE and PDw SPACE were assessed. The validation results indicate that the automatic segmentation algorithm performed best on the T2w DESS images. The SPACE sequence has lower scan time, better diagnostic utility and is the most likely 3D sequence to be used in clinical scanning. We found that the SPACE sequence obtained reasonably accurate automated morphological cartilage assessment, although less accurate than DESS.

## Acknowledgements

The research was funded by an ARC Linkage grant (LP100200422).

### Contact

Jurgen Fripp  
Level 5 UQ Health Sciences  
Building 901/16  
Royal Brisbane and Women's  
Hospital Herston  
Queensland 4029  
Australia  
Phone: +61 7 3253 3660  
Fax: +61 7 3253 3690  
Mobile: +61 31 241 277  
jurgen.fripp@csiro.au

### References

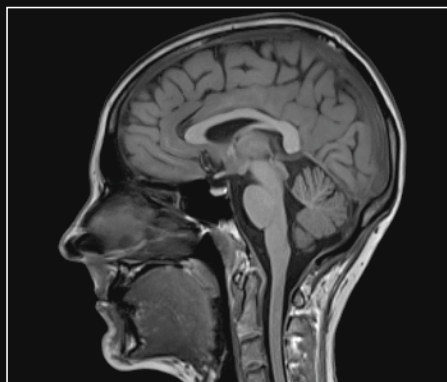
- Crema MD, Roemer FW, Marra MD, Burstein D, Gold GE, Eckstein F, et al. Articular cartilage in the knee: current MR imaging techniques and applications in clinical practice and research. *Radiographics*. 2011 Feb;31(1):37–61.
- Eckstein F, Burstein D, Link TM. Quantitative MRI of cartilage and bone: degenerative changes in osteoarthritis. *NMR Biomed*. 2006 Nov;19(7):822–54.
- Wang Y-XJ, Griffith JF, Ahuja AT. Non-invasive MRI assessment of the articular cartilage in clinical studies and experimental settings. *World J Radiol*. 2010 Jan 28;2(1):44–54.
- Roemer FW, Crema MD, Trattinnig S, Guermazi A. Advances in imaging of osteoarthritis and cartilage. *Radiology*. 2011 Aug;260(2):332–54.
- Eckstein F, Cicuttini F, Raynauld J-P, Waterton JC, Peterfy C. Magnetic resonance imaging (MRI) of articular cartilage in knee osteoarthritis (OA): morphological assessment. *Osteoarthritis Cartil*. 2006;14 Suppl A:A46–75.
- Schneider E, Nevitt M, McCulloch C, Cicuttini FM, Duryea J, Eckstein F, et al. Equivalence and precision of knee cartilage morphometry between different segmentation teams, cartilage regions, and MR acquisitions. *Osteoarthritis Cartil*. 2012 Aug;20(8):869–79.
- Glocker B, Komodakis N, Paragios N, Glaser C, Tziritis G, Navab N. Primal/dual linear programming and statistical atlases for cartilage segmentation. *Med Image Comput Comput Assist Interv*. 2007;10(Pt 2):536–43.
- Folkesson J, Dam EB, Olsen OF, Pettersen PC, Christiansen C. Segmenting articular cartilage automatically using a voxel classification approach. *IEEE Trans Med Imaging*. 2007 Jan;26(1):106–15.
- Grau V, Mewes AUJ, Alcañiz M, Kikinis R, Warfield SK. Improved watershed transform for medical image segmentation using prior information. *IEEE Trans Med Imaging*. 2004 Apr;23(4):447–58.
- Yin Y, Zhang X, Williams R, Wu X, Anderson DD, Sonka M. LOGISMOS—layered optimal graph image segmentation of multiple objects and surfaces: cartilage segmentation in the knee joint. *IEEE Trans Med Imaging*. 2010 Dec;29(12):2023–37.
- Fripp J, Crozier S, Warfield SK, Ourselin S. Automatic segmentation and quantitative analysis of the articular cartilages from magnetic resonance images of the knee. *IEEE Trans Med Imaging*. 2010 Jan;29(1):55–64.
- Eckstein F, Hudelmaier M, Wirth W, Kiefer B, Jackson R, Yu J, et al. Double echo steady state magnetic resonance imaging of knee articular cartilage at 3 Tesla: a pilot study for the Osteoarthritis Initiative. *Ann. Rheum. Dis*. 2006 Apr;65(4):433–41.
- Hunter DJ, Niu J, Zhang Y, Totterman S, Tamez J, Dabrowski C, et al. Change in cartilage morphometry: a sample of the progression cohort of the Osteoarthritis Initiative. *Ann. Rheum. Dis*. 2009 Mar;68(3):349–56.
- Hunter DJ, Bowes MA, Eaton CB, Holmes AP, Mann H, Kwok CK, et al. Can cartilage loss be detected in knee osteoarthritis (OA) patients with 3-6 months' observation using advanced image analysis of 3T MRI? *Osteoarthritis Cartil*. 2010 May;18(5):677–83.
- Wirth W, Larroque S, Davies RY, Nevitt M, Gimona A, Baribaud F, et al. Comparison of 1-year vs 2-year change in regional cartilage thickness in osteoarthritis results from 346 participants from the Osteoarthritis Initiative. *Osteoarthritis Cartil*. 2011 Jan;19(1):74–83.
- Eckstein F, Kunz M, Schutzer M, Hudelmaier M, Jackson RD, Yu J, et al. Two year longitudinal change and test-retest-precision of knee cartilage morphology in a pilot study for the osteoarthritis initiative. *Osteoarthritis Cartil*. 2007 Nov;15(11):1326–32.
- Abramoff, M.D., Magalhaes, P.J., Ram, S.J. *Image Processing with ImageJ*. Biophotonics International. 2004;11(7):36–42.
- Ibáñez L. *The ITK software guide : updated for ITK version 2.4 [the insight segmentation and registration toolkit] [covers installing and programming with ITK] [includes C source code examples and data]*. 2. ed., November 21, 2005. [New York]: Kitware; 2005.
- Fripp J, Crozier S, Warfield SK, Ourselin S. Automatic segmentation of the bone and extraction of the bone-cartilage interface from magnetic resonance images of the knee. *Phys Med Biol*. 2007 Mar 21;52(6):1617–31.
- Dice, L. Measures of the amount of ecologic association between species. *Ecology*. 1945;26:297–302.
- Friedrich KM, Reiter G, Kaiser B, Mayerhöfer M, Deimling M, Jellus V, et al. High-resolution cartilage imaging of the knee at 3T: basic evaluation of modern isotropic 3D MR-sequences. *Eur J Radiol*. 2011 Jun;78(3):398–405.
- Notohamiprodjo M, Horng A, Pietschmann MF, Müller PE, Horger W, Park J, et al. MRI of the knee at 3T: first clinical results with an isotropic PDfs-weighted 3D-TSE-sequence. *Invest Radiol*. 2009 Sep;44(9):585–97.
- Notohamiprodjo M, Horng A, Kuschel B, Paul D, Li G, Raya JG, et al. 3D-imaging of the knee with an optimized 3D-FSE-sequence and a 15-channel knee-coil. *European Journal of Radiology* [Internet]. 2012 May [cited 2012 Jul 3].

# MAGNETOM Prisma Image Gallery

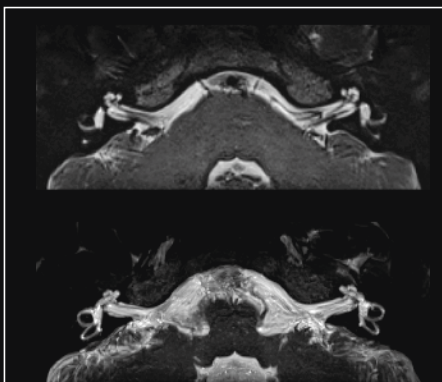
MAGNETOM Prisma\*, Siemens' new and powerful 3T MRI system, is built to tackle the most demanding research challenges. It delivers maximum perfor-

mance under prolonged high-strain conditions opening new possibilities for imaging functional processes and understanding the most threatening diseases.

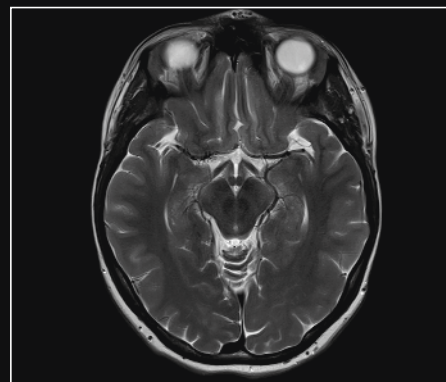
Only one of many high-performance features is the new XR 80/200 gradient system. With its higher gradient amplitude it delivers significantly higher sig-



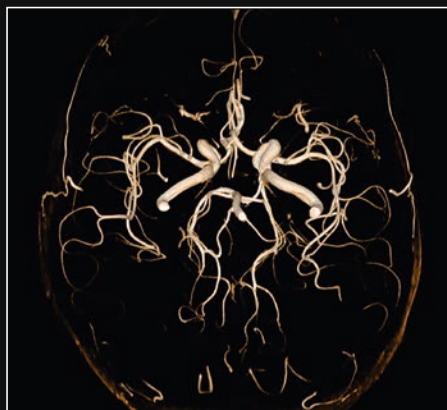
Head, T1 3D MPRAGE sagittal, isotropic, PAT factor 2, effective SL 0.8 mm, matrix 288



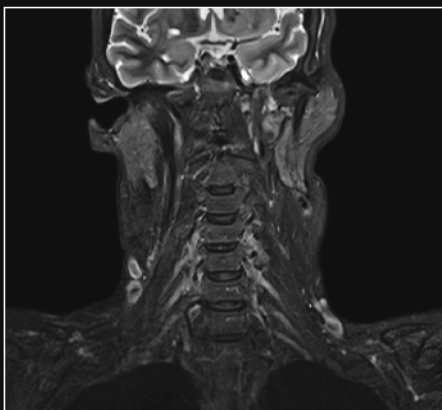
Head IAC, syngo ZOOMit, T2 3D SPACE thin MPR and tihin MIP, FOV 50x160 mm, matrix 320



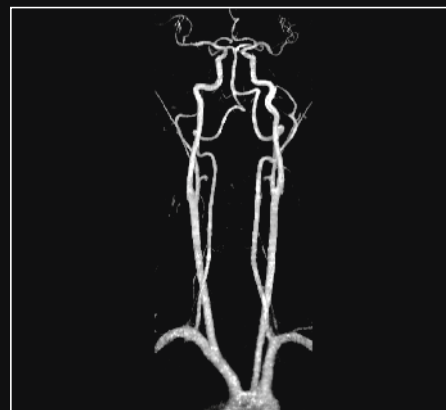
Head, T2 TSE transversal, matrix 512



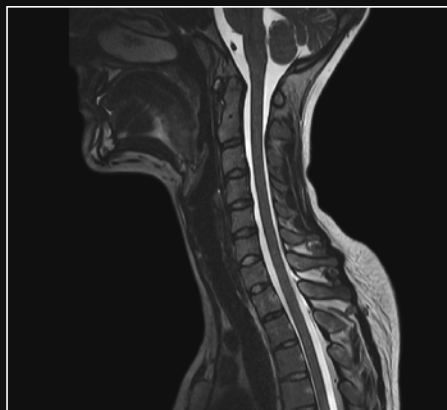
Head Angiography, 3D FLASH TOF, VRT, PAT factor 2, matrix 320  
32-channel Head coil



Head/Neck, T2 TSE Dixon water coronal, PAT factor 2, matrix 320



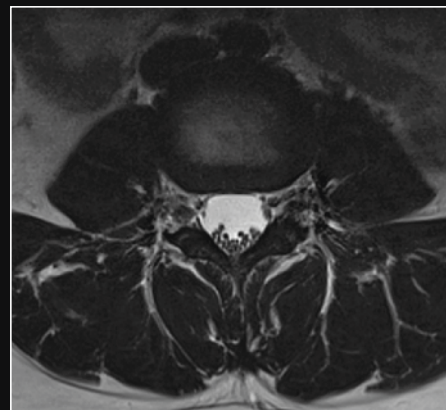
Carotids Angiography, 3D FLASH TOF, MIP, PAT factor 3, matrix 384  
64-channel Head/Neck coil



C-spine, T2 3D SPACE sagittal, PAT factor 2, matrix 320



L-spine, T2 TSE SPAIR sagittal, PAT factor 2, matrix 448



L-spine, T2 TSE transversal, matrix 448

\*The product is under development and not commercially available. Its future availability cannot be ensured.

nal-to-noise ratio, enhancing for example physiological imaging or morphometric measurements. With MAGNETOM Prisma's higher spatial and temporal

resolution you can see excellent anatomical detail, for example displaying functional and structural brain connectivity or smallest lesions with zoomed

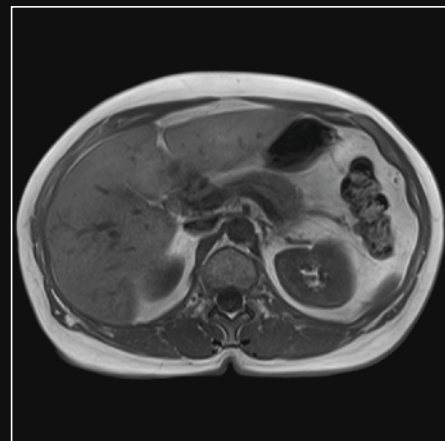
MRI. Additionally, it delivers benchmark 3T magnet homogeneity – the basis for superior quantitative evaluations.



Thoracic, 3D SPACE IR thin MIP, PAT factor 2, matrix 320



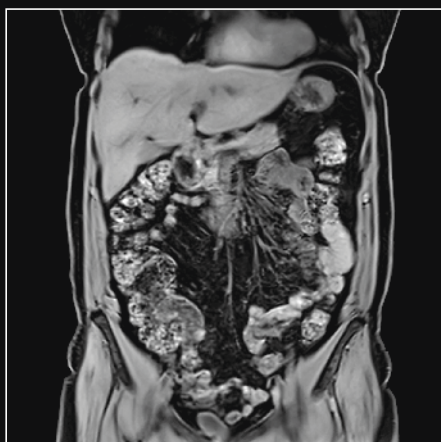
Abdomen, syngo BLADE, T2 TSE coronal, PAT factor 2, matrix 320, FOV 500 mm



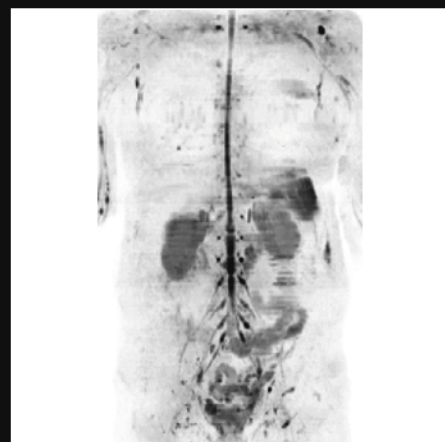
Abdomen, T1 3D VIBE inphase transversal, CAIPIRINHA, PAT factor 4, matrix 320, TA 13 s



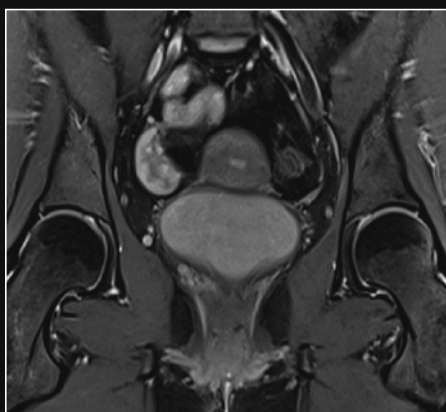
Abdomen, T1 3D VIBE opposed phase coronal, CAIPIRINHA, PAT factor 6, isotropic, matrix 320, FOV 450 mm, TA 18 s



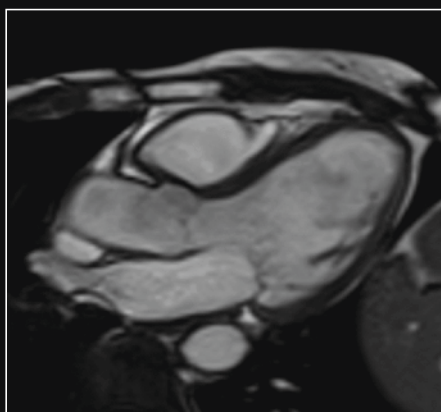
Abdomen, T1 3D VIBE Dixon water coronal, CAIPIRINHA, PAT factor 6, isotropic, matrix 320, FOV 450 mm, TA 18 s



Abdomen coronal, syngo REVEAL, b-value 800, 3 steps composed, PAT factor 2



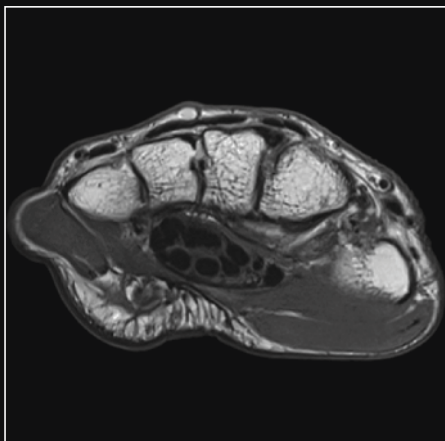
Pelvis female, PD TSE SPAIR coronal, PAT factor 2, matrix 448



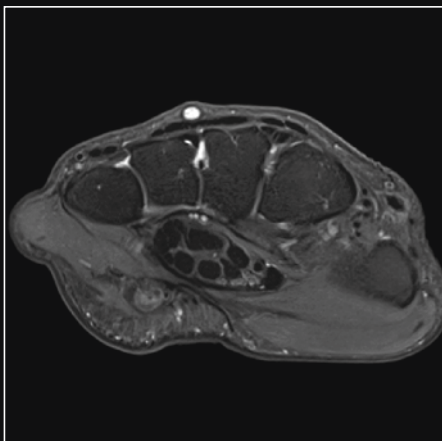
Cardio Function, TrueFISP cine RVOT, PAT factor 3, matrix 208



Cardio Coronary, 3D FLASH SPAIR thin MIP, matrix 320



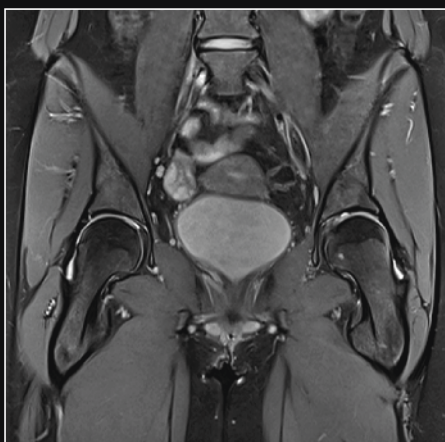
Wrist, PD TSE transversal, PAT factor 2, matrix 320, 16-channel Hand/Wrist coil



Wrist, PD TSE FatSat transversal, matrix 320, 16-channel Hand/Wrist coil



Hips, T1 TSE coronal, PAT factor 2, matrix 512, 18-channel Body/32-channel Spine coil



Hips, PD TSE SPAIR coronal, PAT factor 2, matrix 448, 18-channel Body/32-channel Spine coil



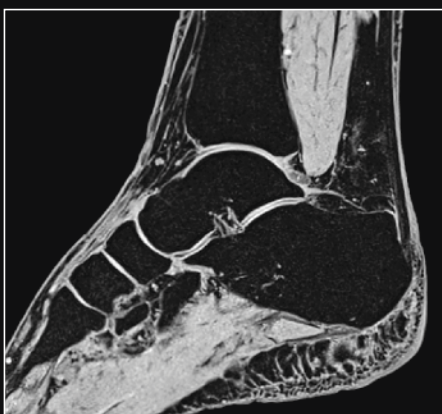
Knee, PD TSE FatSat coronal, PAT factor 2, matrix 384, 15-channel Knee coil



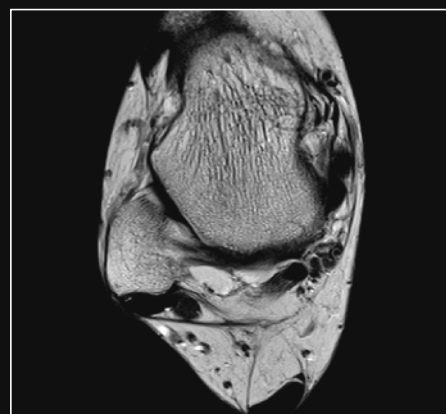
Knee, T2 TSE transversal, matrix 512, 15-channel Knee coil



Ankle, PD TSE FatSat sagittal, PAT factor 2, matrix 384, 16-channel Foot/Ankle coil



Ankle, T1 3D VIBE water excitation sagittal, PAT factor 2, matrix 320, 16-channel Foot/Ankle coil



Ankle, T2 TSE transversal, matrix 320, 16-channel Foot/Ankle coil

# The New, High-Performance MR Gradient System XR 80/200. Design, Benefits and Safe Operation

Daniel Fischer; Eva Eberlein

Siemens Healthcare, Erlangen, Germany

## Introduction

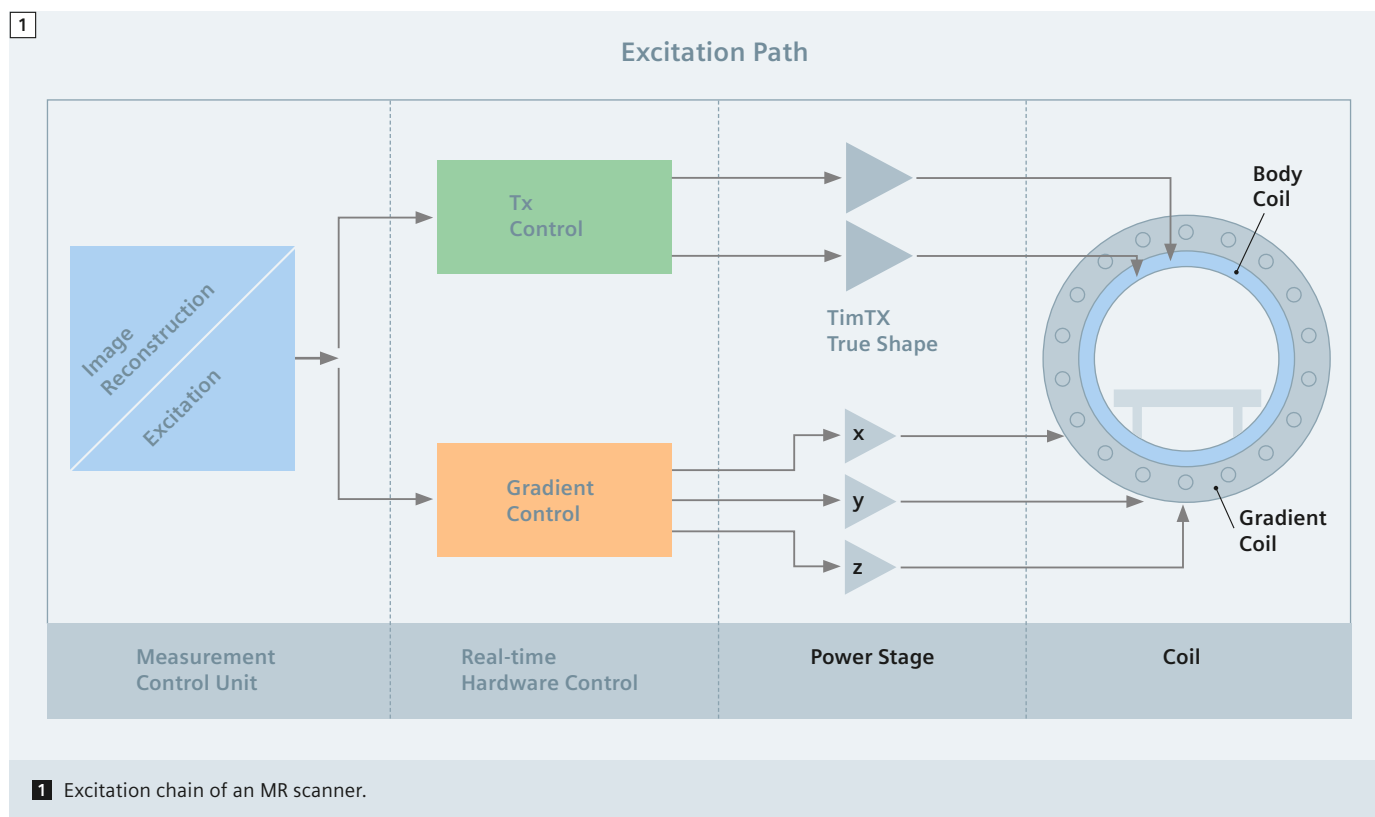
At the RSNA 2012, Siemens introduced MAGNETOM Prisma\*, a new 3 Tesla MR imaging (MRI) scanner. This system is designed to fit the needs of those involved primarily in research activities. The foundation of the system is a new 3T magnet, based on the proven MAGNETOM Trio. It provides the same robust base as Trio did – with high homogeneity, only now with zero helium boil-off. MAGNETOM Prisma combines Siemens' latest technological advancements in MR signal transmit and receive technologies – TimTX

TrueShape and Tim 4G technology, with the latter forming the backbone of other Siemens MR scanners 1.5T MAGNETOM Aera and 3T MAGNETOM Skyra. Both technologies have shown an increase in image quality and imaging speed, providing their value in a number of clinical MRI applications [1]. On top of these components, MAGNETOM Prisma includes XR 80/200, a new, high-end gradient system that delivers high gradient amplitudes and fast switching capabilities in a combination that is currently

unmatched in the market.

This article is to provide insight into the evolution of the new gradient engine: a brief history of gradients in MR, the technical aspects surrounding the XR gradient engine, safety mechanisms, as well as the benefits that MR applications stand to gain from the outstanding performance.

\*The product is still under development and not commercially available yet. Its future availability cannot be ensured.



## A few words on gradients

The gradient system is one of the major sub-systems of any MR scanner. It plays a key role in the creation of the MR image by providing a means to:

- 1) spatially select a region that should be imaged and
  - 2) encode the contents of this region.
- Both selection and encoding are done by applying electric current to the gradient coil, thus creating a field slope on any one of the physical axes x, y, or z. Through precise timing of these additional fields, or gradients, a specific section of an object can be selected and then encoded. By altering the physical characteristics of the selected image region, it can be seen that the gradients have a tremendous influence on the overall quality of the acquired image.

In order to create a gradient pulse in the context of an MR measurement, a lot has to happen, and it all has to happen very fast. The gradient sub-system can be generalized as a chain of several individual units that receive data from their previous neighbor on the chain, process it, and then pass it down the chain to their next neighbor. First in this chain is the measurement control unit, which controls the entire MR pulse sequence and image reconstruction task. This unit has the task of 'ordering' not only gradient pulses, but also the necessary RF pulses and performing the reconstruction algorithms on the received MR data. The 'ordered' gradient pulse information is passed onto the next unit, the gradient control module, which works digitally and in sub-millisecond intervals, executing the desired gradient pulse forms in real-time and performing algorithms on these wave forms in order to compensate for effects such as eddy currents, delays, and other gradient-field-induced abnormalities. Next, the small-signal unit processes the digital signal further and converts it into an analog signal, to be fed into the power stage. Here, the signal is amplified and finally fed to the last member of the chain, the gradient coil, in which the rapidly flowing current creates a gradient field in the region of interest. The two main performance characteristics of any gradient sub-system are the maxi-

mum attainable amplitude (Gmax), which is measured in millitesla per meter (mT/m), and the slew rate (SR), which describes how fast a gradient can attain a desired amplitude and is measured in Tesla per meter per second (T/m/s). Ideally, the gradient sub-system is designed in a way to allow the highest amount of performance (Gmax and SR) without having to compromise one measure for the other. It is not uncommon to find clinical scanners with a Gmax anywhere from 33 mT/m to 45 mT/m, while slew rates can vary from 100 T/m/s to 200 T/m/s. To get an idea as to how gradient performance has evolved over the past 30 years: In 1983 the first super-conducting 0.35T clinical Siemens MAGNETOM system, was commissioned in St. Louis, USA and could deliver a maximum gradient amplitude of 3 mT/m and a slew rate of 3 T/m/s. Ten years later in 1993, the MAGNETOM Vision was introduced and set a new standard in gradient performance for clinical systems with a maximum amplitude of 25 mT/m and a slew rate of 42 T/m/s. Shifting to the new century, MAGNETOM Avanto, the first Tim system, was introduced in 2003 and boasted gradients with a 45 mT/m maximum amplitude and a 200 slew rate. MAGNETOM Prisma raises the gradient performance bar again, delivering maximum gradient amplitude of 80 mT/m and a slew rate of 200. In very few industries has there been such a dramatic enhancement in performance in such a short period of time.

So what are the benefits of maximum amplitude and slew rate? The gradient sub-system has a direct influence on the spatial resolution and acquisition time of the MR image [4]. By increasing the performance of the gradient sub-system, you can increase the spatial resolution and decrease the acquisition time. In terms of MR images, increased gradient performance translates into more signal-to-noise (SNR), fewer distortions, higher in-plane resolution and thinner slices. In short, better image quality. Fast imaging techniques such as echo planar imaging (EPI) and turbo spin echo (TSE) have evolved and thrived in part because

of the higher performance that gradient sub-systems have been able to offer. Diffusion-weighted imaging (DWI) benefits greatly as well because there is a direct relation of the measured ADC data to the square of the diffusion gradient amplitudes. By utilizing higher gradient amplitudes, higher levels of SNR can be achieved, improving DWI and making it even more relevant in the clinical and research environments.

The technical challenge in designing a gradient system is two-fold. On one hand, the desire exists to deliver outstanding performance, which allows the user to realize the previously mentioned imaging benefits. On the other hand, guaranteeing safe operation is paramount. Striking the right balance of performance and safety is the key guiding principle in this process. The characteristics of high gradient performance and safety are largely dependent on the design of the analog components in the gradient sub-system, namely the power amplifier and gradient coil, and play a major role in achieving the desired image quality results. However, the surrounding digital infrastructure also contributes significantly. The following sections give an overview of the XR gradient system in the MAGNETOM Prisma.

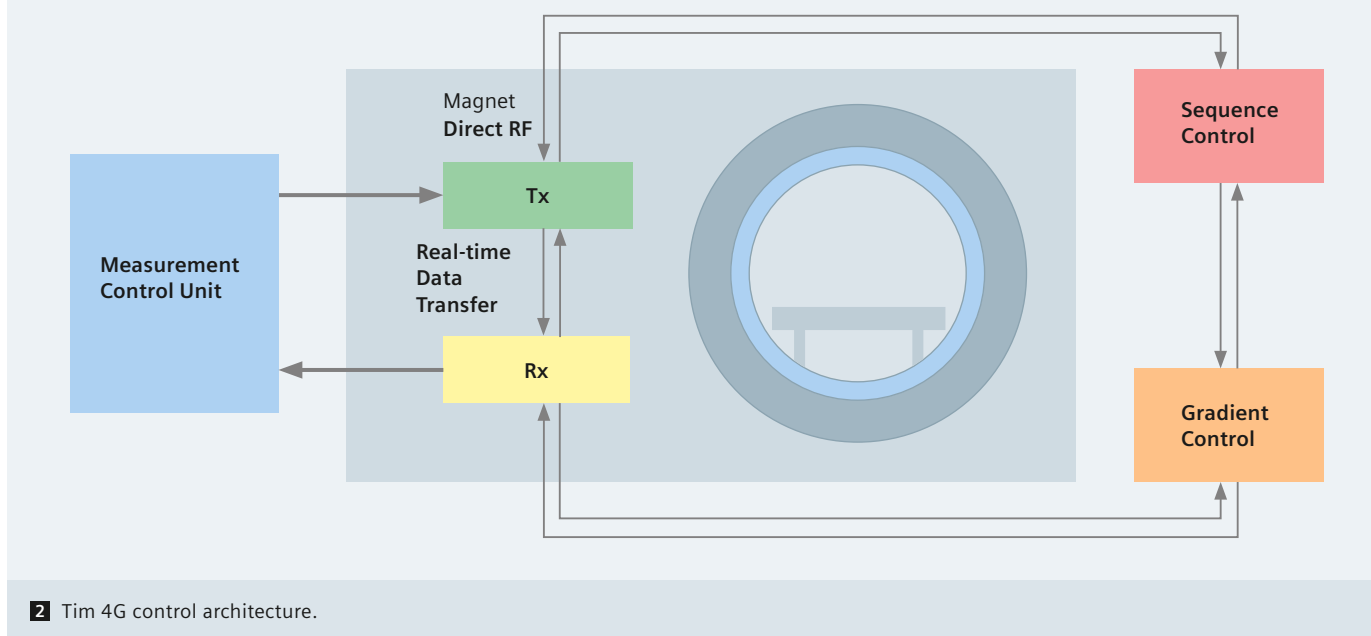
## The XR gradient system

The XR gradient is a key component of the technological foundation upon which the MAGNETOM Prisma is built. This gradient is capable of driving maximum amplitudes of up to 80 mT/m with a slew rate of 200 T/m/s, on each axis, simultaneously. Let's take a deeper look at these aspects as they relate to designing the XR gradient system.

The gradient coil can truly be considered a masterpiece of engineering as it brings a number of separate topics together: physics, electro-magnetics, thermodynamics, mechanics, and manufacturing. As the gradient coil is responsible for precisely encoding the physical characteristics within the measurement volume, it is imperative that particular attention be paid to its design. The XR gradient coil itself is constructed of numerous

2

## Tim 4G Scanner Control Architecture



2 Tim 4G control architecture.

individual layers of different materials, making the coil substantially thicker and, as a result, much heavier than conventional gradient coils. These layers all have a specific function – whether the conductors to create and adjust the gradient fields, the isolation layers to aid in protection from RF disturbances as well as those potentially induced by the coil itself, or the fill layers to ensure a stable and rigid coil. Additionally, a number of these layers are dedicated water-cooling. High gradient performance delivers a strong, stable and linear gradient field. A byproduct of all of this current is induced mechanical vibration [3] and thermal noise as well as heat as a result of simple electrical resistance. Through an efficient force compensation design on all axes, these vibrations can be reduced to a minimum. The sheer size of the gradient coil plays to its advantage, whilst the mass of the coil helps reduce vibrations, acoustic noise, and eddy currents further. Heat must still be dealt with as efficiently as possible. Failure to do so can result in a decrease in contrast and an increase in susceptibility artifacts due to a thermally induced drift of the  $B_0$  frequency, a common effect with fast

imaging techniques such as EPI. With this in mind, the designers of the XR gradient coil utilized a special conductive material that allows thermal energy to be transferred easily to the coolant flowing through these layers in the coil. Each cooling layer is then placed next to a coil conductor, effectively giving each axis its own individual cooling source. In total, the MAGNETOM Prisma has the ability to cool up to 60 kW, thus ensuring that any thermal energy created by the system is also removed from the system, guaranteeing stability and performance at the same time.

Driving the gradient coil is a power amplifier system designed specifically to handle the needs of such a high-performance gradient system. Modular in design and small in footprint, the solid-state amplifier provides 2250 V at maximum voltage for fast switching gradients and up to 900A of peak current for high-amplitude pulses, which this amplifier can achieve simultaneously. It has the total specified power available to it at all times – there is no need to switch to a special hardware mode which would create some compromise with respect to maximum amplitude or slew rate.

It is these specific capabilities that made this amplifier so attractive for the renowned high-performance gradient system supplied by Siemens for the Human Connectome Project (HCP). For this project, two unique MR systems were built, using this amplifier specifically for neurological research. One such system is able to deliver up to 300 mT/m of peak gradient amplitude with a slew rate of 200 T/m/s!

While power is important to drive performance, it is just as important to have the ability to accurately reproduce the pulses from scan to scan. Unless the unit controlling the amplifier and thus the gradient coil is deterministic and precise in its functionality, then stable performance of the entire system cannot be guaranteed. The gradient control unit of the XR gradient system consists of a real-time digital signal-processing unit working in sub-millisecond intervals to control the entire operation of the gradient system as requested by the MR sequence. Like many other control units critical to the MR system functionality, the gradient control unit contains a vast amount of intelligence. It has the ability to influence the state of the entire MR

system through an intelligent real-time data transfer, realized via a fiber-optic communication network. Through this real-time data transfer, which is common on all Tim 4G MR scanners and made possible by DirectRF, all components that rely on data produced by the gradient system – be it for fine-tuning of the RF transmit/receive systems, patient safety data collection, or supplying algorithms with data, can receive it in real-time and integrate it into their data processing chain. The gradient control unit is part of an intelligent network and plays an integral part not only in the operation of the XR gradients, but also the entire MAGNETOM Prisma.

### Safe operation

Unfortunately we cannot continuously increase the amplitudes and slew rates of our gradient pulses and reap their benefits. A rapidly changing magnetic field, which is essentially what MR gradients are meant to produce, have been shown to produce physiological effects such as peripheral nerve stimulation (PNS) in humans [2]. These effects can be uncomfortable. All MR systems with a gradient system that has the potential to stimulate must provide measures in order to ensure that this does not occur. How is it possible to maximize performance of the gradient system while maintaining safe operation under these conditions?

The XR gradient system, like all other Tim 4G scanners, employs several safety measures (or layers) in order to allow the user to not only maximize the performance of the gradient system, but also to ensure that the patient is in no way harmed and safe at all times. Feeding off the vast knowledge that has been accumulated through projects such as the Human Connectome Project, the MAGNETOM Prisma employs three main layers of safety.

First – the prediction. A so-called 'look-ahead', or prediction monitor examines the critical pulses in a measurement protocol and determines whether or not it will be possible to run the protocol without exceeding the stimulation limit. If it is deemed that the protocol will exceed

stimulation limits, then the user is presented with a set of possibilities as to how to adjust the protocol, allowing it to run. If the MR protocol checks out OK, then it is allowed to run. Prior to the actual execution of the sequence, the look-ahead monitor sends measurement parameters to the second safety layer – the online monitor.

The online monitor has the task of calculating the current stimulation level and checking this against that calculated by the prediction model. Each calculation occurs at regular sub-millisecond intervals during a running sequence. Should at any time during a running sequence the measured levels exceed the predicted levels, the measurement is stopped. Upon completion of a measurement, the prediction model obtains the final stimulation results from the online monitor and does a comparison: does the calculated prediction model stimulation correlate with the actual measured stimulation? By checking the prediction model with the online calculation, there is the added security that the hardware is performing as intended and the user is receiving the maximum performance available. If there were a discrepancy, the user would be notified of this. The third and final safety layer involves Tim 4G technology. We are not referring to the high-density coils that Tim 4G is known for, but rather the infrastructure that makes it possible to integrate them flawlessly into a complex system.

Through the intense use of fiber optics that enable the DirectRF real-time data transfer, the scanner can digitally transmit large amounts of raw data over dedicated channels from the receivers located directly at the magnet, to the measurement control unit located in the equipment room in a fast and efficient manner. At the same time, other MR components, such as the transmitter or gradient controller, utilize the same fiber optic technology to communicate with each other, at all times, and in real-time. By doing so, the free exchange of information between MR-critical components is possible. Information such as measurement results, calibration data, status updates, and safety information is

broadcast over this 'network' at all times to all components. Should one component in this network exhibit abnormal behavior, this is registered and the scanner is immediately brought into a safe state. Fiber optics is just part of the digital backbone that makes Tim 4G possible – not just for excellent image quality, but also for robust communication and safe operation of all components at the scanner.

### Outlook

The XR 80/200 gradient system of the MAGNETOM Prisma sets a new standard in gradient performance. The design of a unique gradient coil that is easily able to handle the stresses demanded by MR researchers, coupled with a powerful amplifier and an intelligent control system make this the gradient system the perfect centerpiece for a 3T MR research platform. Ensuring safe operation is of the utmost importance, and multiple, redundant layers of safety make this possible. Many MR applications will surely benefit from the gradient power that the XR 80/200 gradient system provides. Adding the technologies TimTX TrueShape, Tim 4G, and a solid 3T magnet to the XR gradients and you get MAGNETOM Prisma – a powerful and flexible tool that will offer MR researchers innumerable possibilities.

#### References

- 1 Boada, Shepherd, Rosenkrantz, Sigmund, Fütterer, Chandarana, Hagiwara, Rusinek, Mikheev, Bruno, Geppert, Glielmi, Pfeuffer, Parallel Transmission and its Clinical Implementation: Enabling new Clinical Imaging Paradigms, MAGNETOM Flash 2/2013, Vol. 52, pp 104ff.
- 2 Reilly, J.P., Medical and Biological Engineering and Computing March 1989, Volume 27, Issue 2, pp 101-110.
- 3 Mansfield, Haywood, Coxon – Active Acoustic Control in Gradient Coils for MRI Magnetic Resonance in Medicine 46:807–818 (2001).
- 4 Cohen, Echo Planar Imager and functional MRI. Appeared in Bandetti and Moonen: Functional MRI 2000, 137-149.

#### Contact

Daniel Fischer  
Siemens Healthcare  
IM MR PI PPM  
daniel.df.fischer@siemens.com

# PRFS Thermometry Proximal to Cryoablation Ice-ball

Antje Kickhefel<sup>1</sup>; Clifford Weiss<sup>2</sup>; Joerg Roland<sup>1</sup>; Patrick Gross<sup>1</sup>; Fritz Schick<sup>3</sup>; Rares Salomir<sup>4</sup>

<sup>1</sup>Siemens Healthcare, Erlangen, Germany

<sup>2</sup>Johns Hopkins University, Baltimore, MD, USA

<sup>3</sup>Eberhard-Karls University Tübingen, Section on Experimental Radiology, Department of Diagnostic and Interventional Radiology, Tübingen, Germany

<sup>4</sup>University of Geneva, Faculty of Medicine, Geneva, Switzerland

The concepts and information presented in this paper are based on research and are not commercially available.

## Introduction

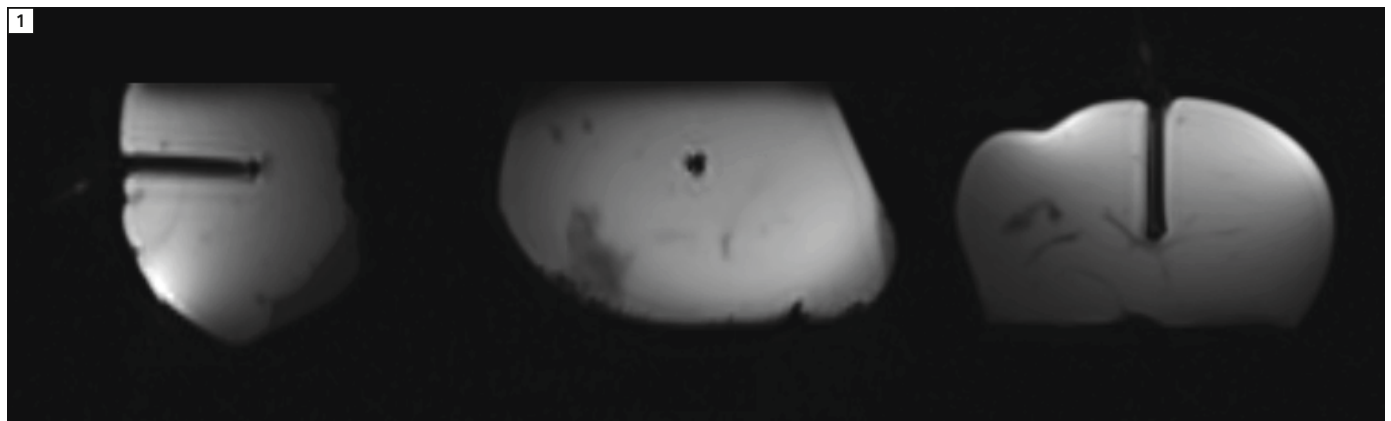
Cryoablation is a promising minimally invasive therapy used to treat malignancies in various organs, and has gained large acceptance in the treatment of prostate and liver cancer [1].

Cryoablation is less painful than high-temperature coagulation techniques such as Laser Induced Thermo Therapy (LITT) or Radio-frequency Ablation (RFA). An additional advantage of cryoablation is the possibility of 'sculpting' the ice-ball using multiple probes, in order to contour complex or large lesions. Magnetic resonance imaging (MRI) guidance of cryoablation allows the monitoring of the ice-ball boundary in three dimensions with excellent contrast

between the frozen and unfrozen tissue and potentially allows noninvasive temperature mapping around the ice-ball [2-9].

Previous studies reported MR thermometry inside the ice-ball based on temperature dependent  $T_2^*$  changes during cryoablation. Given the very short  $T_2^*$  values within the ice-ball, short echo time (TE) values need to be used, in the range  $\leq 1$  ms [2]. Kaye et al. [10] showed exponential dependency of the  $T_2^*$ -relaxation time in the temperature range between  $-20^\circ\text{C}$  to  $-5^\circ\text{C}$ . This exponential behavior is similar for different tissues (liver, heart, kidney, prostate) [11, 12].

Temperature monitoring in the tissues proximal to the ice-ball would be a valuable safety tool, particularly considering at-risk structures adjacent to the target tissue/organ (e.g. nerve bundles, wall of large vessels, urinary bladder). Currently, temperature monitoring around the ice-ball is performed using invasive temperature probes, which must be placed by the operator, a time consuming procedure prone to puncture complications. To the best of our knowledge, little investigation has been reported on using MR to measure the near-zero temperatures induced around the ice-ball. As long as the tissue contains liquid water, the Proton Resonance Frequency Shift (PRFS)



**1** Experimental setup for the two test-case scenarios performed in this study. **(1A)** Pre-frozen ex vivo muscle was defrosted inside a large water bath set at room temperature, acting as a thermostat at  $20^\circ\text{C}$ . The shown image corresponds to a magnitude GRE coronal slice. **(1B)**. An MR-compatible cryogenic probe (4 mm diameter) was used to induce an ice-ball formation in ex vivo liver, initially set at room temperature ( $20^\circ\text{C}$ ). Three orthogonal planes (T1w VIBE acquisition) are illustrated, with shown FOV 15 cm in each frame. Note the apparent size of the cryogenic probe is practically equal to its physical dimension, as seen at current resolution.

method should be applicable. PRFS MR thermometry is currently the preferred method for on-line monitoring of thermal therapy, due to its linear calibration and tissue-type independence [13] (excepting the adipose tissue). Nevertheless, the susceptibility contrast between frozen and unfrozen tissue disturbs the local magnetic field proximal to the ice-ball. This effect is time-dependent as the volume of the ice-ball varies during the procedure and yields temperature estimation errors when using the conventional PRFS method. In particular, the measured values of temperature may be under- or overestimated around the ice-ball depending on the relative orientation from the magnetic field and on the shape of the ice-ball. This study demonstrates a time-effective 3D correction of gradient-recalled (GRE) phase shift around an ice-ball that is due to the susceptibility contrast between frozen and non-frozen tissue. This correction is necessary in order to deliver accurate temperature maps in tissue proximal to the ice-ball using the PRFS method. The study was published first in Magnetic Resonance Materials in Physics, Biology and Medicine [14].

## Material and methods

### Theory

This section summarises the underlying physical model for a time-effective correction of the GRE phase shift induced around the ice-ball during cryotherapy [15]. For more details please see [14]. It must be considered that the magnetic field at one point of an object is the summation of the magnetic contributions of bulk susceptibility ( $\chi$ ) from all other points of the object. For convenience, the vacuum permittivity is set to 1. According to fundamental physics, if there are no circulating currents within a region of matter, the magnetic field strength ( $\vec{H}$ ) in the object can be described as an irrotational field, which means that a magnetic potential ( $\Phi$ ) as a scalar field exists:

$$\vec{H} = -\nabla\Phi \text{ with } \nabla = \left( \frac{\partial}{\partial x}, \frac{\partial}{\partial y}, \frac{\partial}{\partial z} \right) \quad (1)$$

As known from Maxwell's equations, the divergence operator of the magnetic

induction is always zero. Furthermore, magnetic induction and magnetic field strength are related by  $\vec{B} = (1 + \chi)\vec{H}$ . Combining this knowledge enables a relation to be established between the scalar potential and the magnetic susceptibility:

$$\nabla\chi\nabla\Phi + (1 + \chi)\nabla^2\Phi = 0 \quad (2)$$

This magnetic scalar potential can be expressed as a linear summation:

$$\Phi = \Phi_0 + \Phi_{in} + \Phi_{obj} \quad (3)$$

where  $\Phi_0 = -H_0 z$  represents the ideal field of the magnet (i.e.  $\vec{H}_0 = (0, 0, H_0)$  is a uniform field),  $\Phi_{in}$  represents the intrinsic inhomogeneities of the magnet field (including shimming), and  $\Phi_{obj}$  represents the inhomogeneities induced by the object itself.

Neglecting all terms and variables smaller than  $10^{-5}$  and mention that  $\nabla^2\Phi_{in} = 0$  (source-free field in the region of interest) equation (2) and (3) can be combined and simplified to:

$$\nabla^2\Phi_{obj} = H_0 \frac{\partial\chi}{\partial z} \quad (4)$$

If the spatial dependence of  $\chi$  is known, the magnetic induction observed by one NMR nucleus which has an electronic screening coefficient  $\sigma$  can be described as [15]:

$$B_{nuc} \cong \left(1 - \sigma + \frac{1}{3}\chi\right) H_0 + h_{in,z} + h_{obj,z} \quad (5)$$

Using equation (5) and the Fourier Transformation (FT) of partial-derivative operators, equation (4) can be written as:

$$FT(\Phi_{obj}) = -iH_0 \frac{k_z}{k^2} FT(\chi) \quad (6)$$

With  $k^2 = k_x^2 + k_y^2 + k_z^2$  the squared norm of the inverse space distance, the non-thermal phase shift in the complex GRE image due to the time-dependent susceptibility changes between the time points  $t_0$  and  $t$  can be written as:

$$\Delta\varphi_{susc}(t) \cong \gamma \times H_0 \times T_E \times FT^{-1} \left[ \left( \frac{1}{3} - \frac{k_z^2}{k^2} \right) FT[\chi(t) - \chi(t_0)] \right] \quad (7)$$

using standard symbols ( $^1\text{H } \gamma = 42.58 \text{ MHz/T}$ ,  $T_E = \text{echo time}$ ). Further on the susceptibility contrast between frozen and unfrozen (or defrosted) tissue is defined as a constant value, denoted here  $\Delta\chi_{ice}$ , and the shape of the ice-ball

as a 3D binary function with  $S(\vec{r}, t) = 1$  within the ice ball and  $S(\vec{r}, t) = 0$  outside the ice ball.

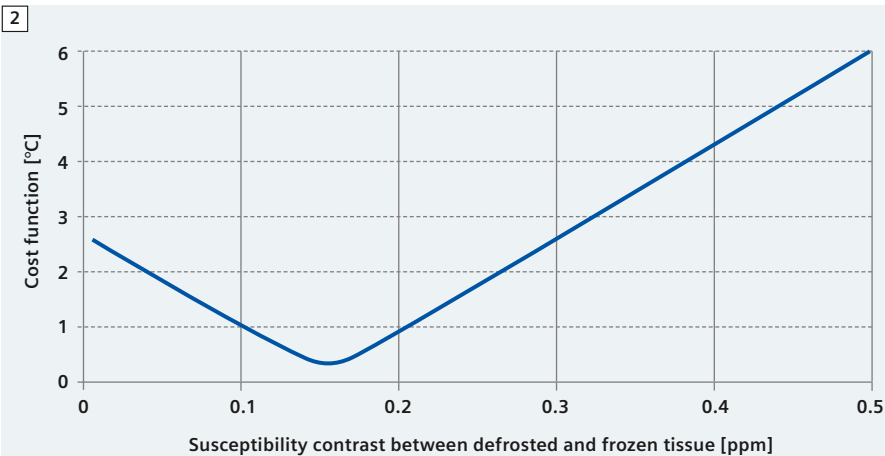
Assuming the value of the susceptibility contrast  $\Delta\chi_{ice}$  is known together with the 3D shape function of the ice-ball at each time-point  $S(t)$ , the master equation for the correction of the PRFS temperature maps (relative temperature changes) in tissue proximal to the ice-ball is:

$$\begin{aligned} \Delta T_{corr}(t) &= \Delta T_{PRFS}(t) + \frac{\Delta\chi_{ice}}{|\alpha|} \times FT^{-1} \\ &\quad \left[ \left( \frac{1}{3} - \frac{k_z^2}{k^2} \right) FT[\Delta S(t)] \right] \\ \text{with } \Delta T_{PRFS}(t) &= \frac{\varphi(t) - \varphi(t_0)}{\Delta \times \gamma \times B_0 \times TE} \quad (8) \end{aligned}$$

where the PRFS temperature coefficient is  $\alpha = -0.0094 \text{ ppm/}^\circ\text{C}$  [13], the average susceptibility contrast between the ice-ball and the tissue is expressed in *ppm* and  $\varphi(t)$  is the actual phase map acquired at time point  $t$ .

### Experimental setup

Experiments were performed at a 1.5T MR-system (MAGNETOM Avanto, Siemens Healthcare, Erlangen, Germany) on ex vivo pork liver. A home-made MR-compatible cryogenic probe was used in order to demonstrate the performance of the correction method, while using an interventional device [14]. High resolution 3D GRE T1-w images VIBE [16] were acquired as preliminary data (Fig. 1), with the following parameters: TE 1.6 ms, TR 4 ms, TA 2.55 min, FA 10°, BW 650 Hz/pixel and spatial resolution of  $1.2 \times 1.2 \times 1.2 \text{ mm}^3$ , and were used for positioning a stack of 25 adjacent slices of MR thermometry (a similar GRE sequence was used as above, modified to a rectangular FOV = 75%, slice thickness 2.4 mm, TR 27.6 ms, TE 20 ms, FA 25°, BW 230 Hz/pixel, GRAPPA 1, temporal resolution 49.6 s and using a single loop coil of 11 cm diameter). The active cryogenic interval corresponded to the circulation of ethanol into the probe, for 20 minutes under MRI monitoring. The MRI acquisition was performed for a further 15 minutes after the peristaltic pump was stopped in order to monitor the initial interval of the return to thermal equilibrium in the tissue.



**2** Illustration of the evolution of the cost function in the correction model over the range of explored susceptibility contrast between defrosted and frozen tissue.

A standard baseline correction for the  $B_0$  drift was implemented using the GRE phase from a 36 pixel-sized region-of-interest (ROI), selected far from the state transition interface.

### Data processing

PRFS thermometry data was corrected off line in this study. To correct for the susceptibility-induced GRE phase shift proximal to the ice-ball, the susceptibility difference between frozen and unfrozen/defrosted tissue has to be determined. The underlying physical hypothesis is that the frontier of the ice-ball has the state transition temperature, uniform at every point of the surface. First, the ice-ball is segmented using a semi-automatic region growing algorithm [17]. That is, the experimental estimation of the shape function  $S(\vec{r}, t)$  is obtained for each measurement. The second step is to determine the average susceptibility difference between the ice-ball and proximal tissue ( $\Delta\chi_{ice}$ ). For this purpose, a cost function ( $F$ ) was defined as the standard deviation (SD) of the series of corrected temperature values, taken from the ice-ball frontier in the central slice that is defined as the slice of maximum cross section through the ice ball.

The third and last step consisted in applying equation (8) for correcting the PRFS temperature maps using the value  $\Delta\chi_{ice}$  determined above. The main steps

of the algorithm are highlighted in Figure 3.

### Results

No MR-signal was obtained within the ice-ball using a TE of 20 ms at 1.5T and therefore no temperature information was available in that region, whereas the semi-automatic segmentation algorithm always performed robustly. Total computing time for correcting one 3D measurement was less than 1s in Matlab<sup>®</sup>.

The susceptibility contrast between non-frozen and frozen *ex vivo* tissue was found to be 0.161 ppm for a best-corrected temperature uncertainty of 0.3°C in pork liver (Fig. 2).

The home-made cryogenic probe showed excellent MR compatibility, the size of the signal void region in a plane orthogonal to the copper cylinder was practically equal to the physical diameter of the cylinder, within the available resolution of the T1-weighted MR images. The induced ice-ball at the end of the cryogenic procedure had the shape of an elongated ellipsoid of diameter 1.2 cm and height 4 cm.

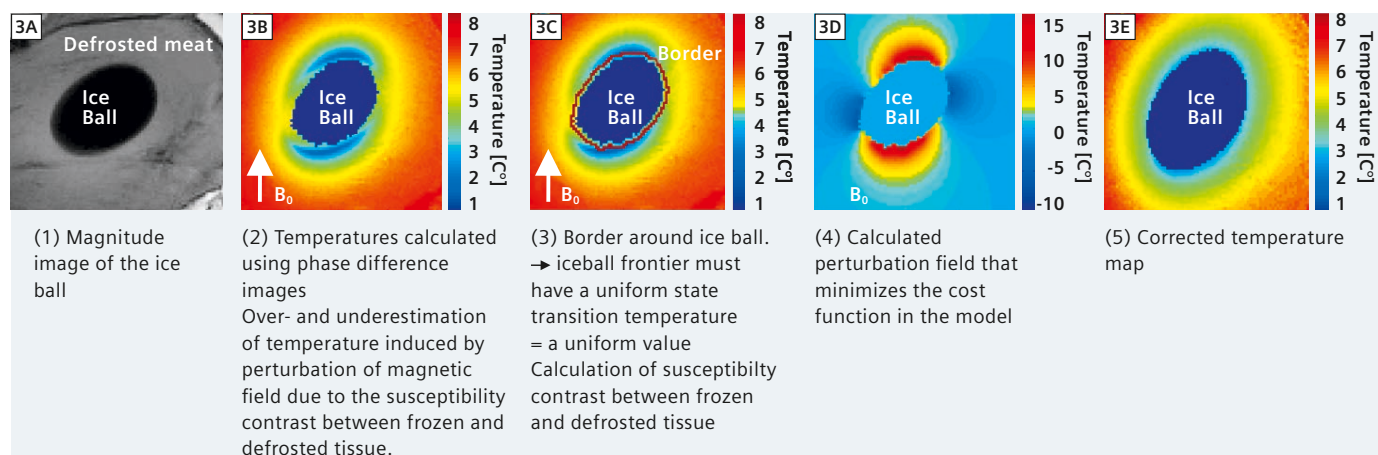
Figure 4 illustrates the performance of the temperature correction method for the cryogenic probe setup. Note, after correction, the temperature values in the tissue layer at the frontier of the ice-ball are uniform and correctly measured at around 0°C. In particular, the

corrected temperature curves considered at two different locations, defined at the same distance from the cryogenic probe but having different position vectors with respect to the  $B_0$  direction, show similar behaviour, as theoretically predicted. The border condition at the margins of the tissue sample was set to 20°C, measured from thermometer data acquired immediately before and after the cryogenic procedure. Without correction, the ice-ball frontier temperature was over- or under-estimated by the conventional PRFS method by  $\pm 10^\circ\text{C}$ .

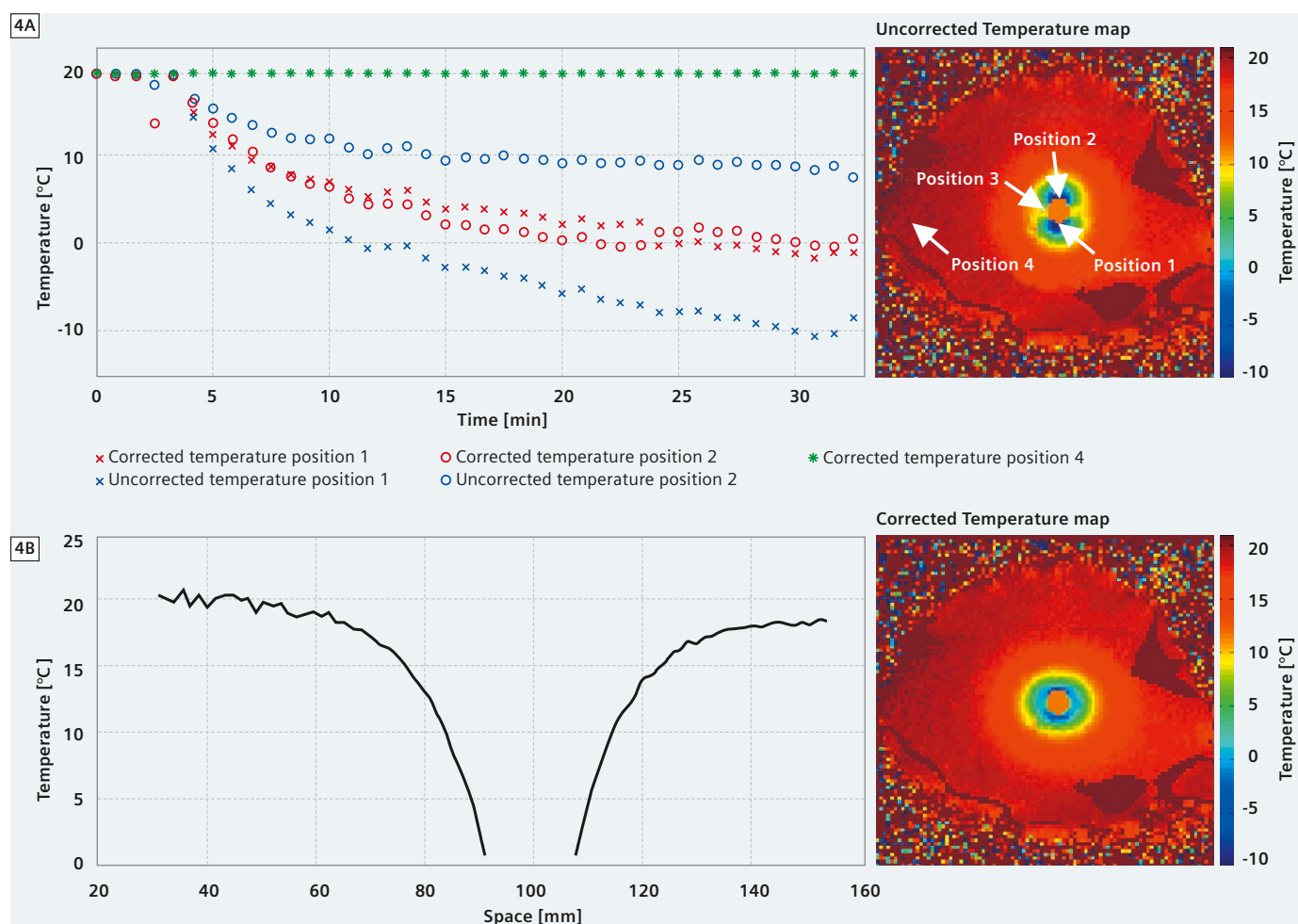
### Discussion

Inducing an ice-ball to treat tumors requires temperature monitoring to protect healthy surrounding tissue, particularly at-risk structures adjacent to the target tissue/organ. Non-freezing cold injuries (NFCI) were documented mainly in the context of accidental casualties. The proposed mechanisms of NFCI include direct axonal damage, ischaemia and ischaemia/reperfusion [18]. Cold immersion (1–2°C) results [18] showed that large myelinated fibres were preferentially damaged, while small myelinated and unmyelinated fibres were relatively spared. The formation of oxygen derived free radicals, which are implicated in ischaemia/reperfusion injuries, have been demonstrated during re-warming of a rabbit hind limb, cooled to 0°C for 20 min [19]. Vasoconstriction, endothelial injury and thromboembolism contribute to vascular insufficiency and ischemia. Thromboembolism, from stasis and endothelial injury, may also be triggered by hemoconcentration and hyperviscosity [20]. The series of enzymatic reactions of the coagulation cascade are strongly inhibited by hypothermia below 28°C [21] that can cause or aggravate bleeding.

The placement of secondary temperature probes into 'structures at risk' proximal to the cryo-ablation site is performed routinely. Not only can the placement of these temperature probes be difficult and time consuming, but they can damage the structures they are trying to protect. Temperature mapping outside of the ice ball would allow for



**3** Workflow of the correction algorithm for the PRFS thermometry in tissue proximal to the ice-ball.



**4** Overview of the experimental results and correction of PRFS thermometry in ex vivo tissue when cryogenic ice-ball was induced by an MR-compatible probe. **(4A)** PRFS temperature maps in a coronal mid-plane through the ice-ball: susceptibility-corrected (left) and phase-subtraction conventional PRFS (right). **(4B)** Plot of the measured temperatures over time in the three positions visualized in frame a). **(4C)** Illustration of the spatial profile of susceptibility-corrected temperature through the centre of the ice-ball (comprising the positions 2 and 3 from above).

non-invasive monitoring of these structures and allow the operator to moderate the ice-ball if a precipitous temperature drop is seen. However, using the phase-subtraction only PRFS method for temperature monitoring in the proximity of frozen tissue results in over- or underestimated values in the typical error range of  $\pm 10^{\circ}\text{C}$ , depending on the ice-ball size/shape and also on the imaging slice orientation.

This range of under- or over-estimation of tissue temperature with conventional PRFS MRT compromises the potential benefit of on-line monitoring of the temperature distribution. To recover accurate temperature maps, our study proposes and validates a numerical algorithm, performed in less than 1 second on a standard CPU, to correct in 3D for the susceptibility-induced GRE phase shift proximal to a cryotherapy ice-ball. Overall, the method described here enables the user to monitor accurately the temperature in the vicinity of an ice-ball, particularly when at-risk structures are adjacent to the target tissue. The method described for the susceptibility artifact correction is based on the fundamental property of isothermal state transition of tissue and allows the PRFS temperature correction without the placement of any probes, which is time consuming and potentially prone to complications.

In contrast to the method described in reference [11] to estimate temperatures inside the ice-ball itself, our aim was to monitor the temperature in regions external and proximal to the ice-ball and therefore to provide a safety tool to enable the physician to avoid collateral damage in surrounding organs or structures of risk.

Finally, the actual correction method does not address motion-related artifacts if any (for instance, concerning liver cryotherapy). Therefore a prerequisite condition here is a motion-robust GRE phase acquisition, prior to applying the susceptibility correction. Coupling motion-correction and susceptibility-correction methods simultaneously is beyond the purpose of the present study and requires further investigations.

## Conclusion

This study demonstrates a time-effective stand-alone method for correcting susceptibility artifacts near an ice-ball induced by the susceptibility contrast between frozen and non-frozen tissue. The post processing method examined provides a fast algorithm requiring only one simple user interaction. It allows the non-invasive and accurate monitoring of near zero temperatures in at risk tissues adjacent to the target lesion using the PRFS method.

### References

- Seifert JK, Morris DL World Survey on the Complications of Hepatic and Prostate Cryotherapy. *World Journal of Surgery*. Volume 23, Number 2, 109-114.
- Wansapura JP, Daniel BL, Vigen KK, Butts K (2005) In vivo MR thermometry of frozen tissue using  $R2^*$  and signal intensity. *Acad Radiol* 12:1080-1084.
- Lu A, Daniel BL, Pauly JM, Butts Pauly K (2008) Improved slice selection for  $R2^*$  mapping during cryoablation with eddy current compensation. *J Magn Reson Imag* 28:190-198.
- Morrison PR, Silverman SG, Tuncali K, Tatli S (2008) MRI-guided cryotherapy. *J Magn Reson Imaging* 27:410-420.
- Matsumoto R, Oshio K, Jolesz FA (1992) Monitoring of laser and freezing induced ablation in the liver with T1-weighted MR imaging. *J Magn Reson Imaging* 2:555-562.
- Shingleton WB, Sewall PE (2001) Percutaneous renal tumor cryoablation with magnetic resonance imaging guidance. *J Urol* 165:773-776.
- Tacke J, Adam G, Haage P, Sellhaus B, Gunther RW (2001) MR-guided percutaneous cryotherapy of the liver: in vivo evaluation with histologic correlation in an animal model. *J Magn Reson Imaging* 13:50-56.
- Gilbert JC, Rubinsky B, Roos MS, Wong STS, Brennan KM (1993) MRImonitored cryosurgery in the rabbit brain. *Magn Reson Imaging* 11:1155-1164.
- Rubinsky B, Gilbert JC, Onik GM, Roos MS, Wong STS, Brennan KM (1993) Monitoring cryosurgery in the brain and in the prostate with proton NMR. *Cryobiology* 30:191-199.
- Kaye EA, Josan S, Lu A, Rosenberg J, Daniel BL, Butts Pauly K (2010) Consistency of Signal Intensity and  $T2^*$  in Frozen Ex Vivo Heart Muscle, Kidney and Liver Tissue. *J Magn Reson Imaging* 31(3): 719-724.
- Butts K, Sinclair J, Daniel BL, Wansapura J, Pauly JM (2001) Temperature quantization and mapping of frozen tissue. *J Magn Reson Imaging* 13:99-104.
- Wansapura JP, Daniel BL, Vigen KK, Butts K (2005) In vivo thermometry of frozen tissue using  $R2^*$  and signal intensity. *Acad Radiol* 12:1080-1084.
- Rieke V, Butts Pauly K (2008) MR thermometry. *J Magn Reson Imaging* 27:376-90
- Kickhefel A, Weiss C, Roland J, Gross P, Schick F, Salomir R. (2012) Correction of susceptibility-induced GRE phase shift for accurate PRFS thermometry proximal to cryoablation iceball. *Magnetic Resonance Materials in Physics, Biology and Medicine*: 25:1:23-31.
- Salomir R, De Senneville BD, Moonen CTW (2003) A Fast Calculation Method for Magnetic Field Inhomogeneity due to an Arbitrary Distribution of Bulk Susceptibility. *Concepts Magn Reson Part B (Magn Reson Engineering)* 19B: 26-34.
- Rofsky NM, Lee VS, Laub G, Pollack MA, Krinsky GA, Thomasson D, Ambrosino MM, Weinreb JC (1999) Abdominal MR imaging with a volumetric interpolated breath-hold examination. *Radiology* 212:876-884.
- Dirk-Jan Kroon. <http://www.mathworks.com/matlabcentral/fileexchange/19084>.
- Irwin MS (1996). Nature and mechanism of peripheral nerve damage in an experimental model of non-freezing cold injury. *Ann R Coll Surg Engl*. 78(4): 372-379.
- Kennett RP, Gilliatt RW (1991). Nerve conduction studies in experimental non-freezing cold injury: II. Generalized nerve cooling by limb immersion. *Muscle Nerve* 14:960-67.
- Biem J, Koehncke N, Classen D, Dosman J (2003). Out of the cold: management of hypothermia and frostbite. *Canadian Med Assoc J*. 168(3): 305-311.
- Rohrer MJ, Natale AM (1992). Effect of hypothermia on the coagulation cascade. *Crit Care Med*. 1992 Oct;20(10):1402-5.

### Contact

Antje Kickhefel, Ph.D.  
Siemens Healthcare  
IM MR R&D CCC AIQ  
Erlangen  
Germany  
[antje.kickhefel@siemens.com](mailto:antje.kickhefel@siemens.com)

*We are looking forward to hearing from you.*

[www.siemens.com/flash-survey](http://www.siemens.com/flash-survey)



Please take a moment to complete a brief reader survey.

Your feedback will help us to produce a high-quality publication that matches your needs and serves as a resource for achieving your clinical, operational and financial goals. We value your feedback.

MAGNETOM Flash – Imprint  
© 2013 by Siemens AG, Berlin and Munich,  
All Rights Reserved

**Publisher:**

**Siemens AG**  
Medical Solutions  
Business Unit Magnetic Resonance,  
Karl-Schall-Straße 6, D-91052 Erlangen,  
Germany

Editor-in-Chief: Milind Dhamankar, M.D.

Associate Editor: Antje Hellwich  
([antje.hellwich@siemens.com](mailto:antje.hellwich@siemens.com))

Editorial Board: Wellesley Were;  
Ralph Strecker; Sven Zühlsdorff, Ph.D.;  
Gary R. McNeal, MS (BME);  
Peter Kreisler, Ph.D.,

Production: Norbert Moser, Siemens AG,  
Medical Solutions

Layout: independent Medien-Design  
Widenmayerstrasse 16, D-80538 Munich

Printer: G. Peschke Druckerei GmbH,  
Schatzbogen 35, D-81829 Munich, Germany

German Federal Data Protection Law: Despatch is made using an address file which is maintained with the aid of an automated data processing system.

MAGNETOM Flash with a total circulation of 35,000 copies is sent free of charge to Siemens MR customers, qualified physicians, technologists, physicists and radiology departments throughout the world. It includes reports in the English language on magnetic resonance: diagnostic and therapeutic methods and their application as well as results and experience gained with corresponding systems and solutions. It introduces from case to case new principles and procedures and discusses their clinical potential.

The statements and views of the authors in the individual contributions do not necessarily reflect the opinion of the publisher.

The information presented in these articles and case reports is for illustration only and is not intended to be relied upon by the reader for instruction as to the practice of medicine. Any health care practitioner reading this information is reminded that they must use their own learning, training and expertise in dealing with their individual patients. This material does not substitute for that duty and is not intended by Siemens Medical Solutions to be used for any purpose in that regard. The drugs and doses mentioned herein are consistent with the approval labeling

for uses and/or indications of the drug. The treating physician bears the sole responsibility for the diagnosis and treatment of patients, including drugs and doses prescribed in connection with such use. The Operating Instructions must always be strictly followed when operating the MR system. The sources for the technical data are the corresponding data sheets. Results may vary. Partial reproduction in printed form of individual contributions is permitted, provided the customary bibliographical data such as author's name and title of the contribution as well as year, issue number and pages of MAGNETOM Flash are named, but the editors request that two copies be sent to them. The written consent of the authors and publisher is required for the complete reprinting of an article.

We welcome your questions and comments about the editorial content of MAGNETOM Flash. Please contact us at [magnetomworld.med@siemens.com](mailto:magnetomworld.med@siemens.com). Manuscripts as well as suggestions, proposals and information are always welcome; they are carefully examined and submitted to the editorial board for attention. MAGNETOM Flash is not responsible for loss, damage, or any other injury to unsolicited manuscripts or other materials. We reserve the right to edit for clarity, accuracy, and space. Include your name, address, and phone number and send to the editors, address above.

**MAGNETOM Flash is also available  
on the internet:**

[www.siemens.com/magnetom-world](http://www.siemens.com/magnetom-world)

# MAGNETOM Flash

The Magazine of MRI

Issue Number 2/2013  
ISMRM Edition  
Not for distribution in the USA

SIEMENS

## Clinical

Advanced Techniques  
in MR Neuroimaging  
Page 6

Neuroimaging of Stroke  
Page 36

Improved EPI DWI of  
the Head and Neck  
using syngo ZOOMit  
Page 68

Combining Throughput  
and Highest Quality  
MRI in an Optimized  
Clinical Workflow  
Page 82

Indications for 24 Hours /  
7 Days Emergency MRI  
Page 128

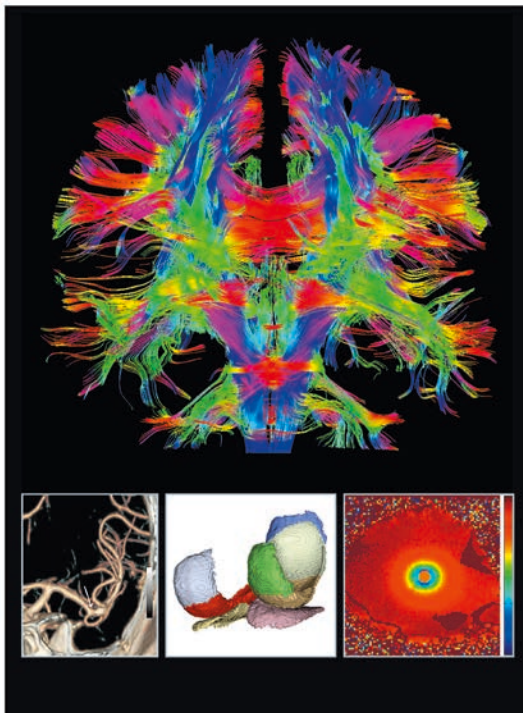
Automated Morphological  
Knee Cartilage Analysis  
of 3D MRI at 3T  
Page 146

## Product News

The New MR Gradient  
System XR 80/200  
Page 160

## Technology

PRFS Thermometry  
Proximal to  
Cryoablation Ice-ball  
Page 164



Please enter your business address

Institution

Department

Function

Title

Name

Street

Postal Code

City

State

Country

MR system used

Please include me in your mailing list for the  
following Siemens Healthcare customer magazine(s):

☐ Medical Solutions

☐ MAGNETOM Flash

☐ SOMATOM Sessions

☐ AXIOM Innovations

Stay up to date with the latest information  
Register for:

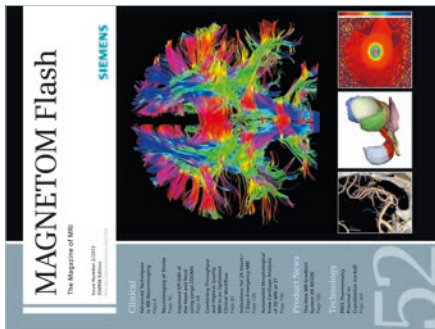
E-mail

☐ Yes, I consent to the above information being used  
for future contact regarding product updates and other  
important news from Siemens.

☐ unsubscribe from info service

Please print clearly!

# MAGNETOM Flash



Siemens AG  
Medical Solutions  
Magnetic Resonance  
Antje Hellwich – Marketing  
P.O. Box 32 60  
D-91050 Erlangen  
Germany



→ Visit [www.siemens.com/magnetom-world](http://www.siemens.com/magnetom-world) for case reports, clinical methods, application tips, talks and much more clinical information.

[www.siemens.com/flash-survey](http://www.siemens.com/flash-survey)  
Please take a moment to give us feedback.

SUBSCRIBE NOW!

– and get your free copy of future  
MAGNETOM Flash! Interesting information from  
the world of magnetic resonance – gratis to your  
desk. Send us this postcard, or subscribe online at  
[www.siemens.com/MAGNETOM-World](http://www.siemens.com/MAGNETOM-World)

## Global Siemens Headquarters

Siemens AG  
Wittelsbacherplatz 2  
80333 Muenchen  
Germany

## Global Siemens Healthcare Headquarters

Siemens AG  
Healthcare Sector  
Henkestrasse 127  
91052 Erlangen  
Germany  
Phone: +49 9131 84-0  
[www.siemens.com/healthcare](http://www.siemens.com/healthcare)

[www.siemens.com/healthcare-magazine](http://www.siemens.com/healthcare-magazine)

Order No. A91MR-1000-99C-7600 | Printed in Germany | CC 1089 041320. | © 04.13, Siemens AG

On account of certain regional limitations of sales rights and service availability, we cannot guarantee that all products included in this brochure are available through the Siemens sales organization worldwide. Availability and packaging may vary by country and is subject to change without prior notice. Some/All of the features and products described herein may not be available in the United States.

The information in this document contains general technical descriptions of specifications and options as well as standard and optional features which do not always have to be present in individual cases.

Siemens reserves the right to modify the design, packaging, specifications and options described herein without prior notice. Please contact your local Siemens sales representative for the most current information.

Note: Any technical data contained in this document may vary within defined tolerances. Original images always lose a certain amount of detail when reproduced.

## Global Business Unit

Siemens AG  
Medical Solutions  
Magnetic Resonance  
Henkestr. 127  
DE-91052 Erlangen  
Germany  
Phone: +49 9131 84-0  
[www.siemens.com/healthcare](http://www.siemens.com/healthcare)

## Local Contact Information

### Asia

Siemens Pte Ltd  
The Siemens Center  
60 MacPherson Road  
Singapore 348615  
Phone: +65 6490-8096

### Canada

Siemens Canada Limited  
Medical Solutions  
2185 Derry Road West  
Mississauga ON L5N 7A6  
Canada  
Phone: +1 905 819-5800

### Europe/Africa/Middle East

Siemens AG  
Medical Solutions  
Henkestr. 127  
91052 Erlangen  
Germany  
Phone: +49 9131 84-0

### Latin America

Siemens S.A.  
Medical Solutions  
Avenida de Pte. Julio A. Roca No 516,  
Piso 7  
C1067ABN Buenos Aires  
Argentina  
Phone: +54 11 4340-8400

### USA

Siemens Medical Solutions U.S.A., Inc.  
51 Valley Stream Parkway  
Malvern, PA 19355-1406  
USA  
Phone: +1-888-826-9702